Republic of Iraq
Ministry of Higher Education &Scientific Research
University of Baghdad
College of Education for Pure Science (Ibn Al–Haitham)
Chemistry Department

Metal Complexes Derived From Bidentate Ligands (N,Se); Synthesis, Spectral Characterisation And Biological Activity

A Thesis

Submitted to the Council of College of
Education for Pure Science (Ibn AL–Haitham)
University of Baghdad in Partial Fulfillment of
the Requirements for the Degree of Doctor of Philosophy (Ph.D.) in Chemistry

By

Talib Hamid Mawat

B.Sc. in Chemistry (2013)
M.Sc. in Chemistry (2016)
College of Education for Pure Science (Ibn AL–Haitham)
University of Baghdad

Supervisor

Prof. Dr. Mohamad J. Al-Jeboori

2019 AC   **1441 AH**

بَسْمِ اللهِ الرَّحْمنِ الرَّحِيمِ

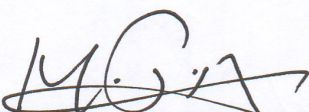{ قَالُوا سُبْحَانَكَ لَا عِلْمَ لَنَا إِلَّا مَا عَلَّمْتَنَا

إِنَّكَ أَنْتَ الْعَلِيمُ الْحَكِيمُ }

صَدَقَ اللهُ العَلُّي العَظِيم

(سورة البقرة/ الآية 32)

Certification

I certify that, this thesis was prepared under my supervision at Department of Chemistry, College of Education for Pure Science (Ibn-Al-Haitham)/ University of Baghdad in partial requirements for the Degree of Doctor of Philosophy in Inorganic Chemistry, and this work has never been submitted or published anywhere else.
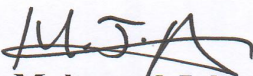
Signature

Name: **Dr. Mohamad Jaber Al-Jeboori** (Supervisor)

Title: Professor

Address: Department of Chemistry, College of Education for Pure Science /Ibn-Al-Haitham University of Baghdad, Iraq.

Date:21/11/2019

In the view of the available recommendation, I forward this thesis for debate by the Examination Committee.

Signature

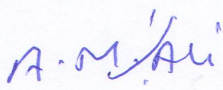Name: **Dr. Mohamad Jaber Al-Jeboori**

Title: Professor

Address: Head of Department of Chemistry, College of Education for Pure Science/(Ibn-Al-Haitham) University of Baghdad, Iraq.

Date:21/11/2019

Examination Committee

We, the examination committee, after reading this thesis and examining the student **Talib Hamid Mawat** in its content. We have found it worthy to be accepted for the degree of Doctor of Philosophy in Inorganic Chemistry with (*Excellent grade*).
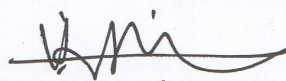
Signature:
Name: **Dr. Abid Allah M. Ali**
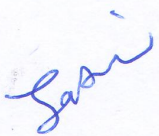Title: Professor
Date: 20/11/2019
Chairman

Signature:
Name: **Dr. Hasan A. Hasan**
Title: Professor
Date: 21/11/2019
Member

Signature:
Name: **Dr. Jasim M. Salih**
Title: Assistant Professor
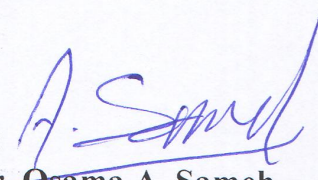Date: 20/11/2019
Member

Signature:
Name: **Dr. Aeed S. Mohammed**
Title: Assistant Professor
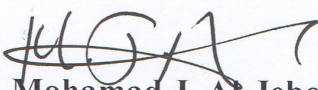Date: 20/11/2019
Member

Signature:
Name: **Dr. Osama A. Sameh**
Title: Assistant Professor
Date: 20/11/2019
Member

Signature:
Name: **Dr. Mohamad J. Al-Jeboori**
Title: Professor
Date: 21/11/2019
(Supervisor)

Approved for the College Committee of Graduate Studies

Signature:
Name: **Dr. Firas Abdulhameed Abdullatif**
Scientific Degree: Assistant Professor
Date: 29/11/2019
Address: Behalf/The Dean of the College of Education for Pure Science-Ibn-Al-Haitham /University of Baghdad

Dedication

To my darling… father who I have lost
him since I was child

To my life…..mother

To my brothers and sisters
With love

Talib
2019

Acknowledgments

Summary

This thesis is based on the synthesis, spectral characterisation, thermal investigation and biological activity of six novel selenosemicarbazone ligands, which derived from Mannich reaction, and their metal complexes. The aim of using selenosemicarbazone compounds is based on the role and applications of Se-based compounds in inorganic chemistry, medicine, pharmaceutical industry, analytical chemistry and biological activity. Further checking on reported data in literature, there is a limited published work on this type of ligands and their complexes Therefore, this fact encouraged us to investigate such compounds and to the best of our knowledge this is the first thesis in Iraq dealing with the synthesis of selenosemicarbazone ligands and their complexes. This thesis consists of four chapters in which;

The first chapter gives an introduction on Mannich-reaction approach and a literature review covering the development of the formation of metal complexes with N, Se coordination core. These include macrocyclic and non-macrocyclic ligands with their metal complexes. Moreover, applications and uses these compounds with their references were mentioned in the introduction along with the aim of the work.

The second chapter covers the experimental part that include materials used in this work, analytical techniques and synthetic procedures used to prepare organic precursors, selenosemicarbazone ligands and their metal complexes. Ligands were prepared in a multi synthetic steps, which divided into a two set depending on type of precursor that used in the formation of ligands. The first set of precursors F1, F2 and F3 were obtained using a one-pot Mannich-reaction. The condensation reaction of benzaldehyde, methoxybenzaldehyde and 4,4`-dimethylaminobenzaldehyde with cyclohexanone and ammonium acetate in a 2:1:1 mole ratio in EtOH medium resulted in the isolation of F1, F2 and F3, respectively. The second set of precursors is based on the preparation of N1, N2 and N3 adopting Mannich-approach by mixing calcium chloride and the title aldehyde and aromatic amine with cyclohexanone and in a 1:1:1:1 mole ratio in EtOH solvent (benzaldehyde and *m*-nitroaniline for N1; 4-methoxybenzaldehyde and aniline for N2, and N3 was prepared by analogous procedure to that for N1 but with the use of 4,4`-dimethylaminobenzaldehyde and *m*-nitroaniline for N3).

The six novel selenosemicarbazone ligands HL^1-HL^6 were synthesised from the reaction of the title precursor with KSeCN and NH$_2$NH$_2$ in a 1:1:3 mole ratio in a mixture of CHCl$_3$:EtOH (1:3) as a solvent. A total of thirty six complexes were synthesised from the reaction of ligands with metal chloride salts in a 2:1 L:M mole ratio, in presence of
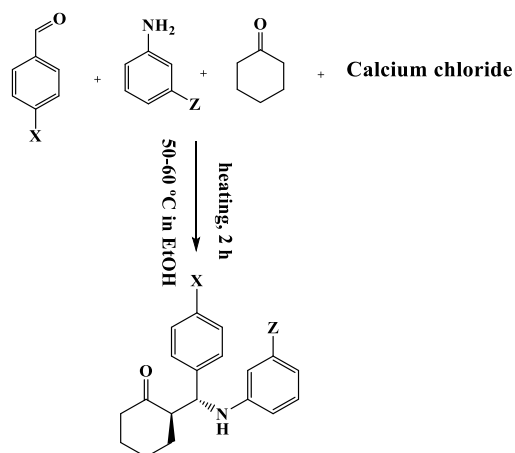
KOH as a base, using a mixture of chloroform/ethanol (1:3) as a reaction medium (see Scheme).

The third chapter (results and discussion) deals with presenting and discussion of the analytical and spectroscopic data that used to conclude the entity of precursors, selenosemicarbazone ligands and their metal complexes. These include the use of; elemental analysis (CHN), atomic absorption (A.A), thermal analysis, chloride ratio, conductance, melting point, FT-IR, UV-Vis, magnetic susceptibility, ^{1}H-, ^{13}C- and ^{77}Se-NMR and ESMS (electrospray mass spectra). The chemical shift of the ^{77}Se-NMR confirmed the incorporation of the Se-atom in the organic segment and the isolation of the selenosemicarbazone ligands and their metal complexes. Further, the presence of one signal in the spectral data of ligands and their diamagnetic complexes indicated the purity, the isolation of one isomer and that the two bound ligands of diamagnetic complexes are equivalents. The ESMS spectroscopic of precursors, ligands and some metals complexes confirmed molecular weight of synthesized compounds. The FT-IR spectra of the complexes of ligands HL^{1}-HL^{6} showed act as a bidentate and behaves as negative species (-1) upon coordination with metal ions. Thermal analysis of ligands HL^{1}-HL^{6} and some metals complexes indicated stability of these compounds in the different temperatures and fragmentations. UV-Vis spectra of complexes were used to predict the arrangement of the ligand around metal ion. The molar conductivity values of complexes were included non-electrolytes and electrolytes with 2:1 ratio. Theoretical approach was used to confirm the coordination mode and the preferred geometry arrangement around metal centre. This was based on using 3D Chem 16 program and checking data against that obtained from the analytical and chemical analysis of complexes.
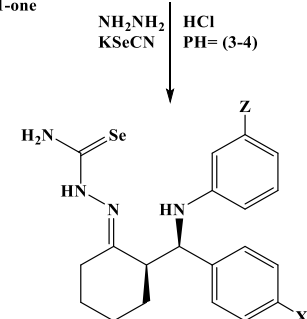
Based on the above analyses, the interaction behavior and mode of bonding and suggested structure of complexes is shown below:

Metal complexes of Mn(II), Co(II) and Ni(II) with HL^{1}-HL^{6} revealed six-coordinate arrangement in which the proposed geometry about metal centre is octahedral. Complexes of Cu(II); Zn(II) and Cd(II) with HL^{1}-HL^{6} revealed the isolation of four-coordinate complexes in which the proposed geometry is square planar and tetrahedral, respectively.
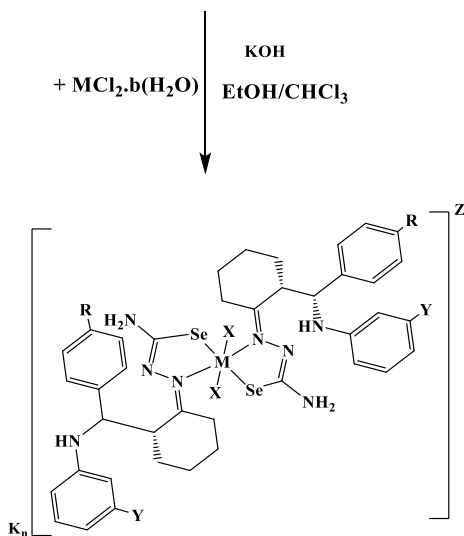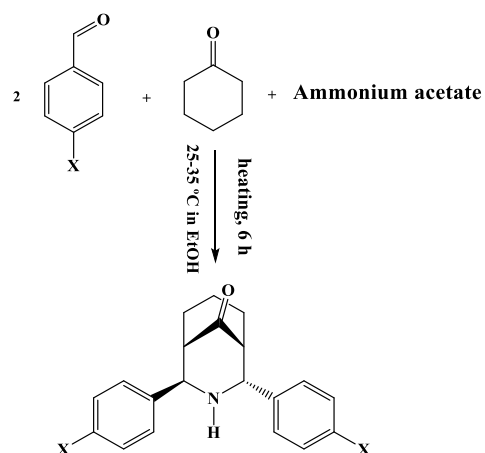
X = 0, Z = NO₂, N1 = 2-(((3-nitrophenyl)amino)(phenyl)methyl)cyclohexan-1-one
X = OMe, Z = 0, N2 = 2-((4-methoxyphenyl)(phenylamino)methyl)cyclohexan-1-one
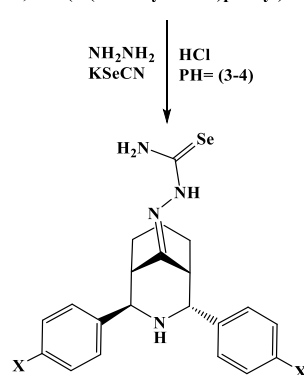X = N(Me)₂, Z = NO₂, N3 = 2-((4-(dimethylamino)phenyl)((3-nitrophenyl)amino)methyl)cyclohexan-1-one

X = 0, F1 = 2,4-diphenyl-3-azabicyclo[3.3.1]nonan-9-one
X = OMe, F2 = 2,4-bis(4-methoxyphenyl)-3-azabicyclo[3.3.1]nonan-9-one
X = N(Me)₂, F3 = 2,4-bis(4-(dimethylamino)phenyl)-3-azabicyclo[3.3.1]nonan-9-one

X = 0, Z = NO₂ (HL⁴)
X = OMe, Z = 0, (HL⁵)
X = N(Me)₂, Z = NO₂, (HL⁶)

X = 0, (HL¹)
X = OMe, (HL²)
X = N(Me)₂, (HL³)
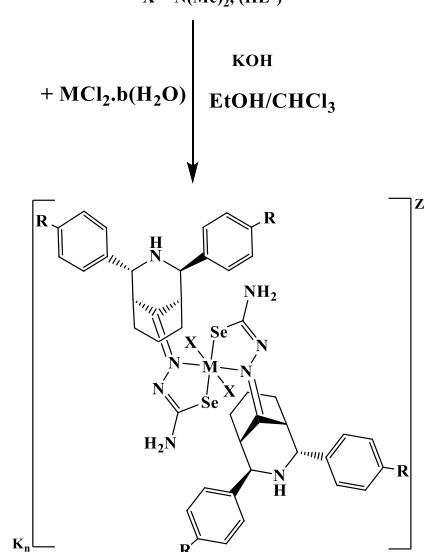
R= 0, Y= NO₂ = HL⁴; R= OCH₃, Y= 0 = HL⁵; R= N(CH₃)₂, Y= NO₂ = HL⁶
M= Mn(II), Co(II), Ni(II); n= 2; X= Cl; Z= -2
M= Cu(II), Zn(II), Cd(II); n= 0; X= 0; Z= 0
b= Number of water molecules

R= 0 = HL¹; R= OCH₃ = HL²; R= N(CH₃)₂ = HL³
M= Mn(II), Co(II), Ni(II); n= 2; X= Cl; Z= -2
M= Cu(II), Zn(II), Cd(II); n= 0; X= 0; Z= 0
b= Number of water molecules

Scheme: Synthetic pathway of HL¹-HL⁶ and metal complexes.

C

Biological activities of compounds (ligands and complexes) were tested toward four strains of bacteria (*E. coli, B. stubtilis*, *St. aureus* and *Klebsiella Pneumoniae*) and four species of fungi (*Candida albicans*, *Candida glabrata*, *Candida tropicalis* and *Candida parapsilsis*). The following trend is observed for the tested compounds;

- Ligands HL^1-HL^6 and their complexes displayed activity against *Esherichia Coli* and *Bacillus subtilis* strains.
- Complexes of Mn(II), Ni(II) and Cu(II) with HL^1 and HL^3 showed no activity against *Staphylococcus aureus* and *Klebsiella Pneumoniae strains*.
- Ligand HL^1 exhibited no activity against *Staphylococcus aureus* and *Klebsiella Pneumoniae strains*. More, HL^3 shows no antimicrobial activity against *Staphylococcus aureus strain*.
- Zinc complex with HL^6 showed the highest antimicrobial activity against *E. coli strain,* compared with other complexes.
- Complexes of zinc and cadmium with the examined ligands HL^1-HL^6 indicated to be more resistance towards tested species, due to their d^{10} configuration.
- Ligands HL^1-HL^6 and their metal complexes showed activity against *Candida glabrata*.
- Ligands HL^1-HL^5 displayed no activity against *Candida parapsilsis*.
- All complexes of HL^1 exhibited no activity against *Candida parapsilsis*.
- Ligands HL^1-HL^3 did not show any activity against *Candida albican*s.
- Complexes of Ni(II) and Cd(II) with HL^1 and complex Cd(II) with HL^4 showed no activity against *Candida albican*s.
- Regarding the activity of tested compounds against *Candida tropicalis*, the following results are observed:
  - a- Complexes of Ni(II) and Cd(II) with HL^1 displayed no-activity.
  - b- Ligands HL^2 and HL^3 showed no-activity.
  - c- Complex of Ni(II) with HL^4 did not exhibit any activity.
  - d- Ligands HL^5 and HL^6 with their metal complexes exhibited higher activity in comparison with other compounds.

List of Contains

LIST OF CONTAINS

IV

List of Tables

List of Figures

List of Schemes

List of Abbreviation

	Abbreviation
ORTEP	Oak Ridge Thermal Ellipsoid Plot
FT-IR	Fourier Transform Infrared
UV-Vis	Ultraviolet-Visible Spectrophotometry
^{1}HNMR	Proton Nuclear Magnetic Resonance Spectroscopy
^{13}CNMR	Carbon(13) Nuclear Magnetic Resonance Spectroscopy
^{77}SeNMR	Selenium (77) Nuclear Magnetic Resonance Spectroscopy
FAB	Fast atom bombardment
MS	Mass spectroscopic
DFT	Density functional theory
HRMS	High resolution mass spectroscopic
ESMS	Electro spray mass spectroscopic
HIV	Human immunodeficiency virus
AIDS	acquired immunodeficiency syndrome
AAS	Atomic absorbance spectroscopic
DMSO	Dimethyl sulfoxide
DMF	N,N-Dimethylformamid
J	Coupling constant
Hz	Hertz
Eq	Equivalent
m.p	Melting point
M. Wt	Molecular Weight
ε_{max}	Molar absorptivity
ppm	Part per million
Δ	Chemical shift
X	Susceptibility
B.M	Bohr magneton
HOMO	Higher occupied molecular orbital
LUMO	Lower unoccupied molecular orbital
TGA	Thermal gravimetric analysis
DTG	Differential thermal gravimetric
DSC	Differential scanning calorimeter
MCF-7	Michigan Cancer Foundation-7
DU145	Prostate cancer cell line
HepG2	Hepatocellular carcinoma

CHAPTER ONE

INTRODUCTION

(1) Introduction

(1.1) General background

Seleno-compounds including seleno-heterocyclic and selenosemicarbzone Schiff-base compounds are an interesting species that inspired organic, inorganic and bioinorganic chemists. The incorporation of nitrogen and selenium atoms in the skeletons of these species allowed them to attract a range of researchers. This may relate to their potential applications in biological chemistry, materials science and biochemistry. The importance of selenosemicarbzone Schiff-base compounds are related to; (i) their ability to be isolated as stable compounds, (ii) be designed as chelating species to give complexes with transition and representative elements [1], and (iii) their role in medicine [2-4], biological system [5,6], coordination, environmental and industrial chemistry [7].

The formation of Mannich-bases is based on a three-component reaction (a primary or a secondary amine, an aldehyde and an enolized ketone). These compounds exhibit high stability and display a range of applications and uses. Selenium-based ligands, in particular selenosemicarbazone, and their complexes have applications in pharmacological activities and biological system, also compounds of selenosemicarbzone have convenient preparation mothed, low toxicity, stability and excellent reactivity [2].

(1.2) Mannich reaction

The Mannich-approach considered as an interesting reaction that plays a vital role in the development of inorganic, bioinorganic and organic chemistry. The one pot-approach is a method that used in this reaction by mixing three components; a ketone, an aldehyde and amine; the final product is β-amino-carbonyl, see Scheme (1-1). Further, compounds that prepared by Mannich reaction have the C-N bond that display applications in medicine, pharmacy and several fields [8-11].
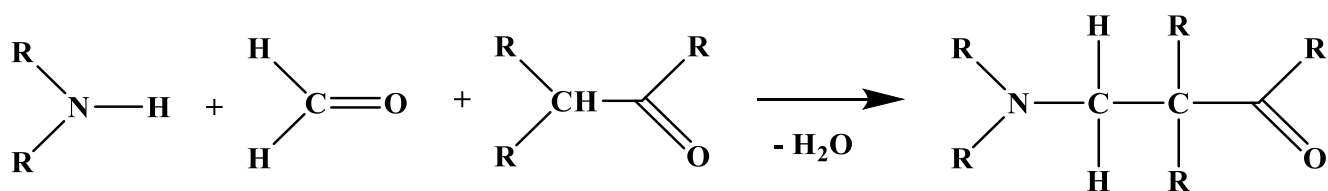
Scheme (1-1): General route for Mannich-base.

(1.3) Synthesis of selenosemicarbazone compounds

The preparation of a range of selenosemicarbazone ligands and their complexes was reported [12]. The addition of cyclohexanone to a mixture of hydrazine hydrate with KSeCN in ethanol gave a Schiff-base that used as an intermediate to prepare the title ligands. The treatment of the intermediate (Schiff-base) with salicylaldehyde selenosemicarbazone and its 1,2-naphthyl-derivative resulted in the isolation of H_2L1^{Se} and H_2L2^{Se}, respectively. The reaction of these ligands with Pd(II) and Pt(II) phosphine complexes gave selenosemicarbazone complexes of the general formula $[M(L^{Se})(P)]$, where M= Pt(II) and Pd(II). The chemical structure of the title compounds was confirmed through several spectroscopic and analytical techniques including X-ray single crystal diffraction. The molecular structure confirmed the isolation of four-coordinate complexes in which the geometry about the metal centre is square planar. Figure (1-1) represents the molecular structure of Pd(II)-complex.
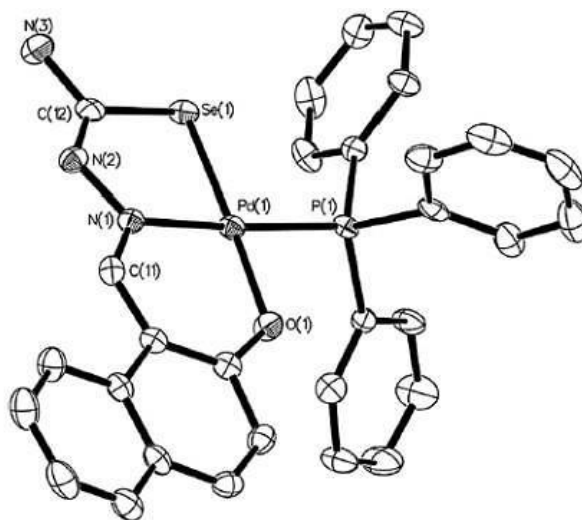
Figure (1-1): ORTEP diagram of $[Pd(L^1Se)(PPh_3)]$.

The Hantzsch-type condensation reaction was used in the preparation of a series of novel functionalised 1,3-selenazole derivatives derived from selenosemicarbazone compounds [2]. The preparation of compounds 6(a-d) and 5(a-d) are summarised in Scheme (1-2). The FTIR, NMR, mass spectroscopy and elemental analysis data were used to confirm the entity of compounds.
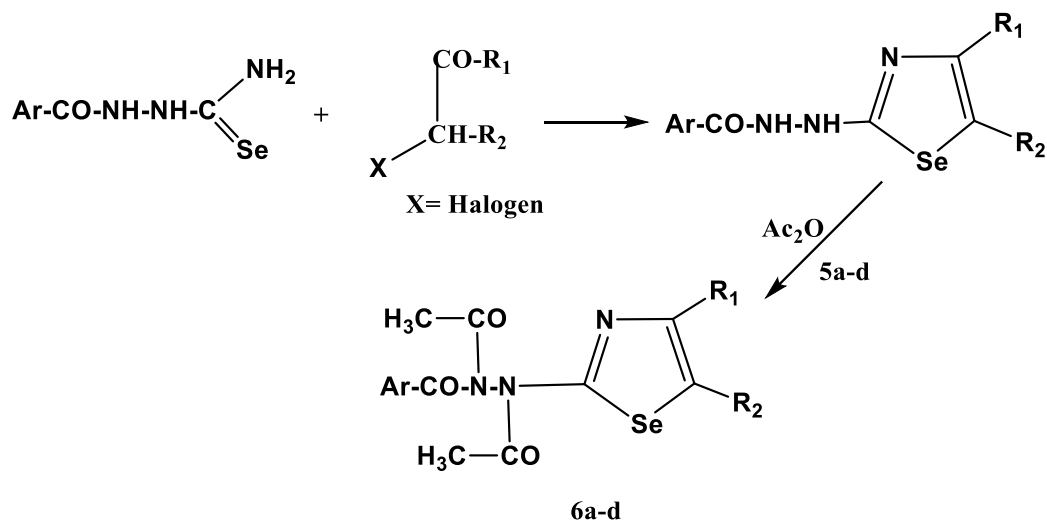
Symbol	5a,6a	5b,6b	5c,6c	5d,6d
Ar	C_6H_5	C_6H_5	C_6H_5Cl (p)	C_6H_5Cl (p)
R_1	CH_3	C_6H_5	CH_3	C_6H_5
R_2	H	H	H	H

Scheme (1-2): The synthesis route of compounds (5a-5d) and (6a-6d).

In 2016 Mahler *et al*. [13] reported the Ishihara reagent that used in the synthesis of selenosemicarbazones by a reaction that involved the replacement of the oxygen atom of semicarbazones with the selenium atom. They reported the formation of eleven selenosemicarbazones (1a-k), as depicted in Scheme (1-3).This study considered as an important approach to guide future Chagas drug design. The title compounds were characterised by several physico-chemical techniques.
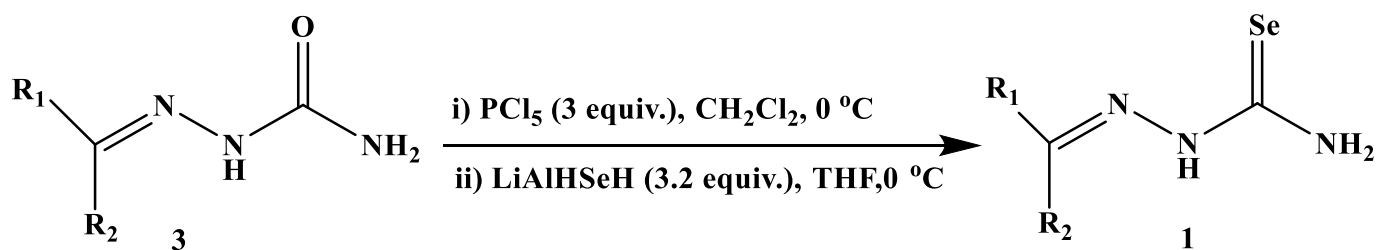
1a: R1 = Ph, R2 = Me, 50%
1b: R1 = m-BrPh, R2 = Me, 36%
1c: R1 = m,p-diClPh, R2 = Me, 13%
1d: R1 = i-prop, R2 = Me, 7%
1e: R1 = m-ClPh, R2 = Me, 25%
1f: R1 = m-CF3Ph, R2 = Et, 65%

1g: R1 = m-MePh, R2 = Me, 15%
1h: R1 = m,p-diClPh, R2 = H, 5%
1i: R1 = m-BrPh, R2 = H, 5%
1j: R1 = p-NMe2Ph, R2 = H, 5%
1k: R1 = p-OMePh, R2 = H, 12%

Scheme (1-3): Synthesis of selenosemicarbazones (1a-k).

The synthesis of a range of selenoureas compounds including PhC(O)NHC(Se)NPhMe, $4\text{-MeC}_6\text{H}_4\text{C(O)NHC(Se)NPhMe}$ and $4\text{-MeC}_6\text{H}_4\text{C(O)NHC(Se)-}$ NEt_2 were reported [14] and displayed in Scheme (1-4). A range of spectroscopic methods were used in the characterisation of compounds.
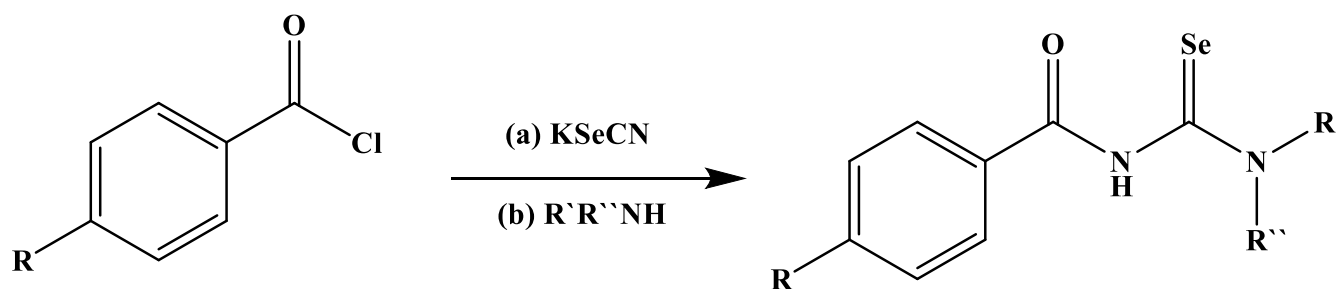
1: R= H, R`= Ph, R``= Me
2: R= Me, R`= Ph, R``= Me
3: R= Me, R`= R``= Et

Scheme (1-4): Preparation path of selenoureas 1-3.

Further, a range of heteroleptic cationic complexes were reported from the reaction of Pt(II), Pd(II) and Ru(II) ions with $4\text{-MeC}_6\text{H}_4\text{C(O)NHC(Se)NEt}_2$. The X-ray diffraction

of [Pd{4-MeC$_6$H$_4$C(O)NC(Se)NEt$_2$}(L-L)][+] confirmed square planar geometry around the Pd centre [14], Figure (1-2).
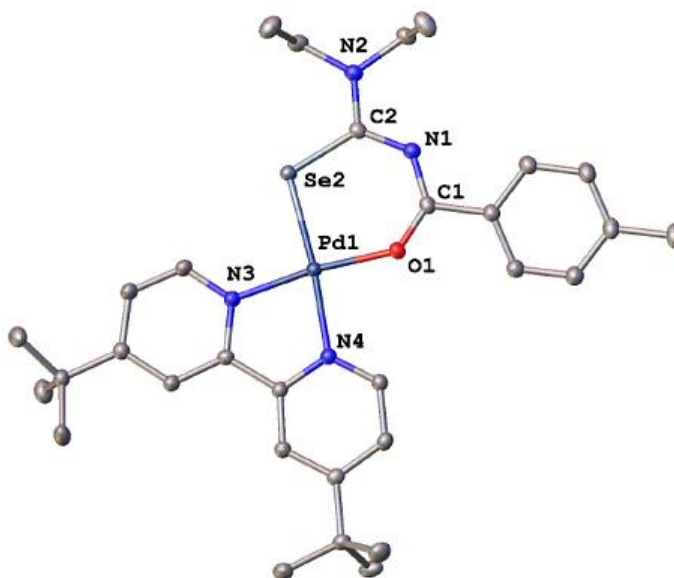
Figure (1-2): Molecular structure of [Pd{4-MeC$_6$H$_4$C(O)NC(Se)NEt$_2$}(L-L)][+].

(1.4) Compounds bearing N, Se donor atoms

A novel selenazoles derivatives were prepared and characterised using NMR, HRMS, elemental analyses, theoretical calculations (DFT B3LYP/6-311++G) and biological activity [15]. The synthesis of the title compounds (4m-4s) are sketched in Scheme (1-5).

R= NO$_2$ = 4m; R= F = 4n
R= CN = 4o; R= Br = 4p
R= Cl = 4r; R= CH$_3$ = 4s
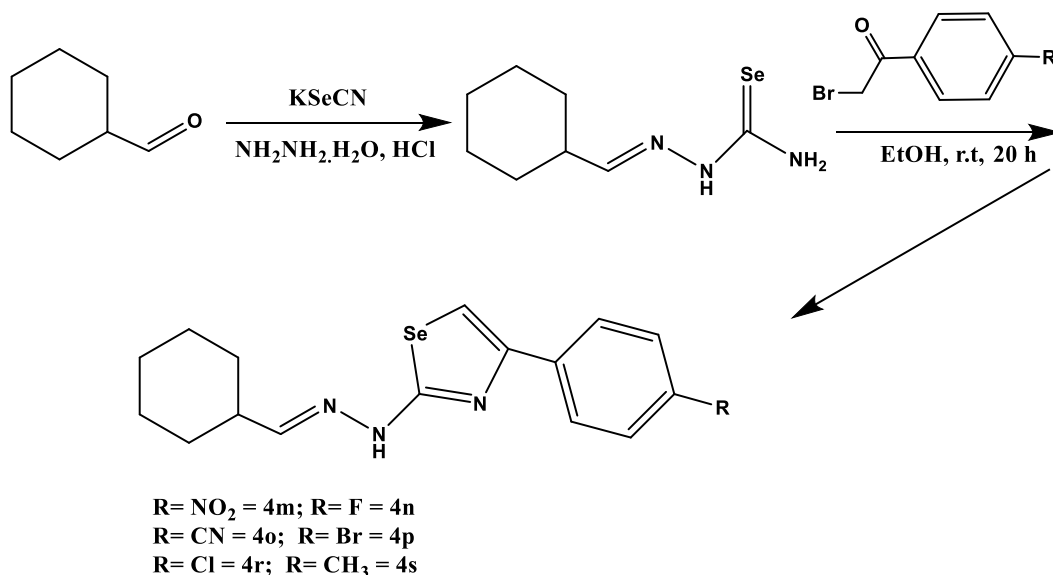
Scheme (1-5): Synthesis route of compounds (4m-4s).

The formation of 4-substituted pyrido[1,2-a][1,3,5]triazine-2-selenone derivatives were prepared by the reaction of acyl chlorides and potassium selenocyanate in the presence of pyridin-2-amine with acetone [16]. A range of techniques were used in the characterisation of compounds. Scheme (1-6) represents the synthetic approach of compounds.
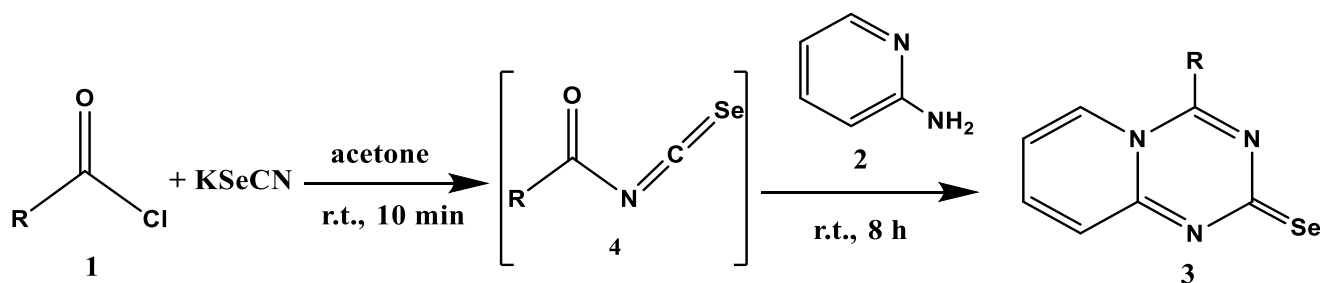
Entry	R	Product	Yield %
1	Ph	3a	70
2	2-Tol	3b	68
3	4-Tol	3c	69
4	2-Cl-C$_6$H$_4$	3d	81
5	3-Cl-C$_6$H$_4$	3e	78
6	4-Cl-C$_6$H$_4$	3f	85
7	Me	3g	60
8	Et	3h	63
9	t-Bu	3i	64

Scheme (1-6): The synthesis route of compounds (3a-3i).

A one-pot approach were used to prepare a range of selenadiazines compounds (3a-3f) by the reaction of aryl isoselenocyanates (1) with different phenacyl halides (2) in the presence of hydrazine hydrate [1]. Physico-chemical techniques were used to investigate the entity of compounds. Further, the molecular structure of compound (3,6-dihydro-5-phenyl-2H-[1,3,4]selenadiazin-2-ylidene)(phenyl)amine (3a) was established by X-ray single crystal diffraction, Figure (1-3).
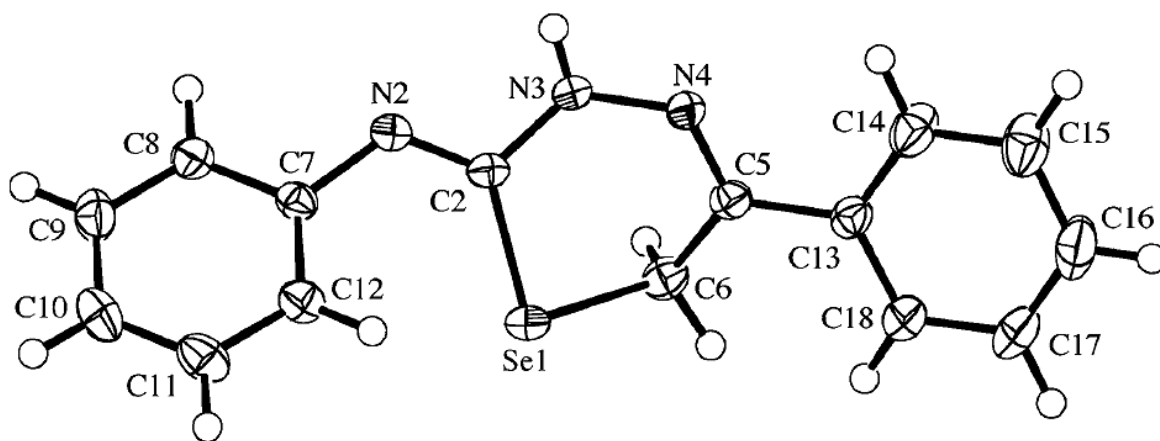
Figure (1-3): X-ray diffraction structure of 3a.

In 2017, Silvestru and co-workers [17] mentioned the synthesis of two selenosemicarbazone ligands 2-[(1′-Me-1′,2′-closo-$C_2B_{10}H_{10}$)SeCH$_2$]C_5H_4N (L^1) and 2,6-[(1′-Me-1′,2′-closo-$C_2B_{10}H_{10}$)SeCH$_2$]$_2C_5H_3$N (L^2) and six complexes; Cs[2-{(1′-Me-1′,2′-nido-$C_2B_9H_9$)SeCH$_2$}C_5H_4N] (1), Cs$_2$[2,6-{(1′-Me-1′,2′-nido-$C_2B_9H_9$)-SeCH$_2$}$_2C_5H_3$N] (2), [Ag(OTf)(L^2)] (3) (OTf=triflate), [Ag(PPh$_3$)(L^2)][OTf] (4), [Cu(L^2)(MeCN)][PF$_6$] (5) and [Cu(L^2)$_2$][PF$_6$] (6). Physico-chemical analyses techniques were used to characterise compounds. The X-ray crystallography confirmed the structures for ligands L^1 and L^2, see Figure (1-4).

L^1   **L^2**
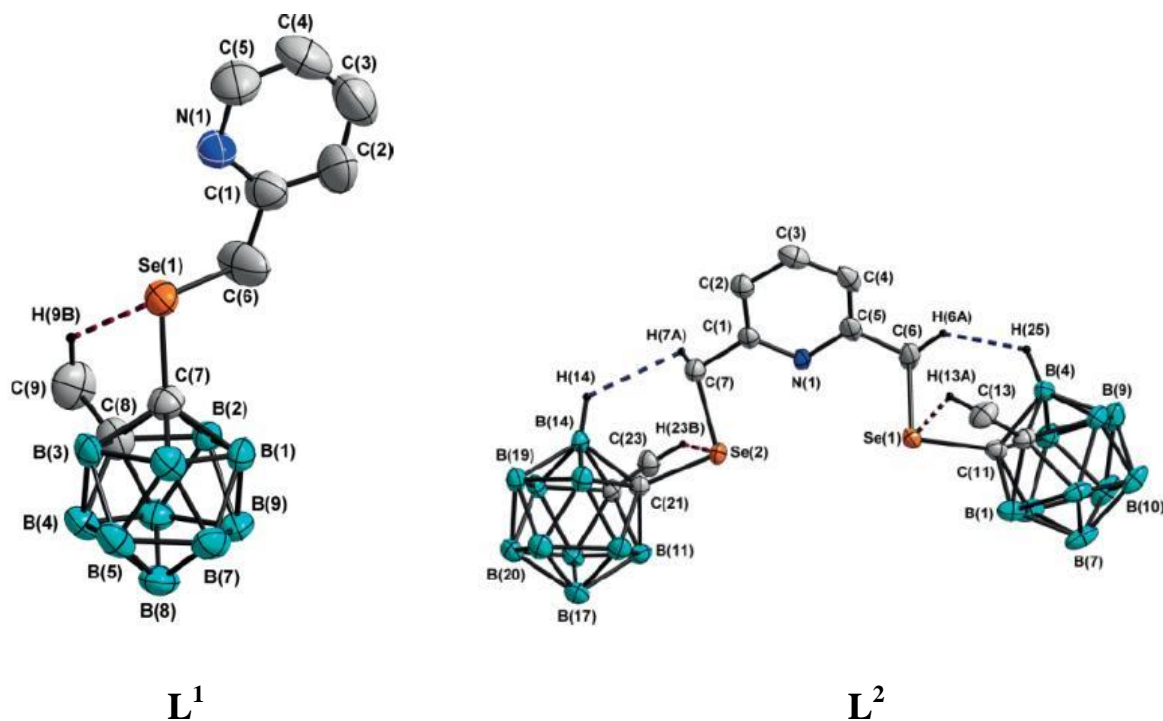
Figure (1-4): Molecular structure of L^1 and L^2.

In 2015, Khanna *et al*. [18] indicated the formation of cycloalkeno-1,2,3-selenadiazoles derivatives named (cyclopenteno, cyclohexeno, cyclohepteno, and cyclooocteno-1,2,3-selenadiazoles) using a one-step reaction that conducted at room temperature. The I.R, UV-Vis, NMR and mass spectroscopic analyses were used to investigate the entity of compounds, see Scheme (1-7).

1,2,3, a n= 1, b n= 2, c n= 3, d n= 4
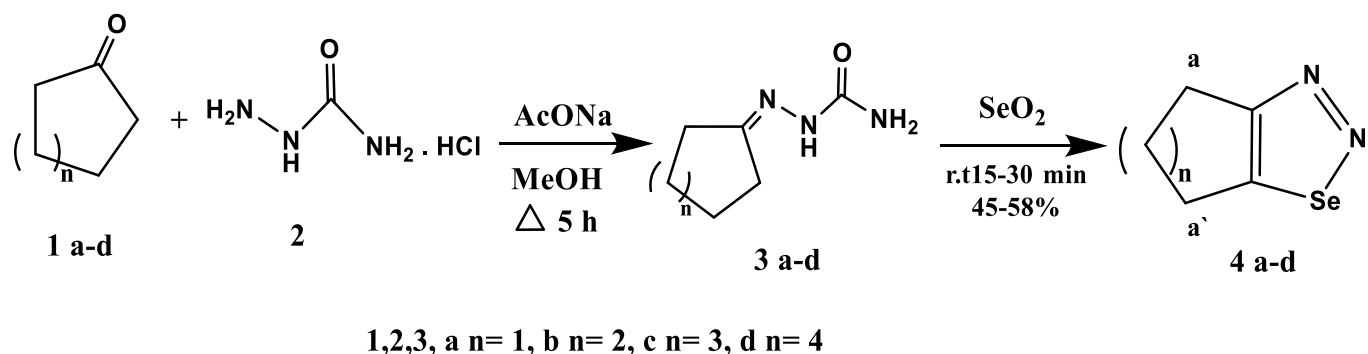
Scheme (1-7): Synthesis route of compounds (4 a-d).

Ishihara *et al*. [19] reported the preparation of seleno-based compounds with two selenium atoms including heterocyclic-Se segment. The synthesis of these types of selenium-containing heterocycles was derived from isoselenocyanates compound. The entity of compounds was confirmed using a range of analytical and spectroscopic methods. The two compounds [2-(phenylimino)-1,3-selenazolidine-3-carboselenoic anilide] (12) and [2-(phenylimino)-1,3-selenazane-3-carboselenoic anilide] (13) were prepared from the reaction of haloamines with two equivalents of isoselenocyanates, see Scheme (1-8).
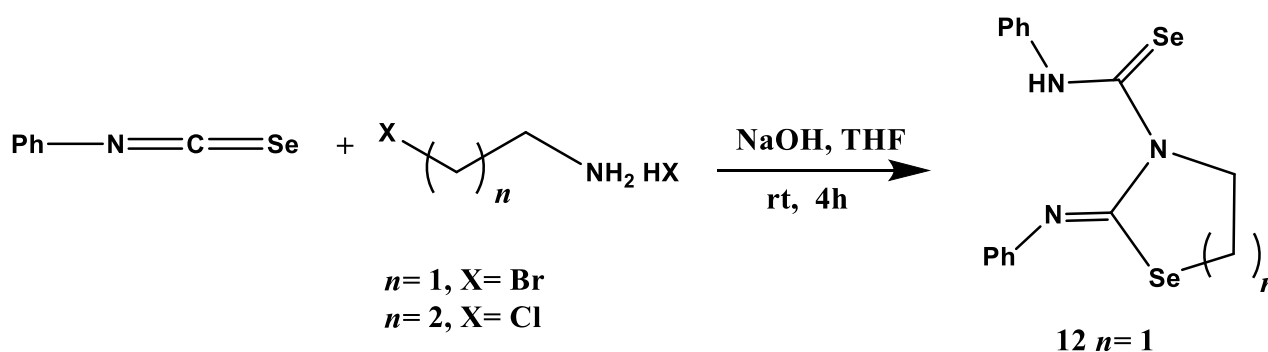
Scheme (1-8): Preparation sketch of compounds 12 and 13.

(1.5) Macrocyclic compounds with N, Se donor atoms

The synthesis of new multidentate macrocyclic ligands with N and Se donor atoms were reported [20]. These ligands were obtained by the condensation reaction of bis(o-formylphenyl)selenide and bis(2-aminoethyl)sulfane. Moreover, the reaction of these ligands with the Ag(I) salts resulted in the isolation of silver (I)-complexes. The chemical structure of ligands and their complexes was confirmed adopting several spectroscopic methods including FTIR, NMR, mass spectroscopic. The chemical structure of compounds is shown in Figure (1-5).

R= CH$_2$CH$_2$ (a)   R= CH$_2$CH$_2$ (c)
R= CH$_2$CH$_2$CH$_2$ (b)   R= CH$_2$CH$_2$CH$_2$ (d)
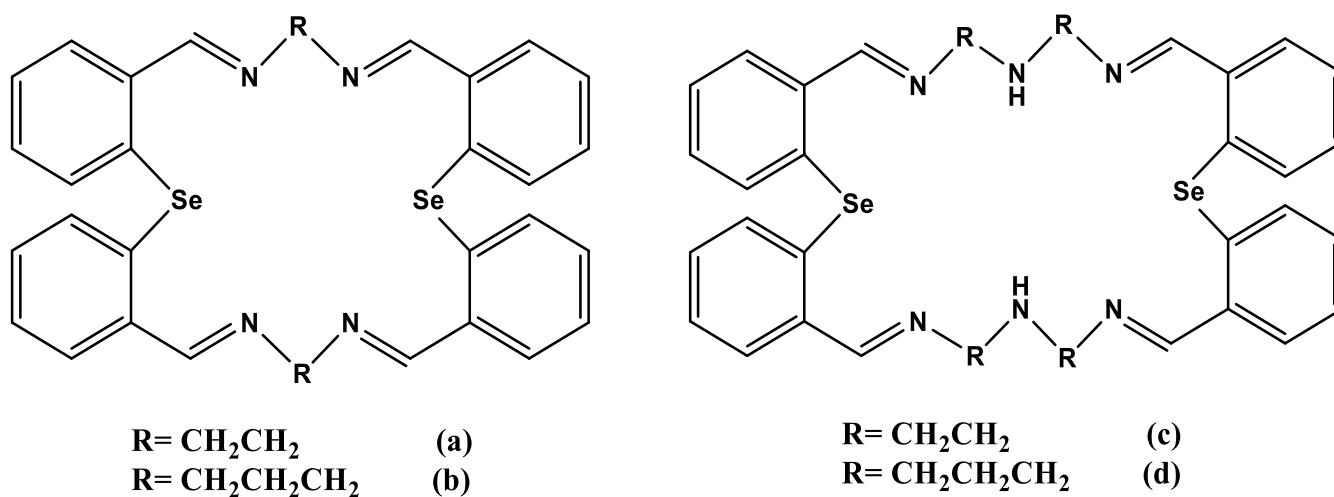
Figure (1-5): Macrocyclic ligands with N and Se donor atoms.

Tripathi *et al.* [21] outlined the formation of a range of macrocyclic compounds including the *hard* (N and O) and the *soft* (Se or Te) donor atoms. The compounds [E{(CH$_2$)nNC(CH$_3$)C$_6$H$_2$(OH)(CH$_3$)CO(CH$_3$)}$_2$] E (E= Se, Te; n= 2,3) were prepared by the reaction of bis (aminoalkyl) selenides/tellurides, {NH$_2$(CH$_2$)n}$_2$E (E= Se, Te; n= 2,3) with 2,6-diacetyl-4-methylphenol, Figure (1-6). These compounds were characterised using spectroscopic tools including the ^{77}Se-NMR and ESMS spectroscopy.

(H₂L)

E= Se; n= 2 (H₂L$_A$). 3 (H₂L$_A$`)
E= Te; n= 2 (H₂L$_B$). 3 (H₂L$_B$`)
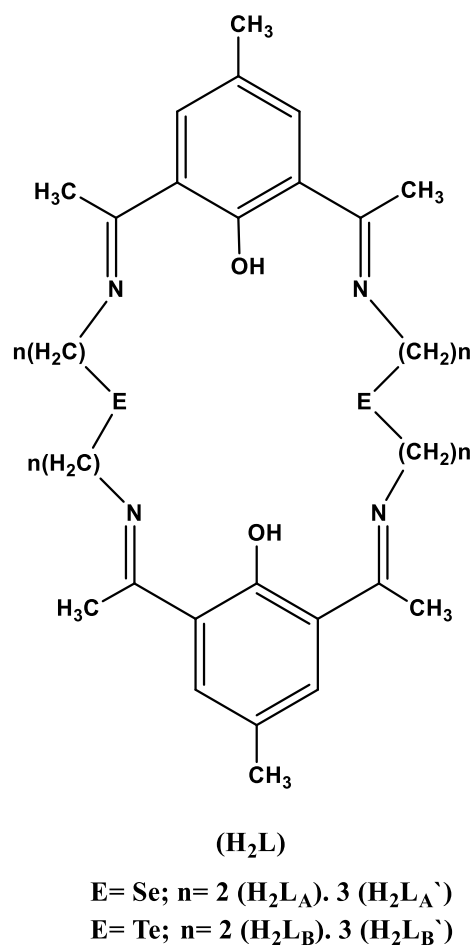
Figure (1-6): A general sketch of macrocyclic ligands (H₂L$_A$ and H₂L$_B$).

(1.6) Non-macrocyclic compounds with N, Se donor atoms

The formation of two selenosemicarbazone ligands 2,6-diacetylpyridine bis (selenosemicarbazone) (H$_2$dapsesc) and 2-{1-[6-(1-selenosemicarbazonoethyl)-2-pyridyl]ethylidene}-hydrazine carbonitrile (H$_2$hcn) were reported. Complexes of Zn(II) and Cd(II) with H$_2$dapsesc and Ni(II) with H$_2$hcn were also isolated [22]. A range of physico-chemical methods were implemented to confirm the entity of ligands and their metal complexes. These studies indicated the isolation of four and five-coordinate complexes with Ni(II) and Zn(II) and Cd(II), respectively. Figure (1-7) represents the chemical structure of the five coordinate Cd(II)-complex.

11
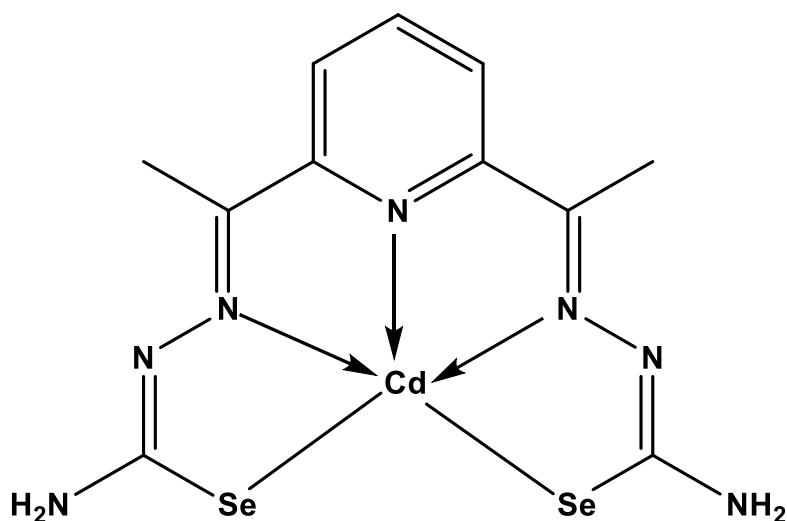
Figure (1-7): A general sketch of five-coordinate of [Cd(dapsesc)] complex.

In 2014, Silvestru and co-workers [23] published the preparation of several kinds of ligands with different donor species including the selenium atom; $[R_2C(OH)CH_2](2-Me_2NCH_2C_6H_4)E$ [R= Me, E= S (1), Se (2), Te (3); R= Ph, E= S (4), Se(5)]. These ligands were used to isolate Ag(I)-complexes of the general formula $[AgOTf\{E[CH_2C(OH)R_2](C_6H_4CH_2NMe_2-2)\}]$ [R= Me, E= S (6), Se (7), Te (8); R= Ph, E= Se (9)]. The structural characterisation of these compounds was based on the FT-IR, NMR and mass spectrometry. The X-ray single crystal of $[Ph_2C(OH)CH_2](2-Me_2NCH_2C_6H_4)Se$ confirmed the entity of the compound, Figure (1-8).
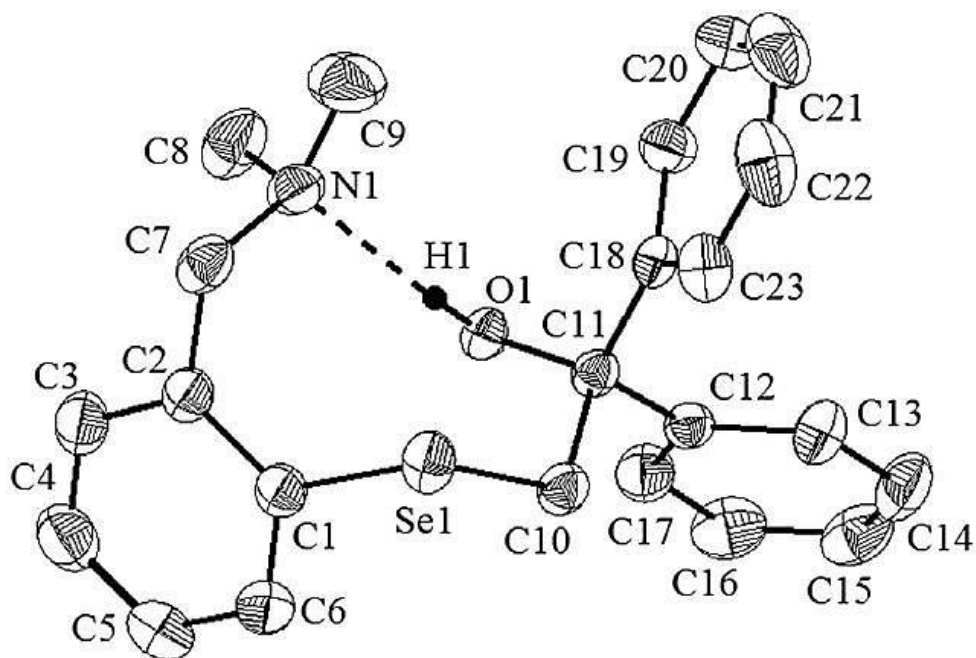
Figure (1-8): ORTEP diagram of [Ph$_2$C(OH)CH$_2$](2-Me$_2$NCH$_2$C$_6$H$_4$)Se] compound.

The reaction of [Cu(CH$_3$CN)$_4$]ClO$_4$ with the bis(methyl)(thia/selena)salen ligands resulted in the isolation of (1) and (2) [{CH$_3$E(o-C$_6$H$_4$)CH=NCH$_2$}$_2$Cu]ClO$_4$; E=S/Se [24]. A variety of analytical and spectroscopic tools were implemented to reveal the entity of (1) and (2). These include; FT-IR, NMR (^{1}H, ^{13}C and ^{77}Se), mass spectroscopy, elemental analysis and cyclic voltammetry. The X-ray single crystal of Cu-complexes (1) and (2) displayed tetrahedral geometry around metal centre, see Figure (1-9).
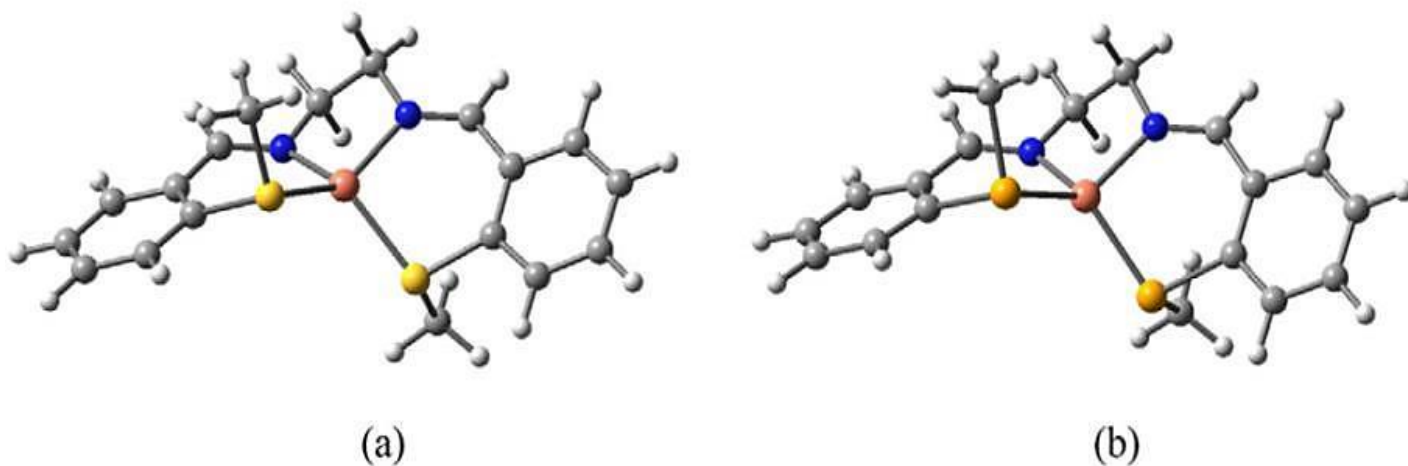
Figure (1-9): ORTEP diagram (50% thermal ellipsoids) of; a) 1 and b) 2.

In 2006, Ishihara and co-workers [25] described the synthesis of a range of derivatives of *N*-benzyl-*N*̀-*p*-toluoylselenourea by the reaction of *p*-toluoyl chloride with KSeCN. The analytical and spectroscopic data of compounds agreed well with the suggested structures. The X-ray single crystal of *N*-benzyl-*N*̀-*p*-toluoylselenourea (3a) was reported, which indicated the presence of two independent molecules in the unit cell; Figure (1-10).
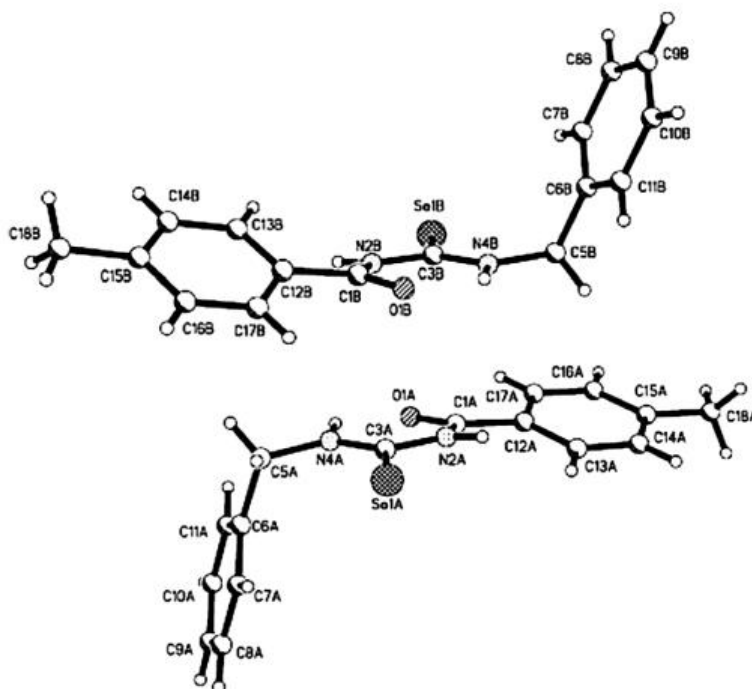
Figure (1-10): ORTEP diagram (50% thermal ellipsoids) of compound 3a.

The preparation of $[2\text{-}(Et_2NCH_2)C_6H_4]_2Se_2$ (1) was achieved by hydrolysis/oxidation of $[2\text{-}(Et_2NCH_2)C_6H_4]SeLi$ derivative. In addition, the reaction of compound (1) with sodium or lithium metal in THF resulted in the formation of $[2\text{-}(Et_2NCH_2)C_6H_4]SeM`$ (M`= Na or Li). The formation of complexes of the general formula $[2\text{-}(R_2NCH_2)C_6H_4Se]_2M$ (R= Me, M= Zn (3), Cd (4); R= Et, M= Zn (5), Cd (6)) were accomplished by reactions of alkali metal selenolates $[2\text{-}(R_2NCH_2)C_6H_4]SeM`$ (R= Me, Et; M`= Li, Na) with MCl_2 (M= Zn, Cd) in a 2:1 molar ratio. The multinuclear NMR (^{1}H, ^{13}C, ^{77}Se and ^{113}Cd), mass spectrometry and X-ray diffraction analysis were used to characterise the title compounds. The X-ray single crystal structure of Zn- and Cd-complexes showed tetrahedral geometry around metal centre [26], see Figure (1-11).
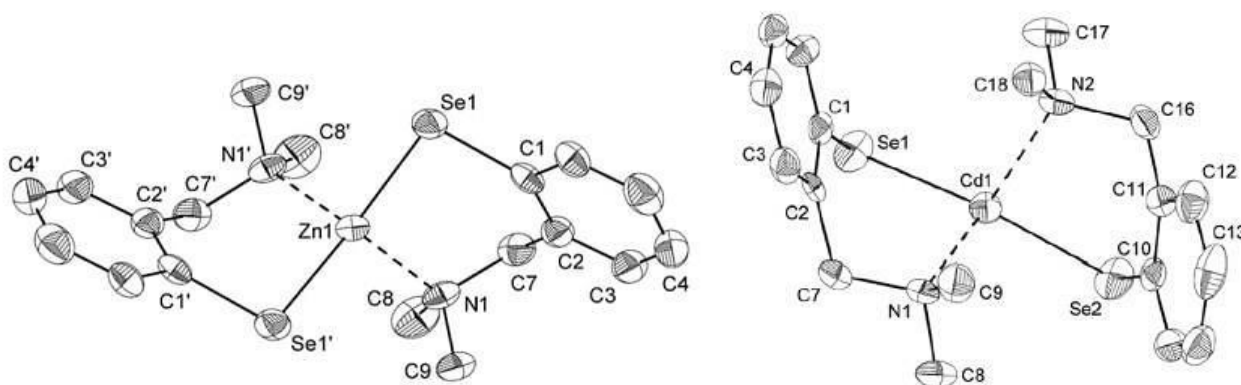
Figure (1-11): Molecular structures of Zn- and Cd-compounds.

Anđelković *et al.* [27] published the isolation of two novel Cd(II) and Zn(II) complexes that derived from the condensation reaction of 2-formylpyridine with selenosemicarbazide. Physico-chemical tools were used in the characterisation of compounds. The X-ray single crystal of Cd(II) complex indicated a five-coordinate arrangement around atom centre, see Figure (1-12).
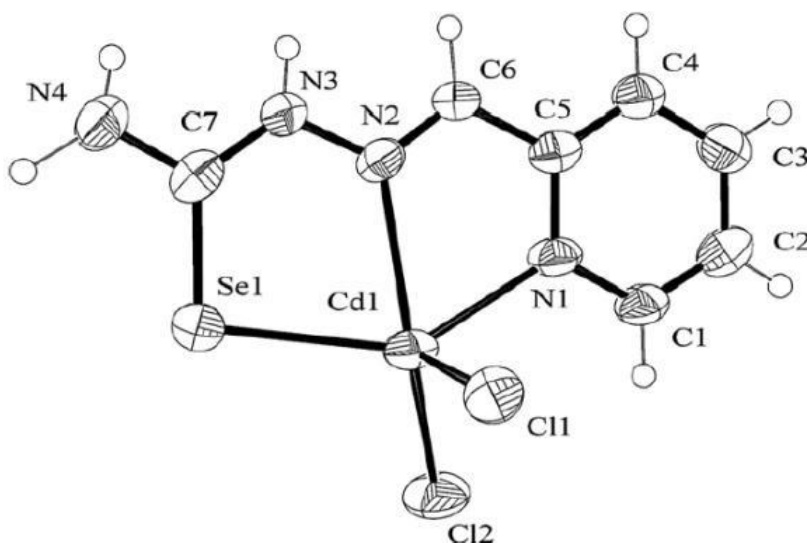
Figure (1-12): The X-ray single crystal structure of Cd(II)-compound.

The formation and characterisation of 2-quinolinecarboxaldehyde selenosemicarbazone (Hqasesc) with Ni(II), Zn(II) and Cd(II) ions were reported [3]. The entity of ligand and its complexes were confirmed using FTIR, NMR (^{1}H, ^{13}C, ^{77}Se and

¹¹³Cd) spectroscopic and elemental analysis. The X-ray single crystal proved the
arrangement about Ni centre is octahedral; see Figure (1-13).
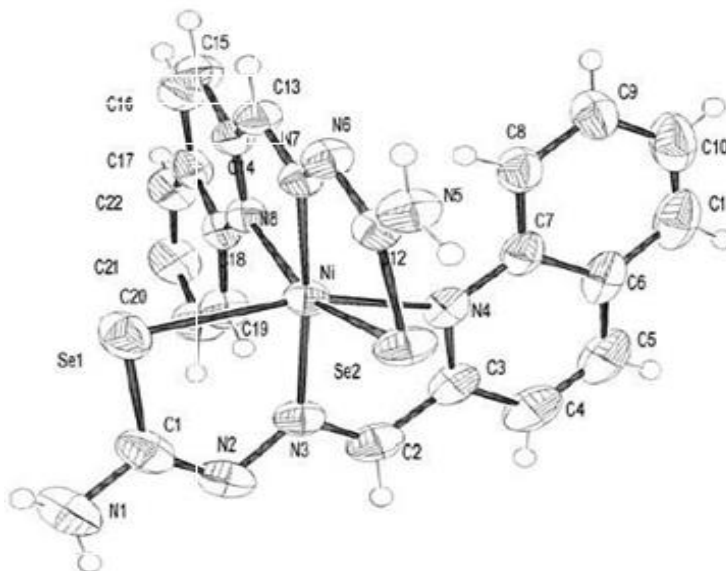
Figure (1-13): ORTEP diagram of [Ni(qasesc)₂].

The ligand 8-quinolinecarboxaldehyde selenosemicarbazone and its complexes with Pd(II), Pt(II), Cd(II), and Ni(II)) were mentioned by Todorovic *et al.* [28]. A range of physico-chimical techniques were implemented to conclude the entity of compounds. The chemical structure of Pd(II)-complex with the square planar arrangement around atom centre is placed in Figure (1-14).
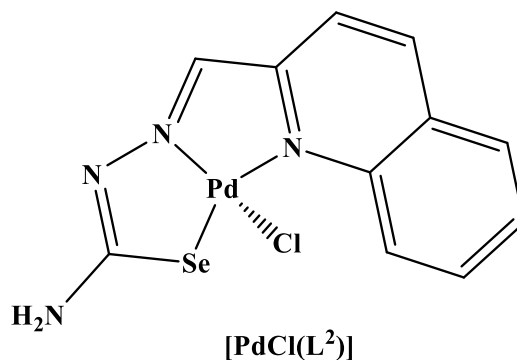
$$[PdCl(L^2)]$$

Figure (1-14): A general chemical sketch of [PdCl(L²)].

17

Heimgartner and co-workers [29] mentioned the synthesis and characterisation of a new range of selenourea derivatives (8) by the addition of morpholine to a solution of imidoylisoselenocyanate (3) in acetone at room temperature. A variety of techniques were implemented to characterise the isolated compounds. The molecular crystal structure of 4-bromo-N`-[(morpholin-4-yl)(selenocarbonyl)]-N-(4-nitrobenzyl) benzimidamide (8b) has determined that depicted in Figure (1-15).
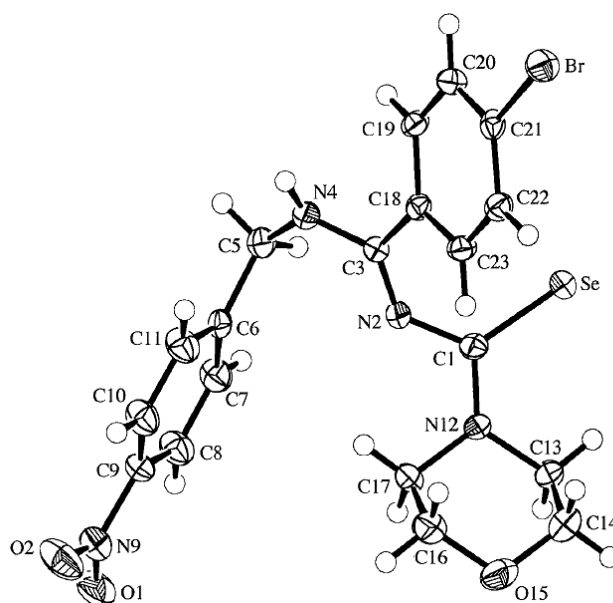
Figure (1-15): ORTEP diagram of compound 8b.

Andjelkovic and co-workers [30] published the synthesis of 2,6-diacetylpyridine-bis(selenosemicarbazone) (dapsesc) ligand. The ligand (dapsesc) was reacted with Ni(II), Zn(II) and Cd(II) ions to form new complexes that confirmed by a variety of physico-chemical methods. These analyses indicated the isolation of five-coordinate complexes with Zn(II) and Cd(II) ions. Further, the X-ray molecular structure of Ni(II) complex confirmed a square planar geometry around metal centre, see Figure (1-16).

18
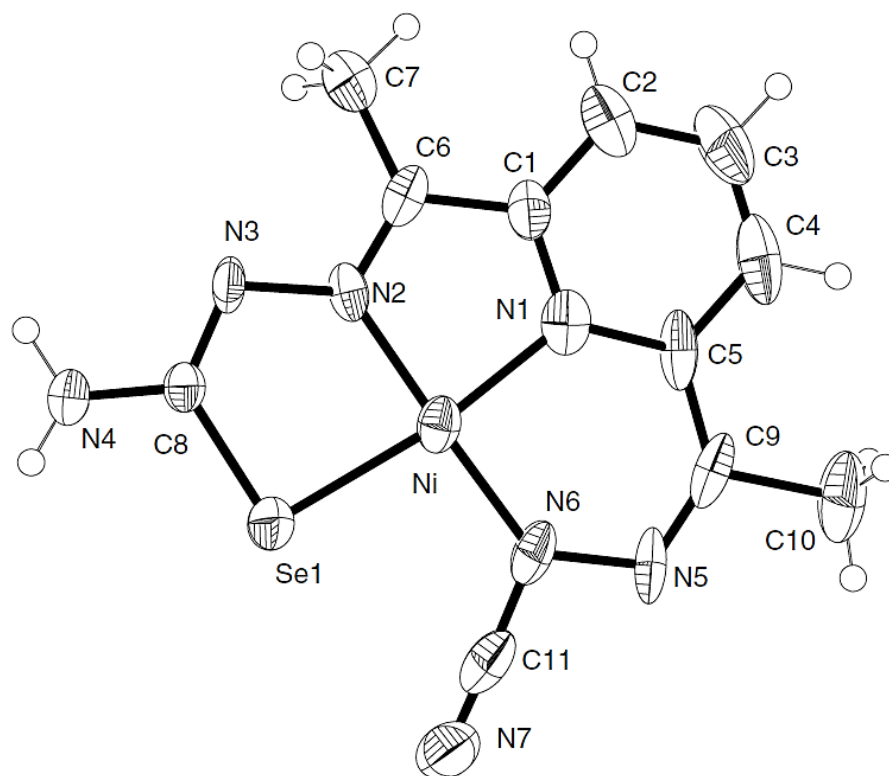
Figure (1-16): The X-ray single crystal diffraction of [Ni(II)dapsesc].

(1.7) Applications and uses of selenosemicarbzone compounds in different fields

Selenosemicarbzone compounds represent an interesting class of Schiff-base species that play a vital role in the development of inorganic, bioinorganic and coordination chemistry. This is due to their ability to form stable complexes with almost transition metals and representative elements. Furthermore, the importance of these organic compounds (with N and Se) and their metal complexes in the in medicine, pharmaceutical industry, analytical chemistry and biological system made them the key issue to be investigated by several research groups.

(1.7.1) Application in medicine and pharmacy

It is well known that selenosemicarbazone compounds and their complexes have shown several biological activities including; antimicrobial, antitumor, anti-inflammatory, antiviral activities, antifungal and anticancer [31]. They also have the role in the treatment of diabetes and HIV/AIDS patients. In the almost reported studies, selenosemicarbazones compounds displayed more activity than sulfur and oxygen analogues compounds [31].

Selenium element is an essential for human metabolism [6]. Due to its high anticancer activity and low toxicity, selenoproteins compounds were explored for their anticancer application. These include epsilon, selenocyanate, selenobetaine [5]. Further, there are a range of organoselenium compounds that indicated an excellent effect on human breast carcinoma MCF-7 cells [32].

Fungal diseases cause a major health problem and a lot of people may infect by these microorganism [33] and these diseases may be lead to death [34]. Moreover, the wide spread of using drugs such as antibiotics, immunosuppressive agents, anticancer, and anti-AIDS drugs lead to the appearance of mutant types of microorganisms that show resistant to drugs [33,35,36]. Therefore, the introduction of selenosemicarbazone compounds as potential agents to tackle this issue that have different acting mechanism, compared with other drugs, may help to overcome the resistant problems [31]. The preparation of new complexes of Ni(II) Zn(II) and Cd(II) with selenosemicarbazone were reported [27]. The isolated complexes exhibited biological activity including; antifungal, antimicrobial, anticancer, anti-inflammatory and antiviral activity. Figure (1-17) represents the four-coordinate structure of [Ni(hen)] complex [hen= 2-{1-[6-(1-selenosemicarbazonoethyl)-2-pyridyl]ethylidene}-hydrazine carbonitrile].
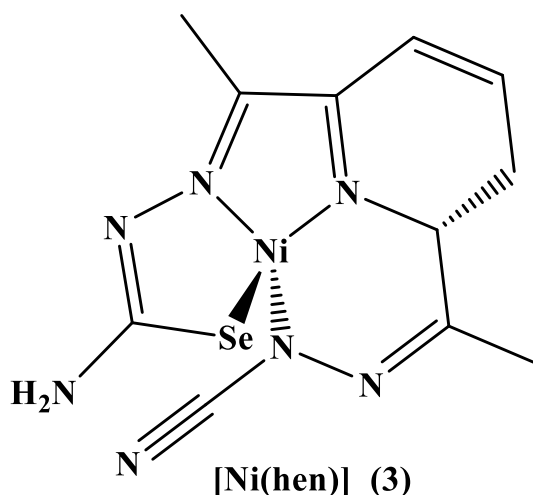
Figure (1-17): The chemical structure of the four-coordinate [Ni(hen)].

The compound (Z)-N,5-diphenyl-3,6-dihydro-2H-1,3,4-selenadiazin-2-imine (3a), Figure (1-18), is one of a series of Se-compounds that reported by Heimgartner *et al.* [1]. The prepared compounds have shown potential applications in the biological and pharmaceutical field including their role as antitumor and antibacterial agents.
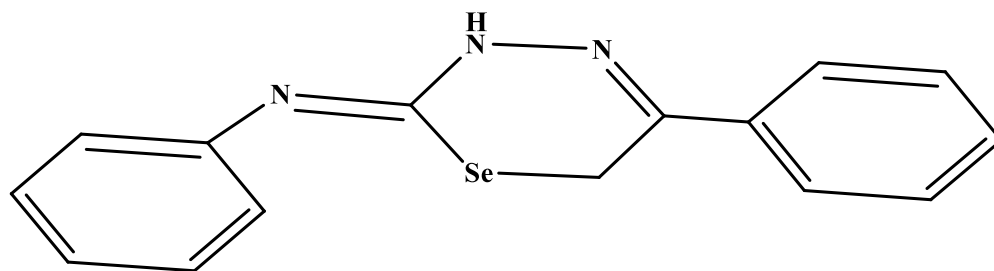
Figure (1-18): A general chemical structure for compound 3a.

The preparation of a series of hydrazinoselenazole derivatives, see Figure (1-19), were aimed to examine the influence of these compounds against two types of human cancer (DU-145) and (Hep-G2) cell lines [2].

Ar= $C_6H_4Cl(p)$
R_1= CH_3
R_2= H
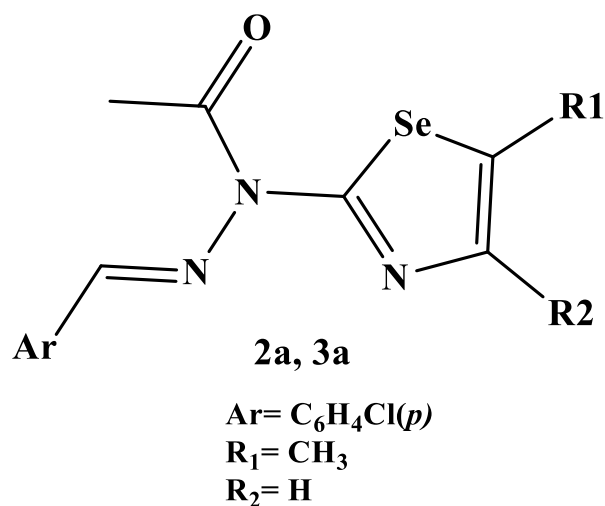
Figure (1-19): A general chemical structure for compounds 2a and 3a.

Srivastava and co-workers [36] indicated the synthesis and characterisation of 2-β-D-ribofuranosylselenazole-4-carboxam (9), Figure (1-20), by phosphorylation of 2-β-D-ribofuranosylselenazole-4-carboxamide (6) with phosphoryl chloride and trimethyl phosphate. The prepared compounds were aimed to act as antitumor agents.

9
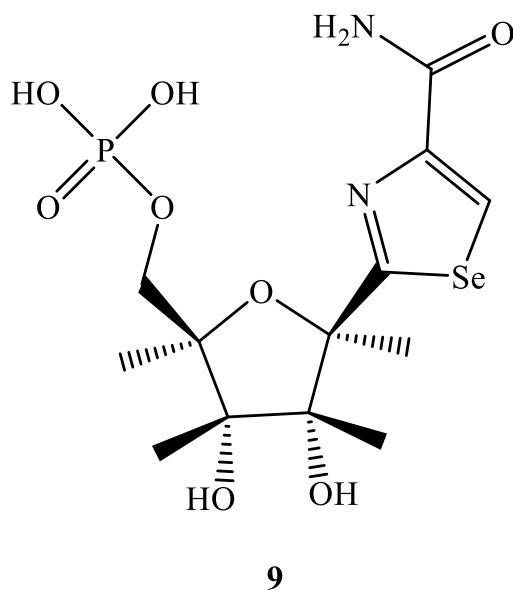
Figure (1-20): Chemical structure of compound 9.

Further, selenoureas compounds have used as anti-infective drugs, cytokine inducers/immunemodulators, antihypertensive and cardiotonic agents [37].

Selenium compounds have proved to be very potent anti-carcinogenic agents in different models, with spontaneous, chemically induced, or transplanted tumours or in culture. An example is the preparation 2-amino-1,4,5,9-tetrahydro-6H-purine-6-thione (493) and 2-amino-1,4,5,9-tetrahydro-6H-purine-6-selenone (494) [38], See Figure (1-21).
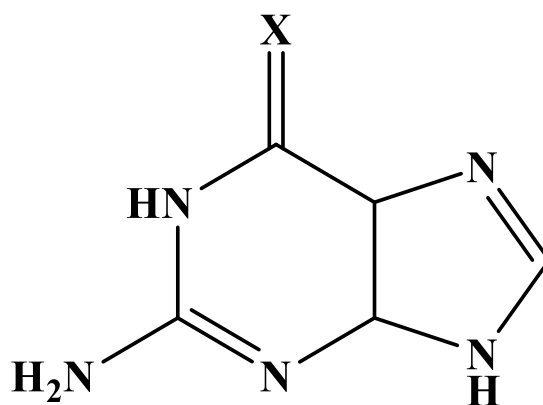
493, X= S
494, X= Se

Figure (1-21): The chemical sketch for (493) and (494).

Al-Smadi and workers [39] described the formation of 1,2,3-selenadiazole derivatives that achieved *via* Lalezari method, Scheme (1-9). These compounds indicated biological activity against several microorganisms.
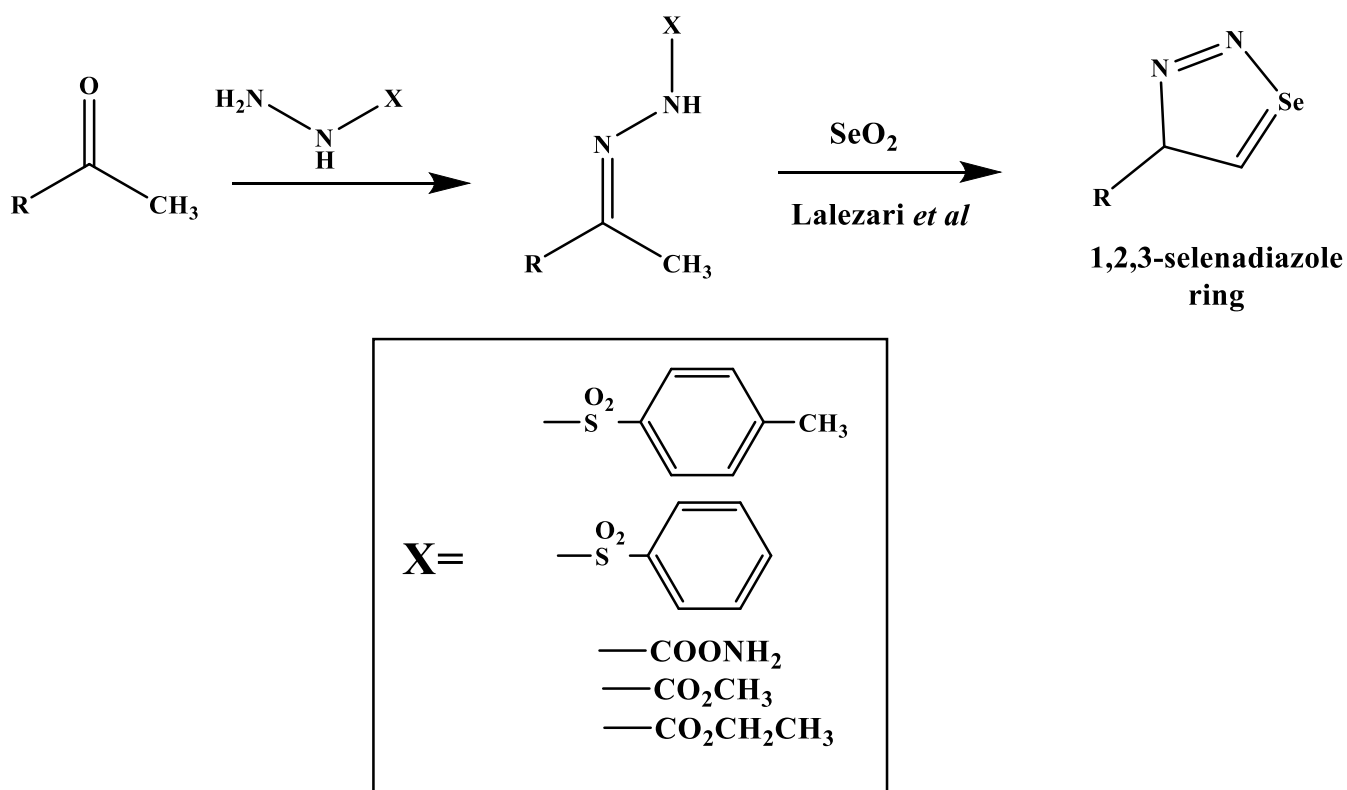
Scheme (1-9): The synthetic route of 1,2,3-selenadiazole derivatives.

Anđelkovic *et al.* [27] reported the synthesis of selenosemicarbazones that showed antimicrobial [40] and antimalarial activity.

Complexes of Cd(II), Zn(II) and Ni(II) with 2-quinolinecarboxaldehyde selenosemicarbazone (Hqasesc) were extensively studied as antibacterial, antiviral and antitumor agents [3]. They displayed strong antitumor, antimicrobial and antiviral activity, compared with thiosemicarbazones and semicarbazones compounds [41,42]. Physico-chemical methods were used to determine the entity of complexes. Figure (1-22) represents the chemical structure of Cd(II)-complex.
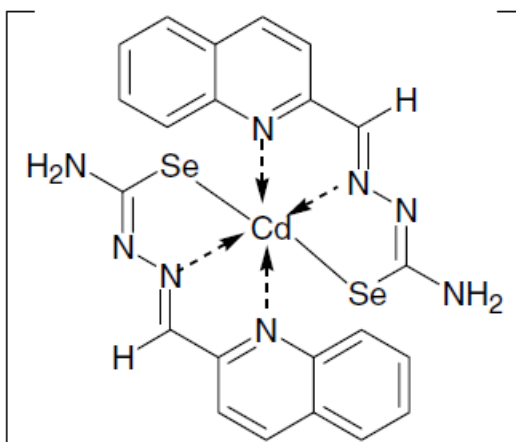
Figure (1-22): Chemical structure of [Cd(qasesc)] compound.

A classic procedure was implemented for the preparation of organoselenium compounds including cycloalkeno-1,2,3-selenadiazoles (cyclopenteno, cyclohexeno, cyclohepteno, and cycloocteno-1,2,3-selenadiazoles). The isolated compounds showed biological activity against *Escherichia coli, Staphylococcus aureus, Salmonella typhi,* and *Pseudomonas aeruginosa* [18].

The formation of Pt(II) and Pd(II) complexes with 8-quinolinecarboxaldehyde selenosemicarbazone was reported by Todorovic *et al.* [28]. The ligand and its complexes were tested against Gram-positive strains of bacteria.

Complexes of Zn(II) and Cd(II) with 2,6-diacetylpyridine-bis(selenosemicarbazone) (dapsesc) were studied for their antibacterial, antiviral, antifungal and antitumor activities [22]. Figure (1-23) showed the proposed geometry of [Zn(dapsesc)] complex.
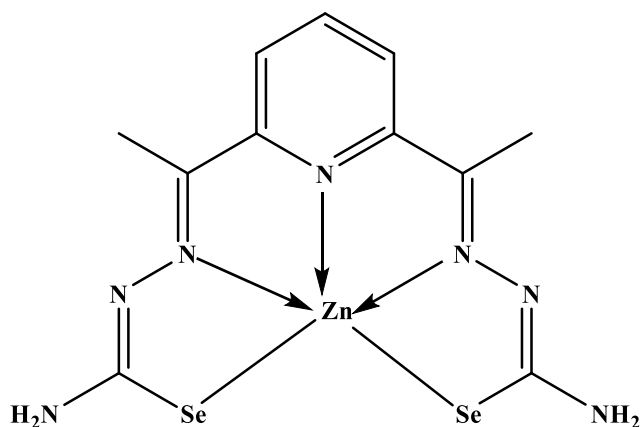
Figure (1-23): The five-coordinate structure of [Zn(dapsesc)] complex.

The synthesis and isolation of Cu(I)-complexes with bis(methyl)(thia/selena) salen ligands were explored. These complexes found a potential application in the DNA binding capacity and may have possible application as groove binder drugs [24].

(1.7.2) Application in biological system

Compounds bearing nitrogen and selenium as donor atoms have been used as enzyme mimics and in the chemotherapeutic application [43,44]. The Se-based compounds have the ability to coordinate and form more stable complexes with metal ions, compared with that of sulfur. The preparation of (E)-2-(1-(3-bromophenyl)ethylidene)hydrazine-1-carbo seleno amide (1b) was reported [13]. The compound (1b), Figure (1-24), was designed as a model for acute Chagas`s disease.
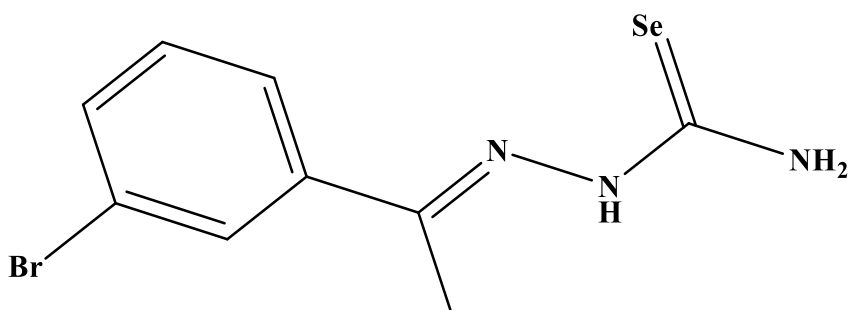
Figure (1-24): Chemical structure of compound 1b.

Selenourea and their derivatives have considered as enzyme inhibition and thymidylate synthase inhibitors. They also have role as antioxidant defense enzymes these include; reduction of hydroperoxides-GPx mimics, reduction of peroxinitriles, lipid peroxidation, tyrosine kinase and iodothyronine inhibitors [37].

(1.7.3) Application in chemistry

Selenosemicarbazone ligands and their complexes played a vital role in the expansion of chemistry such as organic, inorganic and coordination chemistry. The reaction of these ligands with most transition and representative elements can yield stable complexes. Seleno-compounds have shown excellent catalytic activity in a variety of process including Heck coupling [45].

The strong electron-donating ability of selenium has led to the synthesis of many transition metal complexes of organoselenium ligands. The preparation of organoselenium and their sulfur and tellurium analogue and their complexes of silver(I) have shown important applications as catalysis in several chemical reactions [23]. Scheme (1-10) represents the general sketch of the preparation of Ag(I) complexes.

R= Me; E= S(1), Se(2), Te(3)
R= Ph; E= S(4), Se(5)

R= Me; E= S(6), Se(7), Te(8)
R= Ph; E= Se(9)
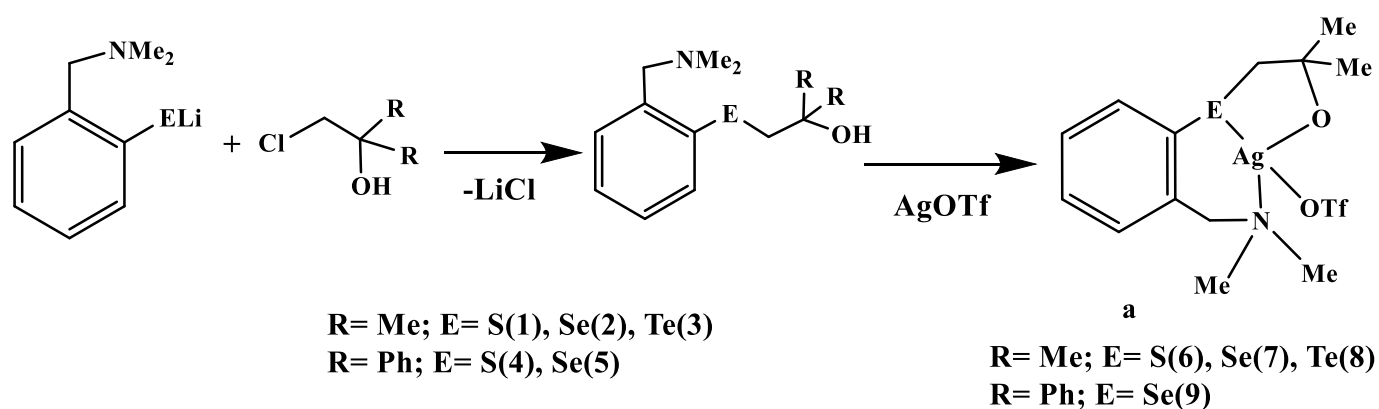
Scheme (1-10): Synthetic route of compounds 1-9.

The formation of PhC(O)NHC(Se)NPhMe, 4-MeC$_6$H$_4$C(O)NHC(Se)NPhMe and 4-MeC$_6$H$_4$C(O)-NHC(Se)NEt$_2$ was aimed to be used in analytical chemistry and spectrophotometric determination of metals. These include their role in the chromatographic metal separation of Pt(II), Pd(II) and Ru(II) [14,46,47].

(1.7.4) Application in industry and agriculture

Selenium is an essential biological trace element that becomes more insufficient in food crops as a result of intensive plant production in many countries [48]. It is an essential constituent of several enzymes in which it is present in the form of the unusual amino acid selenocysteine (SeCys). It is used to replace vitamin E in the diets of rats and chicks for the prevention of vascular, muscular and/or hepatic lesions. Compound of dimethylselenide played a vital role in the improvement of agriculture soil [48].

There are a range of selenosemicarbzone selenols, selenides, seleno-aldehydes and acids, selenium-phosphorus and selenium heterocyclic compounds that have used as insecticides, microbicides, prooxidants, antibacterial and antifungal agents [49].

Further, selenium-based compounds have used as intermediates in the synthesis of some dyes and pigments [7].

(1.8) Aim of the work

In the past, Se-based materials showed limited uses and applications [16]. This is due to the fact that scientists classified these materials as very toxic compounds. However, currently these compounds considered as interesting species and have applications in different fields including; medicinal chemistry, pharmaceutical industry, analytical chemistry, catalysis, and as a mimic in the biological system.

This study involves the formation, physico-chemical characterisation, thermal properties and biological assay of bidentate selenosemicarbazone ligands (bearing N and Se donor atoms) and their metal complexes. Therefore, the aim of current project includes:

- Synthesis of six novel selenosemicarbazone Schiff-base ligands (HL^1-HL^6), in which several synthetic steps were implemented to isolate the required ligand.

- Formation a series of metal complexes from the reaction of the ligands with several metal ions.

- A range of physico-chemical methods were implemented to confirm the entity of ligands and their metal complexes.

- Investigating the stereochemistry and potential structure of the synthesised compounds.

- Investigating the thermal stability for ligands and some metal using TGA, DTG and DSC techniques.

- Studying the biological activity of the selenosemicarbazone ligands and their metal complexes. These include their antibacterial and antifungal behaviour toward four kinds of bacteria (G$^+$ and G$^-$ strains) and four types of fungi family.

CHAPTER TWO

EXPERIMENTAL PART

(2) Experimental part

(2.1) Chemicals

The used laboratory chemicals and reagents and their providers are included in Table (2-1). Chemicals were used without additional purification.

Table (2-1): Reagents and materials used in this study and their providers.

No.	Material	Supplier	Purity %
1	Acetic acid	C.D.H	99.9
2	Acetone	Romil	99.8
3	Ammonium acetate	Chem-supply	97
4	Aniline	C.D.H	99
5	Benzaldehyde	C.D.H	99.8
6	Benzene	Romil	99.8
7	Chloroform	Romil	99.8
8	Cyclohexanone	B.D.H	99.8
9	Dichloromethane	Romil	99.8
10	Diethyl ether	Romil	99.9
11	*p*-Dimethylaminobenzaldehyde	Merck	99
12	Dimethylformamide (DMF)	C.D.H	99
13	Dimethylsulfoxide (DMSO)	Sigma-Aldrich	99
14	Ethanol	Sigma-Aldrich	99.9
15	*p*-Methoxybenzaldehyde	B.D.H	99
16	*m*-Nitroaniline	Merck	99

No.	Material	Supplier	Purity %
17	Methanol	Scharlau	99.9
18	Cd(II)-chloride dehydrate	B.D.H	99
19	Calcium-chloride (anhydrous)	Merck	99
20	Co(II)-chloride hexahydrate	RieDel-DeHaen	99
21	Copper(II)-chloride dehydrate	Fluka	99
22	Hydrochloride acid (36%)	G.C.C	99
23	Manganese(II)-chloride tetrahydrate	B.D.H	99
24	Nickel(II) chloride hexahydrate	B.D.H	99
25	KOH	Scharlau	99.8
26	Potassium selenocyanate	Sigma-Aldrich	97
27	Zn(II)-chloride	Fluka	99

(2.2) Physico-chemical measurements

A range of physico-chemical techniques were used to confirm the entity of precursors, ligands and their metal complexes and as follows;

(2.2.1) Melting point measurements

An electro-thermal Stuart apparatus, model SMP_{30}, was used to determine melting points of compounds.

(2.2.2) Infrared spectra

The Fourier Transfer Infrared spectra were obtained using KBr and CsI discs between 250-4000 cm^{-1} on a Shimadzu (FT–IR)–8400S and Biotic England spectrometers. Spectra were determined at University of Baghdad (College of Education for Pure Science (Ibn Al-Haitham), Central Service Laboratory and College of Science).

(2.2.3) Electronic spectra

The UV-Vis spectra of synthesised compounds were accomplished by a Shimadzu UV-160 between 200-1100 nm. A concentration of 10^{-3} M of tested compounds in DMSO at room temperature using a quartz cell with 1 cm length was used to obtain spectra. The spectra were performed in Ibn Siena Enterprise / Iraqi Ministry of Industry.

(2.2.4) Mass spectra

The electro spray mass spectra (ESMS) of organic compounds (precursors and ligands) and some metal complexes acquired by positive electrospray mass spectroscopy technique (ESMS) using an Agilent LCms sx machine. The spectra recorded at Beirut Arabic University / Lebanon.

(2.2.5) Conductivity measurements

All complexes were measured at room temperature with 10^{-3} M solutions of compounds in DMSO on a EUTECH INSTRUMENTS con 510 digital conductivity meter.

(2.2.6) Metal content

An atomic absorption spectrophotometer (F.A.A) type Shimadzu 680G, was used to measure metals analysis. The analysis was performed at Ibn Siena Enterprise / Iraqi Ministry of Industry.

(2.2.7) Nuclear magnetic resonance spectra

The ^{1}H- and ^{13}C-NMR spectra of the prepared precursors, ligands and diamagnetic complexes were measured in DMSO-d^6 and CDCl$_3$ using a Brücker instrument with 400 and 300 MHz for the ^{1}H and ^{13}C, respectively. A tetramethylsilane (TMS), an internal standard, was used in the ^{1}H-NMR spectra. The title compounds were acquired at Beirut Arabic University / Lebanon. The ^{77}Se-NMR spectra for ligands and their diamagnetic complexes were recorded in DMSO-d^6 using a Brücker 400 MHz instrument with a dimethylselenide (Me$_2$Se) as a reference. The title compounds were measured at Tehran University / Republic Islamic of Iran.

(2.2.8) Elemental microanalyses

Elemental microanalysis (C, H and N) of organic compounds (precursors and ligands) and their metal complexes were measured by EuroEA 3000 instrument. All samples recorded at Central Service Laboratory / College of Education for Pure Science (Ibn Al-Haitham), University of Baghdad.

(2.2.9) Chloride percentage

The method used to measure chloride content is potentiometric titration analysis. It was performed using a potentiometric procedure with 686 – Titro Processor – 665 Dosim A – Metrohm/Swiss apparatus at Ibn Siena Enterprise / Iraqi Ministry of Industry.

(2.2.10) Thermal analysis

TGA, DTG and DSC analyses were performed by STA PT-1000 Linseis Company / Germany instrument with a heating rate 10 °C/min. The compounds measured at Central Service Laboratory / College of Education for Pure Science Ibn Al-Haitham / University of Baghdad.

(2.2.11) Magnetic susceptibility calculation

The susceptibility magnetic moments calculations of the paramagnetic complexes were achieved at room temperature using a Johnson Matthey balance. The title samples were recorded at Central Service Laboratory / College of Science / University of Al-Nahrain.

(2.2.12) Biological assay

The title compounds (ligands and their complexes) were tested toward four types of bacteria *(Escherichia coli, Bacillus stubtilis, Staphylococcus aureus* and *Klebsiella pneumoniac*) and four fungal species (*Candida albican*s, *Candida glabrat*a, *Candida tropicali*s and *Candida parapsilsis*) using agar-well diffusion. The designated wells were borer by a sterile metallic in the media with an area of not less than 6 mm. At a concentration 100 ppm of the test sample. Biological activity was assessed by measuring the diameter of the inhibition zones (mm). All samples recorded at Central Service Laboratory / College of Education for Pure Science Ibn Al-Haitham / University of Baghdad.

(2.2.13) The suggested molecular structure

The predicted molecular structures of the title complexes were optimized using a commercial programme; Chem. Office 2016 3DX Programme.
.

(2.3) Synthesis of the starting material, precursors and ligands

(2.3.1) Synthesis of the starting material (potassium selenocyanate)

The formation of KSeCN was based on a method reported previously [50] as follows;

A mixture of (5.25 g, 80.8 mmol) of potassium cyanide and (6 g, 75.9 mmol) of grey selenium powder was melted on a hotplate using a porcelain evaporating dish at 150 ºC. The melt was mixed manually until the dissolve of all selenium powder. Subsequently, the melt was allowed to cool slowly with constant mixing and then the melt crushed quickly to a fine powder using a porcelain mortar. The above residue was dissolved immediately in a hot acetone (75 ml) and a stream of CO_2 gas was bubbled through the mixture at 50 ºC for 2 h. The solvent was reduced by vacuum and on cooling at room temperature, a solid was formed that collected by filtration and then washed with diethylether (5 ml) and dried in a dark place. Yield: 3.20 g (61%). Analytical data including melting point (m.p= 100-102 ºC) are consistent with that recorded for KSeCN purchased from Sigma-Aldrich.

(2.3.2) Synthesis of precursors

All precursors were prepared according to a traditional method that mentioned in [51,52], which based on a Mannich approach and as follows;

(2.3.2.1) Synthesis of precursor F1

A solution of benzaldehyde (2.8 ml, 26 mmol), ammonium acetate (1 g, 13 mmol) and cyclohexanone (1.3 ml, 13 mmol) [2:1:1] in ethanol (20 ml) was mixed together in a 100 ml round-bottomed flask [51]. The reaction mixture was allowed heating between 30-35 ºC for 6 h, during which time the title compound crushed out as a yellow solid. The solid that isolated by filtration was washed by ethanol several times, and diethylether (10 ml) and then dried in air. Yield: 1.20 g (92%), m.p= 108-110 ºC.

(2.3.2.2) Synthesis of precursors F2 and F3

The method used to prepare F2 and F3 was analogous to that mentioned for F1, but with the use of 4-methoxybenzaldehyde and 4,4`-dimethylaminobenzaldehyde, respectively instead of benzaldehyde. The amounts of other materials used were modified accordingly, and a same isolation procedure was used to give compounds F2 and F3. Table (2-2) represents some physical properties of the precursors. General chemical structure and nomenclature of precursors are depicted in Table (2-3).

(2.3.2.3) Synthesis of precursor N1

A solution of calcium chloride (1.1 g, 10 mmol), benzaldehyde (1 ml, 10 mmol), cyclohexanone (1 ml, 10 mmol) and *m*-nitroaniline (1.4 g, 10 mmol) [1:1:1:1] in ethanol (30 ml) was mixed together in a 150 ml beaker that kept in an ice bath for 30 min. The reaction mixture was allowed heating between 50-60 ºC for 2 h, then stirred at RT for 1 h [52]. The solid that formed was collected by filtration, washed several times with ethanol, and diethylether (10 ml) and then dried in air. Yield: 1.20 g (86%), m.p= 110-112 ºC.
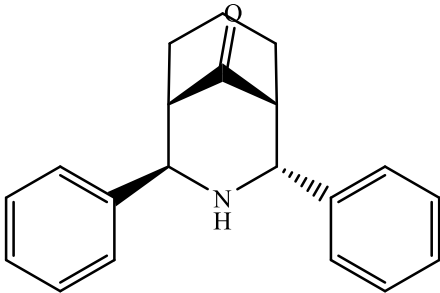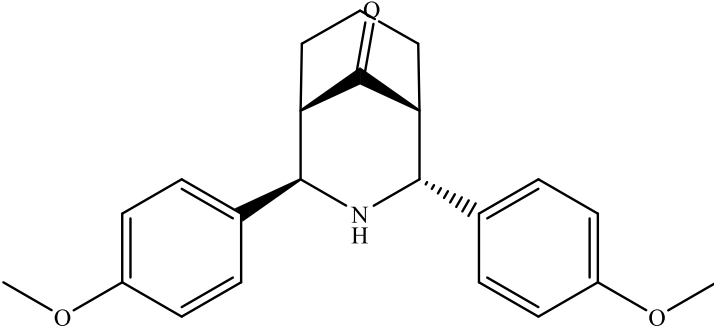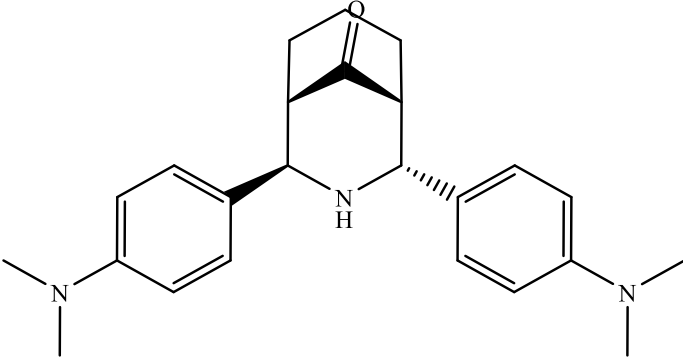
(2.3.2.4) Synthesis of precursor N2 and N3
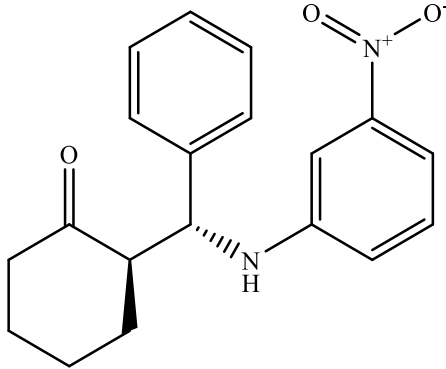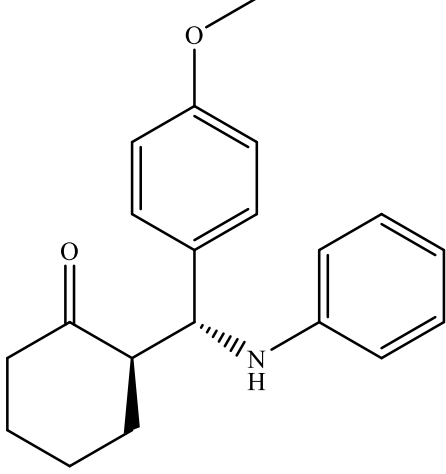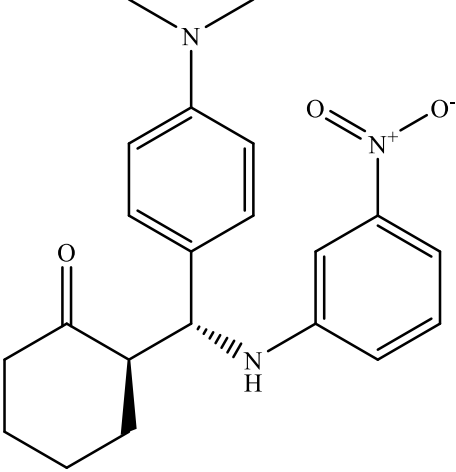
The method used to prepare N2 was analogous to N1 but with the use of 4-methoxybenzaldehyde in place of benzaldehyde and aniline in place of *m*-nitroaniline. Further, N3 was prepared by analogous procedure to that for N1 but with the use of 4,4`-dimethylaminobenzaldehyde in place of benzaldehyde. The amounts of other materials used were modified accordingly, and a similar isolation procedure was used to give compounds N2 and N3. The important physical properties of precursors N1, N2 and N3 are listed in Table (2-2). The general chemical structures and nomenclatures of precursors are depicted in Table (2-3).

Table (2-2): The important physical properties of the precursors F1-F3 and N1-N3.

No.	Precursor	Formula	Wt. (g)	M. wt.	M.p ºC
F1	2,4-diphenyl-3-azabicyclo [3.3.1] nonan-9-one	$C_{20}H_{21}NO$	1.20	291.39	108-110
F2	2,4-bis(4-methoxyphenyl)-3-azabicyclo[3.3.1]nonan-9-one	$C_{22}H_{25}NO_3$	1.05	351.45	122-124
F3	2,4-bis(4-(dimethylamino) phenyl)-3-azabicyclo[3.3.1] nonan-9-one	$C_{24}H_{31}N_3O$	1.02	377.53	131-133
N1	2-(((3-nitrophenyl)amino)(phenyl) methyl) cyclohexan-1-one	$C_{19}H_{20}N_2O_3$	0.85	324.38	110-112
N2	(2S)-2-((4-methoxyphenyl) (phenylamino) methyl)cyclohexan-1-one	$C_{20}H_{23}NO_2$	0.80	309.41	118-120
N3	2-((4-(dimethylamino)phenyl)((3-nitrophenyl)amino)methyl)cyclohexan-1-one	$C_{21}H_{25}N_3O_3$	0.65	367.45	132-134

Table (2-3): Chemical structures and nomenclature of synthesised precursors F1-F3 and N1-N3.

Comp.	Structure	Nomenclature
F1		2,4-diphenyl-3-azabicyclo [3.3.1]nonan-9-one
F2		2,4-bis(4-methoxyphenyl)-3-azabicyclo[3.3.1]nonan-9-one
F3		2,4-bis(4-(dimethylamino) phenyl)-3-azabicyclo [3.3.1]nonan-9-one

Comp.	Structure	Nomenclature
N1		2-(((3-nitrophenyl)amino)(phenyl) methyl)cyclohexan-1-one
N2		2-((4-methoxyphenyl) (phenylamino)methyl)cyclohex an-1-one
N3		2-((4-(dimethylamino) phenyl) ((3-nitrophenyl)amino) methyl) cyclohexan-1one

(2.3.3) Synthesis of HL^1

To a mixture of hydrazine hydrate (0.1 ml, 3 mmol; 99.9%), KSeCN (0.15 g, 1 mmol) and hydrochloride acid (0.1 ml, 3 mmol; 36%) in ethanol (20 ml) was added drop-wise with agitation to a solution of F1 (0.3 g, 1 mmol) in 20 ml of a mixture of CHCl$_3$:EtOH (1:3). The resulted reaction mixture was heated at reflux for 3 h, and filtrated off while it is hot to remove the free grey selenium. The solution was reduced to half under vacuum then kept at room temperature. The solid that formed was collected by filtration, washed with diethylether (5 ml) and dried in air. Yield: 0.21 g (70%), m.p= 270-272 °C.
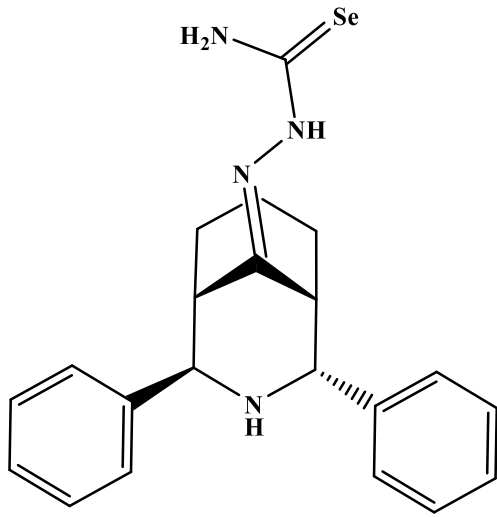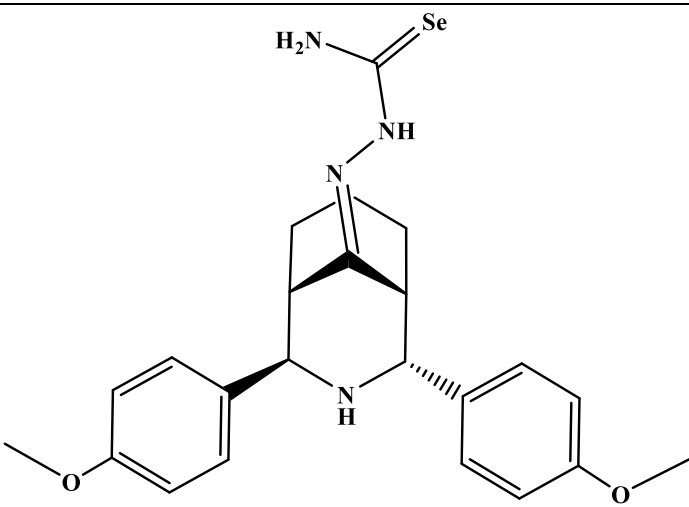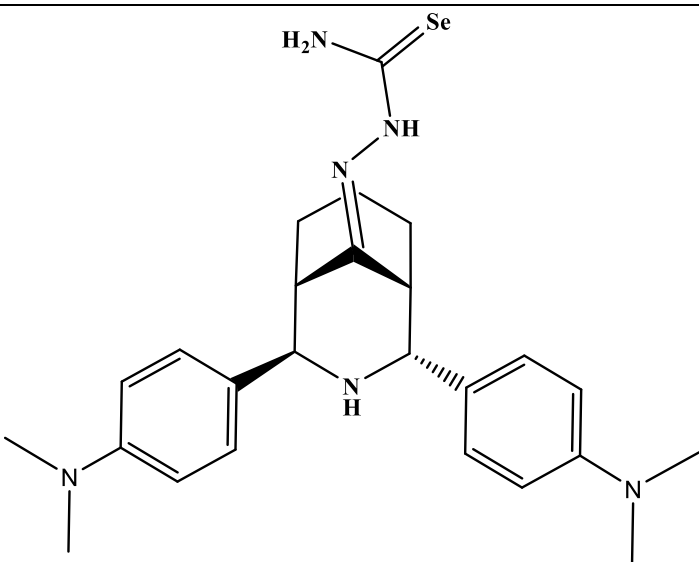
(2.3.3.1) Synthesis of HL^2-HL^6
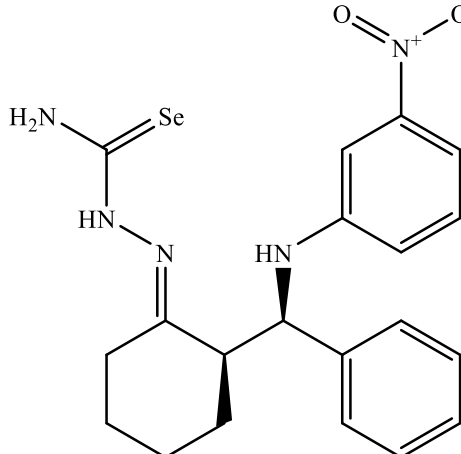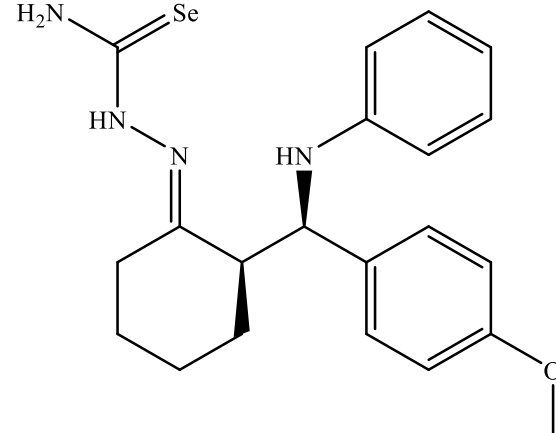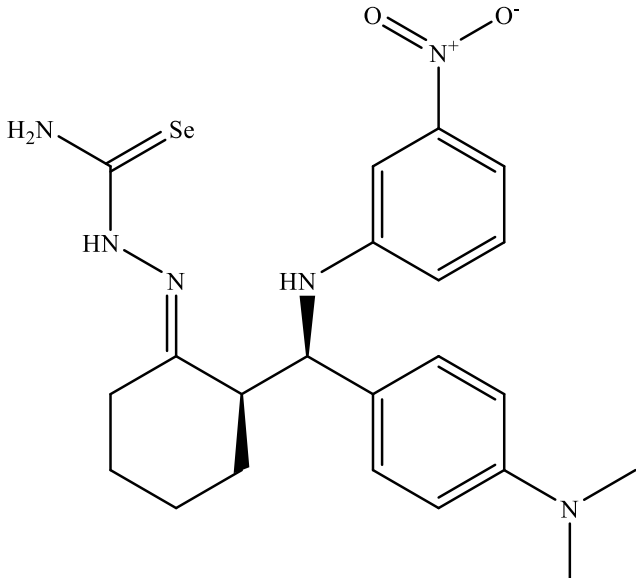
The method adopted to prepare HL^2-HL^6 was similar to that for HL^1, but with the use of precursors F2 and F3 for ligands HL^2 and HL^3, respectively. Whereas ligands HL^4-HL^6 were prepared using precursors N1-N3, respectively. The amount of starting materials used to obtain ligands, colours, yields and melting points are placed in Table (2-4). The structures of the prepared ligands and their nomenclature are included in Table (2-5).

Table (2-4): Weight of precursors, colours, yield percentage and melting points of HL^1- HL^6.

Ligand	Weight of (F1-F3) and (N1-N3) (g)	Yield (%)	Colour	M.p. °C
HL^1	0.30	70	Pale-orange	270-272
HL^2	0.30	66	Deep-orange	265-267
HL^3	0.30	60	Orange	251-253
HL^4	0.30	51	Deep-orange	244-246
HL^5	0.30	50	Deep-orange	243-245
HL^6	0.30	41	Brown	265-267

Table (2-5): Chemical structures and nomenclature of synthesised ligands HL^1-HL^6.

Comp.	Chemical structure	Nomenclature
HL^1		diphenyl-3--2,4)-2 azabicyclo[3.3.1]nonan-9-ylidene)hydrazine-1-carboselenoamide
HL^2		bis(4-methoxyphenyl)--2,4)-2 3-azabicyclo[3.3.1]nonan-9-ylidene)hydrazine-1-carboselenoamide
HL^3		bis(4--2,4)-2 (dimethylamino)phenyl)-3-azabicyclo[3.3.1]nonan-9-ylidene)hydrazine-1-carboselenoamide

Comp.	Chemical structure	Nomenclature
HL^4		E)-2-(2-(((3-nitrophenyl)) amino) (phenyl)methyl) cyclohexylidene)hydrazine-1-carboselenoamide
HL^5		E)-2-(2-((4-)) methoxyphenyl) (phenylamino)methyl) cyclohexylidene)hydrazine-1-carboselenoamide
HL^6		E)-2-(2-((4-) (dimethylamino)phenyl)((3-nitrophenyl)amino) methyl)cyclohexylidene)hyd razine-1-carboselenoamide

(2.4) Synthesis of metal complexes

(2.4.1) Synthesis of complexes with HL^1 ligand

(2.4.1.1) Synthesis of $K_2[Mn(L^1)_2Cl_2]$ complex

A mixture of manganese(II) chloride tetrahydrate (0.024 g, 0.122 mmol) in 10 ml of ethanol was added drop-wise to a solution of HL^1 (0.1 g, 0.243 mmol) in 20 ml of a mixture of $CHCl_3$:EtOH (1:3). The pH of the reaction mixture was adjusted by adding potassium hydroxide, pH= 9, and then allowed to stir for 3 h. The dark blue precipitate that formed was collected on a filter paper, washed with cold pure ethanol (5 ml) and then dried in air. Yield: 0.012 g (50%), m.p= 280-284 ºC.

(2.4.1.2) Synthesis of $K_2[Co(L^1)_2Cl_2]$, $K_2[Ni(L^1)_2Cl_2]$, $[Cu(L^1)_2]$, $[Zn(L^1)_2]$ and $[Cd(L^1)_2]$ complexes

The method implemented to isolate complexes of HL^1 with Co^{II}, Ni^{II}, Cu^{II}, Zn^{II} and Cd^{II} metal was similar to that mentioned in (2.4.1.1) of the formation of $K_2[Mn(L^1)_2Cl_2]$. Table (2-6) displays the important physical features of the title complexes and their reactants quantities.

(2.4.2) Synthesis of HL^2-HL^6 metal complexes
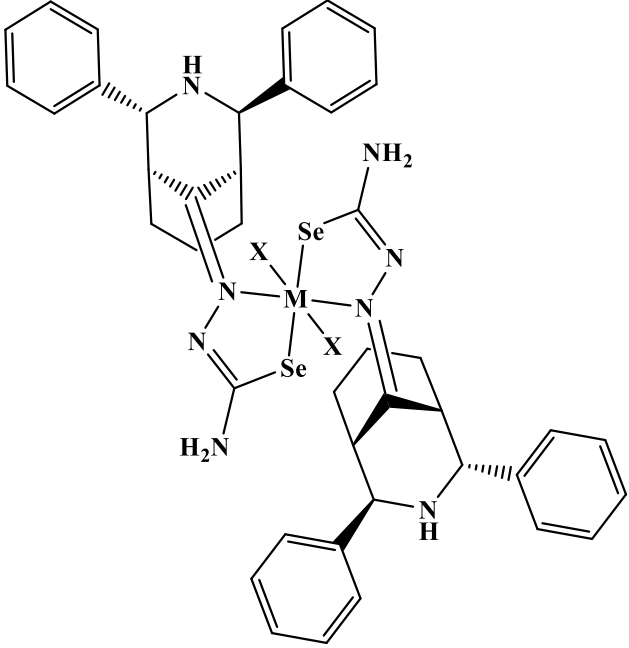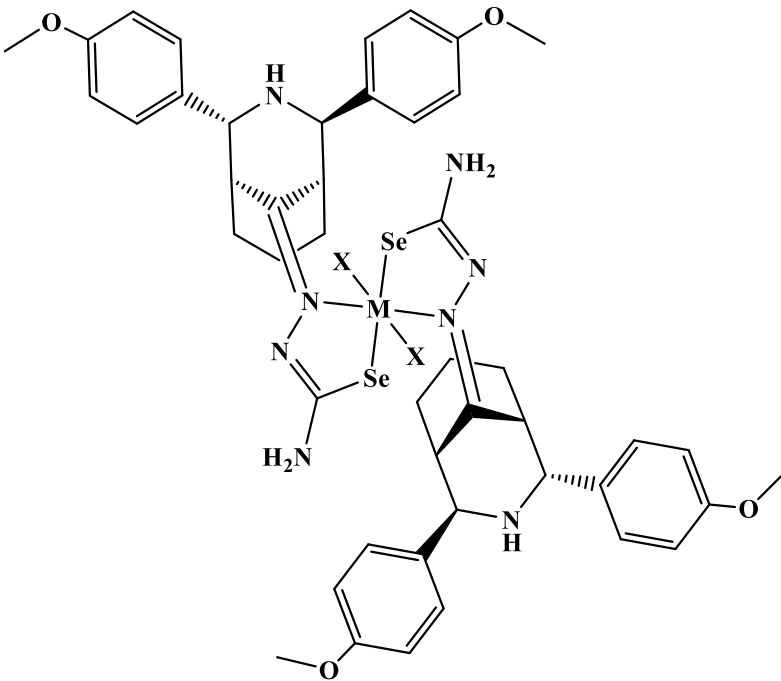
A same method to that reported in the synthesis of $K_2[Mn(L^1)_2Cl_2]$ was implemented to isolate other HL^2, HL^3, HL^4, HL^5 and HL^6 complexes with $MnCl_2.4H_2O$, $CoCl_2.6H_2O$, $NiCl_2.6H_2O$, $CuCl_2.2H_2O$, $ZnCl_2$ and $CdCl_2.2H_2O$ salts. Table (2-6) represent selected physical properties, weight of metal salts and yields of the prepared complexes. The Table (2-7) represents suggested chemical structure of complexes.
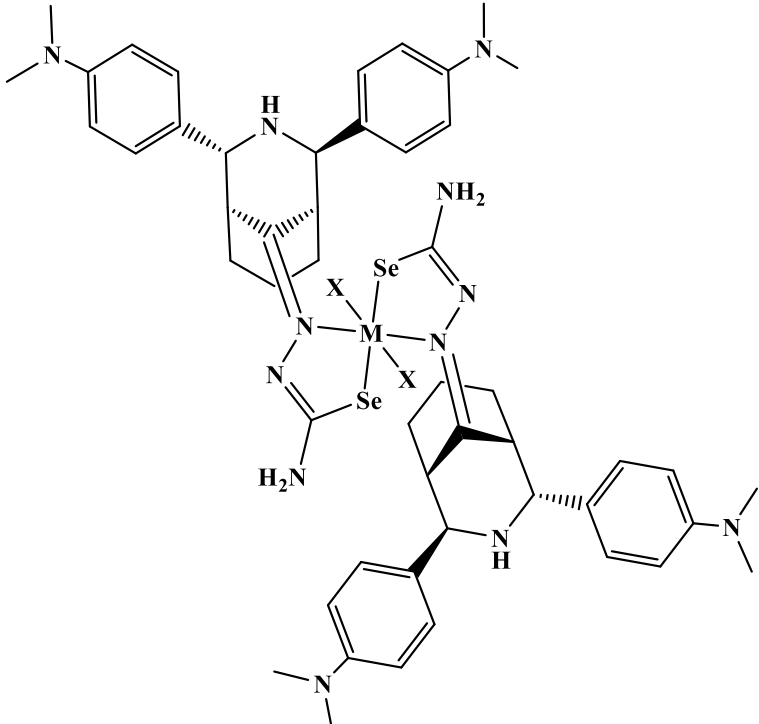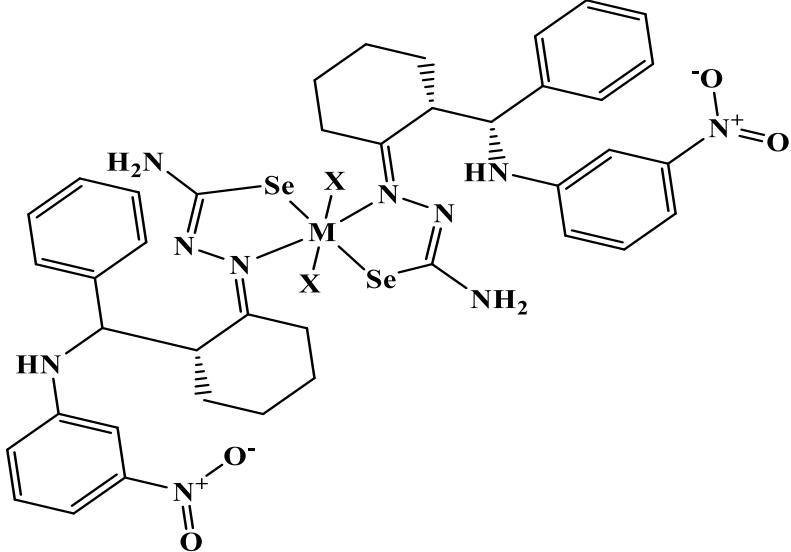
Table (2-6): The important physical properties of complexes with HL^1-HL^6 and their reactants quantities.
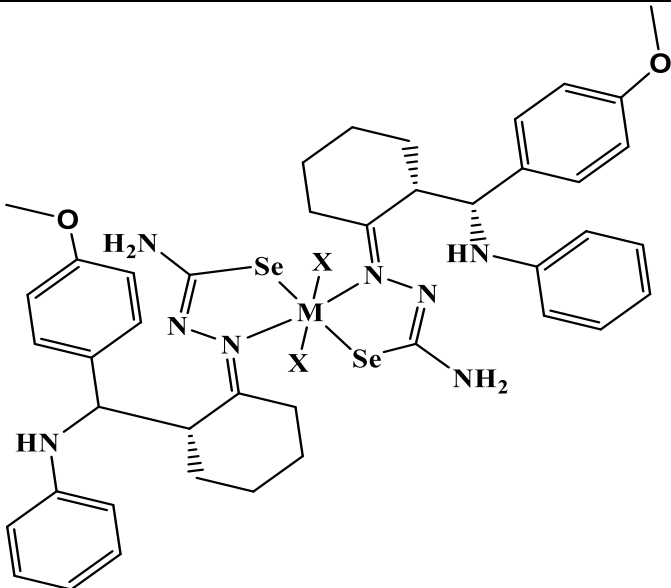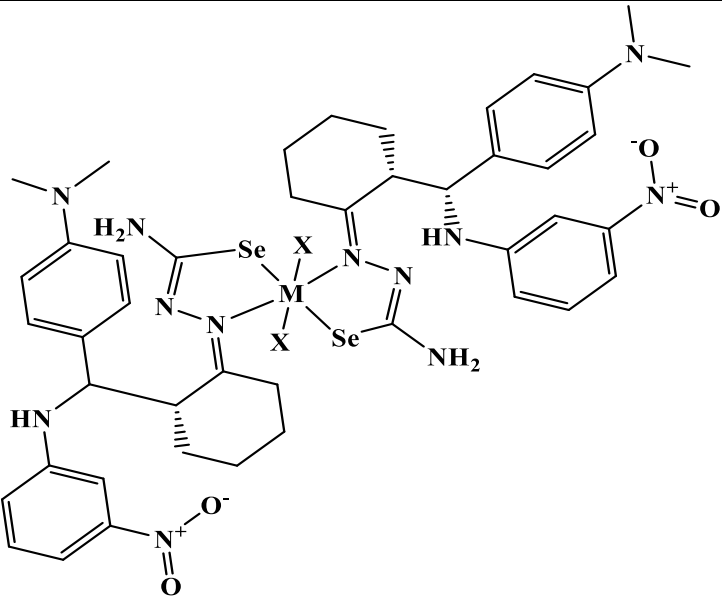
Metal ion	Colour	M.p °C	Wt. of metal salt (g)	Wt. of product (g)	Yield (%)
COMPLEXES OF HL^1					
Mn(II)	Dark-blue	280-284	0.024	0.012	50
Co(II)	Deep-brown	241-244	0.029	0.021	72
Ni(II)	Dark-orange	291-293	0.029	0.022	76
Cu(II)	Light-brown	288-290	0.021	0.013	62
Zn(II)	Light-brown	287-289	0.016	0.010	63
Cd(II)	Deep-brown	304-306	0.027	0.011	41
COMPLEXES OF HL^2					
Mn(II)	Brown	266-268	0.021	0.011	52
Co(II)	Red-brown	245-247	0.025	0.017	68
Ni(II)	Dark-orange	285-287	0.025	0.016	64
Cu(II)	Dark-brown	299-302	0.018	0.012	67
Zn(II)	Light-brown	287-289	0.014	0.011	79
Cd(II)	Deep-brown	296-2 98	0.012	0.009	75
COMPLEXES OF HL^3					
Mn(II)	Deep-brown	277-279	0.020	0.013	65
Co(II)	Brown	287-289	0.024	0.015	63
Ni(II)	Light-orange	290-292	0.024	0.014	58
Cu(II)	Dark-brown	296-298	0.017	0.012	71
Zn(II)	Light-brown	305-307	0.027	0.018	67
Cd(II)	Deep-brown	311-313	0.012	0.008	67

Metal ion	Colour	M.p °C	Wt. of metal salt (g)	Wt. of product (g)	Yield (%)
COMPLEXES OF HL^4					
Mn(II)	Deep-brown	276-278	0.022	0.015	68
Co(II)	Red-brown	287-289	0.027	0.016	59
Ni(II)	Light-orange	299-301	0.027	0.017	63
Cu(II)	Dark-brown	296-298	0.019	0.011	58
Zn(II)	Light-brown	288-290	0.015	0.010	67
Cd(II)	Deep-brown	312-314	0.013	0.009	69
COMPLEXES OF HL^5					
Mn(II)	Brown	276-278	0.023	0.015	65
Co(II)	Dark-brown	287-289	0.028	0.016	57
Ni(II)	deep-orange	299-301	0.028	0.014	50
Cu(II)	Dark-brown	296-298	0.020	0.012	60
Zn(II)	Light-brown	288-290	0.031	0.013	42
Cd(II)	Light-brown	312-314	0.013	0.007	54
COMPLEXES OF HL^6					
Mn(II)	Deep-brown	288-290	0.020	0.014	70
Co(II)	Dark-brown	291-293	0.024	0.015	63
Ni(II)	Deep-orange	306-308	0.024	0.013	54
Cu(II)	Dark-brown	299-301	0.017	0.011	65
Zn(II)	Light-brown	309-311	0.014	0.010	71
Cd(II)	Light-brown	313-315	0.012	0.007	58

Table (2-7): Suggested chemical structure of complexes.

Ligand	Suggested chemical structure	Metal ion
HL^1		M= Mn(II), Co(II) and Ni(II). X= Cl M= Cu(II), Zn(II) and Cd(II). X= 0
HL^2		M= Mn(II), Co(II) and Ni(II). X= Cl M= Cu(II), Zn(II) and Cd(II). X= 0

46

Ligand	Suggested chemical structure	Metal ion
HL^3		M= Mn(II), Co(II) and Ni(II). X= Cl M= Cu(II), Zn(II) and Cd(II). X= 0
HL^4		M= Mn(II), Co(II) and Ni(II). X= Cl M= Cu(II), Zn(II) and Cd(II). X= 0

Ligand	Suggested chemical structure	Metal ion
HL^5		M= Mn(II), Co(II) and Ni(II). X= Cl M= Cu(II), Zn(II) and Cd(II). X= 0
HL^6		M= Mn(II), Co(II) and Ni(II). X= Cl M= Cu(II), Zn(II) and Cd(II). X= 0

CHAPTER THREE

RESULTS AND DISCUSSION

(3) Results and discussion

(3.1) Synthesis and characterisation of precursors and ligands

(3.1.1) Synthesis and characterisation of precursors F1-F3

(3.1.1.1) Synthesis and characterisation of 2,4-diphenyl-3-azabicyclo[3.3.1]nonan-9-one (F1)

The synthesis of F1 is based on a reported method mentioned in [51] as follows:

A one-pot Mannich reaction was used for the preparation of compound F1. The condensation reaction of benzaldehyde with cyclohexanone and ammonium acetate in a 2:1:1 mole ratio at 30-35 ºC in EtOH solvent resulted in the formation of compound F1 in a moderate yield, See Scheme (3-1).

(3.1.1.2) Synthesis and characterisation of F2 and F3

The used method of the preparation of F2 and F3 compounds is the same as that mentioned in the synthesis of starting material F1, but with the use of 4-methoxybenzaldehyde and 4,4`-dimethyl aminobenzaldehyde of F2 and F3 compounds, respectively in place of benzaldehyde with cyclohexanone and ammonium acetate in a 2:1:1 mole ratio. Compounds F2 and F3 in almost quantitative yield, See Scheme (3-1). The compounds F1, F2 and F3 are soluble in the following organic solvents; hot MeOH, acetone, C_6H_6, CH_2Cl_2, $CHCl_3$, DMSO and DMF, Table (3-1). The isolated compounds characterised by elemental analysis (Table (3-2)), FT-IR (Table (3-3)) and ^{1}H-, ^{13}C-NMR and mass spectra.
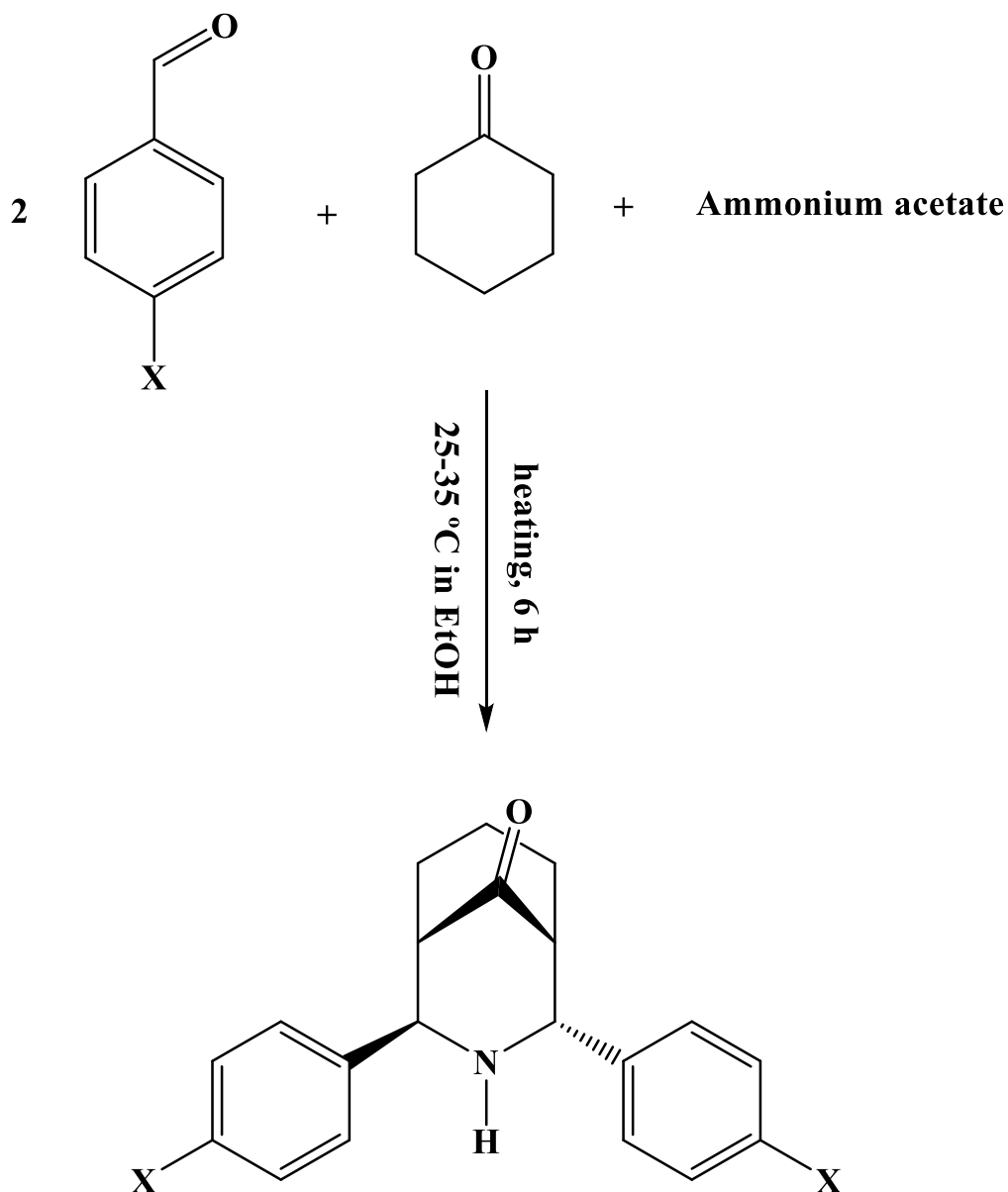
X = 0, F1 = 2,4-diphenyl-3-azabicyclo[3.3.1]nonan-9-one
X = OMe, F2 = 2,4-bis(4-methoxyphenyl)-3-azabicyclo[3.3.1]nonan-9-one
X = N(Me)$_2$, F3 = 2,4-bis(4-(dimethylamino)phenyl)-3-azabicyclo[3.3.1]nonan-9-one

Scheme (3-1): General preparation route of F1, F2 and F3.

(3.1.1.3) Synthesis and characterisation of 2-(((3nitrophenyl)amino) (phenyl)methyl)cyclohexan-1-one (N1)

The synthesis of N1 is based on a reported method mentioned in [52] as follows:

The formation of compound N1 was achieved *via* a one-pot Mannich reaction. The reaction between calcium chloride and benzaldehyde with cyclohexanone and *m*-nitro aniline in a 1:1:1:1 mole ratio in EtOH solvent at heating between 50-60 ºC for 2 h gave compound N1 in almost quantitative yield, see Scheme (3-2).

(3.1.1.4) Synthesis and characterisation of N2 and N3

An analogous method to that mentioned for N1 was implemented for the preparation of N2 and N3 compounds, but with the use of *p*-methoxybenzaldehyde in place of benzaldehyde with cyclohexanone and aniline for as N2. While, 4,4`-dimethyl aminobenzaldehyde was used in place of benzaldehyde with cyclohexanone and *m*-nitroaniline for as N3, in a 1:1:1:1 mole ratio. The mixture was heated between 50-60 ºC in EtOH solvent to give the title compounds N2 and N3 in almost quantitative yield, see Scheme (3-2). The compounds N1, N2 and N3 are soluble in the following organic solvents; hot MeOH, acetone, C_6H_6, CH_2Cl_2, $CHCl_3$, DMSO and DMF, Table (3-1). The isolated precursors were checked by C.H.N (Table (3-2)), FT-IR (Table (3-3)) and ^{1}H-, ^{13}C-NMR and mass spectra.
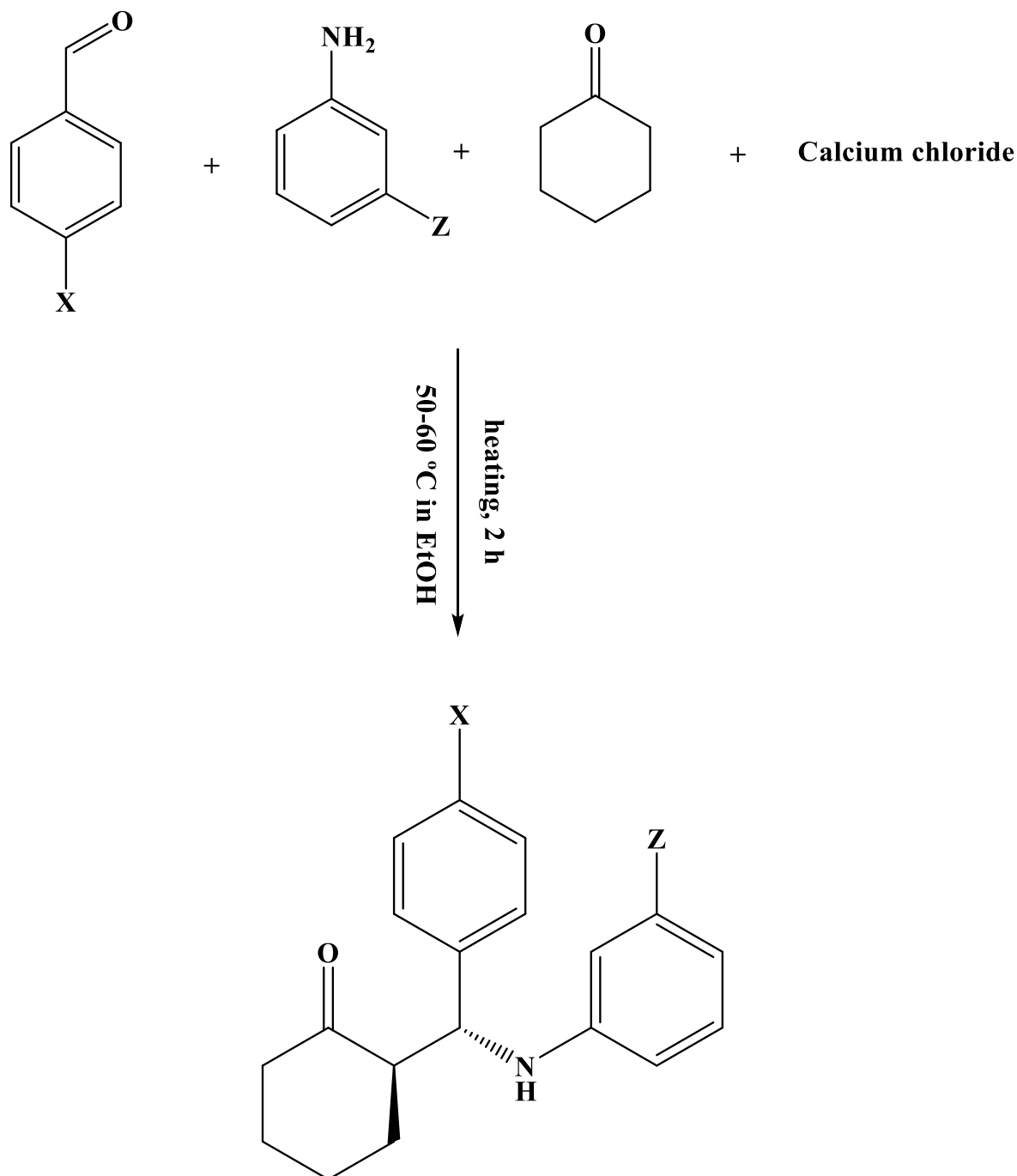
50-60 °C in EtOH

heating, 2 h

X = 0, Z = NO$_2$, N1 = 2-(((3-nitrophenyl)amino)(phenyl)methyl)cyclohexan-1-one
X = OMe, Z = 0, N2 = 2-((4-methoxyphenyl)(phenylamino)methyl)cyclohexan-1-one
X = N(Me)$_2$, Z = NO$_2$, N3 = 2-((4-(dimethylamino)phenyl)((3-nitrophenyl)amino)methyl)cyclohexan-1-one

Scheme (3-2): General synthetic route of precursors N1-N3.

(3.1.2) Synthesis and characterisation of ligands

(3.1.2.1) Synthesis and characterisation of HL^1

The preparation of HL^1 was derived from the reaction of precursor F1 with KSeCN and NH_2NH_2 in a 1:1:3 mole ratio in a mixture of $CHCl_3$:EtOH (1:3). The reaction mixture was heated at reflux for 3h, and the title ligand was formed when solvent removed under reduced pressure, Scheme (3-3).

(3.1.2.2) Synthesis and characterisation of HL^2-HL^6

The method used for the preparation of ligands HL^2-HL^6 is similar to that mentioned for HL^1, but with F2 and F3 in place of F1 for ligands HL^2 and HL^3, respectively. Further, precursors N1, N2 and N3 were used in place of F1-F3 to prepare ligands HL^4, HL^5 and HL^6, respectively (Scheme (3-3)). Physico-chemical tools were used for the characterisation of ligands including; elemental analysis (Table (3-2)), FT-IR (Table 3-4)), ^{1}H-, ^{13}C-, ^{77}Se-NMR, mass spectra and thermal analysis. Table (3-1) includes the solubility of ligands in common solvents.

X = 0, (F1)
X = OMe, (F2)
X = N(Me)$_2$, (F3)

X = 0, Z = NO$_2$ (N1)
X = OMe, Z = 0, (N2)
X = N(Me)$_2$, Z = NO$_2$, (N3)

NH$_2$NH$_2$ | HCl
KSeCN | PH= (3-4)

NH$_2$NH$_2$ | HCl
KSeCN | PH= (3-4)

X = 0, (HL^1)
X = OMe, (HL^2)
X = N(Me)$_2$, (HL^3)

X = 0, Z = NO$_2$ (HL^4)
X = OMe, Z = 0, (HL^5)
X = N(Me)$_2$, Z = NO$_2$, (HL^6)
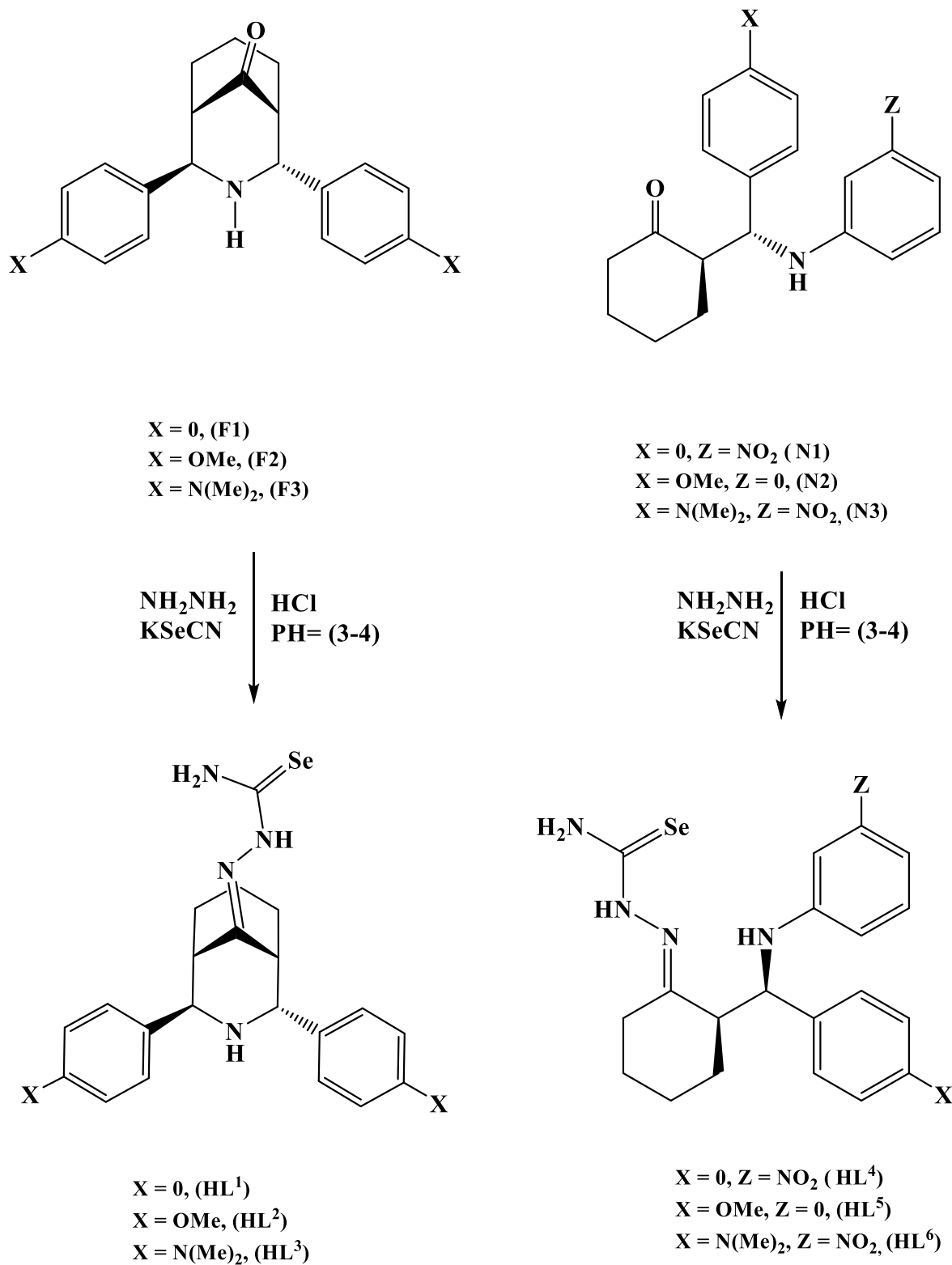
Scheme (3-3): General preparation route of ligands HL^1-HL^6.

54

Table (3-1): Solubility of organic compounds (precursors and ligands) in a variety of solvents.

Compound	H_2O	C_6H_6	DMSO	DMF	CH_3OH	C_2H_5OH	$CHCl_3$
F1	-	+	+	+	-	-	+
F2	-	+	+	+	-	-	+
F3	-	+	+	+	-	-	+
N1	-	+	+	+	-	-	+
N2	-	+	+	+	-	-	+
N3	-	+	+	+	÷	-	+
HL^1	-	+	+	+	-	-	+
HL^2	-	+	+	+	-	-	+
HL^3	-	+	+	+	-	-	+
HL^4	-	+	+	+	-	-	+
HL^5	-	+	+	+	-	-	+
HL^6	-	+	+	+	-	-	+

(+)= soluble, (-)= insoluble, (÷)= sparingly soluble

Table (3-2): Microanalyses results and some physical properties for precursors and ligands.

Compound	Empirical formula	M.wt g/mol	Yield (%)	M.p. ºC	Colour	Found/(Calc.)%		
						C	H	N
F1	$C_{20}H_{21}NO$	291.39	93	108-110	Yellow	82.33 (82.36)	7.20 (7.21)	4.79 (4.81)
F2	$C_{22}H_{25}NO_3$	351.45	81	122-124	Deep yellow	75.09 (75.12)	7.09 (7.11)	3.97 (3.98)
F3	$C_{24}H_{31}N_3O$	377.53	78	131-133	Deep yellow	76.24 (76.29)	8.01 (8.21)	11.12 (11.13)
N1	$C_{19}H_{20}N_2O_3$	324.38	86	110-112	Off white	70.22 (70.29)	6.15 (6.17)	8.61 (8.63)
N2	$C_{20}H_{23}NO_2$	309.41	80	118-120	Off white	77.51 (77.57)	7.41 (7.43)	4.51 (4.53)
N3	$C_{21}H_{25}N_3O_3$	367.45	65	132-134	Deep yellow	68.55 (68.58)	6.79 (6.80)	11.40 (11.43)
HL^1	$C_{21}H_{24}N_4Se$	411.41	70	270-272	Pale orange	61.20 (61.25)	5.81 (5.83)	13.60 (13.61)
HL^2	$C_{23}H_{28}N_4O_2Se$	471.46	66	265-267	Dark orange	58.51 (58.54)	5.93 (5.94)	11.87 (11.88)
HL^3	$C_{25}H_{34}N_6Se$	497.55	60	251-253	Orange	60.28 (60.30)	6.80 (6.83)	16.84 (16.88)
HL^4	$C_{20}H_{23}N_5O_2Se$	444.40	51	244-246	Dark orange	53.98 (54.01)	5.17 (5.18)	15.74 (15.75)
HL^5	$C_{21}H_{26}N_4OSe$	429.43	50	243-245	Dark orange	58.65 (58.68)	6.01 (6.06)	13.01 (13.04)
HL^6	$C_{22}H_{28}N_6O_2Se$	487.47	41	265-267	Brown	54.12 (54.16)	5.71 (5.74)	17.20 (17.23)

(3.2) FT-IR spectra of starting materials, precursors and ligands

(3.2.1) FT-IR spectra of starting materials

The FT-IR spectra of benzaldehyde, cyclohexanone, ammonium acetate, aniline and KSeCN are depicted in Figure (3.1 a, b, c and d), respectively.
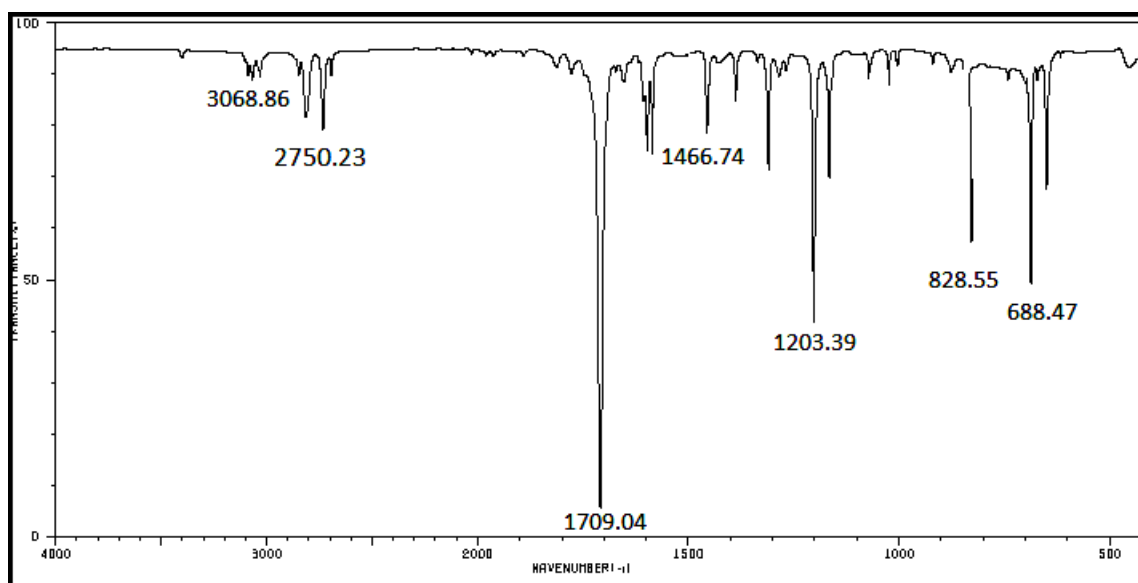
Figure (3-1 a): FT-IR chart of benzaldehyde.
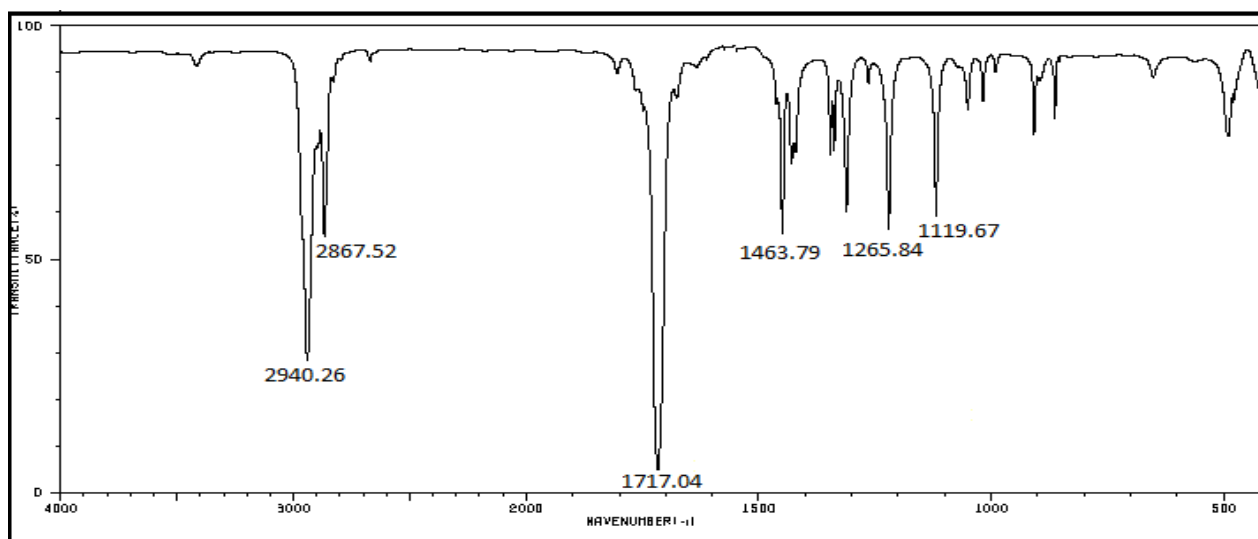
Figure (3-1 b): FT-IR chart of cyclohexanone.
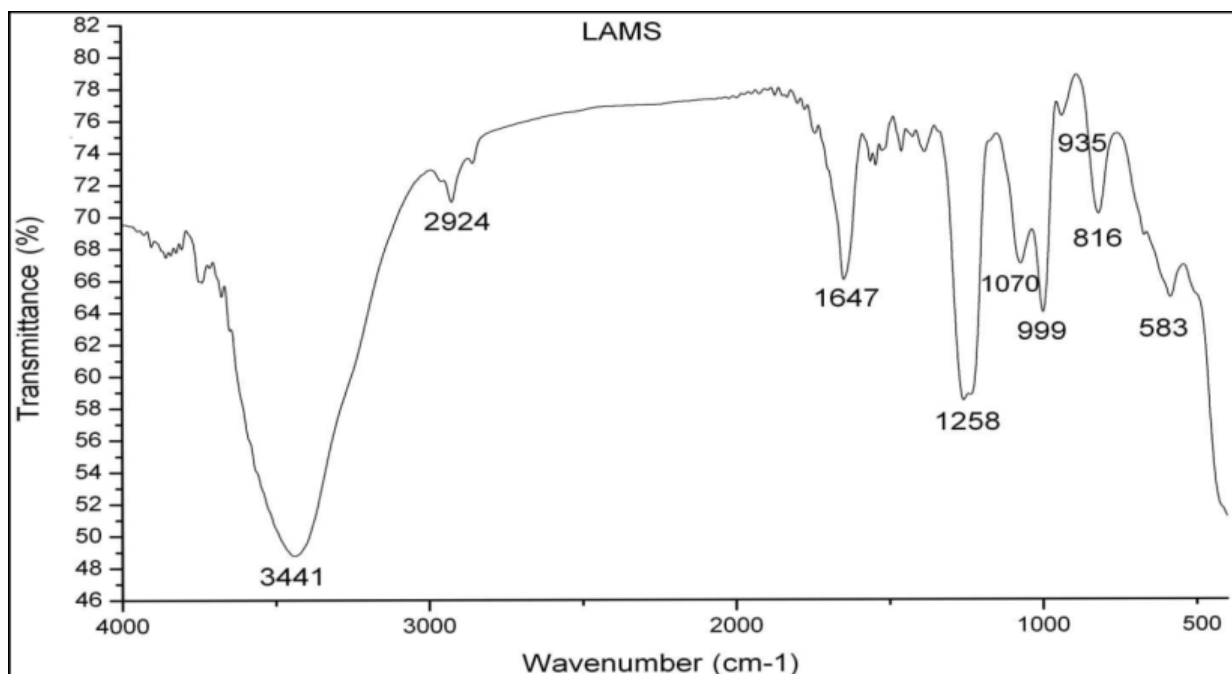
Figure (3-1 c): FT-IR chart of ammonium acetate.
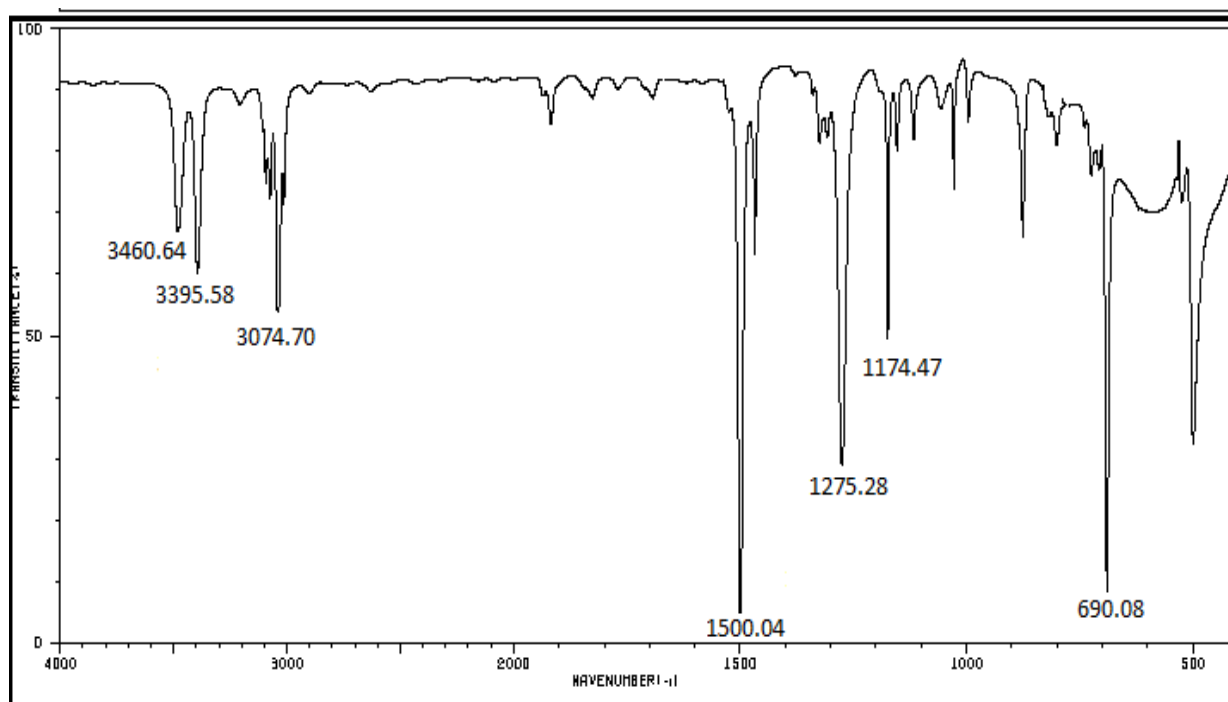
Figure (3-1 d): FT-IR chart of aniline.
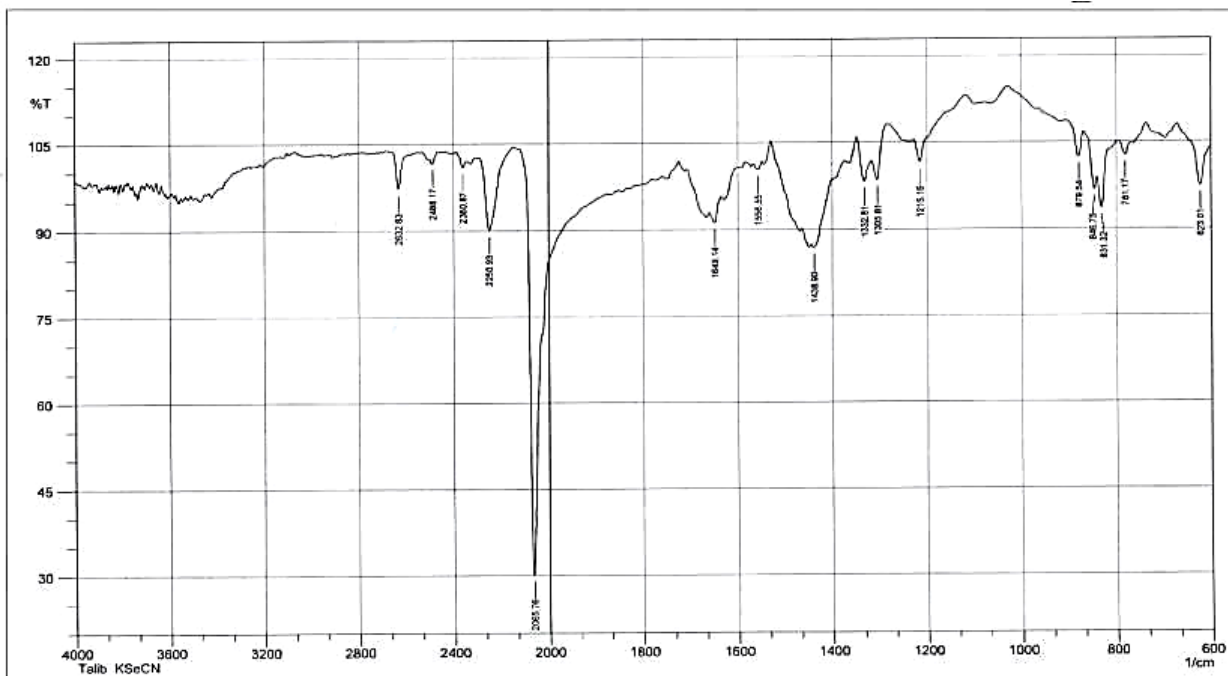
Figure (3-1 e): FT-IR chart of KSeCN.

(3.2.2) FT-IR spectra of precursors

(3.2.2.1) FT-IR spectrum of 2,4-diphenyl-3-azabicyclo[3.3.1]nonan-9-one (F1)

The FT-IR spectrum of F1, Figure (3-2), is checked against the FT-IR of benzaldehyde (Figure (3-1 a)), cyclohexanone (Figure (3-1 b)) and ammonium acetate (Figure (3-1 c)). The spectrum of F1 indicates a band at 3305 cm^{-1} attributed to ν(N-H) stretching of the secondary amine [53], compared with ammonium acetate spectrum. Peaks at 1707 and 1600 cm^{-1} correlated to ν(C=O) of ketone moiety [54] and ν(C=C) group of aromatic system [55], respectively. Band that attributed to δ(N-H) was recorded at 1456 cm^{-1}. The assignments of functional bands are included in Table (3-3).
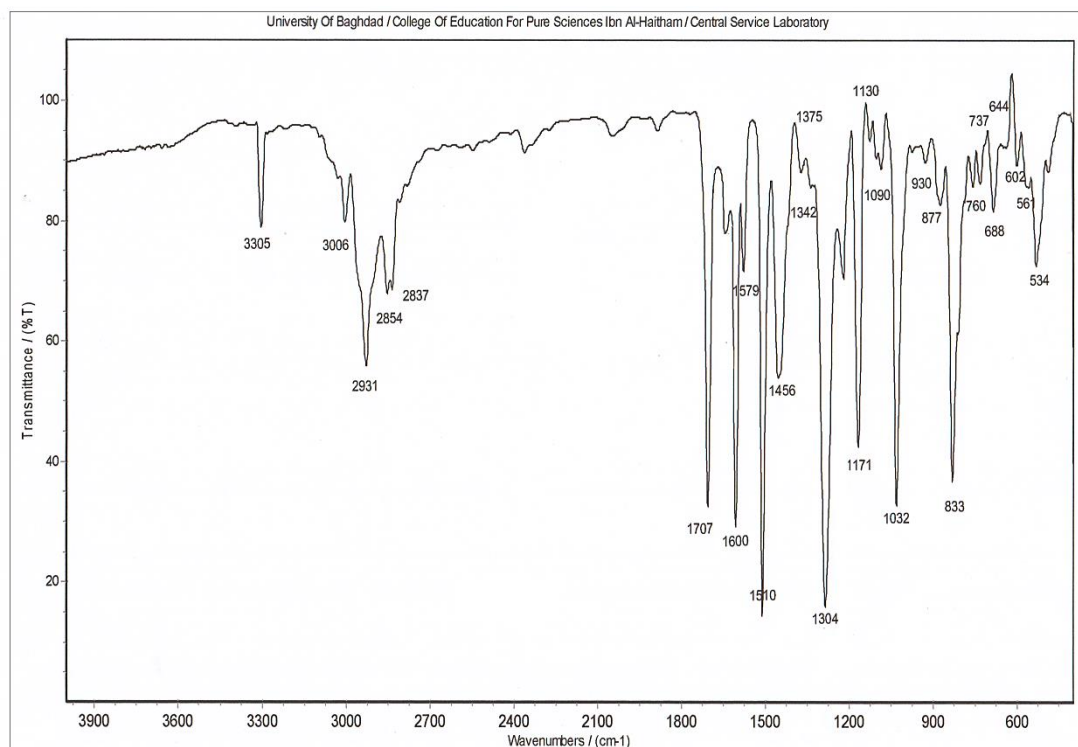
Figure (3-2): FT-IR chart of F1.

(3.2.2.2) FT-IR spectra of precursors F2 and F3

The FT-IR spectra of precursors F2 and F3 are shown in Figures (3-3 and 3-4). The spectra revealed a similar pattern of bands to that of F1 and a similar explanation may implement to discuss the spectra. The assignments of characteristic functional groups are tabulated in Table (3-3).

60
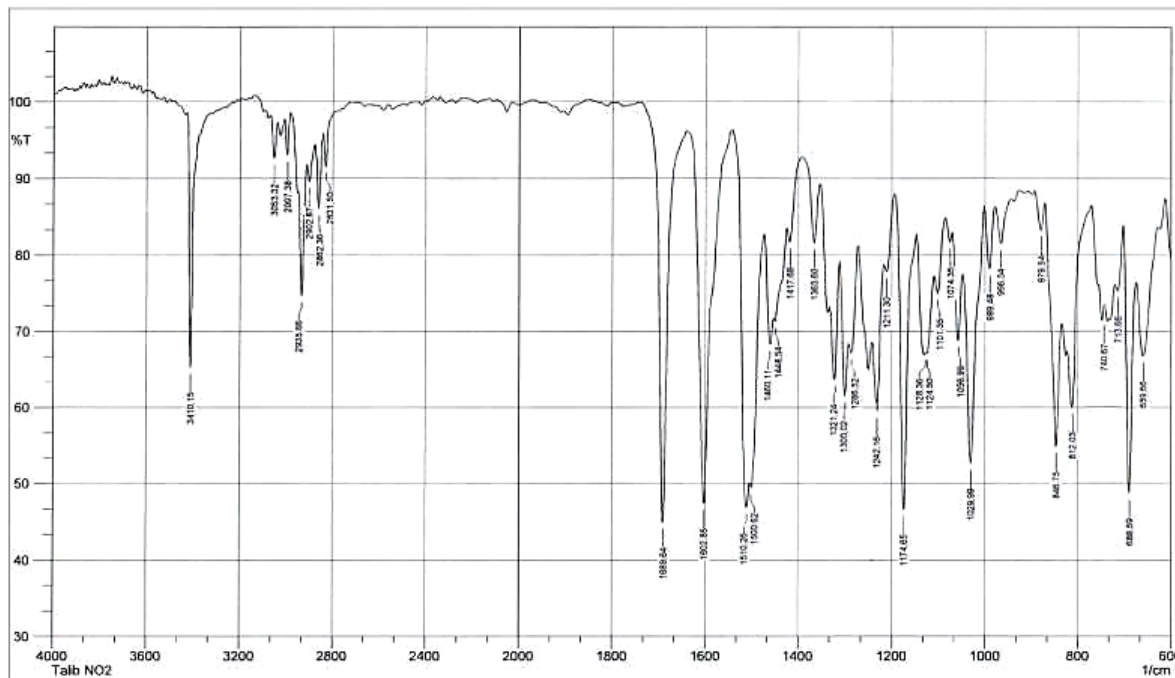
Figure (3-3): FT-IR chart of F2.
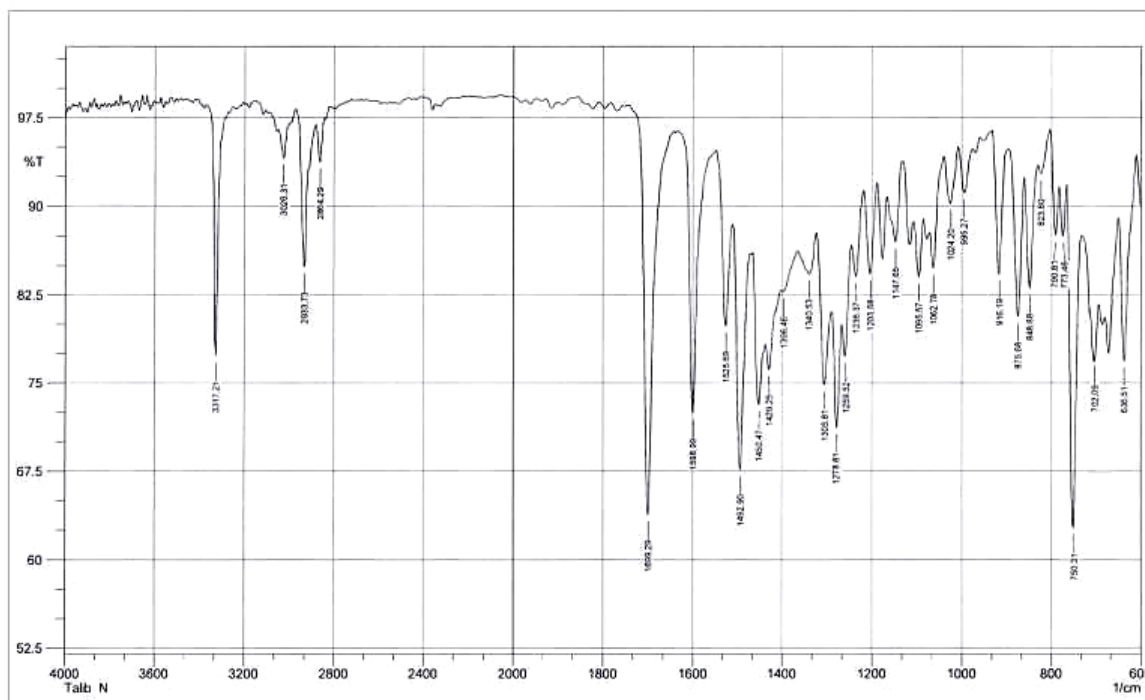
Figure (3-4): FT-IR chart of F3.

(3.2.2.3) FT-IR spectrum of 2-(((3 nitrophenyl)amino) (phenyl)methyl) cyclohexan-1-one (N1)

The FT-IR spectrum of N1, see Figure (3-5), is checked against the FT-IR of benzaldehyde (Figure (3-1 a)), cyclohexanone (Figure (3-1 b)) and aniline (Figure (3-1 d)). The FT-IR of N1 indicates a band at 3379 cm^{-1} that attributed to ν(N-H) stretching of the secondary amine [53], compared with the aniline spectrum. Bands at 1703 and 1601, 1527 cm^{-1} assigned to ν(C=O) of ketone group [54] and ν(C=C) group of the aromatic system [55], respectively. Band that attributed to δ(N-H) was recorded at 1450 cm^{-1}. The assignments of functional groups are listed in Table (3-3).
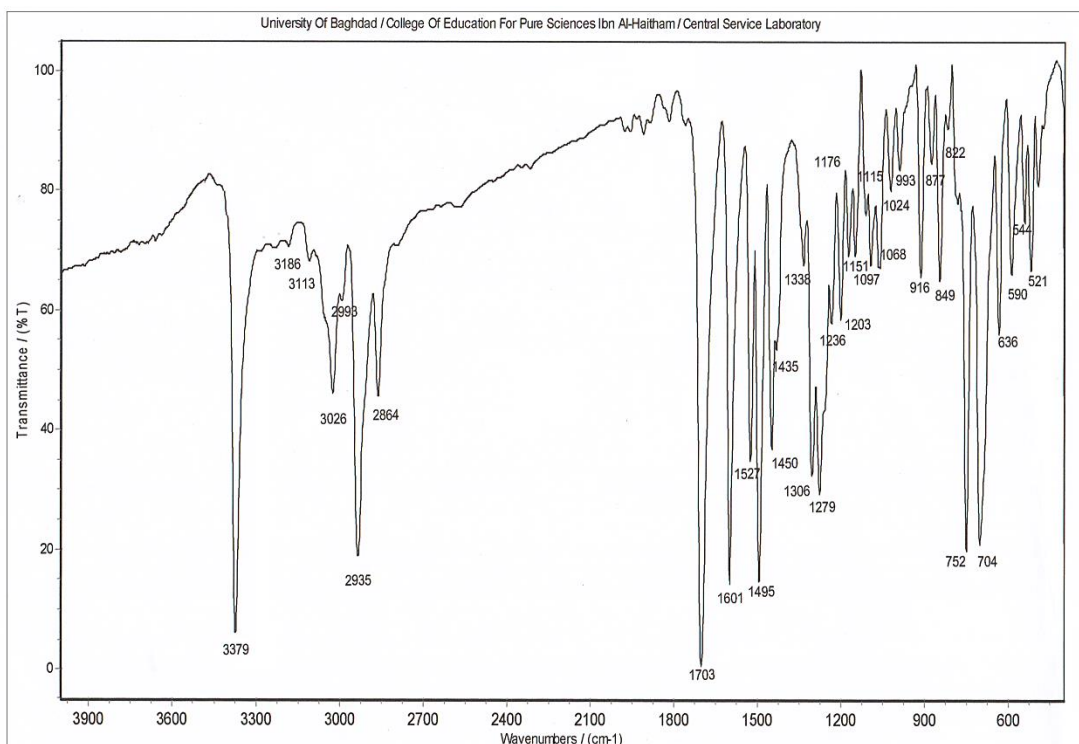
Figure (3-5): FT-IR chart of N1.

(3.2.2.4) FT-IR spectra of precursors N2 and N3

The FT-IR spectra of N2 and N3 depict in Figures (3-6 and 3-7). The obtained spectra recorded analogues features to that observed in N1. Therefore, a similar explanation can implement to explain the spectra. The assignments of the functional groups are listed in Table (3-3).
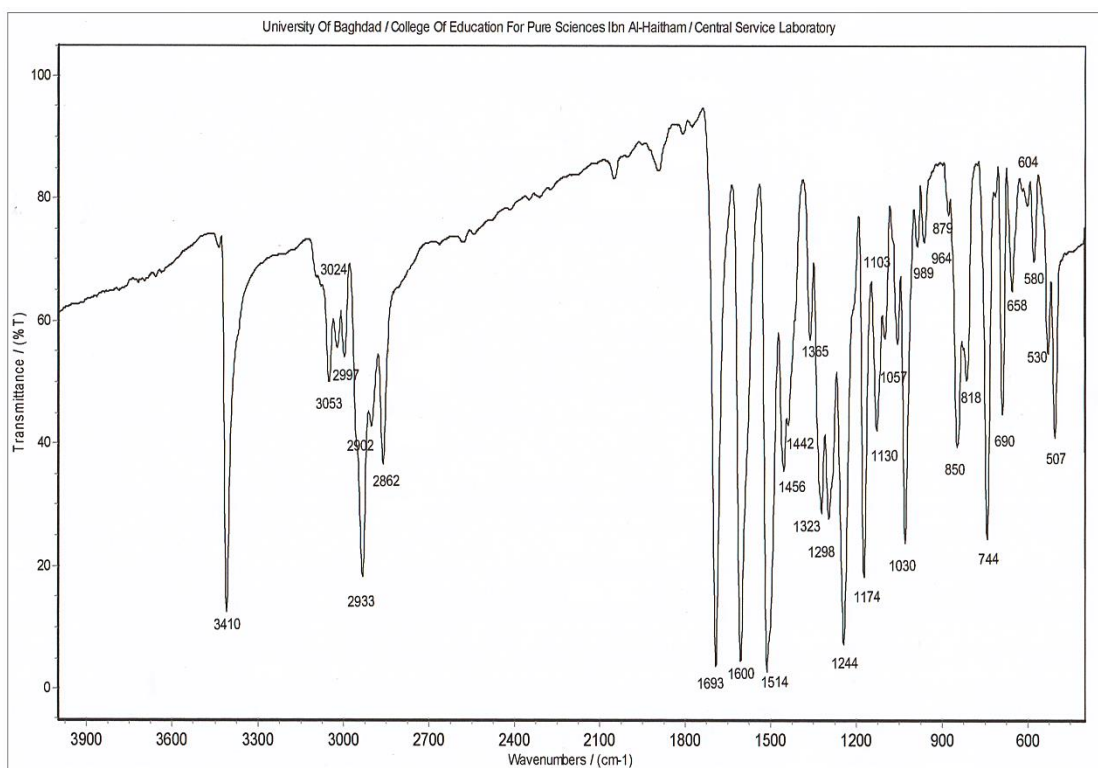
Figure (3-6): FT-IR chart of N2.
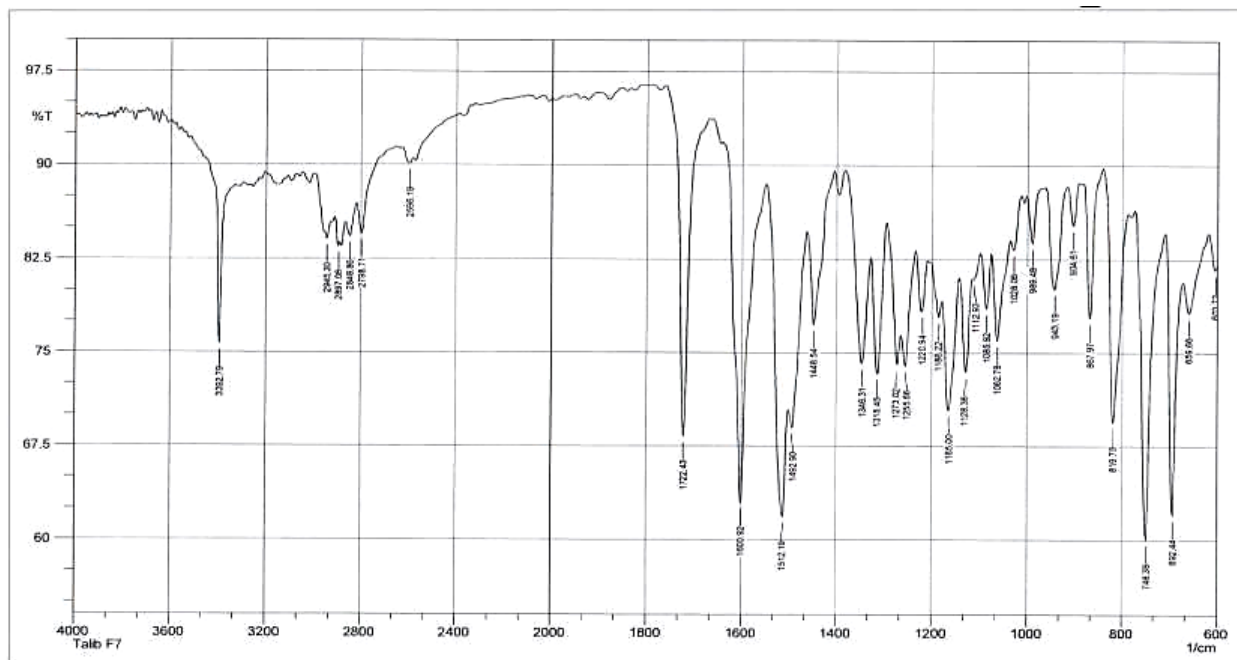
Figure (3-7): FT-IR chart of N3.

Table (3-3): Infrared data (cm^{-1}) of starting materials, F1-F3 and N1-N3.

Compound	ν(N-H)$_{Strech.}$	ν(C-H)$_{Aro.}$	ν(C-H)$_{Ali.}$	ν(C=O)	ν(C=C)	ν(N-H)$_{Bend.}$	ν(C-H) O.O.P
F1	3305	3006	2931	1707	1600	1456	833
F2	3410	3053	2935	1689	1602	1460	846
F3	3317	3026	2933	1699	1598	1492	750
N1	3379	3113	2935	1703	1601 1527	1450	752 704
N2	3410	3053	2933	1693	1600 1514	1456	850 744
N3	3392	2945	2897	1722	1600 1512	1448	819 748

(3.2.3) FT-IR spectra of ligands

(3.2.3.1) FT-IR spectrum of HL^1

The FT-IR of diphenyl-3-azabicyclo[3.3.1]nonan-9-ylidene)hydrazine-1-carboselenoamide (HL^1), Figure (3-8), comparison with the FT-IR spectra of KSeCN (Figure (3-1 e)), and precursor F1 (Figure (3-2)). The FT-IR of HL^1 showed bands at 3375 and 3368, 3337 and 3305 cm^{-1} assigned to ν(N4-H), ν(N3-H) and ν(N1-H) stretching [3], respectively. The spectrum displayed bands at 1641 and 1604 cm^{-1} assigned to ν(C=N)$_{imine}$ and ν(N-C=Se) group [3,56], respectively. While bands at 1579 and 1510 cm^{-1} due to ν(C=C)$_{aromatic}$ [55], The former band confirmed the formation of the Schiff-base *via* condensation reaction. The spectrum revealed a new band at 1250 cm^{-1}, which may be attributed to ν(C-Se) group [30]. The spectrum indicated no peak in the range 2400-2500 cm^{-1} may assign to ν(Se-H) [3], indicating the ligand exists in the selenone form [56]. The assignment of the prominent bands is included in Table (3-4).
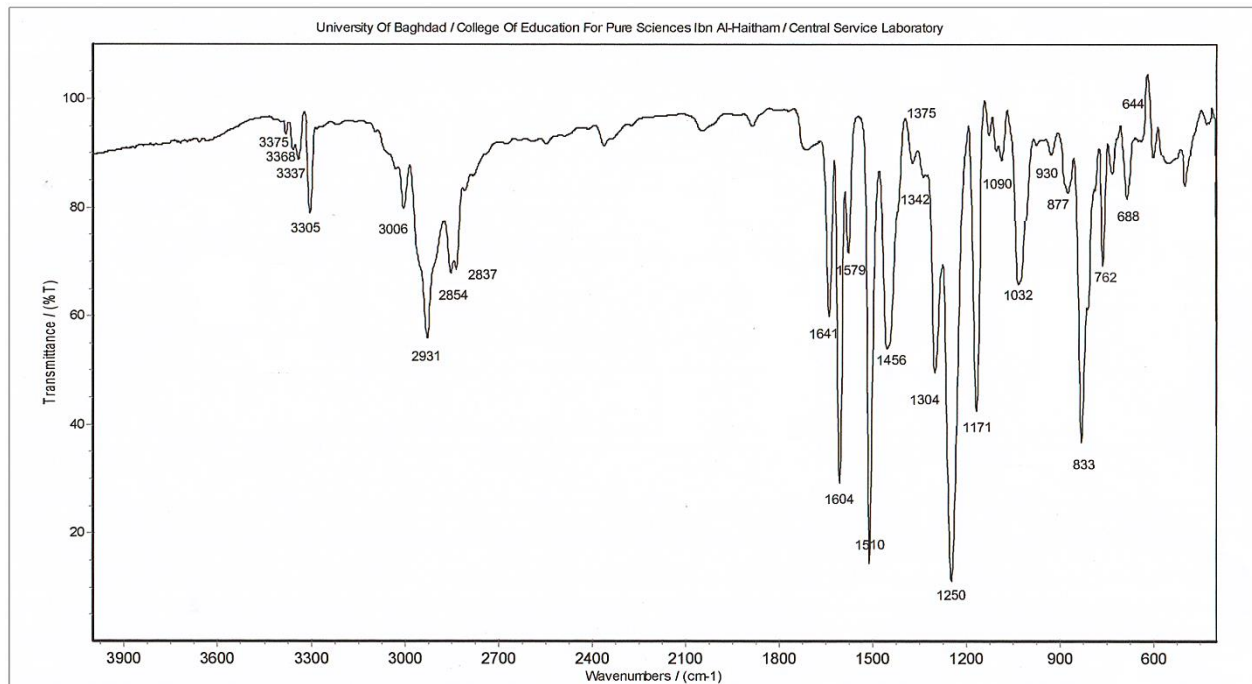
Figure (3-8): FT-IR chart of HL^1.

(3.2.3.2) FT-IR Spectra of ligands HL^2-HL^6

The spectra of HL^2-HL^6 are included in Figures (3-9) to (3-13). The assignments of the prominent peaks are listed in Table (3-4). The FT-IR data exhibit a same fashion with the expected peaks to that of HL^1, and a similar analysis is implemented to explain the spectra.
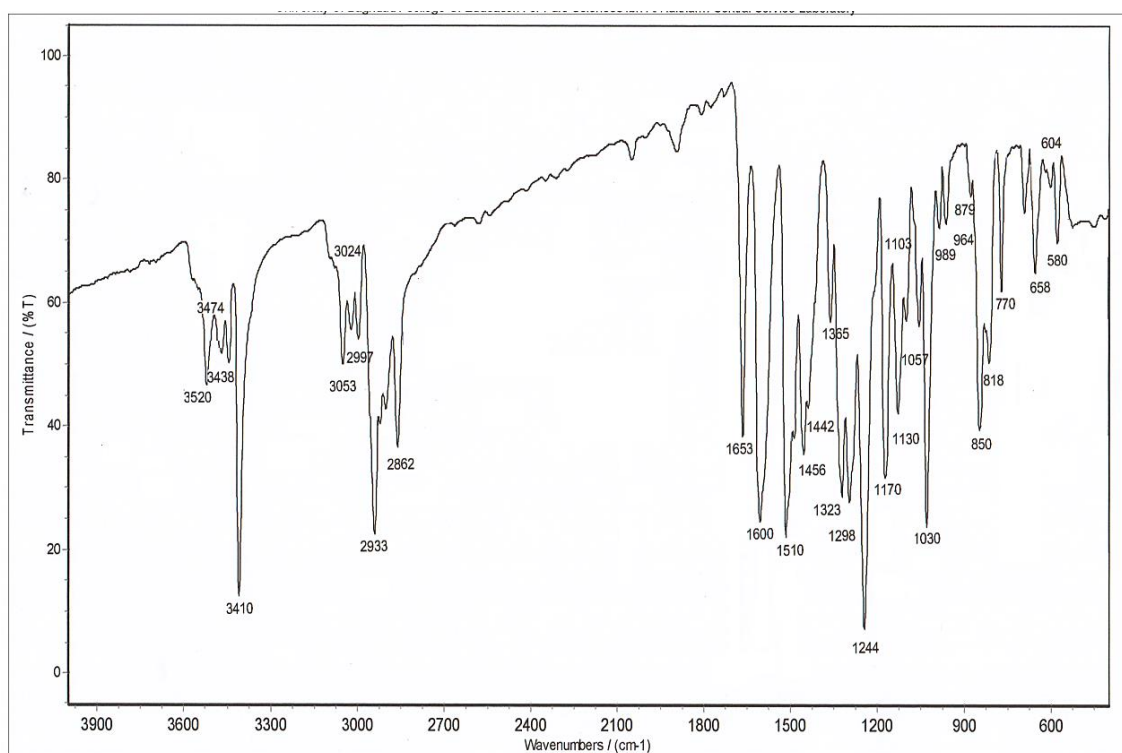
Figure (3-9): FT-IR chart of HL^2.
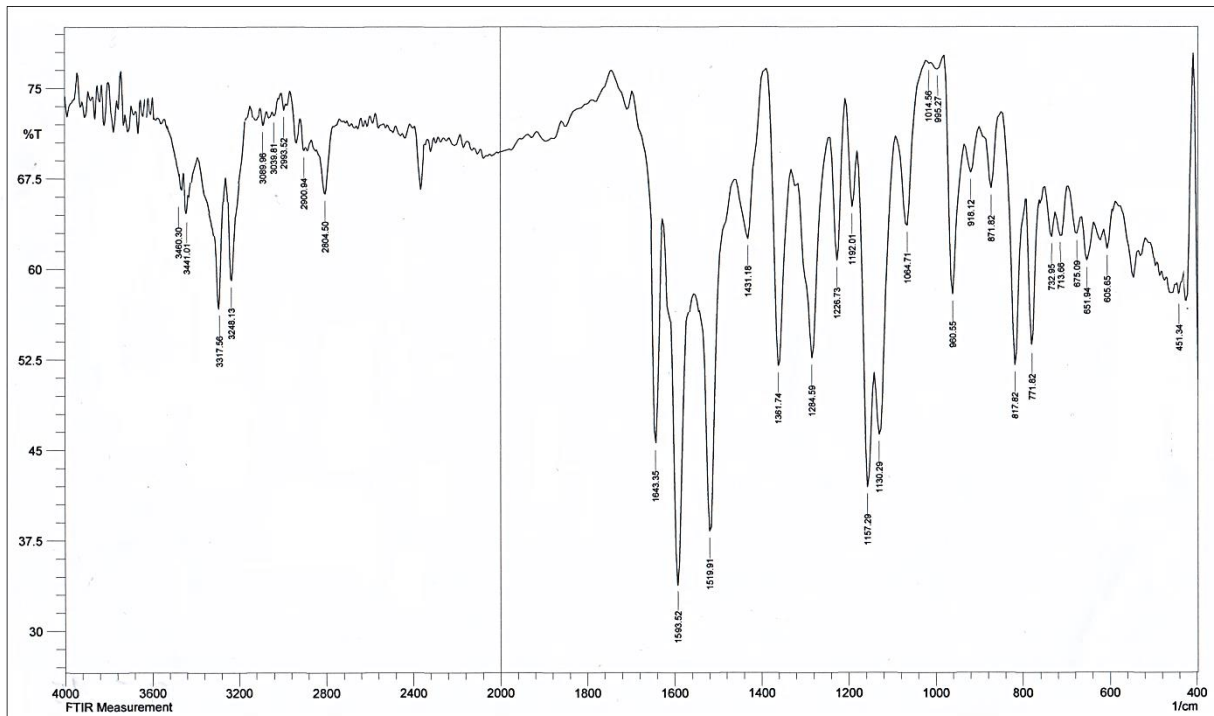
Figure (3-10): FT-IR chart of HL³.
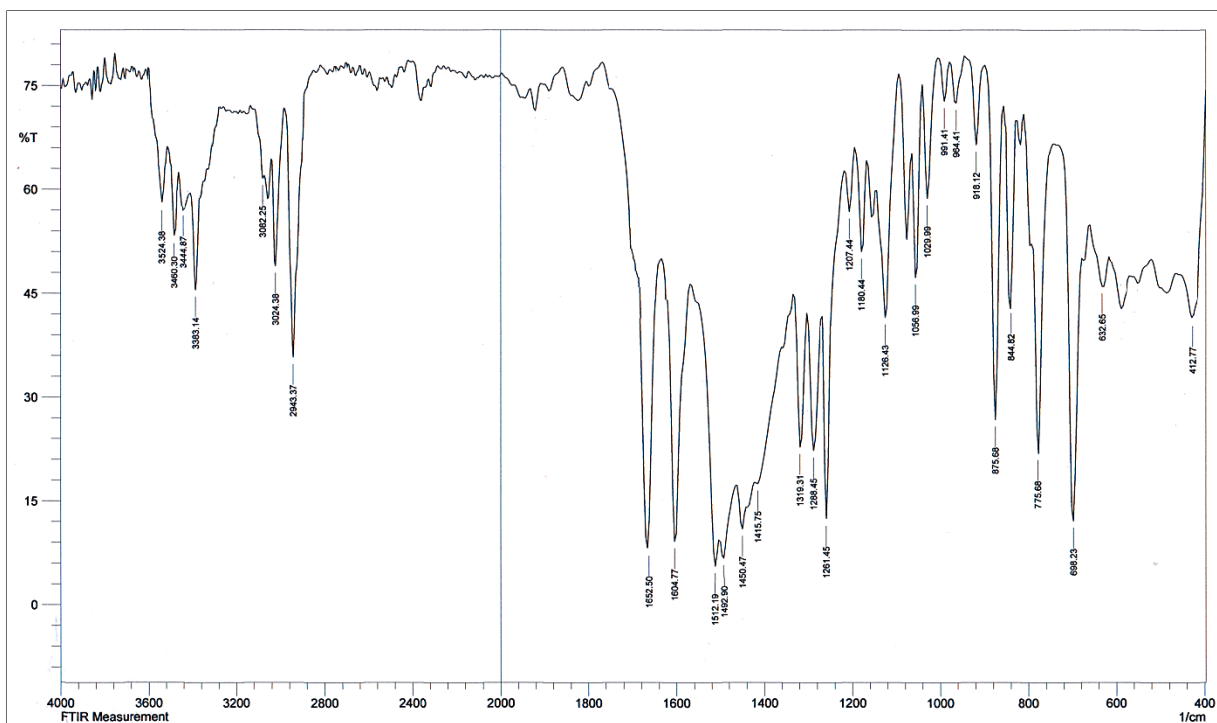
Figure (3-11): FT-IR chart of HL⁴.
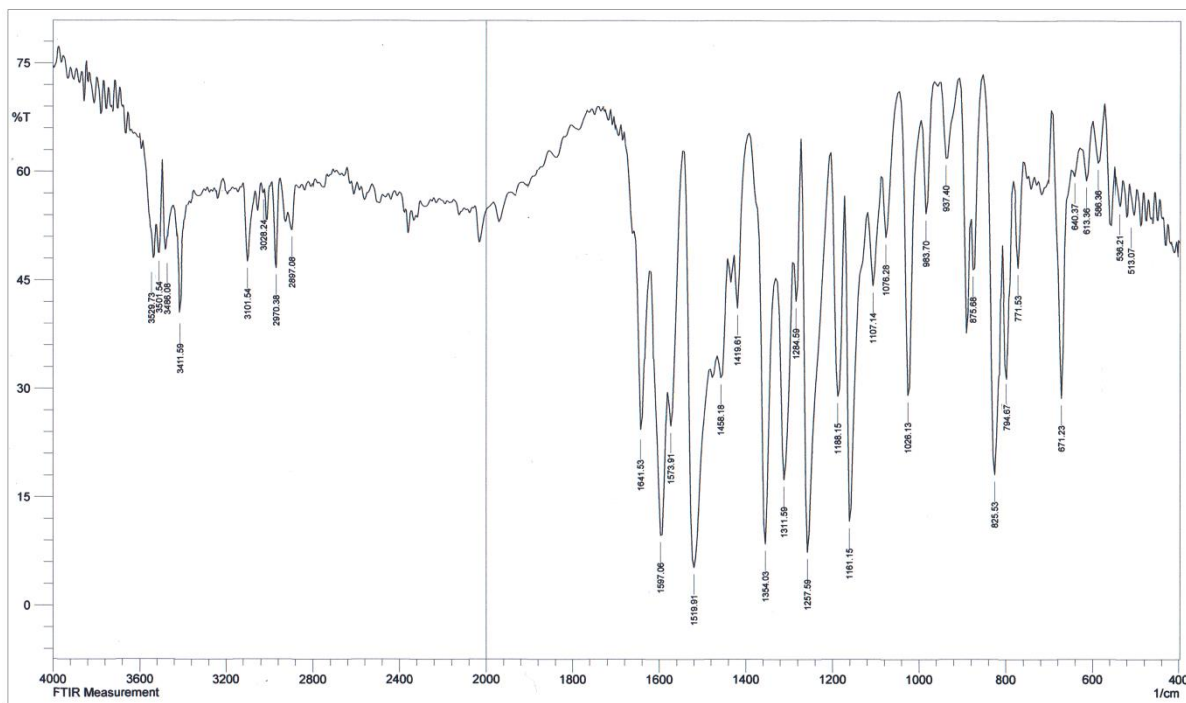
Figure (3-12): FT-IR chart of HL^5.
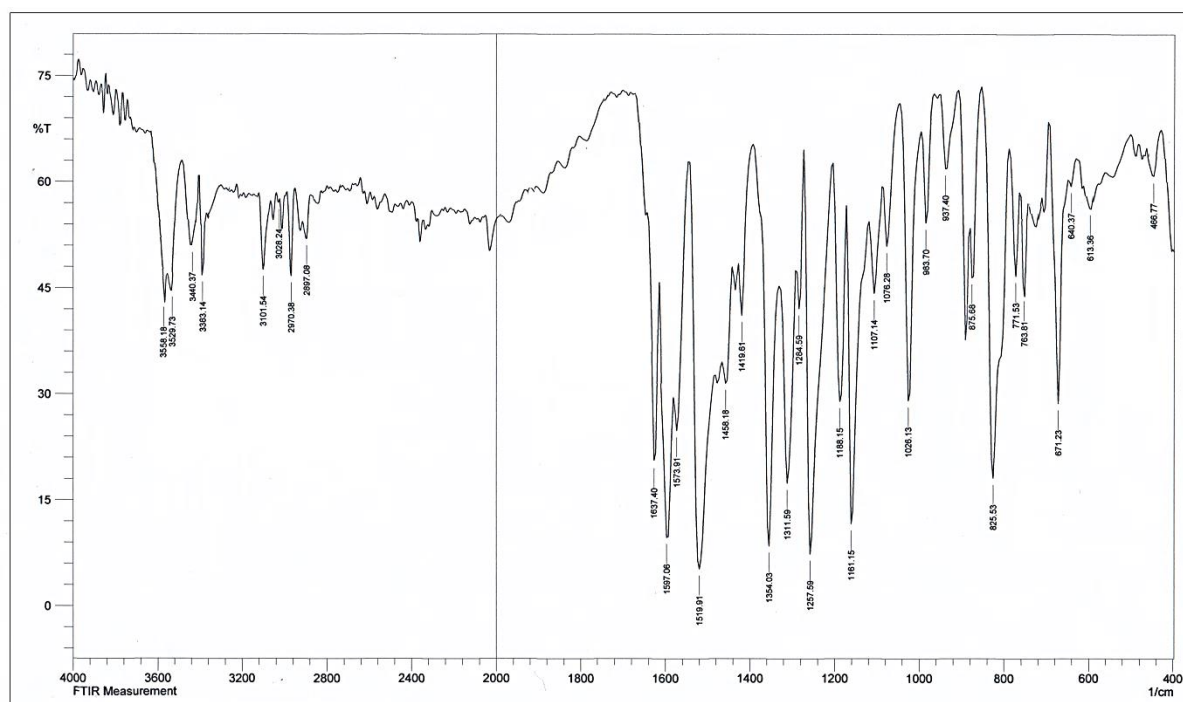
Figure (3-13): FT-IR chart of HL^6.

69

Table (3-4): Infrared data (cm^{-1}) of ligands HL^1-HL^6.

Compound	v(N4-H)	v(N3-H)	v(N1-H)	v(C-H) Aro. v(C-H) Ali.	v(C=N)	v(N-C=Se) v(C=C)	v(C-Se)	v(C-N)	v(N-H) Bend.	v(C-H) O.O.P.
HL^1	3375 3368	3337	3305	3006 2931	1641	1604 1579	1250 762	1171	1456	833 688
HL^2	3520 3474	3438	3410	3053 2933	1653	1600 1510	1244 770	1170	1456	850 818
HL^3	3460 3441	3248	3317	3089 2804	1643	1593 1519	1284 771	1157	1431	871 817
HL^4	3524 3460	3444	3383	3024 2943	1652	1604 1512	1261 775	1180	1450	875 844
HL^5	3529 3501	3486	3411	3101 2970	1641	1597 1573	1257 771	1161	1519	825 794
HL^6	3558 3529	3440	3383	3101 2970	1637	1597 1573	1257 763	1161	1519	825 771

70

(3.3) ^{1}H- and ^{13}C-NMR data of precursors and ligands

(3.3.1) ^{1}H-NMR spectrum of 2,4-diphenyl-3-azabicyclo[3.3.1]nonan-9-one (F1)

The ^{1}H-NMR spectrum of F1 in DMSO-d^6 is displayed in Figure (3-14). The ^{1}H-NMR exhibits peak at δ_H= 1.26 ppm corresponding to 2 protons that related to (2H, m, C$_{10}$-*H*). The chemical shift of (C$_{9,9'}$-*H*) that equivalent to four protons appears as a multiple at 1.44 ppm. Signal appeared at δ_H= 2.82 ppm (2H, m) attributed to (C$_{8,8'}$-*H*). The resonance at δ_H= 2.21 ppm (2H, d, J_{HH}= 4.4 Hz) is related to (C$_{7,7'}$-*H*). The (N-*H*) peak of the amine moiety is detected at δ_H= 4.30 ppm (1H, s). In the aromatic region, resonances recorded at δ_H= 7.30 and 7.41 ppm attributed to (C$_{1,1'}$-*H*; 2H, t, J_{HH}= 9.7 Hz) and (C$_{2,2',6,6'}$-*H*; 4H, t, J_{HH}= 9.7 Hz), respectively. Further, peak at 7.59 ppm (4H, d, J_{HH}= 9.5 Hz) correlated to (C$_{3,3',5,5'}$-*H*) [57,58]. Peaks related to the DMSO-d^6 and water traces in the solvent are observed at *ca.* δ_H= 2.50 and 3.34 ppm, respectively. The ^{1}H-NMR data are included in Table (3-5).
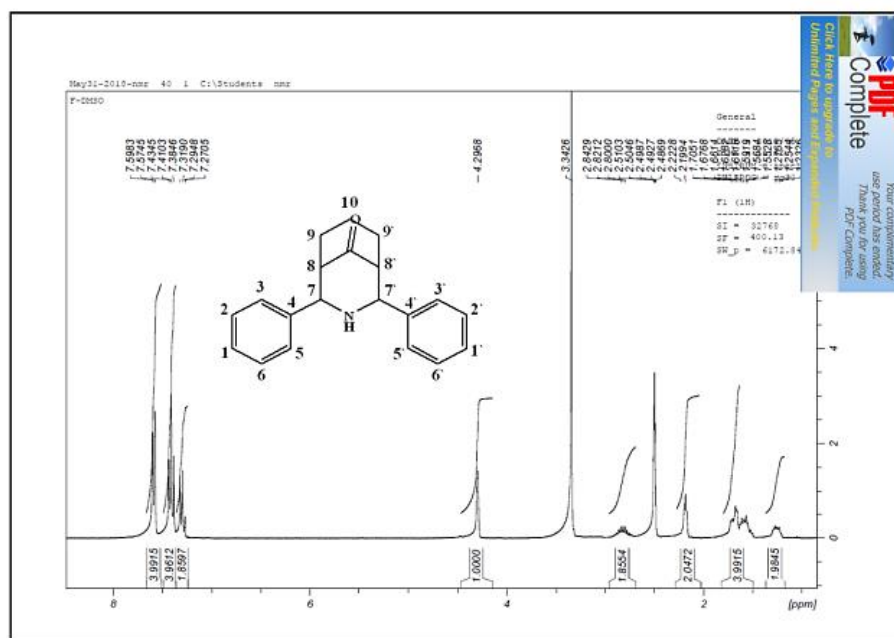
Figure (3-14): ^{1}H-NMR chart of precursor F1 in DMSO-d^6.

(3.3.2) ^{1}H-NMR spectrum of 2,4-bis(4-methoxyphenyl)-3-azabicyclo [3.3.1]nonan-9-one (F2) and 2,4-bis (4-(dimethylamino) phenyl) -3-azabicyclo [3.3.1]nonan-9-one (F3)

The ^{1}H-NMR spectra of precursors F2 and F3 display in Figures (3-15) and (3-16), respectively. The spectra exhibit almost a similar pattern of signals to that of F1 and an analogue reasoning may be used to discuss the spectra. Furthermore, in the spectrum of F2 the signal of the methoxy moieties appeared as a singlet at δ_H= 3.76 ppm (6H, s, 2 x OCH3). While, the signal at δ_H= 3.76 ppm (12H, s) related to (2 x dimethyl amino) group for precursor F3. The ^{1}H-NMR data and their assignment are listed in Table (3-5).
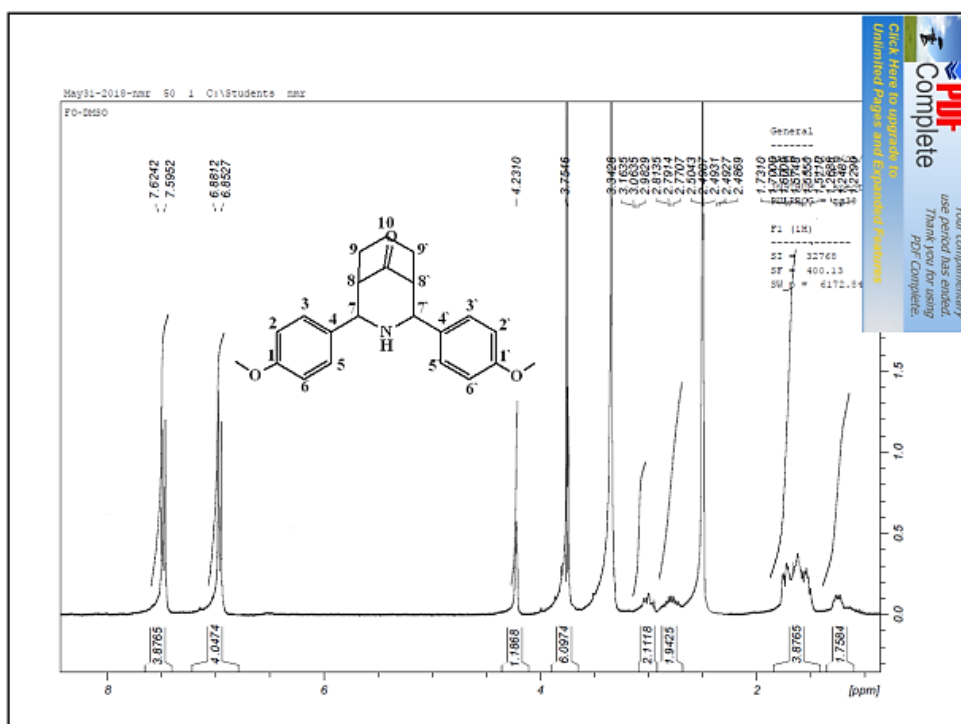
Figure (3-15): ^{1}H-NMR chart of precursor F2 in DMSO-d[6].
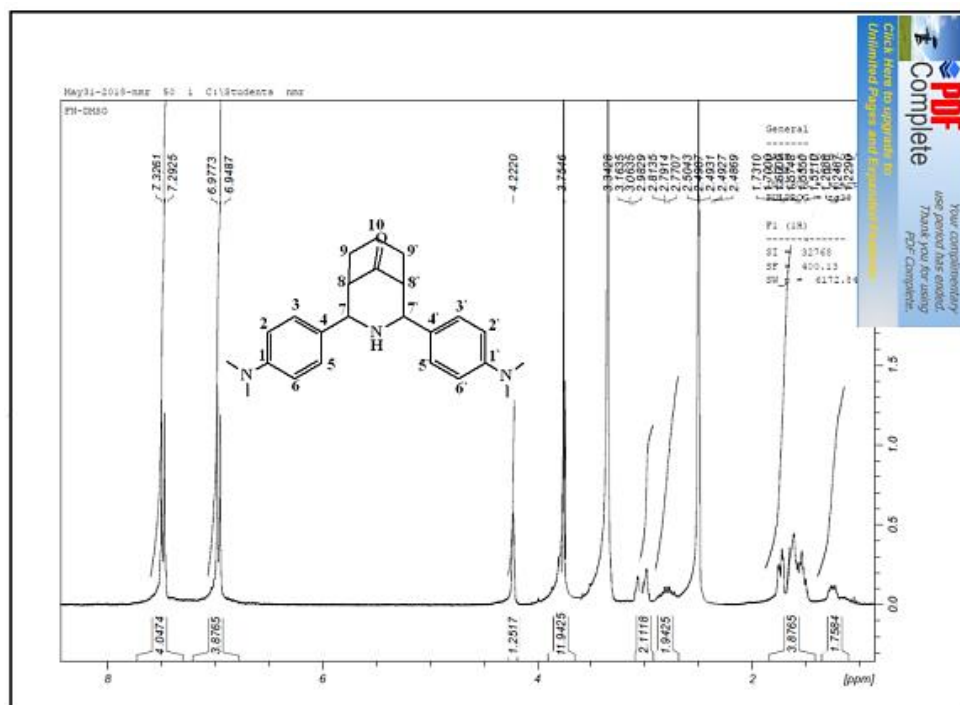
Figure (3-16): ^{1}H-NMR chart of precursor F3 in DMSO-d^6.

(3.3.3) ^{1}H-NMR spectrum of 2-(((3-nitrophenyl)amino)(phenyl) meth-yl) cyclohexan-1-one (N1)

The ^{1}H-NMR of N1 in DMSO-d^6, Figure (3-17), revealed a multiplet peak at δ_H= 1.22 ppm equal to 2 protons attributed to (2H, m, C4 -*H*). The chemical shifts at δ_H= 1.56 ppm (2H, m), 1.77 ppm (2H, m) and 2.34 ppm (2H, m) correlated to (C$_5$-*H*), (C$_3$-*H*) and (C$_6$-*H*) protons, respectively. Signal at δ_H= 2.74 ppm (1H, m) assigned to (C$_2$-*H*) proton. The (C$_7$-*H*) signal is seen as doublet of doublet at δ_H= 4.84 ppm (1H, dd, J_{HH}= 9.1, 8.6 Hz). The (N-*H*) signal of the amine appeared at δ_H= 6.04 ppm (1H, d, J_{HH}= 10.7 Hz). A detected peak at δ_H= 7.55 ppm (1H, s) attributed to (C$_9$-*H*) proton, while resonance at 7.26 ppm (1H, dd, J_{HH}= 10.8, 9.6 Hz) attributed to (C$_{12}$-*H*) proton. The chemical shifts of (C$_{11}$-*H*) and (C$_{13}$-*H*) protons appeared at δ_H= 7.17 ppm (1H, d, J_{HH}= 10.8 Hz) and 6.95 ppm (1H, d, J_{HH}= 9.6 Hz), respectively. The peak at δ_H= 6.75 ppm (1H, t, J_{HH}= 9.6 Hz) assigned to (C$_{17}$-*H*) proton. Chemical shifts at δ_H= 6.54 ppm (2H, d, J_{HH}= 10.4 Hz) and 6.43 ppm (2H,

73

dd, J_{HH}= 10.4, 9.6 Hz) attributed to (C$_{15,15'}$-*H*) and (C$_{16,16'}$-*H*), respectively [59]. Signals related to the DMSO-d^6 and H$_2$O traces in the solvent are recorded at *ca.* δ_H= 2.50 and 3.34 ppm, respectively. The assignment of the ^{1}H-NMR chemical shifts is shown in Table (3-6).
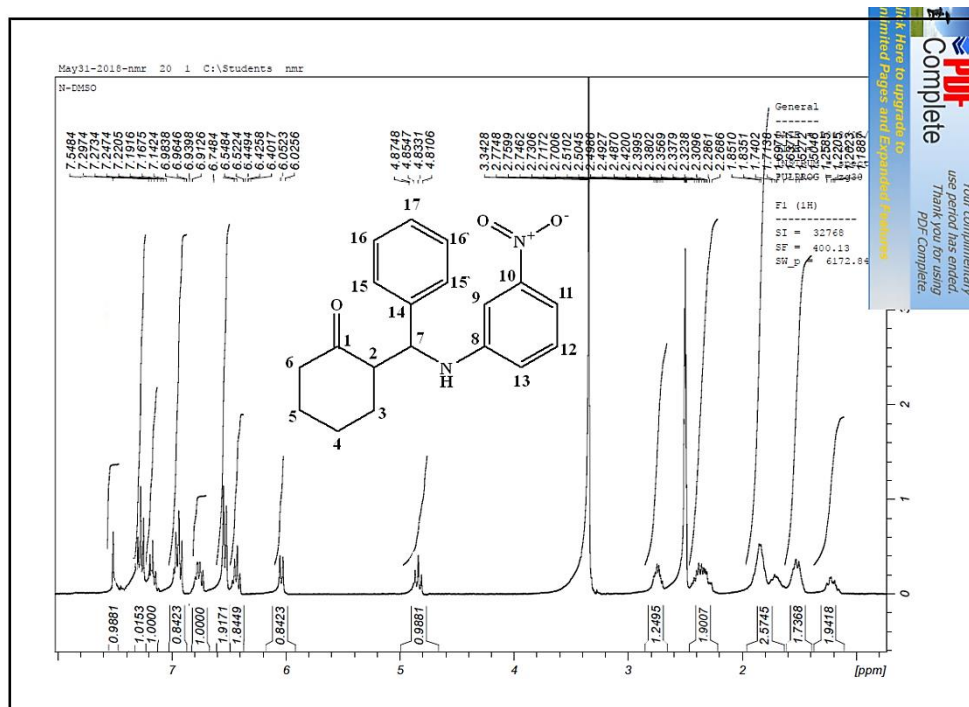
Figure (3.17): ^{1}H-NMR chart of precursor N1 in DMSO-d^6.

(3.3.4) ^{1}H-NMR spectrum of 2-((4-methoxyphenyl) (phenylamino) methyl) cyclohexan-1-one (N2) and 2-((4-(dimethylamino)phenyl) ((3-nitrophenyl)amino)methyl)cyclohexan-1-one (N3)

The ^{1}H-NMR spectra of precursors N2 and N3 are placed in Figures (3-18) and (3-19), respectively. The spectra exhibit almost an analogue pattern to that of N1 and a similar discussion may be used to correlate the spectra. Further, in the spectrum of N2 signal that attributed to the methoxy groups appeared as a singlet at δ_H= 3.69 ppm (3H, s, OCH3). Whereas, the chemical shift that related to dimethylamino group for precursor N3 reported at δ_H= 2.82 ppm (6H, s). The ^{1}H-NMR data and their assignment are tabulated in Table (3-6).
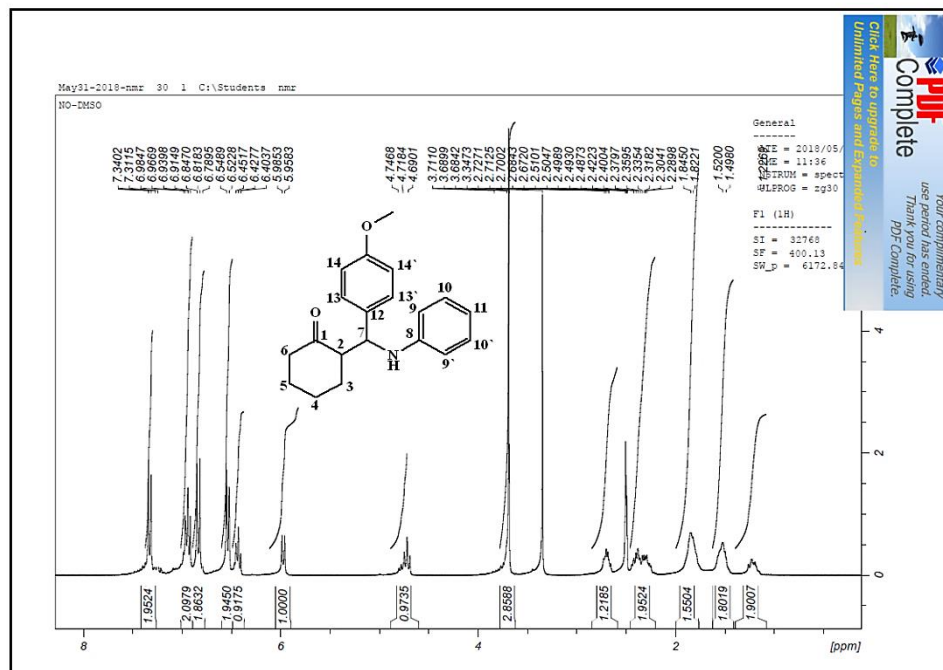
Figure (3-18): ^{1}H-NMR chart of precursor N2 in DMSO-d^6.
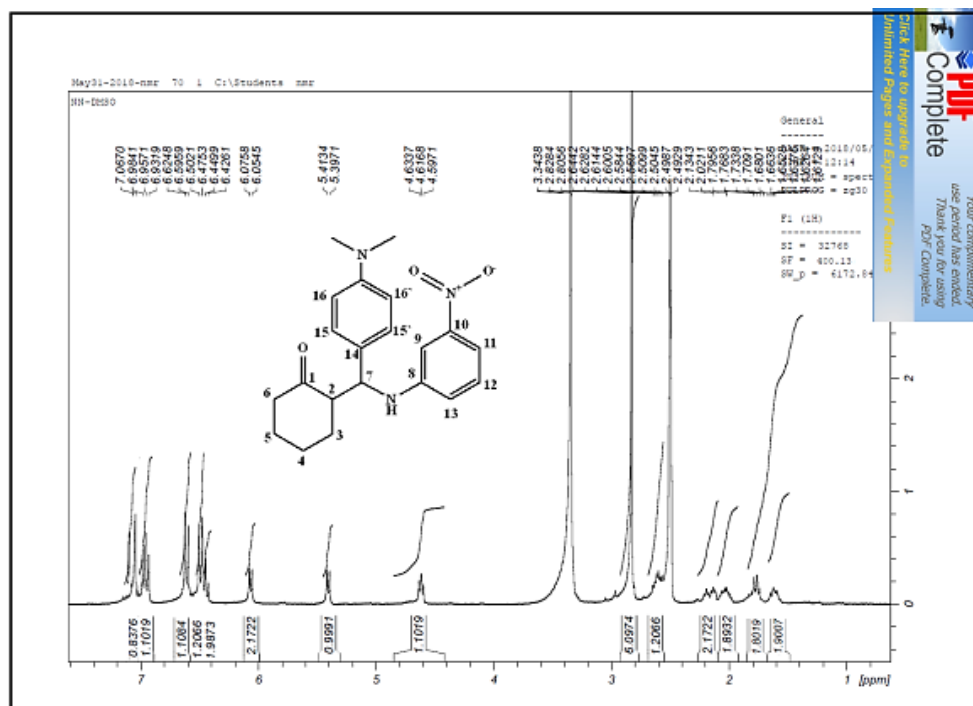
Figure (3-19): ^{1}H-NMR chart of precursor N3 in DMSO-d^6.

(3.3.5) ^{1}H-NMR spectrum of 2-(2,4-diphenyl-3-azabicyclo[3.3.1]nonan-9-ylidene)hydrazine-1-carboselenoamide (HL^1)

The ^{1}H-NMR of HL^1, Figure (3-20), in DMSO-d^6 solution indicated a signal at δ_H= 1.25 ppm (2H, m) related to (C$_{10}$-H) proton. The chemical shift at δ_H= 1.62 ppm (4H, m) assigned to (C$_{9,9'}$-H). Peak noticed at δ_H= 1.82 ppm (1H, br.) equivalent to one proton assigned to (N1-H) group. Peaks observed at δ_H= 2.22 ppm (2H, d, J_{HH}= 9.4 Hz) and 2.82 ppm (2H, m) attributed to (C$_{7,7'}$-H) protons and (C$_{8,8'}$-H) protons, respectively. Peak detected at δ_H= 4.97 ppm (2H, s) equivalent to two protons assigned to (N4-H) group. The doublet at δ_H= 7.60 ppm (4H, d, J_{HH}= 9.4 Hz) attributed to (C$_{3,3',5,5'}$-H) protons. Peak due to (C$_{2,2',6,6'}$-H) recorded at δ_H= 7.41 ppm (4H, t, J_{HH}= 9.7 Hz). Resonance recorded at δ_H= 7.30 ppm (2H, t, J_{HH}= 9.7 Hz) and 8.11 ppm (1H, br.) related to (C$_{1,1'}$-H) protons and (N3-H) group. Chemical shifts at *ca.* δ_H= 2.50 and 3.34 ppm attributed solvent residual for DMSO-d^6 and H$_2$O traces in the NMR solvent, respectively. The ^{1}H-NMR data are tabulated in Table (3-5).
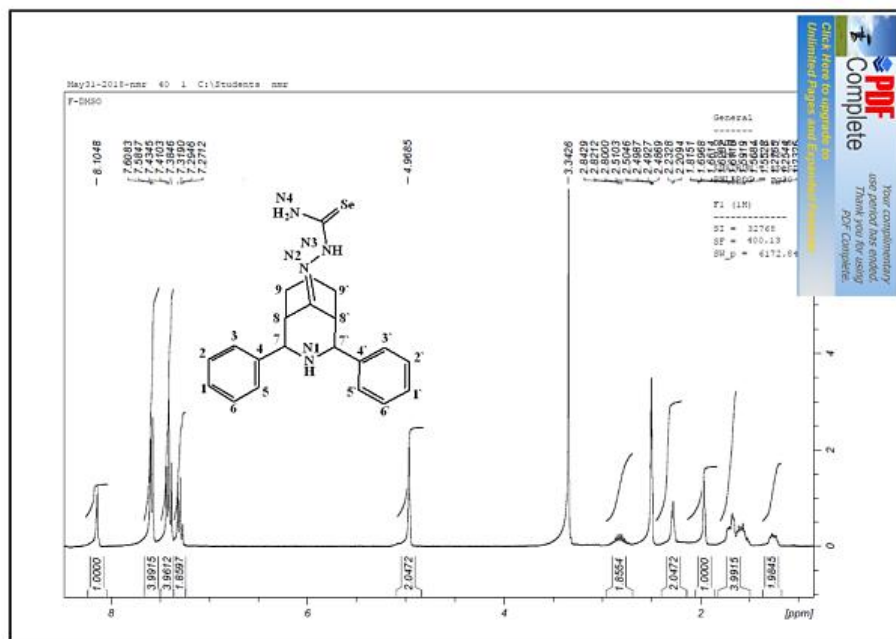
Figure (3-20): ^{1}H-NMR chart of HL^1 in DMSO-d^6.

76

(3.3.6) ^{1}H-NMR spectrum of 2-(2,4-bis(4-methoxyphenyl)-3-azabicyclo [3.3.1]nonan-9-ylidene)hydrazine-1-carboselenoamide (HL^2)

The ^{1}H-NMR of HL^2 in DMSO-d^6 solvent displayed in Figure (3.21). The ^{1}H-NMR exhibits a peak at δ_H= 1.25 ppm (2H, m) related to (C$_{10}$-*H*) protons. The chemical shift δ_H= 1.61 ppm (4H, m) assigned to (C$_{9,9}$-*H*) protons. The peak that equivalent to one proton, which attributed to (N1-*H*) group detected at δ_H= 1.98 ppm (1H, s). Peaks observed at δ_H= 2.79 ppm (2H, m) and 3.06 ppm (2H, dd, J_{HH}= 4.2, 4.0 Hz) related to (C$_{8,8}$-*H*) and (C$_{7,7}$-*H*), respectively. A peak at δ_H= 3.76 ppm (6H, s) is correlated to (2 x OCH$_3$) group. The broad peak that detected at δ_H= 4.63 ppm (2H, br.), equal to two protons, attributed to (N4-*H*) group. Moreover, the (C$_{3,3`,5,5`}$-*H*) signal appeared at δ_H= 7.59 ppm (4H, d, J_{HH}= 11.6 Hz), while (C$_{2,2`,6,6`}$-*H*) protons detected at 6.87 ppm (4H, d, J_{HH}= 11.6 Hz). The peak observed at 7.96 ppm (1H, s) equivalent one proton is related to (N3-*H*) moiety. Chemical shifts at *ca*. δ_H= 2.50 and 3.34 ppm attributed solvent residual for DMSO-d^6 and H$_2$O traces in the NMR solvent, respectively. The ^{1}H-NMR data are included in Table (3-5).
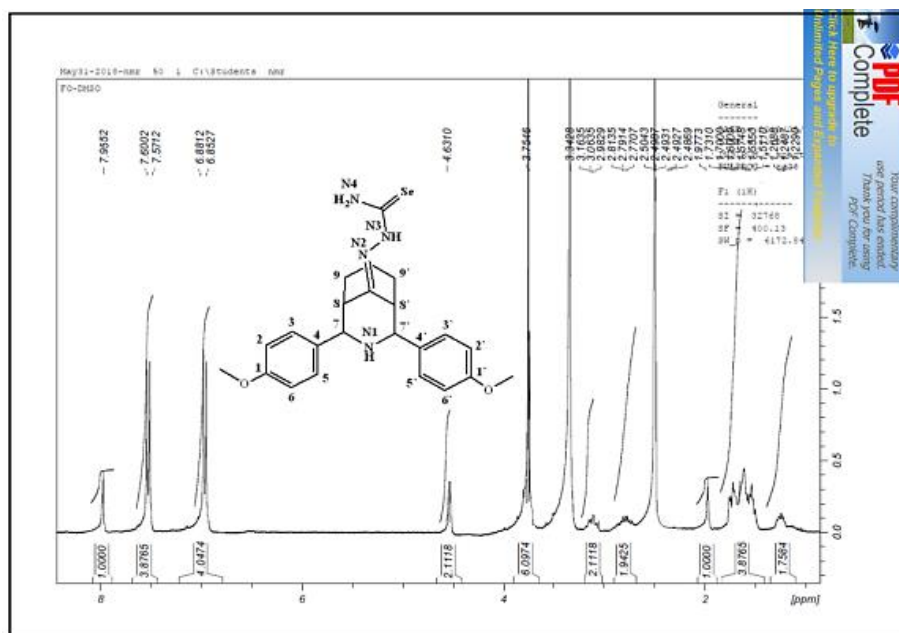
Figure (3-21): ^{1}H-NMR chart of HL^2 in DMSO-d^6.

(3.3.7) ^{1}H-NMR spectrum of 2-(2,4-bis(4-(dimethylamino)phenyl)-3-azabicyclo[3.3.1]nonan-9-ylidene)hydrazine-1-carboselenoamide (HL^3)

The ^{1}H-NMR, in DMSO-d^6 solvent, of HL^3 is placed in Figure (3-22). In the spectrum, the peak at δ_H= 1.25 ppm (2H, m) is related to (C$_{10}$-*H*) protons. Chemical shifts at δ_H= 1.61 ppm (4H, m) and 1.97 ppm (1H, s) assigned to (C$_{9,9'}$-*H*) protons and (N1-*H*) group, respectively. Peaks observed at δ_H= 2.79 ppm (2H, m) and 3.01 ppm (2H, dd, J_{HH}= 4.9, 4.3 Hz) related to (C$_{8,8'}$-*H*) and (C$_{7,7'}$-*H*) protons, respectively. The chemical shift that attribute to methyl groups protons (2 x dimethylamino) appeared as expected as a singlet at δ_H= 3.76 ppm (12H, s). Peak detected at δ_H= 4.12 ppm (2H, br.) equal to two protons correlated to (N4-*H*) group. The chemical shifts recorded at δ_H= 7.48 ppm (4H, d, J_{HH}= 11.5 Hz) and δ_H= 7.00 ppm (4H, d, J_{HH}= 11.5 Hz) related to (C$_{3,3',5,5'}$-*H*) and (C$_{2,2',6,6'}$-*H*) protons, respectively. The chemical shift that correlated to (N3-*H*) group appeared as a singlet at 8.01 ppm (1H, br.). Peaks observed at *ca*. δ_H= 2.50 and 3.34 ppm are related to the solvent residual for DMSO-d^6 and H$_2$O traces in the solvent, respectively. The ^{1}H-NMR data are listed in Table (3-5).
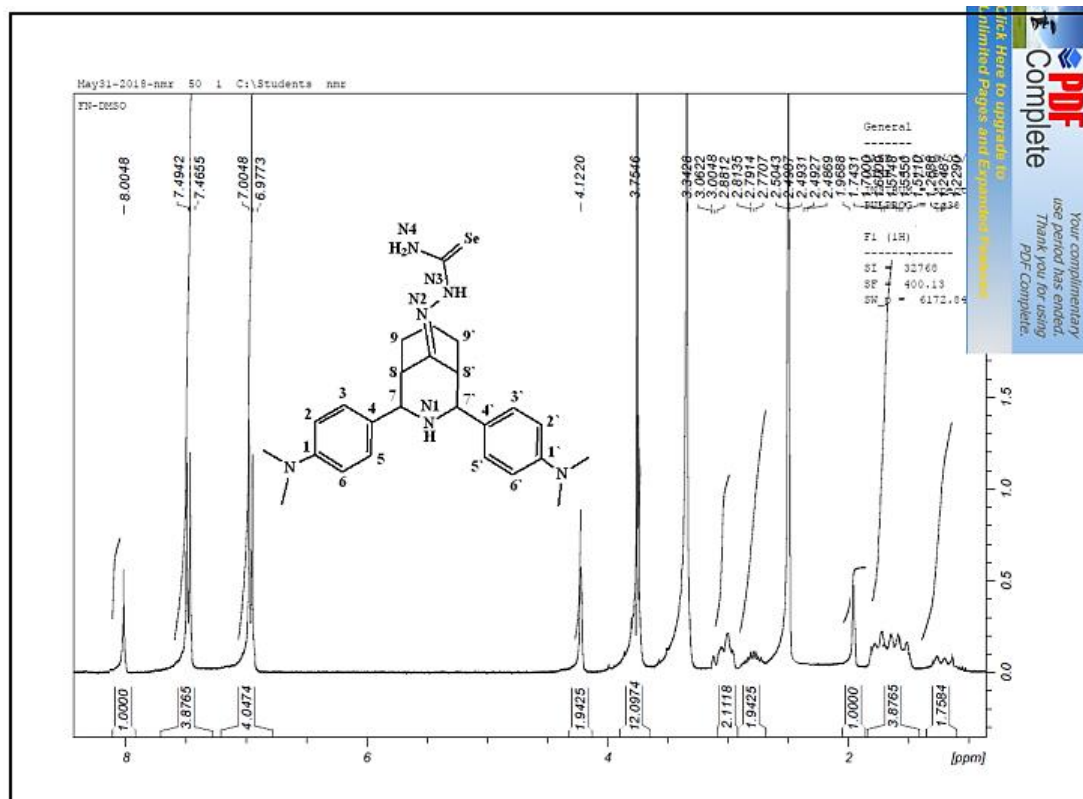
Figure (3-22): ^{1}H-NMR chart of HL^3 in DMSO-d^6.

Table (3-5): ^{1}H-NMR data of the precursors F1-F3 and ligands HL^1-HL^3 with their chemical shifts in ppm (δ).

Compound	$(C_{7,7'}\text{-}H)$	$(C_{8,8'}\text{-}H)$ $(C_{9,9'}\text{-}H)$	$(C10\text{-}H)$	$(C_{1,1'}\text{-}H)$	$(C_{2,2', 6,6'}\text{-}H)$ $(C_{3,3', 5,5'}\text{-}H)$	$(N1\text{-}H)$	$(N3\text{-}H)$	$(N4\text{-}H)$	$(2 \times OCH_3)$ $(2 \times N(CH_3)_2)$
F1	2.21	2.82 1.44	1.26	7.30	7.41 7.59	4.30	–	–	– –
F2	3.07	2.79 1.61	1.25	–	6.87 7.61	4.23	–	–	3.76 –
F3	3.07	2.79 1.61	1.25	–	6.96 7.31	4.22	–	–	– 3.76
HL^1	2.22	2.82 1.62	1.25	7.30	7.41 7.60	1.82	8.11	4.97	– –
HL^2	3.06	2.79 1.61	1.25	–	6.87 7.59	1.98	7.96	4.63	3.76 –
HL^3	3.01	2.79 1.61	1.25	–	7.00 7.48	1.97	8.01	4.12	– 3.76

(3.3.8) ^{1}H-NMR spectrum of (E)-2-(2-(((3-nitrophenyl) amino) (phenyl) methyl)cyclohexylidene)hydrazine-1-carboselenoamide (HL^4)

The ^{1}H-NMR of HL^4 in DMSO-d^6, Figure (3-23), indicates a peak at δ_H= 1.22 ppm (2H, m) equal to 2 protons that related to (C$_4$-H). The chemical shifts at δ_H= 1.52 ppm (2H, m), δ_H= 1.74 ppm (2H, m) and 2.34 ppm (2H, m) attributed to (C$_5$-H), (C$_3$-H) and (C$_6$-H) protons, respectively. The signal at δ_H= 2.75 ppm (1H, m) assigned to (C$_2$-H) proton. A peak equivalent to two protons that detected at δ_H= 4.40 ppm (2H, s) correlated to (N4-H) segment. The (C$_7$-H) signal is seen as a doublet of doublet at δ_H= 4.78 ppm (1H, dd, J_{HH}= 11.4, 10.2 Hz). The (N1-H) group appeared at δ_H= 6.04 ppm (1H, d, J_{HH}= 10.7 Hz). Resonances at δ_H= 7.33 ppm (1H, s) assigned to (C$_9$-H) proton. Moreover, signal δ_H= 7.26 ppm (1H, dd, J_{HH}= 10.8, 9.6 Hz) is attributed to (C$_{12}$-H) proton. While, the chemical shifts of (C$_{11}$-H) and (C$_{13}$-H) protons appeared at δ_H= 7.17 ppm (1H, d, J_{HH}= 10.8 Hz) and δ_H= 6.92 ppm (1H, d, J_{HH}= 9.6 Hz), respectively. The resonance at δ_H= 6.75 ppm (1H, t, J_{HH}= 9.4 Hz) assigned to (C$_{17}$-H) proton. Peaks at δ_H= 6.54 ppm (2H, d, J_{HH}= 10.4 Hz) and 6.43 ppm (2H, dd, J_{HH}= 10.4, 9.4 Hz) attributed to (C$_{15,15`}$-$H$) and (C$_{16,16`}$-H), respectively. The broad peak observed at 7.75 ppm (1H, br.) equivalent one proton related to (N3-H) moiety. The spectrum shows two peaks at *ca*. δ_H= 2.50 and 3.34 ppm related to the solvent residual for DMSO-d^6 and H$_2$O traces in the solvent, respectively. The ^{1}H-NMR chemical shifts are shown in Table (3-6).
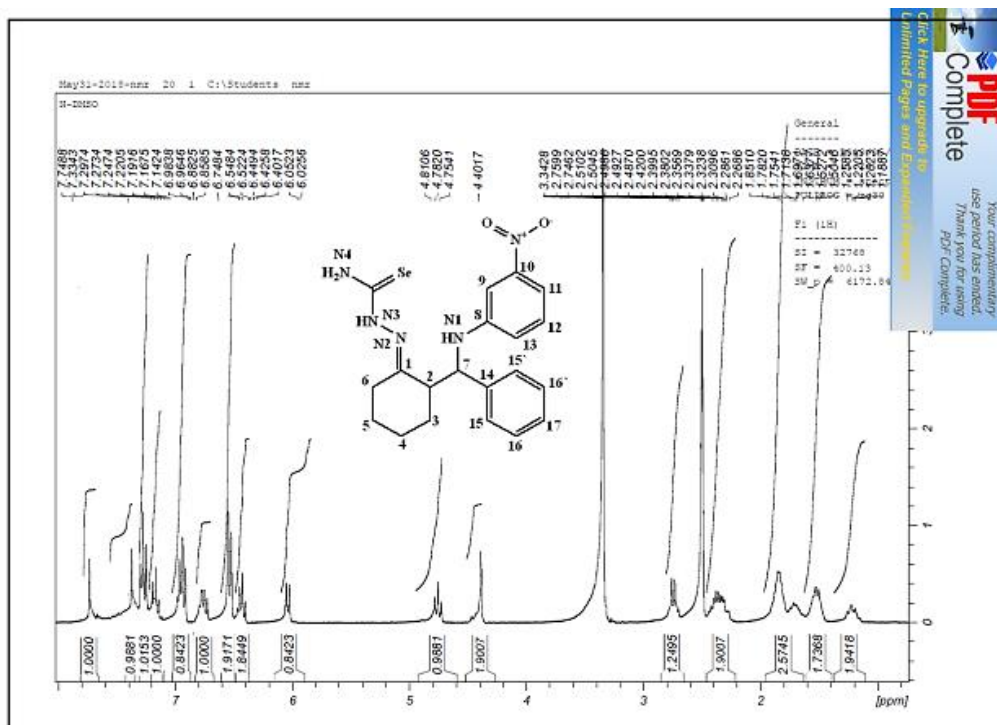
Figure (3-23): ^{1}H-NMR chart of HL^4 in DMSO-d^6.

(3.3.9) ^{1}H-NMR spectrum of (E)-2-(2-((4-methoxyphenyl) (phenylamino) methyl)cyclohexylidene)hydrazine-1-carboselenoamide (HL^5)

The ^{1}H-NMR of HL^5 in DMSO-d^6, Figure (3-24), recorded a resonance at δ_H= 1.23 ppm (2H, m) with 2 protons integration correlated to (C$_4$-*H*). Signals at δ_H= 1.51 ppm (2H, m), δ_H= 1.83 ppm (2H, m) and 2.36 ppm (2H, m) attributed to (C$_5$-*H*), (C$_3$-*H*) and (C$_6$-*H*), respectively. A peak seen at δ_H= 2.70 ppm (1H, m) assigned to (C$_2$-*H*) proton. The chemical shift at δ_H= 3.71 ppm (3H, s) is assigned to methoxy moiety. The peak detected at δ_H= 4.19 ppm (2H, br.), equivalent to two protons, related to (N4-*H*) group. The (C$_7$-*H*) signal is seen as doublet of doublet at δ_H= 4.72 ppm (1H, dd, J_{HH}= 11.4, 10.3 Hz). The (N1-*H*) signal appeared at δ_H= 5.97 ppm (1H, d, J_{HH}= 10.8 Hz). Resonance at δ_H= 7.43 ppm (2H, d, J_{HH}= 11.2 Hz) assigned to (C$_{13,13'}$-*H*) protons. While (C$_{10,10'}$-*H*) protons

appeared δ_H= 6.97 ppm (2H, dd, J_{HH}= 10.5, 9.6 Hz). Chemical shifts at δ_H= 6.82 ppm (2H, d, J_{HH}= 11.2 Hz) and δ_H= 6.54 ppm (2H, d, J_{HH}= 10.5 Hz) attributed to ($C_{14,14'}$-*H*) and ($C_{9,9'}$-*H*) respectively. The chemical shift at δ_H= 6.43 ppm (1H, t, J_{HH}= 9.6 Hz) and 8.12 ppm (1H, s) assigned to (C_{11}-*H*) proton and (N3-*H*) moiety, respectively. The spectrum shows two signals at *ca.* δ_H= 2.50 and 3.34 ppm attributed to the remaining of DMSO in the DMSO-d^6 and H_2O traces in the solvent, respectively. Table (3-6) included the ^{1}H-NMR data.
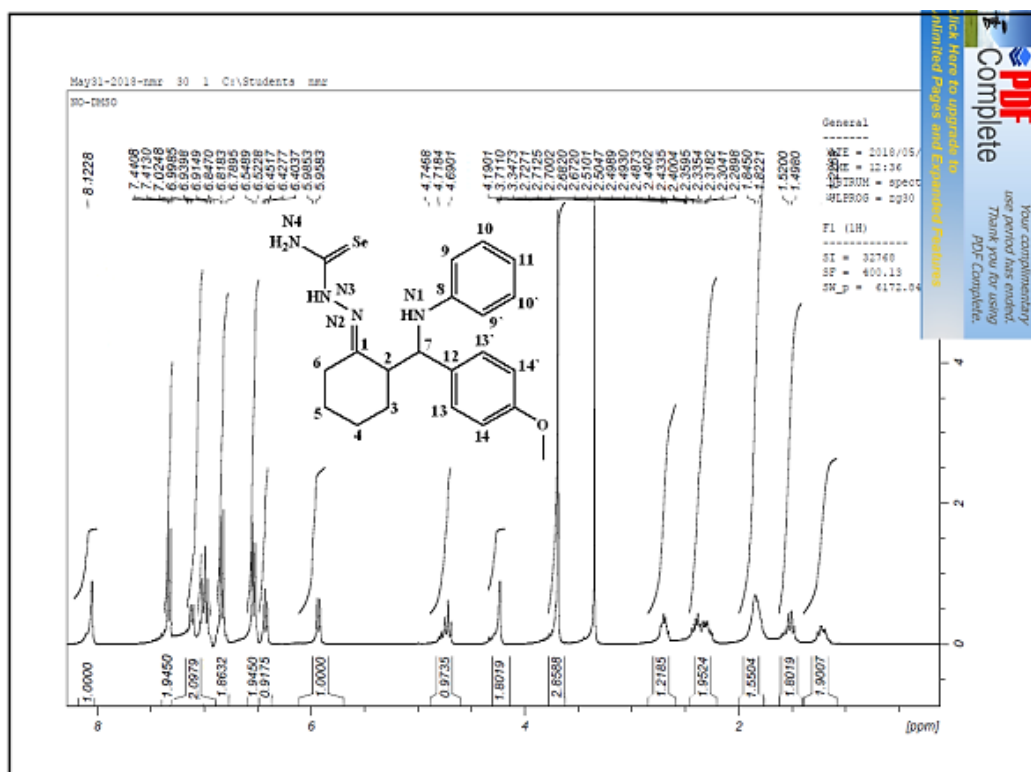
Figure (3-24): ^{1}H-NMR chart of HL^5 in DMSO-d^6.

(3.3.10) ^{1}H-NMR spectrum of (E)-2-(2-((4-(dimethylamino)phenyl)((3-nitrophenyl)amino)methyl)cyclohexylidene)hydrazine-1-carboselenoamide (HL^6)

The ^{1}H-NMR of HL^6 is recorded in DMSO-d^6 solvent and allocated in Figure (3-25). Peaks seen at δ_H= 1.65 ppm (2H, m) and δ_H= 1.76 ppm (2H, m) attributed to (C$_4$-*H*) and (C$_5$-*H*) protons, respectively. Chemical shifts at δ_H= 2.02 ppm (2H, m) and δ_H= 2.08 ppm (2H, m) attributed to (C$_3$-*H*) and (C$_6$-*H*) protons, respectively. The peak that detected at δ_H= 2.65 ppm (1H, m) attributed to (C$_2$-*H*) proton. The peaks at δ_H= 2.82 ppm (6H, s) assigned to methyl group protons (dimethyl amino). The peak that related to the (N4-*H*) group was detected at the expected chemical shift at δ_H= 4.19 ppm (2H, s). The (C$_7$-*H*) signal is seen as a doublet of doublet at δ_H= 4.50 ppm (1H, dd, J_{HH}= 6.8, 4.4 Hz). The (N1-*H*) signal appeared at δ_H= 5.63 ppm (1H, d, J_{HH}= 6.8 Hz). Resonances at δ_H= 7.17 ppm (1H, s) and 6.96 ppm (1H, dd, J_{HH}= 10.8, 9.4 Hz) assigned to (C$_9$-*H*) and (C$_{12}$-*H*), respectively. While, (C$_{11}$-*H*) and (C$_{13}$-*H*) chemical shifts appeared at δ_H= 6.71 ppm (1H, d, J_{HH}= 10.8 Hz) and δ_H= 6.49 ppm (1H, d, J_{HH}= 9.4 Hz), respectively. Resonances at δ_H= 6.44 ppm (2H, d, J_{HH}= 8.5 Hz) and δ_H= 6.17 ppm (2H, d, J_{HH}= 8.5 Hz) correlated to (C$_{15,15`}$-*H*) and (C$_{16,16`}$-*H*), respectively. The broad peak observed at 7.36 ppm (1H, br.) equivalent one proton is related to (N3-*H*) group. The spectrum shows two peaks at *ca.* δ_H= 2.50 and 3.34 ppm related to the remaining DMSO residual in DMSO-d^6 and H$_2$O hints in the solvent, respectively. The ^{1}H-NMR data are tabulated in Table (3-6).
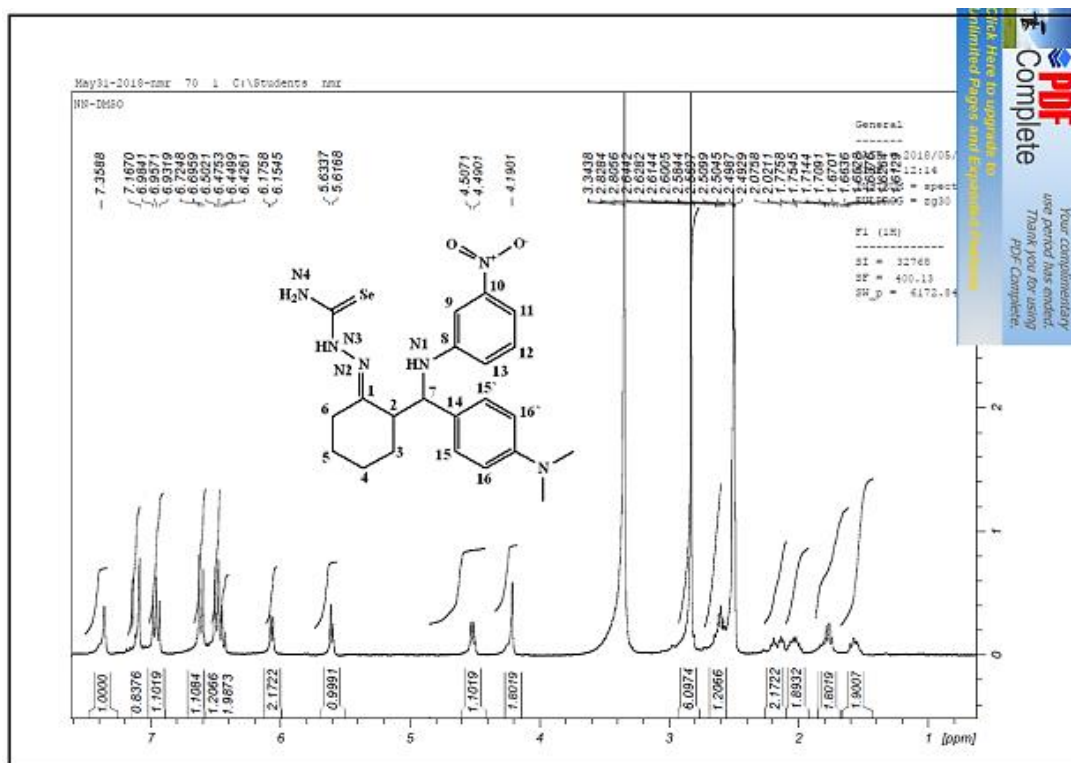
Figure (3-25): ^{1}H-NMR chart of HL^6 in DMSO-d^6.

Table (3-6): ^{1}H-NMR data of the precursors N1-N3 and ligands HL^4-HL^6 with their chemical shift in ppm (δ).

Compound	(C2-*H*) (C3-*H*)	(C4-*H*) (C5-*H*)	(C6-*H*) (C7-*H*)	(C9-*H*) (C11-*H*)	(C12-*H*) (C13-*H*)	(C$_{9,9'}$-*H*) (C$_{10,10'}$-*H*)	(C$_{13,13'}$-*H*) (C$_{14,14'}$-*H*)	(C$_{15,15'}$-*H*) (C$_{16,16'}$-*H*)	(C17-*H*)	(N1-*H*)	(N3-*H*)	(N4-*H*)	(OCH$_3$) (N(CH$_3$)$_2$)
N1	2.74 1.77	1.22 1.56	2.34 4.84	7.55 7.17	7.26 6.95	– _	– _	6.54 6.43	6.75	6.04	–	–	– –
N2	2.70 1.83	1.23 1.51	2.35 4.72	_ 6.43	_ _	6.54 6.95	7.33 6.82	– _	_	5.97	–	–	3.69 –
N3	2.65 2.02	1.69 1.75	2.13 4.62	7.07 6.62	6.96 6.49	– _	– _	6.44 6.07	_	5.41	–	–	– 2.82
HL^4	2.75 1.74	1.22 1.52	2.34 4.78	7.33 7.17	7.26 6.92	– _	– _	6.54 6.43	6.75	6.04	7.75	4.40	– –
HL^5	2.70 1.83	1.23 1.51	2.36 4.72	_ 6.43	_ _	6.54 6.97	7.43 6.82	– _	_	5.97	8.12	4.19	3.71 –
HL^6	2.65 2.02	1.65 1.76	2.08 4.50	7.17 6.71	6.96 6.49	– _	– _	6.44 6.17	_	5.63	7.36	4.19	– 2.82

(3.3.11) ^{13}C-NMR spectrum of 2,4-diphenyl-3-azabicyclo[3.3.1]nonan-9-one (F1)

The ^{13}C-NMR spectrum of F1 is placed in Figure (3-26). The spectrum that recorded in DMSO-d^6 displayed two set of resonances in the aliphatic and aromatic region. Chemical shifts at δc= 20.52 and 28.49 ppm related to (C$_{10}$) and (C$_{9,9'}$), respectively. Signals due to (C$_{7,7'}$) and (C$_{8,8'}$) detected at 53.22 and 63.72 ppm, respectively. Resonances assigned for (C$_{1,1'}$), (C$_{3,3',5,5'}$), (C$_{2,2',6,6'}$) and (C$_{4,4'}$) were recorded at 126.84, 127.00, 128.20 and 141.75 ppm, respectively. Finally, the C=O of the carbonyl group recorded as estimated in the downfield region at δc= 215.85 ppm. The ^{13}C-NMR resonances are listed in Table (3-7).
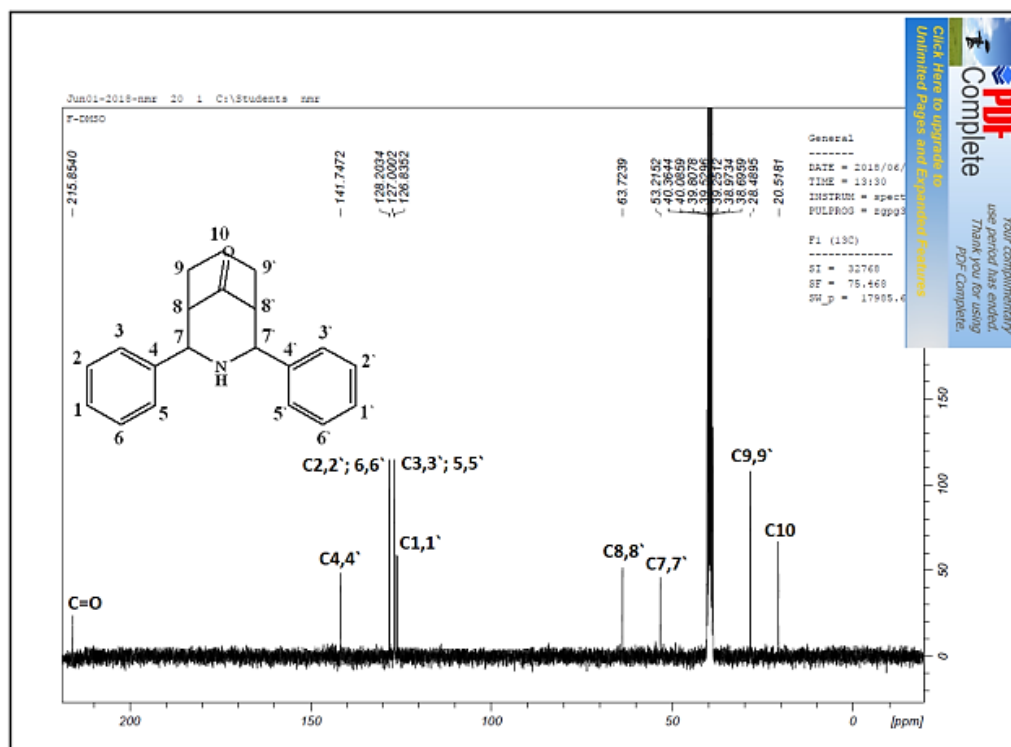
Figure (3-26): ^{13}C-NMR chart of precursor F1 in DMSO-d^6.

(3.3.12) ^{13}C-NMR spectrum of 2,4-bis(4-methoxyphenyl)-3-azabicyclo [3.3.1]nonan-9-one (F2) and 2,4-bis(4-(dimethylamino)phenyl)-3-azabicyclo[3.3.1]nonan-9-one (F3)

The ^{13}C-NMR spectra of F2 and F3 are placed in Figures (3-27) and (3-28), respectively. The spectra exhibit almost a similar pattern of signals to that of F1 and a similar reasoning may be used to explain the spectra. Further, in the spectrum of F2 the chemical shift at δc= 45.23 ppm was assigned to C-methoxy. While, in the F3 spectrum the signal at δc= 40.23 ppm is related to two dimethyl amino segment. The ^{13}C-NMR data and their assignment are included in Table (3-7).
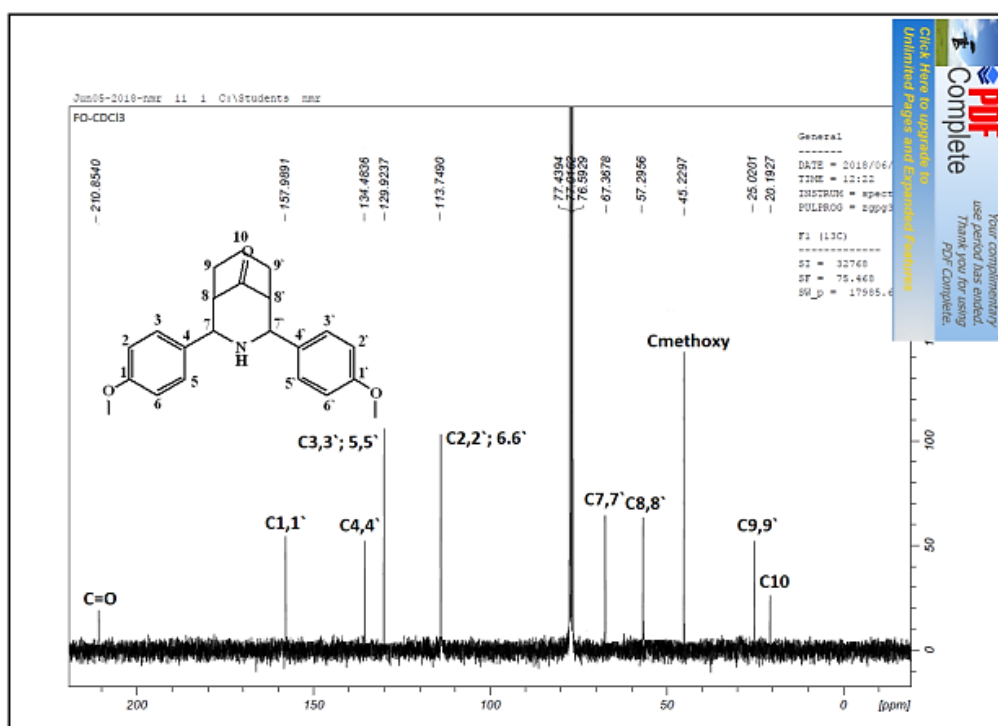
Figure (3-27): ^{13}C-NMR chart of precursor F2 in CDCl$_3$.

88
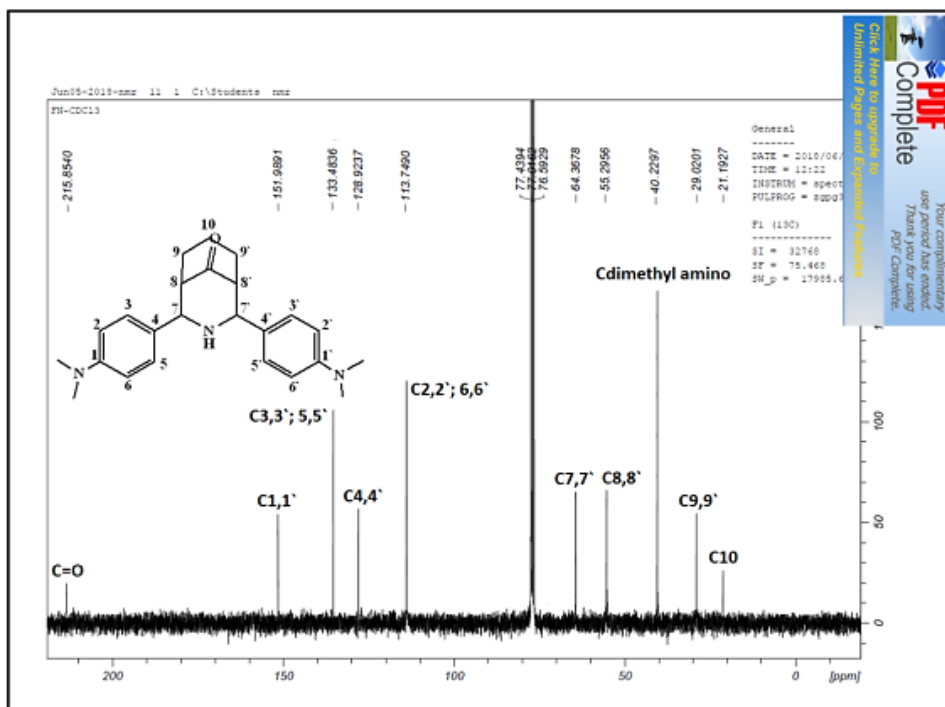
Figure (3-28): ^{13}**C-NMR chart of precursor F3 in CDCl$_3$.**

(3.3.13) ^{13}C-NMR spectrum of 2-((((3-nitrophenyl) amino) (phenyl) methyl) cyclohexan-1-one (N1)

The ^{13}C-NMR of N1 is allocated in Figure (3-29). The NMR that performed in DMSO-d^6 revealed signals in the aliphatic region at δc= 22.89, 27.90, 30.61 and 40.97 ppm, which related to (C$_3$), (C$_4$), (C$_5$) and (C$_6$), respectively. Chemical shifts that assigned to (C$_2$) and (C$_7$, C-H) were observed at δc= 55.69 and 56.25 ppm, respectively. The spectrum indicated resonances in the aromatic region at 112.93, 115.73, 120.71 and 125.06 ppm, assigned to (C$_9$), (C$_{11}$), (C$_{13}$) and (C$_{12}$), respectively. Further, signals that detected at 127.49, 130.04 and 133.90 ppm were assigned to (C$_{17}$), (C$_{15,15`}$) and (C$_{16,16`}$). A chemical shift at 142.21 ppm attributed to (C$_{14}$), while signals at 150.91 and 158.99 ppm assigned to (C$_8$, C-NH) and (C$_{10}$, C-NO$_2$), respectively. Finally, the resonance at δc= 210.94 ppm is

attributed to C=O moiety of the carbonyl group. The ^{13}C-NMR resonances are included in Table (3-8).
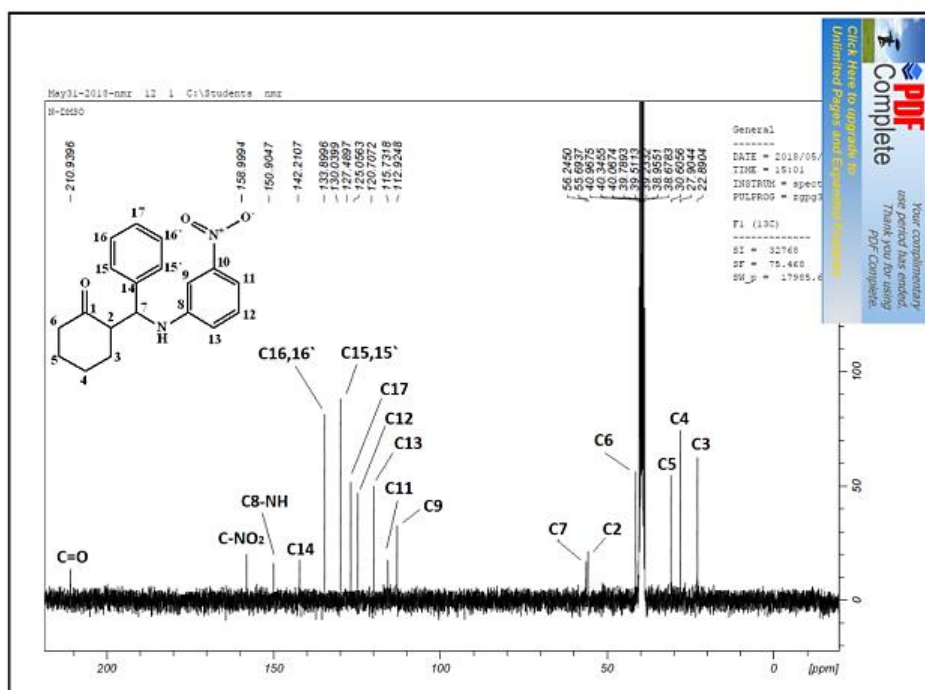
Figure (3-29): ^{13}C-NMR chart of precursor N1 in DMSO-d^6.

(3.3.14) ^{13}C-NMR spectrum of 2-((4-methoxyphenyl) (phenylamino) methyl)cyclohexan-1-one (N2) and 2-((4-(dimethylamino)phenyl)((3-nitrophenyl)amino)methyl)cyclohexan-1-one (N3)

The ^{13}C-NMR of N2 and N3 are placed in Figures (3-30) and (3-31), respectively. The spectra exhibit almost an analogue pattern to that of N1 and a similar explanation may be used to discuss the spectra. Furthermore, in the spectrum of N2 peak detected at δc= 55.09 ppm assigned to C-methoxy, and the chemical shift at δc= 45.23 ppm in the spectrum of N3 assigned to C-dimethyl amino group. The ^{13}C-NMR data and their assignment are tabulated in Table (3-8).
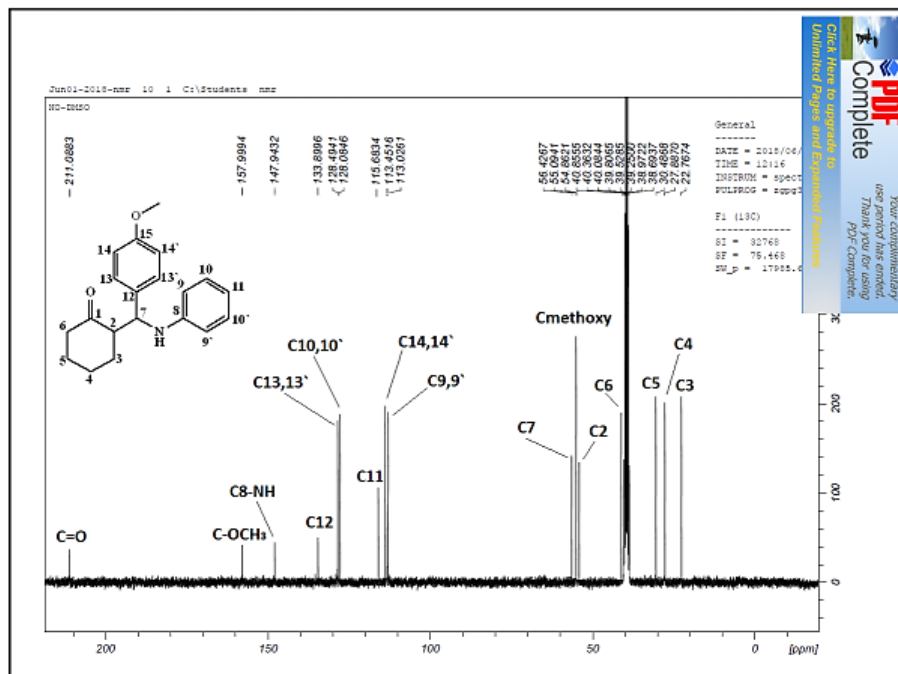
Figure (3-30): ^{13}C-NMR chart of precursor N2 in DMSO-d^6.
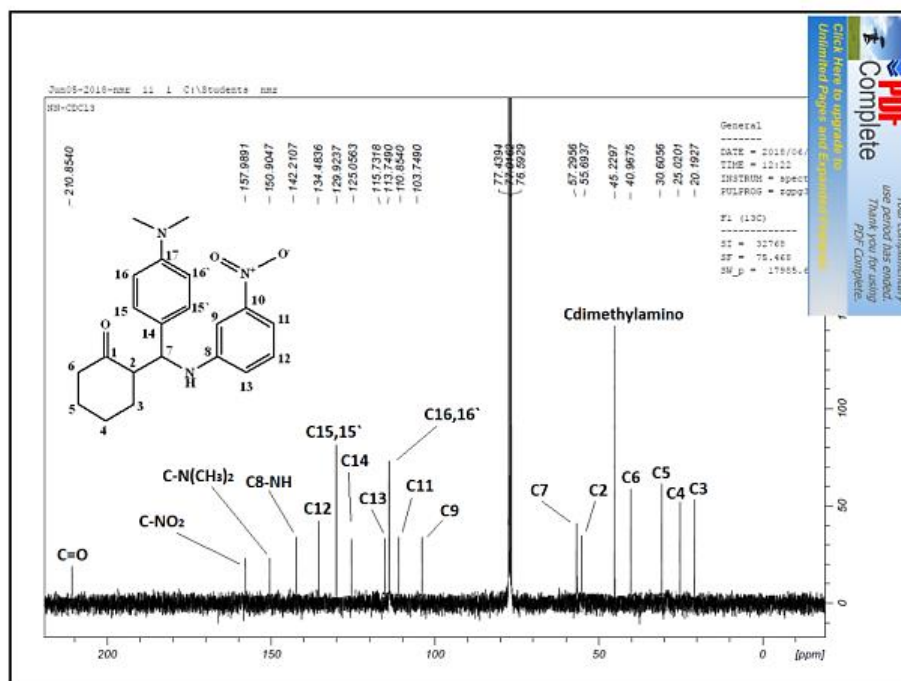
Figure (3-31): ^{13}C-NMR chart of precursor N3 in CDCl$_3$.

91

(3.3.15) ^{13}C-NMR spectrum of 2-(2,4-diphenyl-3-azabicyclo[3.3.1]nonan-9-ylidene)hydrazine-1-carboselenoamide (HL[1])

The ^{13}C-NMR of HL[1], Figure (3-32), indicates a two set of peaks in the aliphatic and aromatic region. The chemical shift in the aliphatic area that related to (C_{10}) appeared as expected at δc= 22.52 ppm. Signals related to ($C_{9,9'}$) and ($C_{7,7'}$) were detected at δc= 28.49 and 61.75 ppm, respectively. The spectrum recorded separately the chemical shifts of C_8 and $C_{8'}$ at δc= 50.22 and 52.20 ppm, respectively indicating the two carbons are non-equivalent. Signals attributed to ($C_{1,1'}$), ($C_{3,3',5,5'}$) and ($C_{2,2',6,6'}$) were observed at δc= 125.85, 126.20 and 127.00 ppm, respectively. Peak that attributed to ($C_{4,4'}$) was seen in the expected region at δc= 140.22 ppm. Further, chemical shift at 161.75 ppm were related to C=N of the imine moiety. Whereas peak at 172.22 ppm due to the C=Se group [3,12]. The ^{13}C-NMR resonances are placed in Table (3-7).
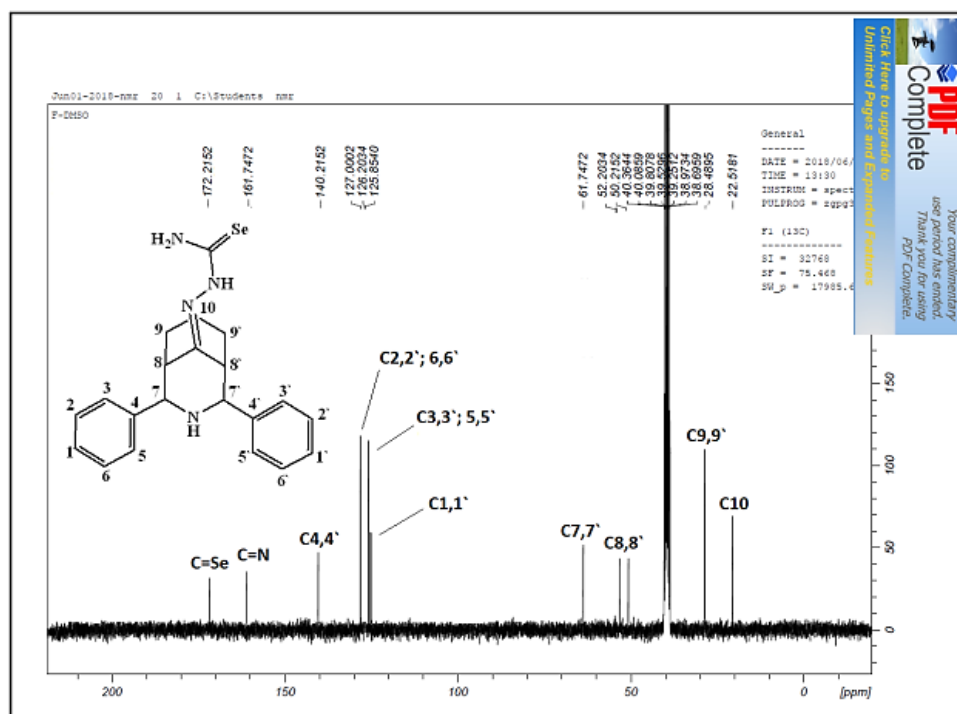
Figure (3-32): ^{13}C-NMR chart of HL[1] in DMSO-d[6].

(3.3.16) ^{13}C-NMR spectrum of 2-(2,4-bis(4-methoxyphenyl)-3-azabicyclo [3.3.1]nonan-9-ylidene)hydrazine-1-carboselenoamide (HL^2)

The ^{13}C-NMR of HL^2 is placed in Figure (3-33). The peak that related to (C$_{10}$) is appeared as expected in the aliphatic region at δc= 21.75 ppm. Signals related to (C$_{9,9'}$) and (C$_{7,7'}$) were observed at δc= 29.37 and 64.37 ppm, respectively. Chemical shifts of C$_8$ and C$_{8'}$ appeared at δc= 44.23 and 49.75 ppm indicating the two carbons are non-equivalent. Resonance at δc= 53.30 ppm was related to C-methoxy. Peak detected at δc= 113.44 ppm assigned to (C$_{2,2',6,6'}$), while signal at δc= 128.92 ppm was attributed to (C$_{3,3',5,5'}$). Further, resonances at 132.48 and 150.99 ppm related to (C$_{4,4'}$) and (C$_{1,1'}$, C-OCH$_3$). Finally, the chemical shifts of the C=N of the imine moiety appeared as expected downfield at δc= 159.99 and the C=Se group recorded at δc= 170.44 ppm [3,12], respectively. The ^{13}C-NMR chemical shifts are included in Table (3-7).
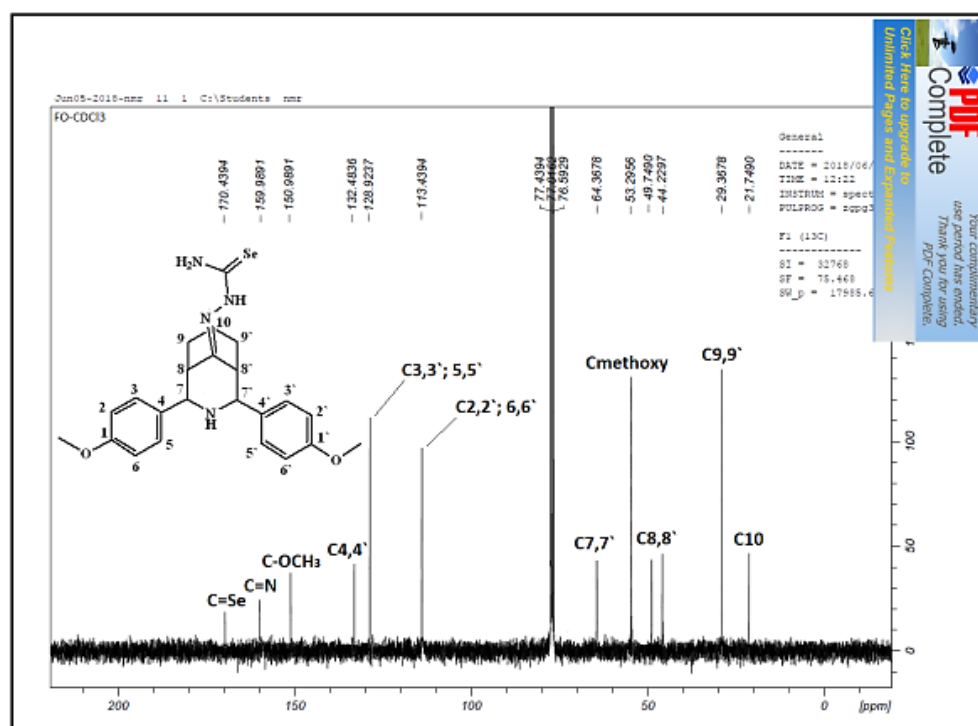
Figure (3-33): ^{13}C-NMR chart of HL^2 in CDCl$_3$.

93

(3.3.17) ^{13}C-NMR spectrum of 2-(2,4-bis(4-(dimethylamino)phenyl)-3-azabicyclo[3.3.1]nonan-9-ylidene)hydrazine-1-carboselenoamide (HL^3)

The ^{13}C-NMR of HL^3 in CDCl$_3$ is placed in Figure (3-34). The chemical shift of (C$_{10}$) is recorded at δc= 21.75 ppm. Signals related to (C$_{9,9`}$), and (C$_{7,7`}$) were observed at δc= 29.37 and 64.37 ppm, respectively. The spectrum indicated two chemical shifts at δc= 51.99 and 55.30 ppm correlated to C$_8$ and C$_{8`}$ indicating the two carbons are non-equivalent. Resonance at δc= 40.23 ppm was related to C-dimethylamino. Peak detected at δc= 113.75 ppm assigned to (C$_{2,2`,6,6`}$), while signal at δc= 128.92 ppm was attributed to (C$_{3,3`,5,5`}$). Further, resonances at 132.48 and 151.99 ppm related to (C$_{4,4`}$) and (C$_{1,1`}$, (C-N(CH$_3$)$_2$), respectively. Finally, a peak recorded at δc= 159.99 ppm correlated to C=N imine moiety. The chemical shift of the C=Se group observed at δc= 171.44 ppm [3,12]. The ^{13}C-NMR resonances are included in Table (3-7).
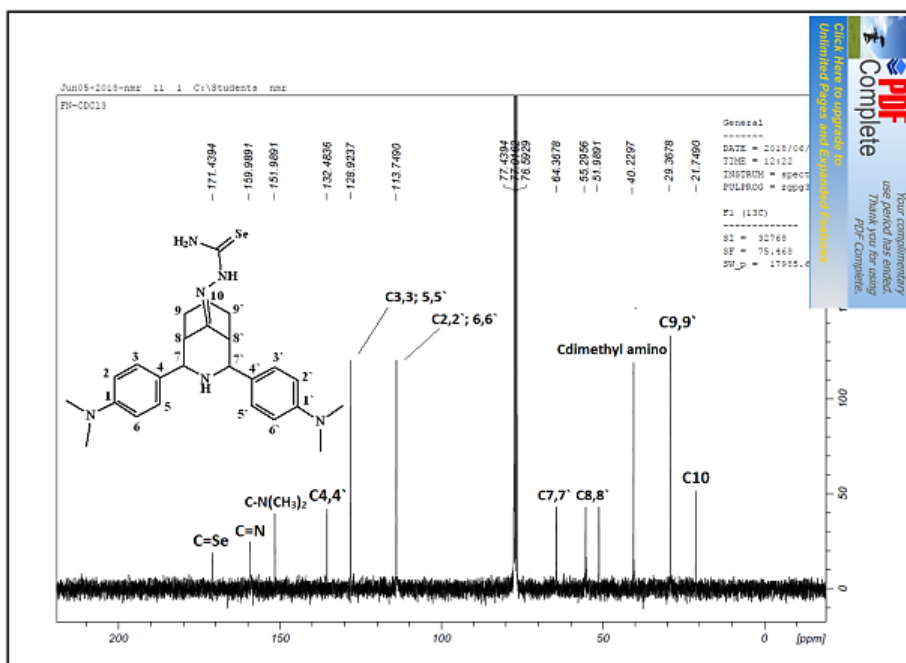
Figure (3-34): ^{13}C-NMR chart of HL^3 in CDCl$_3$

Table (3-7): ^{13}C-NMR data of precursors F1-F3 and ligands HL^1-HL^3 with their resonances in ppm (δ).

Compound	(C_{10})	$(C_{9,9^`})$	$(C_{8,8^`})$	$(C_{7,7^`})$	$(C_{2,2^`,6,6^`})$ $(C_{3,3^`,5,5^`})$	$(C_{4,4^`})$	$(C_{1,1^`})$	$(C=O)$	$(C=N)$	$(C=Se)$	$(2 \times OCH_3)$ $(2 \times N(CH_3)_2)$
F1	20.52	28.49	63.72	53.22	128.20 127.00	141.75	126.84	215.85	_	_	– –
F2	20.19	25.02	57.30	67.37	113.75 129.92	134.48	157.99	210.85	_	_	45.23 –
F3	21.19	29.02	55.30	64.37	113.75 133.48	128.92	151.99	215.85	_	_	– 40.23
HL^1	22.52	28.49	50.22 52.20	61.75	127.00 126.20	140.22	125.85	_	161.75	172.22	– –
HL^2	21.75	29.37	44.23 49.75	64.37	113.44 128.92	132.48	150.99	_	159.99	170.44	53.30 –
HL^3	21.75	29.37	51.99 55.30	64.37	113.75 128.92	132.48	151.99	_	159.99	171.44	– 40.23

(3.3.18) ^{13}C-NMR spectrum of (E)-2-(2-(((3-nitrophenyl) amino) (phenyl) methyl)cyclohexylidene)hydrazine-1-carboselenoamide (HL^4)

The ^{13}C-NMR chart of HL^4 is placed in Figure (3-35). In the aliphatic region, signals appeared at δc= 22.89, 27.90, 30.61 and 40.97 ppm related to (C$_3$), (C$_4$), (C$_5$) and (C$_6$), respectively. Resonances correlated to (C$_2$) and (C$_7$, C-H) were observed at δc= 55.91 and δc= 58.21 ppm, respectively. The spectrum showed peaks in the aromatic region at 112.93, 115.73, 126.04 and 132.89 ppm assigned to (C$_9$), (C$_{11}$), (C$_{13}$) and (C$_{12}$), respectively. Further, signals detected at 127.06, 128.04 and 130.61 ppm assigned to (C$_{17}$), (C$_{15,15'}$) and (C$_{16,16'}$), respectively. A chemical shift at 143.21 ppm attributed to (C$_{14}$), while signals at 152.91 and 155.68 ppm assigned to (C$_8$, C-NH) and (C$_{10}$, C-NO$_2$) groups, respectively. Finally, the imine moiety displayed at δc= 160.94 ppm, while the C=Se group recorded at δc= 175.94 ppm [3,12]. The ^{13}C-NMR resonances are included in Table (3-8).
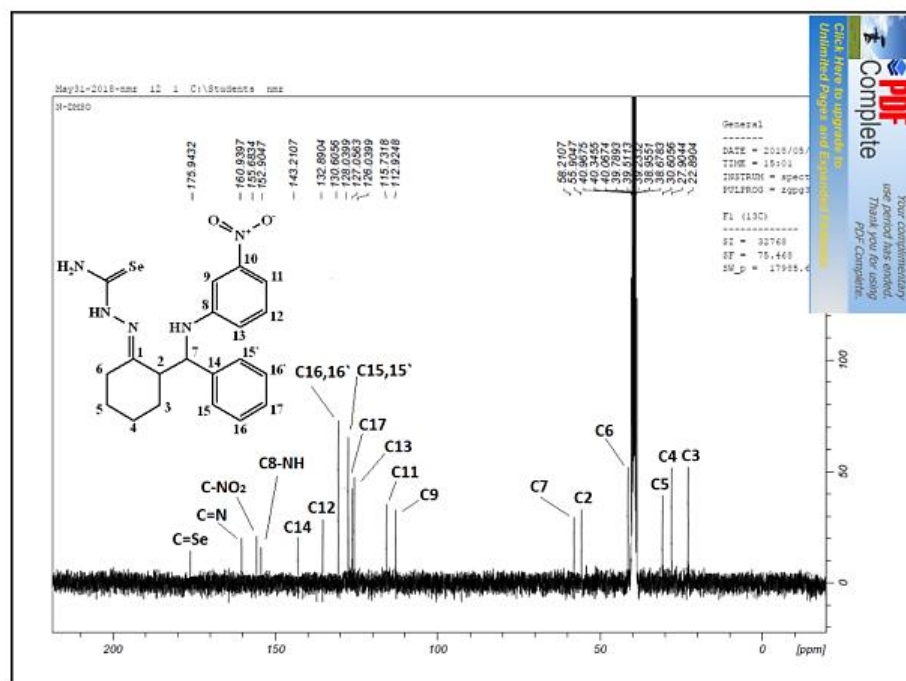
Figure (3-35): ^{13}C-NMR chart of HL^4 in DMSO-d^6.

96

(3.3.19) ^{13}C-NMR spectrum of (E)-2-(2-((4-methoxyphenyl) (phenylamino) methyl)cyclohexylidene)hydrazine-1-carboselenoamide (HL^5)

The ^{13}C-NMR of HL^5 is allocated in Figure (3-36). The spectrum revealed two sets of peaks in the aliphatic and aromatic region. In the aliphatic region, signals at δc= 24.77, 27.89, 30.49 and 40.86 ppm related to (C$_3$), (C$_4$), (C$_5$) and (C$_6$), respectively. Chemical shifts that assigned to (C$_2$) and (C$_7$, C-H) group were observed at δc= 54.86 and δc= 57.43 ppm respectively. Peak detected at δc= 55.09 ppm assigned to C-methoxy. In the aromatic region, chemical shifts assigned to (C$_{9,9'}$) and (C$_{14,14'}$) were detected at δc= 113.03 and δc= 114.45 ppm, respectively, while (C$_{11}$) appeared at δc= 115.68 ppm. Further, signals related to (C$_{10,10'}$) and (C$_{13,13'}$) detected at δc= 128.09 and 128.49 ppm, respectively. A chemical shift at 133.90 ppm attributed to (C$_{12}$), while signals at 147.94 and 155.68 ppm assigned to (C$_8$, C-NH) and (C$_{15}$, C-OCH$_3$) groups, respectively. Finally, the C=N of the imine moiety appears at δc= 159.99 ppm and the C=Se group at δc= 174.94 ppm [3,12]. The ^{13}C-NMR resonances are included in Table (3-8).
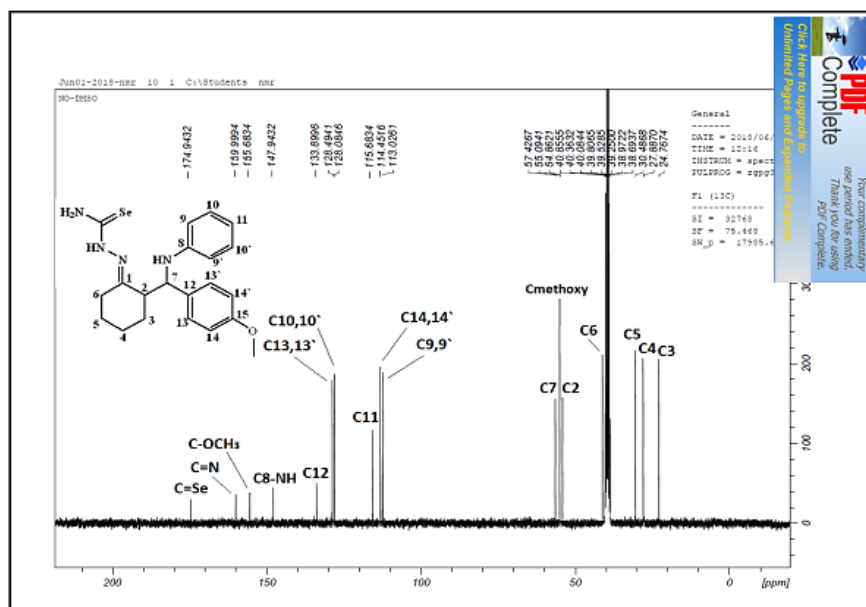
Figure (3-36): ^{13}C-NMR chart of HL^5 in DMSO-d^6.

97

(3.3.20) ^{13}C-NMR spectrum of (E)-2-(2-((4-(dimethylamino)phenyl)((3-nitro phenyl)amino)methyl)cyclohexylidene)hydrazine-1-carboselenoamide (HL^6)

The ^{13}C-NMR chart of HL^6 is placed in Figure (3-37). In the aliphatic region, signals at δc= 24.77, 27.89, 30.61 and 41.97 ppm related to (C$_3$), (C$_4$), (C$_5$) and (C$_6$), respectively. Peak detected at δc= 45.23 ppm assigned to C-dimethylamino. Chemical shifts related to (C$_2$) and (C$_7$, C-H) group were observed at δc= 50.69 and 54.30 ppm, respectively. In the aromatic region, the spectrum indicated signals at 103.75, 110.94, 113.75 and 134.99 ppm related to (C$_9$), (C$_{11}$), (C$_{13}$) and (C$_{12}$), respectively. Chemical shifts assigned to (C$_{16,16'}$), (C$_{14}$) and (C$_{15,15'}$) were detected at 115.73, 125.06 and 129.92 ppm, respectively. Peak attributed to (C$_{17}$, C-N(CH$_3$)$_2$) appeared at δc= 142.91 ppm. Furthermore, signals related to (C$_8$, C-NH) and (C$_{10}$, C-NO$_2$) were observed at δc= 147.94 and δc= 155.68 ppm, respectively. A resonance at 160.64 ppm correlated to C=N group, while signal at δc= 176.94 ppm assigned to C=Se group [3,12]. The ^{13}C-NMR resonances are included in Table (3-8).
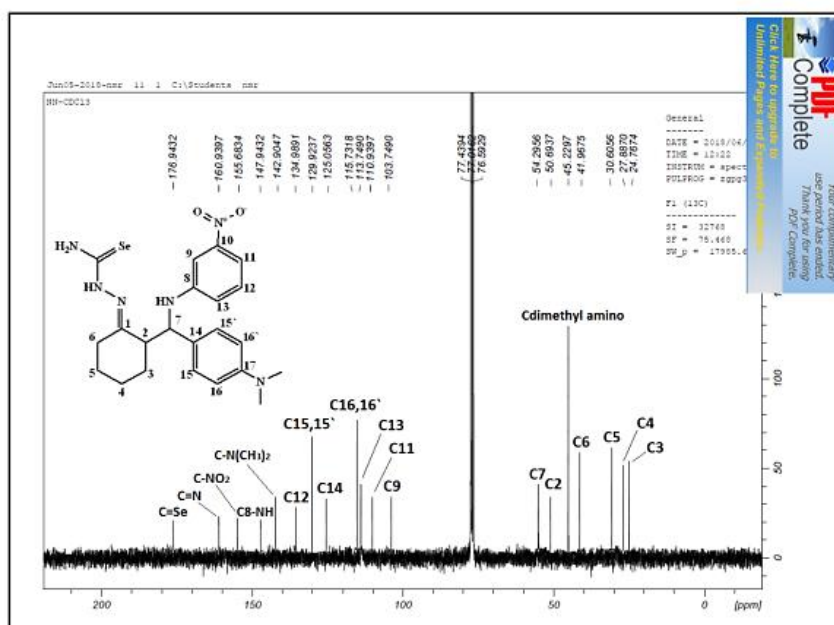
Figure (3-37): ^{13}C-NMR chart of HL^6 in CDCl$_3$.

Table (3-8): ^{13}C-NMR data of precursors N1-N3 and ligands HL^4-HL^6 with their resonances in ppm (δ).

Compound	(C$_2$) (C$_3$)	(C$_4$) (C$_5$)	(C$_6$) (C$_7$)	(C$_9$) (C$_{11}$)	(C$_{12}$) (C$_{13}$)	(C$_{14}$) (C$_{15}$)	(C$_{15,15'}$) (C$_{16,16'}$)	(C$_{9,9'}$) (C$_{10,10'}$)	(C$_{13,13'}$) (C$_{14,14'}$)	(C$_8$-NH) (C$_{10}$-NO$_2$)	(C$_{15}$-OCH$_3$) (C$_{17}$)	(C$_{17}$-N(CH$_3$)$_2$) (C=O)	(C=Se) (C=N)	(OCH$_3$) (N(CH$_3$)$_2$)
N1	55.69	27.90	40.97	112.93	125.06	142.21	130.04	_	_	150.91	_	_	_	_
	22.89	30.61	56.25	115.73	120.71	_	133.90	_	_	158.99	127.49	210.94	_	_
N2	54.86	27.89	40.86	_	133.90	_	_	113.03	128.49	147.94	157.99	_	_	55.09
	22.77	30.49	56.43	115.68	_	_	_	128.09	113.45	_	_	211.09	_	_
N3	55.69	25.02	40.97	103.75	134.48	125.06	129.92	_	_	142.21	_	150.91	_	_
	20.19	30.61	57.30	110.85	115.73	_	113.75	_	_	157.99	_	210.85	_	45.23
HL^4	55.91	27.90	40.97	112.93	132.89	143.21	128.04	_	_	152.91	_	_	175.94	_
	22.89	30.61	58.21	115.73	126.04	_	130.61	_	_	155.68	127.06	_	160.94	_
HL^5	54.86	27.89	40.86	_	133.90	_	_	113.03	128.49	147.94	155.68	_	174.94	55.09
	24.77	30.49	57.43	115.68	_	_	_	128.09	114.45	_	_	_	159.99	_
HL^6	50.69	27.89	41.97	103.75	134.99	125.06	129.92	_	_	147.94	_	142.91	176.94	_
	24.77	30.61	54.30	110.94	113.75	_	115.73	_	_	155.68	_	_	160.64	45.23

99

(3.4) ^{77}Se-NMR spectra of ligands

(3.4.1) ^{77}Se-NMR spectrum of 2-(2,4-diphenyl-3-azabicyclo[3.3.1]nonan-9-ylidene)hydrazine-1-carboselenoamide (HL^1)

The ^{77}Se-NMR data of HL^1 is recorded in DMSO-d^6 solvent and placed in Figure (3-38). The ^{77}Se-NMR showed one peak at δ_{Se}= 179.36 ppm assigned to C=Se group, confirming the presence of the C=Se moiety in its selenone form in the solution. This finding is within the range of reported Se-compounds adopt the selenone form [12]. Further, this finding supported by the ^{13}C-NMR data that confirmed the existence of the C=Se group in its selenone form (see ^{13}C-NMR section (3.3.15), page 92), [3,12]. Furthermore, in the solid state the FT-IR spectrum showed no band about 2300 cm^{-1} may assign to ν(Se-H), (see FT-IR section (3.2.3.1), page 66), confirming the existence of the ligand in its selenone form [3,27]. The ^{77}Se-NMR data included in Table (3-9).
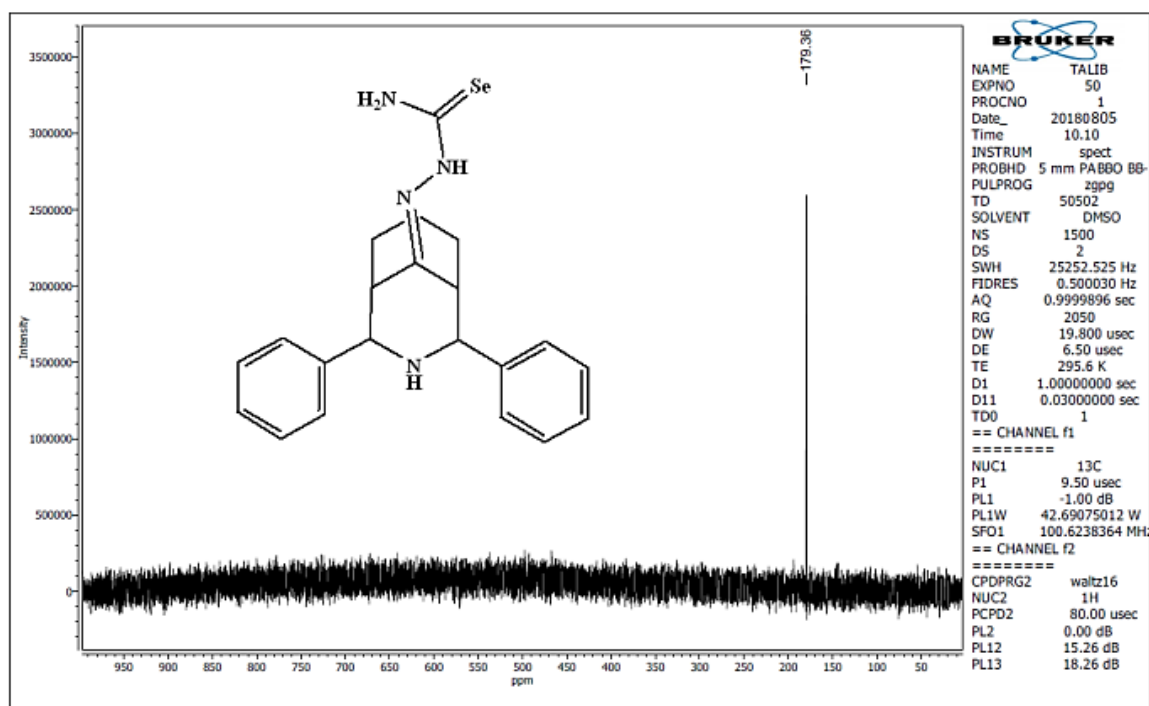
Figure (3-38): ^{77}Se-NMR chart of HL^1 in DMSO-d^6.

(3.4.2) ^{77}Se-NMR spectrum of ligands HL^2-HL^6

The ^{77}Se-NMR spectra of HL^2 and HL^3 are depicted in Figures (3-39) and (3-40), respectively. The spectra indicated resonances at δ_{Se}= 206.80 and 198.50 ppm related to C=Se groups as selenone form for HL^2 and HL^3, respectively. The down field of these chemical shift values of ligands, compared with that of HL^1 may be related to the introduction of different substituents groups on the backbone of the phenyl group OCH$_3$ and N(CH$_3$)$_2$. These groups may lead to the delocalisation of the electronic density on these moieties and the appearance of the C=Se group downfield [3,12]. The ^{77}Se-NMR spectra of HL^4-HL^6 are placed in Figures (3-41) to (3-43). The spectra displayed peaks at δ_{Se}= 217.60, 226.39 and 240.51 ppm related to C=Se groups of HL^4, HL^5 and HL^6, respectively. These data indicated the present of the C=Se moiety in the selenone form. The introduction of NO$_2$, OCH$_3$ and N(CH$_3$)$_2$ may be influenced the chemical shift position of the C=Se group [3,27]. The ^{77}Se-NMR resonances are included in Table (3-9).
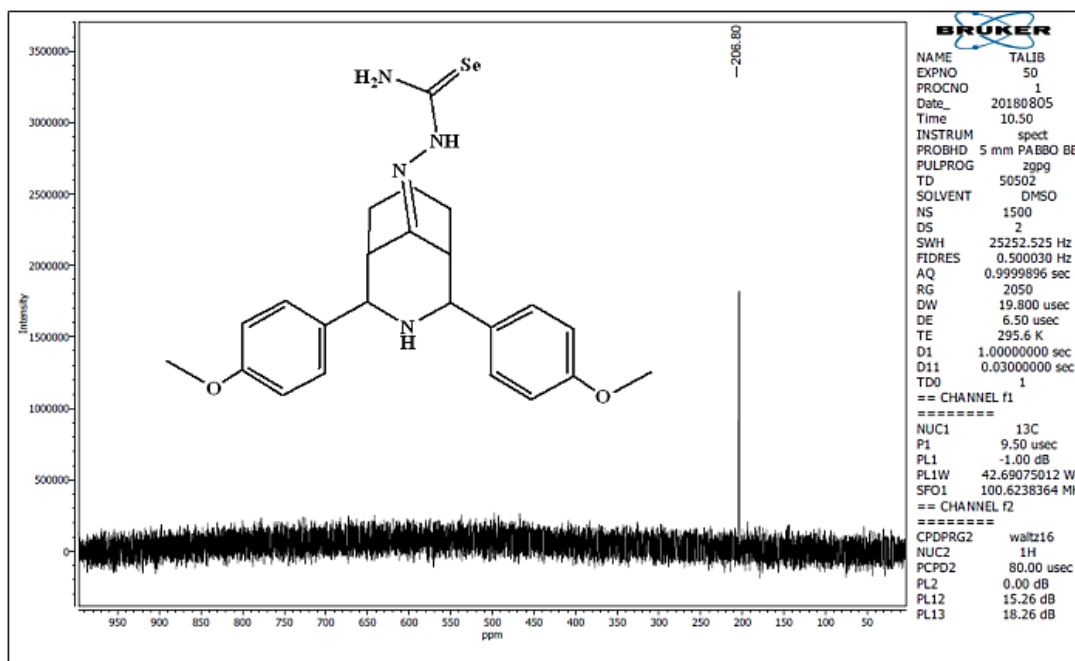
Figure (3-39): ^{77}Se-NMR chart of HL^2 in DMSO-d^6.
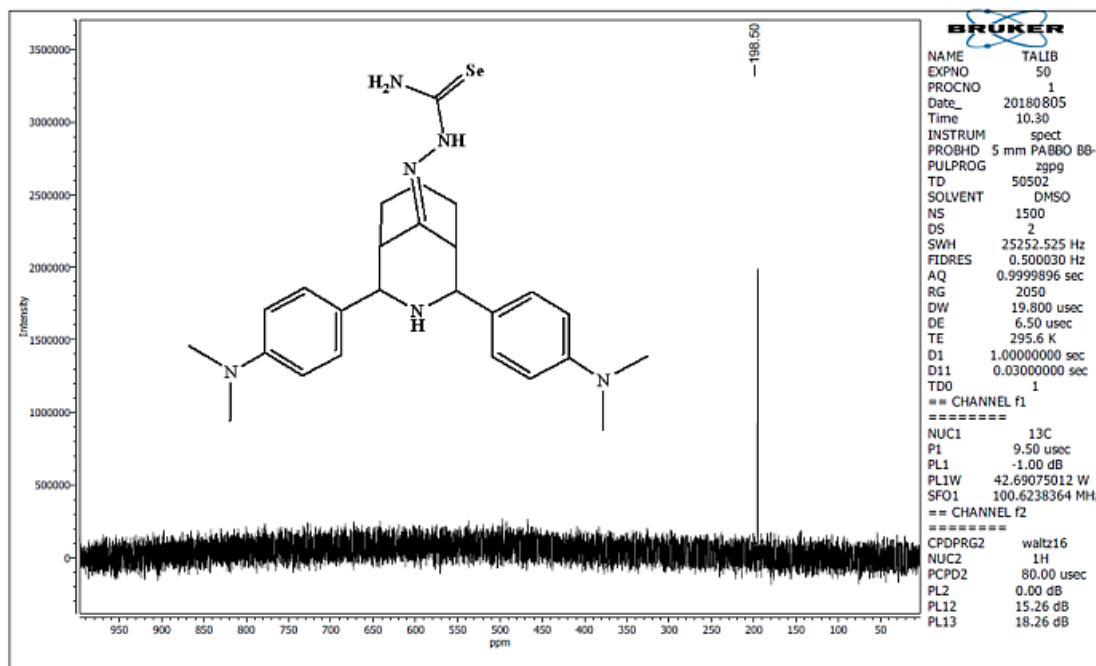
Figure (3-40): ^{77}**Se-NMR chart of HL**^{3} **in DMSO-d**^{6}**.**
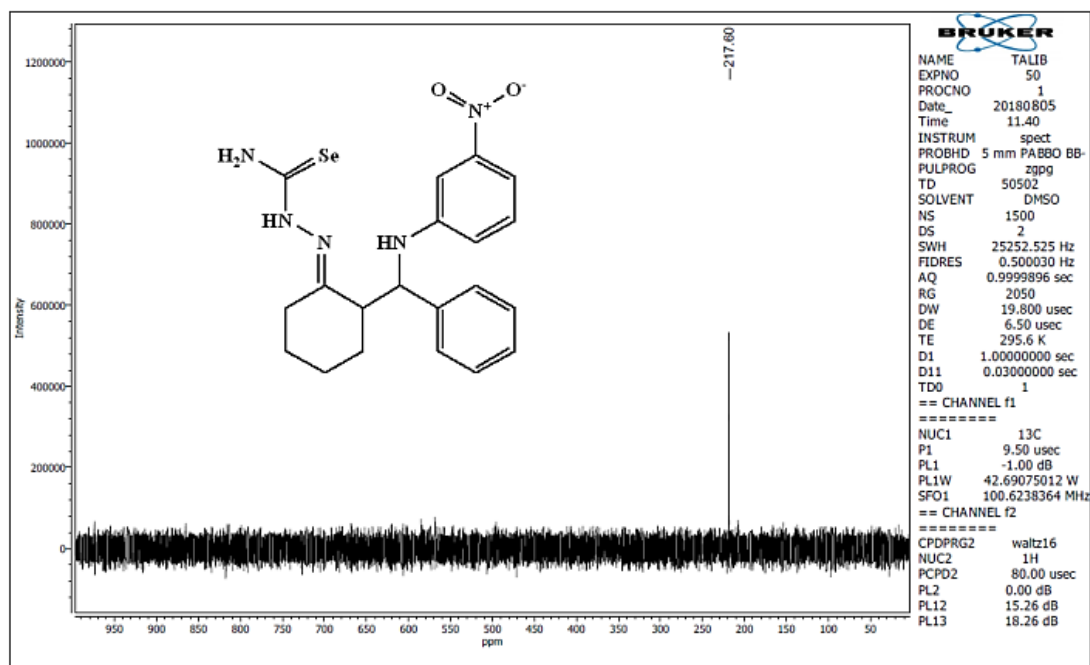
Figure (3-41): ^{77}**Se-NMR chart of HL**^{4} **in DMSO-d**^{6}**.**
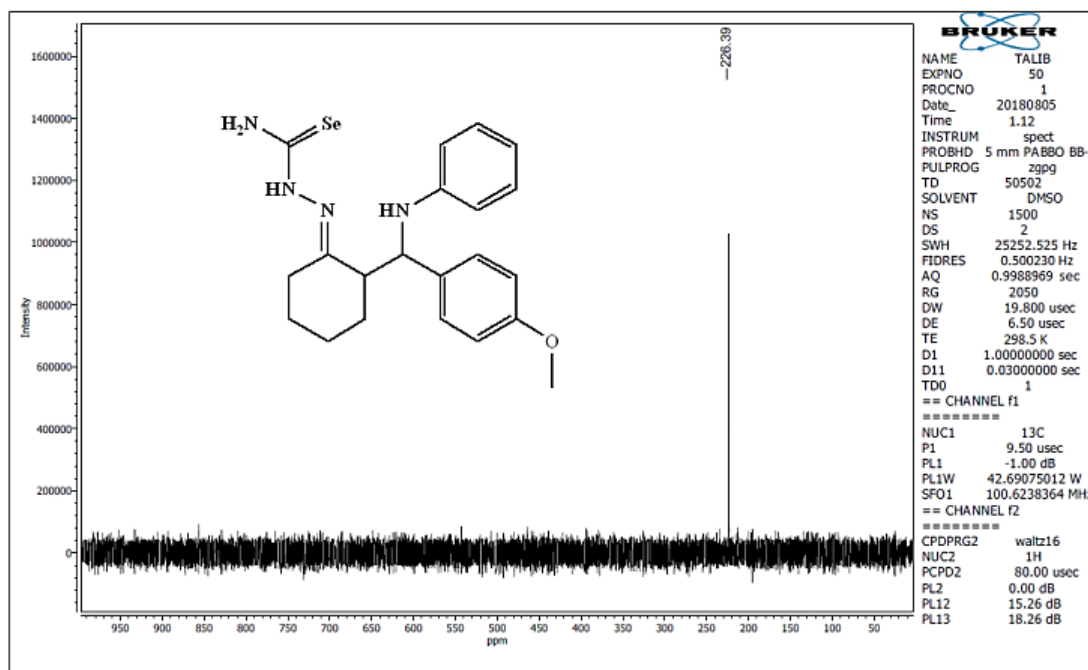
Figure (3-42): ^{77}Se-NMR chart of HL^5 in DMSO-d^6.
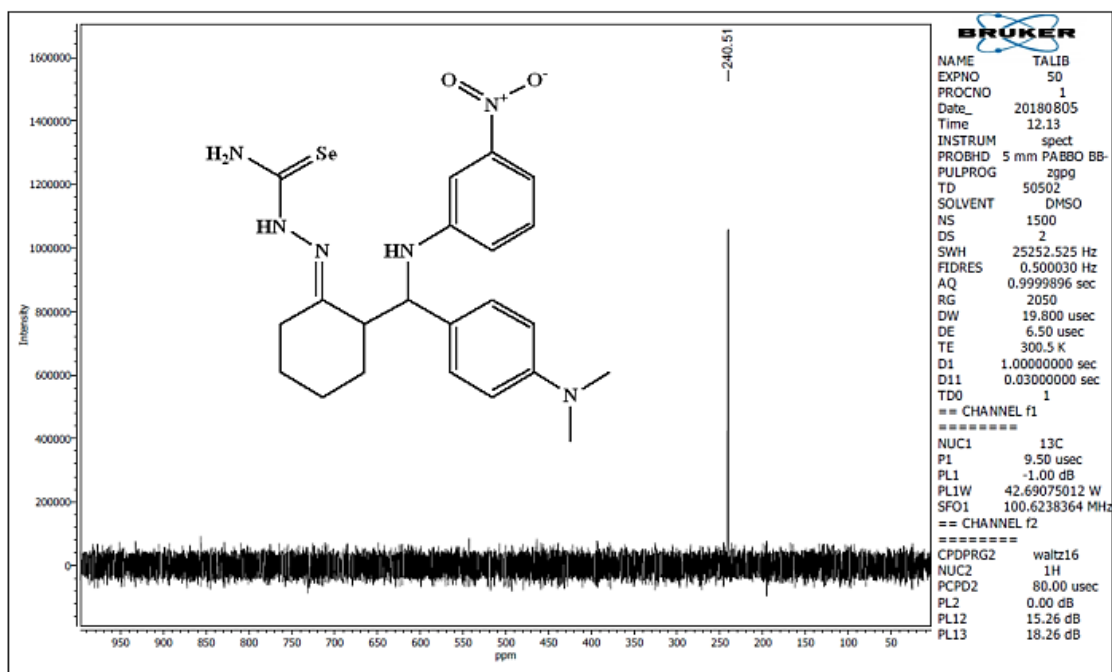
Figure (3-43): ^{77}Se-NMR chart of HL^6 in DMSO-d^6.

103

Table (3-9): ^{77}Se-NMR chemical shifts of HL^1-HL^6 with their assignment and resonances in ppm (δ).

Compound	Chemical shift for (C-Se) selenone group in ppm (δ)
HL^1	179.36
HL^2	206.80
HL^3	198.50
HL^4	217.60
HL^5	226.39
HL^6	240.51

(3.5) Mass spectra of precursors and ligands

(3.5.1) Mass spectrum of 2,4-diphenyl-3-azabicyclo[3.3.1]nonan-9-one (F1)

The electrospray (+) mass spectrum of F1 is placed in Figure (3-44). The parent ion peak of F1 detected at m/z= 291.4 amu (M)$^+$ (100%) for $C_{20}H_{21}NO$, calculates= 291.4. Peaks detected at m/z= 194.4 (87%), 158.4 (24%), 130.3 (35%) and 77.3 (15%) assigned to [M-(C$_6$H$_7$O)+H)]$^+$, [M-{(C$_6$H$_7$O+H)+(CH$_4$N+3H$_2$)}]$^+$, [M-{(C$_6$H$_7$O+H)+(CH$_4$N+3H$_2$)+ (C$_2$H$_4$)}]$^+$ and [M-{(C$_6$H$_7$O+H)+(CH$_4$N+3H$_2$)+(C$_2$H$_4$)+(C$_4$H$_5$)}]$^{+,}$ respectively. The fragmentation pattern of F1 compound is shown in Scheme (3-4).

File :C:\MSDCHEM\3\DATA\Snapshot\3000482.D
Operator :
Acquired : 1 Jul 2018 12:44 using Electro Spray Method Normal
Instrument : Instrumen
Sample Name: F
Misc Info :
Vial Number: 1
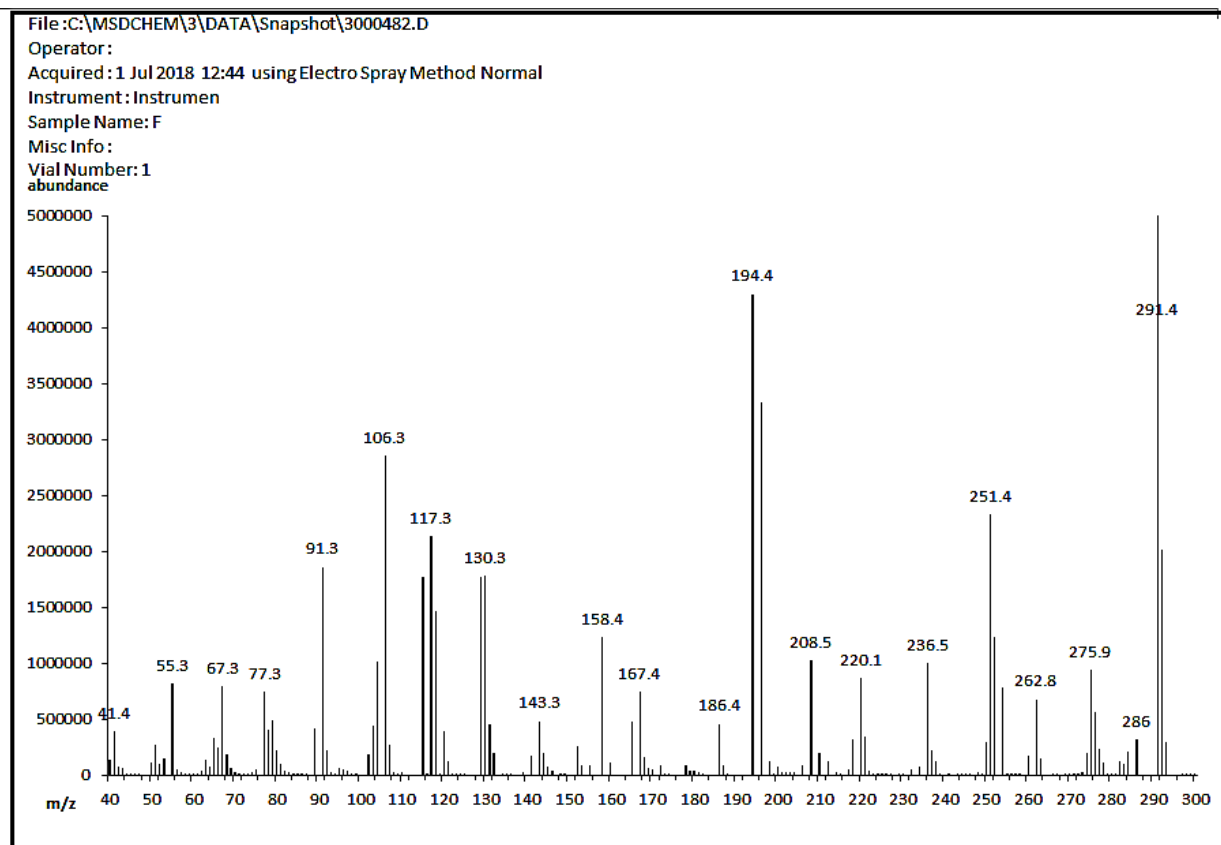
Figure (3-44): The electrospray (+) mass spectrum of F1.
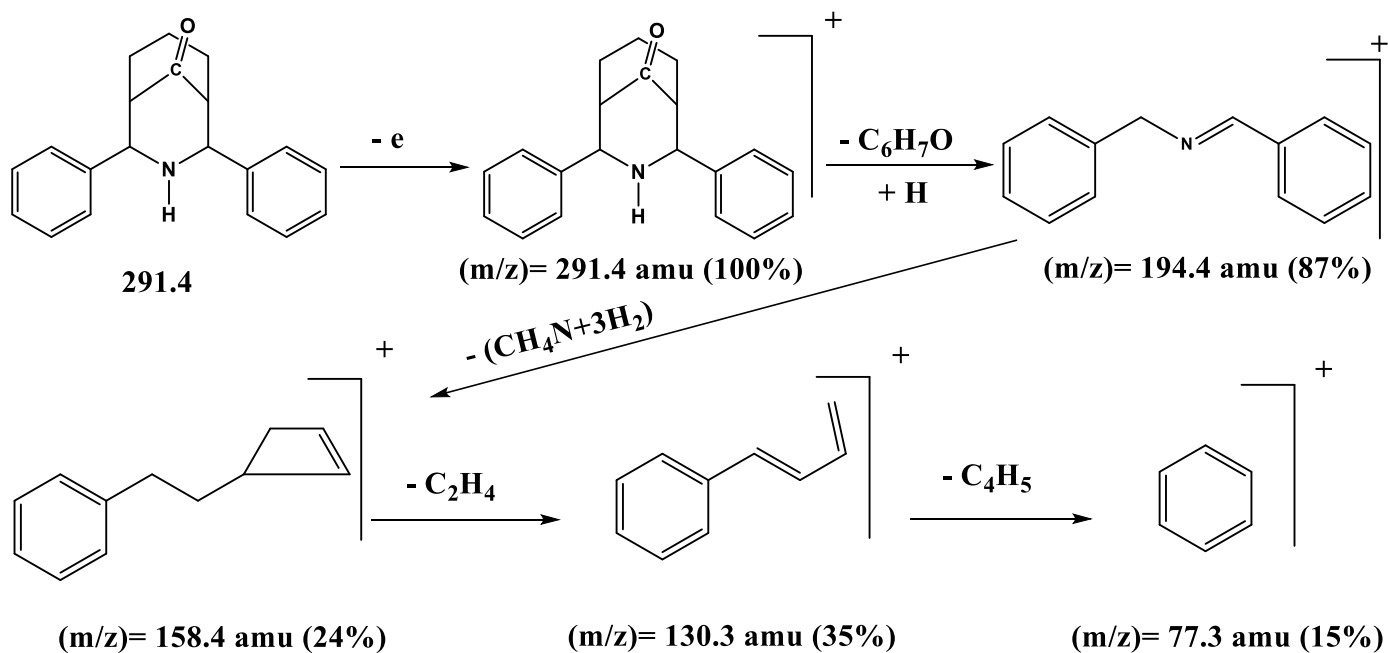
Scheme (3-4): Fragmentation outline and relative abundance of F1.

(3.5.2) Mass spectrum of 2,4-bis(4-methoxyphenyl)-3-azabicyclo [3.3.1] nonan-9-one (F2)

The electrospray (+) mass spectrum of F2 is placed in Figure (3-45). The parent ion molecule of F2 is recorded at m/z= 351.4 amu (M)$^+$ (67%) for $C_{22}H_{25}NO_3$, calculates= 351.4. Peaks detected at m/z = 254.5 (100%), 188.4 (90%), 159.4 (35%), 91.4 (15%) and 41.4 (5%) assigned to [M-(C_6H_9O)]$^+$, [M-{(C_6H_9O)+(C_5H_6)}]$^+$, [M-{(C_6H_9O)+(C_5H_6)+ (CH_2NH)}]$^+$, [M-{(C_6H_9O)+(C_5H_6)+(CH_2NH)+(C_4H_4O)}]$^+$ and [M-{(C_6H_9O)+(C_5H_6)+ (CH_2NH)+(C_4H_4O)+(C_4H_2)}]$^+$, respectively. The fragmentation pattern of F2 compound is detailed in Scheme (3-5).

106

File :C:\MSDCHEM\3\DATA\Snapshot\3000482.D
Operator :
Acquired : 1 Jul 2018 11:44 using Electro Spray Method Normal
Instrument : Instrumen
Sample Name: FO
Misc Info :
Vial Number: 1
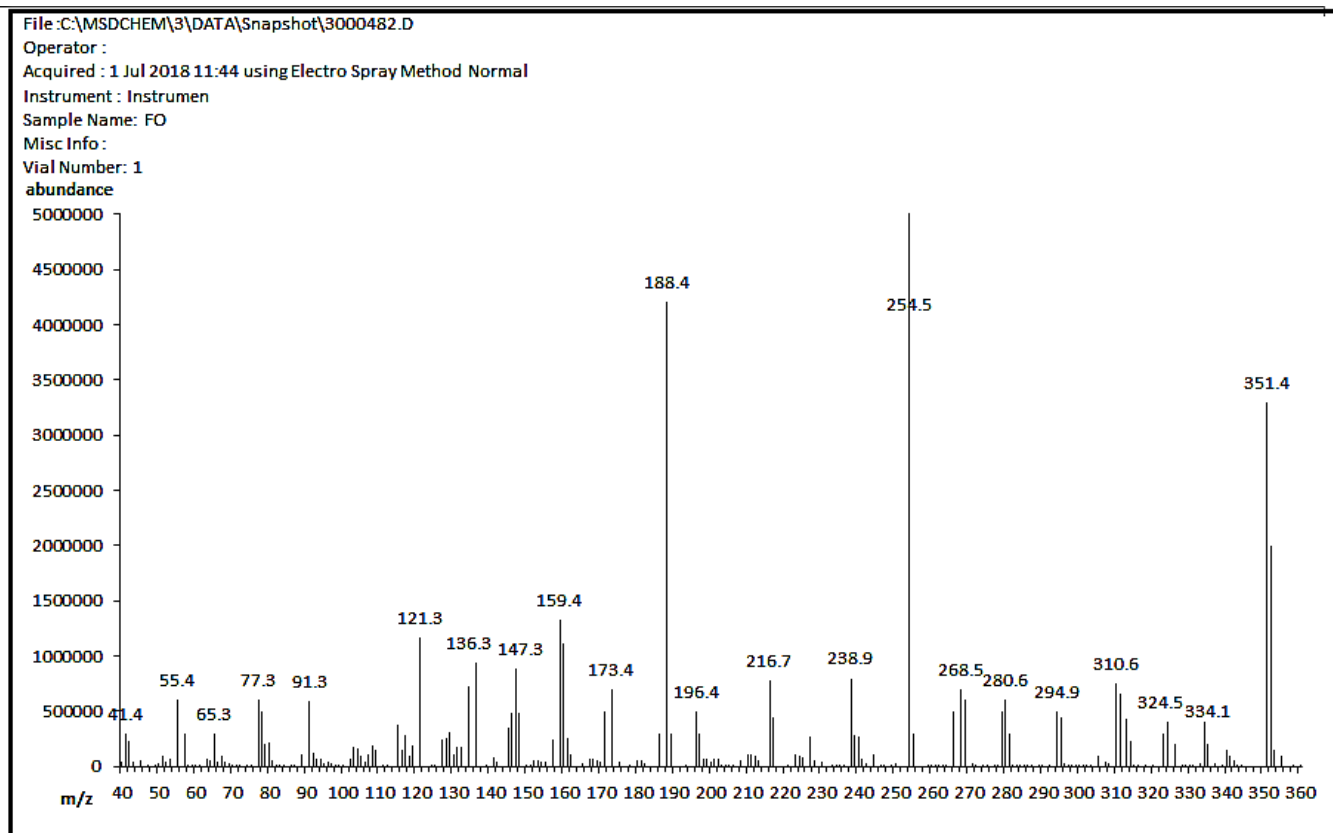
Figure (3-45): The electrospray (+) mass spectrum of F2.
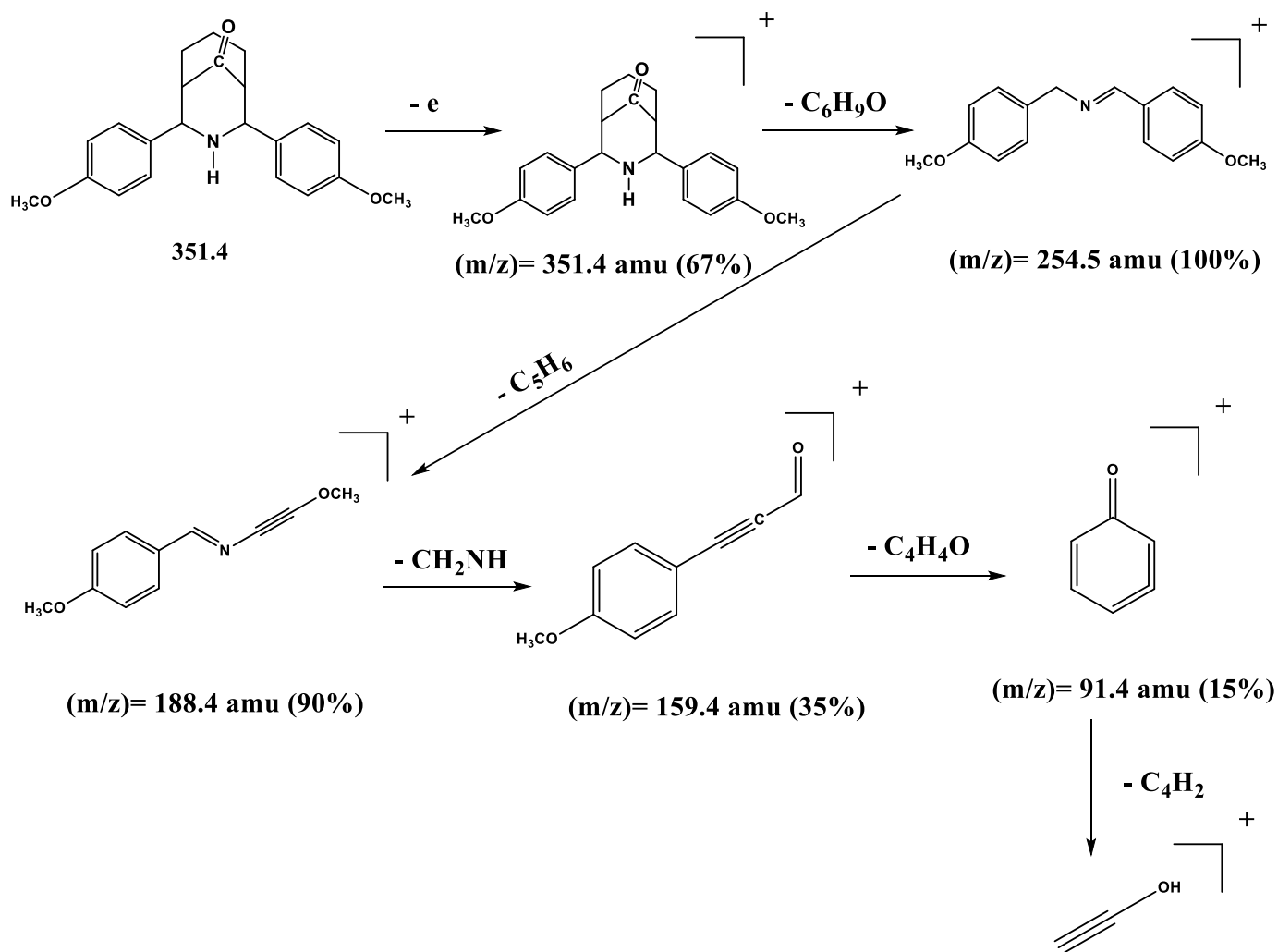
Scheme (3-5): Fragmentation outline and relative abundance of F2.

(3.5.3) Mass spectrum of 2,4-bis(4-(dimethylamino)phenyl)-3-azabicyclo [3.3.1]nonan-9-one (F3)

The electrospray (+) mass spectrum of F3 is shown in Figure (3-46). The parent ion peak of F3 is showed at m/z= 377.5 amu $(M)^+$ (86%) for $C_{24}H_{31}N_3O$, calculates= 377.5. Peaks detected at m/z= 291.4 (67%), 194.4 (100%), 117.3 (37%), 94.4 (20%) and 44.3

(5%) assigned to $[M-(C_5H_{12}N)]^+$, $[M-\{(C_5H_{12}N))+(C_6H_{11}N)\}]^+$, $[M-\{(C_5H_{12}N))+$ $(C_6H_{11}N)+(C_6H_5)\}]^+$, $[M-\{(C_5H_{12}N))+(C_6H_{11}N)+(C_6H_5)+(C_2H_2)\}]^+$ and $[M-\{(C_5H_{12}N))+$ $(C_6H_{11}N)+(C_6H_5)+(C_2H_2)+(C_4H_2)\}]^+$, respectively. The fragmentation pattern of F2 compound is shown in Scheme (3-6).

File :C:\MSDCHEM\3\DATA\Snapshot\3000482.D
Operator :
Acquired : 1 Jul 2018   12:58 using Electro Spray Method Normal
Instrument : Instrumen
Sample Name: FN
Misc Info :
Vial Number: 1
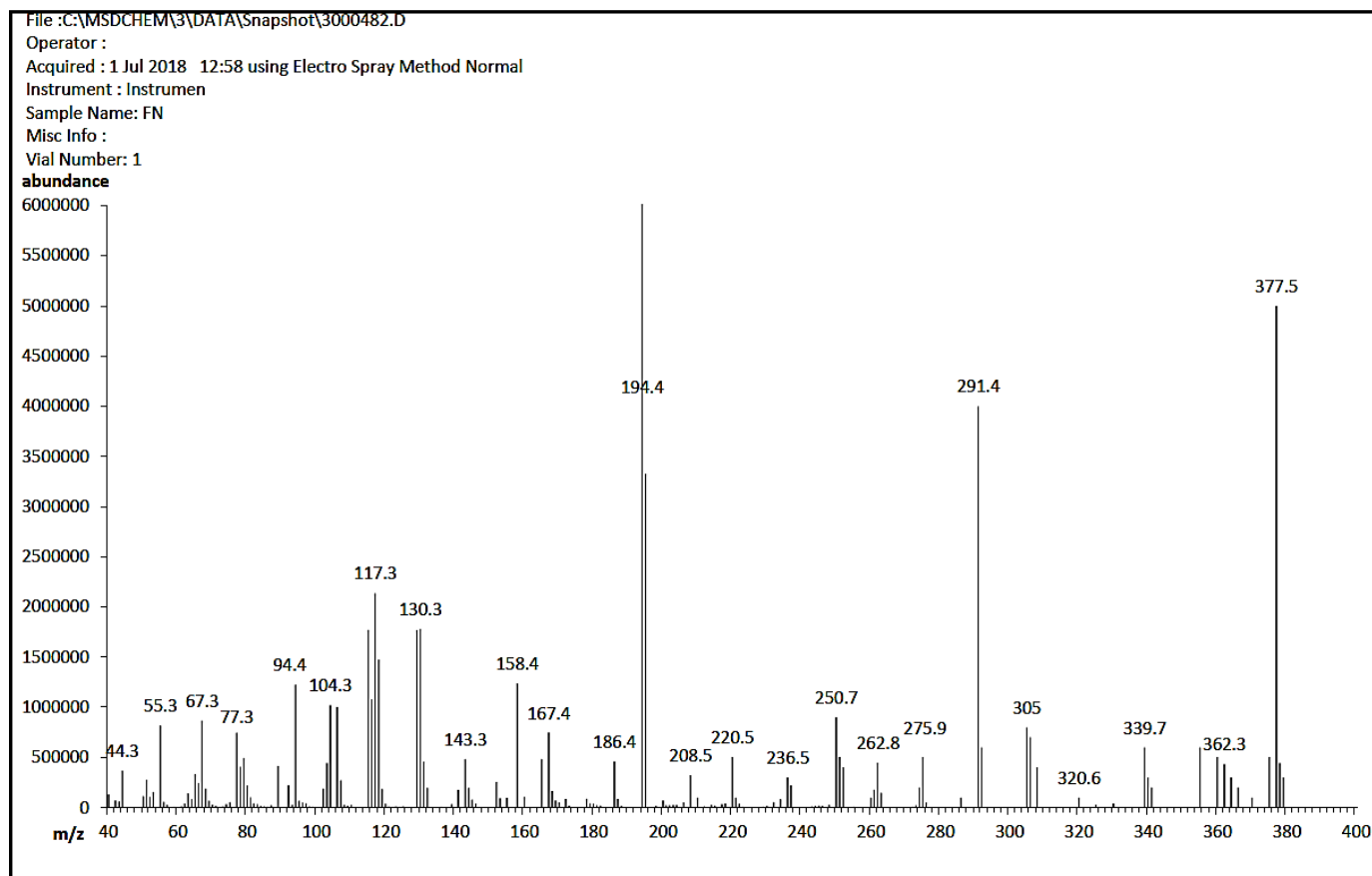
Figure (3-46): The electrospray (+) mass spectrum of F3.
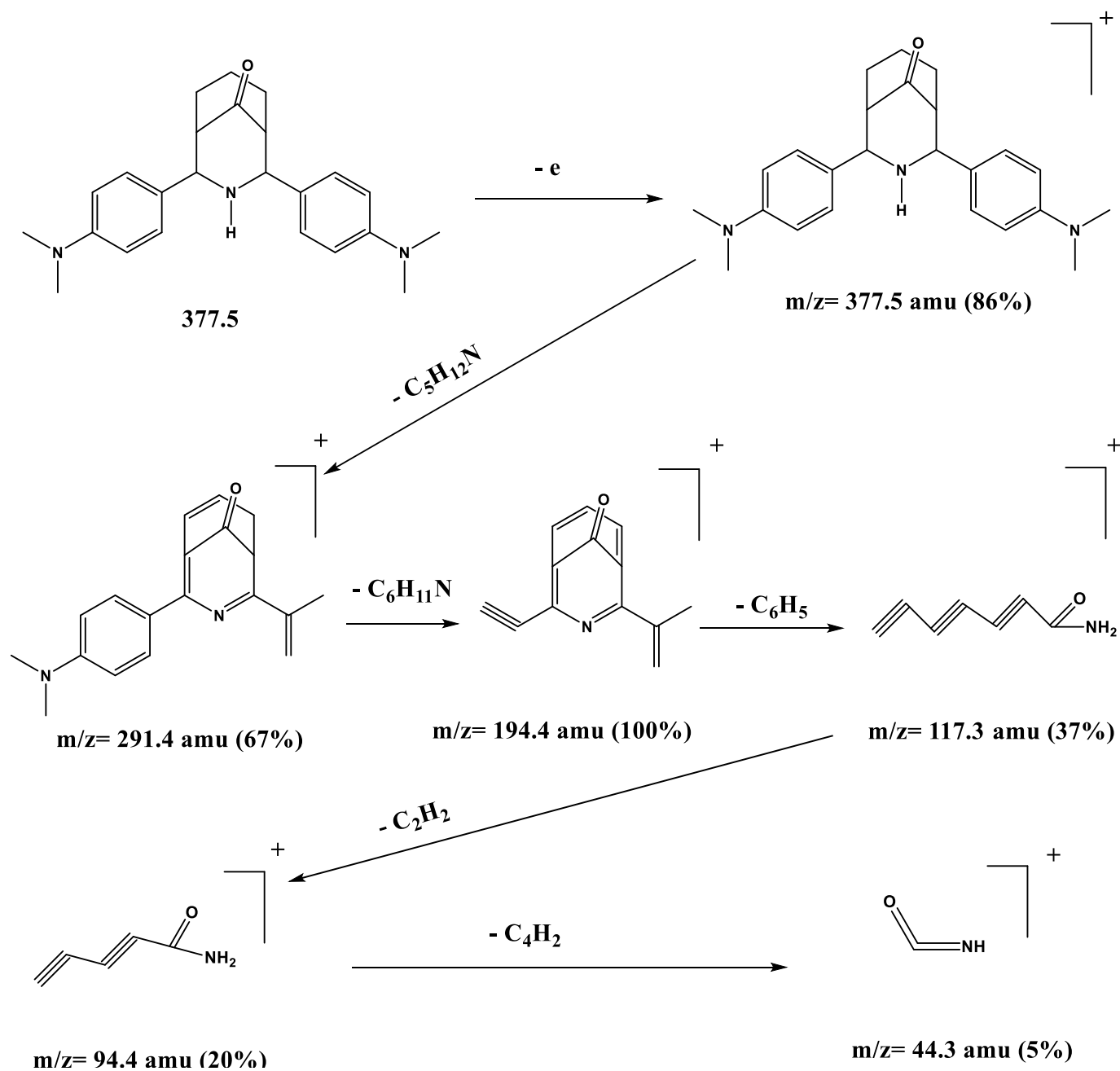
Scheme (3-6): Fragmentation outline and relative abundance of F3.

(3.5.4) Mass spectrum of 2-(((3-nitrophenyl) amino) (phenyl) methyl) cyclohexan-1-one (N1)

The electrospray (+) mass spectrum of N1, Figure (3-47), shows the parent molecule of N1 at m/z= 325.7 amu $(M+H)^+$ (68%) for $C_{19}H_{20}N_2O_3$, requires= 324.5. Peaks detected at m/z = 250.4 (50%), 182.5 (93%), 130.4 (100%), 104.6 (75%) and 41.4 (13%) related to $[M+H-(C_2H_5NO_2)]^+$, $[(M+H)-\{(C_2H_5NO_2)+(C_4H_6N)\}]^+$, $[(M+H)-\{(C_2H_5NO_2)+(C_4H_6N)+(C_4H_4)\}]^+$, $[(M+H)-\{(C_2H_5NO_2)+(C_4H_6N)+(C_4H_4)+(C_2H_2)\}]^+$ and $[(M+H)-\{(C_2H_5NO_2)+(C_4H_6N)+(C_4H_4)+(C_2H_2)+(C_5H_3)\}]^+$, respectively. The fragmentation pattern of N1 compound is shown in Scheme (3-7).

File :C:\MSDCHEM\3\DATA\Snapshot\3000482.D
Operator :
Acquired : 1 Jul 2018   10:12 using Electro Spray Method Normal
Instrument : Instrumen
Sample Name: N
Misc Info :
Vial Number: 1
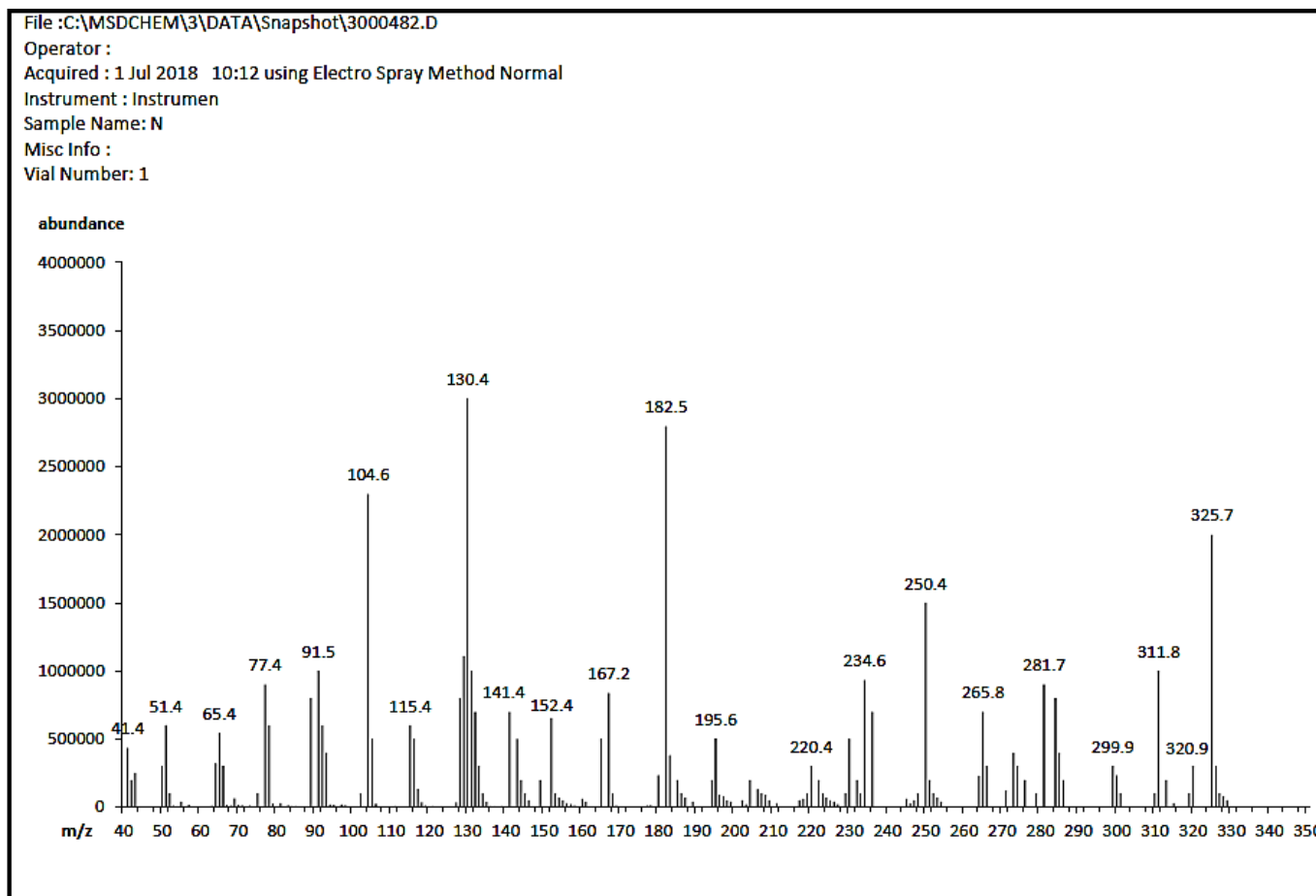
Figure (3-47): The electrospray (+) mass spectrum of N1.
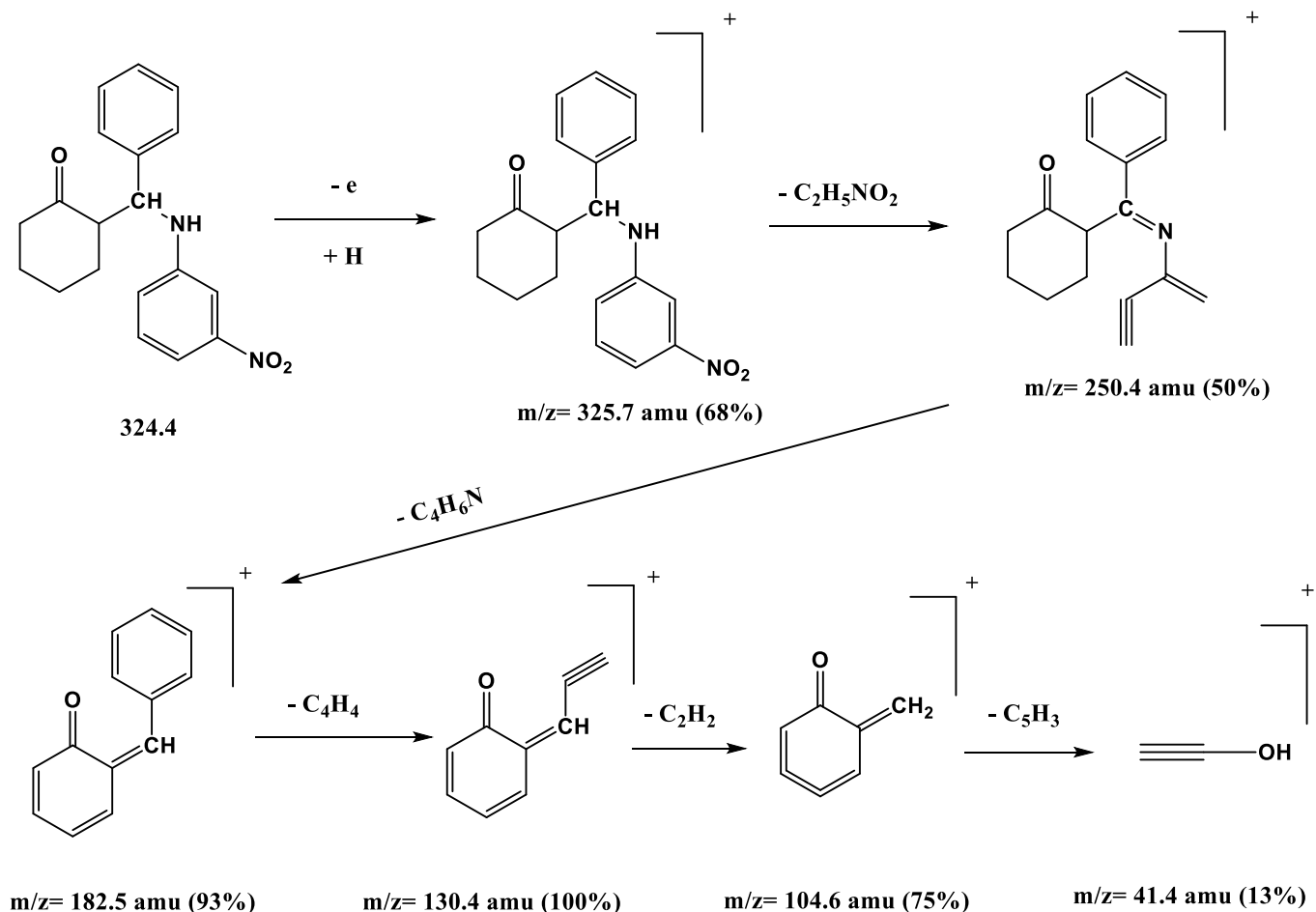
Scheme (3-7): Fragmentation outline and relative abundance of N1.

(3.5.5) Mass spectrum of 2-((4-methoxyphenyl) (phenylamino) methyl) cyclohexan-1-one (N2)

The electrospray (+) mass spectrum of N2 is placed in Figure (3-48). The parent ion peak of N2 is displayed at m/z= 310.4 amu $(M+H)^+$ (27%) for $C_{20}H_{23}NO_2$, calculates= 309.4. Peaks detected at m/z= 262.7 (60%), 212.1 (100%), 160.7 (42%), 104.3 (25%) and 77.3 (14%) attributed to $[M+H-(C_2H_8O)]^+$, $[(M+H)-\{(C_2H_8O)+(C_4H_2)\}]^+$, $[(M+H)-\{(C_2H_8O)+(C_4H_2)+(C_4H_4)\}]^+$, $[(M+H)-\{(C_2H_8O)+(C_4H_2)+(C_4H_4)+(C_3H_4O)\}]^+$ and $[(M+H)-$

$\{(C_2H_8O)+(C_4H_2)+(C_4H_4)+(C_3H_4O)+(HCN)\}]^{+,}$ respectively. The fragmentation pattern of N2 compound is shown in Scheme (3-8).
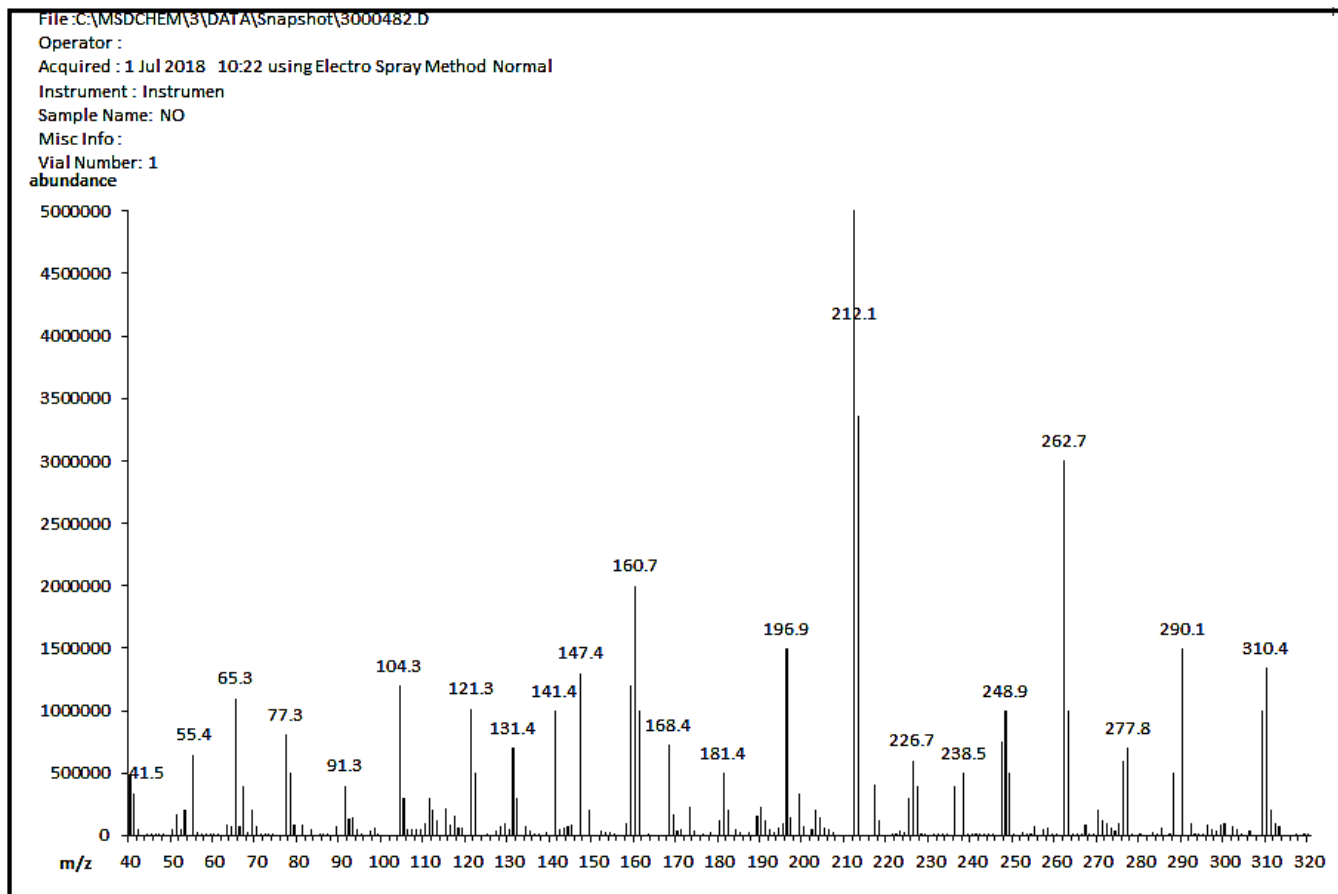
Figure (3-48): The electrospray (+) mass spectrum of N2.
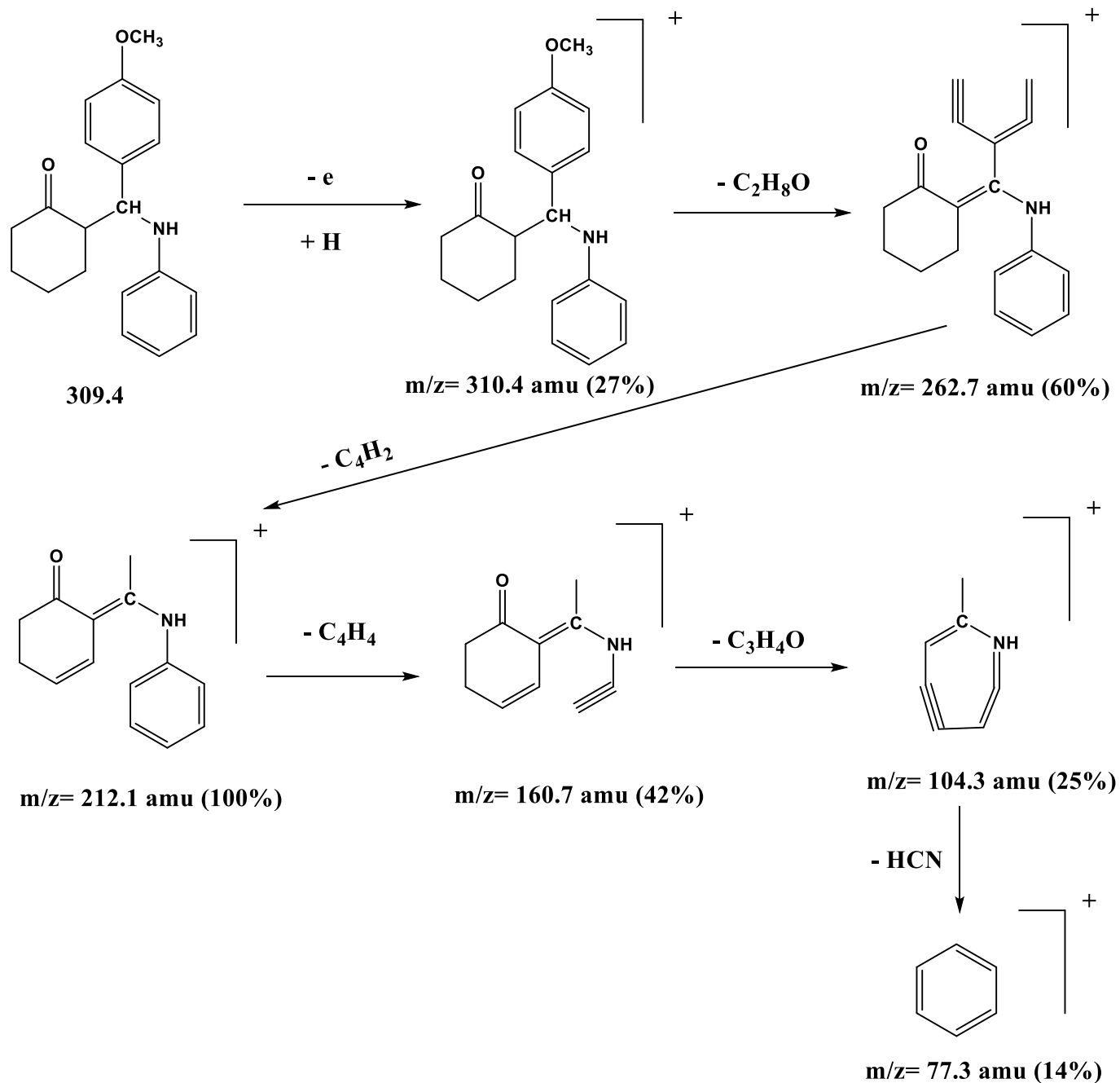
Scheme (3-8): Fragmentation outline and relative abundance of N2.

(3.5.6) Mass spectrum of 2-((4-(dimethylamino)phenyl)((3-nitrophenyl) amino)methyl)cyclohexan-1-one (N3)

The electrospray (+) mass spectrum of N3 is placed in Figure (3-49). The ESMS indicated peak at m/z= 367.5 amu that attributed to $(M)^+$ (39%) for $C_{21}H_{25}N_3O_3$, requires= 367.5. Peaks detected at m/z= 279.5 (36%), 212.4 (100%), 182.5 (56%), 128.5 (67%) and 65.4 (7%) assigned to $[M-(C_3H_5NO_2+H)]^+$, $[M-\{(C_3H_5NO_2+H)+(C_4H_5N)\}]^+$, $[M-\{(C_3H_5NO_2+H)+(C_4H_5N)+(CH_4N)\}]^+$, $[M-\{(C_3H_5NO_2+H)+(C_4H_5N)+(CH_4N)+(C_4H_6)\}]^+$ and $[M-\{(C_3H_5NO_2+H)+(C_4H_5N)+(CH_4N)+(C_4H_6)+(C_5H_2+H)\}]^+$, respectively. The fragmentation pattern of N3 compound is shown in Scheme (3-9).
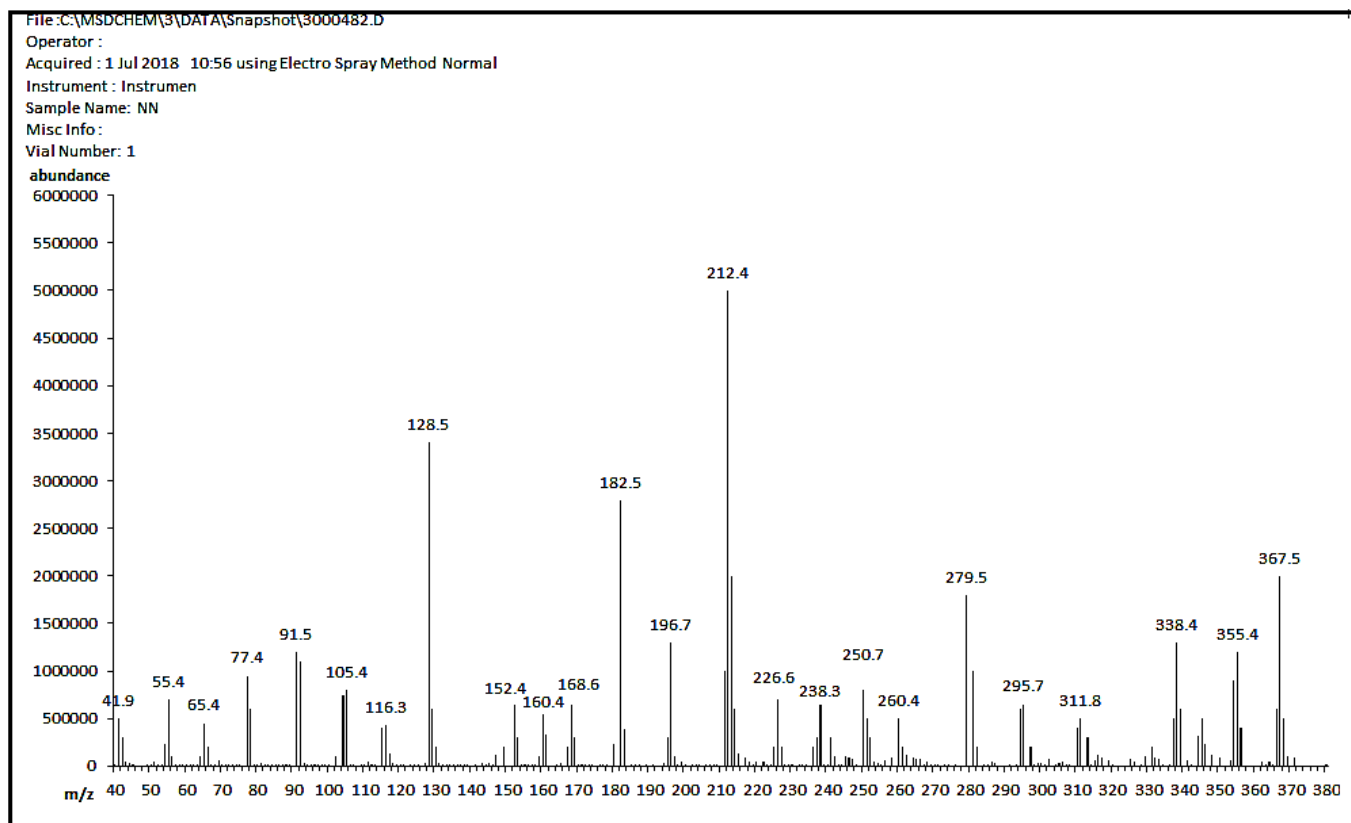
Figure (3-49): The electrospray (+) mass spectrum of N3.
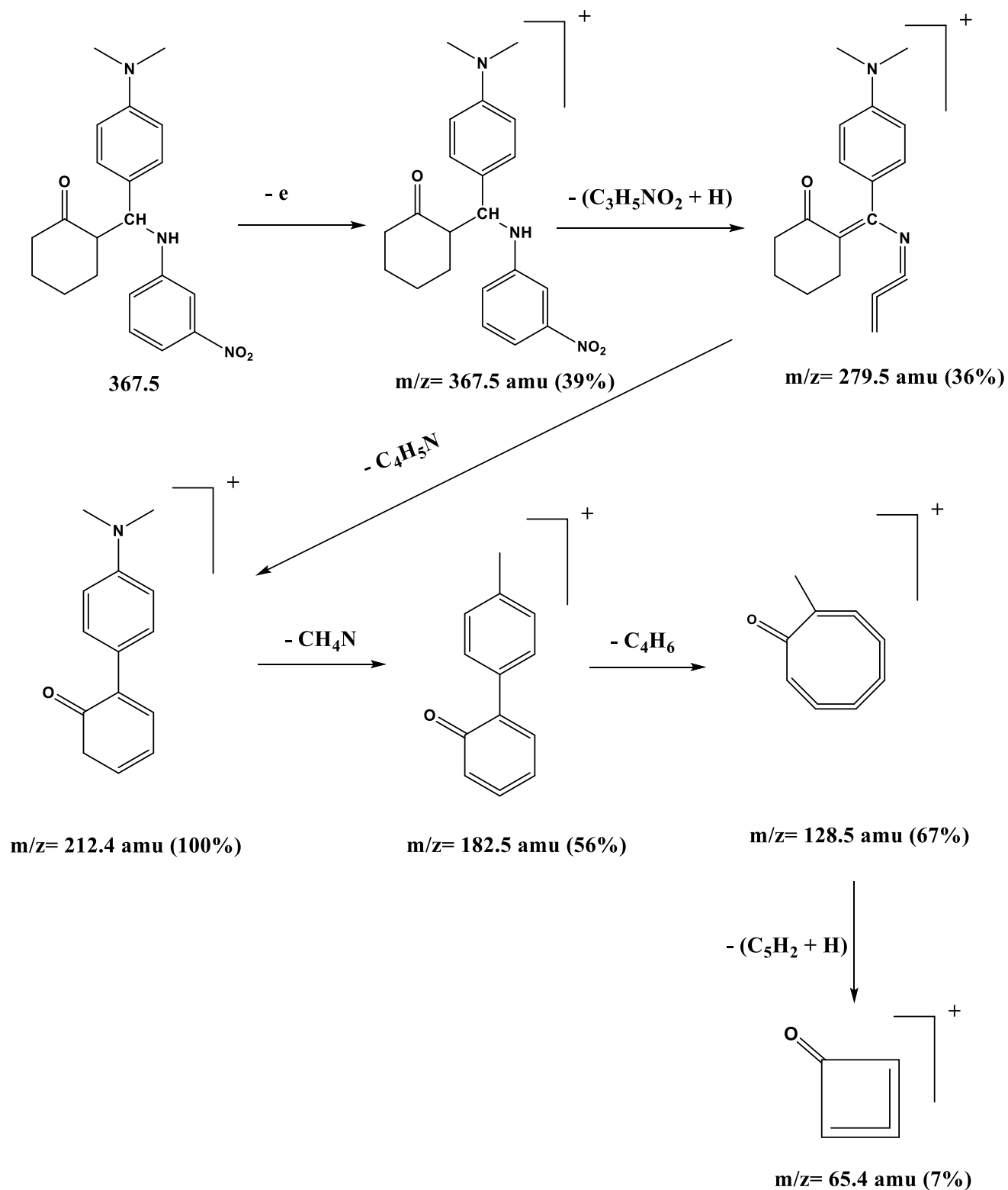
Scheme (3-9): Fragmentation outline and relative abundance of N3.

(3.5.7) Mass spectrum of 2-(2,4-diphenyl-3-azabicyclo[3.3.1]nonan-9-ylidene)hydrazine-1-carboselenoamide (HL^1)

The electrospray (+) mass spectrum of HL^1 is displayed in Figure (3-50). The parent ion peak of the HL^1 is noticed at m/z= 434.4 amu (M+Na)$^+$ (20%) for $C_{21}H_{24}N_4Se$, calculates= 411.4. Peaks detected at m/z= 291.4 (70%), 194.4 (100%), 106.3 (48%) and 55.3 (14%) correspond to [M+Na-(CH$_2$N$_2$Se)]$^+$, [(M+Na)-{(CH$_2$N$_2$Se)+(C$_6$H$_{11}$N)}]$^+$, [(M+Na)-{(CH$_2$N$_2$Se)+(C$_6$H$_{11}$N)+(C$_7$H$_4$)}]$^+$ and [(M+Na)-{(CH$_2$N$_2$Se)+(C$_6$H$_{11}$N)+(C$_7$H$_4$)+(C$_4$H$_2$+H)}]$^+$, respectively. Scheme (3-10) outlines the fragmentation steps of HL^1.

File :C:\MSDCHEM\3\DATA\Snapshot\3000482.D
Operator :
Acquired : 2 Jul 2018 10:56 using Electro Spray Method Normal
Instrument : Instrumen
Sample Name: FK
Misc Info :
Vial Number: 1
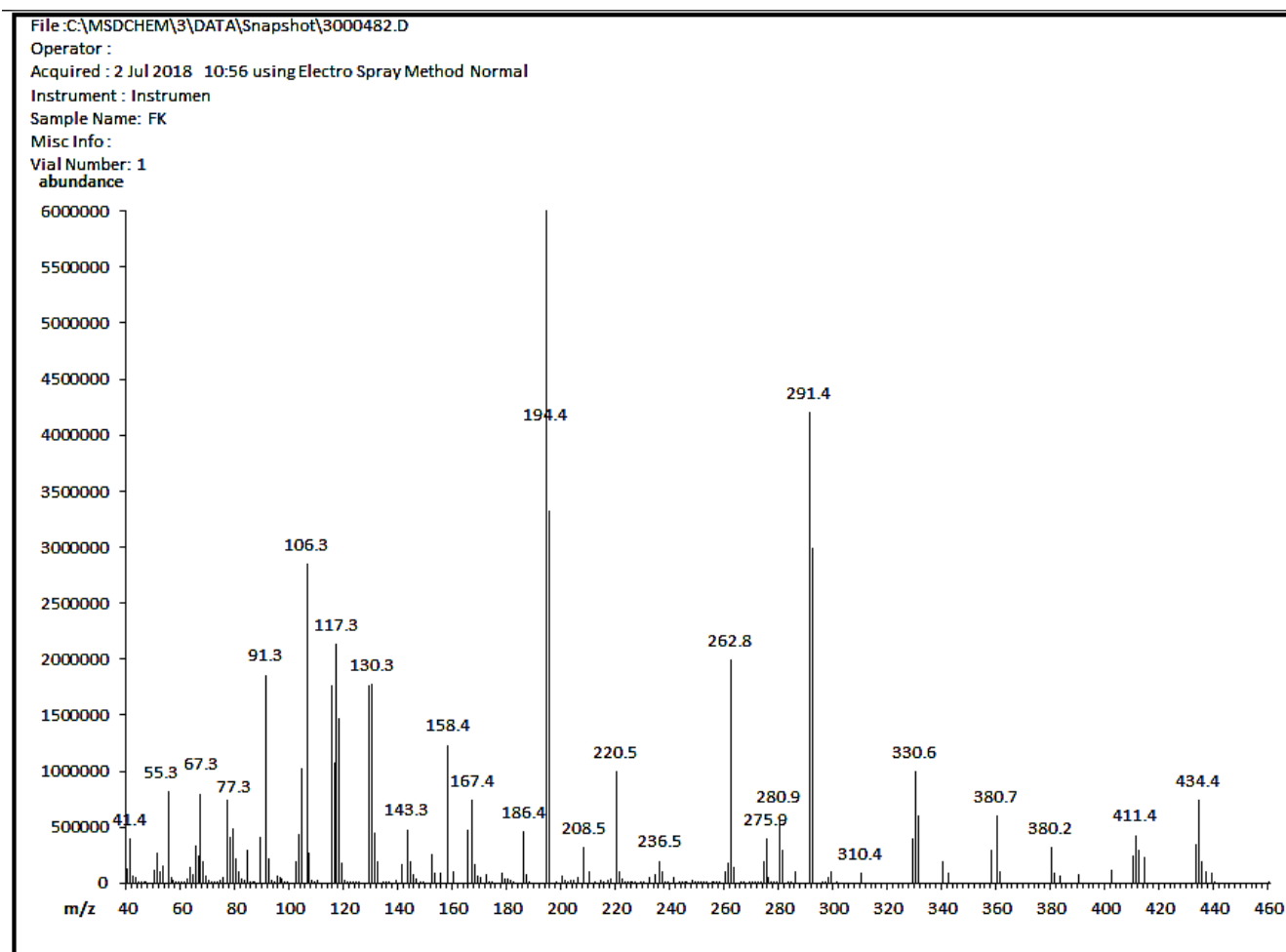
Figure (3-50): The electrospray (+) mass spectrum of HL^1.
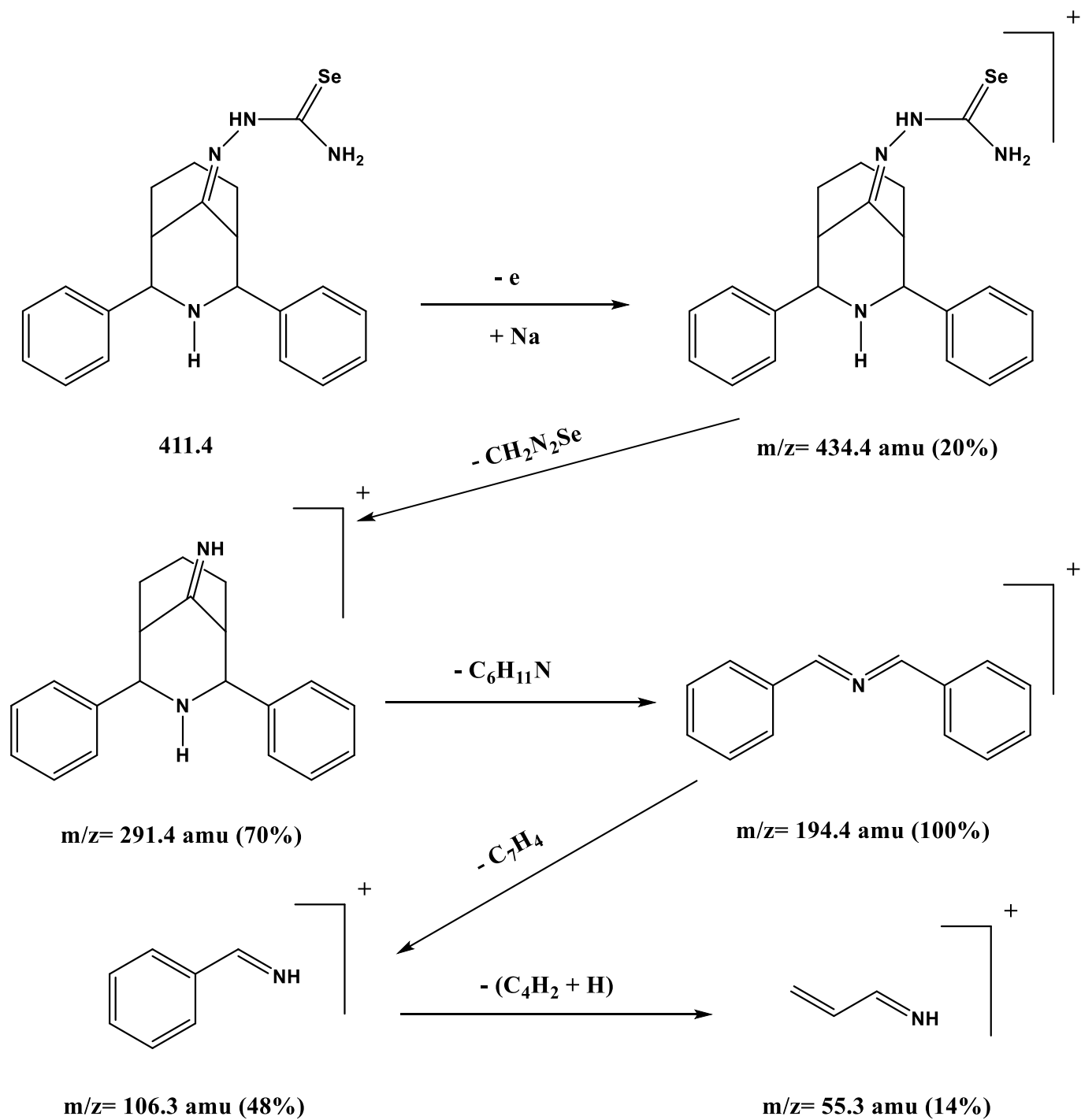
Scheme (3-10): Fragmentation outline and relative abundance of HL[1].

(3.5.8) Mass spectrum of 2-(2,4-bis(4-methoxyphenyl)-3-azabicyclo [3.3.1] nonan-9-ylidene)hydrazine-1-carboselenoamide (HL^2)

The electrospray (+) mass spectrum of HL^2, Figure (3-51), recorded the molecular of the ligand at m/z= 472.5 amu (M+H)$^+$ (20%) for C$_{23}$H$_{28}$N$_4$O$_2$Se, requires= 471.4. Peaks detected at m/z= 352.4 (69%), 254.5 (100%), 188.4 (59%) and 77.3 (27%) correlated to [M+H-(CH$_2$N$_2$Se)]$^+$, [(M+H)-{(CH$_2$N$_2$Se)+(C$_6$H$_{12}$N)}]$^+$, [(M+H)-{(CH$_2$N$_2$Se)+(C$_6$H$_{12}$N)+(C$_4$H$_2$O)}]$^+$ and [(M+H)-{(CH$_2$N$_2$Se)+(C$_6$H$_{12}$N)+(C$_4$H$_2$O)+(C$_7$H$_{11}$O)}]$^+$, respectively. Scheme (3-11) includes the fragmentation steps of HL^2.
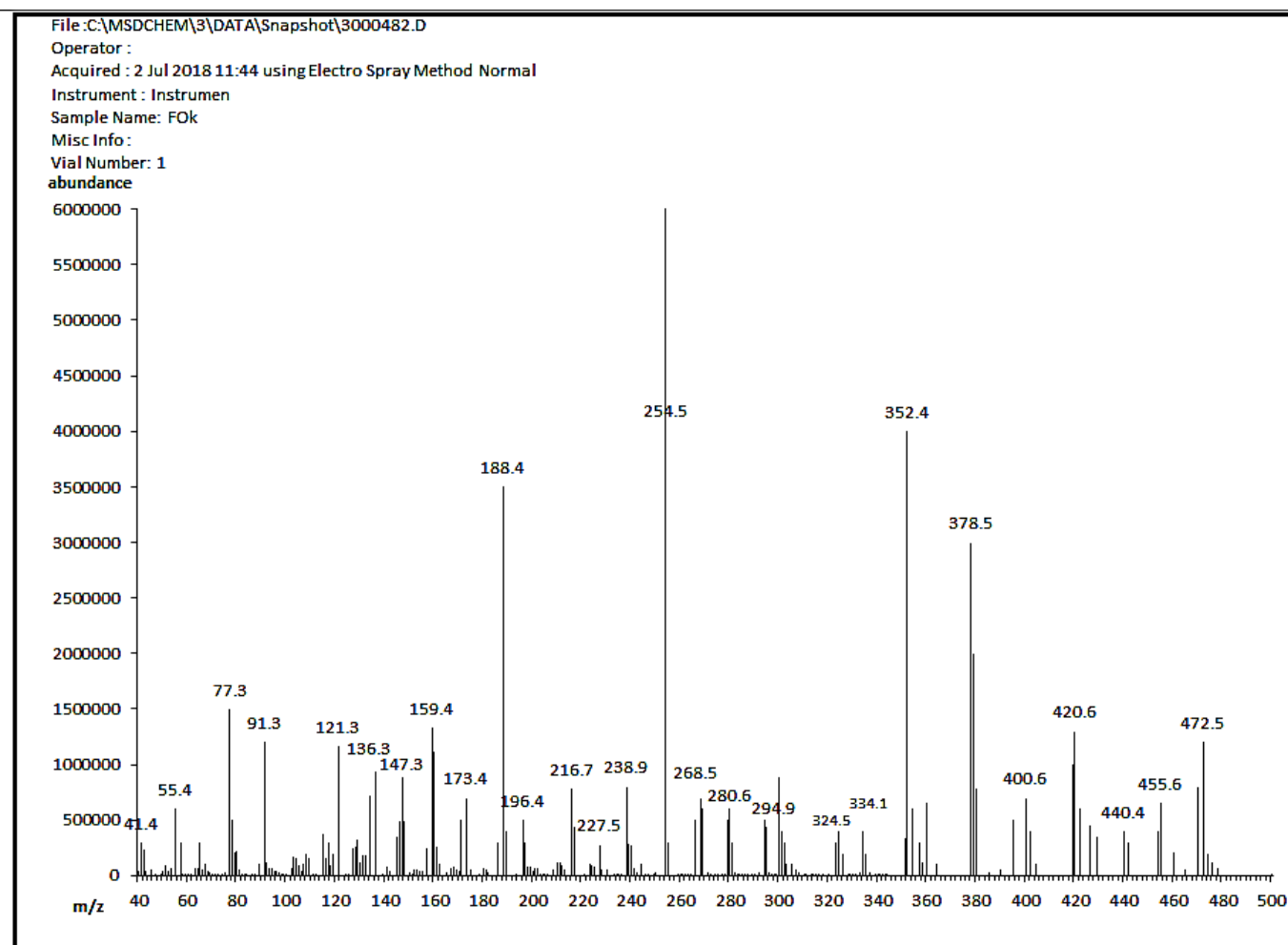
Figure (3-51): The electrospray (+) mass spectrum of HL^2.
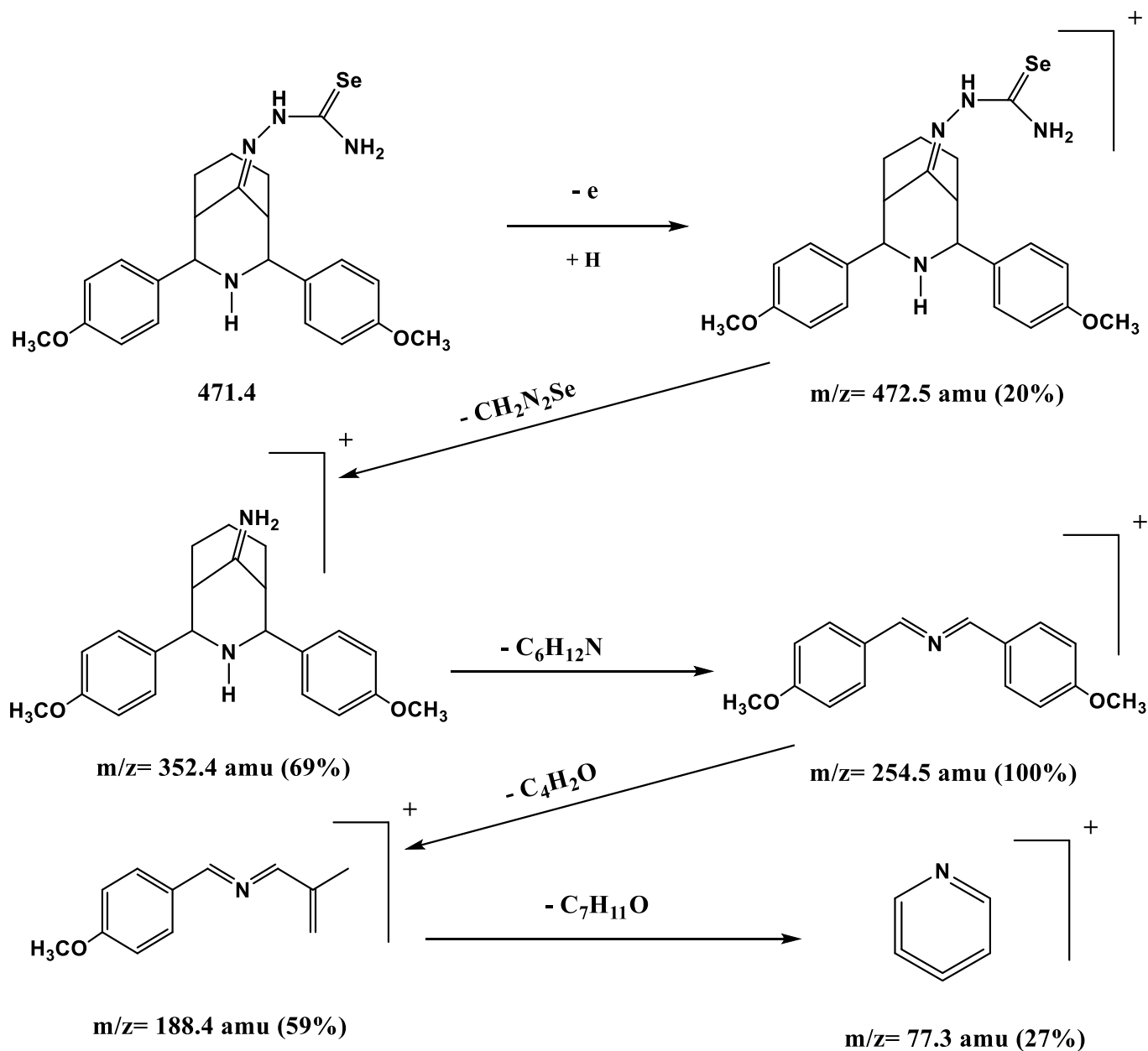
Scheme (3-11): Fragmentation outline and relative abundance of HL^2.

(3.5.9) Mass spectrum of 2-(2,4-bis(4-(dimethylamino)phenyl)-3-azabicyclo [3.3.1]nonan-9-ylidene)hydrazine-1-carboselenoamide (HL^3)

The electrospray (+) mass spectrum of HL^3 is shown in Figure (3-52). The parent ion peak of HL^3 is recorded at m/z= 498.5 amu (M+H)$^+$ (16%) for $C_{25}H_{34}N_6Se$, calculates= 497.5. Peaks detected at m/z= 291.4 (69%), 194.4 (100%), 115.3 (30%) and 55.3 (13%) assigned to $[M+H-(C_7H_4N_3Se)]^+$, $[(M+H)-\{(C_7H_4N_3Se)+(C_6H_{10}N+H)\}]^+$, $[(M+H)-\{(C_7H_4N_3Se)+(C_6H_{10}N+H)+(C_5H_5N)\}]^+$ and $[(M+H)-\{(C_7H_4N_3Se)+(C_6H_{10}N+H)+(C_5H_5N)+(C_4H_{12})\}]^+$, respectively. Scheme (3-12) includes the fragmentation steps of HL^3.
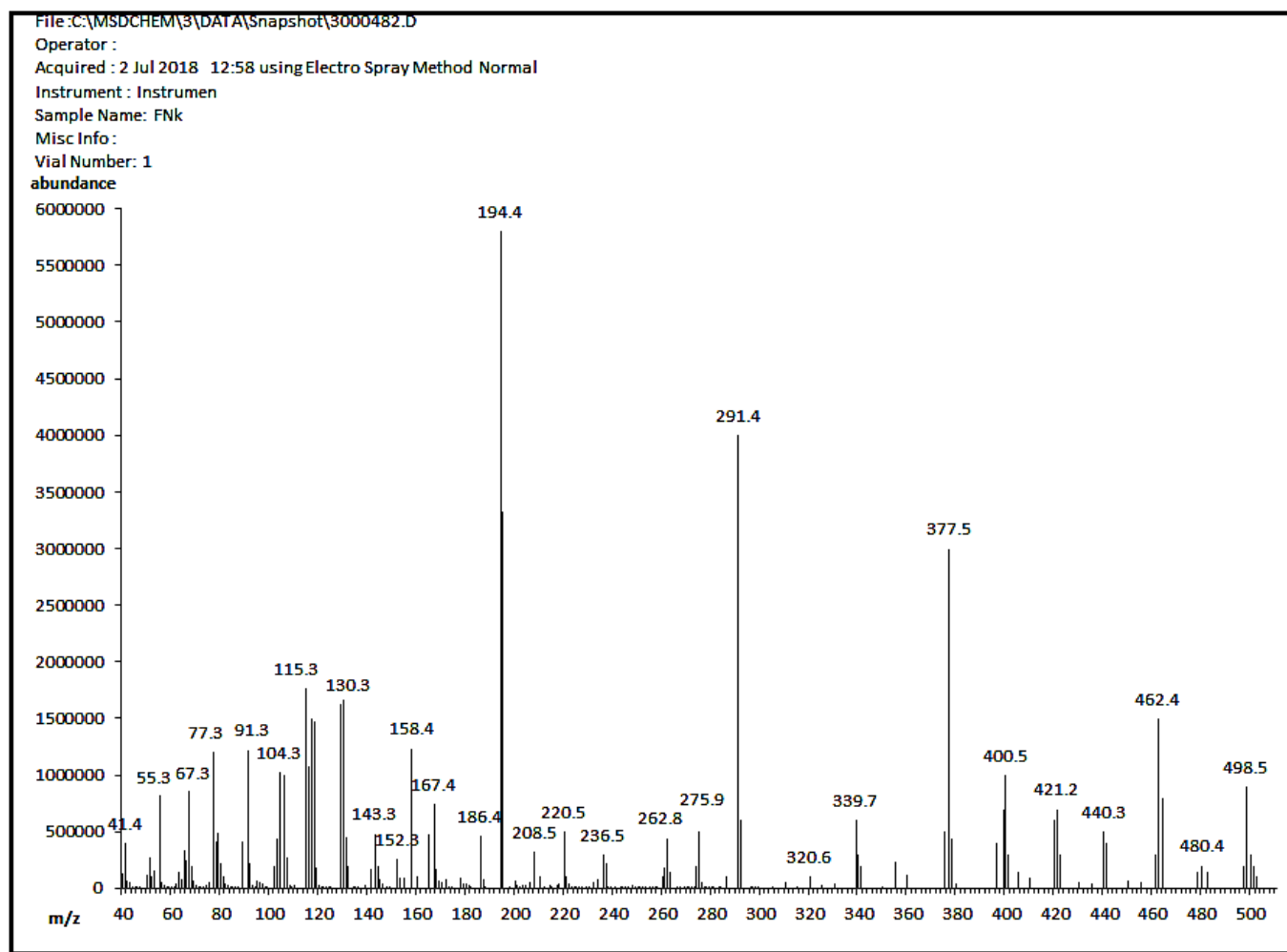
Figure (3-52): The electrospray (+) mass spectrum of HL^3.

497.5

m/z= 498.5 amu (16%)

- e

+ H

- C$_7$H$_4$N$_3$Se

m/z= 291.4 amu (69%)

- (C$_6$H$_{10}$N + H)

m/z= 194.4 amu (100%)

- C$_5$H$_5$N

- C$_4$H$_{12}$

m/z= 115.3 amu (30%)

m/z= 55.3 amu (13%)
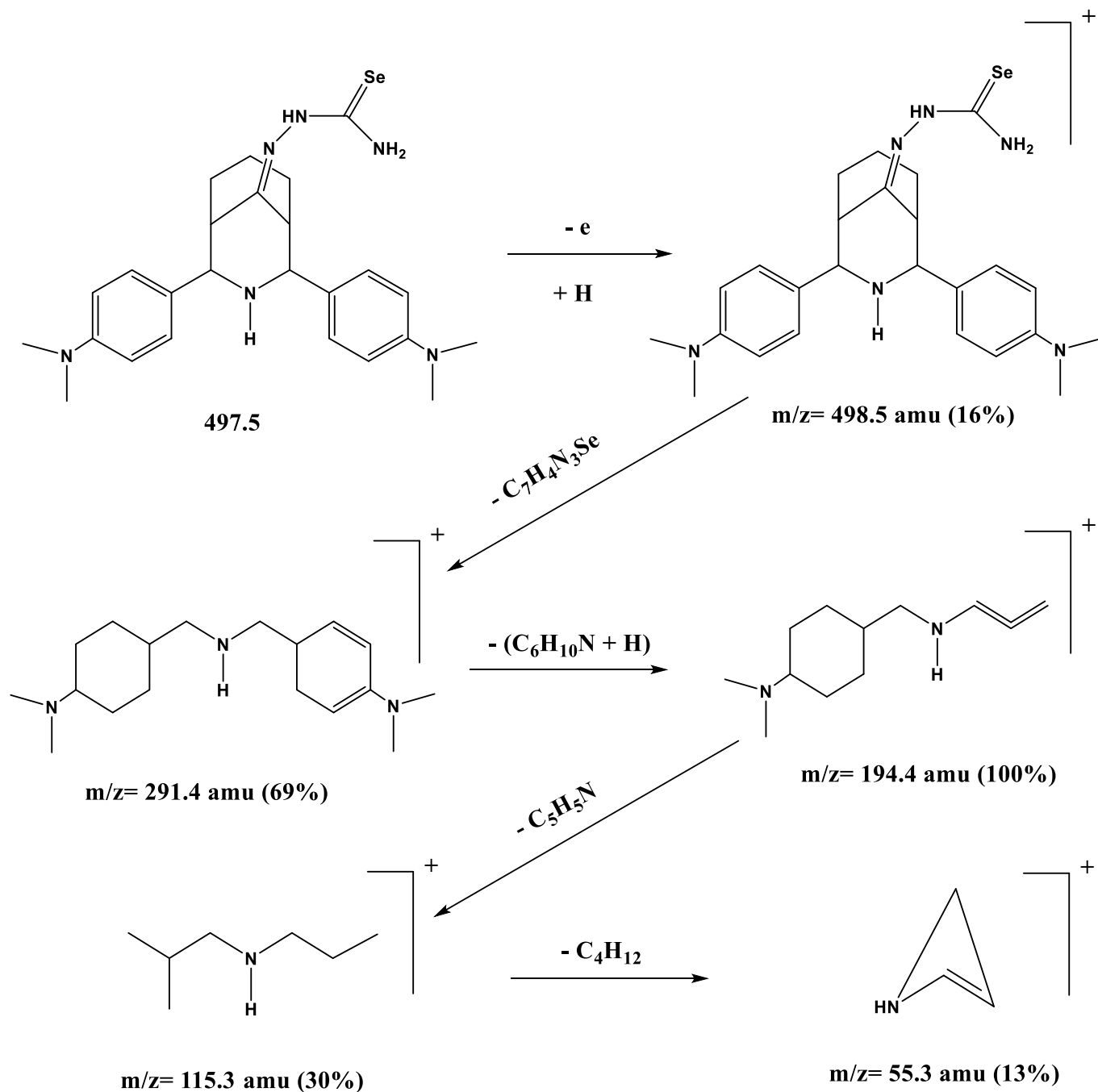
Scheme (3-12): Fragmentation outline and relative abundance of HL^3.

(3.5.10) Mass spectrum of (E)-2-(2-(((3-nitrophenyl) amino) (phenyl) methyl)cyclohexylidene)hydrazine-1-carboselenoamide (HL^4)

The electrospray (+) mass spectrum of HL^4, Figure (3-53), indicated the molecular ion peak at m/z= 445.6 amu (M+H)$^+$ (21%) for $C_{20}H_{23}N_5O_2Se$, requires= 444.4. Peaks measured at m/z= 325.7 (73%), 250.4 (53%), 182.5 (100%) and 91.5 (36%) assigned to [M+H-(CH$_2$N$_2$Se)]$^+$, [(M+H)-{(CH$_2$N$_2$Se)+(C$_2$H$_5$NO$_2$)}]$^+$, [(M+H)-{(CH$_2$N$_2$Se)+ (C$_2$H$_5$NO$_2$)+(C$_5$H$_8$)}]$^+$, and [(M+H)-{(CH$_2$N$_2$Se)+(C$_2$H$_5$NO$_2$)+(C$_5$H$_8$)+(C$_6$H$_5$N)}]$^+$, respectively. Scheme (3-13) includes the fragmentation steps of HL^4.
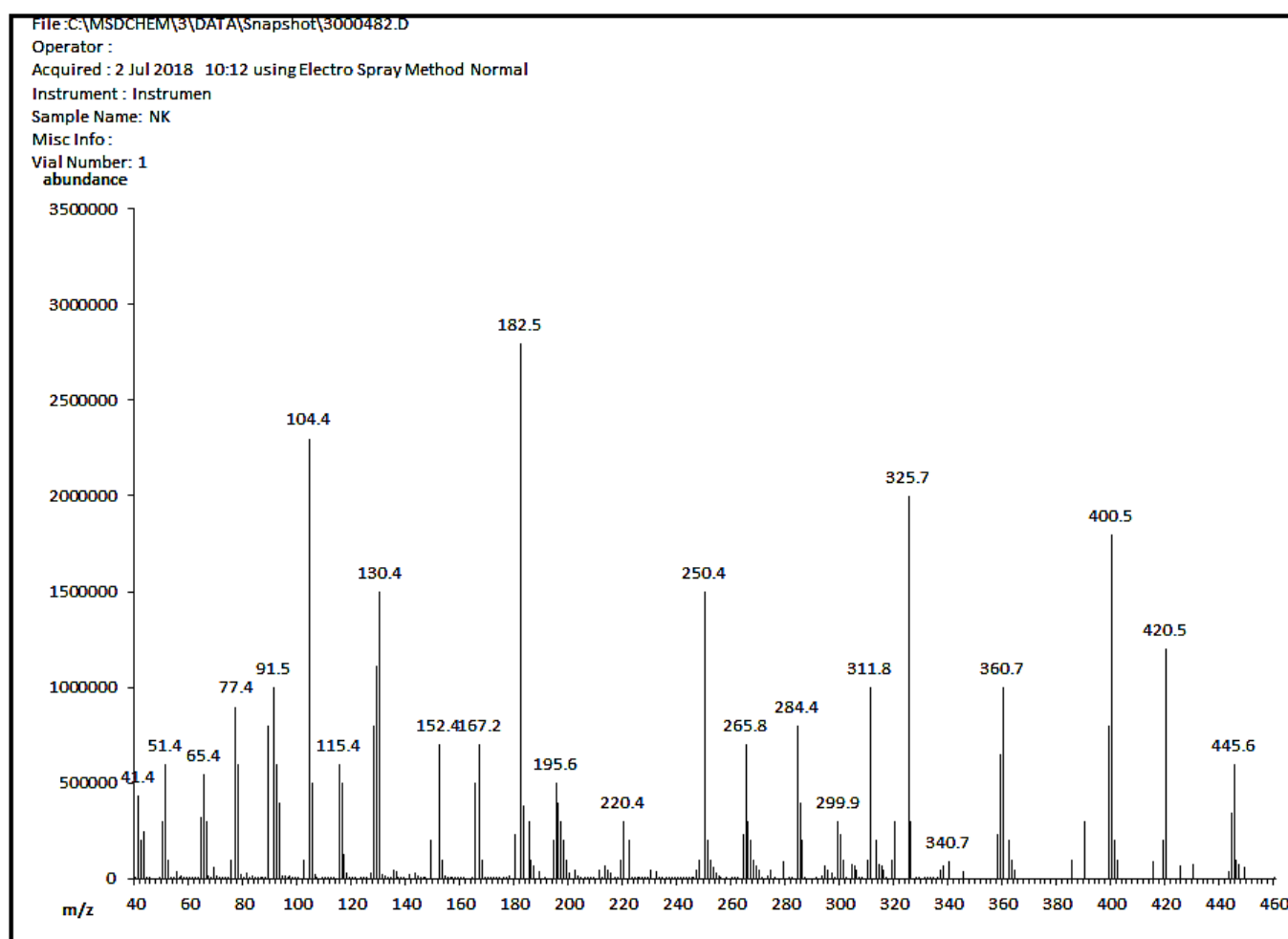
Figure (3-53): The electrospray (+) mass spectrum of HL^4.
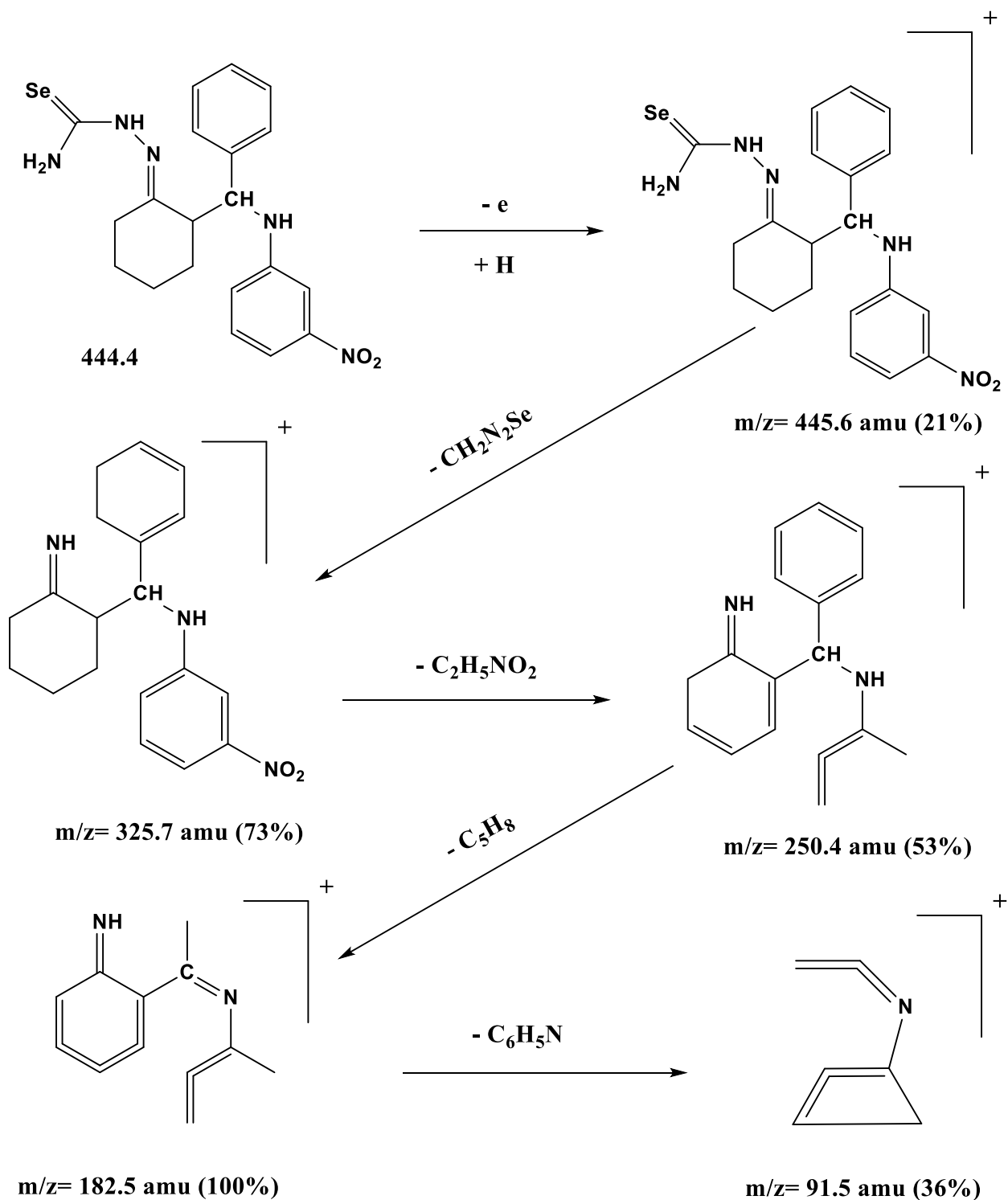
Scheme (3-13): Fragmentation outline and relative abundance of HL^4.

(3.5.11) Mass spectrum of (E)-2-(2-((4-methoxyphenyl) (phenylamino) methyl)cyclohexylidene)hydrazine-1-carboselenoamide (HL^5)

The electrospray (+) mass spectrum of HL^5 is displayed in Figure (3-54). The parent ion peak of HL^5 is seen at m/z= 452.4 amu (M+Na)$^+$ (13%) for $C_{21}H_{26}N_4OSe$, calculates= 429.4. Peaks detected at m/z= 334.4 (9%), 212.1 (100%), 147.4 (23%) and 55.4 (12%) assigned to $[M+Na-(C_6H_7O)]^+$, $[(M+Na)-\{(C_6H_7O)+(CH_3N_2Se)\}]^+$, $[(M+Na)-\{(C_6H_7O)+(CH_3N_2Se)+(C_5H_5)\}]^+$ and $[(M+Na)-\{(C_6H_7O)+(CH_3N_2Se)+(C_5H_5)+(C_6H_6N)\}]^+$, respectively. Scheme (3-14) includes the fragmentation steps of HL^5.

File :C:\MSDCHEM\3\DATA\Snapshot\3000482.D
Operator :
Acquired : 2 Jul 2018 10:22 using Electro Spray Method Normal
Instrument : Instrumen
Sample Name: NOK
Misc Info :
Vial Number: 1
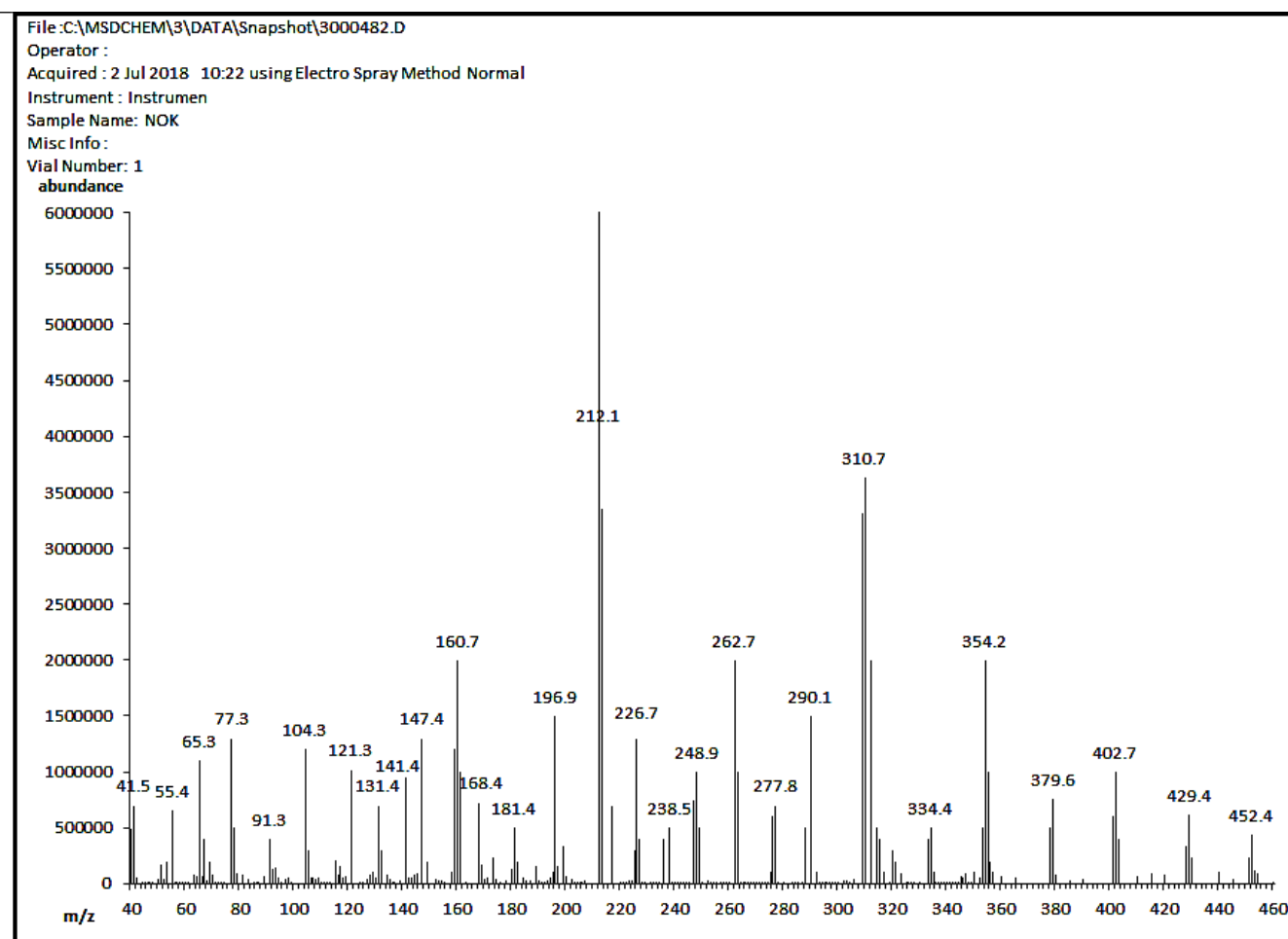
Figure (3-54): The electrospray (+) mass spectrum of HL^5.
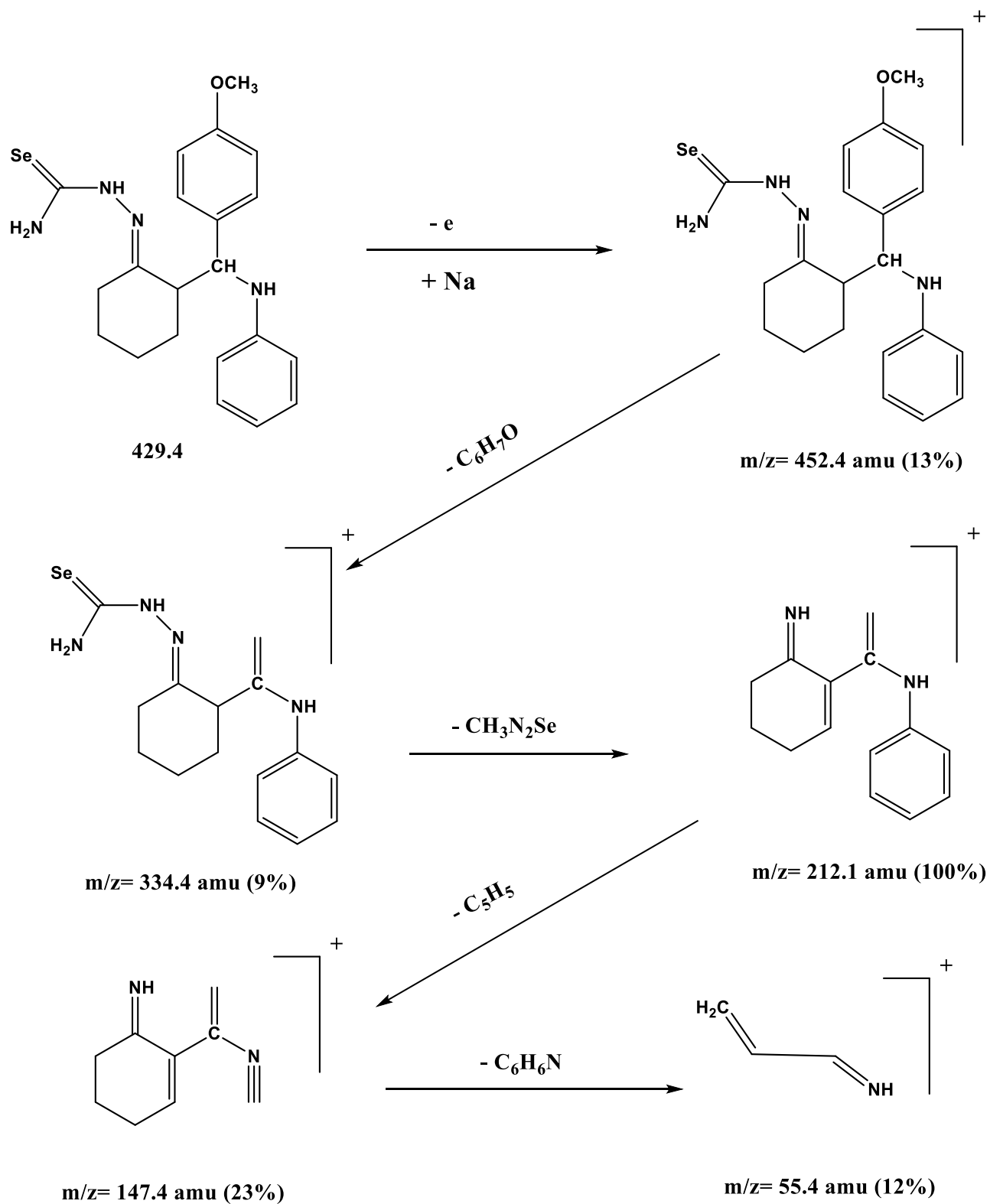
Scheme (3-14): Fragmentation outline and relative abundance of HL^5.

(3.5.12) Mass spectrum of (E)-2-(2-((4-(dimethylamino)phenyl)((3-nitrophenyl)amino)methyl)cyclohexylidene)hydrazine-1-carboselenoamide (HL^6)

The electrospray (+) mass spectrum of HL^6 is displayed in Figure (3-55). The parent ion peak of HL^6 is showed at m/z= 488.5 amu (M+H)$^+$ (23%) for $C_{22}H_{28}N_6O_2Se$, calculates= 487.5. Peaks detected at m/z= 367.8 (57%), 212.4 (100%), 128.5 (69%) and 55.4 (20%) assigned to [M+H-(CH$_3$N$_2$Se+H)]$^+$, [(M+H)-{(CH$_3$N$_2$Se+H)+(C$_{11}$H$_9$N)}]$^+$, [(M+H)-{(CH$_3$N$_2$Se+H)+(C$_{11}$H$_9$N)+(C$_3$H$_2$NO$_2$+H)}]$^+$ and [(M+H)-{(CH$_3$N$_2$Se+H)+ (C$_{11}$H$_9$N)+(C$_3$H$_2$NO$_2$+H)+(C$_5$H$_{12}$+H)}]$^+$, respectively. Scheme (3-15) includes the fragmentation steps of HL^6.
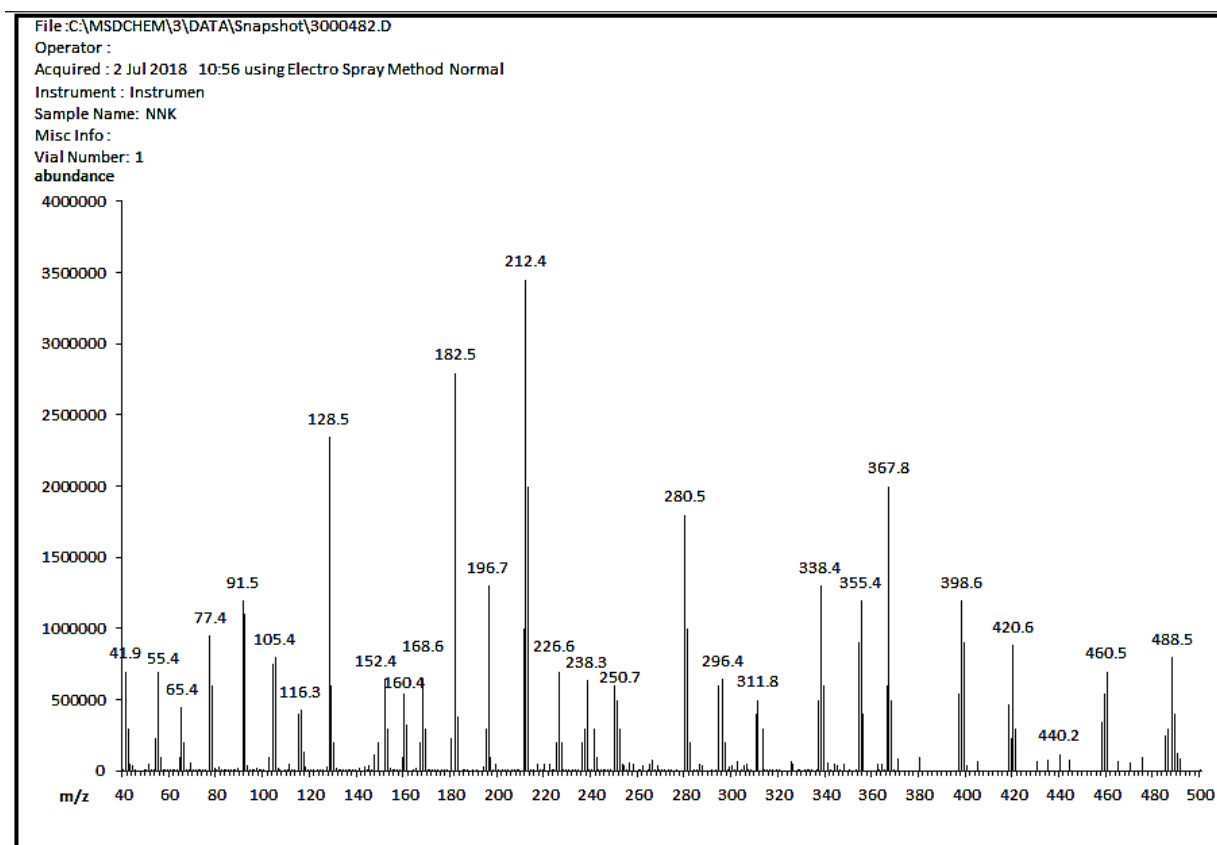
Figure (3-55): The electrospray (+) mass spectrum of HL^6.
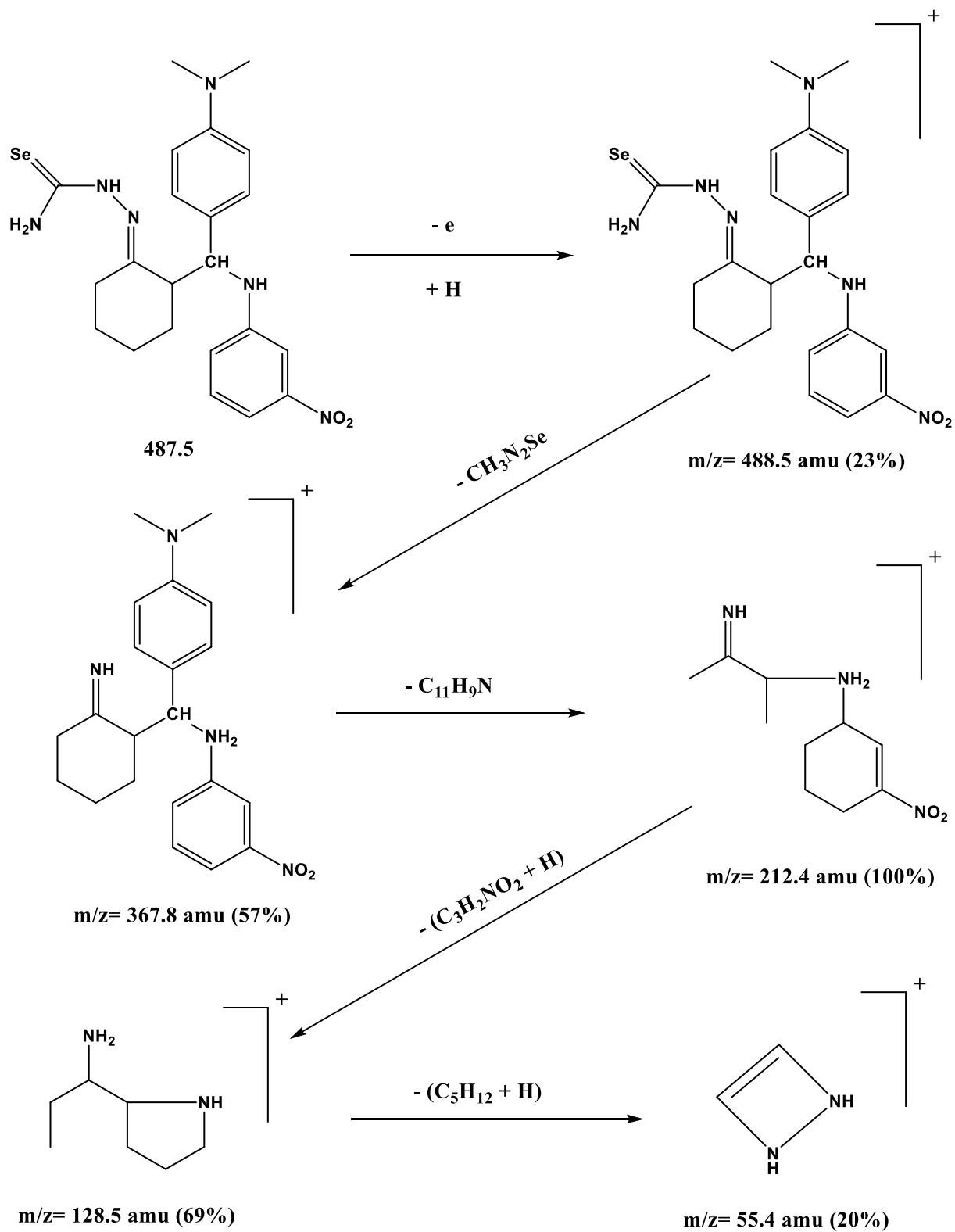
Scheme (3-15): Fragmentation outline and relative abundance of HL^6.

(3.6) Electronic spectra of ligands

(3.6.1) Electronic spectra of ligands HL^1-HL^6

(3.6.1.1) Electronic data of HL^1

The electronic transition analysis of HL^1 in DMSO solvent is placed in Figure (3-56). The data reveals an intense bands at 263 nm (38023 cm^{-1}; ε_{max}= 560 dm^3 mol^{-1} cm^{-1}) and 315 nm (31746 cm^{-1}; ε_{max}= 1234 dm^3 mol^{-1} cm^{-1}) related to $\pi\rightarrow\pi^*$ and $n\rightarrow\pi^*$ electronic transitions, respectively [60-62]. The electronic data includes in Table (3-10).
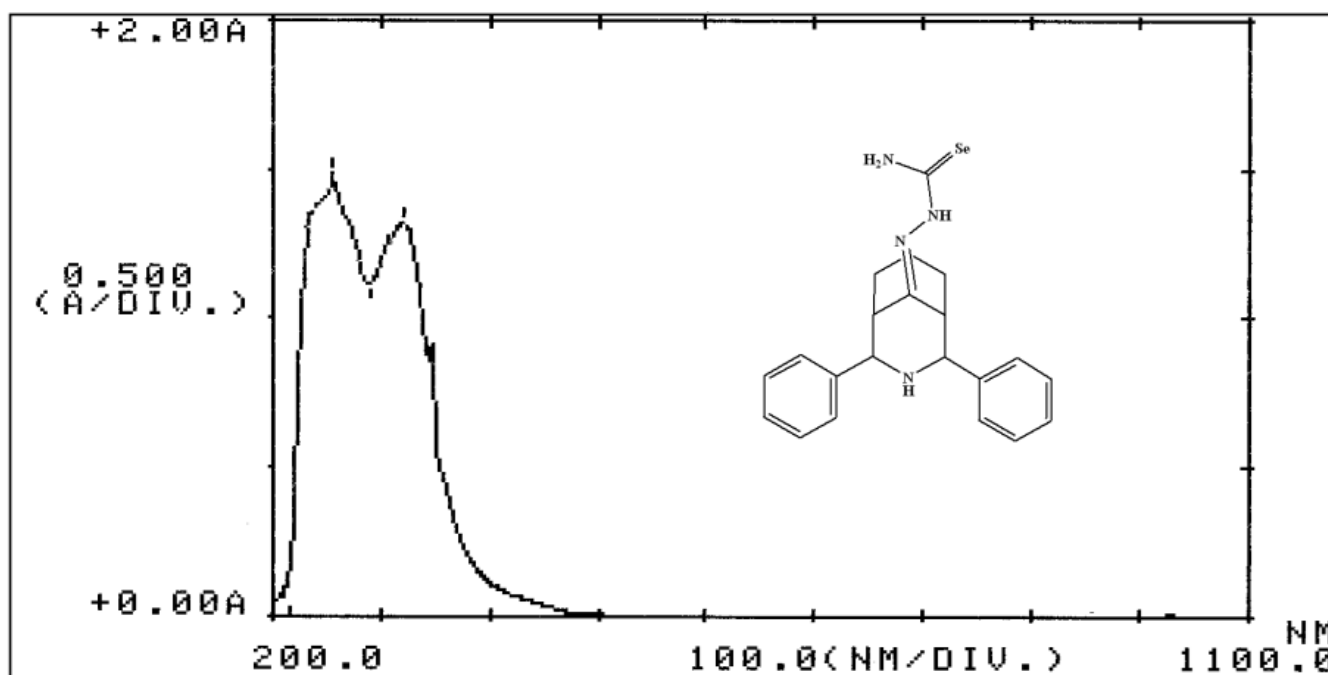
Figure (3-56): Electronic chart of HL^1 in DMSO solvent.

(3.6.1.2) Electronic data of HL^2

The electronic transition data of HL^2, in DMSO solvent is displayed in Figure (3-57). The spectrum exhibits bands at 266 nm (37594 cm^{-1}; ε_{max}= 450 dm^3 mol^{-1} cm^{-1}), 350 nm (28571 cm^{-1}; ε_{max}= 1980 dm^3 mol^{-1} cm^{-1}) and 380 nm (26316 cm^{-1}; ε_{max}= 2134 dm^3 mol^{-1}

cm^{-1}) correlated to $\pi\rightarrow\pi^*$, $n\rightarrow\pi^*$ and C.T. transitions, respectively [60-62]. The electronic data presents in Table (3-10).
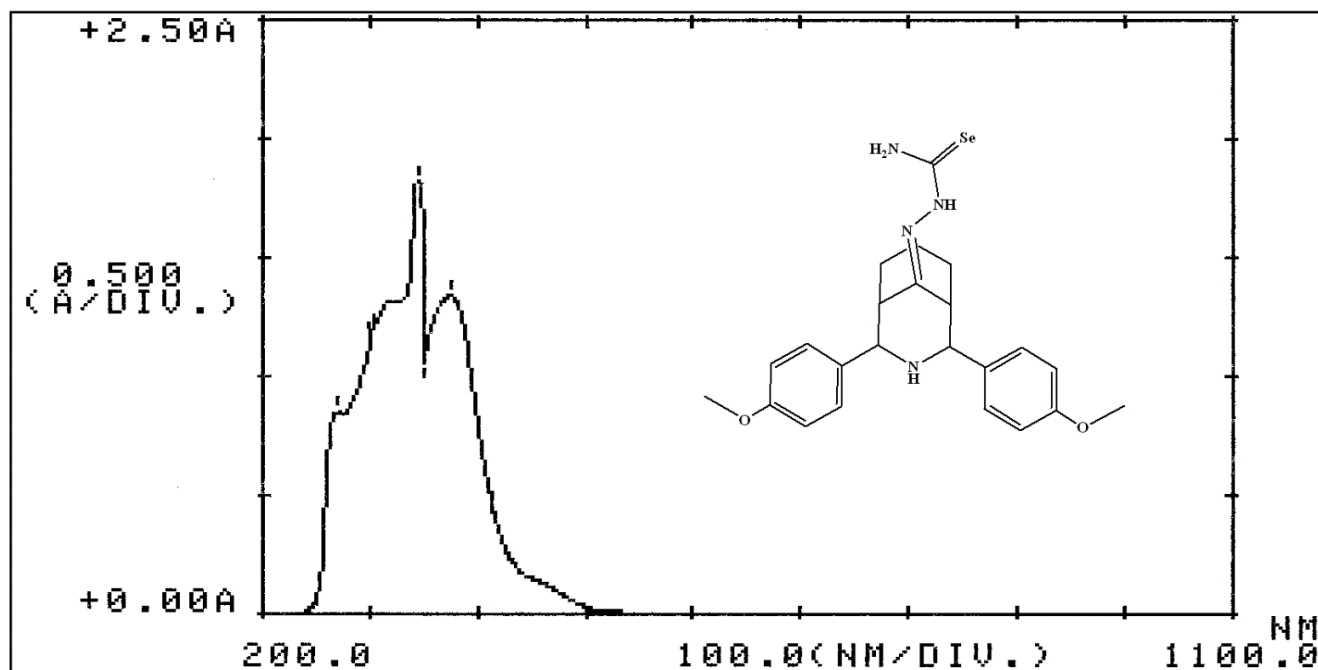
Figure (3-57): Electronic chart of HL^2 in DMSO solvent.

(3.6.1.3) Electronic data of HL^3

The electronic spectral data of HL^3 in DMSO solvent, Figure (3-58), revealed three absorption bands at 270 nm (37037 cm^{-1}; ε_{max}= 987 dm^3 mol^{-1} cm^{-1}), 310 nm (32258 cm^{-1}; ε_{max}= 1305 dm^3 mol^{-1} cm^{-1}) and 365 nm (27397 cm^{-1}; ε_{max}= 718 dm^3 mol^{-1} cm^{-1}) attributed to $\pi\rightarrow\pi^*$, $n\rightarrow\pi^*$ and C.T. transitions, respectively [60-62]. These data includes in Table (3-10).
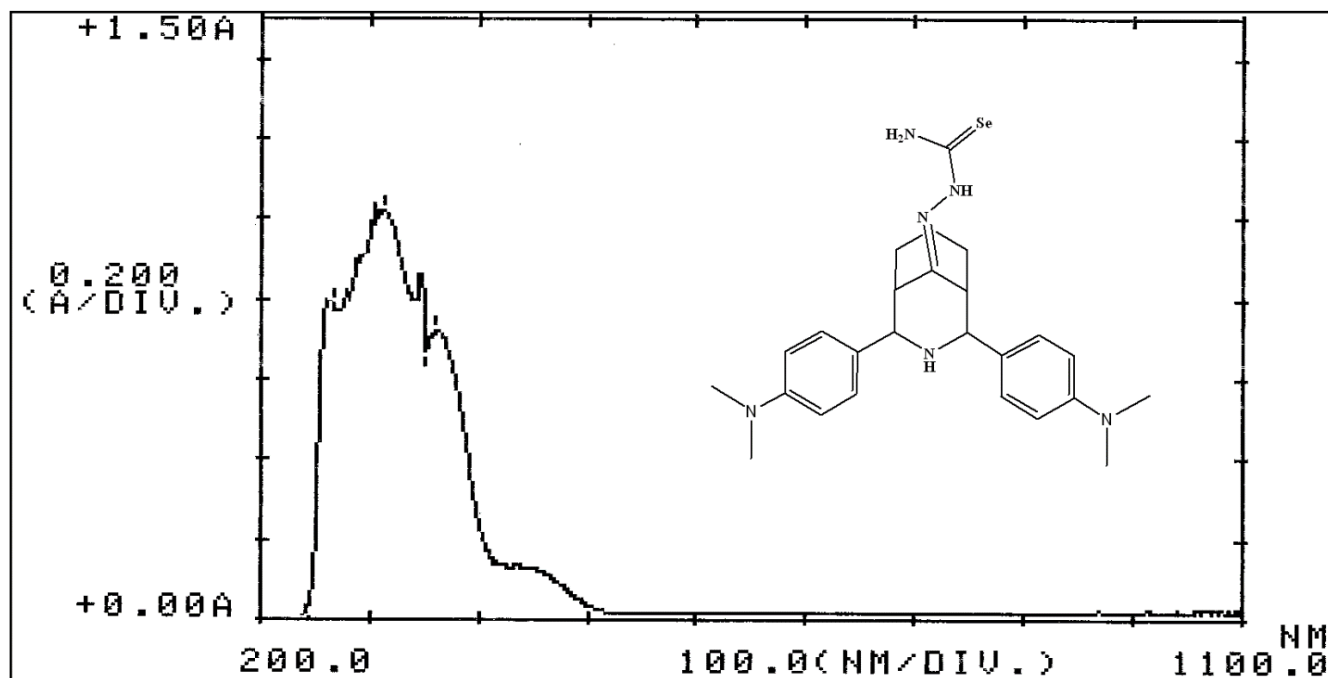
Figure (3-58): Electronic chart of HL^3 in DMSO solvent.

(3.6.1.4) Electronic data of HL^4

The electronic spectral data of HL^4, Figure (3-59), exhibits peak at 265 nm (37736 cm^{-1}; ε_{max}= 1123 dm^3 mol^{-1} cm^{-1}) related to $\pi\rightarrow\pi*$ transition. A peak at 310 nm (32258 cm^{-1}; ε_{max}= 988 dm^3 mol^{-1} cm^{-1}) related to n$\rightarrow\pi*$ transition [60-62]. The absorption data of the ligand is given in Table (3-10).
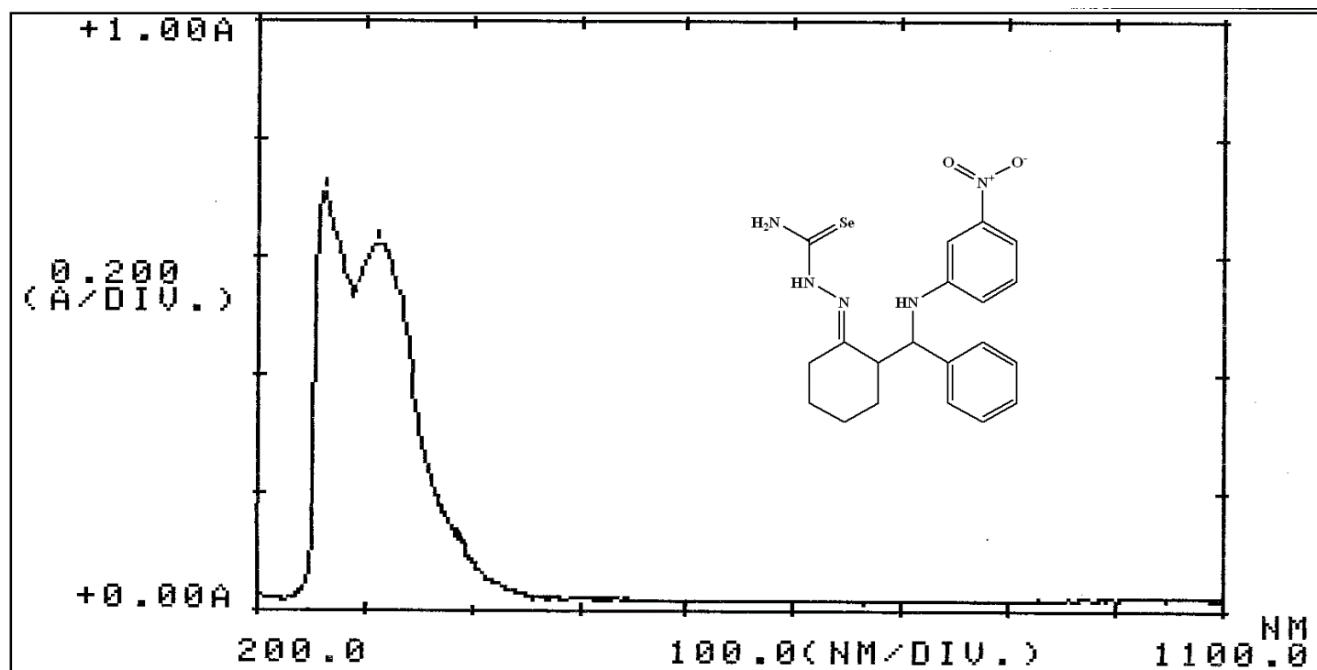
Figure (3-59): Electronic chart of HL^4 in DMSO solvent.

(3.6.1.5) Electronic data of HL^5

The electronic spectral data for HL^5, Figure (3-60), reveals bands at 262 nm (38168 cm^{-1}; ε_{max}= 1343 dm^3 mol^{-1} cm^{-1}) and 315 nm (31746 cm^{-1}; ε_{max}= 1063 dm^3 mol^{-1} cm^{-1}) related to $\pi\rightarrow\pi^*$ and n$\rightarrow\pi^*$ transitions, individually [60-62]. The absorption data is given in Table (3-10).
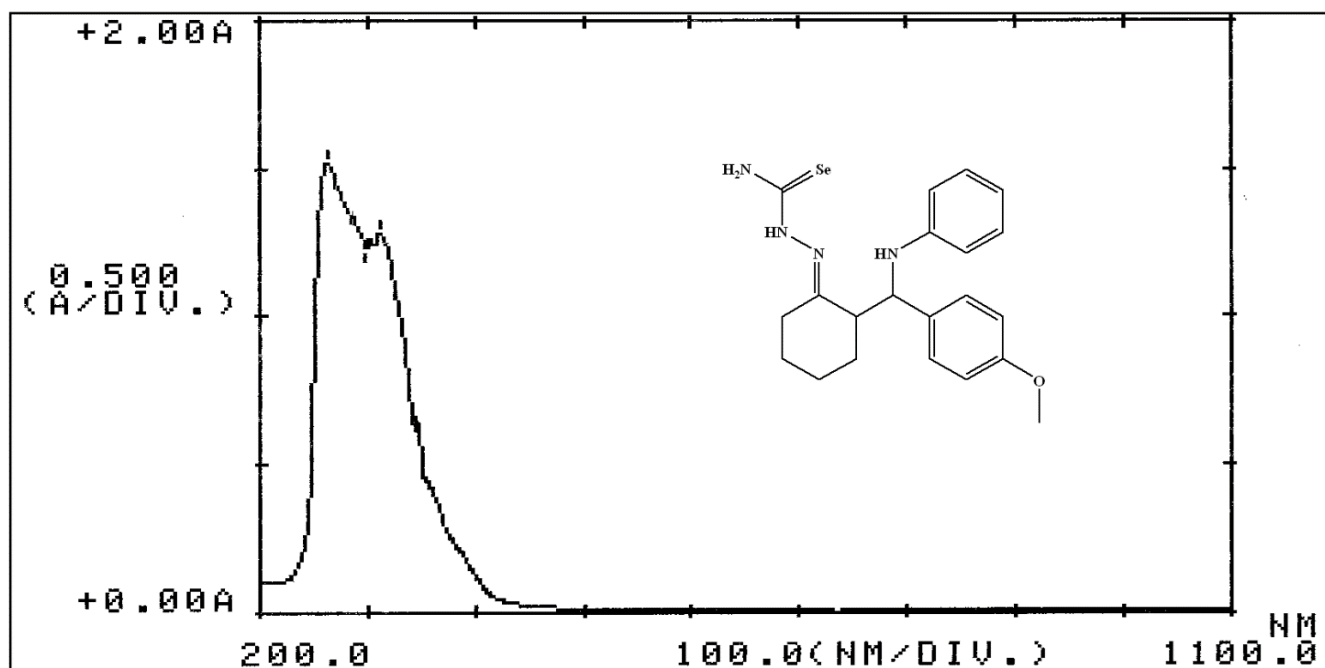
Figure (3-60): Electronic chart of HL^5 in DMSO solvent.

(3.6.1.6) Electronic data of HL^6

The electronic spectral data of HL^6 in DMSO solvent, Figure (3-61), reveals two absorption bands at 272 nm (36765 cm^{-1}; ε_{max}= 1443 dm^3 mol^{-1} cm^{-1}) and 318 nm (31447 cm^{-1}; ε_{max}= 1366 dm^3 mol^{-1} cm^{-1}) assigned to $\pi\rightarrow\pi*$ and n$\rightarrow\pi*$ transitions, respectively [60-62]. The electronic data includes in Table (3-10).
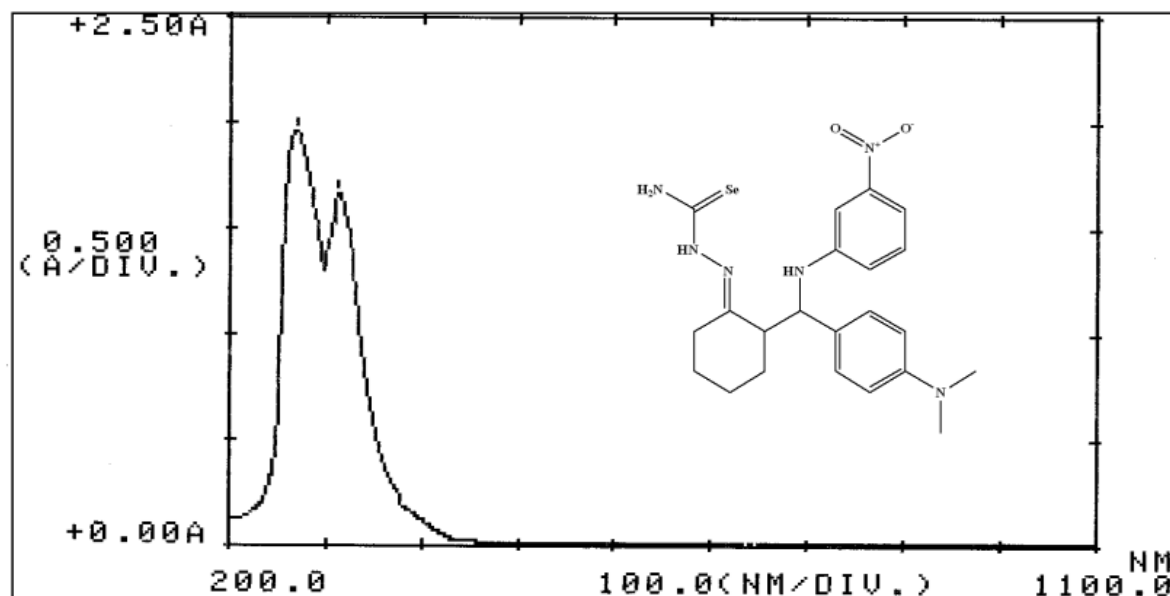
Figure (3-61): Electronic chart of HL^6 in DMSO solvent.

Table (3-10): UV-Vis data of HL^1-HL^6 in DMSO solvents.

Compound	Peak value λ_{nm}	Wave number (cm^{-1})	Molar extinction coefficient ε_{max} $(dm^3\ mol^{-1}\ cm^{-1})$	Assignment
HL^1	263	38023	560	$\pi\rightarrow\pi^*$
	315	31746	1234	$n\rightarrow\pi^*$
HL^2	266	37594	450	$\pi\rightarrow\pi^*$
	350	28571	1980	$n\rightarrow\pi^*$
	380	26316	2134	C. T.
HL^3	270	37037	987	$\pi\rightarrow\pi^*$
	310	32258	1305	$n\rightarrow\pi^*$
	365	27397	718	C. T.
HL^4	265	37736	1123	$\pi\rightarrow\pi^*$
	310	32258	988	$n\rightarrow\pi^*$
HL^5	262	38168	1343	$\pi\rightarrow\pi^*$
	315	31746	1063	$n\rightarrow\pi^*$
HL^6	272	36765	1443	$\pi\rightarrow\pi^*$
	318	31447	1366	$n\rightarrow\pi^*$

(3.7) Synthesis and characterisation of complexes

(3.7.1) Synthesis and characterisation of HL^1-HL^6 complexes

The synthesis of complexes is included in Scheme (3-16). The isolation of the title metal complexes was achieved from the reaction of the title ligand with metal chloride salts in a 2:1 L:M mole ratio. The reaction was carried out, in presence of KOH as a base, in a mixture of chloroform/ethanol in a 1:3 ratio with stirring. Upon complexation, ligands singly deprotonated and behave as (-1) and pure complexes collected by filtration in good yields as coloured solids.

Table (3-11) shows the ability of complexes to be soluble in a range of solvents. A range of spectral tools (FT-IR, UV-Vis, A.A., ES mass and ^{1}H-, ^{13}C- and ^{77}Se-NMR spectroscopy), microanalyses, magnetic moment measurements, chloride content, melting point, thermal analysis and conductivity measurements were used to characterise the complexes. Table (3-12) represents the micro-analyses data and selected physical properties of complexes.

R= 0 = HL^1; R= OCH$_3$ = HL^2; R= N(CH$_3$)$_2$ = HL^3

M= Mn(II), Co(II), Ni(II); n= 2; X= Cl; Z= -2

M= Cu(II), Zn(II), Cd(II); n= 0; X= 0; Z= 0

b= Number of water molecules

R= 0, Y= NO$_2$ = HL^4; R= OCH$_3$, Y= 0 = HL^5; R= N(CH$_3$)$_2$, Y= NO$_2$ = HL^6

M= Mn(II), Co(II), Ni(II); n= 2; X= Cl; Z= -2

M= Cu(II), Zn(II), Cd(II); n= 0; X= 0; Z= 0

b= Number of water molecules
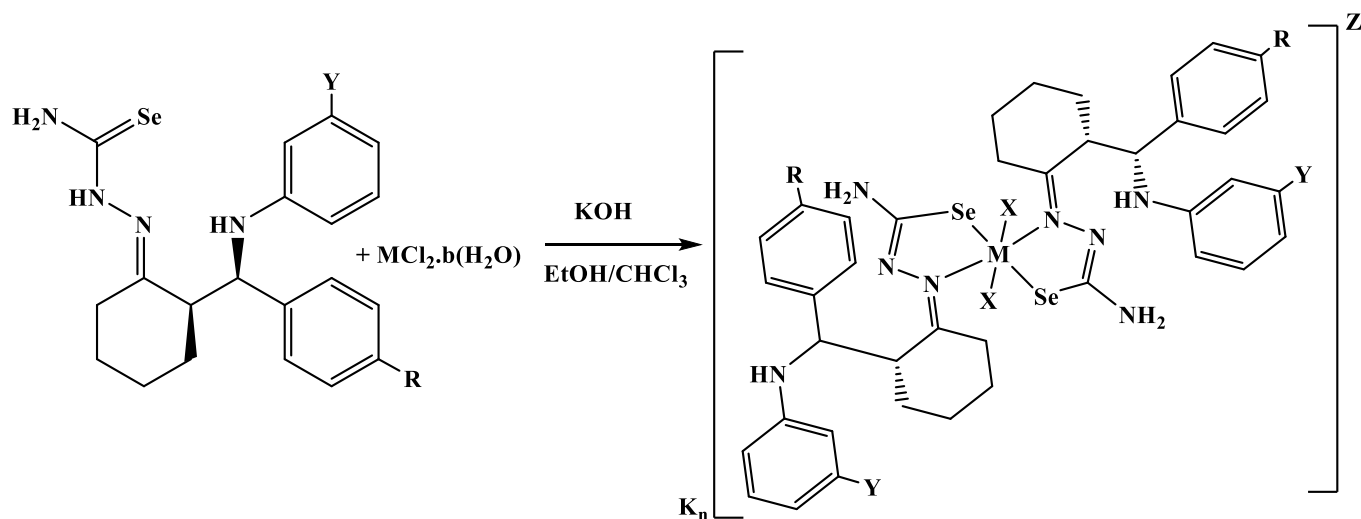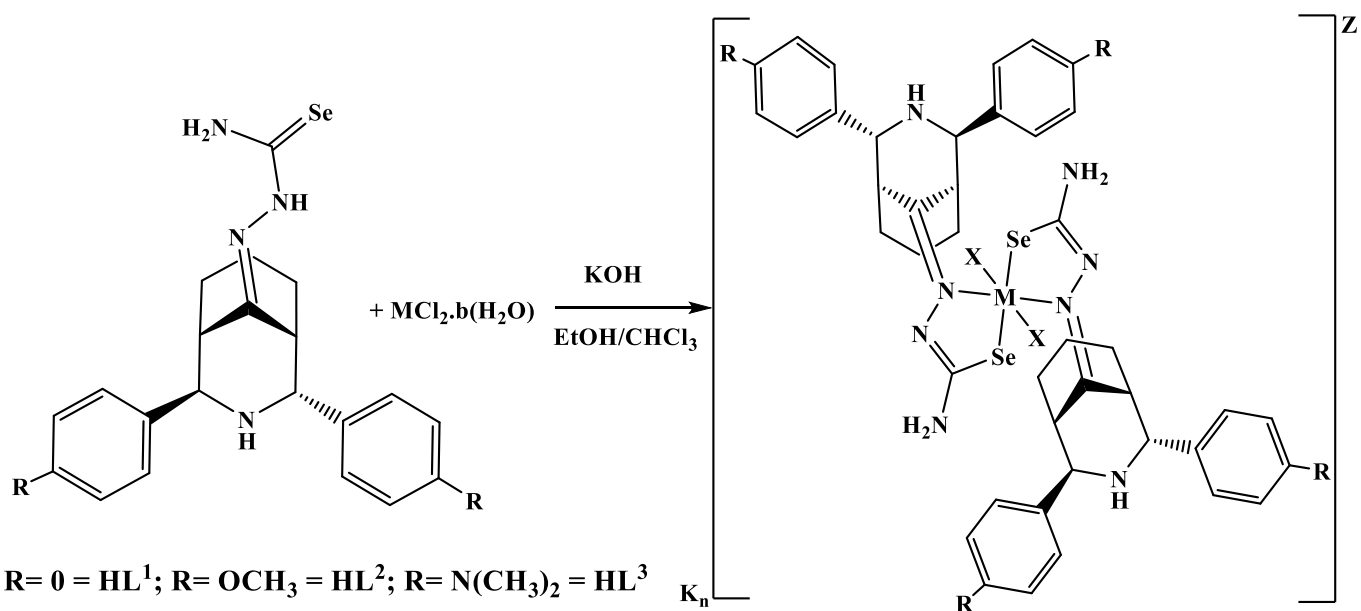
Scheme (3-16): General synthesis sketch of HL^1-HL^6 complexes.

Table (3-11): Solubility of metal complexes of HL^1-HL^6 in a range of solvents.

Complex	H_2O	DMSO	DMF	CH_3OH	C_2H_5OH	$CHCl_3$
$K_2[Mn(L^1)_2Cl_2]$	-	+	+	-	-	+
$K_2[Co(L^1)_2Cl_2]$	-	+	+	-	-	+
$K_2[Ni(L^1)_2Cl_2]$	-	+	+	-	-	+
$[Cu(L^1)_2]$	-	+	+	-	-	+
$[Zn(L^1)_2]$	-	+	+	-	-	+
$[Cd(L^1)_2]$	-	+	+	÷	-	+
$K_2[Mn(L^2)_2Cl_2]$	-	+	+	-	-	+
$K_2[Co(L^2)_2Cl_2]$	-	+	+	-	-	+
$K_2[Ni(L^2)_2Cl_2]$	-	+	+	-	-	+
$[Cu(L^2)_2]$	-	+	+	-	-	+
$[Zn(L^2)_2]$	-	+	+	-	-	+
$[Cd(L^2)_2]$	-	+	+	÷	-	+
$K_2[Mn(L^3)_2Cl_2]$	-	+	+	-	-	+
$K_2[Co(L^3)_2Cl_2]$	-	+	+	-	-	+
$K_2[Ni(L^3)_2Cl_2]$	-	+	+	-	-	+
$[Cu(L^3)_2]$	-	+	+	-	-	+
$[Zn(L^3)_2]$	-	+	+	-	-	+
$[Cd(L^3)_2]$	-	+	+	÷	-	+
$K_2[Mn(L^4)_2Cl_2]$	-	+	+	-	-	+
$K_2[Co(L^4)_2Cl_2]$	-	+	+	-	-	+
$K_2[Ni(L^4)_2Cl_2]$	-	+	+	-	-	+
$[Cu(L^4)_2]$	-	+	+	-	-	+
$[Zn(L^4)_2]$	-	+	+	-	-	+
$[Cd(L^4)_2]$	-	+	+	÷	-	+

(+)= soluble, (-)= insoluble, (÷)= partially soluble

Complex	H_2O	DMSO	DMF	CH_3OH	C_2H_5OH	$CHCl_3$
$K_2[Mn(L^5)_2Cl_2]$	-	+	+	-	-	+
$K_2[Co(L^5)_2Cl_2]$	-	+	+	-	-	+
$K_2[Ni(L^5)_2Cl_2]$	-	+	+	-	-	+
$[Cu(L^5)_2]$	-	+	+	-	-	+
$[Zn(L^5)_2]$	-	+	+	-	-	+
$[Cd(L^5)_2]$	-	+	+	÷	-	+
$K_2[Mn(L^6)_2Cl_2]$	-	+	+	-	-	+
$K_2[Co(L^6)_2Cl_2]$	-	+	+	-	-	+
$K_2[Ni(L^6)_2Cl_2]$	-	+	+	-	-	+
$[Cu(L^6)_2]$	-	+	+	-	-	+
$[Zn(L^6)_2]$	-	+	+	-	-	+
$[Cd(L^6)_2]$	-	+	+	÷	-	+

(+)= soluble, (-)= insoluble, (÷)= partially soluble

Table (3-12): Physico-chemical data of HL^1-HL^6 complexes.

Chemical formula	M.wt g/mol	Yield (%)	Colour	M.p ºC	Microanalysis Found, (Calc.)%				
					C	H	N	M	Cl
COMPLEXES OF HL^1									
$K_2[MnC_{42}H_{46}Cl_2N_8Se_2]$	1024.84	50	Dark blue	280-285	49.10 (49.18)	4.47 (4.49)	10.90 (10.93)	5.32 (5.37)	6.80 (6.83)
$K_2[CoC_{42}H_{46}Cl_2N_8Se_2]$	1028.84	72	Deep brown	241-244	48.95 (48.99)	4.45 (4.47)	10.88 (10.89)	5.70 (5.74)	6.77 (6.80)
$K_2[NiC_{42}H_{46}Cl_2N_8Se_2]$	1028.60	76	Dark orange	291-294	48.94 (49.00)	4.44 (4.47)	10.86 (10.89)	5.70 (5.74)	6.79 (6.81)
$[CuC_{42}H_{46}N_8Se_2]$	884.35	62	Light brown	288-291	56.98 (57.00)	5.18 (5.20)	12.64 (12.67)	7.20 (7.24)	-
$[ZnC_{42}H_{46}N_8Se_2]$	886.19	63	Light brown	287-289	56.85 (56.87)	5.17 (5.19)	12.60 (12.64)	7.30 (7.34)	-
$[CdC_{42}H_{46}N_8Se_2]$	933.22	41	Deep brown	304-306	53.99 (54.01)	4.90 (4.93)	11.98 (12.00)	11.95 (12.00)	-

Chemical formula	M.wt g/mol	Yield (%)	Colour	M.p ºC	Microanalysis Found, (Calc.)%				
					C	H	N	M	Cl
COMPLEXES OF HL²									
$K_2[MnC_{46}H_{54}Cl_2N_8O_4Se_2]$	1144.94	52	Brown	266-269	48.16 (48.21)	4.70 (4.72)	9.72 (9.78)	4.79 (4.80)	6.10 (6.11)
$K_2[CoC_{46}H_{54}Cl_2N_8O_4Se_2]$	1148.94	68	Red brown	245-248	48.00 (48.04)	4.66 (4.70)	9.71 (9.75)	5.12 (5.14)	6.07 (6.09)
$K_2[NiC_{46}H_{54}Cl_2N_8O_4Se_2]$	1148.70	64	Dark orange	285-287	48.01 (48.05)	4.68 (4.70)	9.73 (9.75)	5.10 (5.14)	6.02 (6.09)
$[CuC_{46}H_{54}N_8O_4Se_2]$	1004.46	67	Dark brown	299-303	54.92 (54.96)	5.35 (5.37)	11.12 (11.15)	6.33 (6.37)	-
$[ZnC_{46}H_{54}N_8O_4Se_2]$	1006.29	79	Light brown	287-289	54.84 (54.86)	5.35 (5.37)	11.11 (11.13)	6.44 (6.46)	-
$[CdC_{46}H_{54}N_8O_4Se_2]$	1053.32	75	Deep brown	296-2 99	52.35 (52.41)	5.11 (5.13)	10.60 (10.63)	10.60 (10.63)	-
COMPLEXES OF HL³									
$K_2[MnC_{50}H_{66}Cl_2N_{12}Se_2]$	1197.12	65	Deep brown	277-279	50.09 (50.12)	5.50 (5.51)	14.00 (14.03)	4.56 (4.59)	5.80 (5.85)
$K_2[CoC_{50}H_{66}Cl_2N_{12}Se_2]$	1201.11	63	Brown	287-289	49.90 (49.95)	5.47 (5.50)	13.95 (13.99)	4.90 (4.91)	5.81 (5.83)
$K_2[NiC_{50}H_{66}Cl_2N_{12}Se_2]$	1200.87	58	Lightorange	290-293	49.95 (99.96)	5.44 (5.50)	13.96 (13.99)	4.90 (4.91)	5.80 (5.83)
$[CuC_{50}H_{66}N_{12}Se_2]$	1056.63	71	Dark brown	296-299	56.77 (56.78)	6.24 (6.25)	15.88 (15.90)	6.04 (6.06)	-
$[ZnC_{50}H_{66}N_{12}Se_2]$	1058.46	67	Light brown	305-308	56.65 (56.69)	6.20 (6.24)	15.85 (15.87)	6.12 (6.14)	-
$[CdC_{50}H_{66}N_{12}Se_2]$	1105.49	67	Deep brown	311-314	54.23 (54.28)	5.95 (5.97)	15.16 (15.20)	10.11 (10.13)	-

Chemical formula	M.wt g/mol	Yield (%)	Colour	M.p ºC	Microanalysis Found, (Calc.)%				
					C	H	N	M	Cl
COMPLEXES OF HL⁴									
$K_2[MnC_{40}H_{44}Cl_2N_{10}O_4Se_2]$	1090.81	68	Deep brown	276-279	43.96 (44.00)	4.00 (4.03)	12.80 (12.84)	5.02 (5.04)	6.40 (6.42)
$K_2[CoC_{40}H_{44}Cl_2N_{10}O_4Se_2]$	1094.81	59	Red brown	287-289	43.80 (43.84)	4.00 (4.02)	12.75 (12.79)	5.33 (5.39)	6.35 (6.39)
$K_2[NiC_{40}H_{44}Cl_2N_{10}O_4Se_2]$	1094.57	63	Light orange	299-303	43.81 (43.85)	4.00 (4.02)	12.75 (12.79)	5.34 (5.39)	6.37 (6.40)
$[CuC_{40}H_{44}N_{10}O_4Se_2]$	950.32	58	Dark brown	296-298	50.46 (50.51)	4.60 (4.63)	14.70 (14.73)	6.71 (6.74)	-
$[ZnC_{40}H_{44}N_{10}O_4Se_2]$	952.16	67	Light brown	288-291	50.40 (50.41)	4.60 (4.62)	14.65 (14.70)	6.80 (6.83)	-
$[CdC_{40}H_{44}N_{10}O_4Se_2]$	999.19	69	Deep brown	312-314	48.00 (48.04)	4.38 (4.40)	14.00 (14.01)	11.18 (11.21)	-
COMPLEXES OF HL⁵									
$K_2[MnC_{42}H_{50}Cl_2N_8O_2Se_2]$	1060.87	65	Brown	276-278	47.46 (47.51)	4.69 (4.71)	10.53 (10.54)	5.15 (5.18)	6.56 (6.60)
$K_2[CoC_{42}H_{50}Cl_2N_8O_2Se_2]$	1064.87	57	Dark brown	287-289	47.30 (47.33)	4.66 (4.70)	10.50 (10.52)	5.50 (5.54)	6.55 (6.57)
$K_2[NiC_{42}H_{50}Cl_2N_8O_2Se_2]$	1064.63	50	Deep orange	299-302	47.31 (47.34)	4.66 (4.70)	10.50 (10.52)	5.51 (5.54)	6.55 (6.58)
$[CuC_{42}H_{50}N_8O_2Se_2]$	920.38	60	Dark brown	296-298	54.71 (54.76)	5.40 (5.43)	12.14 (12.17)	6.92 (6.95)	-
$[ZnC_{42}H_{50}N_8O_2Se_2]$	922.22	42	Light brown	288-291	54.62 (54.65)	5.40 (5.42)	12.12 (12.15)	7.01 (7.05)	-
$[CdC_{42}H_{50}N_8O_2Se_2]$	969.25	54	Light brown	312-314	51.97 (52.00)	5.12 (5.16)	11.53 (11.56)	11.53 (11.56)	-
COMPLEXES OF HL⁶									
$K_2[MnC_{44}H_{54}Cl_2N_{12}O_4Se_2]$	1176.95	70	Deep brown	288-291	44.82 (44.86)	4.56 (4.59)	14.22 (14.27)	4.65 (4.67)	5.91 (5.95)
$K_2[CoC_{44}H_{54}Cl_2N_{12}O_4Se_2]$	1180.95	63	Dark brown	291-293	44.68 (44.71)	4.55 (4.57)	14.20 (14.23)	4.98 (5.00)	5.90 (5.93)
$K_2[NiC_{44}H_{54}Cl_2N_{12}O_4Se_2]$	1180.71	54	Deep orange	306-308	44.69 (44.72)	4.55 (4.57)	14.20 (14.23)	4.97 (5.00)	5.90 (5.93)
$[CuC_{44}H_{54}N_{12}O_4Se_2]$	1036.46	65	Dark brown	299-302	50.91 (50.94)	5.20 (5.21)	16.18 (16.21)	6.14 (6.18)	-
$[ZnC_{44}H_{54}N_{12}O_4Se_2]$	1038.30	71	Light brown	309-313	50.83 (50.85)	5.18 (5.20)	16.15 (16.18)	6.24 (6.26)	-
$[CdC_{44}H_{54}N_{12}O_4Se_2]$	1085.33	58	Light brown	313-315	48.61 (48.65)	4.95 (4.98)	15.45 (15.48)	10.30 (10.32)	-

(3.8) FT-IR spectra of complexes

(3.8.1) FT-IR spectra of HL^1 complexes

(3.8.1.1) FT-IR data of $K_2[Mn(L^1)_2Cl_2]$

The FT-IR data of HL^1 complexes are presented in Table (3-13). The spectrum of $K_2[Mn(L^1)_2Cl_2]$, Figure (3-62), displays peaks related to $\nu(C=N)$ and $\nu(C-Se)$ [30] stretches at 1637 and 754 cm^{-1}, respectively. The former band was shifted to lower frequency, compared with the free ligand. This may relate to redistribute electron density of metal to ligand system ($d\pi \rightarrow p\pi^*$), HOMO$\rightarrow$LUMO [63,64]. The shifting to lower frequency indicates strong bonding nature between the metal ions and the iminic C=N group. The shift in the $\nu(C=N)$ confirmed the involvement of nitrogen atoms of imine moieties in the coordination to the metal ions [65-67]. The C-Se band was shifted to lower wave number and detected at 1219 cm^{-1}, referred to that in HL^1 at 1250 cm^{-1}, indicating the presence of the C-Se group in its selenide form [30]. Further, the appearance of the N=C-Se group at 1614 cm^{-1} in the spectrum of complex, compared with that at 1604 cm^{-1} in HL^1, indicated the deprotonation of N3-H of the H-N-C=Se moiety and supporting the presence of the C-Se in its selenide form at 754 cm^{-1}.

Bands at 3433 and 3400 cm^{-1} related to $\nu(N4-H)$ group and band at 3305 cm^{-1} assigned to $\nu(N1-H)$ group. The appearance of these bands in the spectra of complex confirmed the non-involvement of nitrogen atoms in the coordination [3]. Further, the spectrum of the Mn(II) complex revealed new bands that are not detected in the ligand spectrum, allocated at 405 and 469 cm^{-1} that attributed to $\nu(Mn-N)$ [68]. At lower frequency, the FT-IR of $K_2[Mn(L^1)_2Cl_2]$, exhibited band at 364 cm^{-1} that attributed to $\nu(M-Se)$ [69]. The band at 273 cm^{-1} attributed to $\nu(Mn-Cl)$ [27].
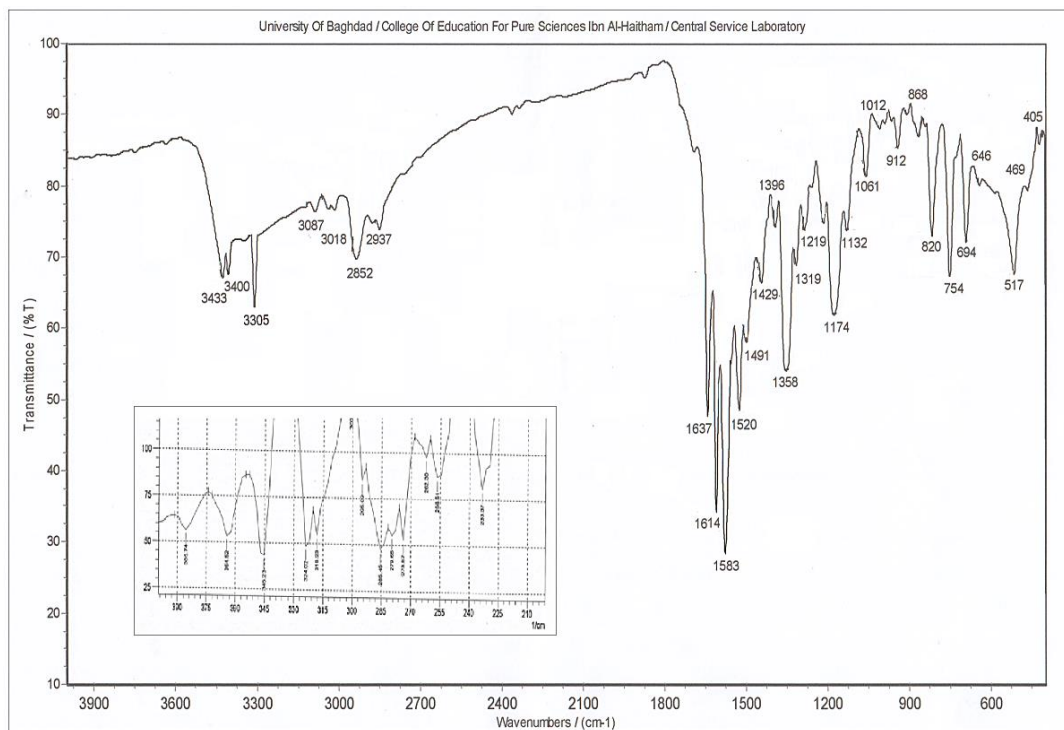
Figure (3-62): FT-IR chart of K$_2$[Mn(L^1)$_2$Cl$_2$].

(3.8.1.2) FT-IR data of K$_2$[Co(L^1)$_2$Cl$_2$], K$_2$[Ni(L^1)$_2$Cl$_2$], [Cu(L^1)$_2$], [Zn(L^1)$_2$] and [Cd(L^1)$_2$] complexes

The FT-IR of the above complexes, Figures (3-63) to (3-67), indicated band in the range 1634-1638 cm^{-1} assigned to ν(C=N) group [3]. This band was shifted to lower frequency, compared with that in HL^1. The reduced bond order may be redistribute electron density of metal to ligand system (dπ→pπ*), HOMO→LUMO [63,64]. The shifting to lower frequency indicates strong bonding nature between the metal ions and the iminic C=N group. The shift in the ν(C=N) confirmed the involvement of nitrogen atoms of imine moieties in the coordination to the metal ions [65-67]. While, band in the range 1610-1618 cm^{-1} related to N=C-Se group. This band shifted to higher wave number, compared with that at 1604 cm^{-1} for HL^1, indicated the deprotonation of N3-H of the H-N-C=Se moiety and supporting the presence of the C-Se in its selenide form. Bands displayed

in the range 3377-3471 and 3304-3305 cm^{-1} were assigned to ν(N4-H) and ν(N1-H) groups, respectively [3]. Band detected in the range 727-736 cm^{-1} attributed to ν(C-Se) group [30]. The appropriate shift of this band, referred to that in HL^{1}, is attributed to complex fabrication. New bands that appeared between 416-420 and 454-466 cm^{-1} are due to ν(M-N) stretch [68], indicating the connection of the nitrogen atoms in the coordination to metal centre. At lower frequency, the bands between 333-350 cm^{-1} that assigned to ν(M-Se) [69]. The spectrum indicated bands at 254 and 275 cm^{-1} related to ν(Co-Cl) and ν(Ni-Cl) respectively [27]. These results are displayed in Table (3-13).
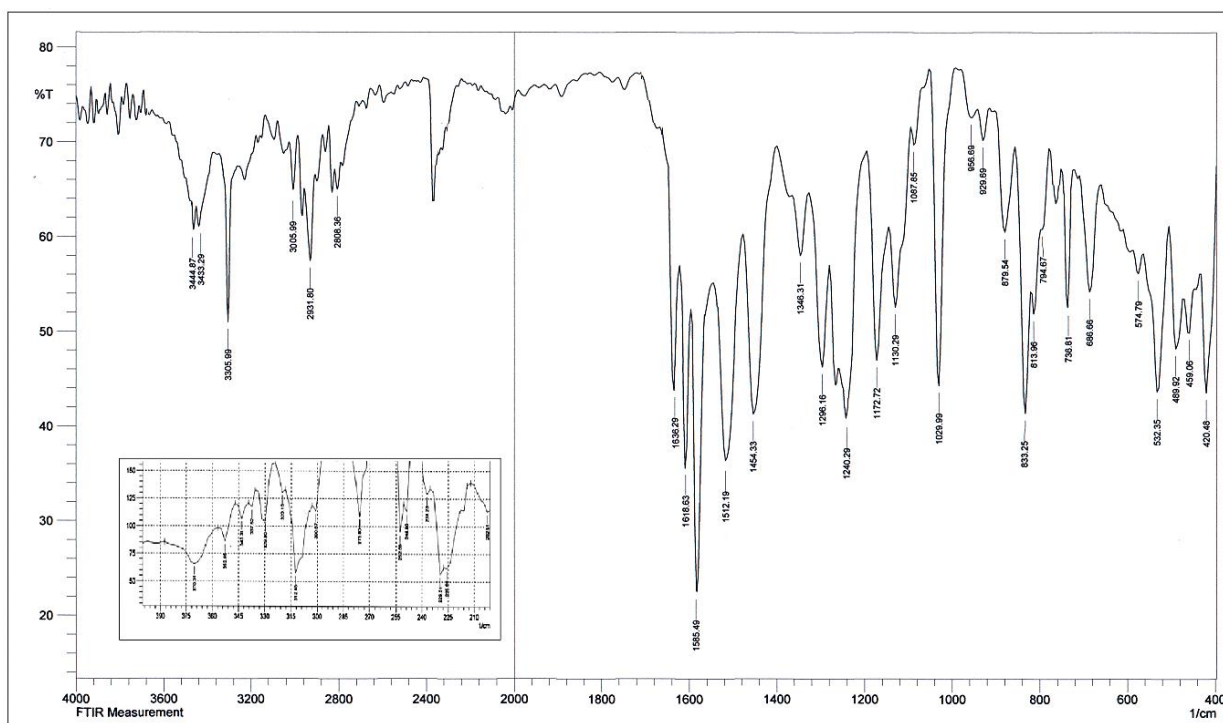
Figure (3-63): FT-IR chart of K$_2$[Co(L^1)$_2$Cl$_2$].
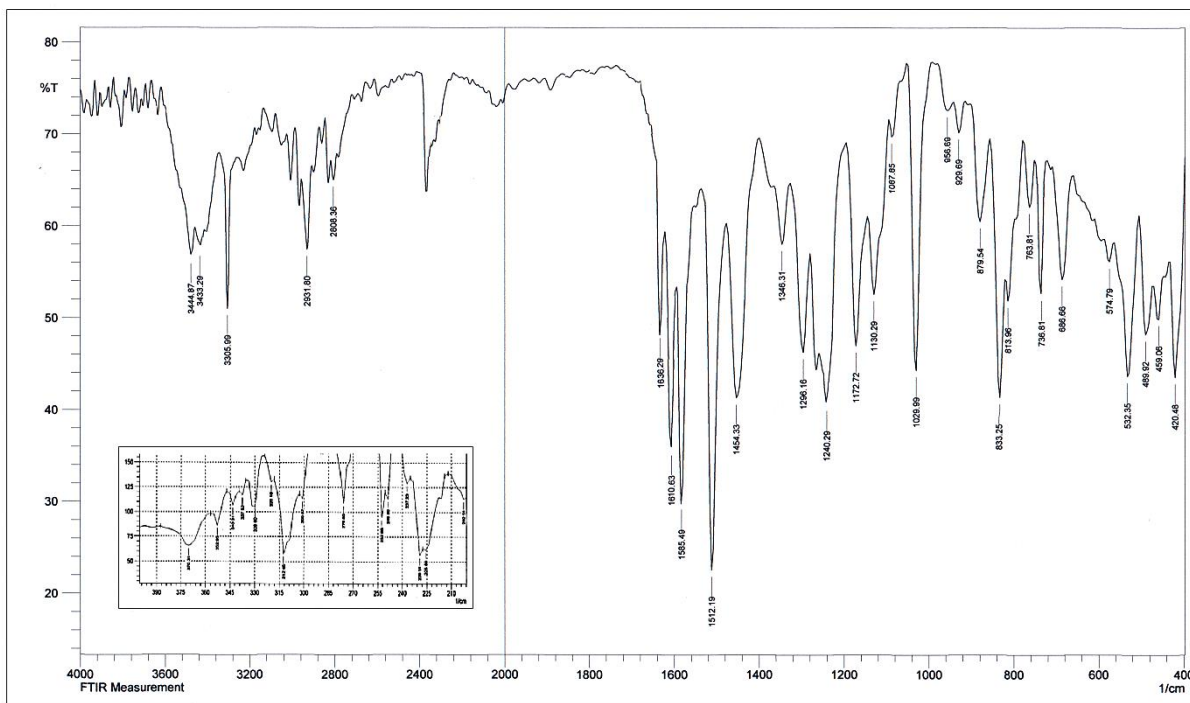
Figure (3-64): FT-IR chart of $K_2[Ni(L^1)_2Cl_2]$.
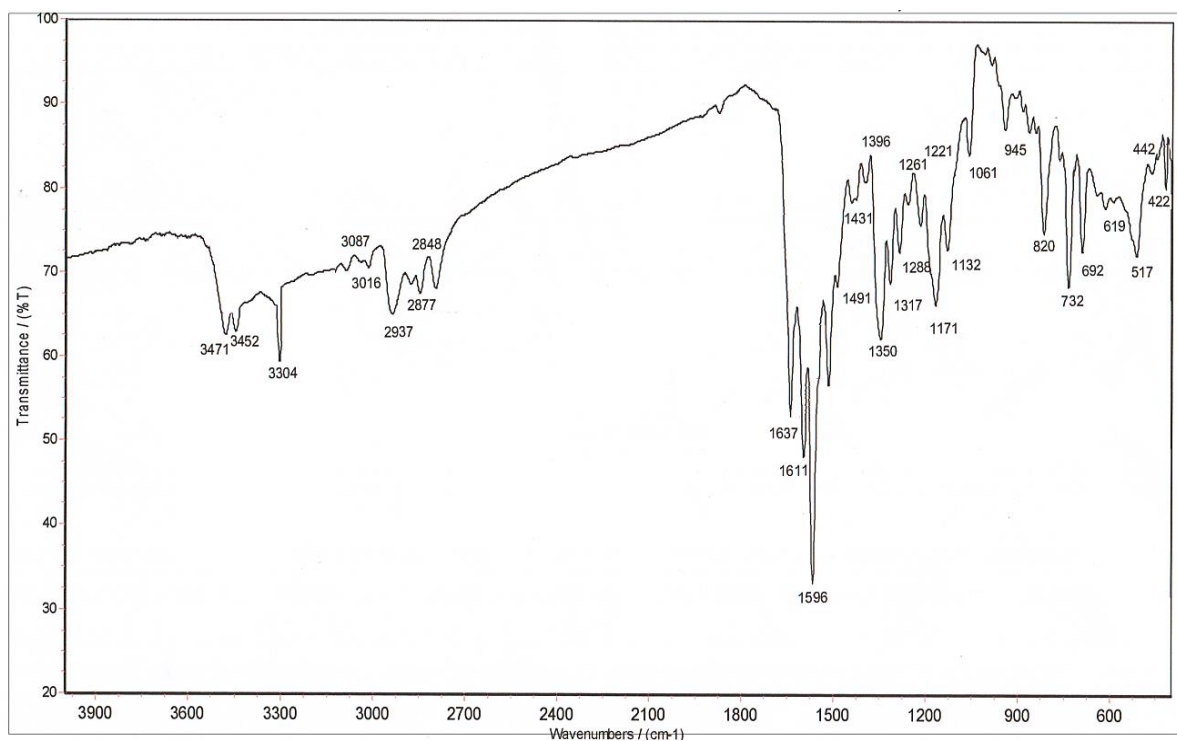
Figure (3-65): FT-IR chart of $[Cu(L^1)_2]$.

144
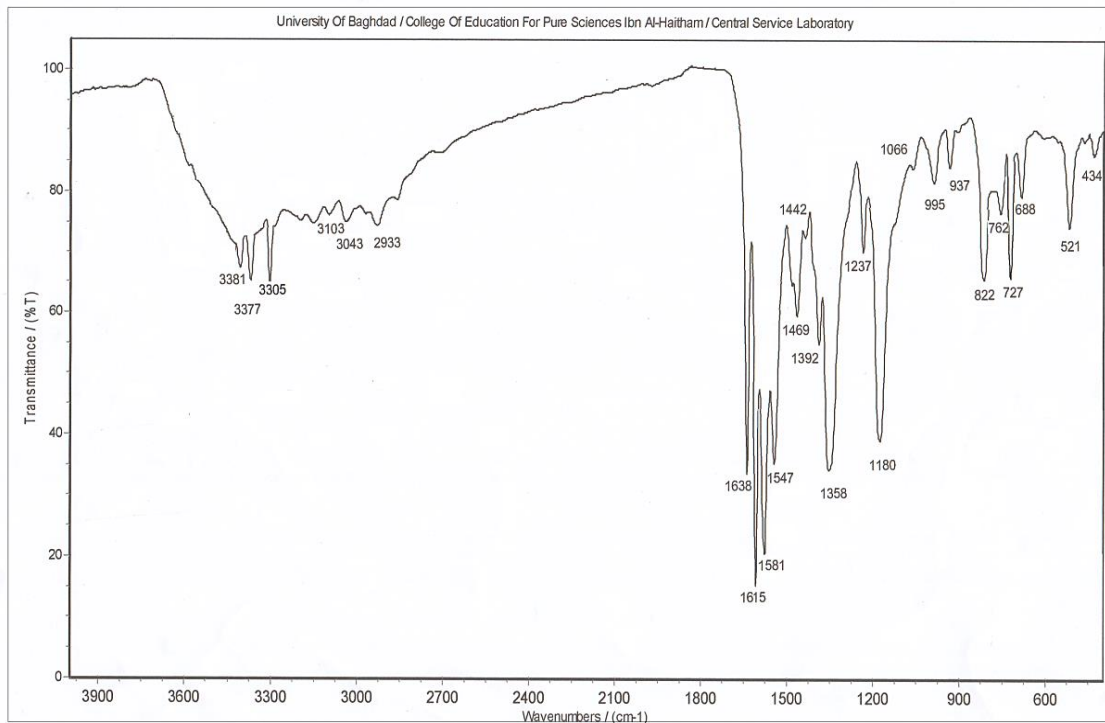
Figure (3-66): FT-IR chart of [Zn(L^1)$_2$].
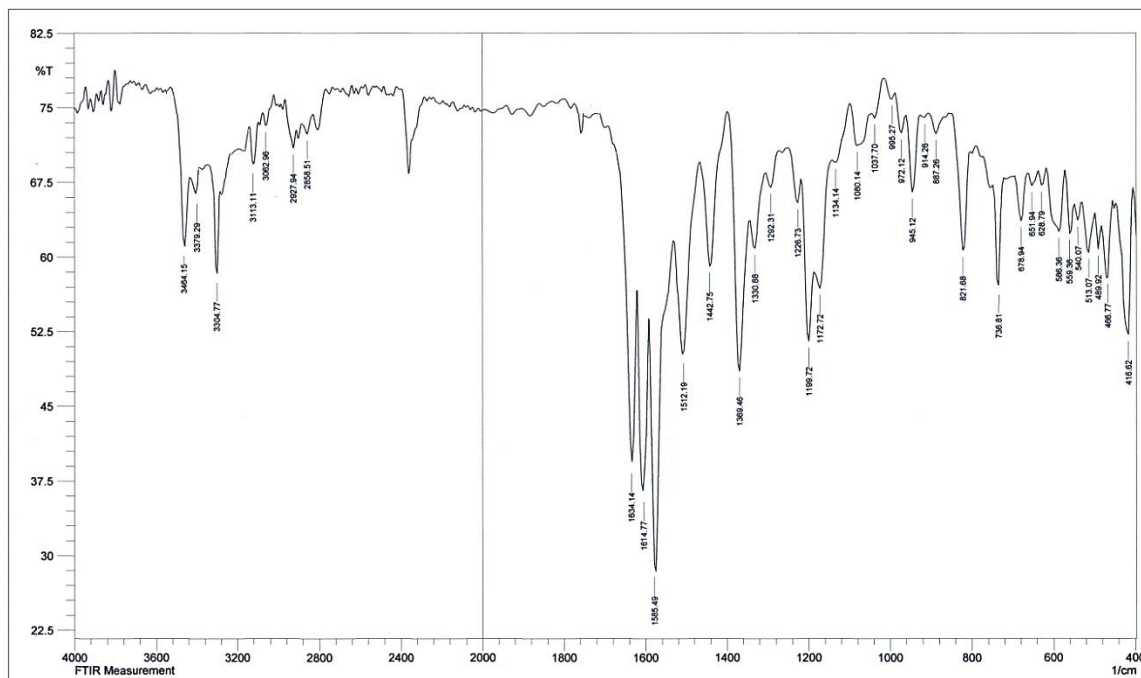
Figure (3-67): FT-IR chart of [Cd(L^1)$_2$].

Table (3-23): Infrared data (cm^{-1}) of HL^1 and its complexes.

Compound	v(N4-H)	v(N3-H)	v(N1-H)	v(C-H)Aro. v(C-H)Ali.	v(C=N)	v(N-C=Se) v(N=C-Se)	v(C=C)	v(C-Se)	v(M-N)	v(M-Se)	v(M-Cl)
HL^1	3375 3368	3337	3305	3006 2931	1641	1602 –	1579 1510	1250 762	–	–	–
K$_2$[Mn(L^1)$_2$Cl$_2$]	3433 3400	–	3305	3087 2852	1637	– 1614	1583 1520	1219 754	405 469	364	273
K$_2$[Co(L^1)$_2$Cl$_2$]	3444 3433	–	3305	3005 2931	1636	– 1618	1585 1512	1240 736	420 459	335	254
K$_2$[Ni(L^1)$_2$Cl$_2$]	3444 3433	–	3305	3009 2931	1636	– 1610	1585 1512	1240 736	420 459	333	275
[Cu(L^1)$_2$]	3471 3452	–	3304	3087 2937	1637	– 1611	1596 1545	1221 732	422 442	334	–
[Zn(L^1)$_2$]	3381 3377	–	3305	3103 2933	1638	– 1615	1581 1547	1237 727	434	350	–
[Cd(L^1)$_2$]	3464 3379	–	3304	3113 2927	1634	– 1614	1585 1512	1226 736	416 466	339	–

146

(3.8.2) FT-IR spectra of HL^2 complexes

(3.8.2.1) FT-IR data of K$_2$[Mn(L^2)$_2$Cl$_2$]

The FT-IR data of Mn(II) complex with HL^2 is included in Table (3-14). The FT-IR chart of K$_2$[Mn(L^2)$_2$Cl$_2$], Figure (3-68), revealed band at 1646 cm^{-1} assigned to ν(C=N) group that shifted to lower frequency [70], in comparison with that at 1653 cm^{-1} in the free ligand. This shift is due to π-back bonding, which resulted from redistribute electron density of metal to ligand system (d$\pi\rightarrow$pπ^*), HOMO$\rightarrow$LUMO [63,64]. More, the shifting to lower frequency indicates strong bonding nature between the metal ions and the iminic C=N group. The shift in the ν(C=N) confirmed the involvement of nitrogen atoms of imine moieties in the coordination to the metal ions [65-67]. The spectrum indicated band at 752 cm^{-1} due to C-Se group that suffered lower shifting, compared with this peak that appeared at 770 cm^{-1} in the spectrum of HL^2. This shifting may attribute to the chelation of the ligand through selenium atoms to the metal ion [30]. Further, the spectrum showed band at 1222 cm^{-1} account for C-Se group. This band was detected at lower wave number, compared with that peak appeared at 1244 cm^{-1} in HL^2, demonstrating the coordination of the Se atom to the metal centre in its selenide form [30]. Further, the spectrum of the complex revealed band at 1619 cm^{-1} assigned to N=C-Se group. This band recorded in higher wave number, compared with that at 1600 cm^{-1} in HL^2, indicating the deprotonation of the N3-H of the H-N-C=Se moiety and supporting the presence of the C-Se in its selenide. Bands that detected at 3444; 3460 and 3412 cm^{-1} related to ν(N4-H) and ν(N1-H) group, respectively [30]. The wave number values of these bands are similar to that found in the free ligand indicating the non-involvement of nitrogen atoms in the coordination [3].

Bands appeared at 412 and 439 cm^{-1} related to ν(Mn-N) [68]. In addition, the FT-IR of K$_2$[Mn(L^2)$_2$Cl$_2$], exhibited band at 340 cm^{-1} assigned to ν(M-Se) vibrational mode [69]. The band at 257 cm^{-1} attributed to ν(Mn-Cl) [27].

Figure (3-68): FT-IR chart of $K_2[Mn(L^2)_2Cl_2]$.

(3.8.2.2) FT-IR data of $K_2[Co(L^2)_2Cl_2]$, $K_2[Ni(L^2)_2Cl_2]$, $[Cu(L^2)_2]$, $[Zn(L^2)_2]$ and $[Cd(L^2)_2]$ complexes

The FT-IR of the above complexes (Figures (3-69) to (3-73)), displayed bands in the range 1637-1645 and 710-760 cm^{-1} due to ν(C=N) imine and ν(C-Se) group, respectively [70,30]. These bands appeared at lower wave number, in comparison with that in HL^2, indicating the involvement of the Se and the nitrogen of the imine group in the coordination to the metal centre. An analogous reasoning to that stated in the spectrum of the Mn(II) complex may be implemented to explain the lower shifting of these groups [63,64]. More, the spectra of complexes recorded band in the range 1611-1618 cm^{-1} assigned to N=C-Se segment [30]. This band shifted to higher wave number, compared

148

with that at 1600 cm^{-1} in HL^2, indicating the deprotonation of the N3-H of the H-N-C=Se moiety and supporting the presence of the C-Se in its selenide form. Bands displayed in the range 3444-3512 and 3407-3411 cm^{-1} were assigned to ν(N4-H) and ν(N1-H) groups, respectively [3,30]. New bands that detected between 412-424 and 439-489 cm^{-1} are due to ν(M-N) stretches [68], indicating the involvement of the nitrogen atoms in the coordination to metal centre. Further, bands detected around 344-355 cm^{-1} attributed to ν(M-Se) [69]. The spectra of Co(II) and Ni(II) complex indicated bands at 257 and 256 cm^{-1} related to ν(Co-Cl) and ν(Ni-Cl), respectively [27]. The FT-IR data are tabulated in Table (3-14).
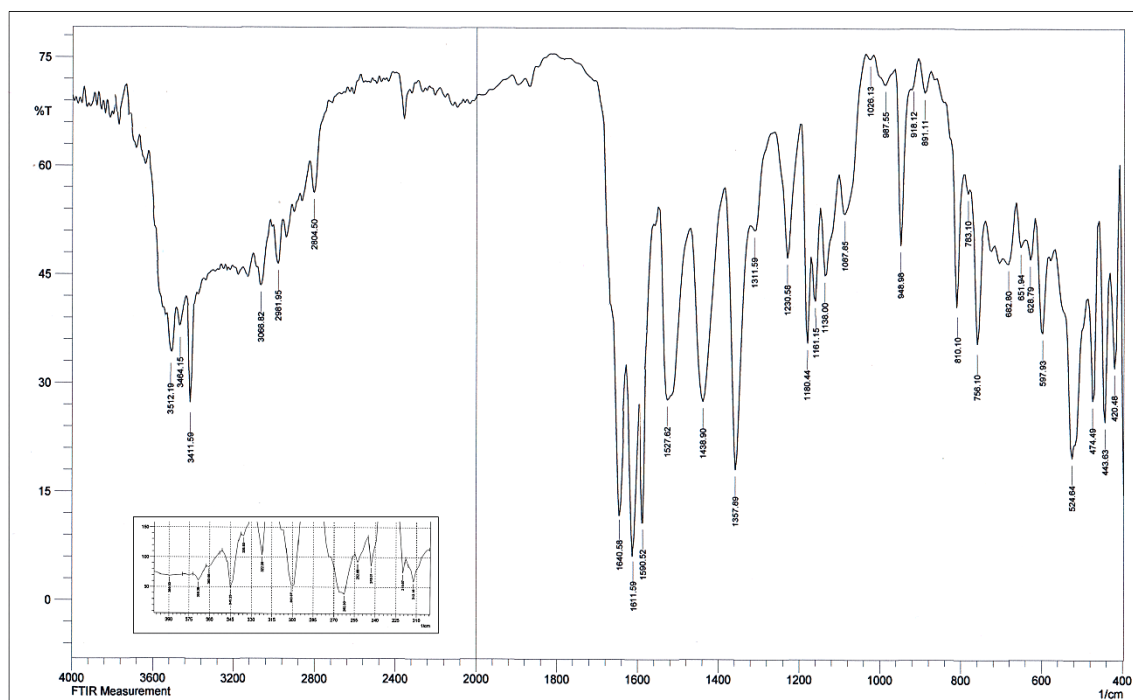
Figure (3-69): FT-IR chart of K$_2$[Co(L^2)$_2$Cl$_2$].
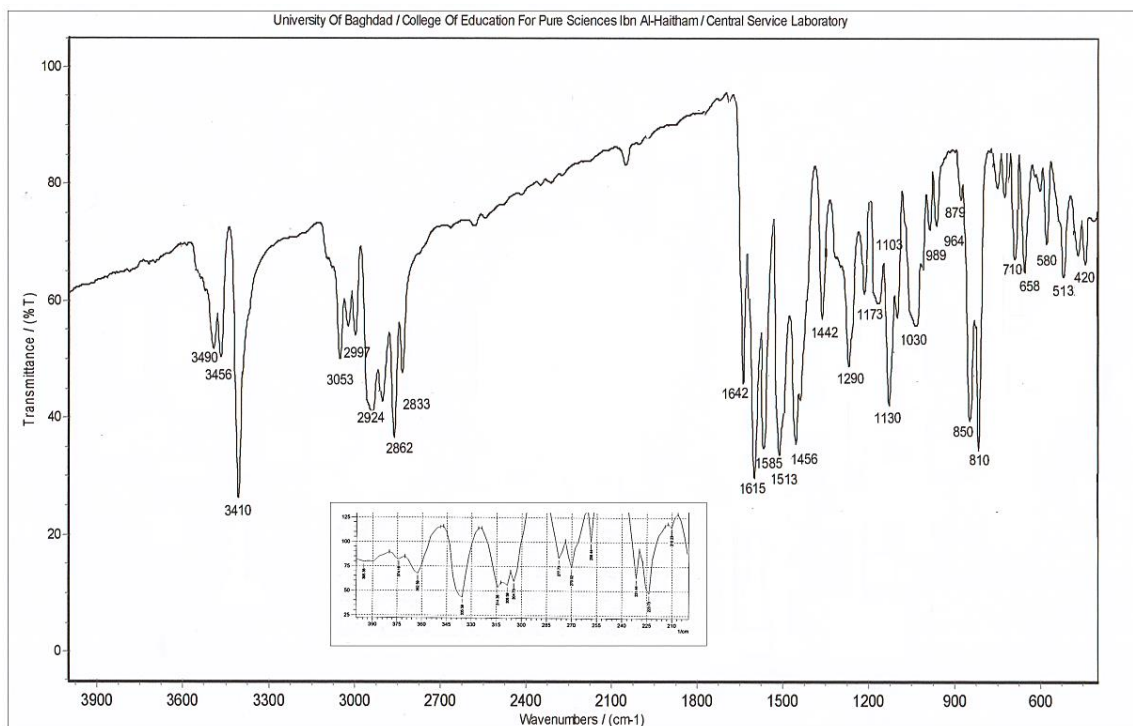
Figure (3-70): FT-IR chart of K$_2$[Ni(L^2)$_2$Cl$_2$].
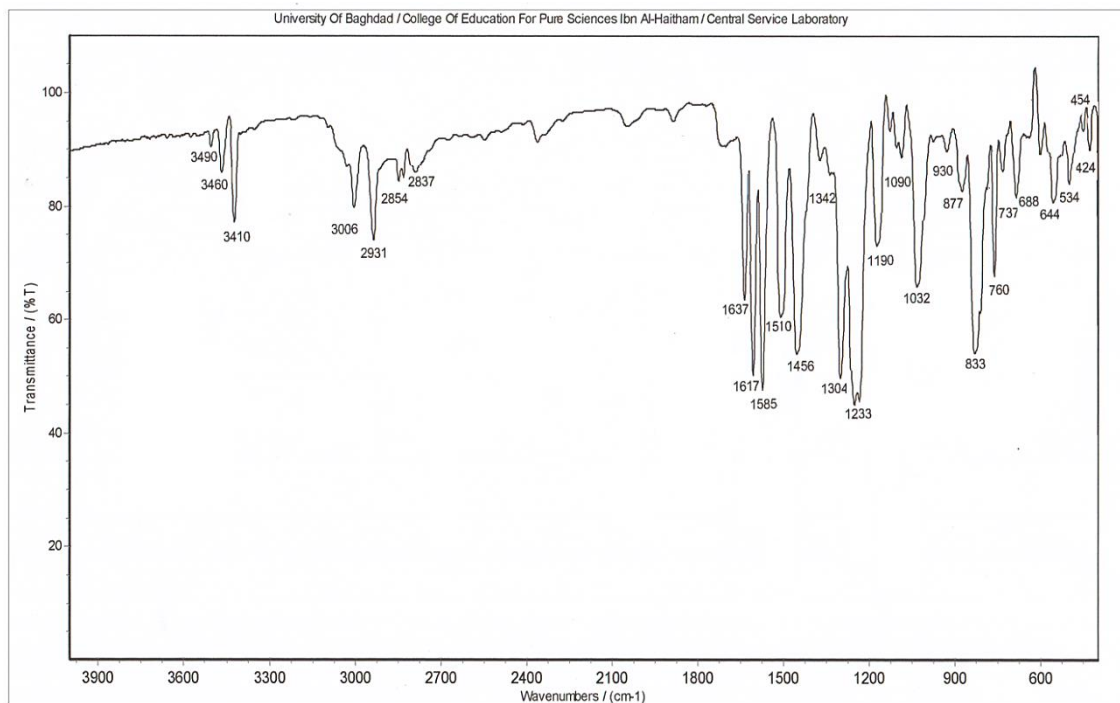
Figure (3-71): FT-IR chart of [Cu(L^2)$_2$].

150
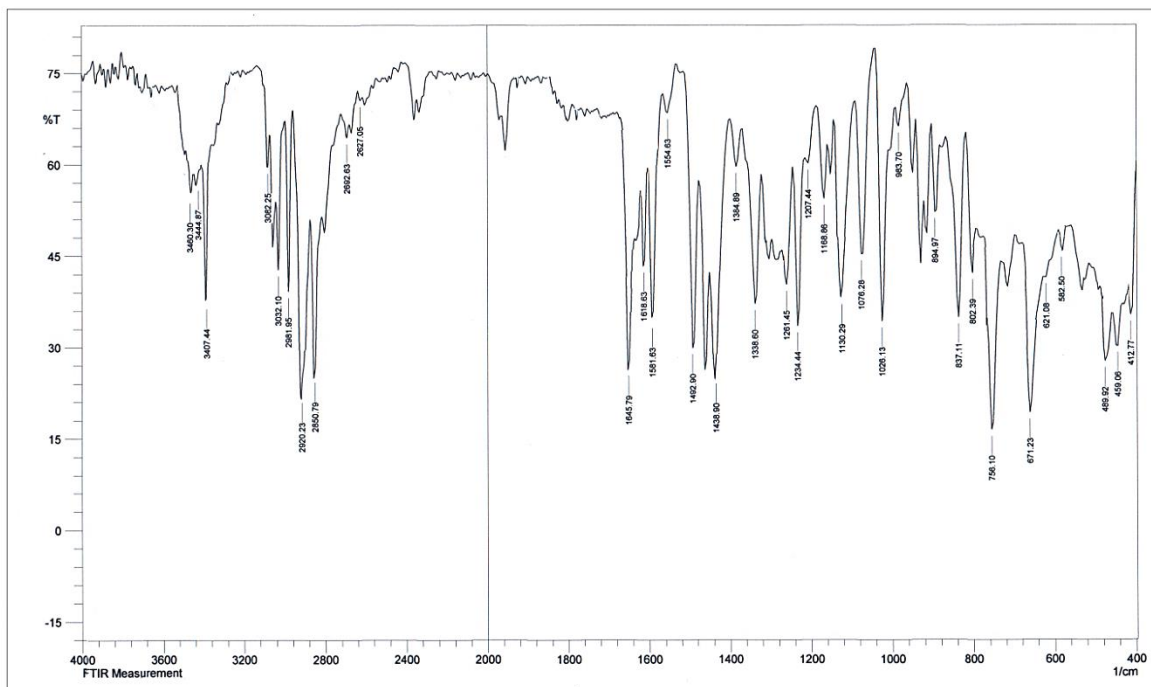
Figure (3-72): FT-IR chart of [Zn(L^2)$_2$].
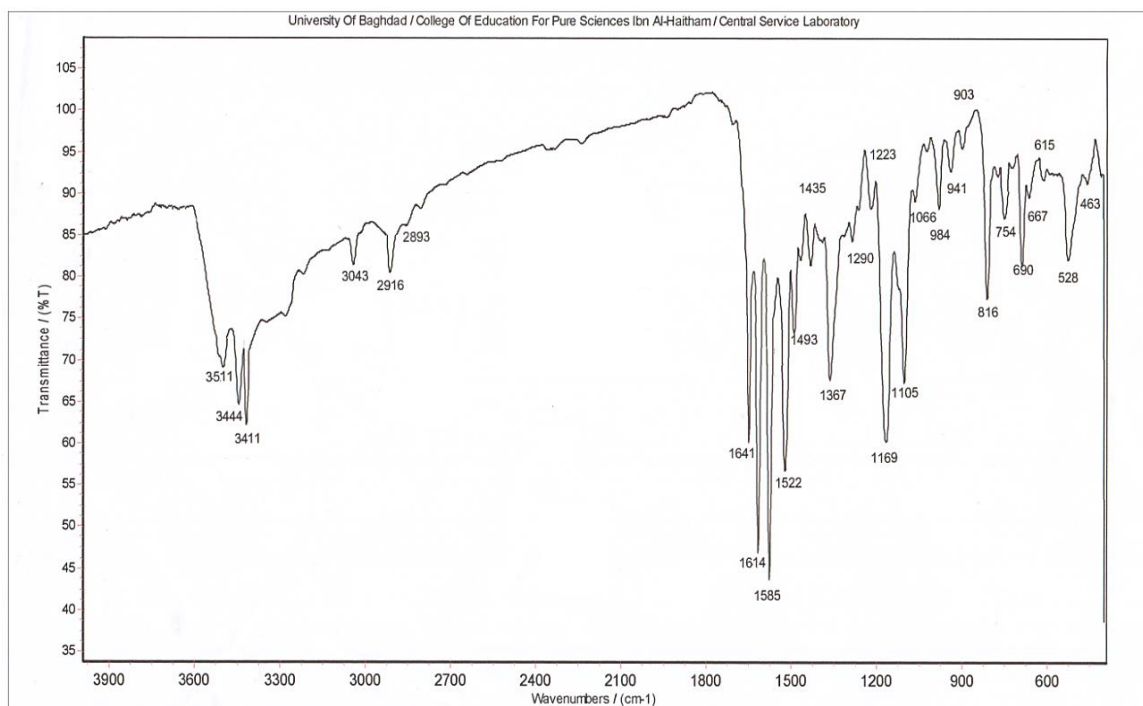
Figure (3-73): FT-IR chart of [Cd(L^2)$_2$].

Table (3-14): Infrared data (cm^{-1}) of HL^2 and its complexes.

Compound	ν(N4-H)	ν(N3-H)	ν(N1-H)	ν(C-H)Aro. ν(C-H)Ali.	ν(C=N)	ν(N-C=Se) ν(N=C-Se)	ν(C=C)	ν(C-Se)	ν(M-N)	ν(M-Se)	ν(M-Cl)
HL^2	3520 3474	3438	3410	3053 2933	1653	1600 –	1500 1510	1244 770	–	–	–
K$_2$[Mn(L^2)$_2$Cl$_2$]	3460 3444	–	3412	3016 2943	1646	– 1619	1590 1512	1222 752	412 439	340	257
K$_2$[Co(L^2)$_2$Cl$_2$]	3512 3464	–	3411	3066 2981	1640	– 1611	1590 1527	1230 756	420 443	348	257
K$_2$[Ni(L^2)$_2$Cl$_2$]	3490 3456	–	3410	3053 2924	1642	– 1615	1585 1513	1239 710	420	351	256
[Cu(L^2)$_2$]	3490 3460	–	3410	3006 2931	1637	– 1617	1585 1510	1233 760	424	355	–
[Zn(L^2)$_2$]	3460 3444	–	3407	3032 2981	1645	– 1618	1581 1554	1234 756	412 459	346	–
[Cd(L^2)$_2$]	3511 3444	–	3411	3043 2916	1641	– 1614	1585 1522	1223 754	463	344	–

152

(3.8.3) FT-IR spectra of HL^3 complexes

(3.8.3.1) FT-IR data of K$_2$[Mn(L^3)$_2$Cl$_2$]

The FT-IR data of K$_2$[Mn(L^3)$_2$Cl$_2$] with HL^3 is listed in Table (3-15). Bands detected at 1636 and 732 cm^{-1} related to v(C=N) and v(C-Se) groups, respectively [70,30]. These bands suffered a lower shift, as compared with that in HL^3. An analogue reasoning to that included in section (3.8.2.1) may be used to justify the reduced bond order of the C=N and C-Se moieties, upon complexation [65-67]. Furthermore, a peak at 1226 cm^{-1} correlated to C-Se group. This band is shifted to lower frequency, as compared with that appeared at 1284 cm^{-1} in HL^3 indicating the C-Se group adopts a selenide fashion upon coordination to the Mn(II) centre [30]. More, the spectrum indicated no band may attribute to N3-H of the H-N-C=Se moiety. The spectrum shows a band at 1610 cm^{-1} assigned to N=C-Se group. This band may confirm the deprotonation of the N3-H of the H-N-C=Se upon complexation.

Bands detected at 3440; 3512 and 3317 cm^{-1} related to v(N4-H) and v(N1-H) group, respectively [30]. The appearance of these bands, with similar values to that detected in HL^3, in the spectrum of the Mn(II) complex confirmed the non-involvement of nitrogen atoms in the coordination [3].

New bands appeared in the spectrum of the Mn(II) complex, which are not detected in the spectrum of the ligand, noticed at 420 and 459 cm^{-1} correlated to v(Mn-N) [68]. The spectrum of K$_2$[Mn(L^3)$_2$Cl$_2$], (Figure (3-74)), recorded peaks at 337 and 270 cm^{-1} attributed to v(M-Se) [69] and v(Mn-Cl) [27], respectively.
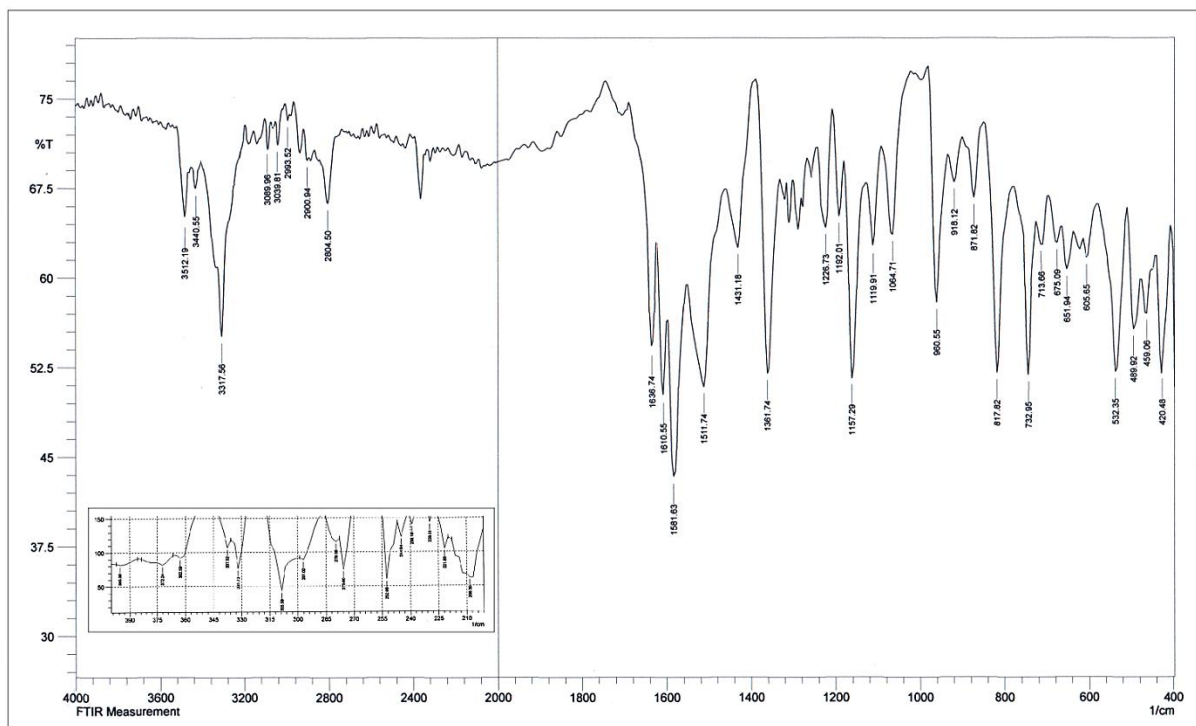
Figure (3-74): FT-IR chart of K$_2$[Mn(L^3)$_2$Cl$_2$].

(3.8.3.2) FT-IR data of K$_2$[Co(L^3)$_2$Cl$_2$], K$_2$[Ni(L^3)$_2$Cl$_2$], [Cu(L^3)$_2$], [Zn(L^3)$_2$] and [Cd(L^3)$_2$] complexes

The FT-IR data of Co(II), Ni(II), Cu(II), Zn(II) and Cd(II) complexes, Figures (3-75) to (3-79), indicated band between 1637-1641 cm^{-1} assigned to ν(C=N) group [70]. This band suffered shifting to lower wave number in comparison with that in HL^3 at 1643 cm^{-1} [63,64]. The shift to lower wave number indicting the coordination between N atoms and metal ions [65-67]. The band recorded between 1610-1618 cm^{-1} attributed to N=C-Se group [30]. This band shifted to higher wave number in the spectra of complexes, compared with that in HL^3 at 1593 cm^{-1} indicated the Se bound to the metal ion in its

154

selenide form. Further, the chelation between Se and metal ions confirmed by reduction in the bond order of the C-Se due to the deprotonation of the N3-H group [30]. The spectra display bands in the range 3358-3496 and 3312-3319 cm^{-1} that attribute to ν(N4-H) and ν(N1-H), respectively [3,30]. New bands that recorded between 405-438 and 432-463 cm^{-1} are due to ν(M-N) stretches [68], indicating the involvement of the nitrogen atoms in the coordination to metal centre. In addition, the spectra of complexes revealed bands between 345-364 cm^{-1} that related to ν(M-Se) [69]. At lower wave number, peaks detected in the spectra of Co(II) and Ni(II) complexes at 252 and 256 cm^{-1} assigned to ν(Co-Cl) and ν(Ni-Cl), respectively [27]. The prominent FT-IR peaks are displayed in Table (3-15).
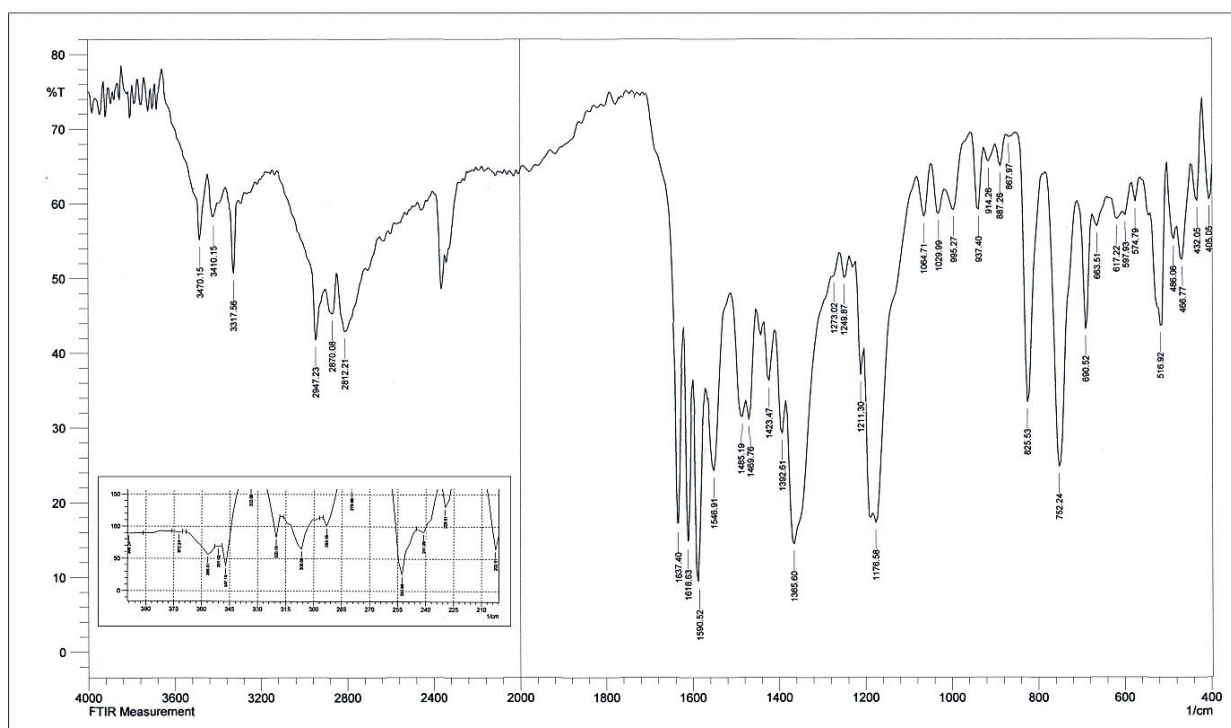
Figure (3-75): FT-IR chart of K$_2$[Co(L^3)$_2$Cl$_2$].
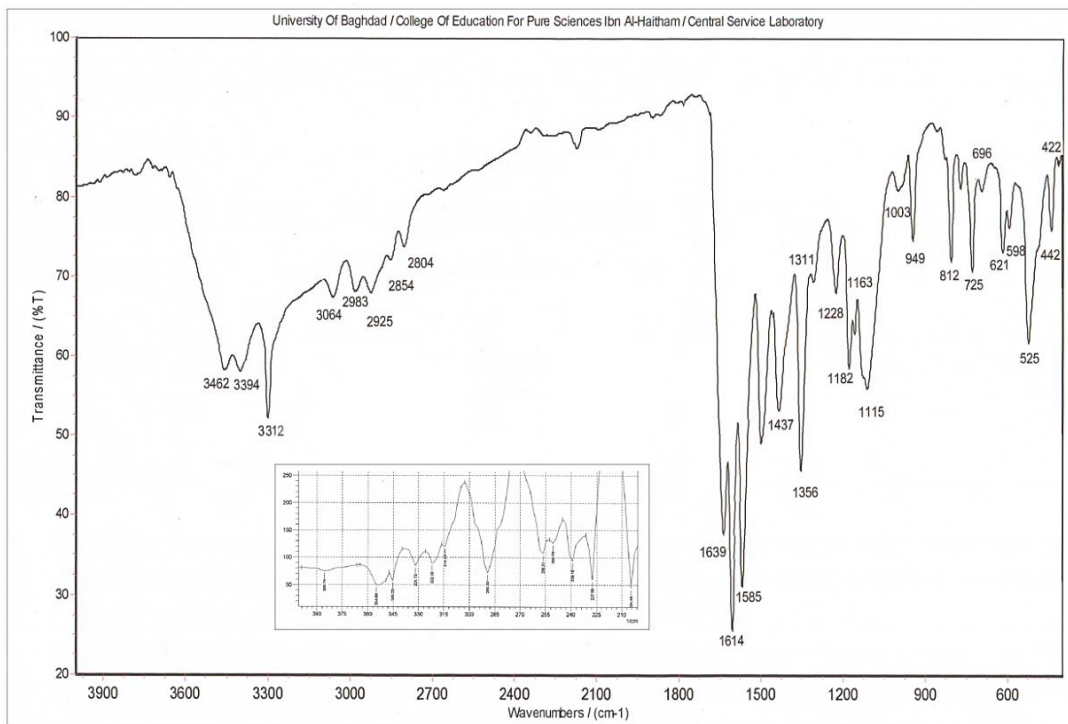
Figure (3-76): FT-IR chart of $K_2[Ni(L^3)_2Cl_2]$.
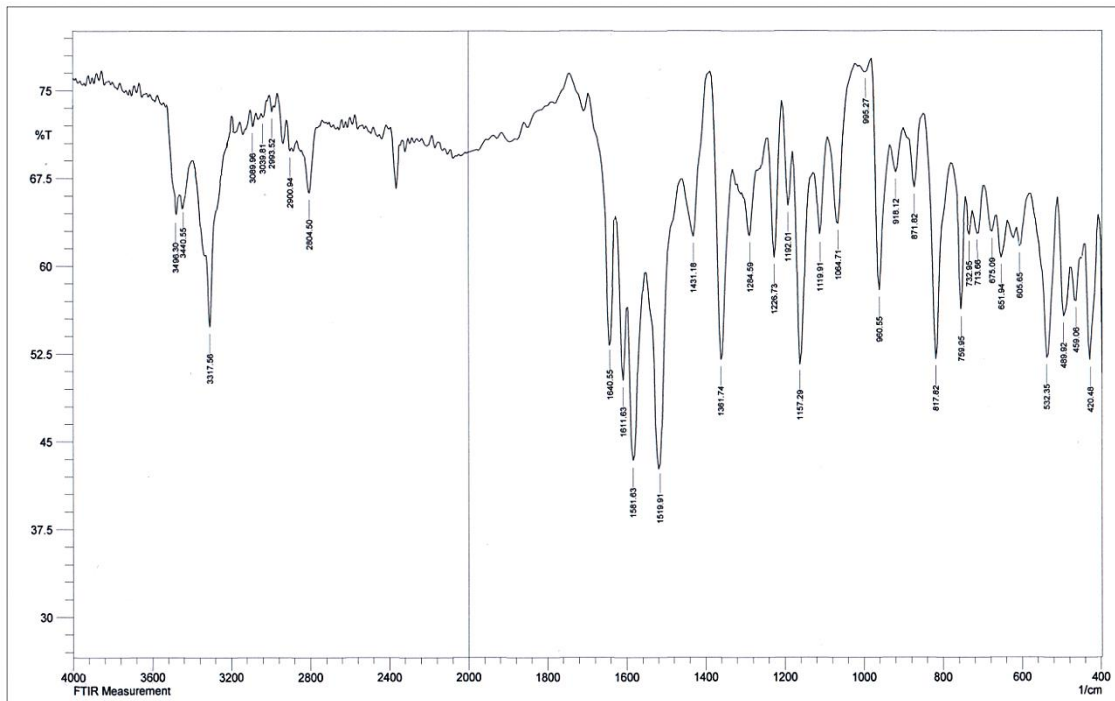
Figure (3-77): FT-IR chart of $[Cu(L^3)_2]$.
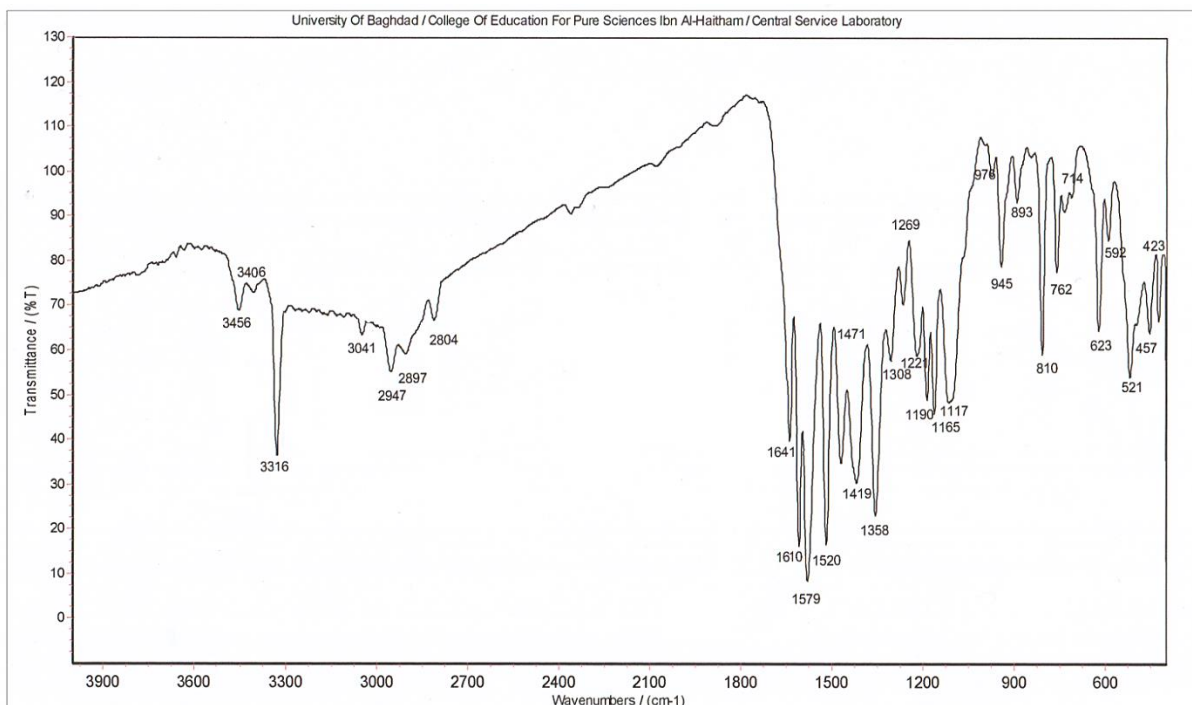
Figure (3-78): FT-IR chart of [Zn(L³)₂].
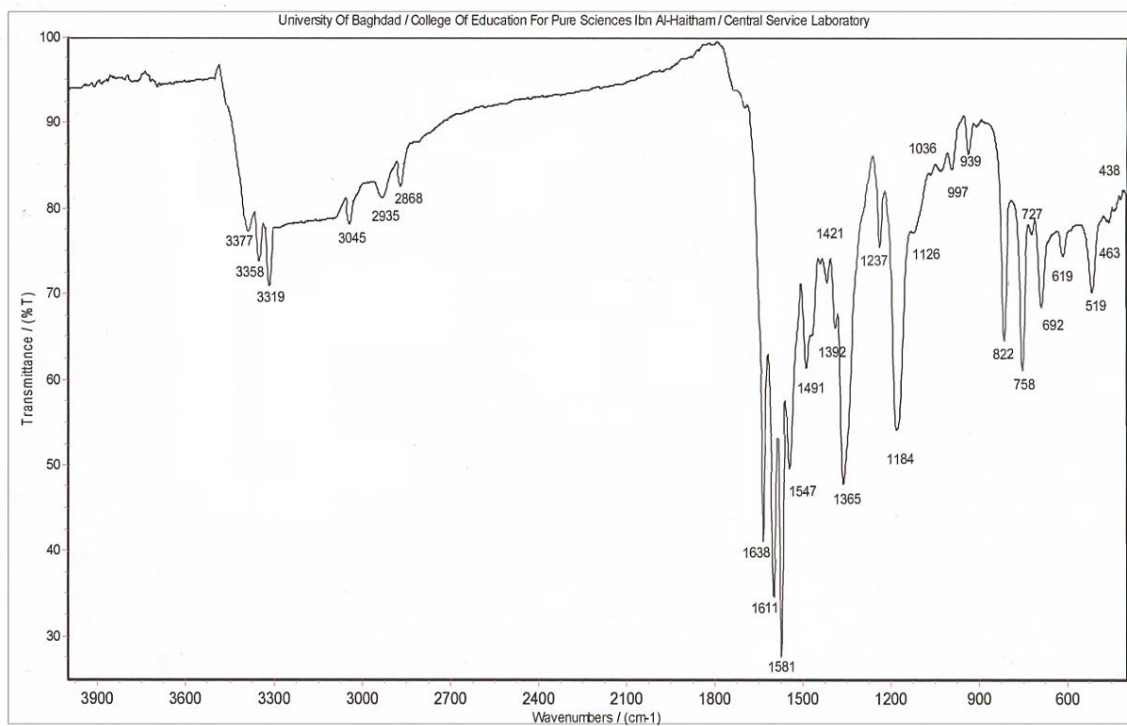
Figure (3-79): FT-IR chart of [Cd(L³)₂].

Table (3-15): Infrared data (cm^{-1}) of HL^3 and its complexes.

Compound	v(N4-H)	v(N3-H)	v(N1-H)	v(C-H)Aro. v(C-H)Ali.	v(C=N)	v(N-C=Se) v(N=C-Se)	v(C=C)	v(C-Se)	v(M-N)	v(M-Se)	v(M-Cl)
HL^3	3460 3441	3248	3317	3089 2804	1643	1593 –	1519	1284 771	–	–	–
K$_2$[Mn(L^3)$_2$Cl$_2$]	3512 3440	–	3317	3039 2804	1636	– 1610	1581 1511	1226 732	420 459	337	270
K$_2$[Co(L^3)$_2$Cl$_2$]	3470 3410	–	3317	2947 2870	1637	– 1618	1590 1546	1249 752	405 432	347	252
K$_2$[Ni(L^3)$_2$Cl$_2$]	3462 3394	–	3312	3064 2983	1639	– 1614	1585 1510	1228 725	422 442	345	256
[Cu(L^3)$_2$]	3496 3440	–	3317	3069 2900	1640	– 1611	1581 1519	1226 759	420 459	335	–
[Zn(L^3)$_2$]	3456 3406	–	3316	3041 2947	1641	– 1610	1579 1520	1269 762	423 457	351	–
[Cd(L^3)$_2$]	3377 3358	–	3319	3045 2935	1638	– 1611	1581 1547	1237 758	438 463	364	–

(3.8.4) FT-IR spectra of HL^4 complexes

(3.8.4.1) FT-IR data of K$_2$[Mn(L^4)$_2$Cl$_2$]

The FT-IR of HL^4 complexes are presented in Table (3-16). The FT-IR of K$_2$[Mn(L^4)$_2$Cl$_2$], Figure (3-80), shows bands related to ν(C=N) and ν(C-Se) stretches at 1646 and 736 cm^{-1}, respectively [70,30]. These bands were shifted to lower wave number, compared with that in HL^4. The shift of the imine group C=N may attribute the π-back bonding, from the metal ion to the ligand, that occurred in the system (dπ-pπ*) [63,64]. This is due to the involvement of the nitrogen atoms of imine moieties in the coordination to the metal ions [65-67]. The C-Se band was moved to a lower wave number and recorded at 1226 cm^{-1}, compared with that in HL^4 at 1261 cm^{-1}, indicating the presence of the C-Se group in its selenide form [30]. Further, the spectrum indicated a peak at 1614 cm^{-1} correlated to N=C-Se segment, as compared with that at 1604 cm^{-1} in HL^4. This may relate to the deprotonation of N3-H of the H-N-C=Se moiety and supporting the presence of the C-Se in its selenide fashion at 736 cm^{-1}.

The spectrum of the Mn(II) complex showed bands at 3379; 3464 and 3336 cm^{-1} related to ν(N4-H) and ν(N1-H), respectively [30]. The spectrum indicated the non-involvement of nitrogen atoms N4 and N1 in the coordination [3]. In addition, the spectrum of the Mn(II) complex showed new bands, which are not detected in the spectrum of the ligand, allocated at 416 and 466 cm^{-1} that related to ν(Mn−N) [68]. At lower frequency, the FT-IR of K$_2$[Mn(L^4)$_2$Cl$_2$], exhibited band at 366 cm^{-1} that attributed to the ν(M-Se) [69]. The band at 262 cm^{-1} attributed to ν(Mn-Cl) [27].
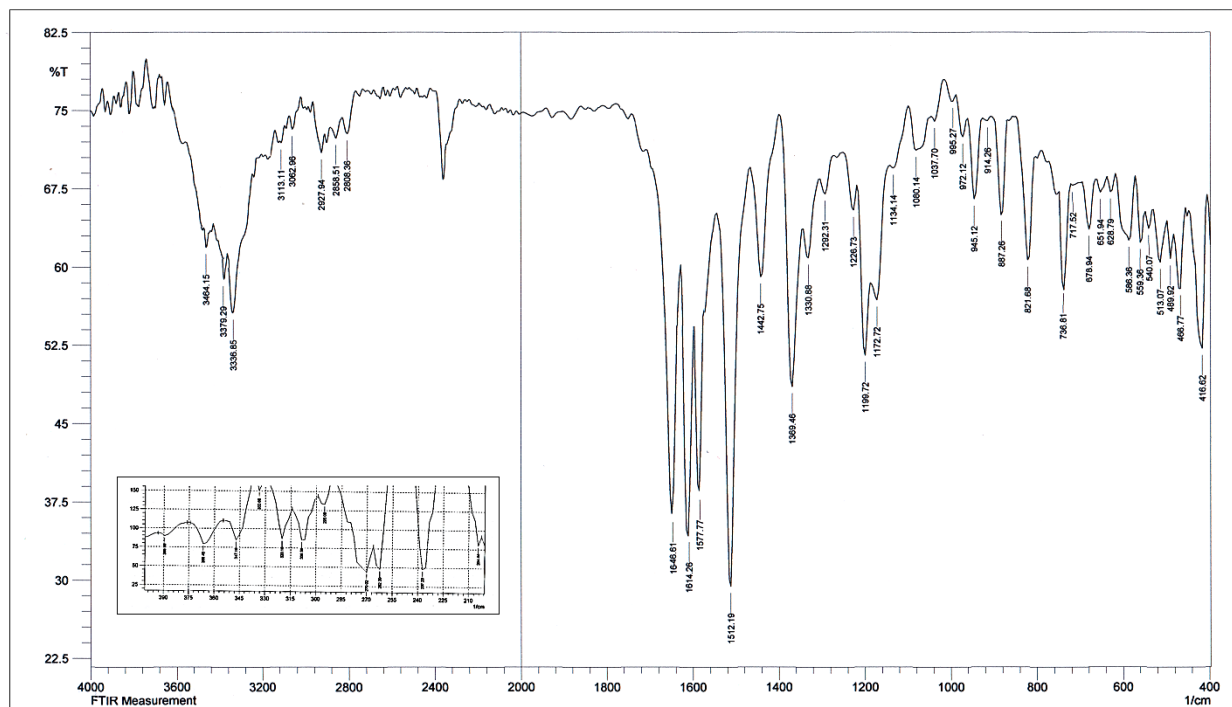
Figure (3-80): FT-IR chart of K$_2$[Mn(L^4)$_2$Cl$_2$].

(3.8.4.2) FT-IR data of K$_2$[Co(L^4)$_2$Cl$_2$], K$_2$[Ni(L^4)$_2$Cl$_2$], [Cu(L^4)$_2$], [Zn(L^4)$_2$] and [Cd(L^4)$_2$] complexes

The FT-IR of the above complexes is depicted in Figures (3-81) to (3-85). The spectra indicated band located between 1639-1646 cm^{-1} assigned to ν(C=N). This peak was shifted to lower wave number, compared with that in HL^4 [70]. The reduced bond order may be related to the π-back bonding (redistribution of metal electron density into the ligand π-system, HOMO→LUMO) [63,64]. Further, the change in the value of the C=N group may indicate the coordination between the nitrogen atom [65-67]. The spectra revealed band in the range 1610-1616 cm^{-1} related to N=C-Se segment. This band shifted to higher wave number, compared with HL^4 at 1604 cm^{-1}, indicated the deprotonation of the N3-H and the participation of the Se atom in the coordination to the metal centre [30].

Bands displayed in the range 3410-3512 and 3375-3383 cm^{-1} were assigned to ν(N4-H) and ν(N1-H) groups, respectively [3,30]. Band detected in the range 729-759 cm^{-1} attributed to ν(C-Se) group [30]. The appropriate shift of this band, compared with that in HL^4, related to complex formation. New bands that appeared between 412-420 and 447-474 cm^{-1} are due to ν(M-N) stretches [68], indicated the involvement of the nitrogen atoms in the coordination to metal centre. At lower frequency, bands recorded between 345-372 cm^{-1} assigned to ν(M-Se) [69]. In the spectra of the Co(II) and Ni(II) complex bands at 252 and 270 cm^{-1} related to ν(Co-Cl) and ν(Ni-Cl), respectively [27]. These assignments of the prominent functional groups are listed in Table (3-16).
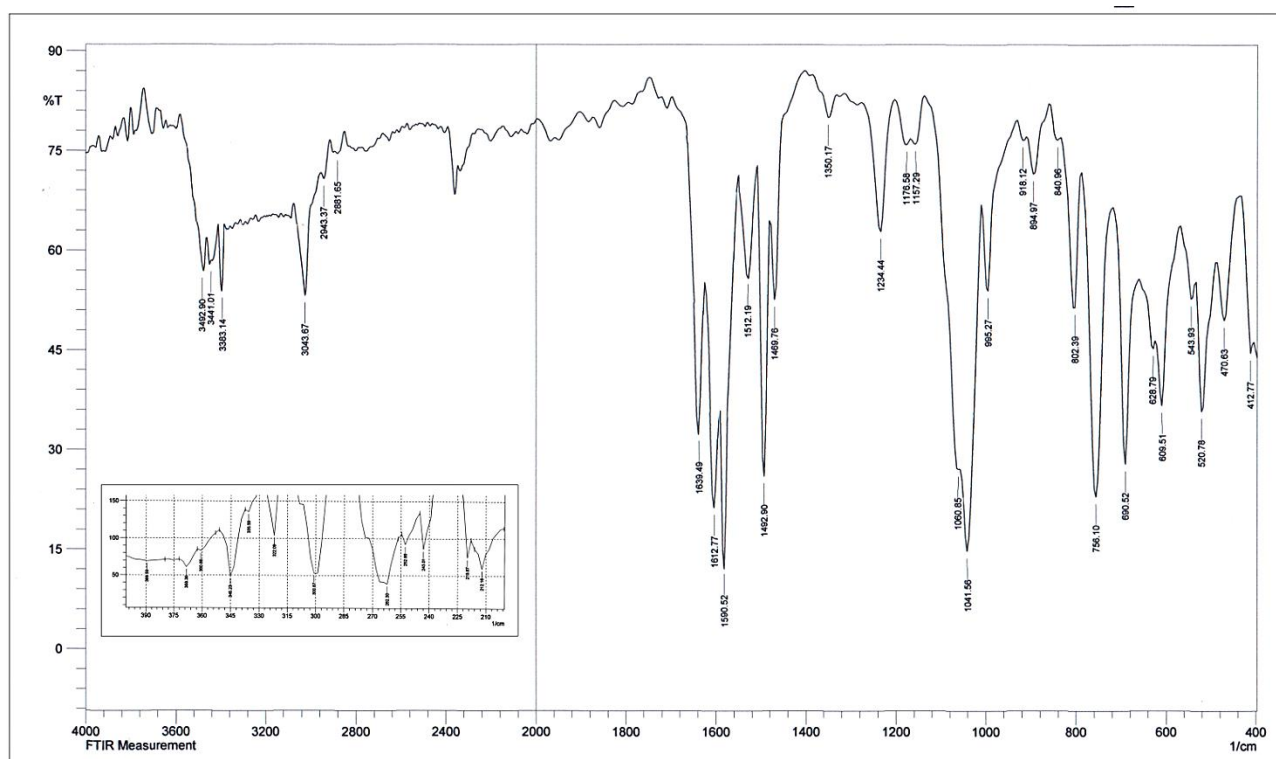
Figure (3-81): FT-IR chart of K$_2$[Co(L^4)$_2$Cl$_2$].
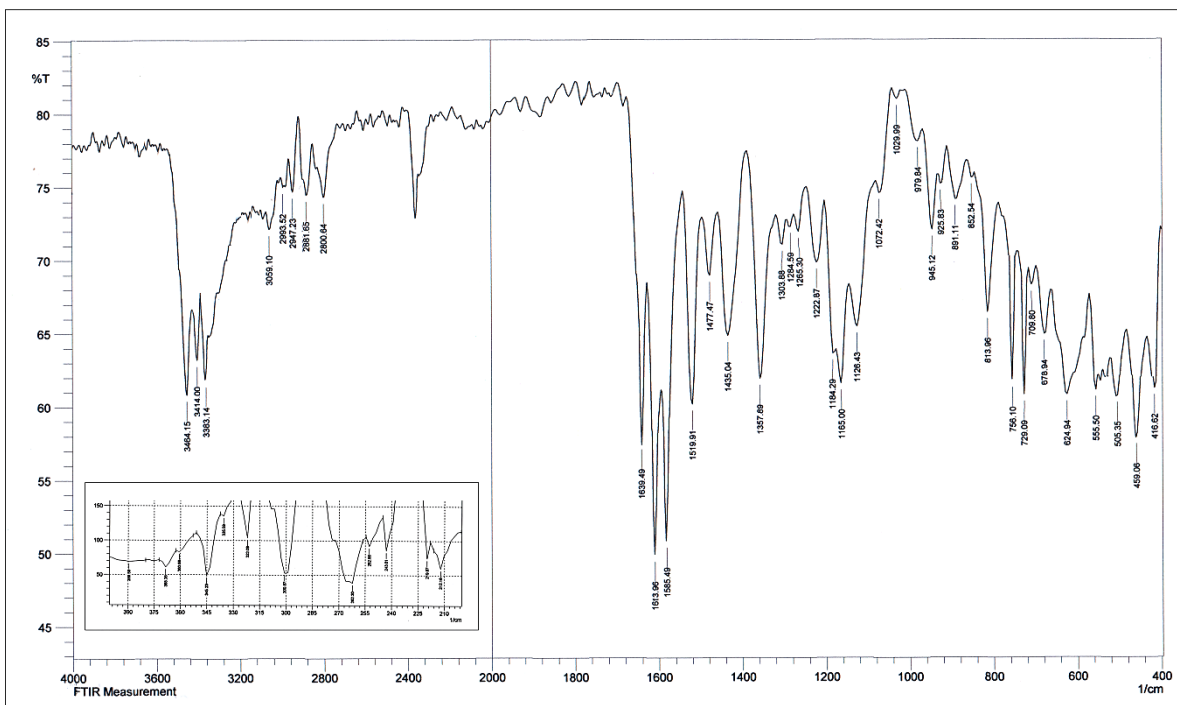
Figure (3-82): FT-IR chart of K$_2$[Ni(L^4)$_2$Cl$_2$].
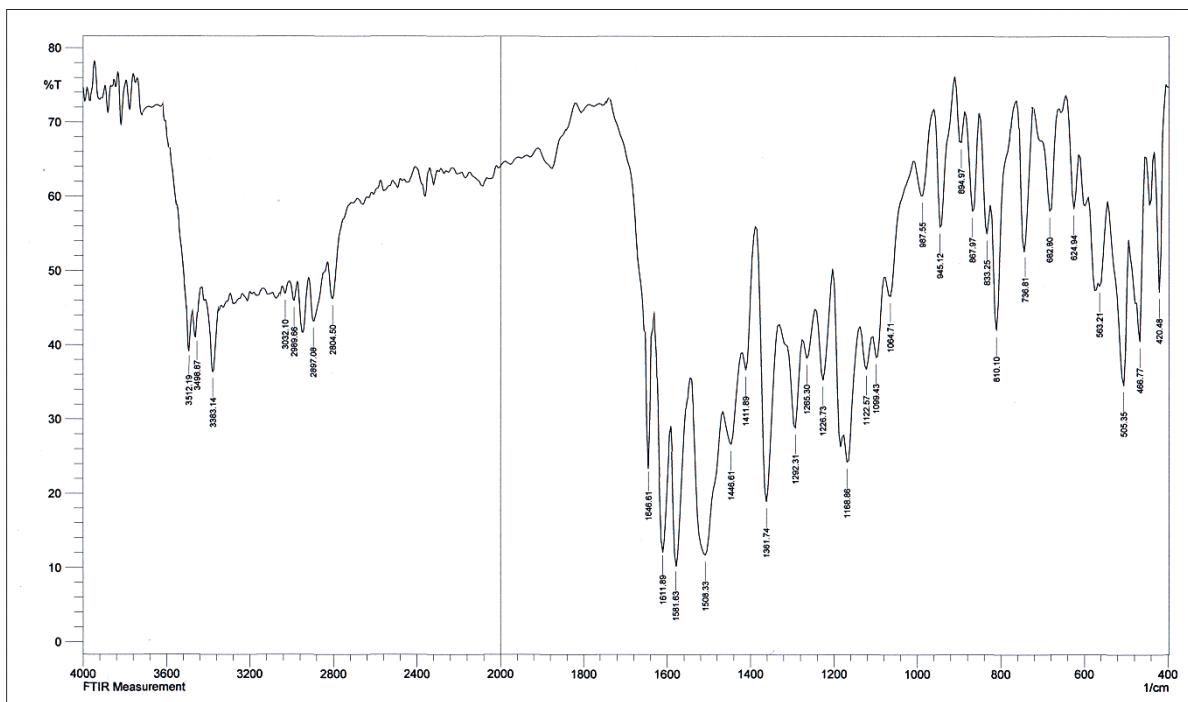
Figure (3-83): FT-IR chart of [Cu(L^4)$_2$].
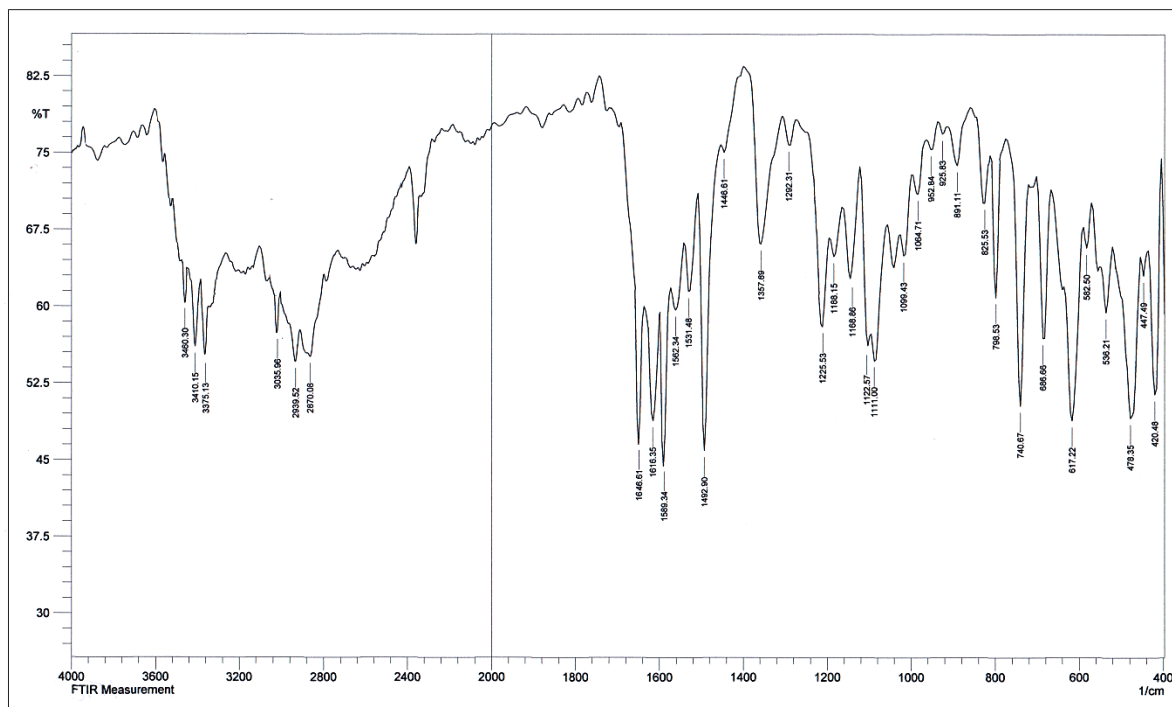
Figure (3-84): FT-IR chart of [Zn(L^4)$_2$].
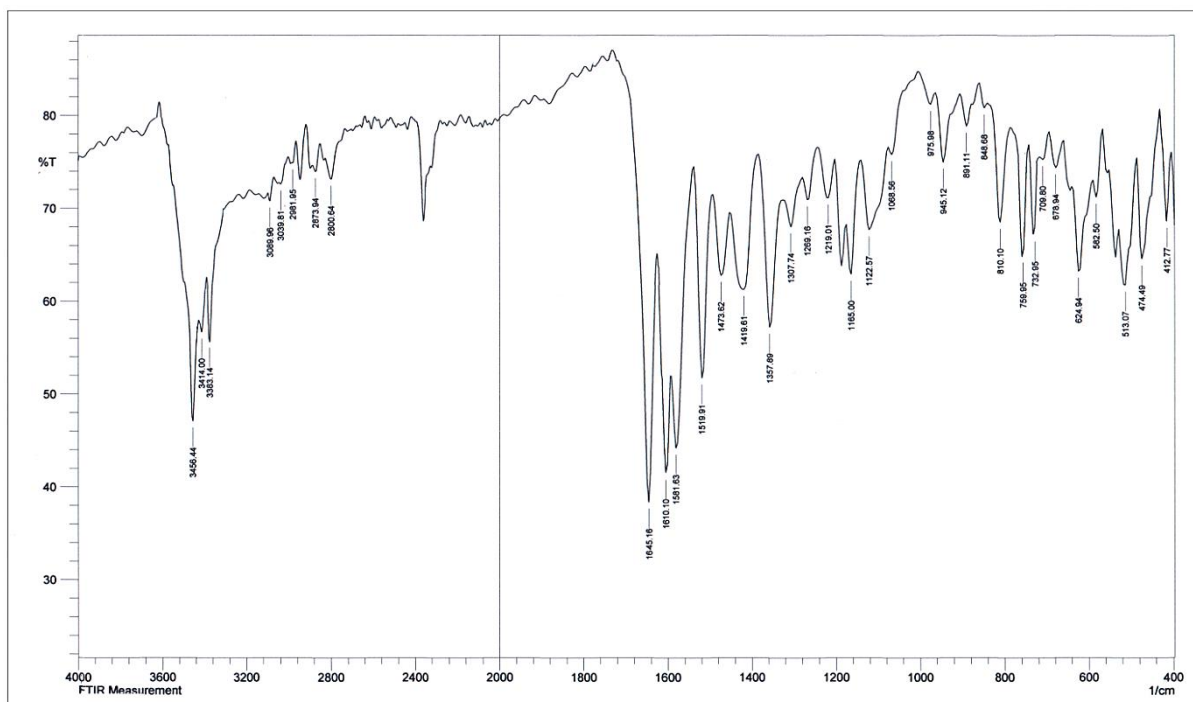
Figure (3-85): FT-IR chart of [Cd(L^4)$_2$]

Table (3-16): Infrared data (cm^{-1}) of HL^4 and its complexes.

Compound	ν(N4-H)	ν(N3-H)	ν(N1-H)	ν(C-H)Aro. ν(C-H)Ali.	ν(C=N)	ν(N-C=Se) ν(N=C-Se)	ν(C=C)	ν(C-Se)	ν(M-N)	ν(M-Se)	ν(M-Cl)
HL^4	3524 3460	3444	3383	3024 2943	1652	1604 –	1512	1261 775	–	–	–
K$_2$[Mn(L^4)$_2$Cl$_2$]	3464 3379	–	3336	3113 2927	1646	– 1614	1577 1512	1226 736	416 466	366	262
K$_2$[Co(L^4)$_2$Cl$_2$]	3492 3441	–	3383	3043 2943	1639	– 1612	1590 1512	1234 756	412 470	345	252
K$_2$[Ni(L^4)$_2$Cl$_2$]	3464 3414	–	3383	3059 2947	1639	– 1613	1585 1519	1222 729	416 459	366	270
[Cu(L^4)$_2$]	3512 3496	–	3383	3032 2989	1646	– 1611	1581 1508	1226 736	420 466	372	–
[Zn(L^4)$_2$]	3460 3410	–	3375	3035 2939	1646	– 1616	1589 1562	1225 740	420 447	355	–
[Cd(L^4)$_2$]	3456 3414	–	3383	3089 2981	1645	– 1610	1581 1519	1219 759	412 474	361	–

(3.8.5) FT-IR spectra of HL^5 complexes

(3.8.5.1) FT-IR data of $K_2[Mn(L^5)_2Cl_2]$

The FT-IR data of HL^5 and their complexes is offered in Table (3-17). The FT-IR of $K_2[Mn(L^5)_2Cl_2]$ is placed in Figure (3-86). The spectrum displays a similar fashion to that reported for the Mn(II) complex with HL^4. An analogue explanation may be implemented to discuss the lower shift of $\nu(C=N)$ and $\nu(C-Se)$ group [70], and the appearance of the N=C-Se at higher wave number, as compared with that in HL^5. The spectrum indicated the non-involvement of N4-H and N1-H group in the coordination to the Mn(II) centre [30]. Bands recorded at 420 and 443 cm^{-1} attributed to $\nu(Mn-N)$ [68]. At lower frequency region, the FT-IR of $K_2[Mn(L^5)_2Cl_2]$, exhibited band at 347 cm^{-1} that related to $\nu(M-Se)$ [69]. The band at 270 cm^{-1} attributed to $\nu(Mn-Cl)$ [27].
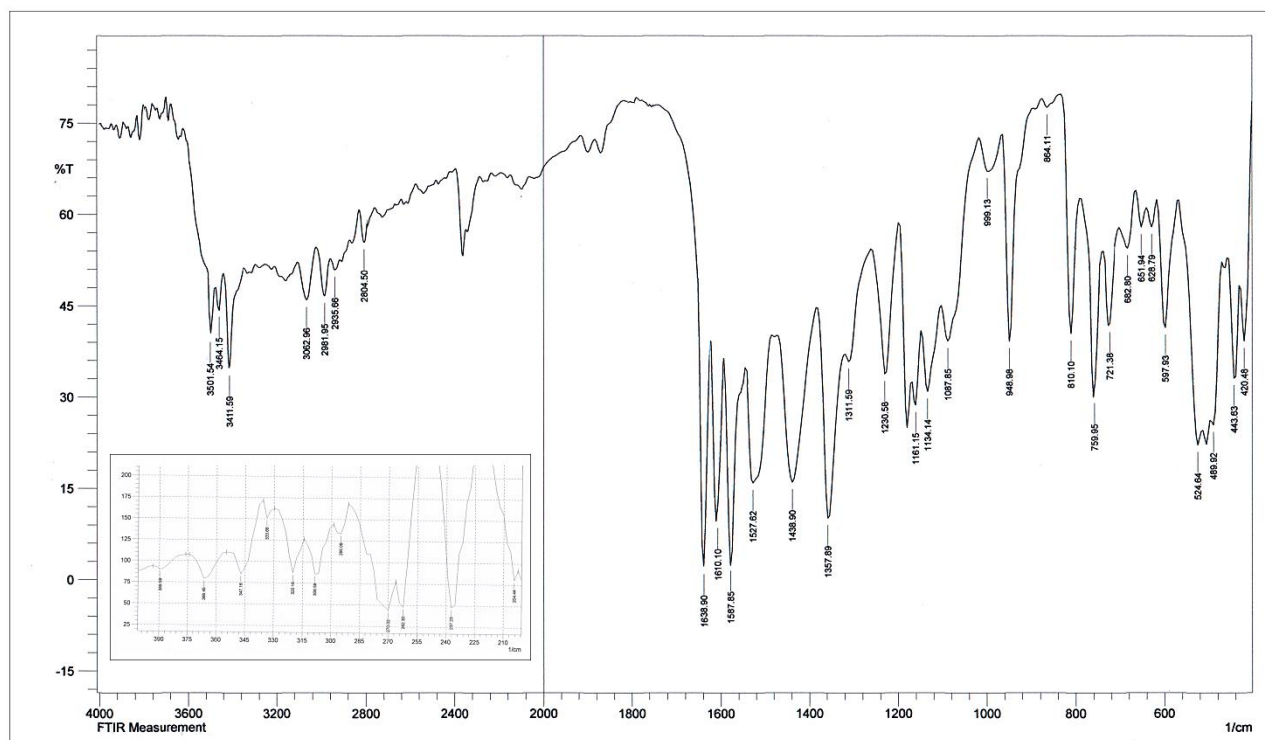
Figure (3-86): FT-IR chart of $K_2[Mn(L^5)_2Cl_2]$.

(3.8.5.2) FT-IR data of $K_2[Co(L^5)_2Cl_2]$, $K_2[Ni(L^5)_2Cl_2]$, $[Cu(L^5)_2]$, $[Zn(L^5)_2]$ and $[Cd(L^5)_2]$ complexes

The FT-IR of the above compounds is depicted in Figures (3-87) to (3-91). The FT-IR of the title complexes exhibited a similar fashion to that of the $K_2[Mn(L^5)_2Cl_2]$ complex and an analogous reasoning may implement to interpret the obtained data. The assignment of the prominent vibrational bands is listed in Table (3-17).
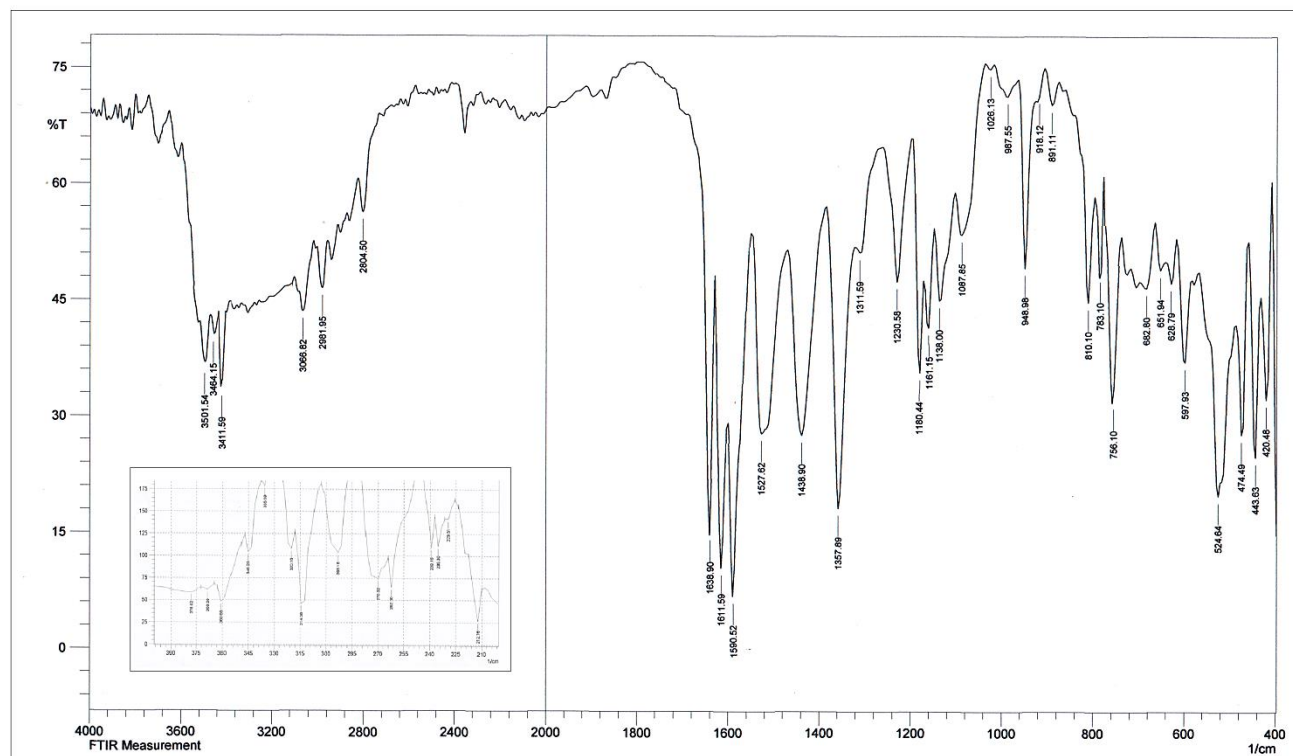
Figure (3-87): FT-IR chart of $K_2[Co(L^5)_2Cl_2]$.
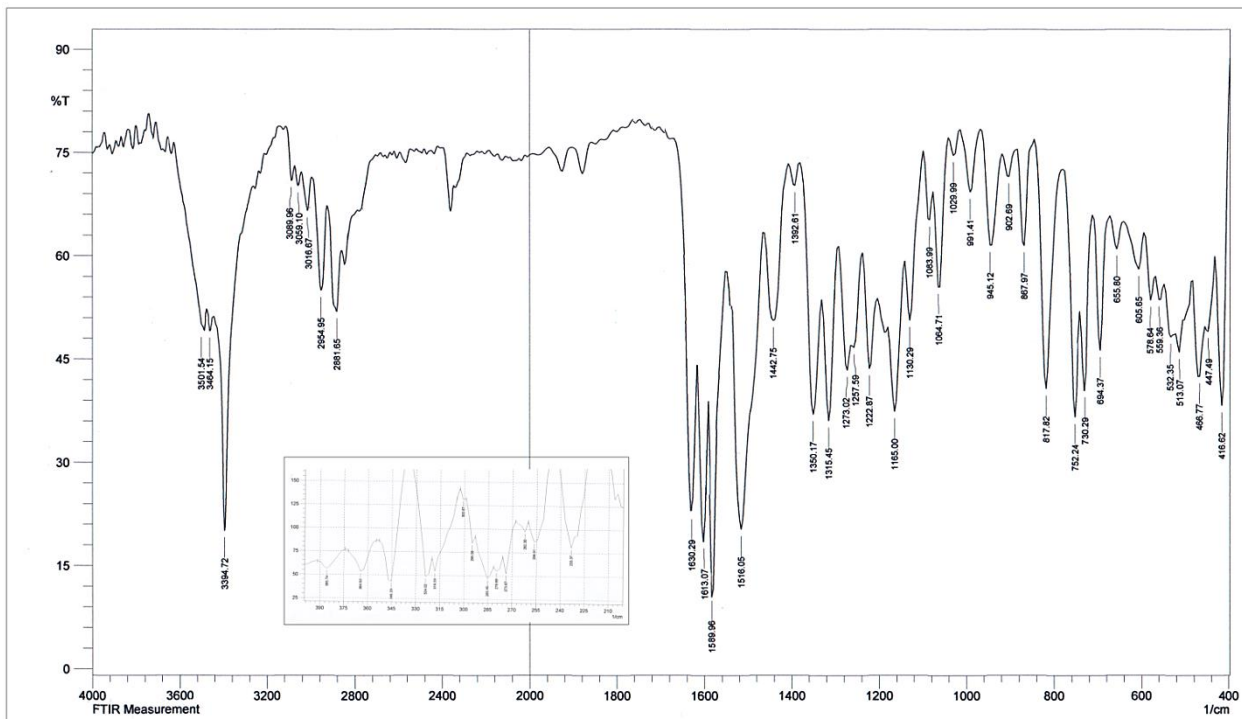
Figure (3-88): FT-IR chart of K$_2$[Ni(L^5)$_2$Cl$_2$].
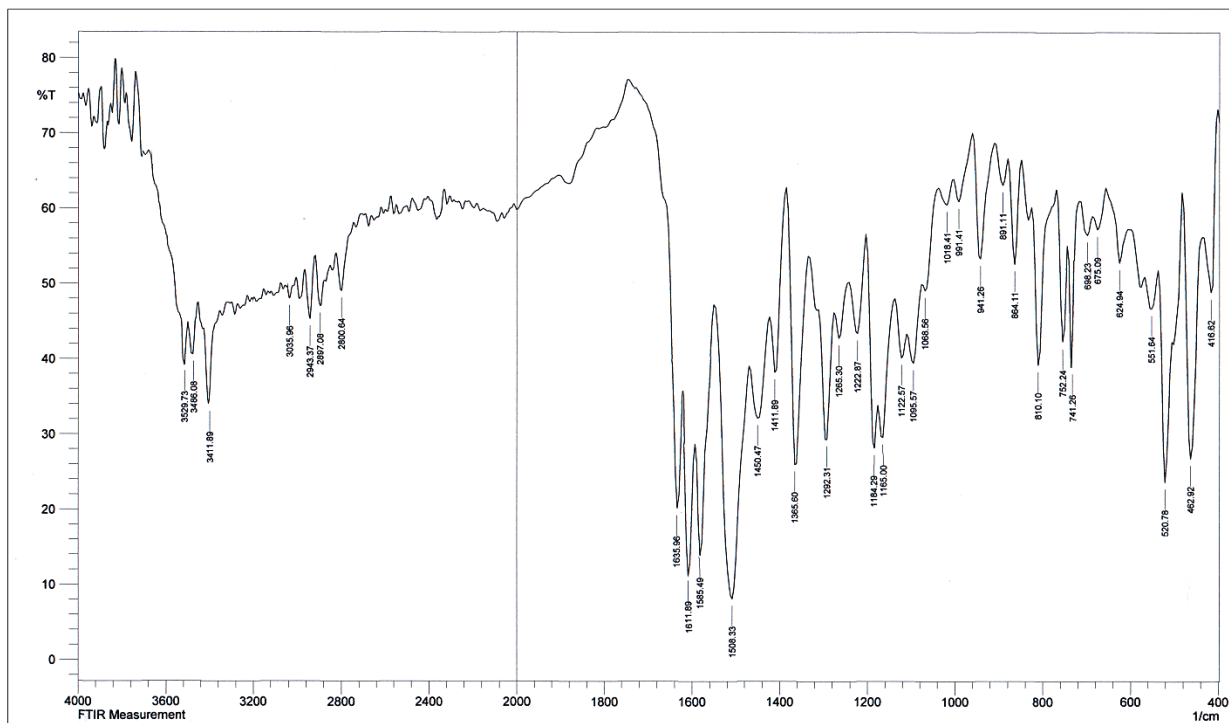
Figure (3-89): FT-IR chart of [Cu(L^5)$_2$].

167
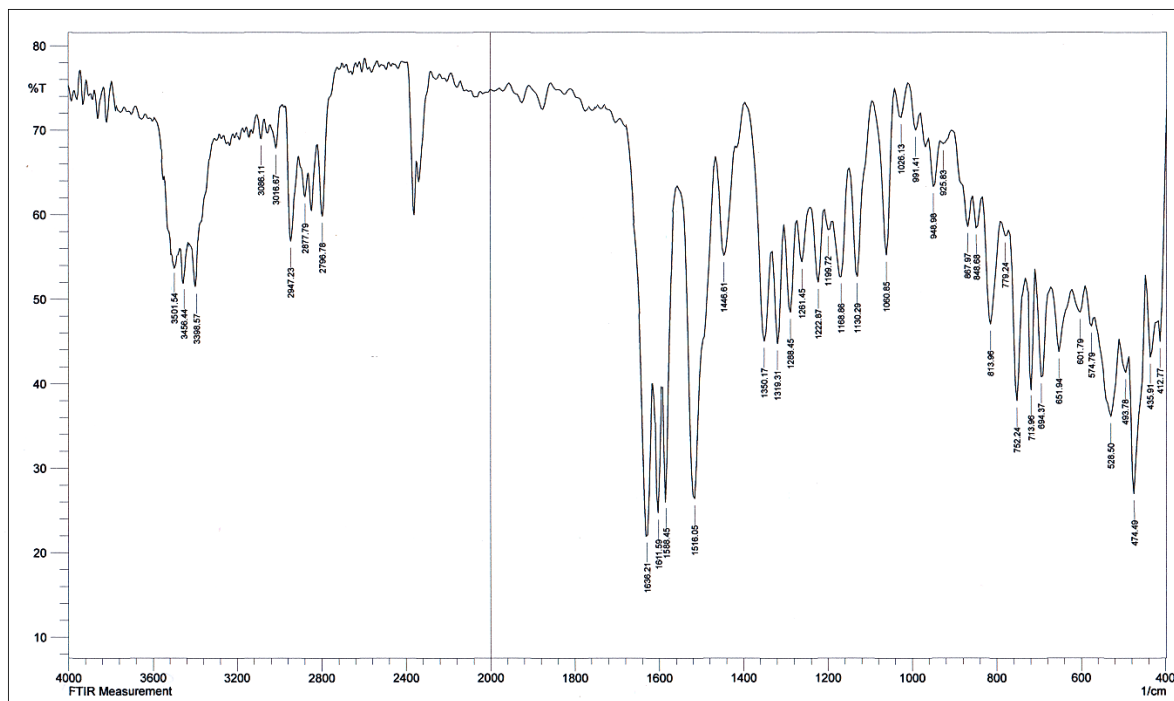
Figure (3-90): FT-IR chart of [Zn(L^5)$_2$].
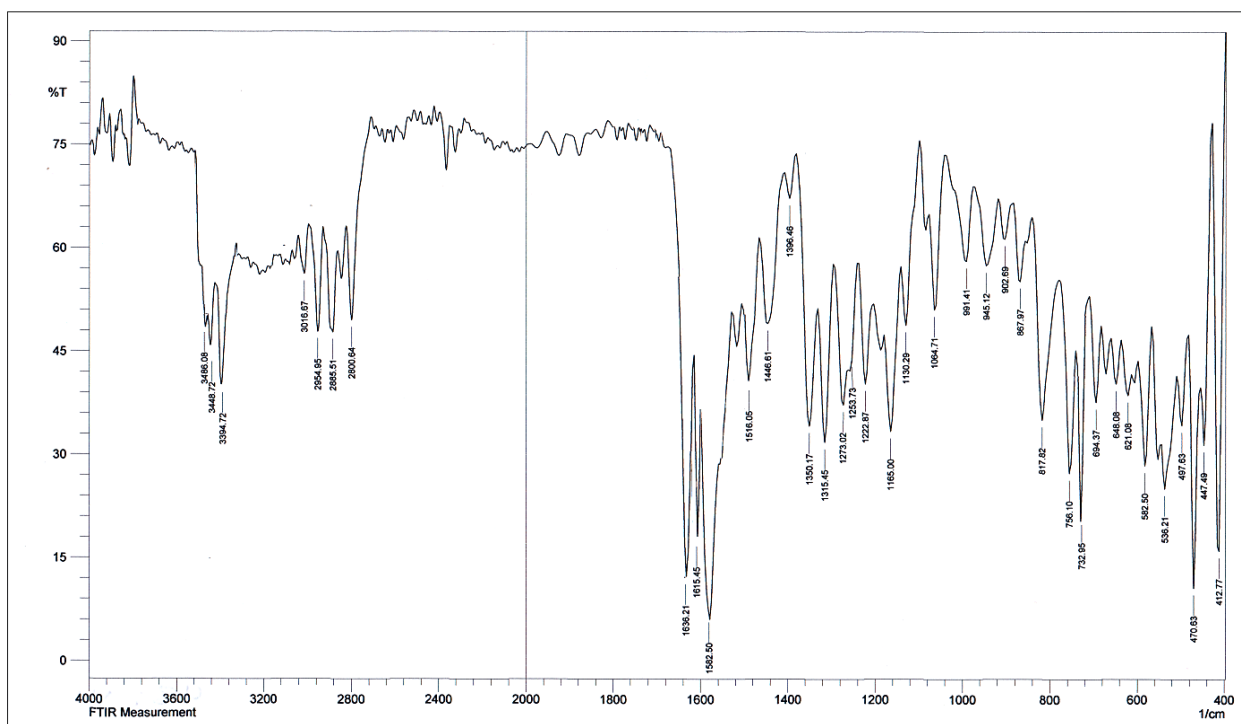
Figure (3-91): FT-IR chart of [Cd(L^5)$_2$].

168

Table (3-17): Infrared data (cm^{-1}) of HL^5 and its complexes.

Compound	v(N4-H)	v(N3-H)	v(N1-H)	v(C-H)Aro. v(C-H)Ali.	v(C=N)	v(N-C=Se) v(N=C-Se)	v(C=C)	v(C-Se)	v(M-N)	v(M-Se)	v(M-Cl)
HL^5	3529 3501	3486	3411	3101 2970	1641	1597 –	1573 1519	1257 771	–	–	–
K$_2$[Mn(L^5)$_2$Cl$_2$]	3501 3464	–	3411	3062 2981	1638	– 1610	1587 1527	1230 759	420 443	347	270
K$_2$[Co(L^5)$_2$Cl$_2$]	3501 3464	–	3411	3066 2981	1638	– 1611	1590 1527	1230 756	420 443	360	262
K$_2$[Ni(L^5)$_2$Cl$_2$]	3501 3464	–	3394	3016 2954	1630	– 1613	1589 1516	1222 752	416 447	345	285
[Cu(L^5)$_2$]	3529 3486	–	3411	3035 2943	1635	– 1611	1585 1508	1222 741	416 462	352	–
[Zn(L^5)$_2$]	3501 3456	–	3396	3086 2947	1636	– 1611	1588 1516	1222 752	412 435	346	–
[Cd(L^5)$_2$]	3486 3448	–	3394	3016 2954	1636	– 1615	1582 1516	1222 756	412 447	350	–

(3.8.6) FT-IR spectra of HL^6 complexes

(3.8.6.1) FT-IR data of K$_2$[Mn(L^6)$_2$Cl$_2$]

The essential infrared data of the K$_2$[Mn(L^6)$_2$Cl$_2$] is presented in Table (3-18). The FT-IR of K$_2$[Mn(L^6)$_2$Cl$_2$], Figure (3-92), shows characteristic bands at 1623, 752 assigned to v(C=N)imine [70], and v(C-Se) group [30], respectively. These bands suffered shifting to lower wave number, as compared with that in HL^6. An analogue explanation to that mentioned in section (3.8.4.1) was used to discuss the above shift. Bands seen at 1249 and 1611 cm^{-1}, were correlated to v(C-Se) and N=C-Se, respectively. These bands indicated the coordination of the C-Se group to the metal centre in its selenide form [30].

The spectrum Mn(II) complex confirmed the non-involvement of N4-H and N1-H group in the coordination to metal ion [3]. Bands detected at 405 and 432 cm^{-1} refer to v(Mn-N) [68]. At lower frequency region, the FT-IR of Mn-complex, exhibited band at 360 cm^{-1} that allocated to the v(M-Se) [69]. The band at 274 cm^{-1} attributed to v(Mn-Cl) [27].
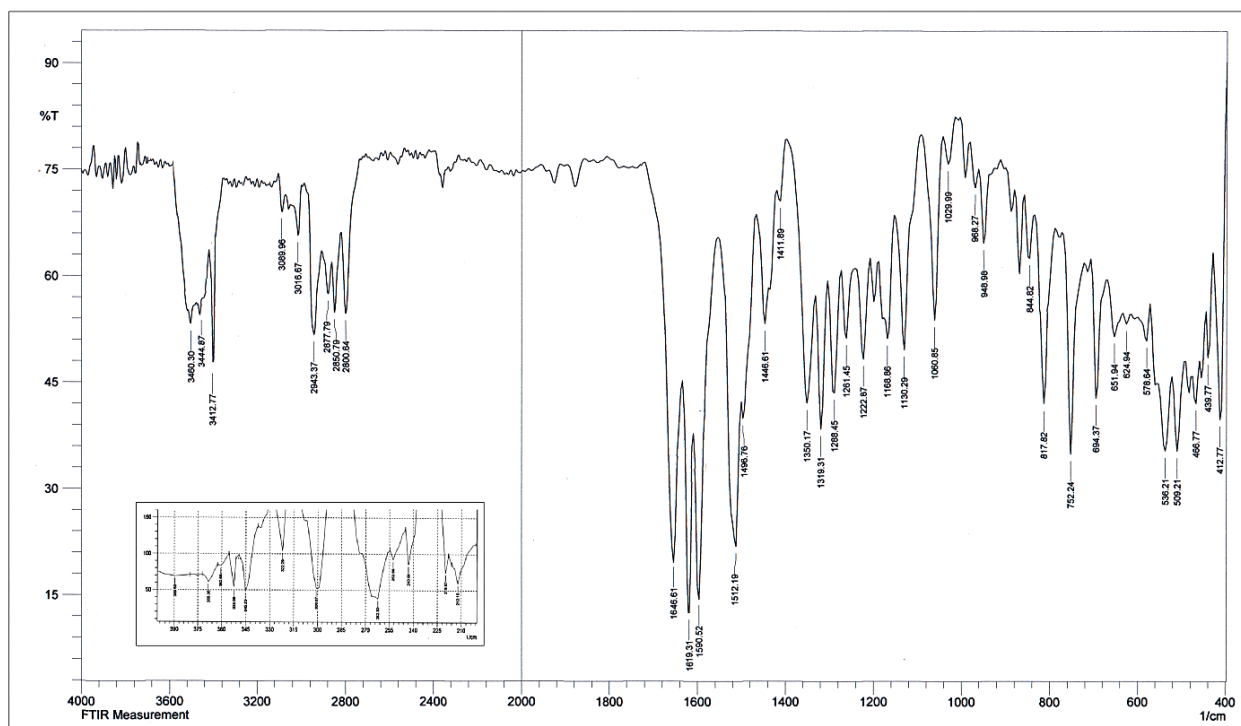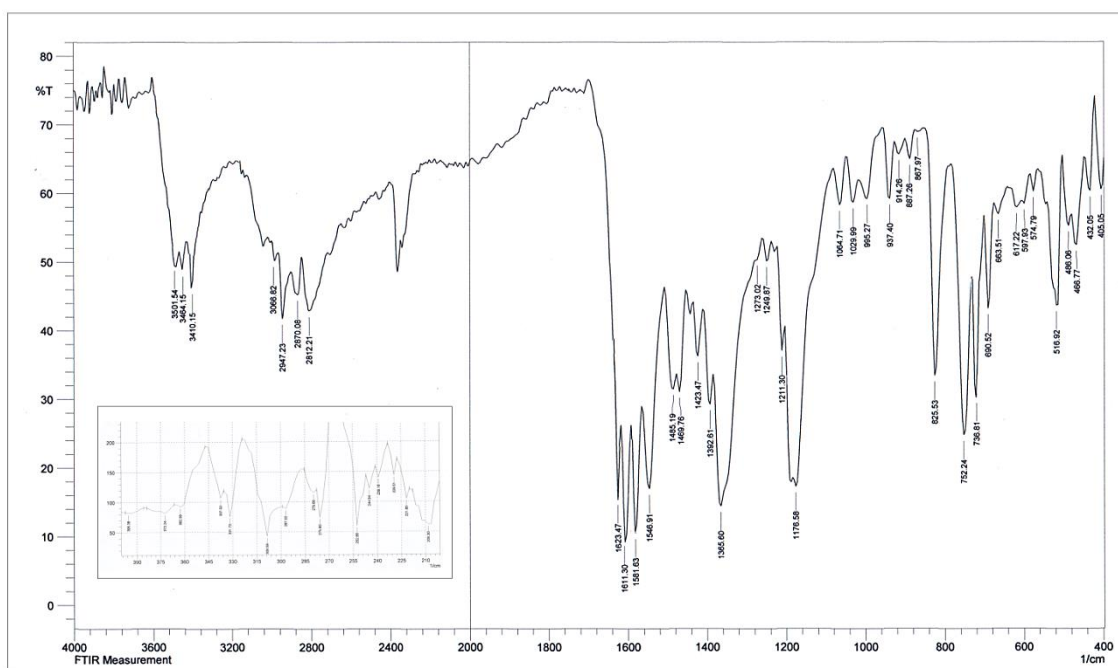

Figure (3-92): FT-IR chart of K$_2$[Mn(L^6)$_2$Cl$_2$].

(3.8.6.2) FT-IR data of $K_2[Co(L^6)_2Cl_2]$, $K_2[Ni(L^6)_2Cl_2]$, $[Cu(L^6)_2]$, $[Zn(L^6)_2]$ and $[Cd(L^6)_2]$ complexes

The FT-IR of the above complexes is shown in Figures (3-93) to (3-97). The FT-IR of the isolated complexes exhibited an analogue fashion to that of the $K_2[Mn(L^6)_2Cl_2]$ and a similar explanation may implement to discuss data. The assignment of the prominent vibrational bands is listed in Table (3-18).
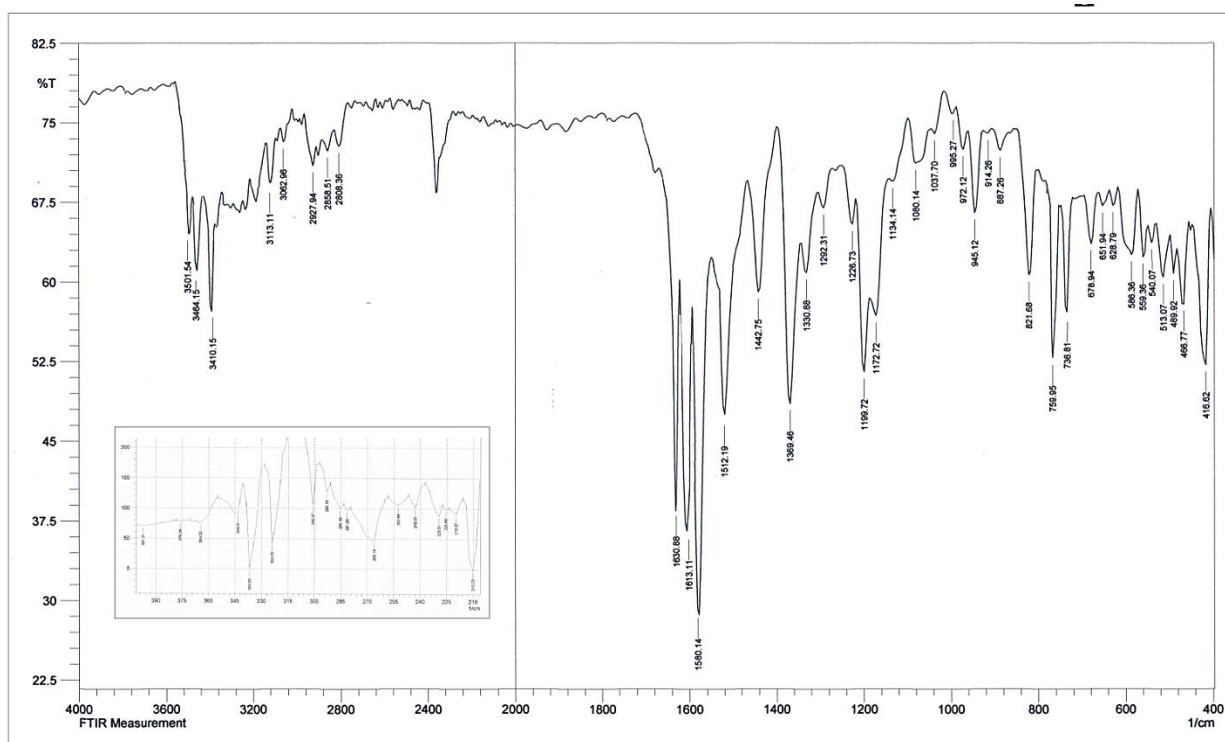
Figure (3-93): FT-IR chart of $K_2[Co(L^6)_2Cl_2]$.
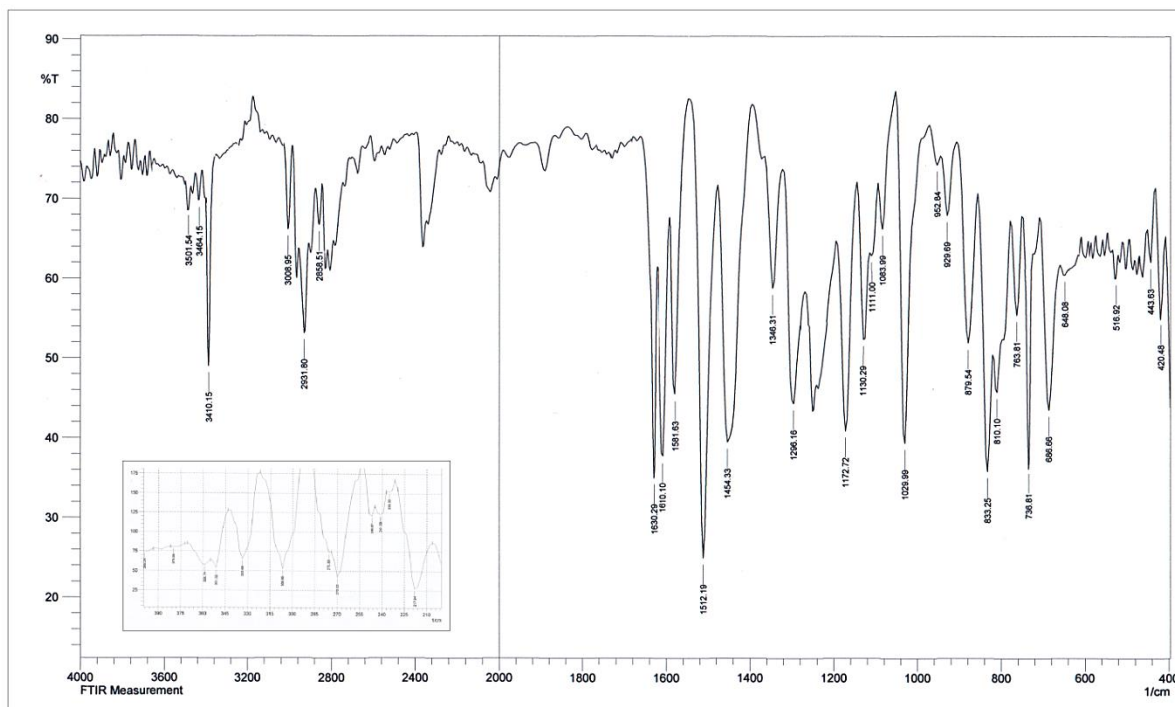
Figure (3-94): FT-IR chart of K$_2$[Ni(L^6)$_2$Cl$_2$].
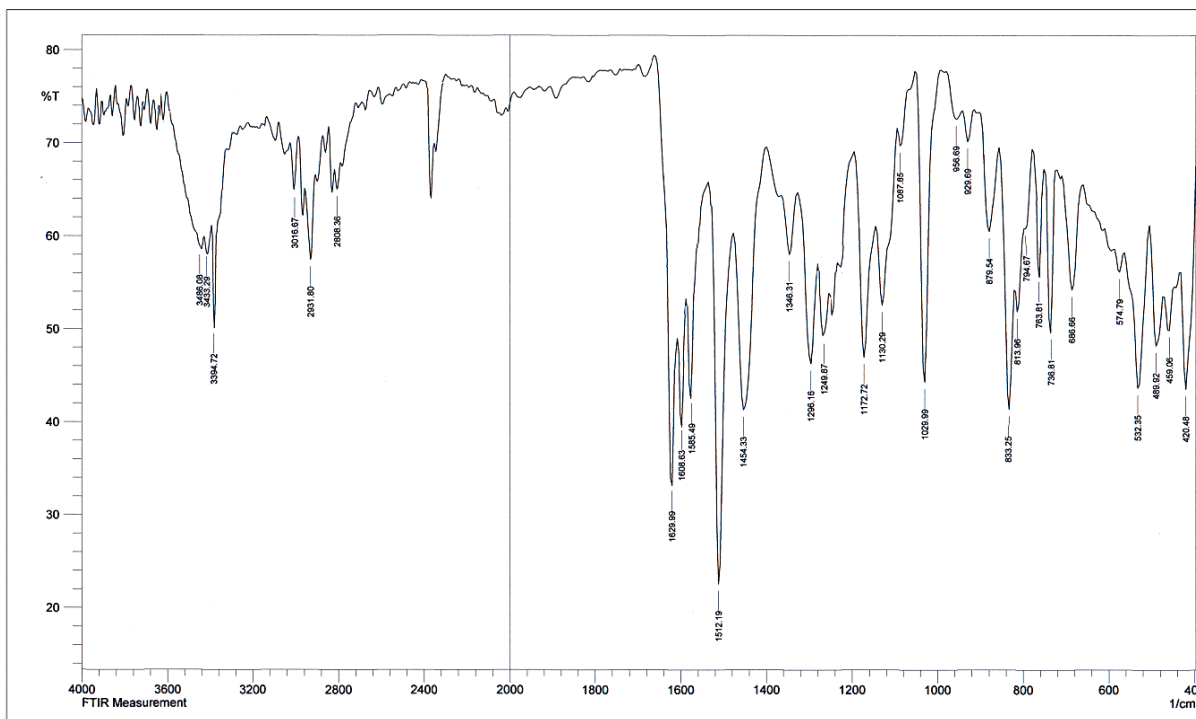
Figure (3-95): FT-IR chart of [Cu(L^6)$_2$].

172
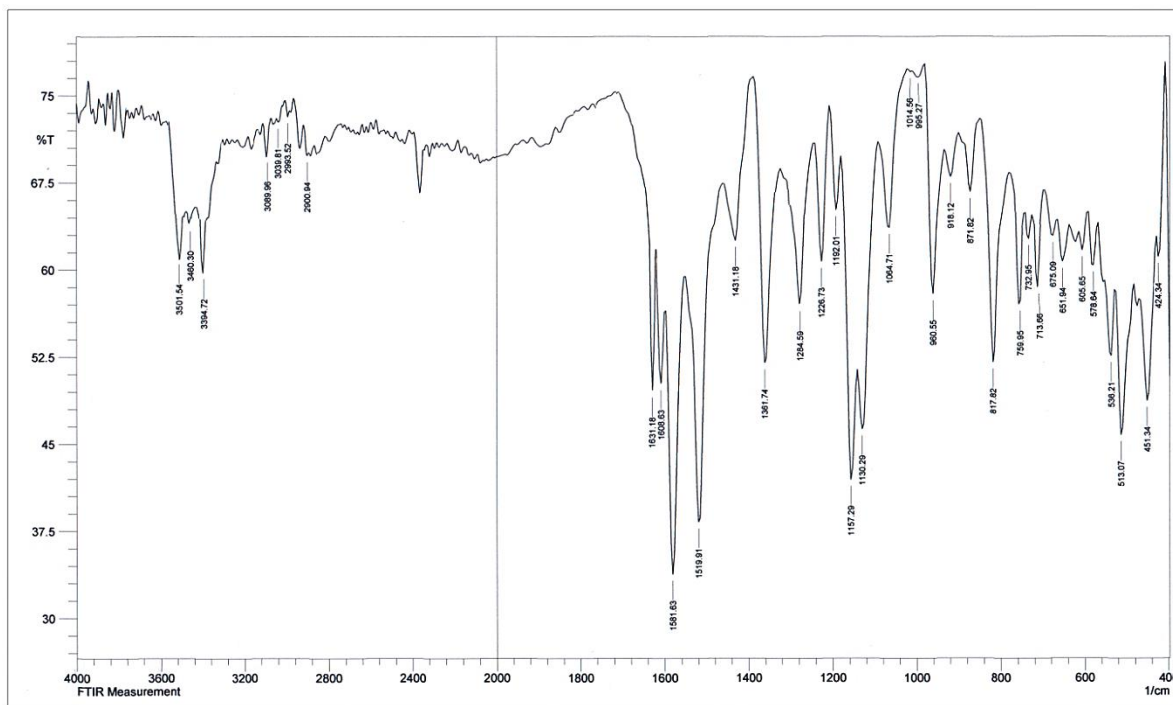
Figure (3-96): FT-IR chart of [Zn(L^6)$_2$].
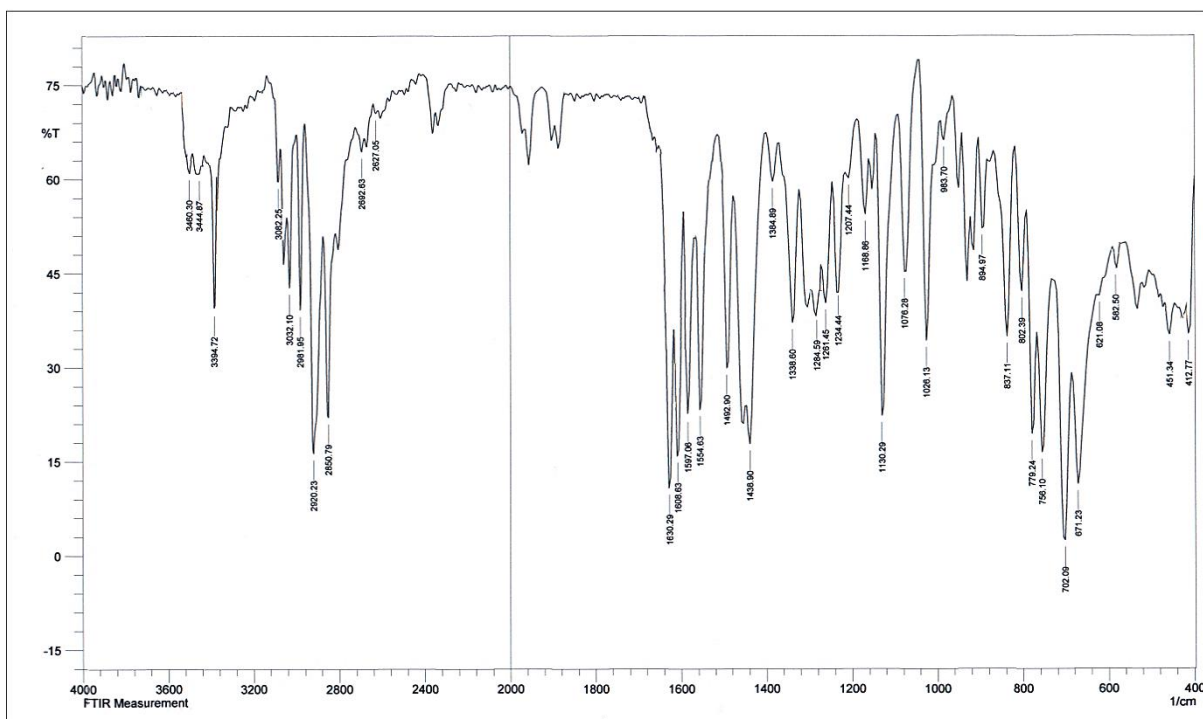
Figure (3-97): FT-IR chart of [Cd(L^6)$_2$]

173

Table (3-18): Infrared data (cm^{-1}) of HL^6 and its complexes.

Compound	v(N4-H)	v(N3-H)	v(N1-H)	v(C-H)Aro. v(C-H)Ali.	v(C=N)	v(N-C=Se) v(N=C-Se)	v(C=C)	v(C-Se)	v(M-N)	v(M-Se)	v(M-Cl)
HL^6	3558 3529	3440	3383	3101 2970	1637	1597 –	1573 1519	1257 763	–	–	–
K$_2$[Mn(L^6)$_2$Cl$_2$]	3501 3464	–	3410	3066 2947	1623	– 1611	1581 1548	1249 752	405 432	360	274
K$_2$[Co(L^6)$_2$Cl$_2$]	3501 3464	–	3410	3113 2927	1630	– 1613	1580 1512	1226 759	416 466	339	264
K$_2$[Ni(L^6)$_2$Cl$_2$]	3501 3464	–	3410	3006 2931	1630	– 1610	1581 1512	1245 736	420 443	350	270
[Cu(L^6)$_2$]	3436 3433	–	3394	3016 2931	1629	– 1608	1585 1512	1249 736	420 459	344	–
[Zn(L^6)$_2$]	3501 3460	–	3394	3089 2993	1631	– 1608	1581 1519	1226 759	424 451	375	–
[Cd(L^6)$_2$]	3460 3444	–	3394	3082 2920	1630	– 1608	1597 1554	1234 702	412 451	353	–

174

(3.9) Electronic spectra of complexes

(3.9.1) Electronic spectra of $K_2[Mn(L^1)_2Cl_2]$, $K_2[Co(L^1)_2Cl_2]$, $K_2[Ni(L^1)_2Cl_2]$, $[Cu(L^1)_2]$, $[Zn(L^1)_2]$ and $[Cd(L^1)_2]$ complexes

The electronic data of HL^1 complexes are included in Figures (3-98) to (3-103). The spectra displayed peaks linked to the ligand field transitions ($\pi \rightarrow \pi^*$ and $n \rightarrow \pi^*$) [60-62], Table (3-19). The Mn(II) complex revealed peak in the visible region (d-d transitions) at 845 nm (11834 cm^{-1}; ε_{max}= 30 dm^3 mol^{-1} cm^{-1}) correlated to $^6A_1g \rightarrow {}^4T_1g^{(G)}$ transition, confirming a distorted octahedral geometry about Mn(II) ion [71-73]. The Co(II) complex recorded peaks at 541 nm (18484 cm^{-1}; ε_{max}= 22 dm^3 mol^{-1} cm^{-1}) and 831 nm (12034 cm^{-1}; ε_{max}= 34 dm^3 mol^{-1} cm^{-1}) due to $^4T_1g^{(F)} \rightarrow {}^4A_2g^{(F)}$ and $^4T_1g^{(F)} \rightarrow {}^4T_1g^{(P)}$, respectively. This spectrum is characteristic for Co(II) complexes with distorted octahedral geometries about cobalt atom [74-76]. The Ni(II) complex recorded peaks at 751 nm (13316 cm^{-1}; ε_{max}= 50 dm^3 mol^{-1} cm^{-1}) and 865 nm (11561 cm^{-1}; ε_{max}= 82 dm^3 mol^{-1} cm^{-1}) correlated to $^3A_2g \rightarrow {}^3T_2g^{(F)}$ and $^3A_2g \rightarrow {}^3T_1g^{(F)}$ transitions, respectively indicating a distorted octahedral geometry about Ni atom [77]. The Cu(II) complex indicated a peak at 867 nm (11534 cm^{-1}; ε_{max}= 104 dm^3 mol^{-1} cm^{-1}) attributed to d-d transition type $^2B_1g \rightarrow {}^2B_2g$, confirming a distorted square planar arrangement about Cu atom [78]. The spectrum of $[Zn(L^1)_2]$, showed peak at 285 nm (35088 cm^{-1}; ε_{max}= 965 dm^3 mol^{-1} cm^{-1}) and 391 nm (25576 cm^{-1}; ε_{max}= 1789 dm^3 mol^{-1} cm^{-1}) correlated to intra-ligand field. More, the electronic spectrum of $[Cd(L^1)_2]$, picked peaks at 280 nm (35714 cm^{-1}; ε_{max}= 877 dm^3 mol^{-1} cm^{-1}) and 396 nm (25253 cm^{-1}; ε_{max}= 2341 dm^3 mol^{-1} cm^{-1}) due to the intra-ligand field. The spectra of the d^{10} system along with their analytical analyses data revealed the formation of four-coordinate compounds in which the geometry about metal centre is a distorted tetrahedral [79,80]. The electronic data with the proposed structure of the metal complexes are listed in Table (3-19).

Figure (3-98): UV-Vis of K$_2$[Mn(L^1)$_2$Cl$_2$] in DMSO solvent.

Figure (3-99): UV-Vis of K$_2$[Co(L^1)$_2$Cl$_2$] in DMSO solvent.

176

Figure (3-100): UV-Vis of $K_2[Ni(L^1)_2Cl_2]$ in DMSO solvent.
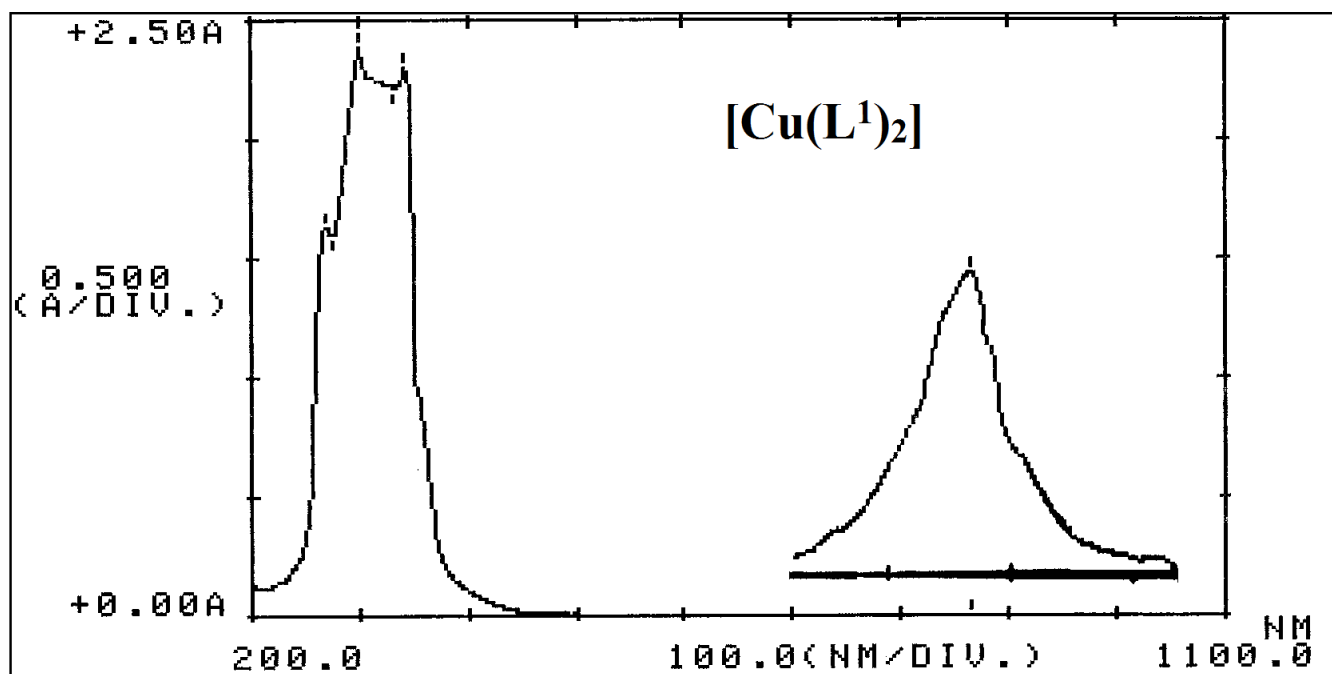
Figure (3-101): UV-Vis of $[Cu(L^1)_2]$ in DMSO solvent.

177
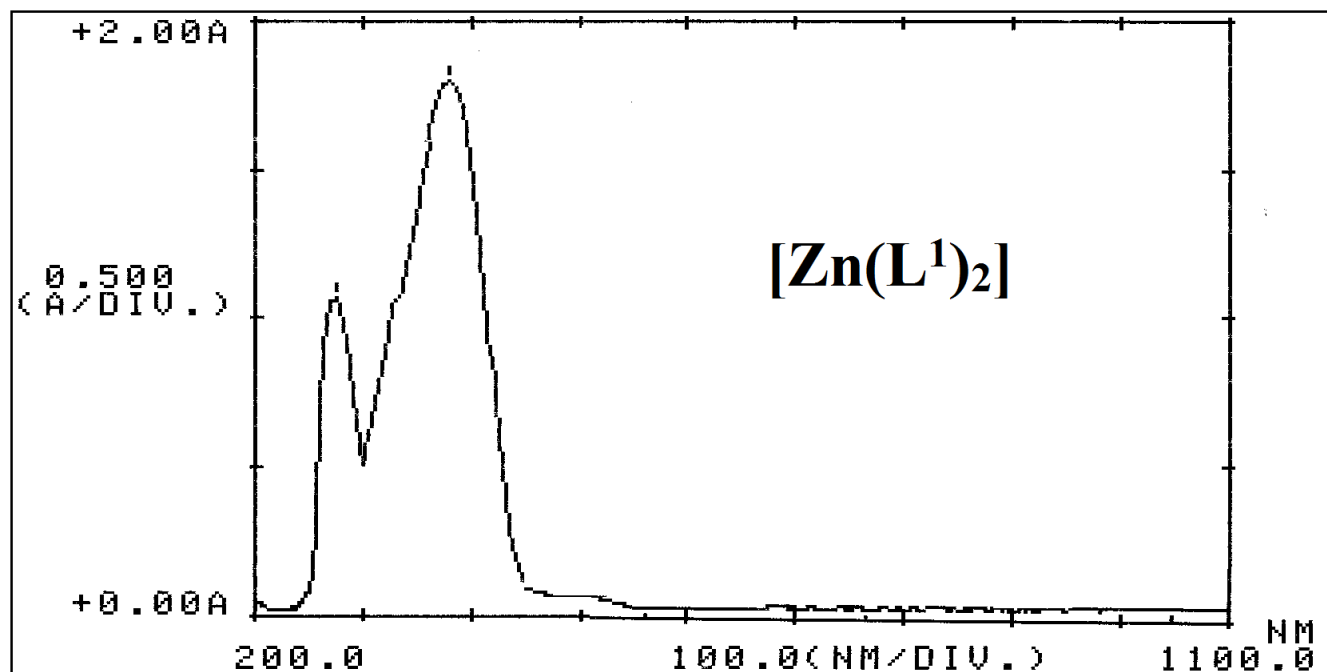
Figure (3-102): UV-Vis of [Zn(L^1)$_2$] in DMSO solvent.
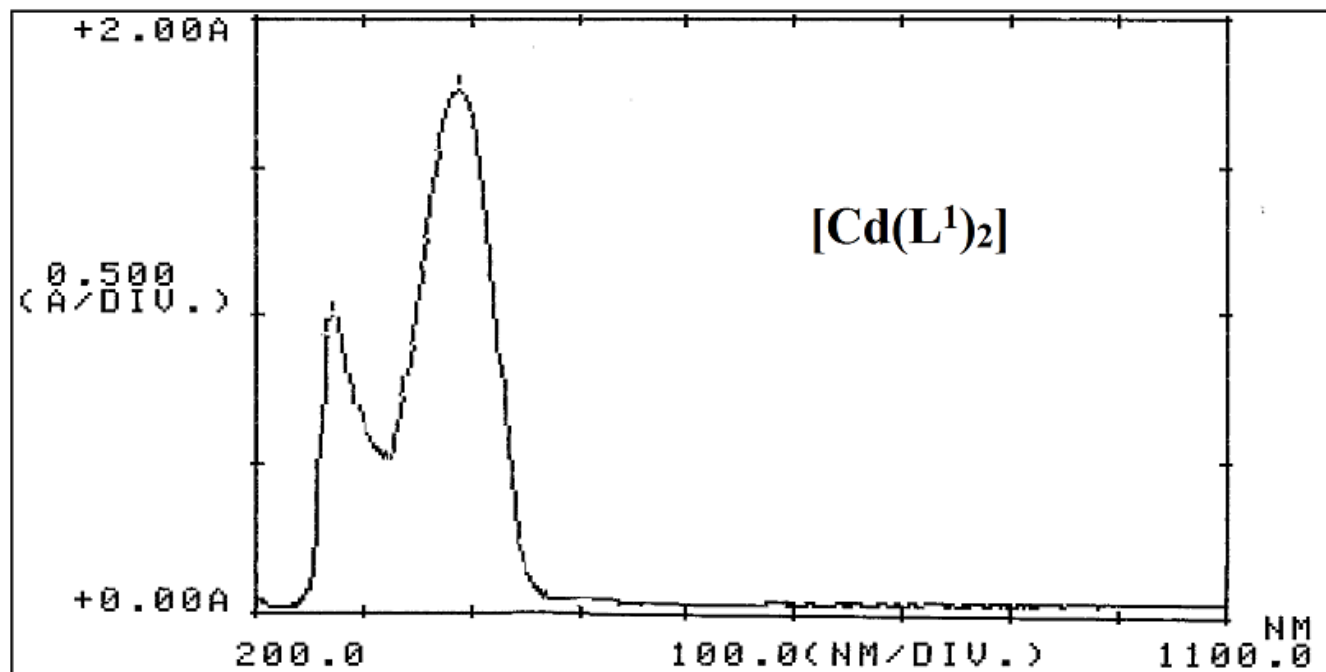
Figure (3-103): UV-Vis of [Cd(L^1)$_2$] in DMSO solvent.

Table (3-19): Electronic data of HL^1 complexes in DMSO solutions.

Compound	Peak position λnm	Wave number (cm^{-1})	Molar extinction coefficient ε_{max} (dm^3 mol^{-1} cm^{-1})	Assignment	Proposed structure
HL^1	263	38023	560	$\pi\rightarrow\pi^*$	
	315	31746	1234	$n\rightarrow\pi^*$	
K$_2$[Mn(L^1)$_2$Cl$_2$]	275	36364	670	$\pi\rightarrow\pi^*$	Distorted octahedral
	305	32787	1465	$n\rightarrow\pi^*$	
	467	21413	280	C.T.	
	845	11834	30	$^6A_1g^{(F)}\rightarrow{}^4T_1g^{(G)}$	
K$_2$[Co(L^1)$_2$Cl$_2$]	295	33898	870	$\pi\rightarrow\pi^*$	Distorted octahedral
	350	28571	1123	$n\rightarrow\pi^*$	
	370	27027	1650	C.T.	
	541	18484	22	$^4T_1g^{(F)}\rightarrow{}^4A_2g^{(F)}$	
	831	12034	34	$^4T_1g^{(F)}\rightarrow{}^4T_1g^{(P)}$	
K$_2$[Ni(L^1)$_2$Cl$_2$]	295	33898	987	$\pi\rightarrow\pi^*$	Distorted octahedral
	348	28736	1450	$n\rightarrow\pi^*$	
	751	13316	50	$^3A_2g\rightarrow{}^3T_2g^{(F)}$	
	845	11834	82	$^3A_2g\rightarrow{}^3T_1g^{(F)}$	
[Cu(L^1)$_2$]	280	35714	1040	$\pi\rightarrow\pi^*$	Distorted square planar
	301	33223	2130	$n\rightarrow\pi^*$	
	355	28169	1980	C.T.	
	867	11534	104	$^2B_1g\rightarrow{}^2B_2g$	
[Zn(L^1)$_2$]	285	35088	965	$\pi\rightarrow\pi^*$	Tetrahedral
	391	25576	1789	$n\rightarrow\pi^*$	
[Cd(L^1)$_2$]	280	35714	877	$\pi\rightarrow\pi^*$	Tetrahedral
	396	25253	2341	$n\rightarrow\pi^*$	

(3.9.2) Electronic spectra of K$_2$[Mn(L^2)$_2$Cl$_2$], K$_2$[Co(L^2)$_2$Cl$_2$], K$_2$[Ni(L^2)$_2$Cl$_2$], [Cu(L^2)$_2$], [Zn(L^2)$_2$] and [Cd(L^2)$_2$] complexes

The UV-Vis spectra for Mn(II), Co(II), Ni(II) and Cu(II)) complexes of HL^2 exhibited peaks that attributed to ligand field ($\pi\rightarrow\pi^*$ and $n\rightarrow\pi^*$) transitions. However, the spectra of complexes of Zn(II) and Cd(II) showed peaks attributed to $\pi\rightarrow\pi^*$, $n\rightarrow\pi^*$ and charge transfer (C.T.) [60-62], see Figures (3-104) to (3-109). The Mn(II) complex reveals bands at 551 nm (18149 cm^{-1}; ε_{max}= 18 dm^3 mol^{-1} cm^{-1}) and 733 nm (13643 cm^{-1}; ε_{max}= 22 dm^3 mol^{-1} cm^{-1}) correlated to $^6A_1g^{(F)}\rightarrow{}^4T_2g^{(G)}$ and $^6A_1g\rightarrow{}^4T_1g^{(G)}$ transitions, respectively,

indicating a distorted octahedral structure about Mn(II) ion [71-73]. The Co(II) complex shows more peaks in the d-d area at 492 nm (20325 cm^{-1}; ε_{max}= 120 dm^3 mol^{-1} cm^{-1}) and 734 nm (13624 cm^{-1}; ε_{max}= 60 dm^3 mol^{-1} cm^{-1}) due to $^4T_1g^{(F)} \rightarrow {}^4A_2g^{(F)}$ and $^4T_1g \rightarrow {}^4T_2g^{(F)}$ transitions, respectively. This spectrum is characteristic for Co(II) complexes that adopt distorted octahedral structures [74-76]. The spectrum of the Ni(II) complex showed additional bands at 451 nm (22173 cm^{-1}; ε_{max}= 176 dm^3 mol^{-1} cm^{-1}), 650 nm (15385 cm^{-1}; ε_{max}= 66 dm^3 mol^{-1} cm^{-1}) and 815 nm (12270 cm^{-1}; ε_{max}= 34 dm^3 mol^{-1} cm^{-1}) assigned to $^3A_2g \rightarrow {}^3T_1g^{(P)}$, $^3A_2g \rightarrow {}^3T_2g^{(F)}$ and $^3A_2g \rightarrow {}^3T_1g^{(F)}$ transitions, respectively, confirming a distorted octahedral sphere about nickel atom [77]. The UV-Vis the Cu(II) complex recorded bands at 762 nm (13123 cm^{-1}; ε_{max}= 35 dm^3 mol^{-1} cm^{-1}) and 871 nm (11481 cm^{-1}; ε_{max}= 57 dm^3 mol^{-1} cm^{-1}) attributed to $^2B_1g \rightarrow {}^2B_2g$ and $^2B_1g \rightarrow {}^2A_2g$ transitions, respectively. Accordingly, the proposed geometry about Cu atom is a distorted square planar [78]. The spectrum of [Zn(L^2)$_2$], recorded bands at 284 nm (35211 cm^{-1}; ε_{max}= 844 dm^3 mol^{-1} cm^{-1}), 340 nm (29412 cm^{-1}; ε_{max}= 932 dm^3 mol^{-1} cm^{-1}) and 375 nm (26667 cm^{-1}; ε_{max}= 1345 dm^3 mol^{-1} cm^{-1}) assigned to intra-ligand field and charge transfer (C.T) transitions, respectively. Tetrahedral is expected geometry of the Zn-complex [79]. The UV-Vis of [Cd(L^1)$_2$], showed bands at 280 nm (35714 cm^{-1}; ε_{max}= 766 dm^3 mol^{-1} cm^{-1}), 342 nm (29240 cm^{-1}; ε_{max}= 987 dm^3 mol^{-1} cm^{-1}) and 374 nm (26738 cm^{-1}; ε_{max}= 1322 dm^3 mol^{-1} cm^{-1}) due to the intra-ligand field and charge transfer, respectively, confirming tetrahedral geometry around Cd atom [80]. The electronic data with the proposed structures of compounds are summarises in Table (3-20).

Figure (3-104): UV-Vis of K₂[Mn(L²)₂Cl₂] in DMSO solvent.

Figure (3-105): UV-Vis of K₂[Co(L²)₂Cl₂] in DMSO solvent.

181

Figure (3-106): UV-Vis of $K_2[Ni(L^2)_2Cl_2]$ in DMSO solvent.
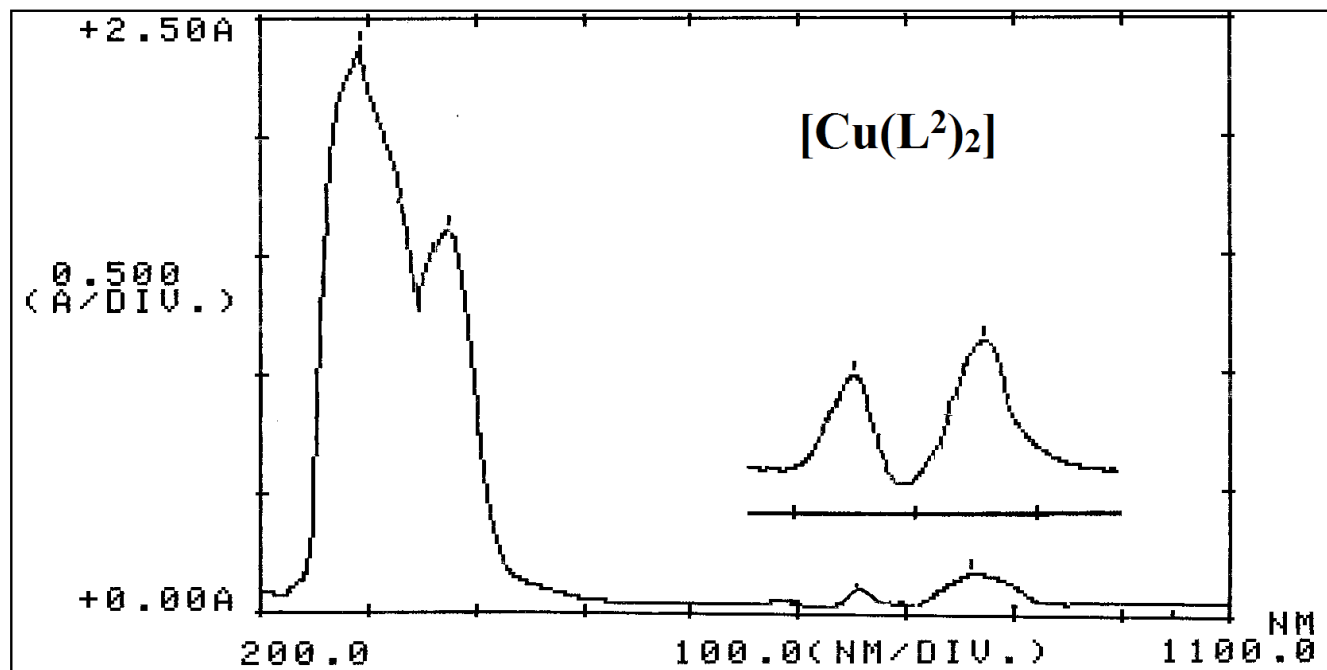
Figure (3-107): UV-Vis of $[Cu(L^2)_2]$ in DMSO solvent.

182
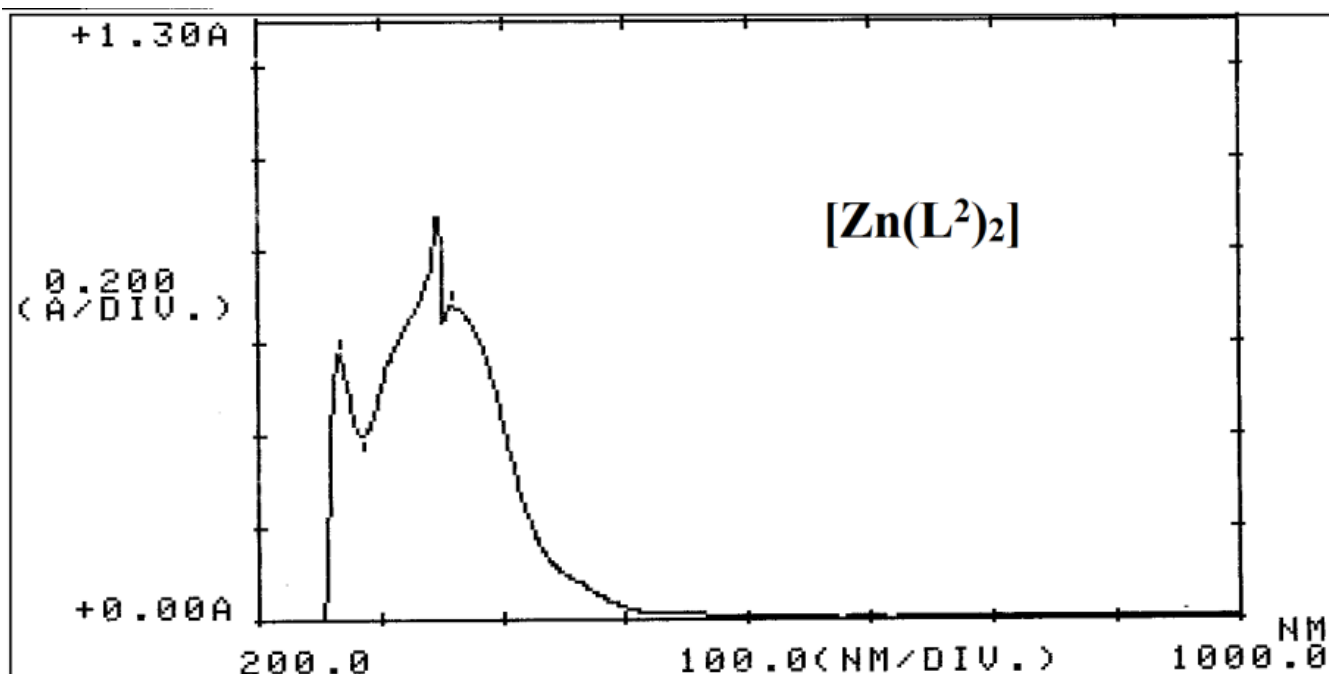
Figure (3-108): UV-Vis of [Zn(L^2)$_2$] in DMSO solvent.
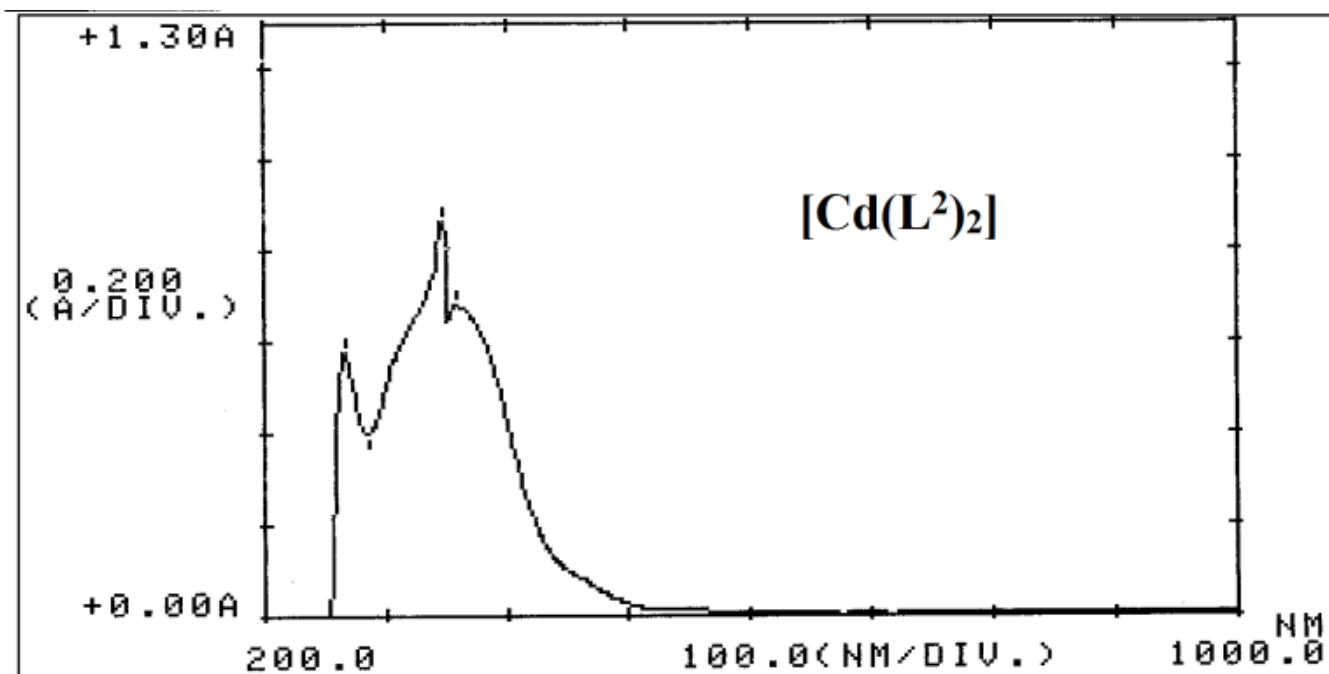
Figure (3-109): UV-Vis of [Cd(L^2)$_2$] in DMSO solvent.

183

Table (3-20): Electronic data of HL^2 complexes in DMSO solutions.

Compound	Peak position λnm	Wave number (cm^{-1})	Molar extinction coefficient ε_{max} (dm^3 mol^{-1} cm^{-1})	Assignment	Proposed structure
HL^2	266	37594	450	$\pi \rightarrow \pi^*$	
	350	28571	1980	$n \rightarrow \pi^*$	
	380	26316	2134	C.T.	
K$_2$[Mn(L^2)$_2$Cl$_2$]	280	35714	350	$\pi \rightarrow \pi^*$	Distorted octahedral
	385	25974	1760	$n \rightarrow \pi^*$	
	551	18149	18	$^6A_1g^{(F)} \rightarrow {}^4T_2g^{(G)}$	
	733	13643	22	$^6A_1g \rightarrow {}^4T_1g^{(G)}$	
K$_2$[Co(L^2)$_2$Cl$_2$]	287	34843	1870	$\pi \rightarrow \pi^*$	Distorted octahedral
	386	25907	986	$n \rightarrow \pi^*$	
	492	20325	120	$^4T_1g^{(F)} \rightarrow {}^4A_2g^{(F)}$	
	734	13624	60	$^4T_1g \rightarrow {}^4T_2g^{(F)}$	
K$_2$[Ni(L^2)$_2$Cl$_2$]	290	34483	2190	$\pi \rightarrow \pi^*$	Distorted octahedral
	351	28490	2310	$n \rightarrow \pi^*$	
	451	22173	176	$^3A_2g \rightarrow {}^3T_1g^{(P)}$	
	650	15385	66	$^3A_2g \rightarrow {}^3T_2g^{(F)}$	
	815	12270	34	$^3A_2g \rightarrow {}^3T_1g^{(F)}$	
[Cu(L^2)$_2$]	295	33898	2432	$\pi \rightarrow \pi^*$	Distorted square planar
	380	26316	1456	$n \rightarrow \pi^*$	
	762	13123	35	$^2B_1g \rightarrow {}^2B_2g$	
	871	11481	57	$^2B_1g \rightarrow {}^2A_2g$	
[Zn(L^2)$_2$]	284	35211	844	$\pi \rightarrow \pi^*$	Tetrahedral
	340	29412	932	$n \rightarrow \pi^*$	
	375	26667	1345	C.T.	
[Cd(L^2)$_2$]	280	35714	766	$\pi \rightarrow \pi^*$	Tetrahedral
	342	29240	987	$n \rightarrow \pi^*$	
	374	26738	1322	C.T.	

(3.9.3) Electronic spectra of K$_2$[Mn(L^3)$_2$Cl$_2$], K$_2$[Co(L^3)$_2$Cl$_2$], K$_2$[Ni(L^3)$_2$Cl$_2$], [Cu(L^3)$_2$], [Zn(L^3)$_2$] and [Cd(L^3)$_2$]

The spectra of HL^3 complexes, Figures (3-110) to (3-115), appeared transitions related to intra-ligand ($\pi \rightarrow \pi^*$ and $n \rightarrow \pi^*$) were shifted to lower frequency compared with the spectrum of the free ligand, indicating an interaction between the ligand and metal

centre [60-62]. The Mn(II) complex revealed a peak at 752 nm (13298 cm^{-1}; ε_{max}= 76 dm^3 mol^{-1} cm^{-1}) due to $^6A_1g{\rightarrow}^4T_1g^{(G)}$ transition, demonstrating a distorted octahedral geometry about Mn(II) ion [71-73]. The peak at 754 nm (13263 cm^{-1}; ε_{max}= 45 dm^3 mol^{-1} cm^{-1}) related to $^4T_1g^{(F)}{\rightarrow}^4T_2g^{(F)}$ transition in the spectrum of Co(II) complex is characteristic for Co(II) complexes with distorted octahedral arrangement about metal centre [74-76]. The Ni(II)-complex revealed bands at 455 nm (21978 cm^{-1}; ε_{max}= 105 dm^3 mol^{-1} cm^{-1}), 748 nm (13369 cm^{-1}; ε_{max}= 32 dm^3 mol^{-1} cm^{-1}) and 835 nm (11976 cm^{-1}; ε_{max}= 30 dm^3 mol^{-1} cm^{-1}) assigned to $^3A_2g{\rightarrow}^3T_1g^{(P)}$, $^3A_2g{\rightarrow}^3T_2g^{(F)}$ and $^3A_2g{\rightarrow}^3T_1g^{(F)}$ transitions, respectively, confirming a distorted octahedral structure about Ni(II) centre [77]. The Cu(II)-complex indicated a peak at 676 nm (14793 cm^{-1}; ε_{max}= 58 dm^3 mol^{-1} cm^{-1}) attributed to d-d transition type $^2B_1g{\rightarrow}^2B_2g$ indicating a distorted square planar arrangement [78]. The two intense absorption peaks of [Zn(L^3)$_2$], which appeared at 282 nm (35461 cm^{-1}; ε_{max}= 944 dm^3 mol^{-1} cm^{-1}) and 302 nm (33113 cm^{-1}; ε_{max}= 1145 dm^3 mol^{-1} cm^{-1}) correlated to intra-ligand field. The [Cd(L^3)$_2$], showed peaks at 281 nm (35587 cm^{-1}; ε_{max}= 1066 dm^3 mol^{-1} cm^{-1}) and 357 nm (28011 cm^{-1}; ε_{max}= 1212 dm^3 mol^{-1} cm^{-1}) due to $\pi{\rightarrow}\pi^*$ and n$\rightarrow\pi^*$, individually. The spectra of the d^{10} system along with their analytical analyses data revealed the formation of four-coordinate compounds in which the geometry about metal centre is a distorted tetrahedral [79,80]. The electronic data with the proposed structure for compounds are listed in Table (3-21).
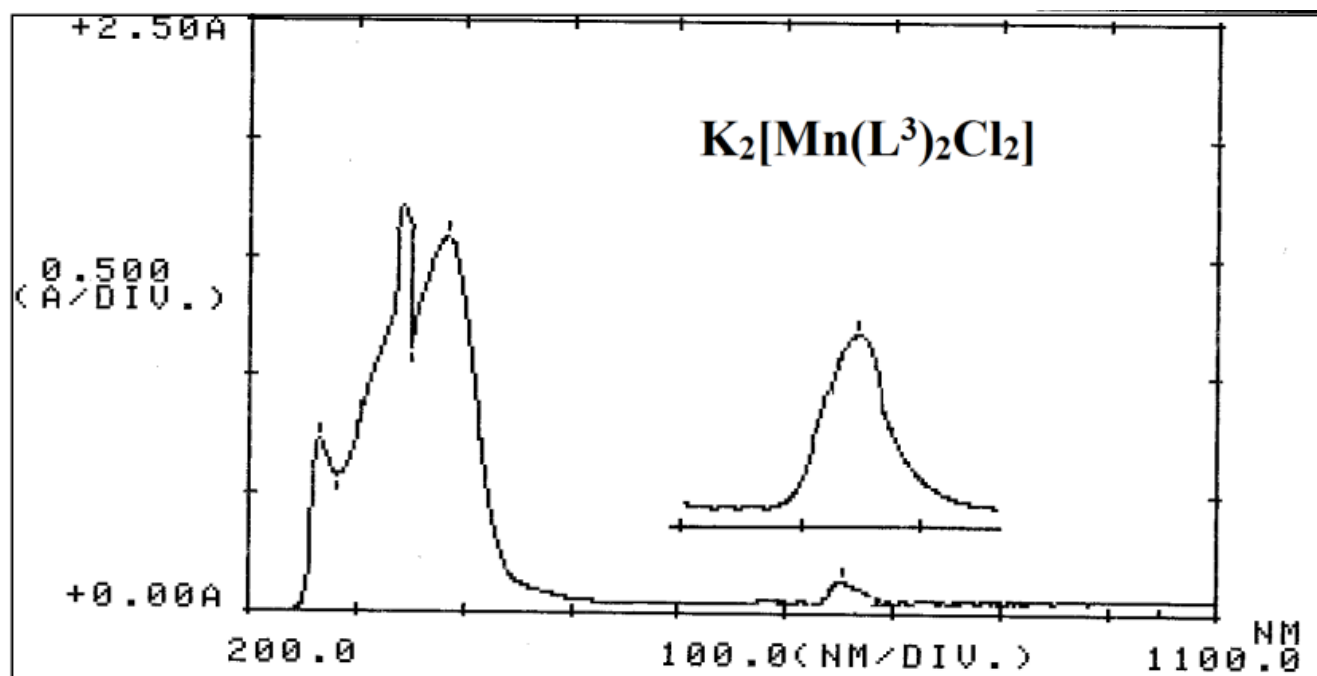
Figure (3-110): UV-Vis of K$_2$[Mn(L^3)$_2$Cl$_2$] in DMSO solvent.
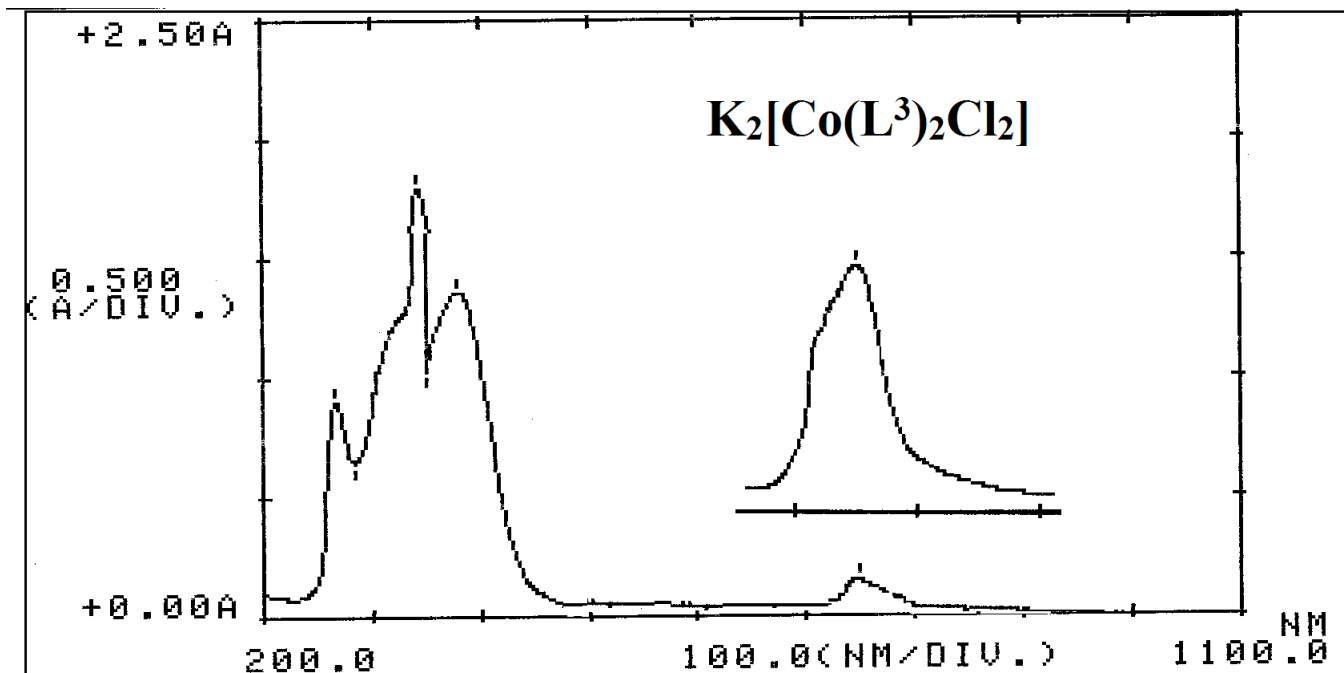
Figure (3-111): UV-Vis of K$_2$[Co(L^3)$_2$Cl$_2$] in DMSO solvent.

186
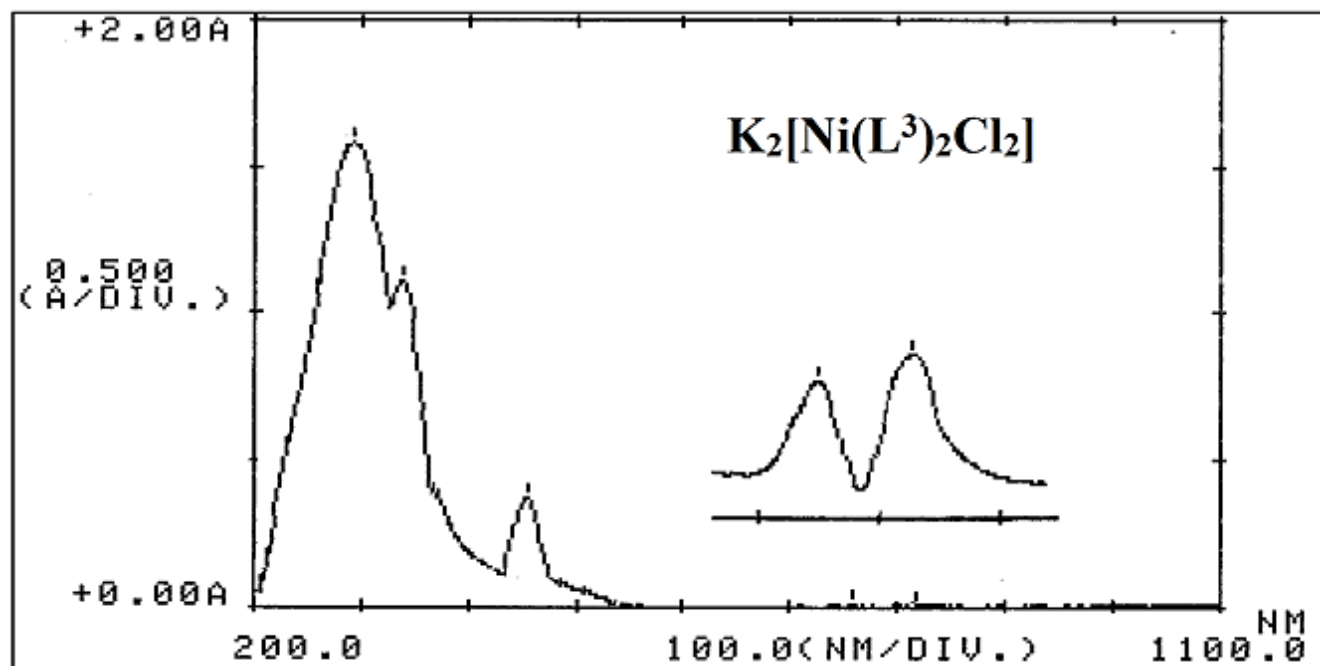
Figure (3-112): UV-Vis of K$_2$[Ni(L^3)$_2$Cl$_2$] in DMSO solvent.
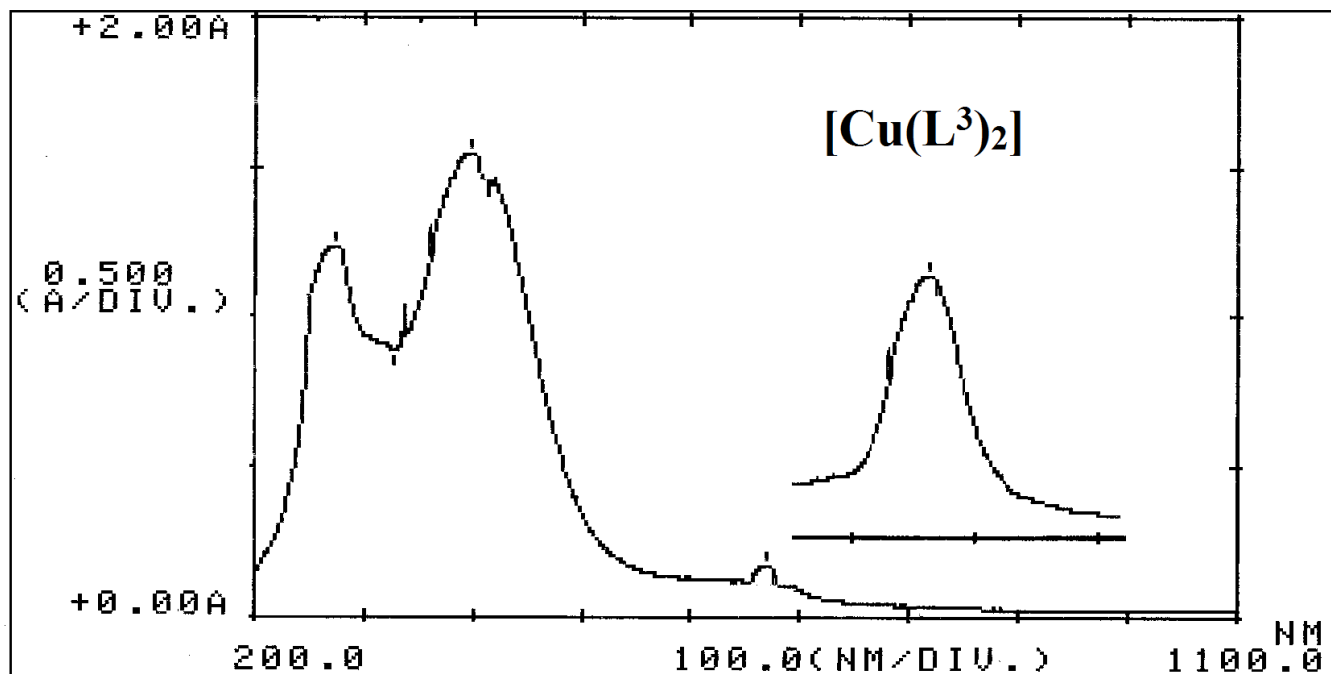
Figure (3-113): UV-Vis of [Cu(L^3)$_2$] in DMSO solvent.
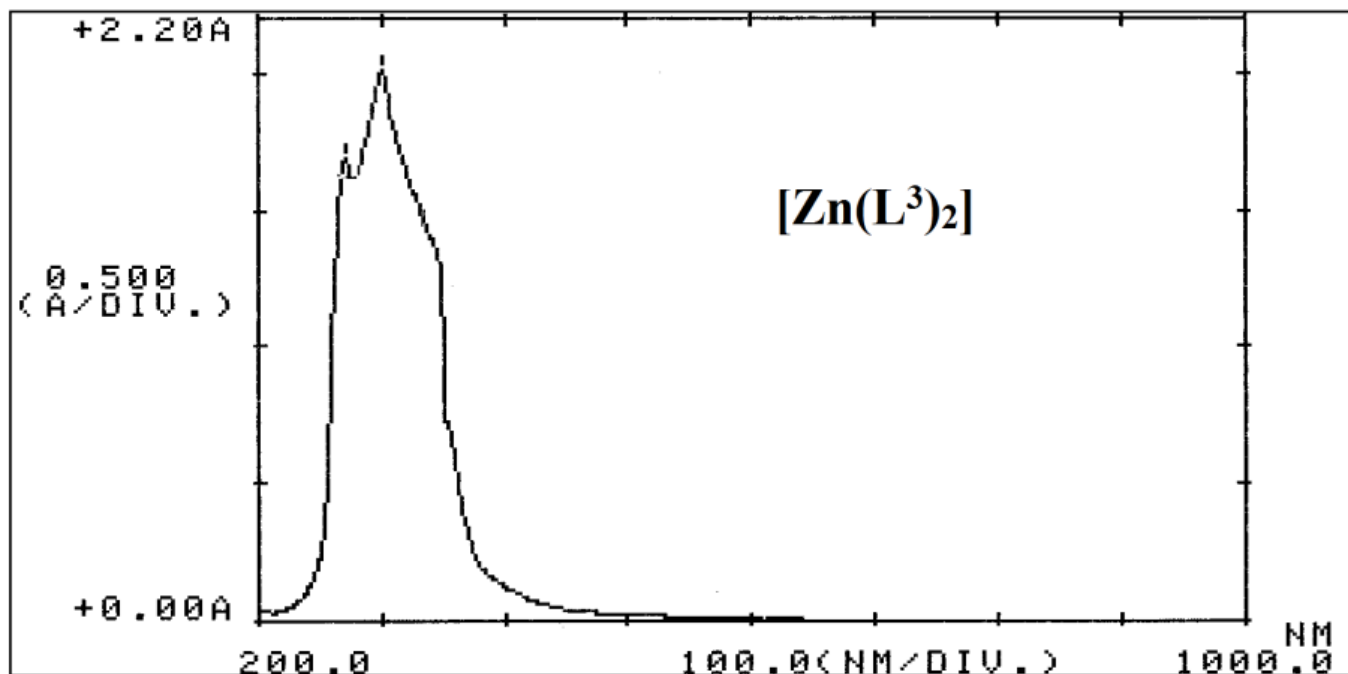
Figure (3-114): UV-Vis of [Zn(L³)₂] in DMSO solvent.

Figure (3-115): UV-Vis of [Cd(L³)₂] in DMSO solvent.

188

Table (3-21): Electronic data of HL^3 complexes in DMSO solutions.

Compound	Peak position λnm	Wave number (cm^{-1})	Molar Extinction coefficient ε_{max} $(dm^3 \, mol^{-1} \, cm^{-1})$	Assignment	Suggested structure
HL^3	270	37037	987	$\pi \rightarrow \pi^*$	
	310	32258	1305	$n \rightarrow \pi^*$	
	365	27397	718	C.T.	
K$_2$[Mn(L^3)$_2$Cl$_2$]	280	35714	770	$\pi \rightarrow \pi^*$	Distorted octahedral
	390	25641	1495	$n \rightarrow \pi^*$	
	752	13298	76	$^6A_1g^{(F)} \rightarrow {^4}T_1g^{(G)}$	
K$_2$[Co(L^3)$_2$Cl$_2$]	279	35842	970	$\pi \rightarrow \pi^*$	Distorted octahedral
	341	29326	1223	$n \rightarrow \pi^*$	
	389	25707	1750	C.T.	
	754	13263	45	$^4T_1g^{(F)} \rightarrow {^4}T_2g^{(p)}$	
K$_2$[Ni(L^3)$_2$Cl$_2$]	298	33557	887	$\pi \rightarrow \pi^*$	Distorted octahedral
	340	29412	1150	$n \rightarrow \pi^*$	
	455	21978	105	$^3A_2g \rightarrow {^3}T_1g^{(P)}$	
	748	13369	32	$^3A_2g \rightarrow {^3}T_2g^{(F)}$	
	835	11976	30	$^3A_2g \rightarrow {^3}T_1g^{(F)}$	
[Cu(L^3)$_2$]	281	35587	1040	$\pi \rightarrow \pi^*$	Square planar
	395	25317	1980	C.T.	
	676	14793	58	$^2B_1g \rightarrow {^2}B_2g$	
[Zn(L^3)$_2$]	282	35461	875	$\pi \rightarrow \pi^*$	Tetrahedral
	302	33113	1889	$n \rightarrow \pi^*$	
[Cd(L^3)$_2$]	281	35587	727	$\pi \rightarrow \pi^*$	Tetrahedral
	357	28011	1441	$n \rightarrow \pi^*$	

(3.9.4) Electronic spectra of K$_2$[Mn(L^4)$_2$Cl$_2$], K$_2$[Co(L^4)$_2$Cl$_2$], K$_2$[Ni(L^4)$_2$Cl$_2$], [Cu(L^4)$_2$], [Zn(L^4)$_2$] and [Cd(L^4)$_2$] complexes

The UV-Vis data for HL^4 complexes revealed peaks correlated to $\pi \rightarrow \pi^*$, $n \rightarrow \pi^*$ transitions (bar Co(II), Ni(II) and Cu(II) complexes which showed $\pi \rightarrow \pi^*$, $n \rightarrow \pi^*$ and C.T. transitions) [60-62], Figures (3-116) to (3-121). The Mn-complex exhibited bands in the visible area at 483 nm (20704 cm^{-1}; ε_{max}= 66 dm^3 mol^{-1} cm^{-1}) and 848 nm (11793 cm^{-1};

ε_{max}= 23 dm^3 mol^{-1} cm^{-1}) allocated to $^6A_1g^{(F)}\rightarrow^4T_2g^{(G)}$ and $^6A_1g^{(F)}\rightarrow^4T_1g^{(G)}$ transitions, indicating a distorted octahedral sphere about Mn(II) ion [71-73]. In addition, the Co(II)-complex reveals a peak at 810 nm (12346 cm^{-1}; ε_{max}= 45 dm^3 mol^{-1} cm^{-1}) due to $^4T_1g^{(F)}\rightarrow^4T_2g^{(F)}$ transition. This spectrum is characteristic for Co(II) complexes that adopt octahedral geometries [74-76]. The Ni(II)-complex chart recorded peaks in the visible section of the spectrum at 450 nm (22222 cm^{-1}; ε_{max}= 86 dm^3 mol^{-1} cm^{-1}) and 751 nm (13316 cm^{-1}; ε_{max}= 50 dm^3 mol^{-1} cm^{-1}) correlated to $^3A_2g\rightarrow^3T_1g^{(P)}$ and $^3A_2g\rightarrow^3T_2g^{(F)}$ transitions, respectively, favouring a distorted octahedral arrangement about Ni(II) atom [77]. The Cu(II)-complex displayed a band at 841 nm (11891 cm^{-1}; ε_{max}= 71 dm^3 mol^{-1} cm^{-1}) attributed to $^2B_1g\rightarrow^2B_2g$ transition, indicating a distorted square planar geometry about Cu(II) atom [78]. The electronic data of the [Zn(L^4)$_2$], exhibited bands at 284 nm (35211 cm^{-1}; ε_{max}= 764 dm^3 mol^{-1} cm^{-1}) and 378 nm (26455 cm^{-1}; ε_{max}= 1045 dm^3 mol^{-1} cm^{-1}) attributed to the intra-ligand field transitions, demonstrating distorted tetrahedral structure about Zn atom [79]. The [Cd(L^4)$_2$], showed bands at 292 nm (34247 cm^{-1}; ε_{max}= 1006 dm^3 mol^{-1} cm^{-1}) and 381 nm (26247 cm^{-1}; ε_{max}= 1345 dm^3 mol^{-1} cm^{-1}) related to the intra-ligand field transitions, confirming tetrahedral geometry around Cd atom [80]. The electronic data with the proposed structure of the compounds are listed in Table (3-22).
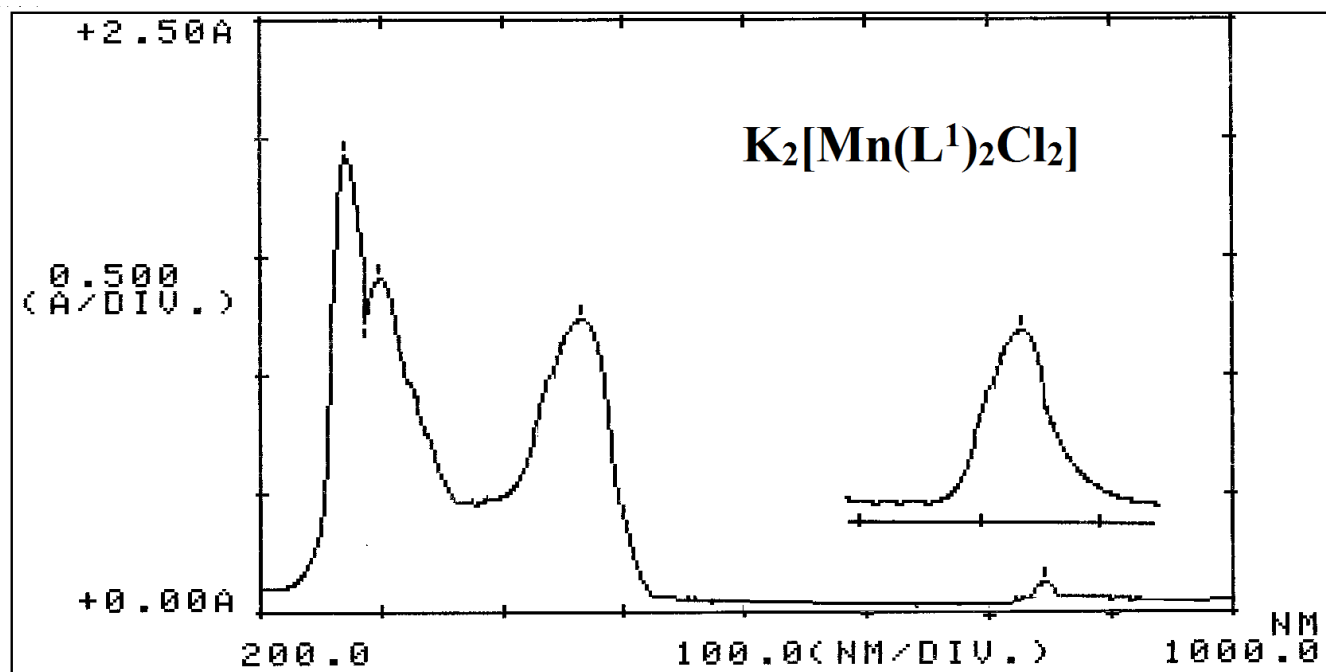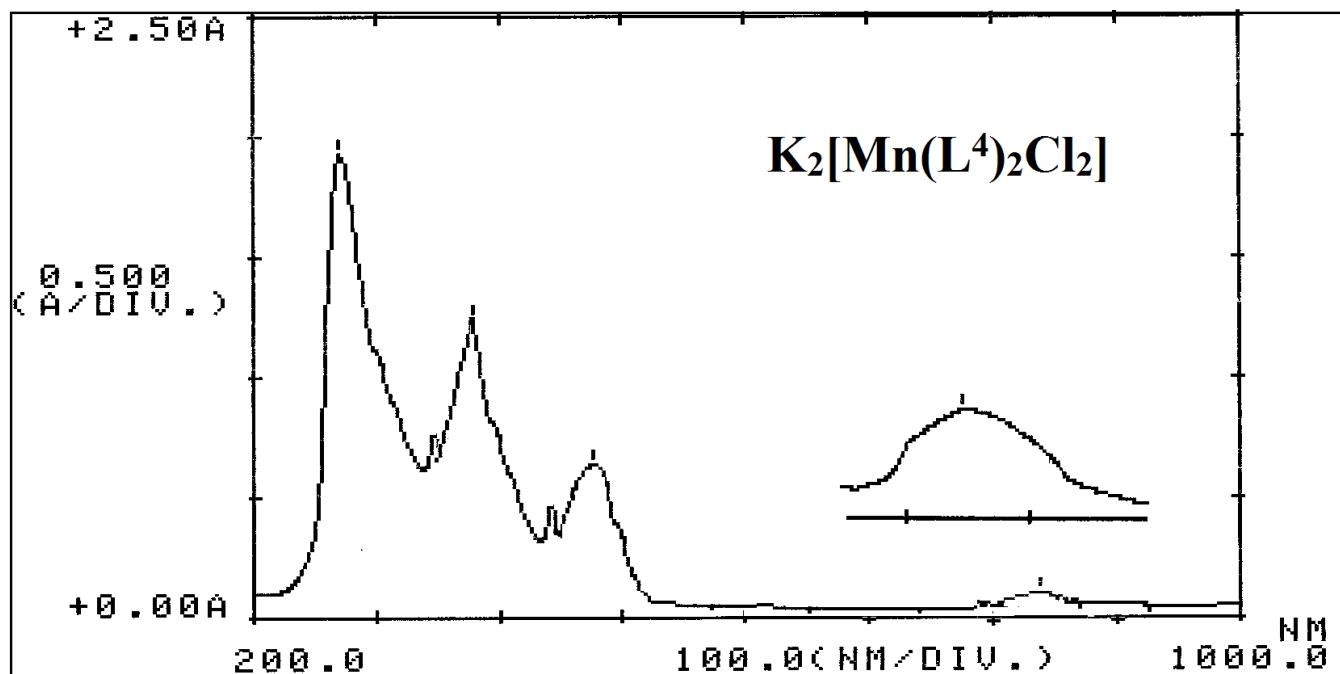
Figure (3-116): UV-Vis of $K_2[Mn(L^4)_2Cl_2]$ in DMSO solvent.
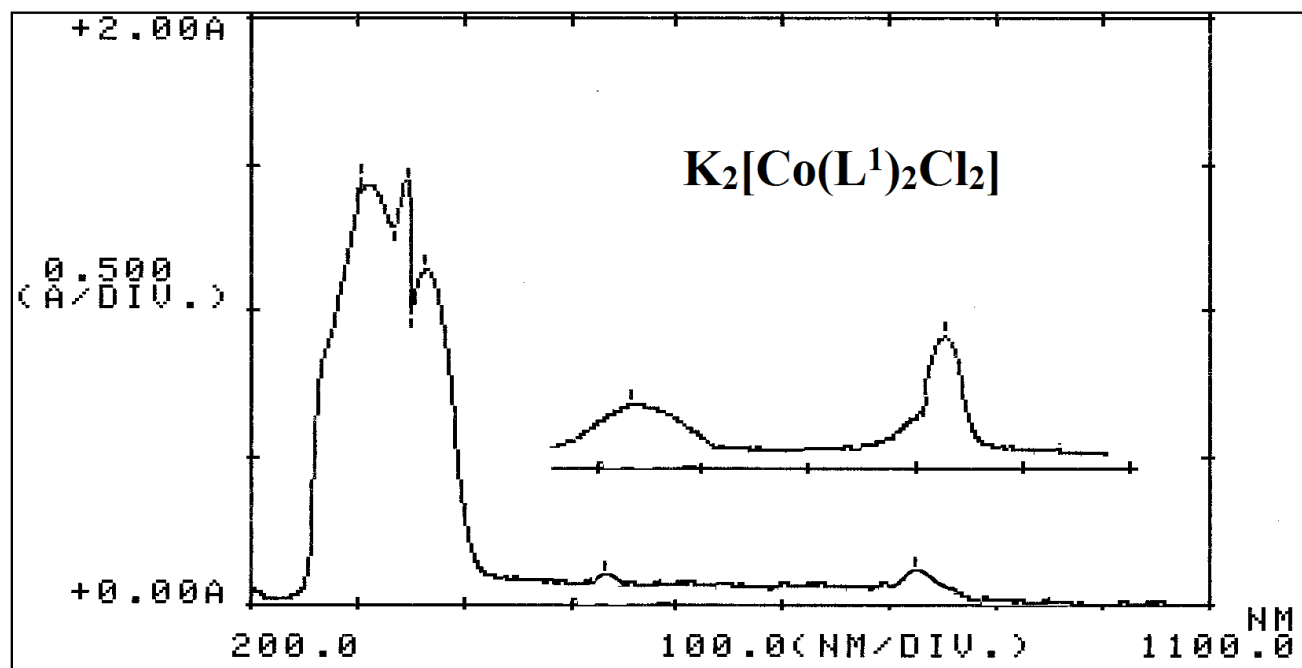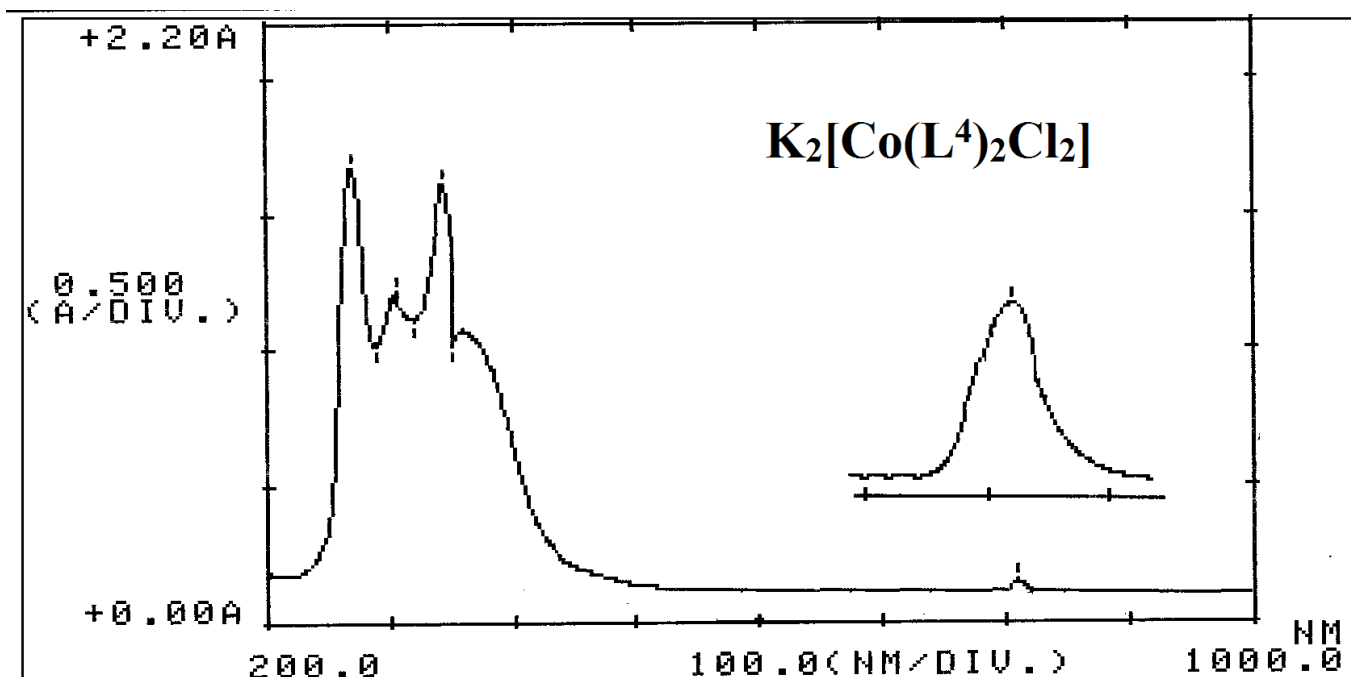

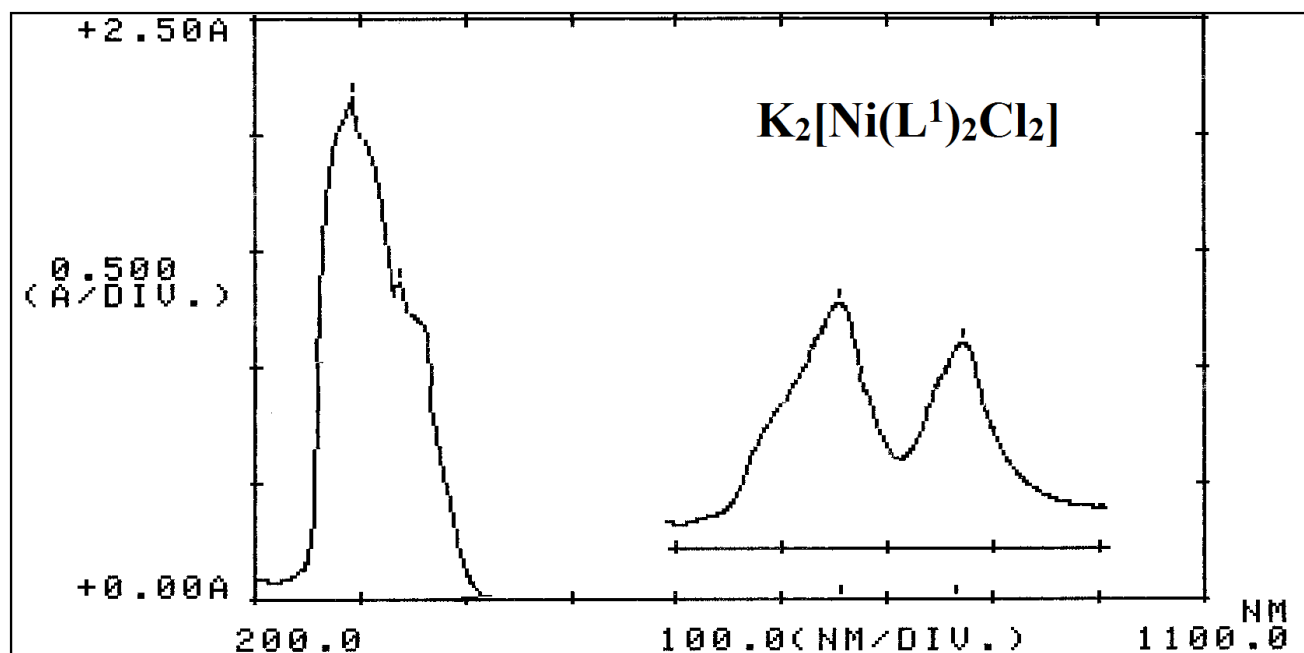**Figure (3-117): UV-Vis of $K_2[Co(L^4)_2Cl_2]$ in DMSO solvent.**

191
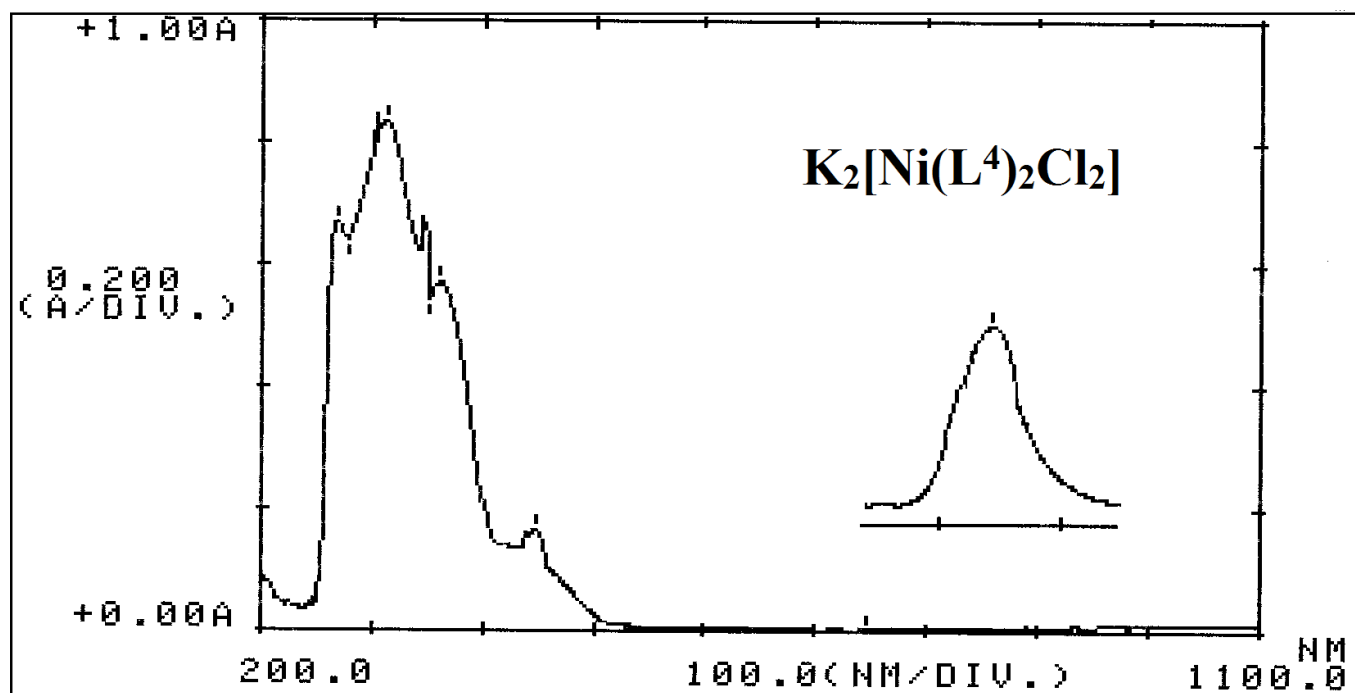
Figure (3-118): UV-Vis of K$_2$[Ni(L^4)$_2$Cl$_2$] in DMSO solvent.
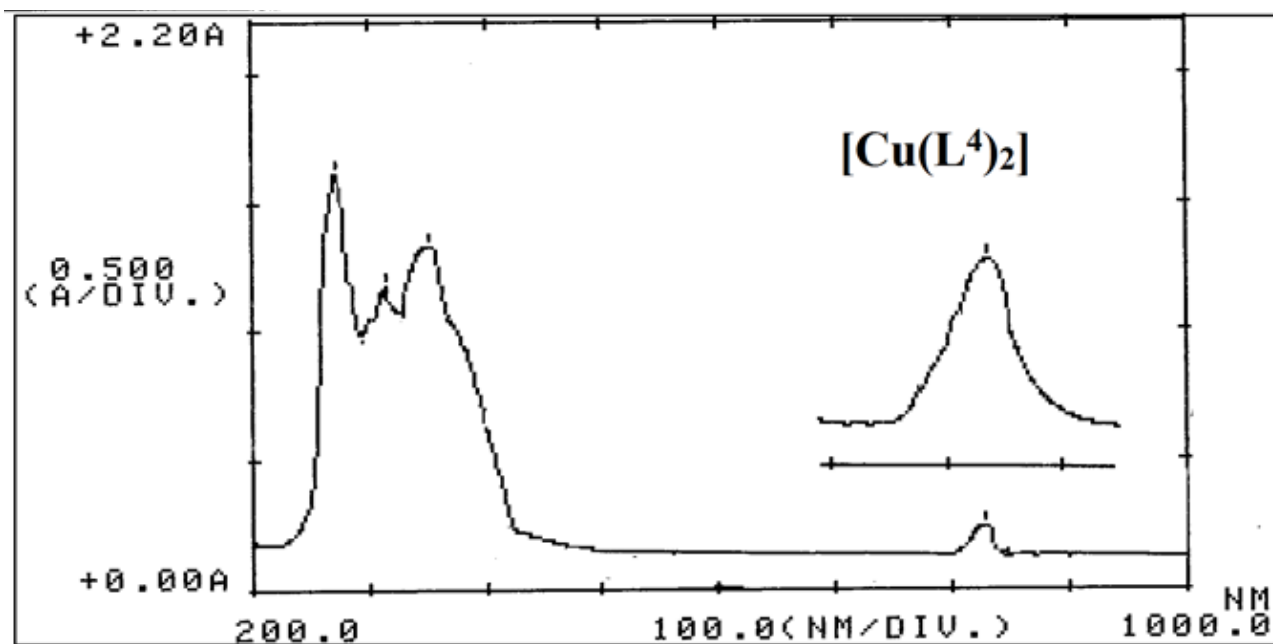
Figure (3-119): UV-Vis of [Cu(L^4)$_2$] in DMSO solvent.

192
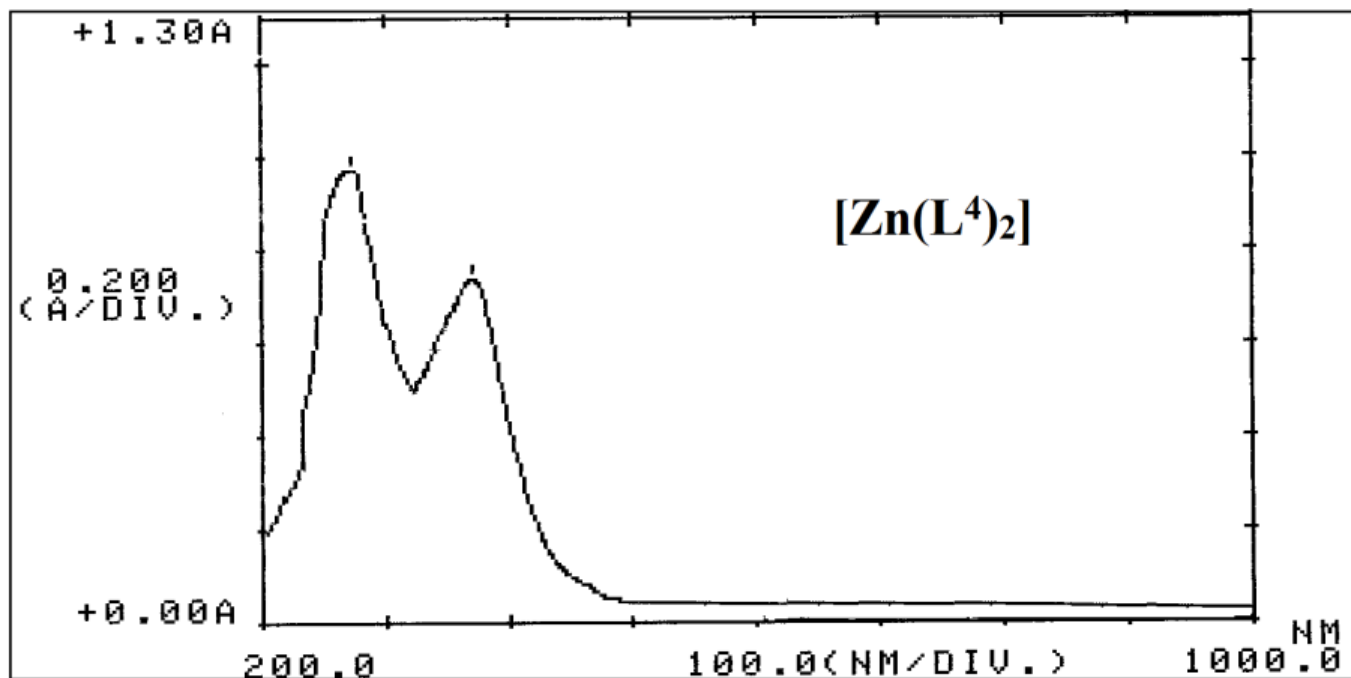
Figure (3-120): UV-Vis of [Zn(L^4)$_2$] in DMSO solvent.
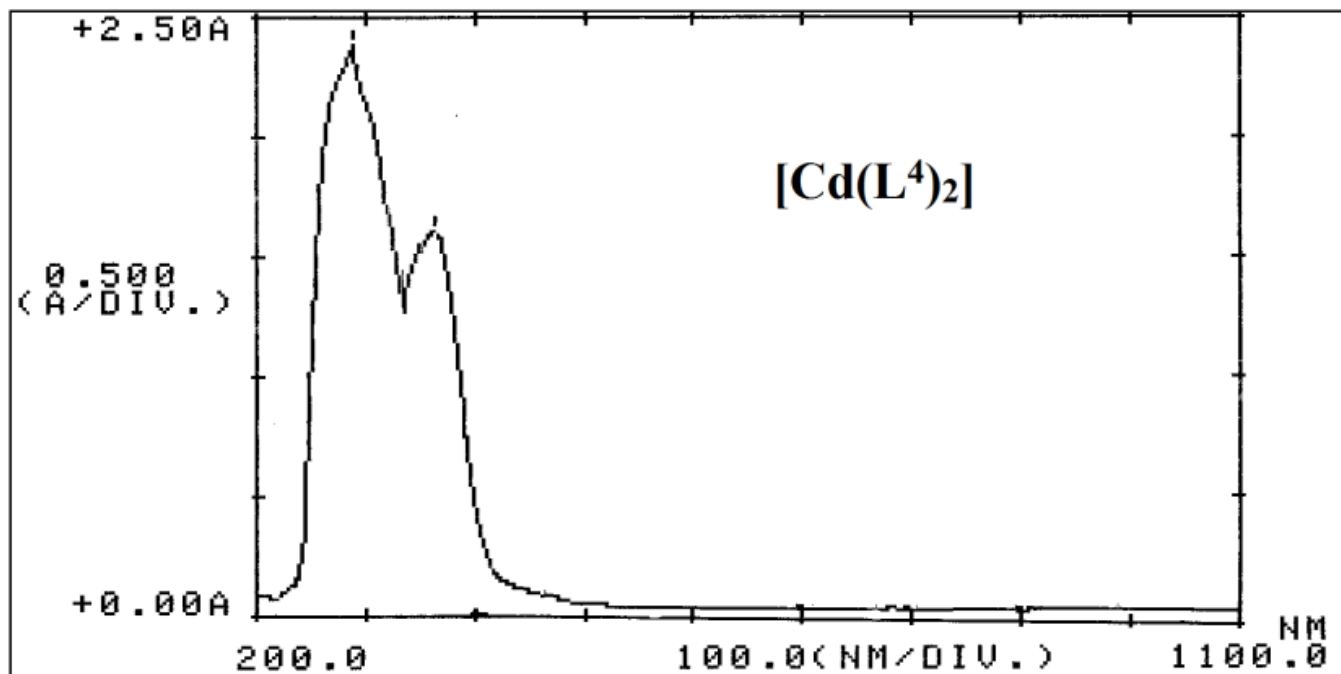
Figure (3-121): UV-Vis of [Cd(L^4)$_2$] in DMSO solvent.

193

Table (3-22): Electronic data of HL^4 complexes in DMSO solutions.

Compound	Peak **position** λnm	**Wave number** (cm^{-1})	**Molar extinction coefficient** ε_{max} (dm^3 mol^{-1} cm^{-1})	**Assignment**	**Suggested structure**
HL^4	265	37736	1123	$\pi\rightarrow\pi^*$	
	310	32258	988	$n\rightarrow\pi^*$	
K$_2$[Mn(L^4)$_2$Cl$_2$]	282	35461	1769	$\pi\rightarrow\pi^*$	Distorted octahedral
	381	26247	1342	$n\rightarrow\pi^*$	
	483	20704	66	$^6A_1g^{(F)}\rightarrow{}^4T_2g^{(G)}$	
	848	11793	23	$^6A_1g^{(F)}\rightarrow{}^4T_1g^{(G)}$	
K$_2$[Co(L^4)$_2$Cl$_2$]	280	35714	1256	$\pi\rightarrow\pi^*$	Distorted octahedral
	305	32787	921	$n\rightarrow\pi^*$	
	345	28986	1145	C.T.	
	810	12346	45	$^4T_1g^{(F)}\rightarrow{}^4T_2g^{(F)}$	
K$_2$[Ni(L^4)$_2$Cl$_2$]	284	35211	933	$\pi\rightarrow\pi^*$	Distorted octahedral
	310	32258	1421	$n\rightarrow\pi^*$	
	375	26667	1388	C.T.	
	450	22222	86	$^3A_2g\rightarrow{}^3T_1g^{(P)}$	
	751	13316	50	$^3A_2g\rightarrow{}^3T_2g^{(F)}$	
[Cu(L^4)$_2$]	278	35971	1166	$\pi\rightarrow\pi^*$	Square planar
	310	32258	875	$n\rightarrow\pi^*$	
	348	28736	1089	C.T.	
	841	11891	71	$^2B_1g\rightarrow{}^2B_2g$	
[Zn(L^4)$_2$]	284	35211	764	$\pi\rightarrow\pi^*$	Tetrahedral
	378	26455	1045	$n\rightarrow\pi^*$	
[Cd(L^4)$_2$]	292	34247	1006	$\pi\rightarrow\pi^*$	Tetrahedral
	381	26247	1345	$n\rightarrow\pi^*$	

(3.9.5) Electronic spectra of K$_2$[Mn(L^5)$_2$Cl$_2$], K$_2$[Co(L^5)$_2$Cl$_2$], K$_2$[Ni(L^5)$_2$Cl$_2$], [Cu(L^5)$_2$], [Zn(L^5)$_2$] and [Cd(L^5)$_2$]

The observed spectra of HL^5 complexes are depicted in Figures ((3-122) to (3-127)). In each case, the spectrum showed intense peaks in the U.V region that assigned to intra-ligand (except Mn(II)-complex showed peaks due to intra-ligand and peak at 395 nm attributed to C.T. transitions) [60-62]. The electronic UV-Vis data of the Mn(II) complex

exhibited bands in the d-d part at 560 nm (17857 cm^{-1}; ε_{max}= 78 dm^3 mol^{-1} cm^{-1}) and 735 nm (13605 cm^{-1}; ε_{max}= 96 dm^3 mol^{-1} cm^{-1}) referred to $^6A_1g^{(F)} \rightarrow {}^4T_2g^{(G)}$ and $^6A_1g \rightarrow {}^4T_1g^{(G)}$ transitions, respectively, demonstrating a distorted octahedral structure about Mn(II) ion [71-73]. The Co(II) complex indicated a band in the d-d part at 776 nm (12887 cm^{-1}; ε_{max}= 21 dm^3 mol^{-1} cm^{-1}) due to $^4T_1g^{(F)} \rightarrow {}^4T_2g^{(F)}$ transition. This spectrum is characteristic for Co(II) complex that adopt a distorted octahedral arrangement around Co atom [74-76]. The chart of Ni(II) complex detected bands at 623 nm (16051 cm^{-1}; ε_{max}= 43 dm^3 mol^{-1} cm^{-1}) and 735 nm (13605 cm^{-1}; ε_{max}= 61 dm^3 mol^{-1} cm^{-1}) correlated to d-d electronic transitions type $^3A_2g \rightarrow {}^3T_2g^{(F)}$ and $^3A_2g \rightarrow {}^3T_1g^{(F)}$, respectively confirming a distorted octahedral structure round Ni(II) atom [77]. The Cu(II) complex pointed out a peak at 680 nm (14706 cm^{-1}; ε_{max}= 40 dm^3 mol^{-1} cm^{-1}), which may be assigned to d-d transition type $^2B_1g \rightarrow {}^2B_2g$, indicating a distorted square planar structure about Cu(II) atom [78]. The [Zn(L^5)$_2$] electronic chart, recorded bands at 279 nm (35211 cm^{-1}; ε_{max}= 764 dm^3 mol^{-1} cm^{-1}) and 365 nm (26455 cm^{-1}; ε_{max}= 1045 dm^3 mol^{-1} cm^{-1}) assigned to the intra-ligand field transitions, designating tetrahedral geometry around Zn(II) ion [79]. The [Cd(L^5)$_2$] chart, showed two intense peaks at 282 nm (34247 cm^{-1}; ε_{max}= 1006 dm^3 mol^{-1} cm^{-1}) and 311 nm (26247 cm^{-1}; ε_{max}= 1345 dm^3 mol^{-1} cm^{-1}) due to the intra-ligand field, confirming tetrahedral geometry around Cd(II) ion [80]. The electronic data with the proposed structure of the compounds are listed in Table (3-23).
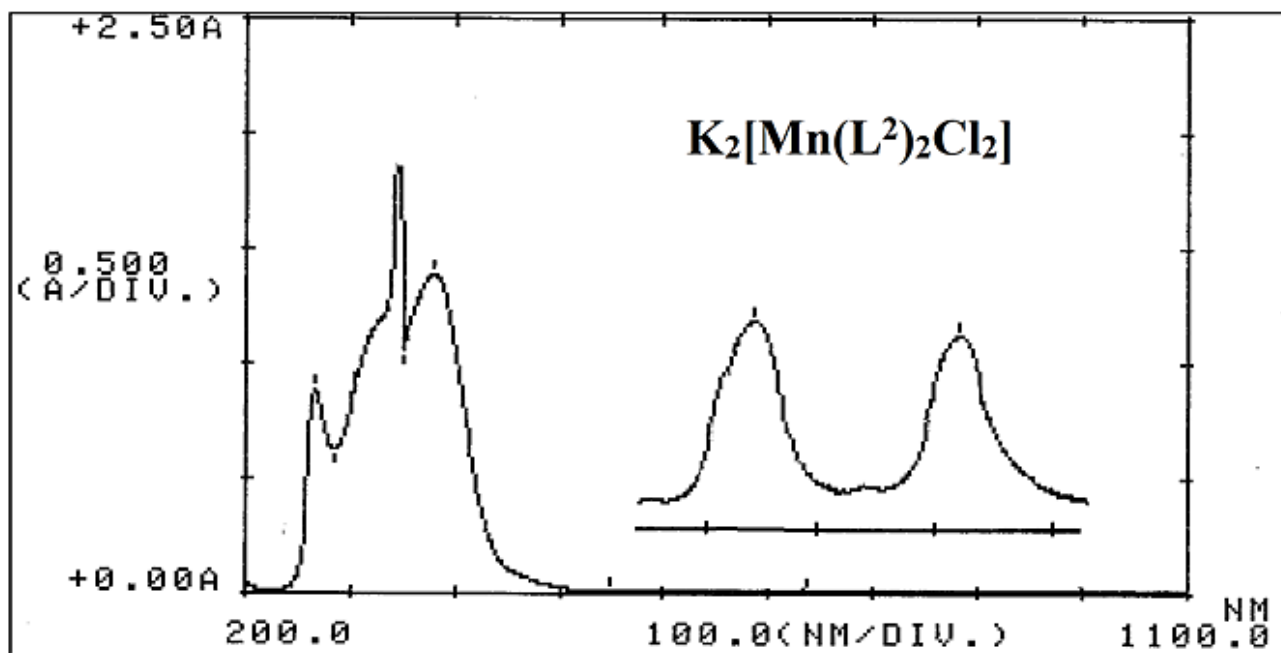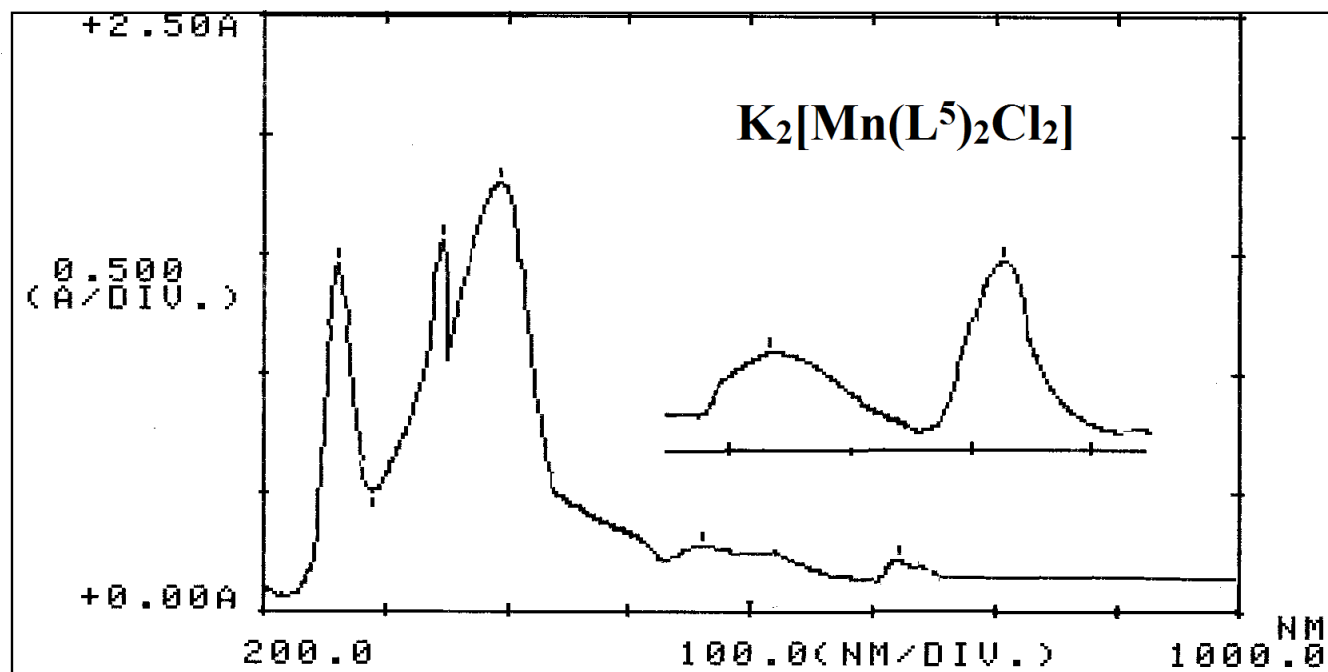
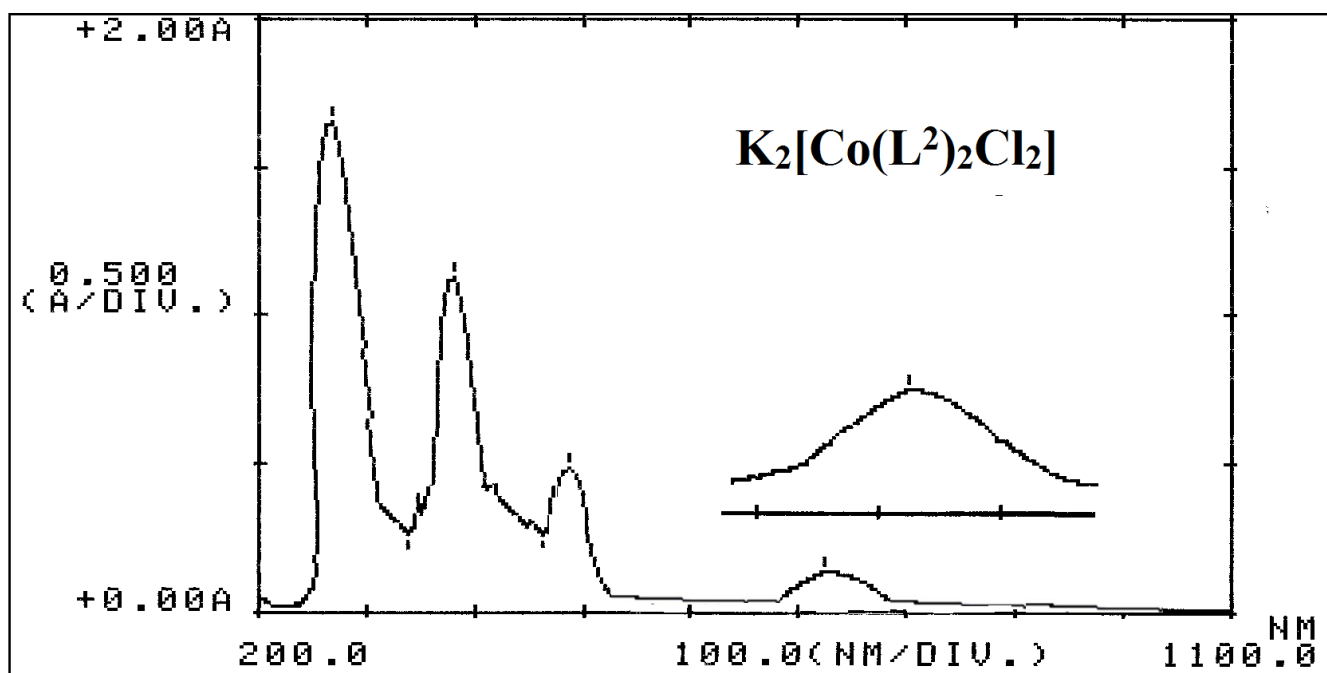**Figure (3-122): UV-Vis of $K_2[Mn(L^5)_2Cl_2]$ in DMSO solvent.**
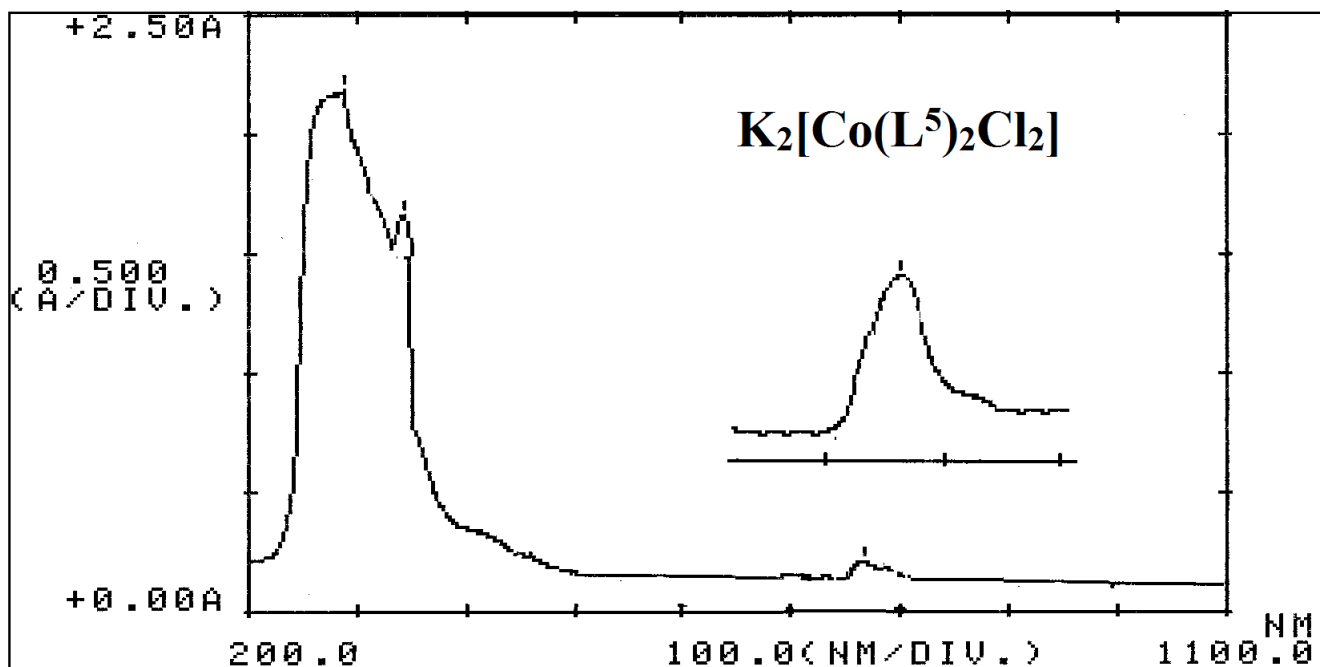
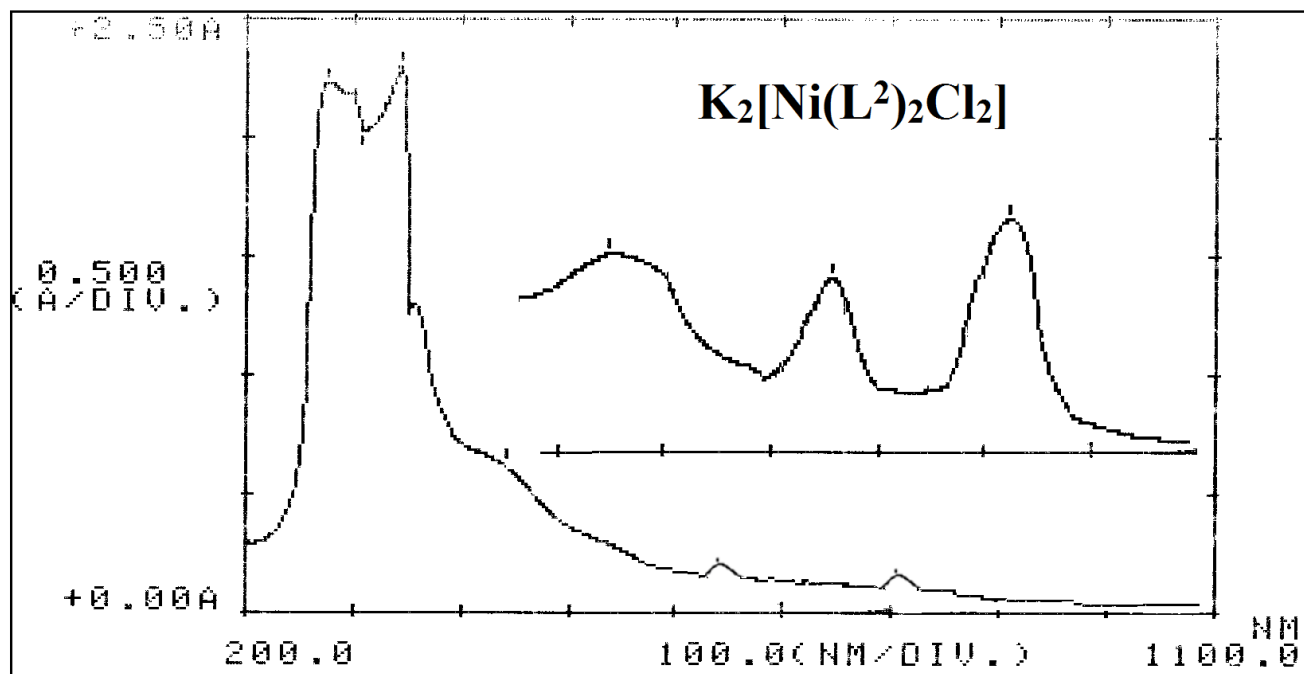**Figure (3-123): UV-Vis of $K_2[Co(L^5)_2Cl_2]$ in DMSO solvent.**

196
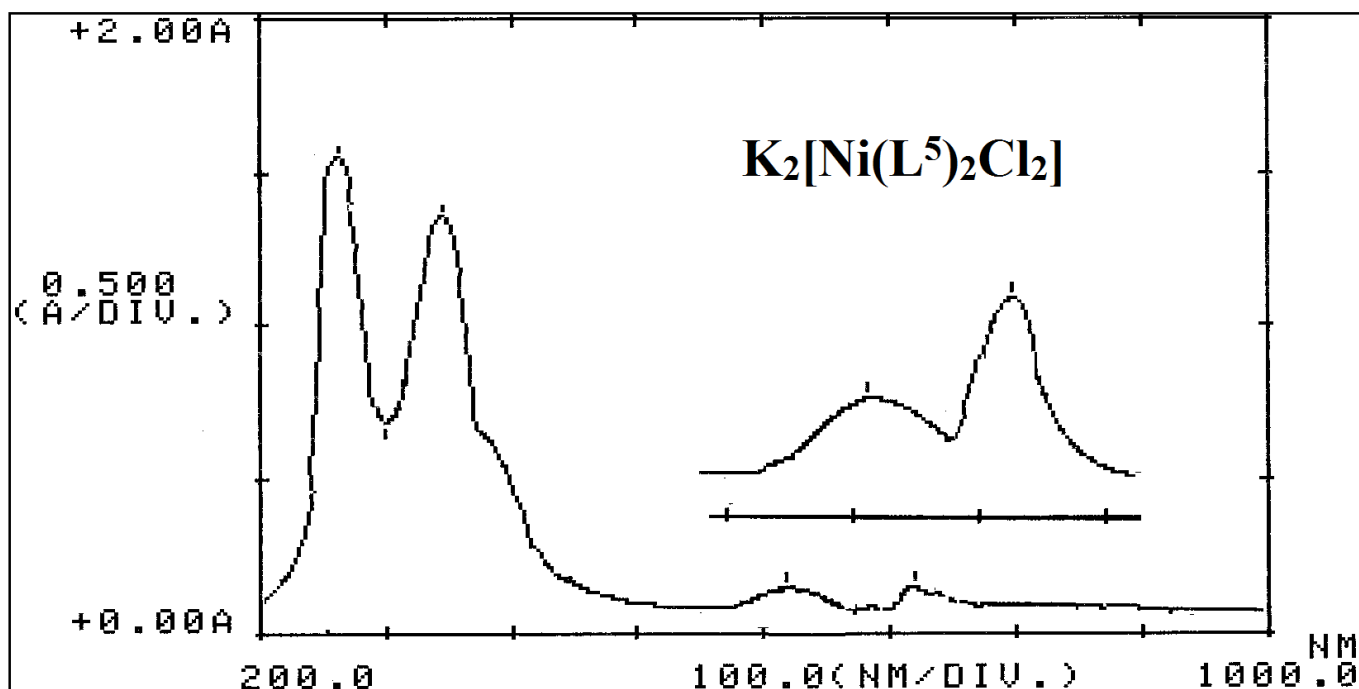
Figure (3-124): UV-Vis of K$_2$[Ni(L^5)$_2$Cl$_2$] in DMSO solvent.
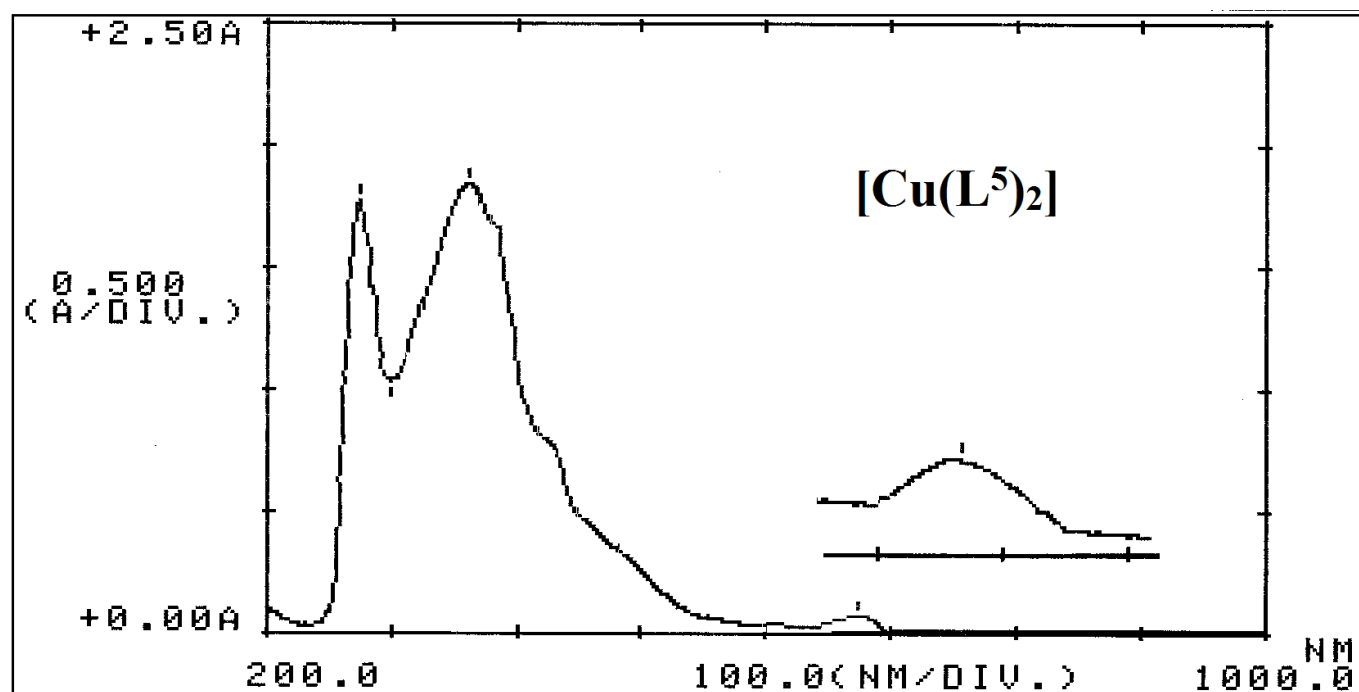
Figure (3-125): UV-Vis of [Cu(L^5)$_2$] in DMSO solvent.

197
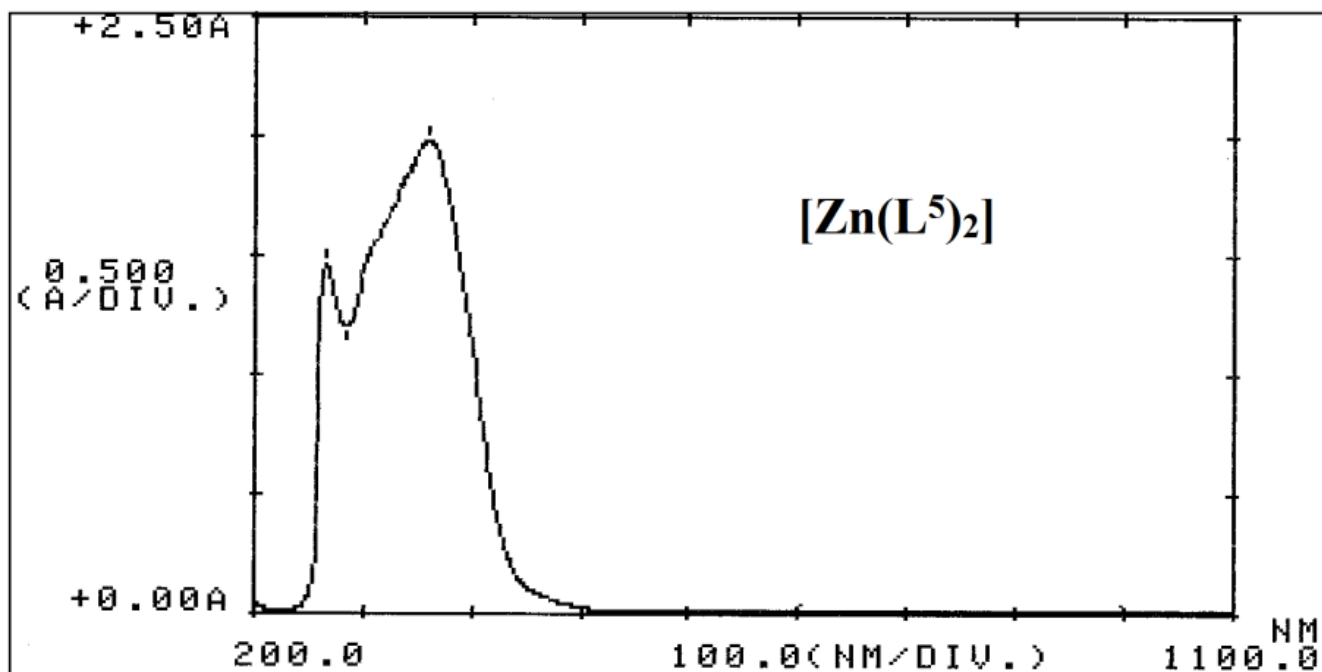
Figure (3-126): UV-Vis of [Zn(L^5)$_2$] in DMSO solvent.
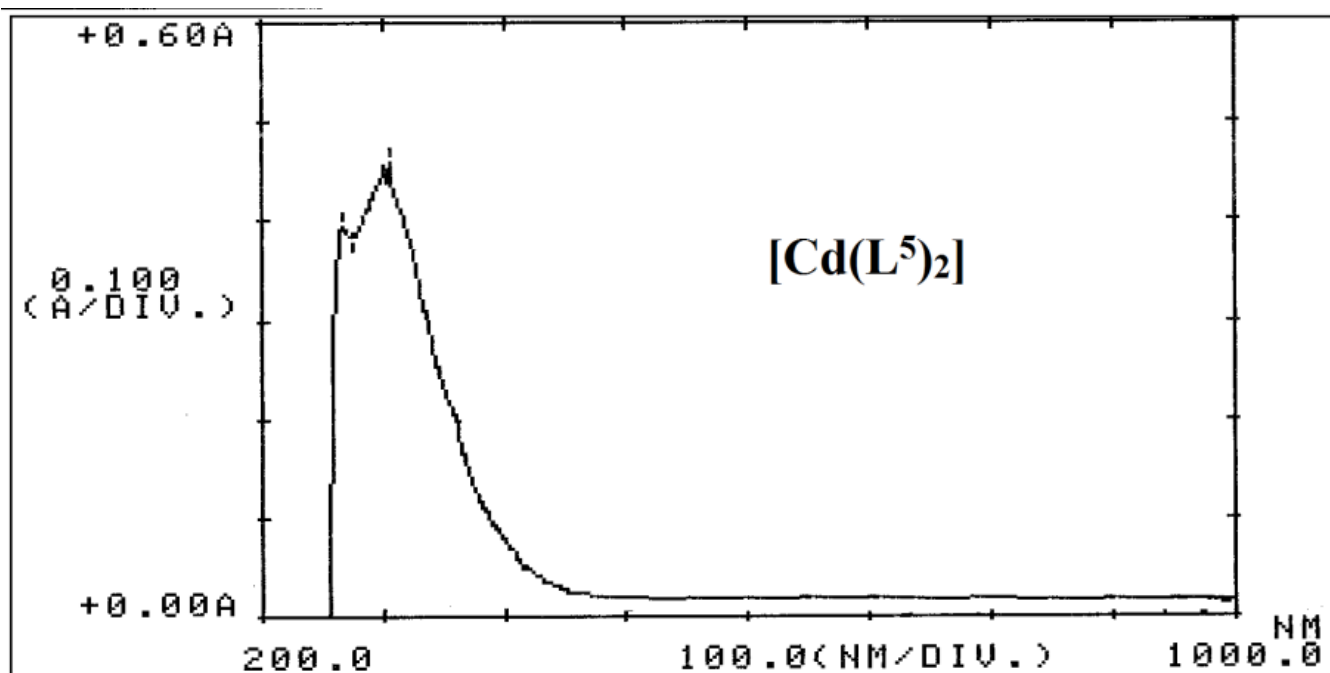
Figure (3-127): UV-Vis of [Cd(L^5)$_2$] in DMSO solvent.

198

Table (3-23): Electronic data of HL^5 complexes in DMSO solvents.

Compound	Peak position λnm	Wave number (cm^{-1})	Molar extinction coefficient ε$_{max}$ (dm^3 mol^{-1} cm^{-1})	Assignment	Suggested structure
HL^5	262	38168	1343	π→π*	
	315	31746	1063	n→π*	
K$_2$[Mn(L^5)$_2$Cl$_2$]	277	36101	734	π→π*	Distorted octahedral
	351	28490	898	n→π*	
	395	25317	987	C.T.	
	560	17857	78	$^6A_1g^{(F)}$→$^4T_2g^{(G)}$	
	735	13605	96	$^6A_1g^{(F)}$→$^4T_1g^{(G)}$	
K$_2$[Co(L^5)$_2$Cl$_2$]	297	33670	1356	π→π*	Distorted octahedral
	338	29586	1275	n→π*	
	776	12887	21	$^4T_1g^{(F)}$→$^4T_2g^{(F)}$	
K$_2$[Ni(L^5)$_2$Cl$_2$]	275	36364	1144	π→π*	Distorted octahedral
	348	28736	1067	n→π*	
	623	16051	43	^3A_2g→$^3T_2g^{(F)}$	
	735	13605	61	^3A_2g→$^3T_1g^{(F)}$	
[Cu(L^5)$_2$]	286	34965	945	π→π*	Square planar
	365	27397	839	n→π*	
	680	14706	40	^2B_1g→^2B_2g	
[Zn(L^5)$_2$]	279	35842	764	π→π*	Tetrahedral
	365	27397	1045	n→π*	
[Cd(L^5)$_2$]	282	35461	1006	π→π*	Tetrahedral
	311	32154	1345	n→π*	

(3.9.6) Electronic spectra of K$_2$[Mn(L^6)$_2$Cl$_2$], K$_2$[Co(L^6)$_2$Cl$_2$], K$_2$[Ni(L^6)$_2$Cl$_2$], [Cu(L^6)$_2$], [Zn(L^6)$_2$] and [Cd(L^6)$_2$]

The UV-Vis data for (Mn(II), Co(II), Ni(II), Cu(II), Zn(II) and Cd(II)) complexes with HL^6 are displayed in Figures ((3-128) to (3-133)). All complexes indicated transitions may relate to π→π* and n→π* transitions that shifted to lower frequency, compared with the spectrum of the free ligand, indicating an interaction between the ligand and metal centre [60-62]. The electronic spectrum in d-d area of Mn(II) complex showed bands at

540 nm (18519 cm^{-1}; ε_{max}= 39 dm^3 mol^{-1} cm^{-1}) and 766 nm (13055 cm^{-1}; ε_{max}= 87 dm^3 mol^{-1} cm^{-1}) which may correlated to $^6A_1g^{(F)} \rightarrow {}^4T_2g^{(G)}$ and $^6A_1g^{(F)} \rightarrow {}^4T_1g^{(G)}$ transitions, respectively, indicating a distorted octahedral structure about Mn(II) ion [71-73]. The Co(II) complex displayed peak at 752 nm (13298 cm^{-1}; ε_{max}= 107 dm^3 mol^{-1} cm^{-1}) related to $^4T_1g^{(F)} \rightarrow {}^4T_2g^{(F)}$ transition, confirming distorted octahedral geometry about Co(II) centre [74-76]. Bands that detected at 640 nm (15625 cm^{-1}; ε_{max}= 77 dm^3 mol^{-1} cm^{-1}) and 839 nm (11919 cm^{-1}; ε_{max}= 112 dm^3 mol^{-1} cm^{-1}) in the Ni(II)-complex are related to transitions type $^3A_2g \rightarrow {}^3T_2g^{(F)}$ and $^3A_2g \rightarrow {}^3T_1g^{(F)}$ respectively [77]. The d-d electronic transition at 740 nm (13514 cm^{-1}; ε_{max}= 52 dm^3 mol^{-1} cm^{-1}) of the Cu(II) complex attributed to $^2B_1g \rightarrow {}^2B_2g$ transition, which may demonstrate distorted square planar geometry [78]. Further, the spectrum of the [Zn(L^6)$_2$], indicated two intense bands at 295 nm (33898 cm^{-1}; ε_{max}= 1064 dm^3 mol^{-1} cm^{-1}) and 390 nm (25641 cm^{-1}; ε_{max}= 976 dm^3 mol^{-1} cm^{-1}) related to the intra-ligand field transitions, confirming tetrahedral geometry around Zn centre [79]. The chart of [Cd(L^6)$_2$], showed bands at 276 nm (36232 cm^{-1}; ε_{max}= 1123 dm^3 mol^{-1} cm^{-1}) and 302 nm (33113 cm^{-1}; ε_{max}= 1645 dm^3 mol^{-1} cm^{-1}) due to the intra-ligand field, indicating tetrahedral geometry around Cd centre [80]. The electronic data with the proposed structure of the compounds are listed in Table (3-24).
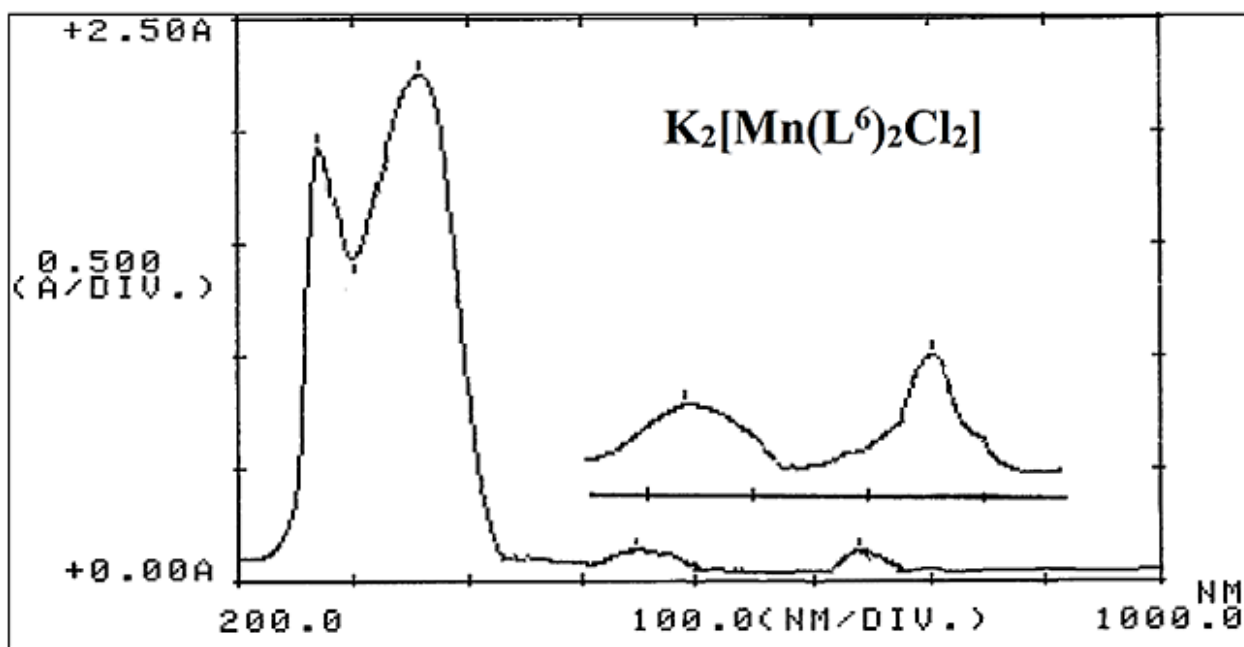
Figure (3-128): UV-Vis of K$_2$[Mn(L^6)$_2$Cl$_2$] in DMSO solvent.
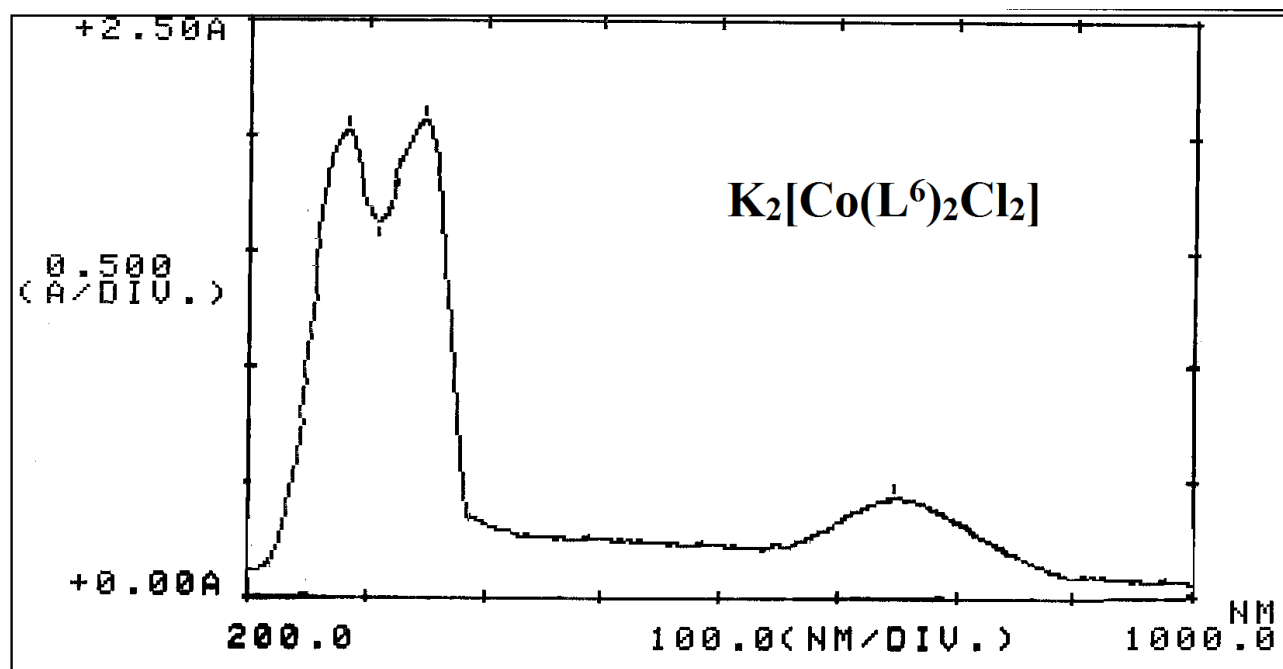
Figure (3-129): UV-Vis of K$_2$[Co(L^6)$_2$Cl$_2$] in DMSO solvent.

201
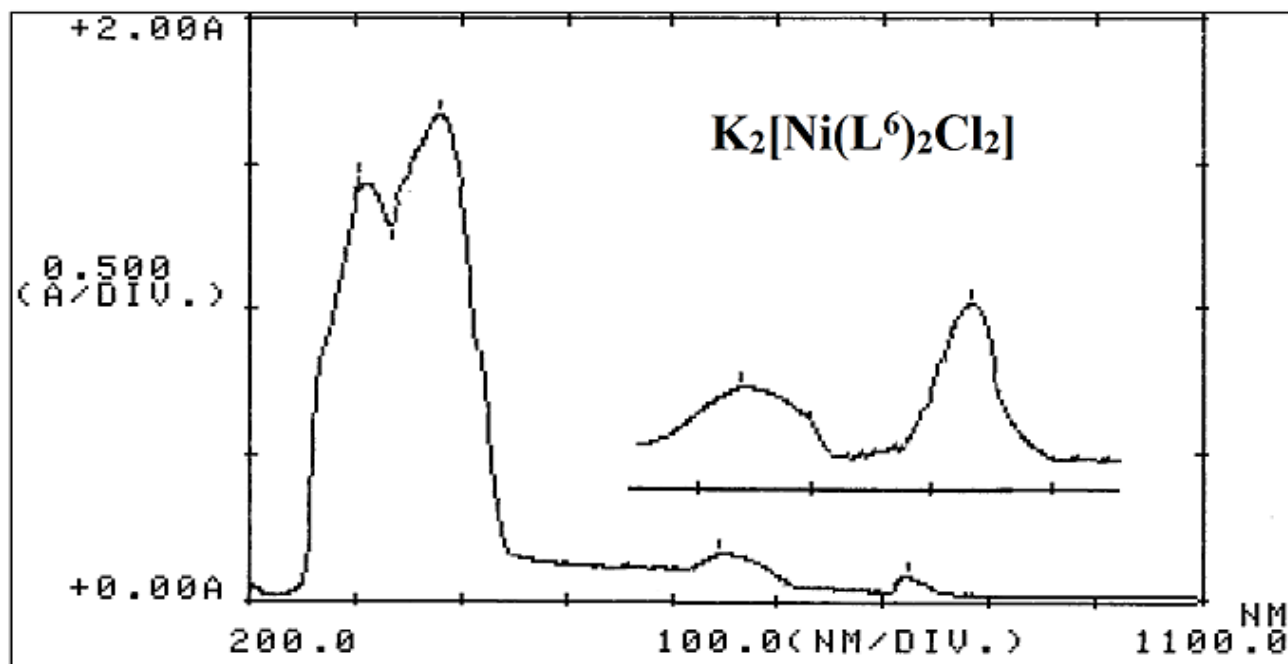
Figure (3-130): UV-Vis of K$_2$[Ni(L^6)$_2$Cl$_2$] in DMSO solvent.
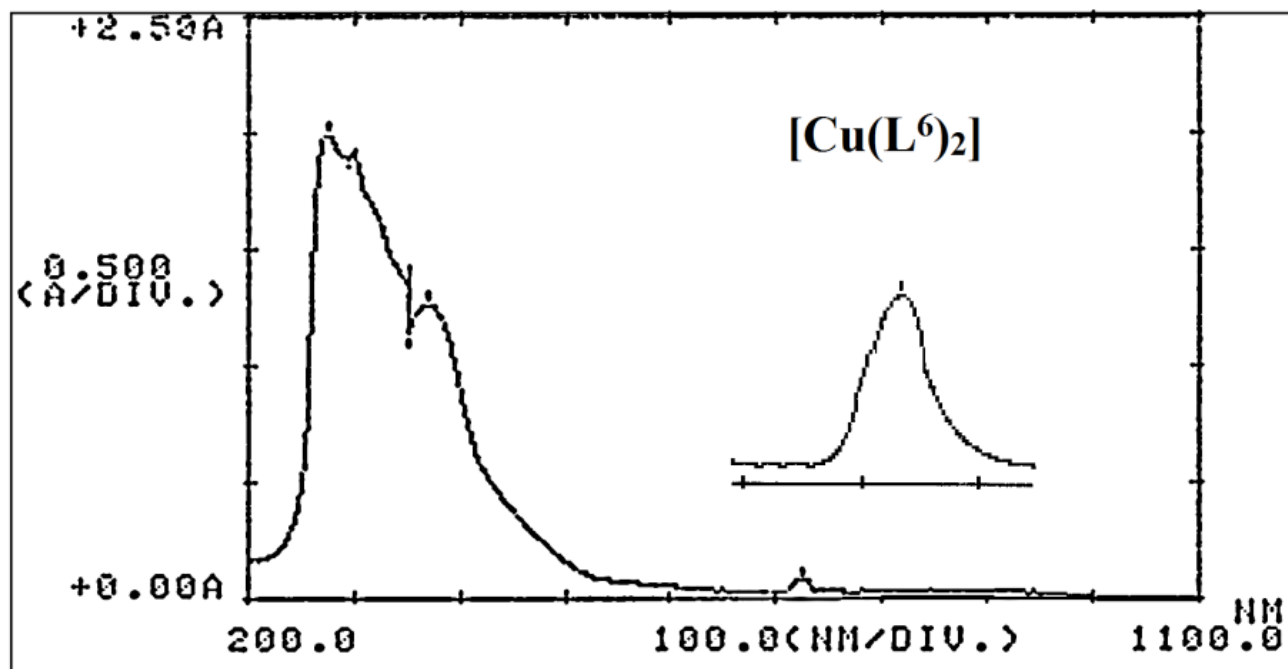
Figure (3-131): UV-Vis of [Cu(L^6)$_2$] in DMSO solvent.

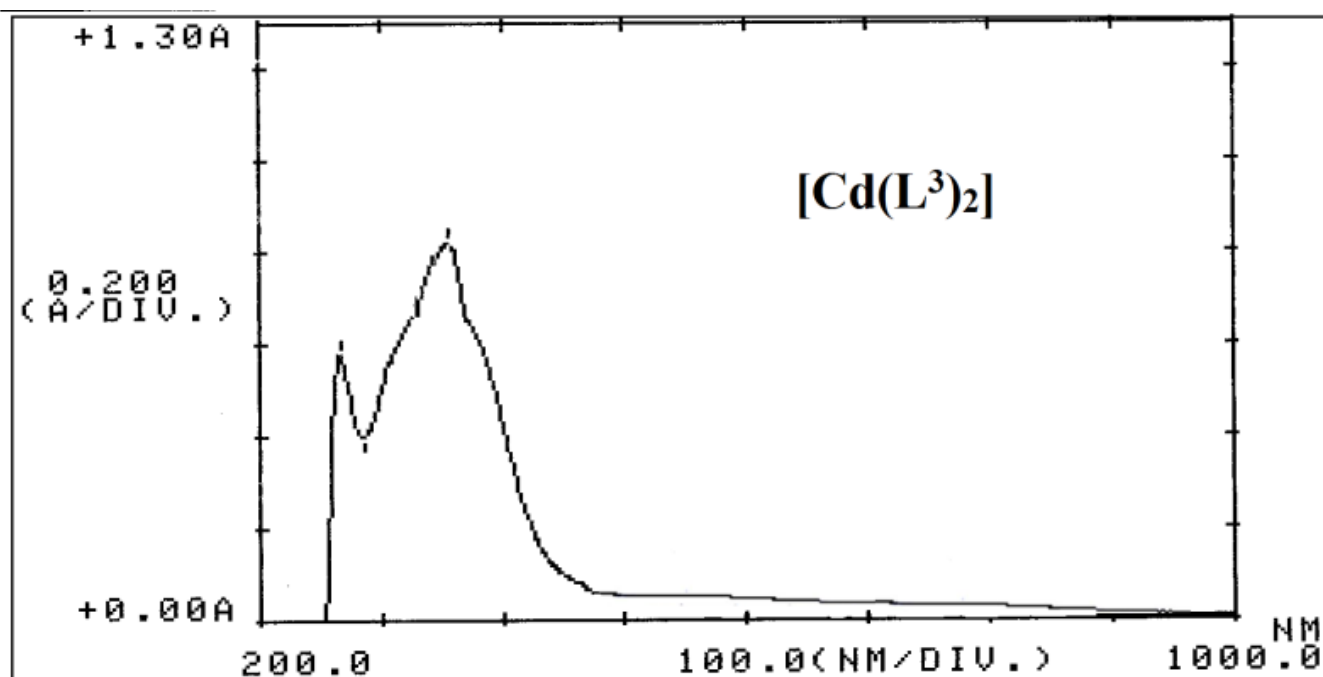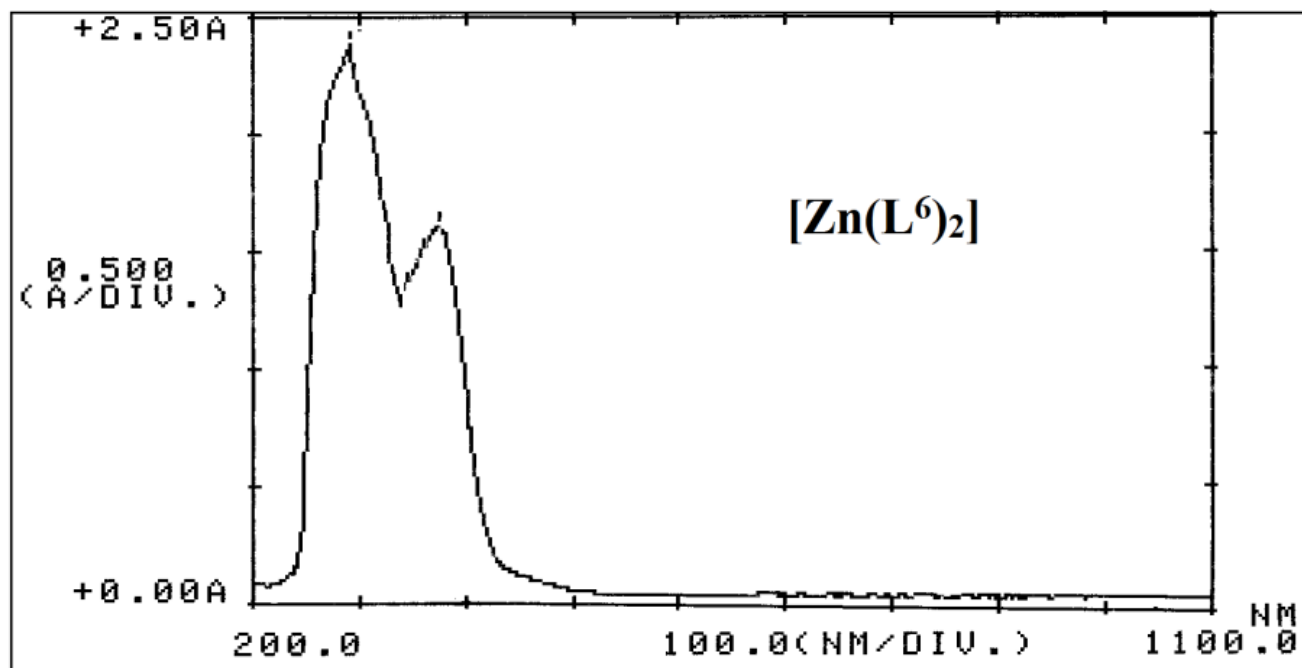**Figure (3-132): UV-Vis of [Zn(L^6)$_2$] in DMSO solvent.**
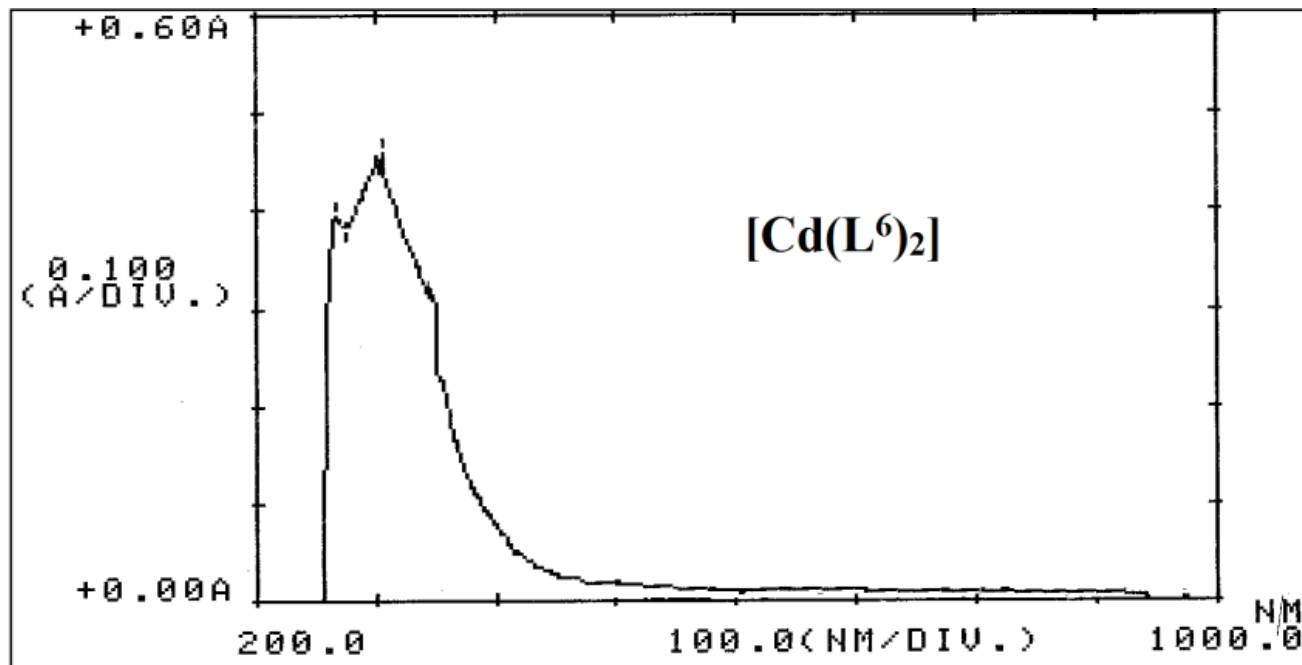
Figure (3-133): UV-Vis of [Cd(L^6)$_2$] in DMSO solvent.

Table (3-24): Electronic data of HL^6 complexes in DMSO solutions.

Compound	Peak position λnm	Wave number (cm^{-1})	Molar extinction coefficient ε_{max} $(dm^3\ mol^{-1}\ cm^{-1})$	Assignment	Suggested structure
HL^6	272	36765	1443	$\pi \rightarrow \pi^*$	
	318	31447	1366	$n \rightarrow \pi^*$	
$K_2[Mn(L^6)_2Cl_2]$	279	35842	876	$\pi \rightarrow \pi^*$	Distorted octahedral
	363	27548	1098	$n \rightarrow \pi^*$	
	540	18519	39	$^6A_1g^{(F)} \rightarrow {}^4T_2g^{(G)}$	
	766	13055	87	$^6A_1g^{(F)} \rightarrow {}^4T_1g^{(G)}$	
$K_2[Co(L^6)_2Cl_2]$	294	34014	988	$\pi \rightarrow \pi^*$	Distorted octahedral
	352	28409	846	$n \rightarrow \pi^*$	
	752	13298	107	$^4T_1g^{(F)} \rightarrow {}^4T_2g^{(F)}$	
$K_2[Ni(L^6)_2Cl_2]$	298	33557	769	$\pi \rightarrow \pi^*$	Distorted octahedral
	380	26316	879	$n \rightarrow \pi^*$	
	640	15625	77	$^3A_2g \rightarrow {}^3T_2g^{(F)}$	
	839	11919	112	$^3A_2g \rightarrow {}^3T_1g^{(F)}$	
$[Cu(L^6)_2]$	281	35587	1234	$\pi \rightarrow \pi^*$	Square planar
	376	26596	968	$n \rightarrow \pi^*$	
	740	13514	52	$^2B_1g \rightarrow {}^2B_2g$	
$[Zn(L^6)_2]$	295	33898	1064	$\pi \rightarrow \pi^*$	Tetrahedral
	390	25641	976	$n \rightarrow \pi^*$	
$[Cd(L^6)_2]$	276	36232	1123	$\pi \rightarrow \pi^*$	Tetrahedral
	302	33113	1645	$n \rightarrow \pi^*$	

(3.10) ^1H- and ^{13}C-NMR spectra of complexes

(3.10.1) ^1H-NMR of $[Zn(L^1)_2]$

The $[Zn(L^1)_2]$ spectra is recorded in DMSO-d^6 and exhibited in Figure (3-134). The ^1H-NMR indicates a peak at 1.25 ppm (4H, m) corresponding to 2 x (C_{10}-H). The signals detected at 1.66, 2.33, 2.82 and 2.94 ppm assigned to 2 x [($C_{9,9'}$-H; 4H, m), (N1-H; 1H, s), ($C_{8,8'}$-H; 2H, m) and ($C_{7,7'}$-H; 2H, d, J_{HH}= 4 Hz)], individually. Peak recorded at 5.02 ppm, which equivalent to four protons due to 2 x (N4-H; 2H, s) group. Resonance detected at 7.59 ppm related to 2 x ($C_{3,3',5,5'}$-H; 4H, d, J_{HH}= 12 Hz). A chemical shift at 7.41 ppm

attributed to 2 x ($C_{1,1'}$-*H*; 2H, t, J_{HH}= 12 Hz). This peak appeared as expected triplet as a result of rigidity that occurred upon complexation, in comparison with that recorded in HL[1] at 7.30 ppm. A peak observed at 7.30 ppm assigned to 2 x ($C_{2,2',6,6'}$-*H*; 2H, t, J_{HH}= 12 Hz). The spectrum indicated no signal could attribute to (N3-*H*), compared with that in the spectrum of the free ligand confirming the deprotonation of the ligand upon complexation. Accordingly, the Se atom bound to the Zn(II) ion in its selenide form. This result is in accordance with that observed in the FT-IR data (see page 142) indicated the complex behaves in a similar fashion in solution and solid state, upon coordination to the metal centre. The ^{1}H-NMR spectral data are tabulated in Table (3-25).
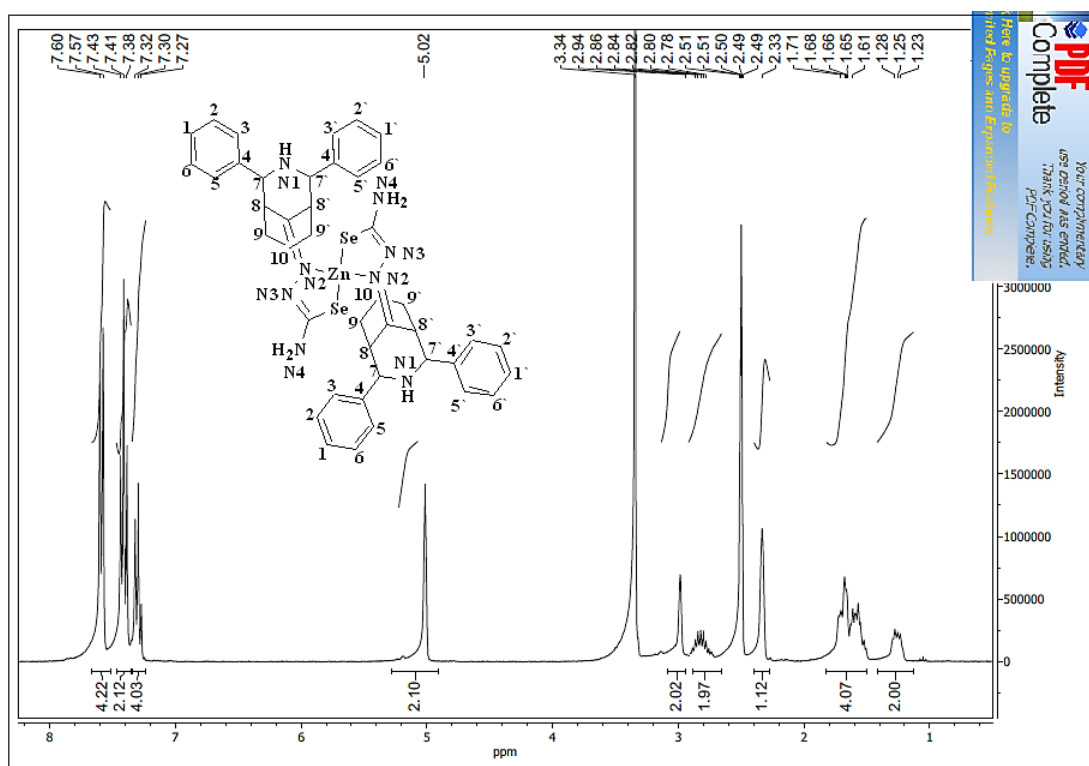
Figure (3-134): ^{1}H-NMR chart of [Zn(L[1])$_2$] in DMSO-d[6].

(3.10.2) ^{1}H-NMR of [Cd(L^1)$_2$]

The ^{1}H-NMR, in DMSO-d^6, of [Cd(L^1)$_2$] is shown in Figure (3-135). This spectrum exhibits almost a similar pattern of signals to that of [Zn(L^1)$_2$] and a same explanation may be used to interpret the spectrum. The spectrum recorded no peak could assign to (N3-*H*), indicating the Se atom adopts selenide form upon complexation to the metal centre. This behaviour has observed in solution and solid state, see page 142. The ^{1}H-NMR peaks of the Cd(II) complex are included in Table (3-25).
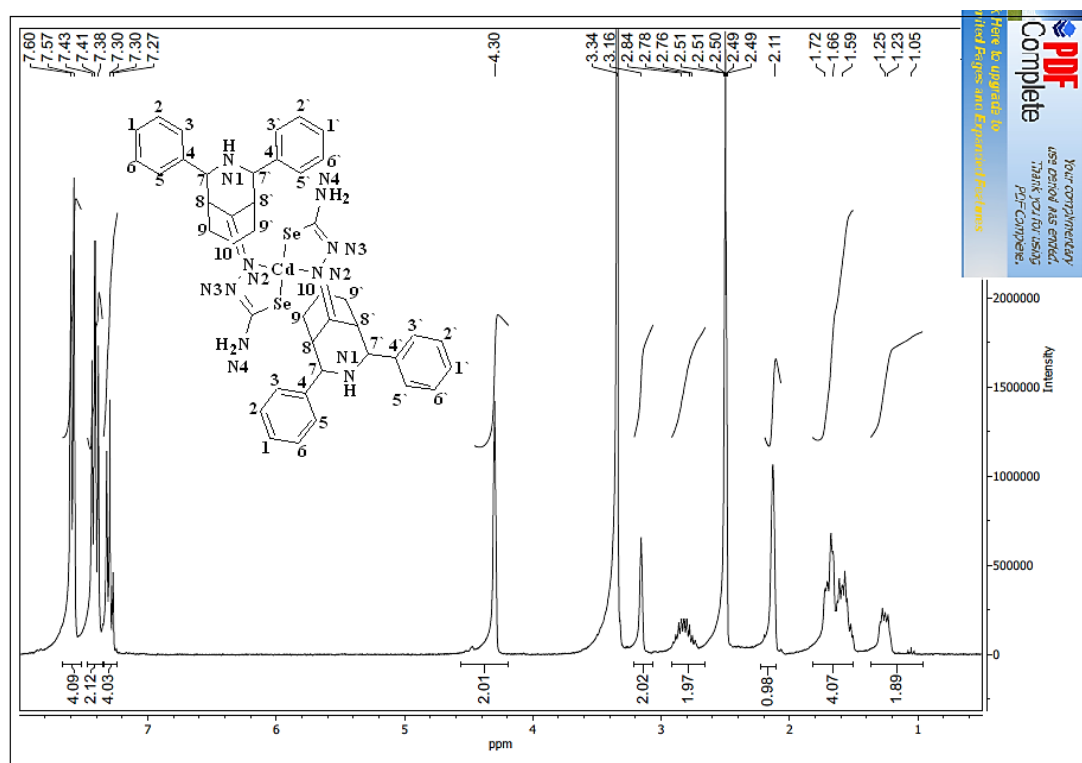
Figure (3-135): ^{1}H-NMR chart of [Cd(L^1)$_2$] in DMSO-d^6.

206

(3.10.3) ^{1}H-NMR of $[Zn(L^2)_2]$

The ^{1}H-NMR spectrum of $[Zn(L^2)_2]$ complex is acquired in DMSO-d^6 solvent and placed in Figure (3-136). A peak at δ_H= 1.24 ppm (4H, m) attributed to 2 x (C$_{10}$-*H*) protons. Signals related to 2 x [(C$_{9,9`}$-*H*; 4H, m), (C$_{8,8`}$-*H*; 2H, m), (C$_{7,7`}$-*H*; 2H, d, J_{HH}= 8 Hz) and (2 x OCH$_3$; 6H, s)] groups, appeared at 1.72, 2.38, 2.66 and 2.82 ppm, respectively.

The singlet peak equivalent to two proton that assigned to 2 x (N1-*H*) groups is recorded at δ_H= 3.05 ppm (2H, s). Further, protons related to 2 x (N4-*H*) groups is shown as singlet at δ_H= 4.65 ppm (4H, s). In the aromatic region, the chemical shift at 7.15 ppm related to 2 x (C$_{3,3`,5,5`}$-*H*; 4H, d, J_{HH}= 12 Hz), which displayed as doublet. This peak appeared upfield, in comparison to that in HL^2 at 7.59 ppm, indicating complex formation. The peak at 6.54 ppm, which equivalent to eight protons assigned to 2 x (C$_{2,2`,6,6`}$-*H*; 4H, d, J_{HH}= 12 Hz). The spectrum indicated no signal could attribute to (N3-*H*), confirming the deprotonation of the ligand and the C-Se group adopts a selenide form upon complex formation. The ^{1}H-NMR data are included in Table (3-25).
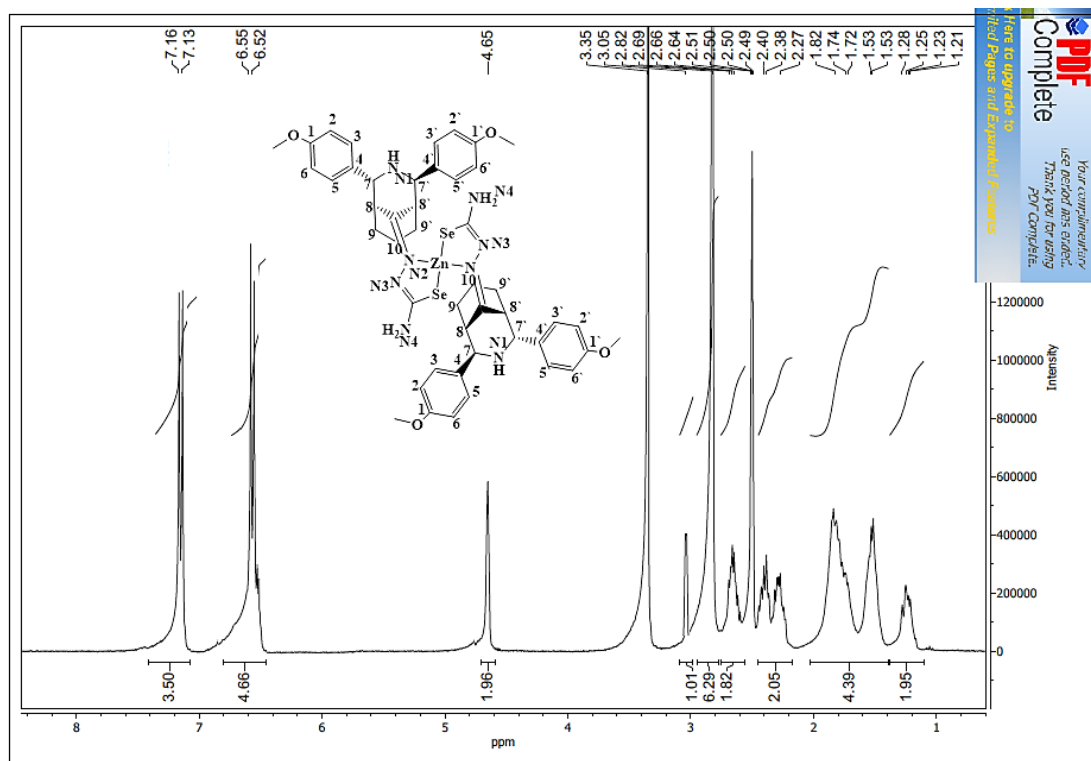
Figure (3-136): ^{1}H-NMR chart of [Zn(L^2)$_2$] in DMSO-d^6.

(3.10.4) ^{1}H-NMR of [Cd(L^2)$_2$]

The ^{1}H-NMR of [Cd(L^2)$_2$] is showed in DMSO-d^6 solvent and included in Figure (3-137). The spectrum exhibited almost a similar pattern of signals to that of [Zn(L^2)$_2$] complex. The chemical shift that corresponds to 2 x (C$_{3,3`,5,5`}$-H; 4H, d, J_{HH}= 12 Hz) detected at 7.21 ppm. This chemical shift appeared at a higher upfield than that in the free ligand at 7.59 ppm. The spectrum indicated the deprotonation of the ligand, no signal could be assigned to (N3-H), and the C-Se moiety adopts a selenide fashion upon complex formation. The ^{1}H-NMR data are included in Table (3-25).
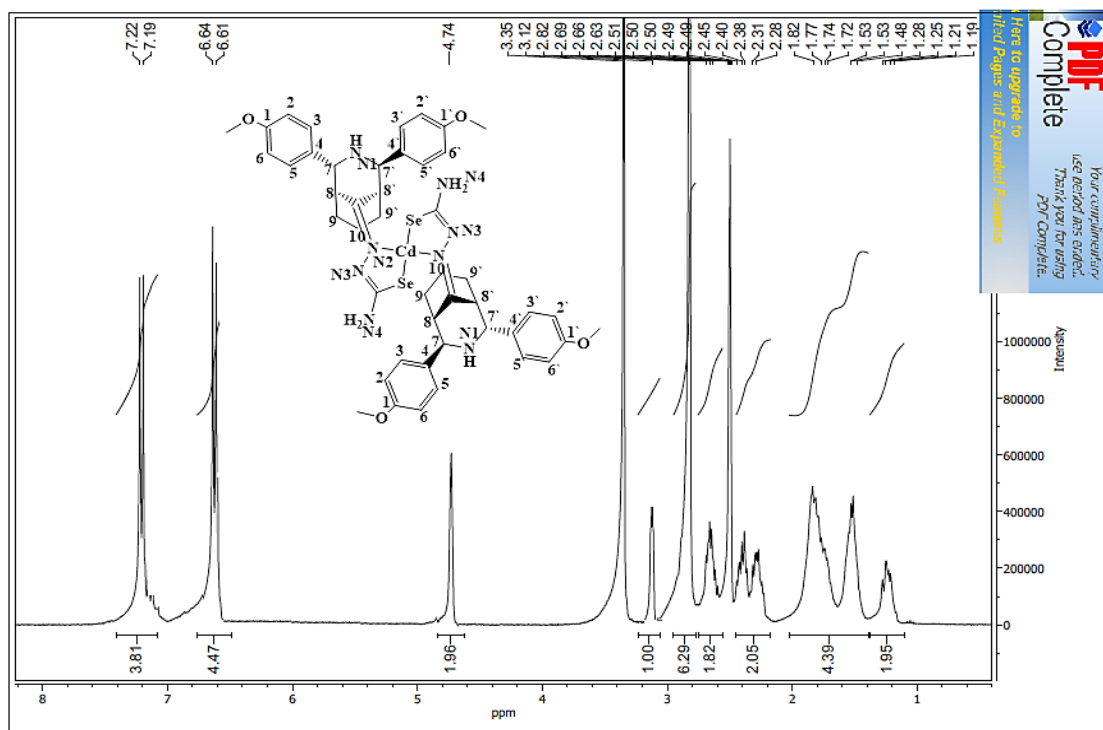
Figure (3-137): ^{1}H-NMR chart of [Cd(L^2)$_2$] in DMSO-d^6.

(3.10.5) ^{1}H-NMR of [Zn(L^3)$_2$]

The [Zn(L^3)$_2$] complex NMR is acquired in DMSO-d^6 solvent and placed in Figure (3-138). The recorded data revealed a two set of signal, in the aromatic and aliphatic region. The chemical shift noticed at δ_H= 1.25 ppm (4H, m) correlated to 2 x (C$_{10}$-H) protons of the cyclohexyl segment. Peaks detected at 1.61, 2.78, 2.98 and 3.75 ppm related to 2 x [(C$_{9,9`}$-$H$; 4H, m), (C$_{8,8`}$-H; 2H, m), (C$_{7,7`}$-H; 2H, d, J_{HH}= 4 Hz) and (2 x (NCH$_3$)$_2$; 12H, s)] protons, respectively. The peak recorded at 2.26 ppm (2H, s), equivalent to two proton, is assigned to 2 x (N1-H) groups. More, protons assigned to 2 x (N4-H) groups appeared as singlet at δ_H= 4.22 ppm (4H, s). The doublet peaks recorded at 7.48 and 6.97 ppm attributed to 2 x [(C$_{3,3`,5,5`}$-H; 4H, d, J_{HH}= 8 Hz) and (C$_{2,2`,6,6`}$-H; 4H, d, J_{HH}= 12 Hz)],

209

respectively. The spectrum indicated no signal could attribute to (N3-*H*), confirming the anionic behaviour of the ligand and the C-Se moiety adopts a selenide fashion upon complex formation. The ^{1}H-NMR resonances are tabulated in Table (3-25).
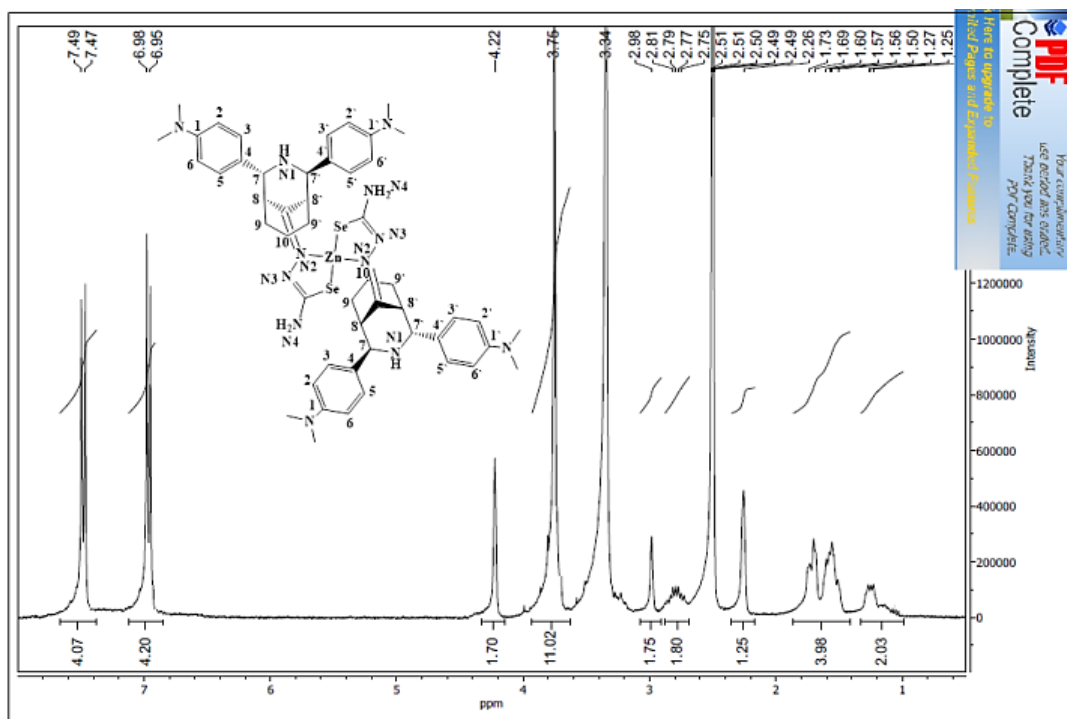
Figure (3-138): ^{1}H-NMR chart of [Zn(L^3)$_2$] in DMSO-d^6.

(3.10.6) ^{1}H-NMR of [Cd(L^3)$_2$]

The spectrum in DMSO-d^6 solution of [Cd(L^3)$_2$] complex is shown in Figure (3-139). This revealed a similar pattern to that of [Zn(L^3)$_2$] and an analogue explanation may be implemented to discuss the spectrum. Furthermore, the spectrum indicated no peak around 8.01 ppm may attribute to (N3-*H*), which confirms the Se atoms bound to the metal centre in its selenide form. The ^{1}H-NMR resonances are tabulated in Table (3-25).
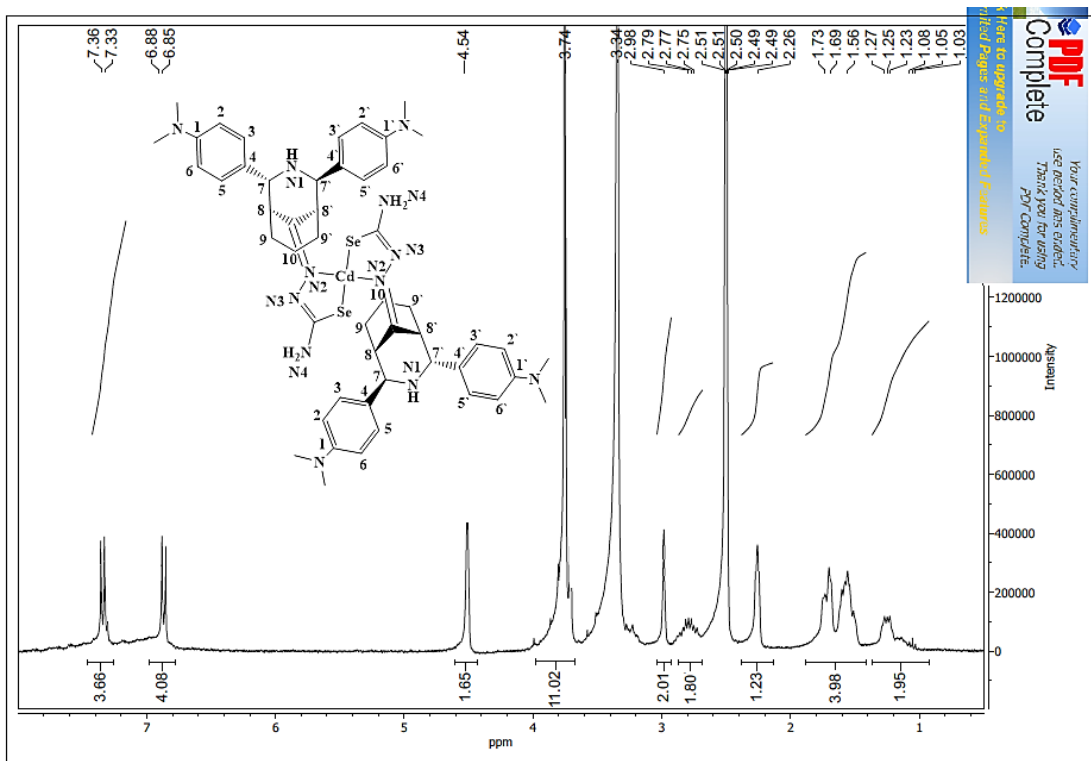
Figure (3-139): ^{1}H-NMR chart of [Cd(L^3)$_2$] in DMSO-d^6.

Table (3-25): ^{1}H-NMR data of HL^1-HL^3 and their complexes with their resonances in ppm (δ).

Compound	(C$_{7,7'}$-H)	(C$_{8,8'}$-H) (C$_{9,9'}$-H)	(C10-H)	(C$_{1,1'}$-H)	(C$_{2,2',6,6'}$-H) (C$_{3,3',5,5'}$-H)	(N1-H)	(N3-H)	(N4-H)	(2 x OCH$_3$) (2 x N(CH$_3$)$_2$)
HL^1	2.22	2.82 1.62	1.25	7.30	7.41 7.60	1.82	8.11	4.97	− −
[Zn(L^1)$_2$]	2.94	2.82 1.66	1.25	7.41	7.30 7.59	2.33	−	5.02	−
[Cd(L^1)$_2$]	3.16	2.78 1.66	1.23	7.41	7.29 7.59	2.11	−	4.30	−
HL^2	3.06	2.79 1.61	1.25	−	6.87 7.59	1.98	7.96	4.63	3.76 −
[Zn(L^2)$_2$]	2.66	2.38 1.72	1.24	−	6.54 7.15	3.05	−	4.65	2.82 −
[Cd(L^2)$_2$]	2.66	2.38 1.72	1.23	−	6.63 7.21	3.12	−	4.74	2.82 −
HL^3	3.01	2.79 1.61	1.25	−	7.00 7.48	1.97	8.01	4.12	− 3.76
[Zn(L^3)$_2$]	2.98	2.78 1.61	1.25	−	6.97 7.48	2.26	−	4.22	− 3.75
[Cd(L^3)$_2$]	2.98	2.77 1.69	1.15	−	6.87 7.35	2.26	−	4.54	− 3.74

(3.10.7) ^{1}H-NMR of [Zn(L^4)$_2$]

The spectrum, in DMSO-d^6 solvent, of [Zn(L^4)$_2$] is depicted in Figure (3-140). The complex revealed peaks in the aliphatic region at δ_H= 1.22, 1.52, 1.85 and 2.35 ppm assigned to 2 x [(C$_4$-*H*; 2H, m), (C$_5$-*H*; 2H, m), (C$_3$-*H*; 2H, m) and (C$_6$-*H*; 2H, m)], respectively. In addition, the two peaks detected at δ_H= 2.74 and 4.77 ppm assigned to 2 x [(C$_2$-*H*; 1H, m) and (C$_7$-*H*; 1H, dd, J_{HH}= 12, 8 Hz)], respectively. A peak equivalent to four protons observed at δ_H= 4.39 ppm (2H, s) assigned to 2 x (N4-*H*) groups. The peak related to 2 x (N1-*H*) recorded as doublet at δ_H= 6.04 ppm (2H, d, J_{HH}= 8 Hz). The spectrum showed peaks δ_H= 7.35 and 7.40 ppm due to 2 x [(C$_{11}$-*H*; 1H, d, J_{HH}= 12 Hz) and (C$_9$-*H*; 1H, s)] groups, respectively. The protons of 2 x [(C$_{12}$-*H*, 1H, dd, J_{HH}= 12, 12 Hz) and (C$_{13}$-*H*, 1H, d, J_{HH}= 12 Hz)] appeared at 7.27 and 7.17 ppm, respectively. These peaks have moved downfield, compared with that observed in HL^4 at 7.26 and 6.92 ppm, respectively. A signal observed at δ_H= 6.94 ppm assigned to 2 x (C$_{17}$-*H*; 1H, t, J_{HH}= 8 Hz) proton. The signals at 6.54 and 6.44 ppm related to 2 x [(C$_{15,15`}$-*H*; 2H, d, $J_{HH}$= 12 Hz) and (C$_{16,16`}$-*H*; 2H, dd, J_{HH}= 8, 12 Hz)], respectively. The spectrum indicated no signal may attribute to (N3-*H*), confirming the Se atom adopts the selenide form upon complexation. The ^{1}H-NMR resonances are shown in Table (3-26).
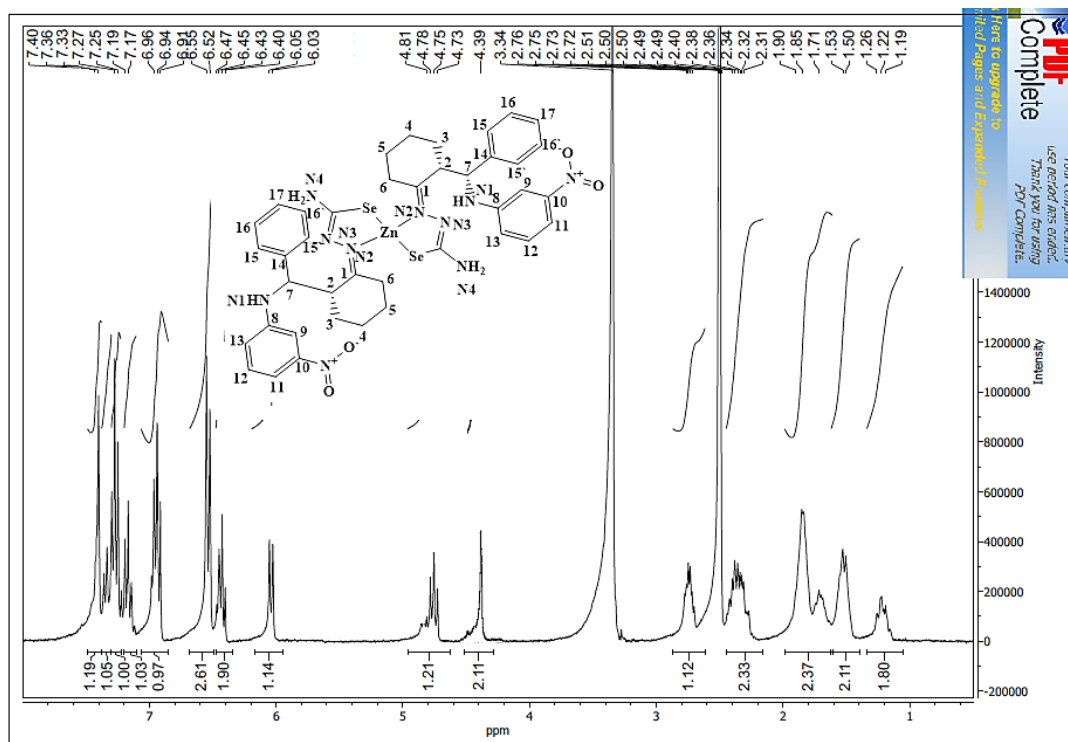
Figure (3-140): ^{1}H-NMR chart of [Zn(L^4)$_2$] in DMSO-d^6.

(3.10.8) ^{1}H-NMR of [Cd(L^4)$_2$]

The [Cd(L^4)$_2$], in DMSO-d^6, is included in Figure (3-141). The spectrum is almost similar to the spectrum of [Zn(L^4)$_2$] complex. Therefore, a similar reasoning that used in the discussion of the Zn(II)-complex can be used to explain the chemical shifts detected in the spectrum of Cd(II)-complex. The ^{1}H-NMR results are shown in Table (3-26).

214
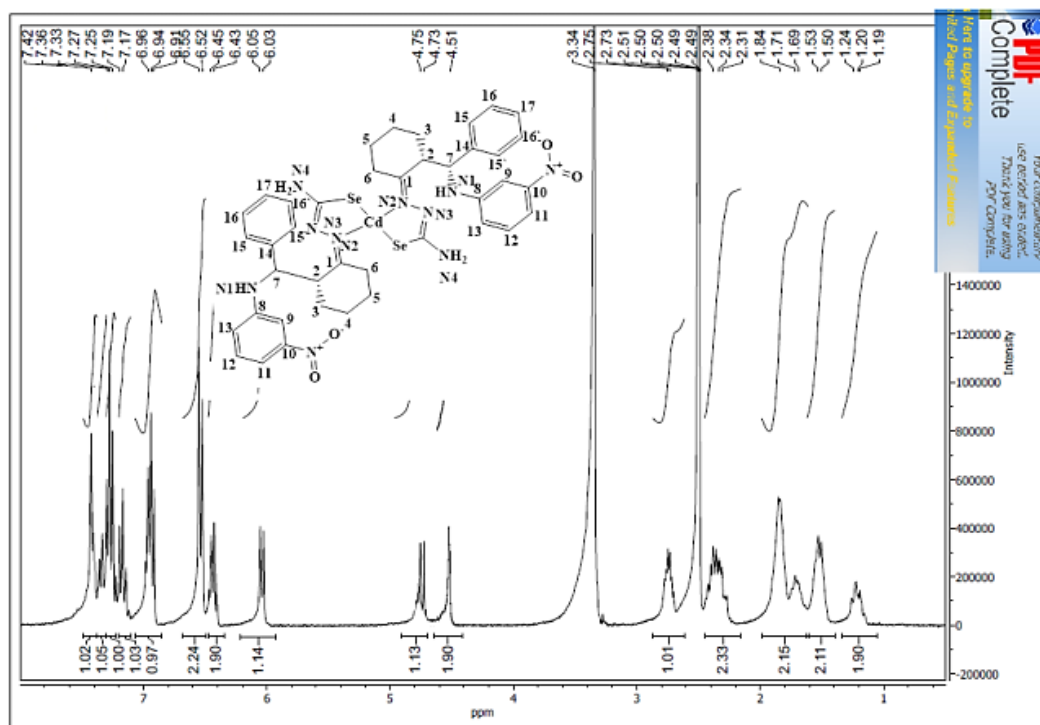
Figure (3-141): ^{1}**H-NMR chart of [Cd(L^4)$_2$] in DMSO-d^6.**

(3.10.9) ^{1}H-NMR of [Zn(L^5)$_2$]

The ^{1}H-NMR, in DMSO-d^6 solution, of [Zn(L^5)$_2$] is located in Figure (3-142). The Zn(II)-complex recorded a set of multiple chemical shifts in the aliphatic region at 1.21, 1.51, 1.77 and 2.36 ppm assigned to 2 x [(C$_4$-H; 2H, m), (C$_5$-H; 2H, m), (C$_3$-H; 2H, m) and (C$_6$-H; 2H, m)] groups, respectively. The signal at δ_H= 2.68 ppm (1H, m) assigned to 2 x (C$_2$-H) groups. The singlet peak of the (2 x methoxy) moiety appeared at δ_H= 3.69 ppm (6H, s). A peak equivalent to four protons that detected at δ_H= 4.37 ppm (2H, s) is related to 2 x (N4-H) groups. A doublet of doublet chemical shift at δ_H= 4.72 ppm is related to 2 x (C$_7$-H; 1H, dd, J_{HH}= 12, 12 Hz). The 2 x (N1-H, 1H, d, J_{HH}= 12 Hz) detected at δ_H= 5.98 ppm. A resonances recorded at δ_H= 7.33 ppm assigned to 2 x (C$_{13,13'}$-H; 2H, d, J_{HH}= 12 Hz), this peak is seen upfield compared with that recorded in HL^5 at 7.43 ppm. The

215

spectrum indicated the 2 x ($C_{10,10'}$-H; 2H, dd, J_{HH}= 12, 8 Hz) chemical shift at δ_H= 6.94 ppm. Further, peaks observed at 6.84 and 6.54 ppm attributed to 2x [($C_{14,14'}$-H; 2H, d, J_{HH}= 12 Hz) and ($C_{9,9'}$-H; 2H, d, J_{HH}= 12 Hz)], respectively. Finally, the chemical shift at δ_H= 6.43 ppm assigned to [(C_{11}-H; 1H, t, J_{HH}= 8 Hz)] proton. The spectrum indicated no proton may assign to (N3-H), compared with that in HL^5, confirming the C-Se segment adopts a selenide fashion upon complex formation. The ^{1}H-NMR resonances are shown in Table (3-26).
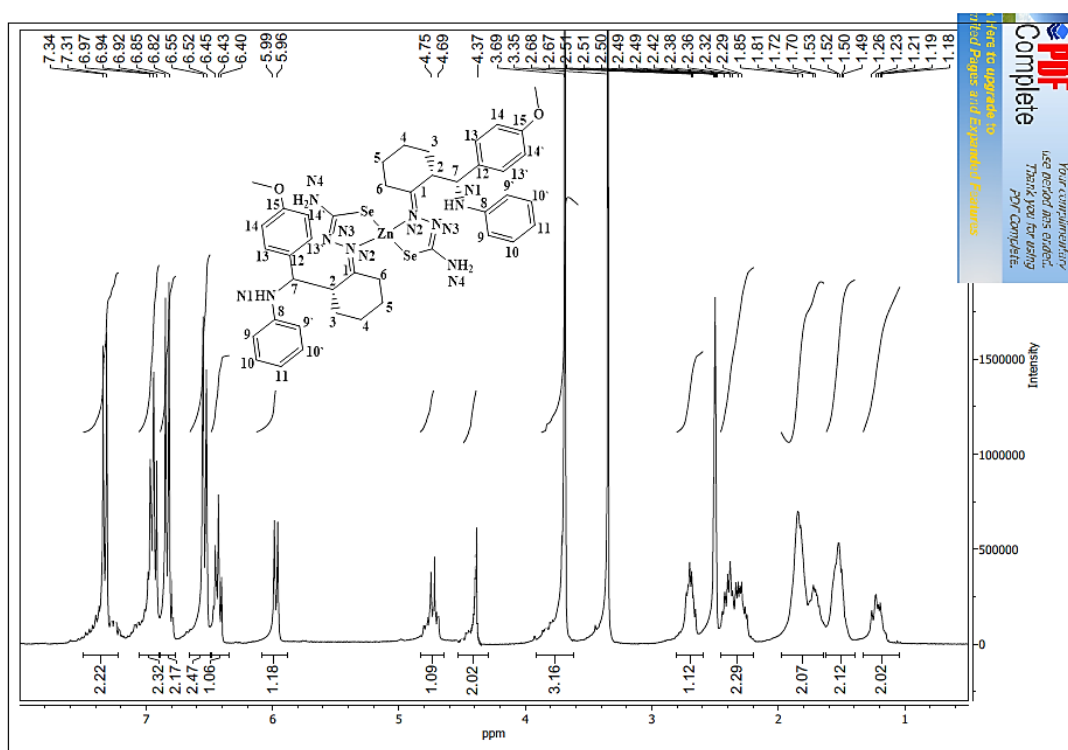
Figure (3-142): ^{1}H-NMR chart of [Zn(L^5)$_2$] in DMSO-d^6.

(3.10.10) ^{1}H-NMR of [Cd(L^5)$_2$]

The [Cd(L^5)$_2$] is acquired in DMSO-d^6 and included in Figure (3-143). In general, the Cd(II)-complex displayed an analogue pattern of signals to that recorded in the spectrum of Zn(II)-complex. Therefore, a similar reasoning that used in the discussion of the Zn(II)-complex can be used to explain all chemical shifts that showed in the spectrum of Cd(II)-complex. The obtained data of the ^{1}H-NMR are shown in Table (3-26).
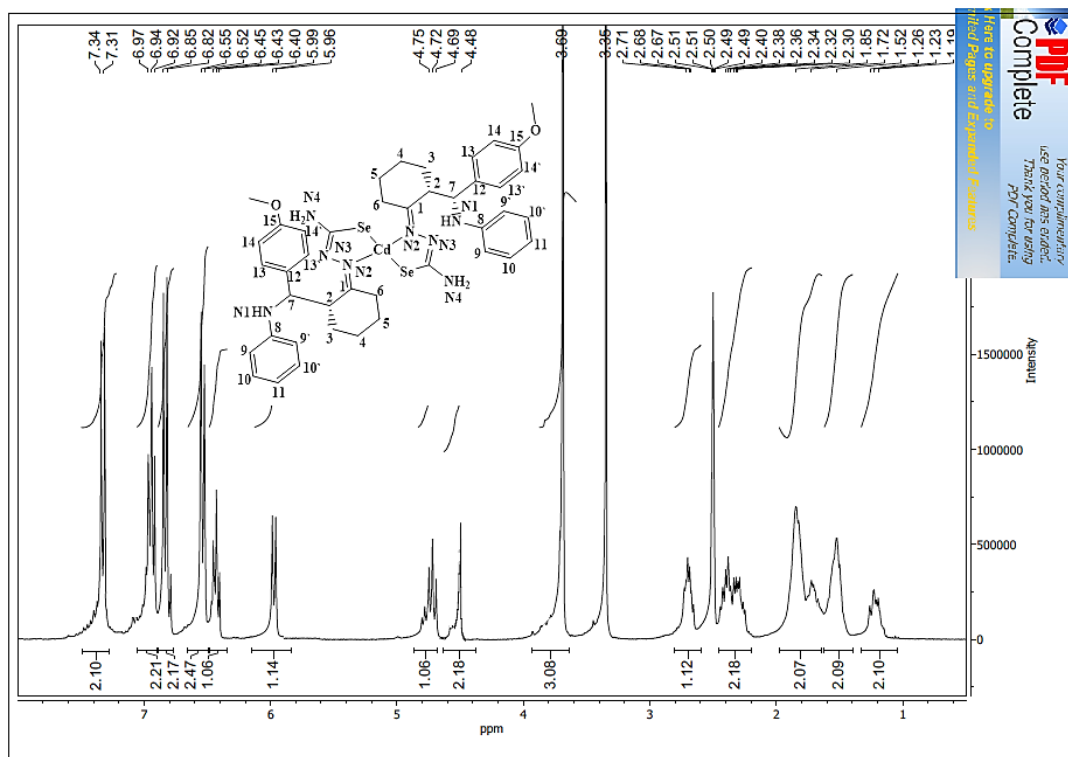
Figure (3-143): ^{1}H-NMR chart of Cd(L^5)$_2$] in DMSO-d^6.

(3.10.11) ^{1}H-NMR of [Zn(L^6)$_2$]

The spectrum, in DMSO-d^6 solution, of [Zn(L^6)$_2$] complex is placed in Figure (3-144). The spectrum revealed a set of multiple peaks in the aliphatic region at 1.05, 1.46, 1.68 and 2.06 ppm that assigned to 2 x [(C$_4$-*H*; 2H, m), (C$_5$-*H*; 2H, m), (C$_3$-*H*; 2H, m) and (C$_6$-*H*; 2H, m)] protons, respectively. The singlet peak observed at δ_H= 2.83 ppm (12H, s) is assigned to metheyl groups (dimethylamino groups of the two ligands). The peak around δ_H= 3.05 ppm (1H, m) assigned to 2 x (C$_2$-*H*) proton. A signal related to 2 x (N4-*H*; 2H, s) observed at δ_H= 4.34 ppm. The doublet of doublet that recorded at δ_H= 4.62 ppm is due to 2 x (C$_7$-*H*; 1H, dd, J_{HH}= 4, 8 Hz). The 2 x (N1-*H*; 1H, d, J_{HH}= 12 Hz) is appeared at δ_H= 5.80 ppm. In the aromatic region, the resonance at δ_H= 7.41 ppm attributed to (2 x C$_9$-*H*; 1H, s), which deshielded in comparison with that in HL^6 at 7.17 ppm. This could be attributed to the influence of the withdrawing groups (NO$_2$ and N(CH$_3$)$_2$). Signal recorded at δ_H= 7.06 and 6.96 ppm attributed to 2 x [(C$_{11}$-*H*; 1H, d, J_{HH}= 8 Hz) and (C$_{12}$-*H*; 1H, dd, J_{HH}= 12, 8 Hz)], respectively. Furthermore, peaks detected at δ_H= 6.48, 6.62 and 6.07 ppm attributed to 2 x [(C$_{13}$-*H*; 1H, d, J_{HH}= 12 Hz), (C$_{15,15'}$-*H*; 2H, d, J_{HH}= 12 Hz) and (C$_{16,16'}$-*H*; 2H, d, J_{HH}= 12 Hz)], respectively. The spectrum showed no signal may assign to (N3-*H*), confirming the C-Se group bound to the Zn centre in its selenide fashion. The ^{1}H-NMR resonances are shown in Table (3-26).
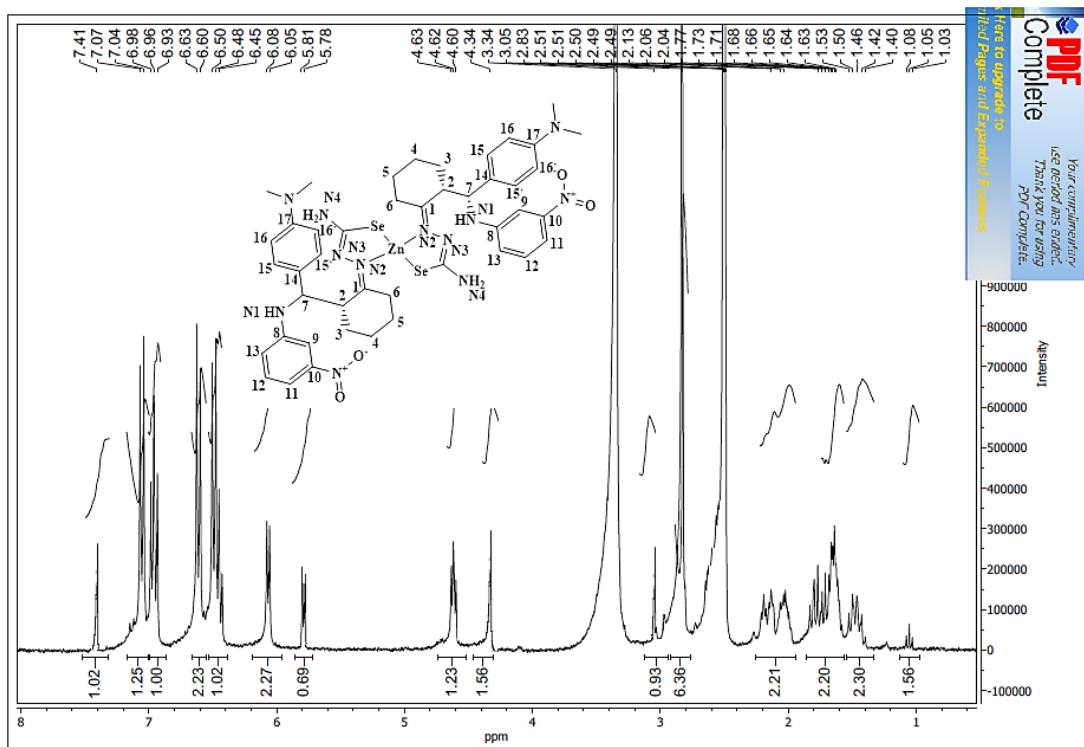
Figure (3-144): ^{1}**H-NMR chart of [Zn(L^6)$_2$] in DMSO-d^6.**

(3.10.12) ^{1}H-NMR of [Cd(L^6)$_2$]

The [Cd(L^6)$_2$] in DMSO-d^6 solvent is exhibited in Figure (3-145). The spectrum displayed almost a similar trend of peaks to that observed in the spectrum of [Zn(L^6)$_2$] complex. Hence, a similar reasoning used to explain the spectrum of Zn(II)-complex may implement to discuss the spectrum of Cd(II)-complex. The ^{1}H-NMR data are shown in Table (3-26).
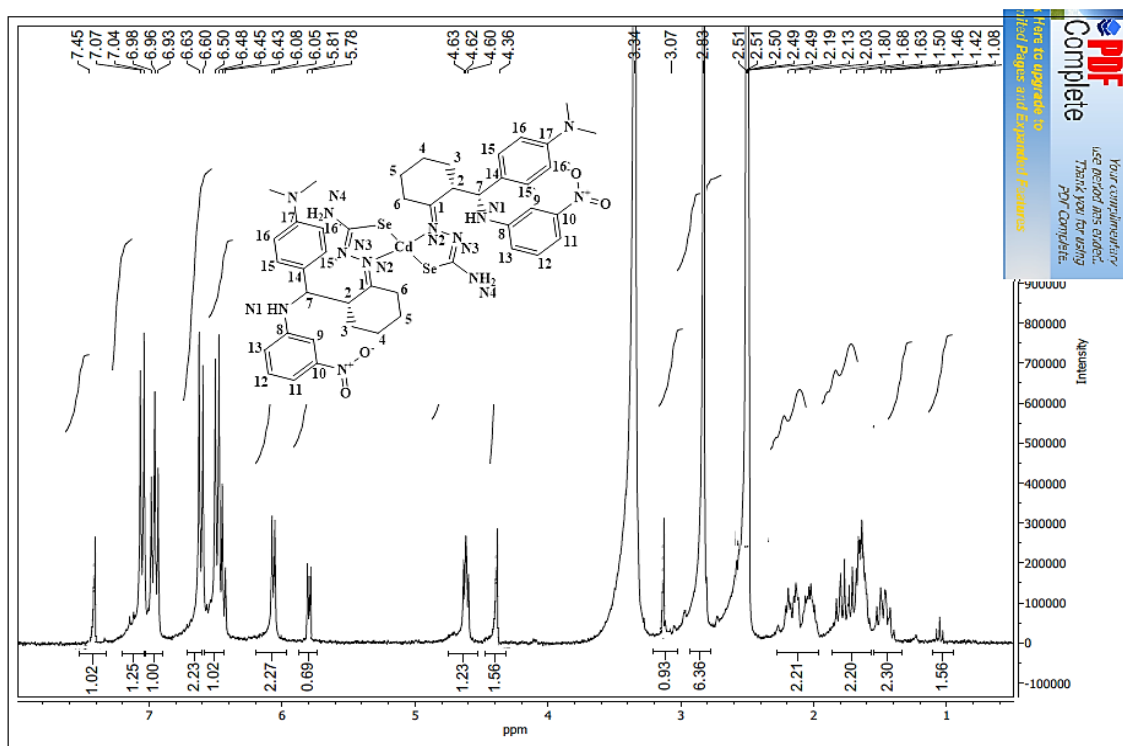
Figure (3-145): ^{1}**H-NMR chart of [Cd(L**^{6}**)**$_2$**] in DMSO-d**^{6}**.**

Table (3-26): ^{1}H-NMR data of HL^4-HL^6 and their complexes with their resonances in ppm (δ).

Compound	(C2-H) (C3-H)	(C4-H) (C5-H)	(C6-H) (C7-H)	(C9-H) (C11-H)	(C12-H) (C13-H)	(C$_{9,9'}$-H) (C$_{10,10'}$-H)	(C$_{13,13'}$-H) (C$_{14,14'}$-H)	(C$_{15,15'}$-H) (C$_{16,16'}$-H)	C17-H)	(N1-H)	(N3-H)	(N4-H)	(2 x OCH$_3$) (2 x N(CH$_3$)$_2$)
HL^4	2.75 1.74	1.22 1.52	2.34 4.78	7.33 7.17	7.26 6.92	– –	– –	6.54 6.43	6.75	6.04	7.75	4.40	– –
[Zn(L^4)$_2$]	2.74 1.85	1.22 1.52	2.35 4.77	7.40 7.35	7.27 7.17	– –	– –	6.54 6.44	6.94	6.04	–	4.39	– –
[Cd(L^4)$_2$]	2.74 1.71	1.20 1.52	2.34 4.74	7.42 7.35	7.27 7.17	– –	– –	6.54 6.44	6.94	6.04	–	4.51	– –
HL^5	2.70 1.83	1.23 1.51	2.36 4.72	– 6.43	– –	6.54 6.97	7.43 6.82	– –	–	5.97	8.12	4.19	3.71 –
[Zn(L^5)$_2$]	2.68 1.77	1.21 1.51	2.36 4.72	– 6.43	– –	6.54 6.94	7.33 6.84	– –	–	5.98	–	4.37	3.69 –
[Cd(L^5)$_2$]	2.68 1.79	1.23 1.52	2.35 4.72	– 6.43	– –	6.54 6.94	7.33 6.84	– –	–	5.98	–	4.48	3.69 –
HL^6	2.65 2.02	1.65 1.76	2.08 4.50	7.17 6.71	6.96 6.49	– –	– –	6.44 6.17	–	5.63	7.36	4.19	– 2.82
[Zn(L^6)$_2$]	3.05 1.68	1.05 1.46	2.06 4.62	7.41 7.06	6.96 6.48	– –	– –	6.62 6.07	–	5.80	–	4.34	– 2.83
[Cd(L^6)$_2$]	3.07 1.68	1.05 1.46	2.13 4.62	7.45 7.06	6.96 6.47	– –	– –	6.62 6.07	–	5.80	–	4.36	– 2.83

(3.10.13) ^{13}C-NMR of [Zn(L^1)$_2$]

The ^{13}C-NMR of [Zn(L^1)$_2$] is recorded in DMSO-d^6 and included in Figure (3-146). A peak that connected to (C$_{10}$) appeared as expected in the aliphatic area at δc= 20.52 ppm. Signals related to (C$_{9,9'}$) and (C$_{7,7'}$) were detected at δc= 28.50 and 53.22 ppm, respectively. A peak recorded at δc= 63.73 ppm attributed to (C$_{8,8'}$) group. Signals that related to (C$_{1,1'}$), (C$_{3,3',5,5'}$) and (C$_{2,2',6,6'}$) were observed at δc= 122.65, 126.85 and 128.22 ppm, respectively. The peak that attributed to (C$_{4,4'}$) was observed in the expected region at δc= 141.77 ppm. Further, a chemical shift at 165.37 ppm is assigned to C=N of the imine moiety. The recorded spectrum indicated that the two imine moieties are equivalent and found downfield, in comparison with that in the free ligand at 161.75 ppm. This is due to the involvement of the imine groups in complexation. More, the recorded signal at 167.86 ppm is related to C-Se group, which suffered upfield shift compared with that in the spectrum of the free ligand that at 172.22 ppm. It is known that, the upfield shifting confirms that the C-Se moiety adopts a selenide fashion in solution [3,12], upon complex formation (compared with that in the free ligand that exists as selenone, see ^{13}C-NMR section (3.3.15), page 92). This phenomenon has also been observed in the solid state (see IR section (3.8.1.2), page 142). The ^{13}C-NMR records are placed in Table (3-27).

222
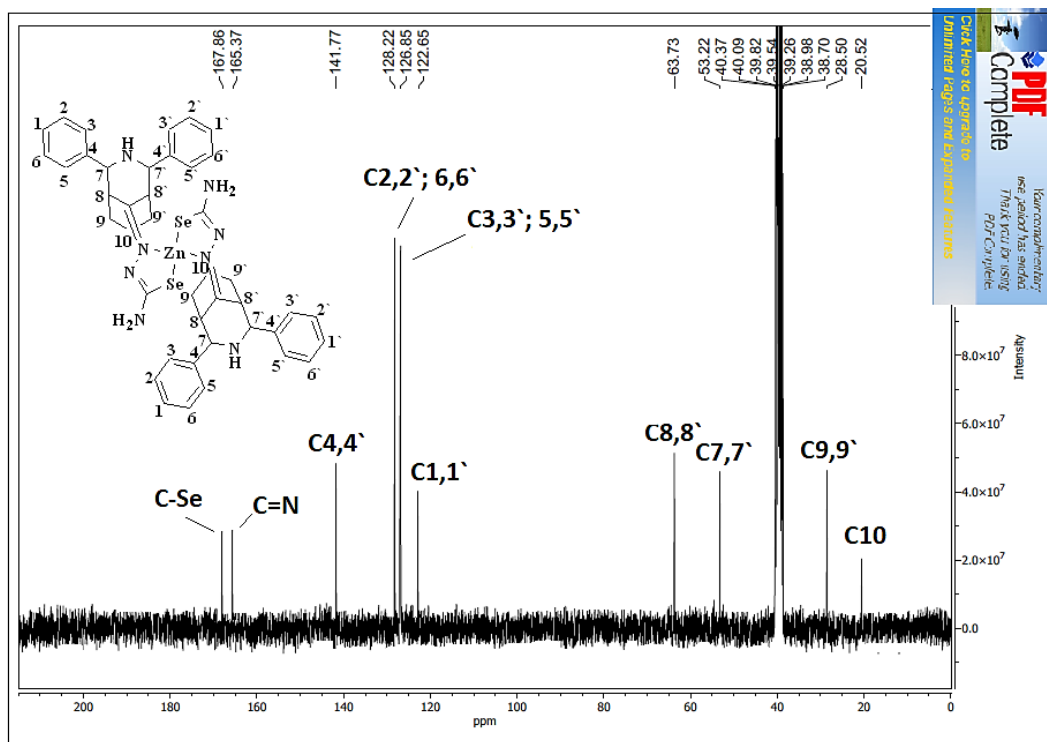
Figure (3-146): ^{13}**C-NMR chart of [Zn(L^1)$_2$] in DMSO-d^6.**

(3.10.14) ^{13}C-NMR of [Cd(L^1)$_2$]

The ^{13}C-NMR of [Cd(L^1)$_2$] is recorded in DMSO-d^6 and placed in Figure (3-147). The spectrum exhibits almost a similar feature to that of [Zn(L^1)$_2$] and an analogue explanation may use to discuss the spectrum. The ^{13}C-NMR data are placed in Table (3-27).
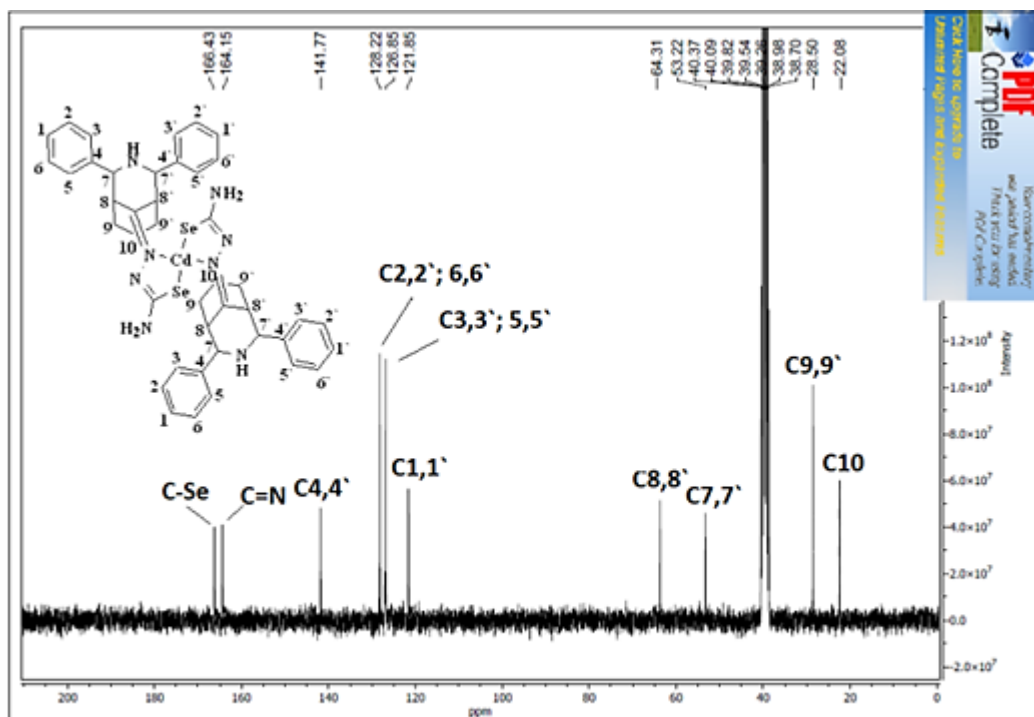
Figure (3-147): ^{13}**C-NMR chart of [Cd(L^1)$_2$] in DMSO-d^6.**

(3.10.15) ^{13}C-NMR of [Zn(L^2)$_2$]

The ^{13}C-NMR of [Zn(L^2)$_2$] is documented in Figure (3-148) and measured in DMSO-d^6 solvent. The spectrum exhibits peaks in the aliphatic and aromatic region. A resonance at δ_C= 22.08 ppm attributed to (C$_{10}$). Peaks detected at 27.12, 47.73 and 53.22 ppm related to (C$_{9,9`}$), (C$_{7,7`}$) and C-dimethoxy, respectively. A signal observed at 63.73 ppm is due to (C$_{8,8`}$) group. Resonances recorded at 114.34, 126.85, 128.22 and 149.84 ppm attributed to (C$_{4,4`}$), (C$_{2,2`,6,6`}$), (C$_{3,3`,5,5`}$) and (C$_{1,1`}$), respectively. Resonance at δ_C= 164.13 ppm assigned to (C=N) imine group. This chemical shift has found downfield, compared with that in HL^2 that at 159.99 ppm, indicating the involvement of the C=N moiety in the coordination to the metal centre. Further, the peak that attributed to C-Se

224

moiety appeared upfield at 166.03 ppm, compared with that in in HL^2 at 170.44 ppm, indicating the involvement of C-Se group in the coordination. The shifting to lower confirms that the C-Se moiety adopts a selenide fashion in solution [3,12], upon complex formation (compared with that in the free ligand that exists as selenone, see ^{13}C-NMR section (3.3.16), page 93). This phenomenon has also been observed in the solid state (see IR section (3.8.2.2), page 148). The appearance of one signal for the imine and C-Se group confirmed the two ligands are equivalents. The ^{13}C-NMR records are placed in Table (3-27).
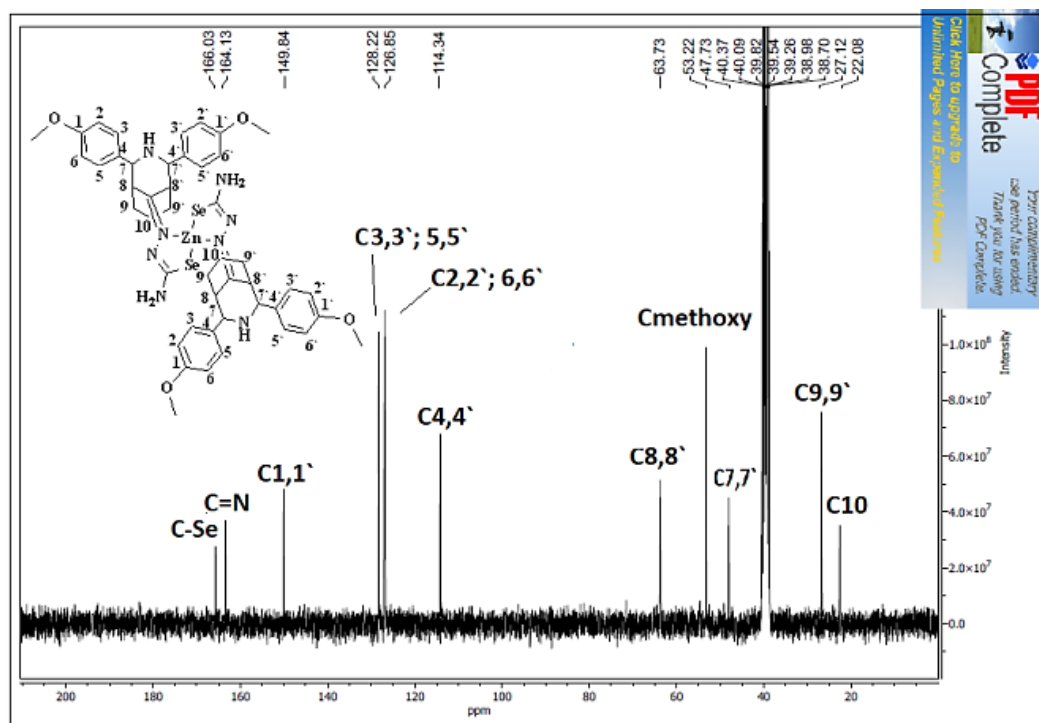
Figure (3-148): [13]**C-NMR chart of** $[Zn(L^2)_2]$ **in DMSO-d**[6]**.**

(3.10.16) ^{13}C-NMR of [Cd(L^2)$_2$]

The ^{13}C-NMR of [Cd(L^2)$_2$] is measured in DMSO-d^6 solvent and placed in Figure (3-149). The spectrum displayed almost an analogue resonances to that recorded in the spectrum of [Zn(L^2)$_2$]. Therefore, a same explanation to that stated in the spectrum of [Zn(L^2)$_2$] may implement to discuss the spectrum. The ^{13}C-NMR data are placed in Table (3-27).
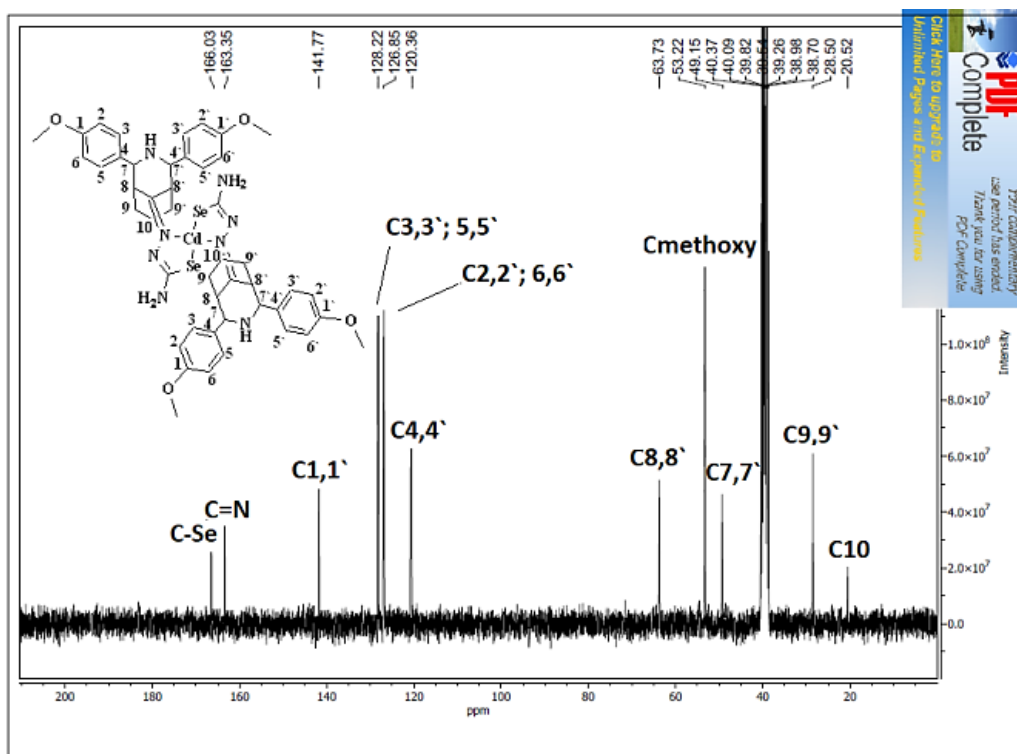
Figure (3-149): ^{13}C-NMR chart of [Cd(L^2)$_2$] in DMSO-d^6.

226

(3.10.17) ^{13}C-NMR of [Zn(L^3)$_2$]

The ^{13}C-NMR of [Zn(L^3)$_2$] in CDCl$_3$ solvent is located in Figure (3-150). The chemical shift that linked to (C$_{10}$) appeared as expected at δc= 21.20 ppm. Signals related to (C$_{9,9'}$), and (C$_{7,7'}$) were observed at δc= 29.03 and 54.24 ppm, respectively. Chemical shifts at δc= 55.30 and 64.38 ppm assigned to C-dimethylamino and (C$_{8,8'}$) group, respectively. Peaks detected at δc= 113.91 and 127.97 ppm may connect to (C$_{2,2',6,6'}$) and (C$_{3,3',5,5'}$), respectively. Further, chemical shifts at 133.50 and 152.62 ppm were related to (C$_{4,4'}$) and (C$_{1,1'}$, C-N(CH$_3$)$_2$), individually. More, the chemical shift at δc= 165.11 ppm of the (C=N) imine moiety was appeared as expected downfield, compared with that in HL^3 at 159.99 ppm, indicating the involvement of the C=N moiety in the coordination. Signal observed at 167.49 ppm due to the C-Se group. This peak was appeared upfield upon complexation, compared with that in HL^3 at 171.44 ppm, indicating the involvement of C-Se group in the coordination [3,12]. The upfield shifting indicates that the C-Se moiety adopts a selenide fashion in solution [3,12], upon complex formation (compared with that in the free ligand that exists as selenone, see ^{13}C-NMR section (3.3.17), page 94). This phenomenon has also been observed in the solid state (see IR section (3.8.3.2), page 154). The ^{13}C-NMR records are included in Table (3-27).
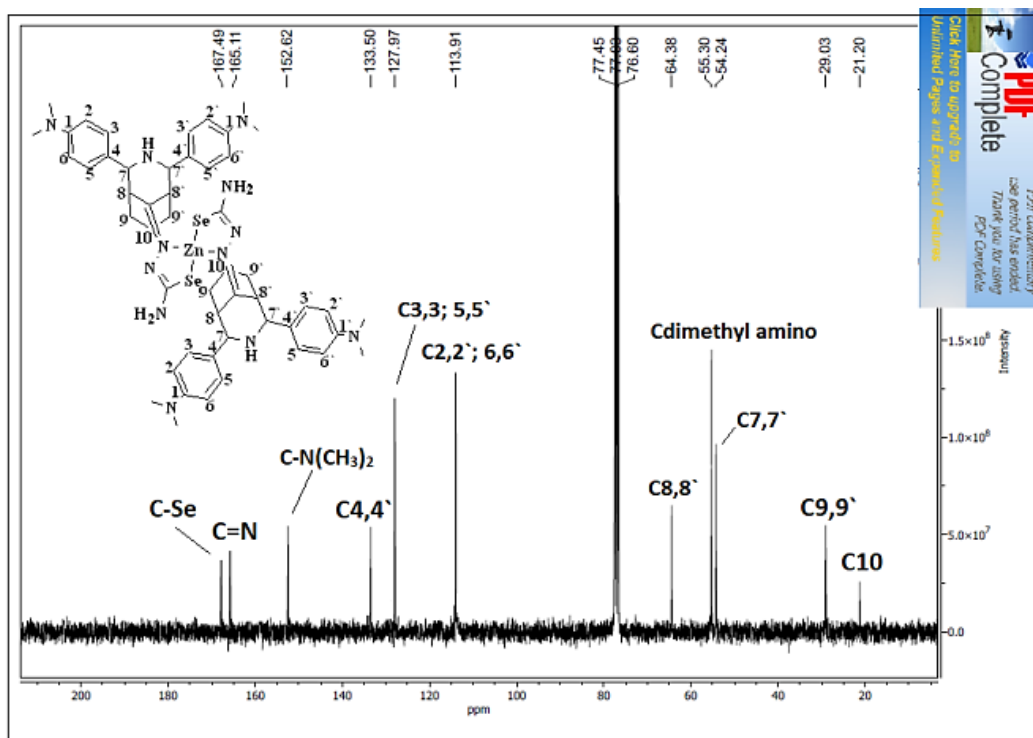
Figure (3-150): ^{13}C-NMR chart of [Zn(L^3)$_2$] in CDCl$_3$.

(3.10.18) ^{13}C-NMR of [Cd(L^3)$_2$]

The ^{13}C-NMR in CDCl$_3$ solution of [Cd(L^3)$_2$] complex, is placed in Figure (3-151). This revealed an analogue set of peaks to that noticed in the spectrum of [Zn(L^3)$_2$] complex. Therefore, a similar reasoning that used in the discussion of the Zn(II)-complex can be used to explain all peaks that detected in the spectrum of Cd(II)-complex. The ^{13}C-NMR resonances are positioned in Table (3-27).
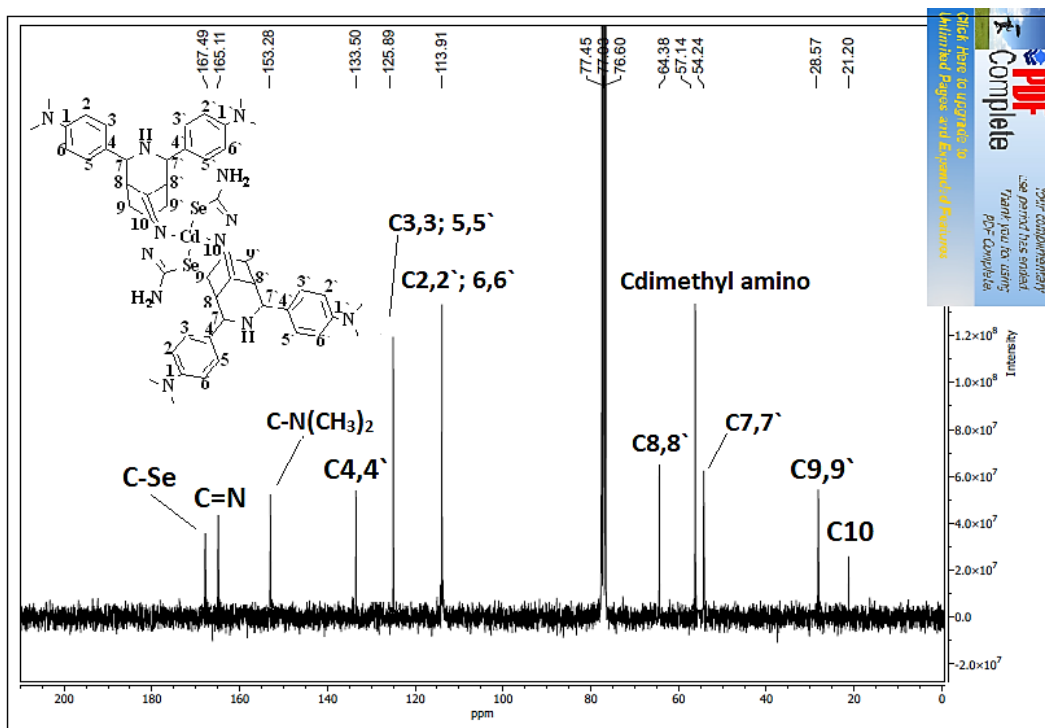
Figure (3-151): ^{13}C-NMR chart of $[Cd(L^3)_2]$ in $CDCl_3$.

229

Table (3-27): ^{13}C-NMR data of HL^1-HL^3 and their complexes with their resonances in ppm (δ).

Compound	(C$_{10}$)	(C$_{9,9'}$)	(C$_{8,8'}$)	(C$_{7,7'}$)	(C$_{2,2', 6,6'}$) (C$_{3,3', 5,5'}$)	(C$_{4,4'}$)	(C$_{1,1'}$)	(C=O)	(C=N)	(C-Se)	(2 x OCH$_3$) (2 x N(CH$_3$)$_2$)
HL^1	22.52	28.49	50.22 52.20	61.75	127.00 126.20	140.22	125.85	–	161.75	172.22	– –
[Zn(L^1)$_2$]	20.52	28.50	63.73	53.22	128.22 126.85	141.77	122.65	–	165.37	167.86	– –
[Cd(L^1)$_2$]	22.08	28.50	64.31	53.22	128.22 126.85	141.77	121.85	–	164.15	166.43	– –
HL^2	21.75	29.37	44.43 49.75	64.37	113.44 128.92	132.48	150.99	–	159.99	170.44	53.30 –
[Zn(L^2)$_2$]	22.08	27.12	63.73	47.73	126.85 128.22	114.34	149.84	–	164.13	166.03	53.22 –
[Cd(L^2)$_2$]	20.52	28.50	63.73	49.15	126.85 128.22	120.36	141.77	–	163.35	166.03	53.22 –
HL^3	21.75	29.37	51.99 55.30	64.37	113.75 128.92	132.48	151.99	–	159.99	171.44	– 40.23
[Zn(L^3)$_2$]	21.20	29.03	64.38	54.24	113.91 127.97	133.50	152.62	–	165.11	167.49	– 55.30
[Cd(L^3)$_2$]	21.20	28.57	64.38	54.24	113.91 125.89	133.50	153.28	–	165.11	167.49	– 57.14

230

(3.10.19) ^{13}C-NMR of $[Zn(L^4)_2]$

The ^{13}C-NMR of $[Zn(L^4)_2]$ complex, in DMSO-d^6, is exhibited in Figure (3-152). In the aliphatic region, the spectrum indicated signals at δc= 22.90, 27.91, 30.61 and 51.03 ppm related to (C_3), (C_4), (C_5) and (C_6), respectively. Chemical shifts that assigned to (C_2) and (C_7, C-H) group were observed at δc= 55.70 and δc= 56.25 ppm, respectively. Peaks detected in the aromatic region at 112.94, 115.75, 126.72 and 135.85 ppm assigned to (C_9), (C_{11}), (C_{13}) and (C_{12}), respectively. Further, signals that noticed at 127.51, 128.55 and 131.46 ppm were related to (C_{17}), ($C_{15,15'}$) and ($C_{16,16'}$), respectively. A peak observed at δc= 142.23 ppm attributed to (C_{14}), while signals at 147.92 and 153.61 ppm assigned to (C_8, C-NH) and (C_{10}, C-NO$_2$) groups, respectively. Finally, the resonance of C=N moiety recorded as estimated at δc= 165.61 ppm, indicated complex formation. While, the C-Se group appeared upfield, compared with HL^4, at δc= 168.43 ppm, confirming the involvement of the C-Se moiety in complex formation [3,12]. The C-Se moiety appeared as a selenide fashion in solution [3,12], upon complex formation (compared with that in the free ligand that exists as selenone, see ^{13}C-NMR section (3.3.18), page 96). This phenomenon has also been presented in the solid state (see IR section (3.8.4.2), page 160). The ^{13}C-NMR resonances are included in Table (3-28).
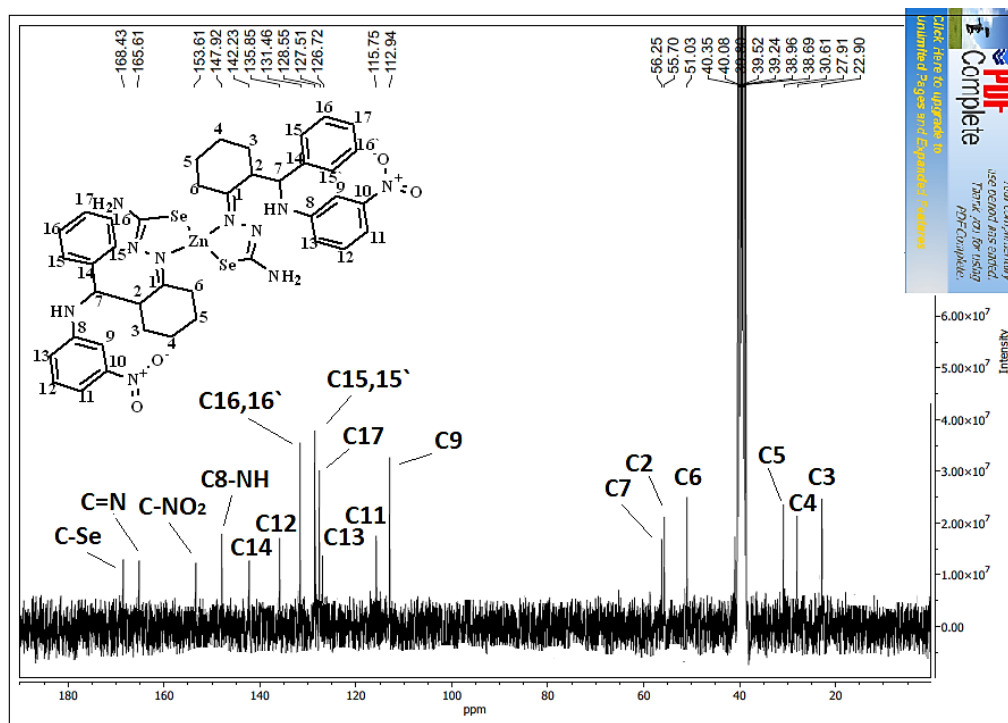
Figure (3-152): ^{13}C-NMR chart of [Zn(L^4)$_2$] in DMSO-d^6.

(3.10.20) ^{13}C-NMR of [Cd(L^4)$_2$]

The [Cd(L^4)$_2$] is measured in DMSO-d^6 and shown Figure (3-153). This spectrum displayed almost a similar trend of peaks to that observed in the spectrum of [Zn(L^4)$_2$] complex. Accordingly, a similar reasoning used to explain the spectrum of [Zn(L^4)$_2$] may implement to discuss the spectrum of [Cd(L^4)$_2$]. The ^{13}C-NMR data are tabulated in Table (3-28).
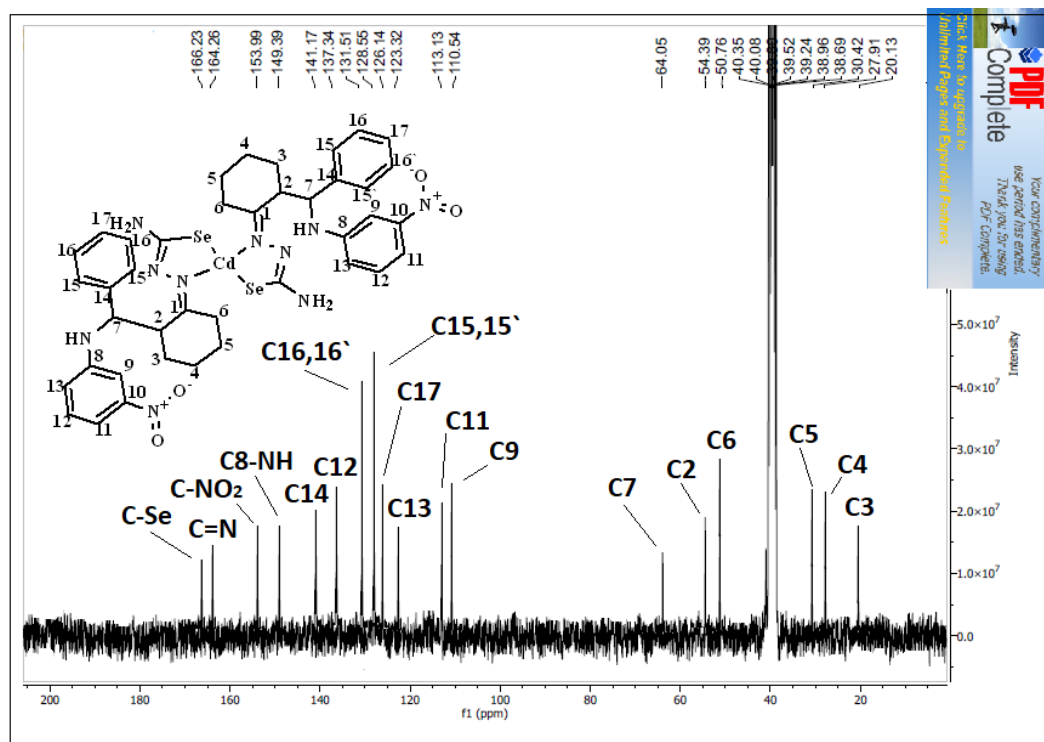
Figure (3-153): ^{13}C-NMR chart of $[Cd(L^4)_2]$ in DMSO-d^6.

(3.10.21) ^{13}C-NMR of $[Zn(L^5)_2]$

The ^{13}C-NMR of $[Zn(L^5)_2]$ complex is run in DMSO-d^6 and placed in Figure (3-154). Signals recorded at δc= 22.77, 27.89, 30.49 and 47.38 ppm are related to (C_3), (C_4), (C_5) and (C_6), respectively. Chemical shifts that assigned to (C_2) and $(C_7$, C-H$)$ group were observed at δc= 54.87 and δc= 56.44 ppm, respectively. A peak detected at δc= 58.98 ppm assigned to C-methoxy. Resonances assigned to $(C_{9,9`})$, $(C_{14,14`})$ and (C_{11}) were detected at δc= 113.04, 113.47 and 115.70 ppm, respectively. Furthermore, signals that related to $(C_{10,10`})$ and $(C_{13,13`})$ were recorded at δc= 126.44 and 128.51 ppm, respectively. A chemical shift at 133.92 ppm attributed to (C_{12}), while signals at 147.96 and 153.91 ppm assigned to $(C_8$, C-NH$)$ and $(C_{15}$, C-OCH$_3)$ groups, respectively. Further, the imine group

233

detected as estimated at δc= 165.35 ppm matched to that in HL[5] at 159.99 ppm, confirming the participation of nitrogen atoms in the coordination to the metal centre. The chemical shift of the C-Se group recorded at δc= 167.45 ppm, which appeared uperfield, as compared with that in HL[5] at 174.94 ppm, indicating the participation of the selenium atom in the coordination to the meal centre [3,12]. The C-Se moiety displayed as a selenide fashion in solution during shifting to lower [3,12], upon complex formation (compared with that in the free ligand that exists as selenone, see ^{13}C-NMR section (3.3.19), page 97). This phenomenon has also been observed in the solid state (see IR section (3.8.5.2), page 166). The ^{13}C-NMR records are shown in Table (3-28).
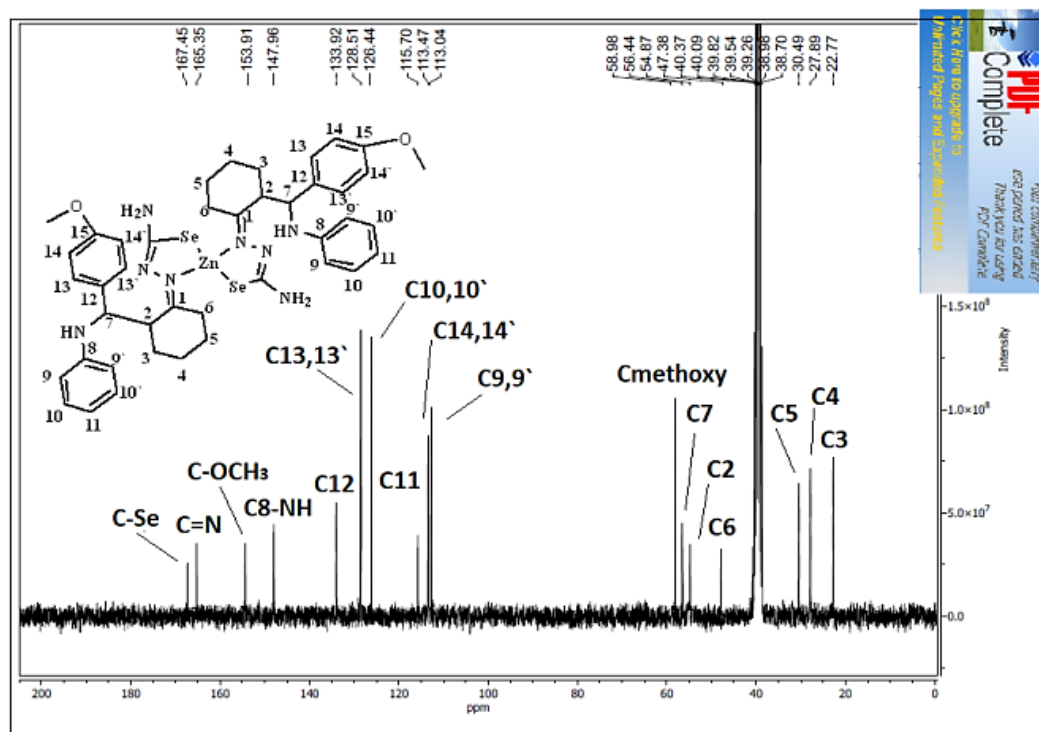
Figure (3-154): ^{13}C-NMR chart of [Zn(L[5])₂] in DMSO-d[6].

(3.10.22) ^{13}C-NMR of [Cd(L^5)$_2$]

The ^{13}C-NMR of [Cd(L^5)$_2$] complex in DMSO-d^6 solvent is placed in Figure (3-155). The obtained data are similar to that observed in the spectrum of [Zn(L^5)$_2$]. Therefore, an analogue explanation may be used to discuss the spectrum on [Cd(L^5)$_2$]. The ^{13}C-NMR data are tabulated in Table (3-28).
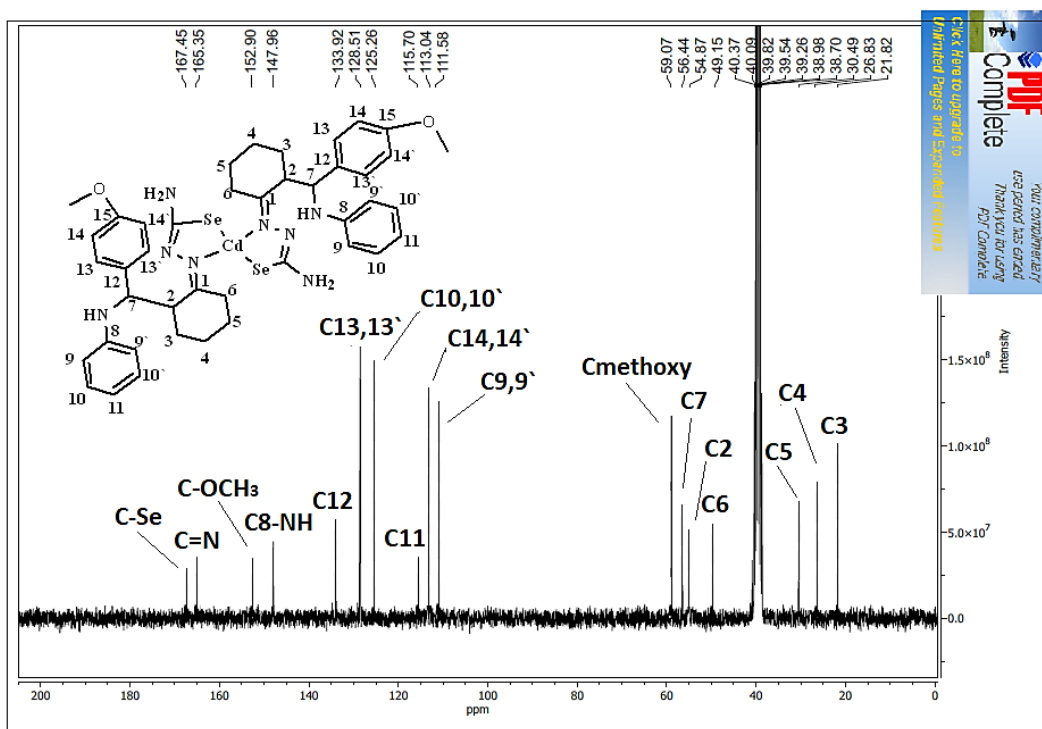
Figure (3-155): ^{13}C-NMR chart of [Cd(L^5)$_2$] in DMSO-d^6.

235

(3.10.23) ^{13}C-NMR of [Zn(L^6)$_2$]

The ^{13}C-NMR of [Zn(L^6)$_2$] in CDCl$_3$ solvent is seen in Figure (3-156). Peaks recorded at δc= 21.20, 29.03, 33.18 and 42.90 ppm related to (C$_3$), (C$_4$), (C$_5$) and (C$_6$), respectively. Signal detected at δc= 47.09 ppm assigned to C-dimethylamino. Chemical shifts that assigned to (C$_2$) and (C$_7$, C-H) group were observed at δc= 54.24 and δc= 55.30 ppm, respectively. Signals that related to the aromatic ring (C$_9$), (C$_{11}$), (C$_{13}$) and (C$_{12}$) were appeared at 101.68, 111.28, 113.91 and 133.50 ppm, respectively. Resonances assigned for (C$_{16,16'}$), (C$_{14}$) and (C$_{15,15'}$) were detected at 116.01, 125.89 and 127.97 ppm, respectively. The peak of (C$_{17}$, C-N(CH$_3$)$_2$) appeared as expected at δc= 140.62 ppm. Further, signals that related to (C$_8$, C-NH) and (C$_{10}$, C-NO$_2$) were detected at δc= 146.44 and 153.25 ppm, respectively. A chemical shift at 165.11 ppm attributed to (C=N) imine group. This peak was shifted by *ca.* 5 ppm, as compared to that in HL^6 (see Table (3-28)), demonstrating the involvement of the C=N moiety in the coordination. A signal recorded at δc= 168.36 ppm assigned to C-Se group. Upon complexation, this group suffered shielding compared to that in the free ligand at 176.94 ppm confirming the involvement of the selenium atom in the coordination to the metal centre [3,12]. This upfield shifting indicates that the C-Se moiety adopts a selenide fashion in solution [3,12], upon complex formation (compared with that in the free ligand that exists as selenone, see ^{13}C-NMR section (3.3.20), page 98). This phenomenon has also been observed in the solid state (see IR section (3.8.6.2), page 171). The ^{13}C-NMR resonances are included in Table (3-28).
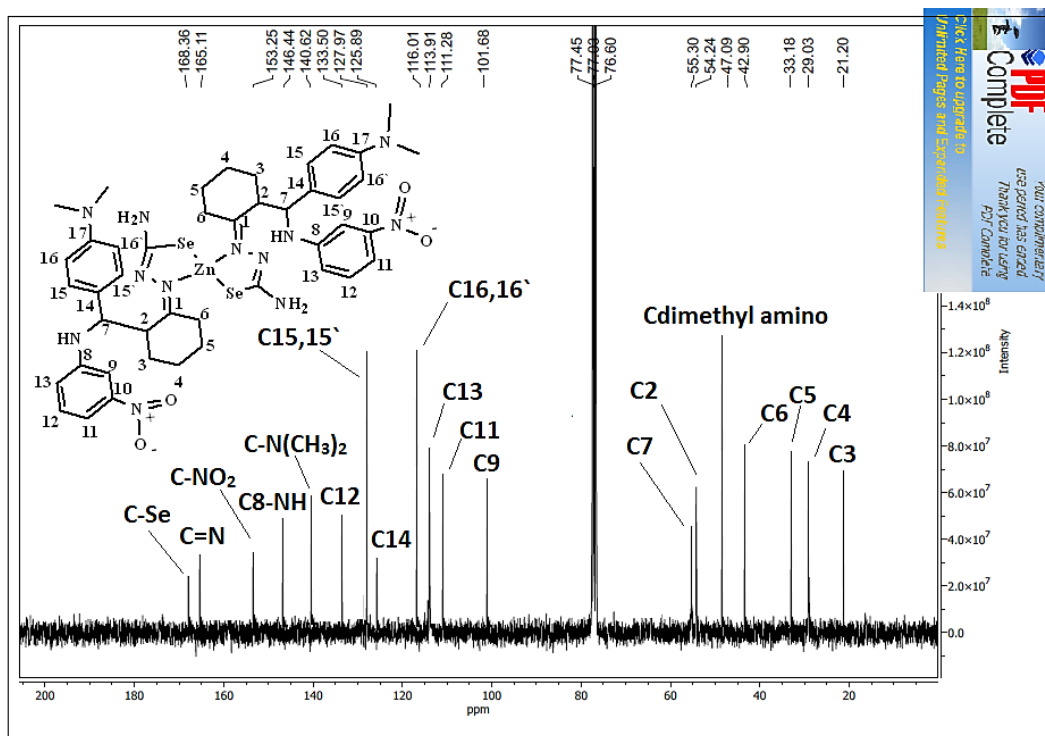
Figure (3-156): ^{13}**C-NMR chart of [Zn(L^6)$_2$] in CDCl$_3$.**

(3.10.24) ^{13}C-NMR of [Cd(L^6)$_2$]

The ^{13}C-NMR of [Cd(L^6)$_2$] complex in CDCl$_3$ solvent is allocated in Figure (3-157). The Cd(II)-complex exhibited almost an analogue pattern of peaks to that observed in the spectrum of Zn(II)-complex and a similar explanation may be used to discuss the spectrum. The ^{13}C-NMR records are listed in Table (3-28).
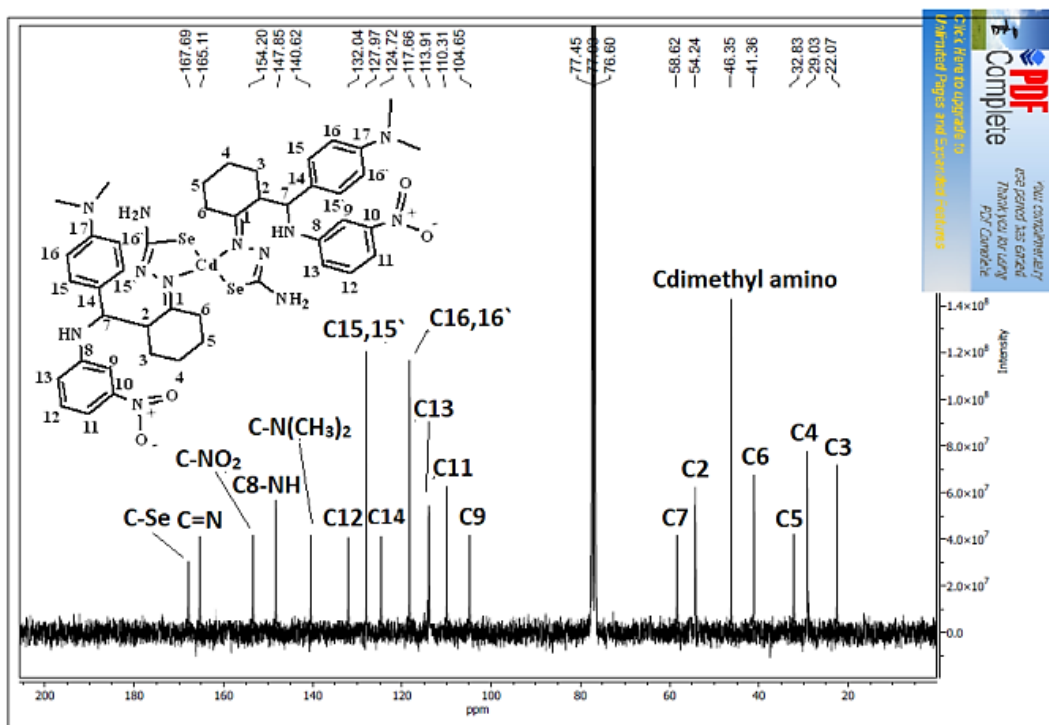
Figure (3-157): ^{13}**C-NMR chart of [Cd(L**^{6}**)**$_2$**] in**

Table (3-28): ^{13}C-NMR data of HL^4-HL^6 and their complexes with their resonances in ppm (δ).

Compound	(C$_2$) (C$_3$)	(C$_4$) (C$_5$)	(C$_6$) (C$_7$)	(C$_9$) (C$_{11}$)	(C$_{12}$) (C$_{13}$)	(C$_{14}$) (C$_{15}$)	(C$_{15,15'}$) (C$_{16,16'}$)	(C$_{9,9'}$) (C$_{10,10'}$)	(C$_{13,13'}$) (C$_{14,14'}$)	(C$_8$-NH) (C$_{10}$-NO$_2$)	(C$_{15}$-OCH$_3$) (C$_{17}$)	(C$_{17}$-N(CH$_3$)$_2$) (C=O)	(C-Se) (C=N)	(2 x OCH$_3$) (2 x N(CH$_3$)$_2$)
HL^4	55.91	27.90	40.97	112.93	132.89	143.21	128.04	_	_	152.91	_	_	175.94	_
	22.89	30.61	58.21	115.73	126.04	_	130.61	_	_	155.68	127.06	_	160.94	_
[Zn(L^4)$_2$]	55.70	27.91	51.03	112.94	135.85	142.23	128.55	_	_	147.92	_	_	168.43	_
	22.90	30.61	56.25	115.75	126.72	_	131.46	_	_	153.61	127.51	_	165.61	_
[Cd(L^4)$_2$]	54.39	27.91	50.76	110.54	137.34	141.17	128.55	_	_	149.39	_	_	166.23	_
	20.13	30.42	64.05	113.13	123.32	_	131.51	_	_	153.99	126.14	_	164.26	_
HL^5	54.86	27.89	40.86	_	133.90	_	_	113.03	128.49	147.94	155.68	_	174.94	55.09
	24.77	30.49	57.43	115.68	_	_	_	128.09	114.45	_	_	_	159.99	_
[Zn(L^5)$_2$]	54.87	27.89	47.38	_	133.92	_	_	113.04	128.51	147.96	153.91	_	167.45	58.98
	22.77	30.49	56.44	115.70	_	_	_	126.44	113.47	_	_	_	165.35	_
[Cd(L^5)$_2$]	54.87	26.83	49.15	_	133.92	_	_	111.58	128.51	147.96	152.90	_	167.45	59.07
	21.82	30.49	56.44	115.70	_	_	_	125.26	113.04	_	_	_	165.35	_
HL^6	50.69	27.89	41.97	103.75	134.99	125.06	129.92	_	_	147.94	_	142.91	176.94	_
	24.77	30.61	54.30	110.94	113.75	_	115.73	_	_	155.68	_	_	160.64	45.23
[Zn(L^6)$_2$]	54.24	29.03	42.90	101.68	133.50	125.89	127.97	_	_	146.44	_	140.62	168.36	_
	21.20	33.18	55.30	111.28	113.91	_	116.01	_	_	153.25	_	_	165.11	47.09
[Cd(L^6)$_2$]	54.24	29.03	41.36	104.65	132.04	124.72	127.97	_	_	147.85	_	140.62	167.69	_
	22.07	32.83	58.62	110.31	113.91	_	117.66	_	_	154.20	_	_	165.11	46.35

(3.11) ^{77}Se-NMR of complexes

(3.11.1) ^{77}Se-NMR of HL[1] complexes

The ^{77}Se-NMR of Zn- and Cd-complex are shown in Figures (3-158) and (3-159), respectively. These spectra were acquired in DMSO-d[6] solvents. The spectra recorded peaks at 389.83 and 392.55 ppm assigned to C-Se group for Zn- and Cd-complex, respectively. These peaks were shifted downfield, compared with that in HL[1] at 179.36 ppm. This shift indicated the C-Se moiety, in solution, bound to the metal centre in its selenide fashion [3,12]. This is in accordance with results reported by Todorovic *et al*. [3]. Furthermore, the upfield shift of the C-Se group in the spectrum of ^{13}C-NMR, compared with that in the free ligand is another evidence of the C-Se moiety to adopt its selenide fashion upon complexation. The selenide fashion of the C-Se group is formed due to deprotonation of the ligand, which resulted in the formation of N=C-Se moiety, compared with free ligand that exists in its selenone fashion (see ^{13}C-NMR section (3.10.13), page 222), [3,12].

Furthermore, the appearance of one signal in the spectra of the complexes indicated the purity of the isolated complexes and the two ligands are symmetrical upon coordination to the metal centre. [69]. The ^{77}Se-NMR records are included in the Table (3-29).
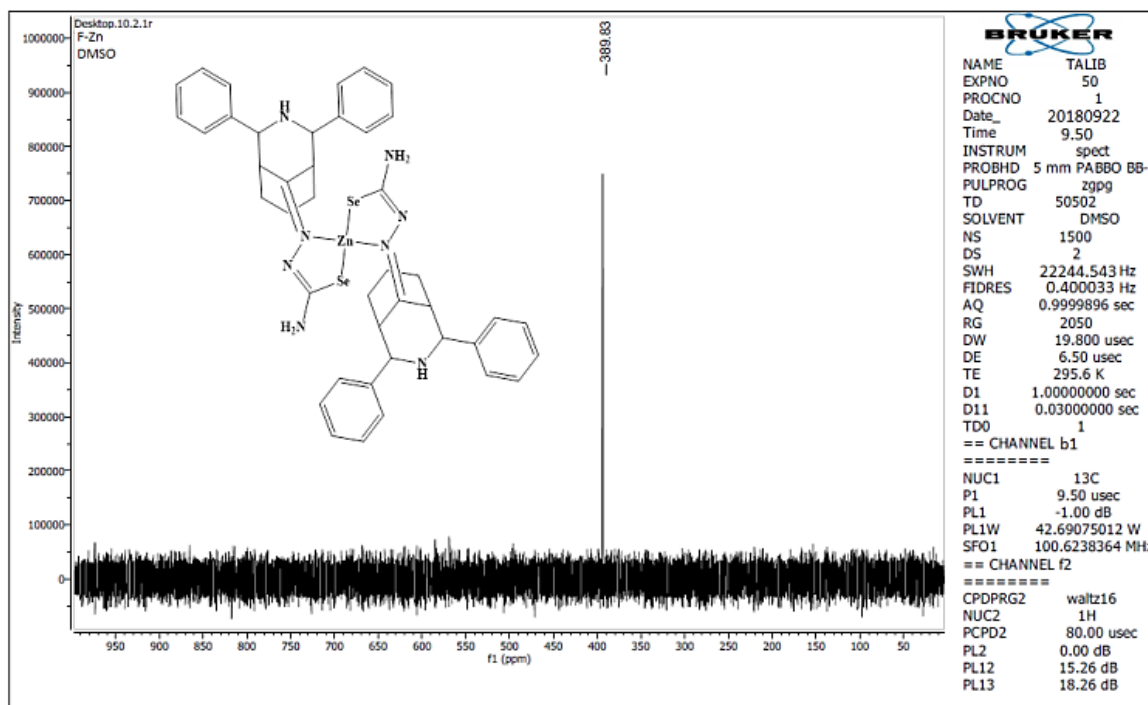
Figure (3-158): ^{77}**Se-NMR chart of [Zn(L^1)$_2$] in DMSO-d^6.**
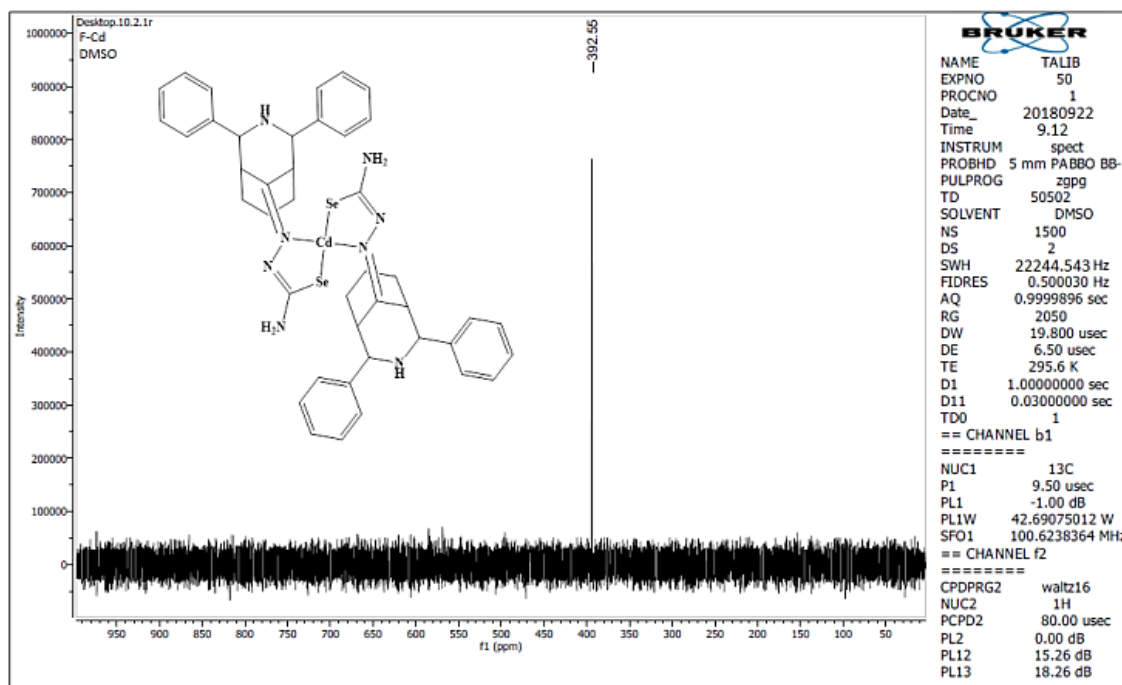
Figure (3-159): ^{77}**Se-NMR chart of [Cd(L^1)$_2$] in DMSO-d^6.**

241

(3.11.2) ^{77}Se-NMR of HL^{2}-HL^{6} complexes

The ^{77}Se-NMR spectra of all compounds are acquired in DMSO-d^{6} solvents. The spectra of HL^{2} complexes placed in Figures (3-160) and (3-161). The spectra showed peaks at 463.82 and 437.75 ppm assigned to C-Se group for Zn- and Cd-complex, respectively. These values appeared downfield, compared with that in HL^{2} at 206.80 ppm.

The spectra of Zn- and Cd-complex of HL^{3} ligand, Figures (3-162) and (3-163), indicated chemical shifts at 496.83 and 492.70 ppm, respectively. These signals have shifted to higher chemical shift, compared with that in HL^{3} at 198.50 ppm.

The ^{77}Se-NMR spectra of Zn(II) and Cd(II) complexes of HL^{4}, Figures (3-164) and (3-165), recorded peaks at 507.86 and 508.28 ppm, respectively. The Zn(II) and Cd(II) complexes of HL^{5}, Figures (3-166) and (3-167), displayed peaks at 520.66 and 537.05 ppm, respectively. While, the spectra of Zn- and Cd-complex of HL^{6}, Figures (3-168) and (3-169), resonances at 538.86 and 672.32 ppm, respectively, which attributed to presence C-Se group. The chemical shifts of these complexes recorded downfield, compared with that displayed at 217.60, 226.39 and 240.51 ppm in HL^{4}, HL^{5} and HL^{6}, respectively. These signals showed a high downfield, compared with that for complexes of HL^{1}-HL^{3}. This may be related to presence groups like (NO$_2$, N(Me)$_2$ and OMe) in ligand structure. An analogue reasoning that mentioned in the discussion of the complexes of HL^{1} could be used to explain the down field shift and the involvement of the C-Se moiety in its selenide form upon [3,12]. The ^{77}Se records are tabulated in Table (3-29).
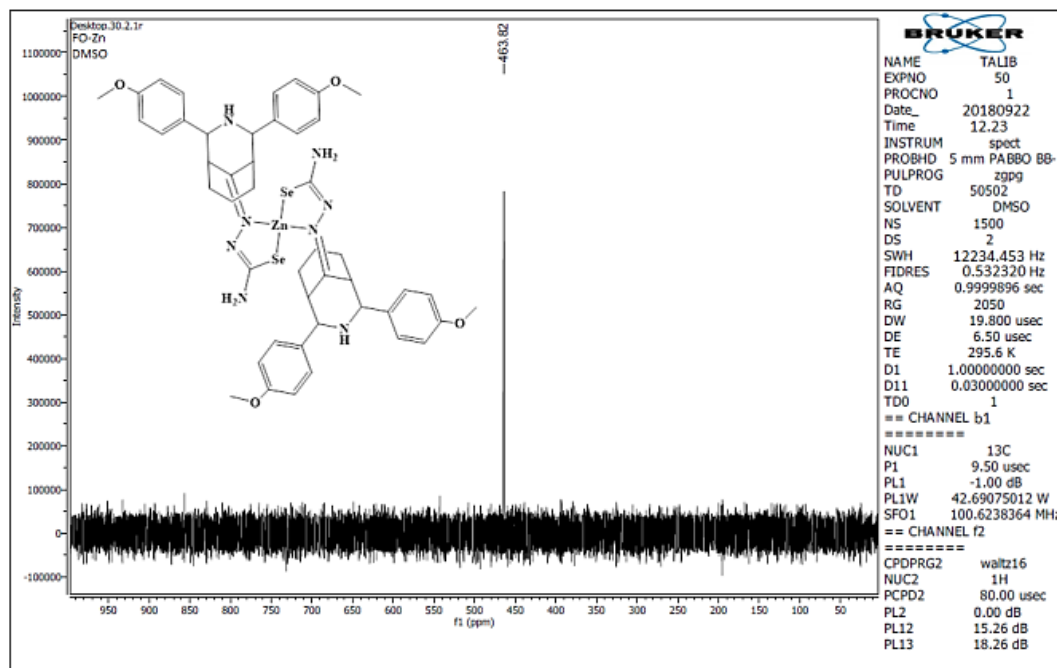
Figure (3-160): ^{77}Se-NMR chart of [Zn(L^2)$_2$] in DMSO-d^6.
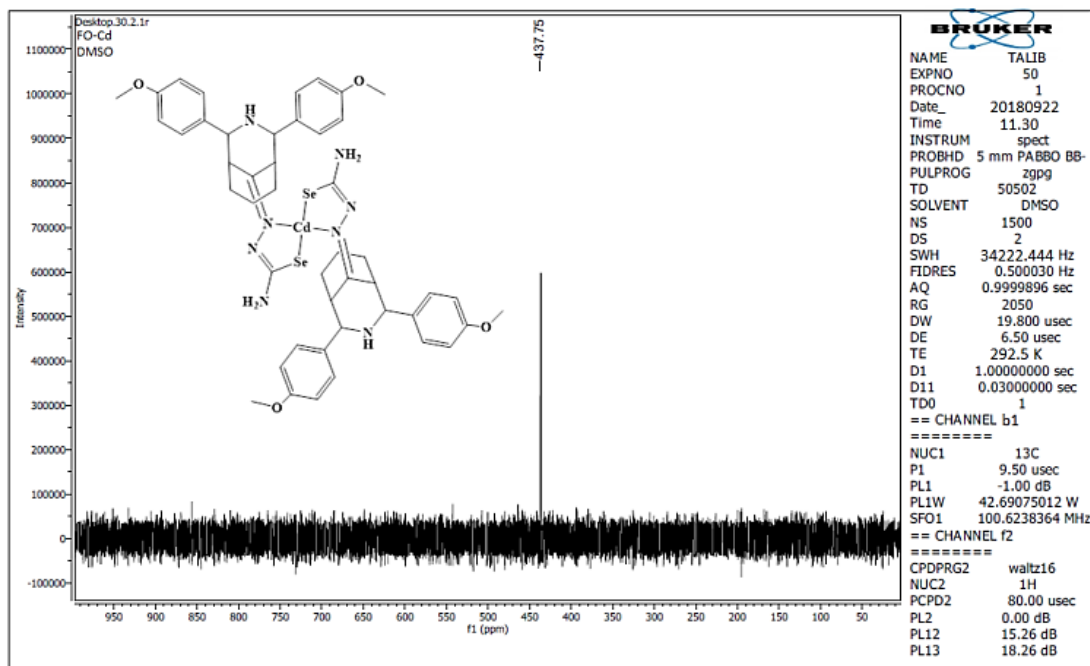
Figure (3-161): ^{77}Se-NMR chart of [Cd(L^2)$_2$] in DMSO-d^6.

243
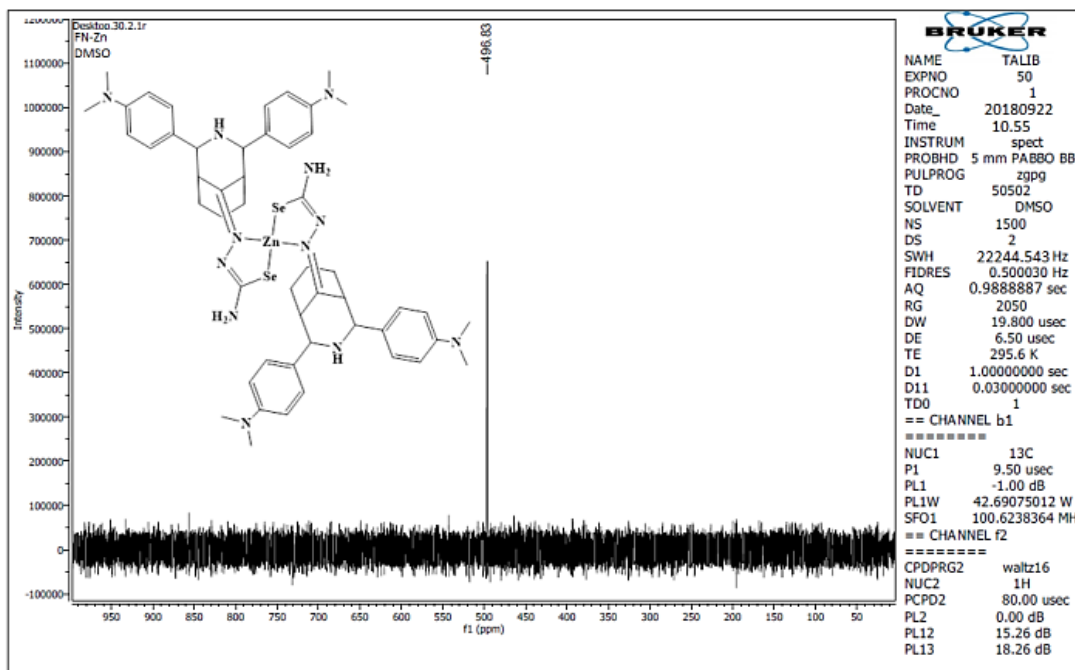
Figure (3-162): ^{77}**Se-NMR chart of [Zn(L^3)$_2$] in DMSO-d^6.**
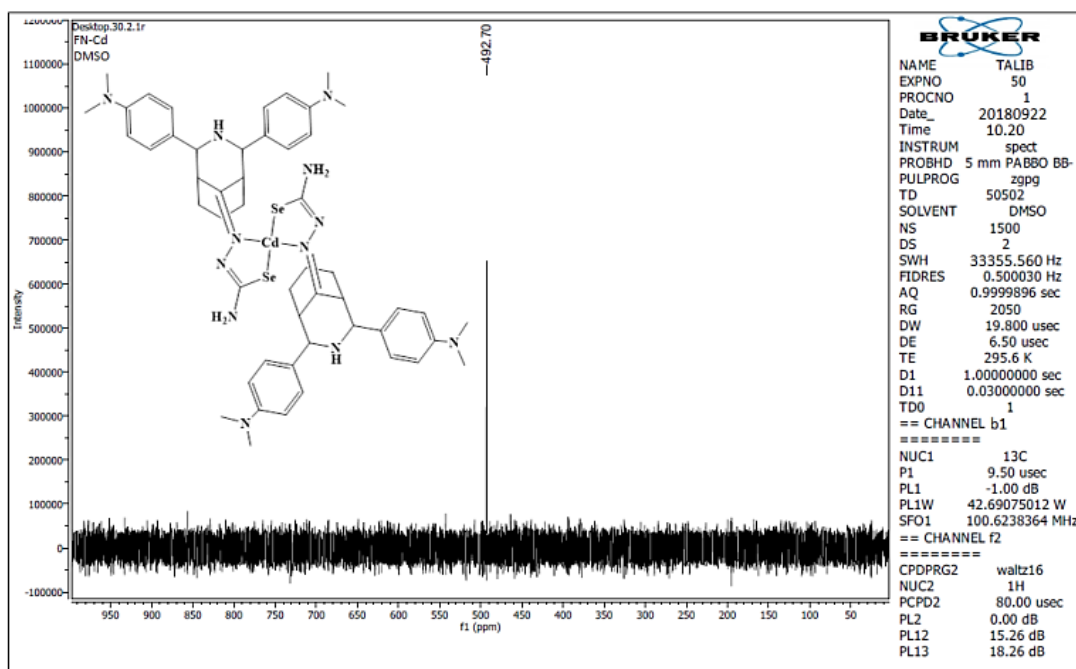
Figure (3-163): ^{77}**Se-NMR chart of [Cd(L^3)$_2$] in DMSO-d^6.**
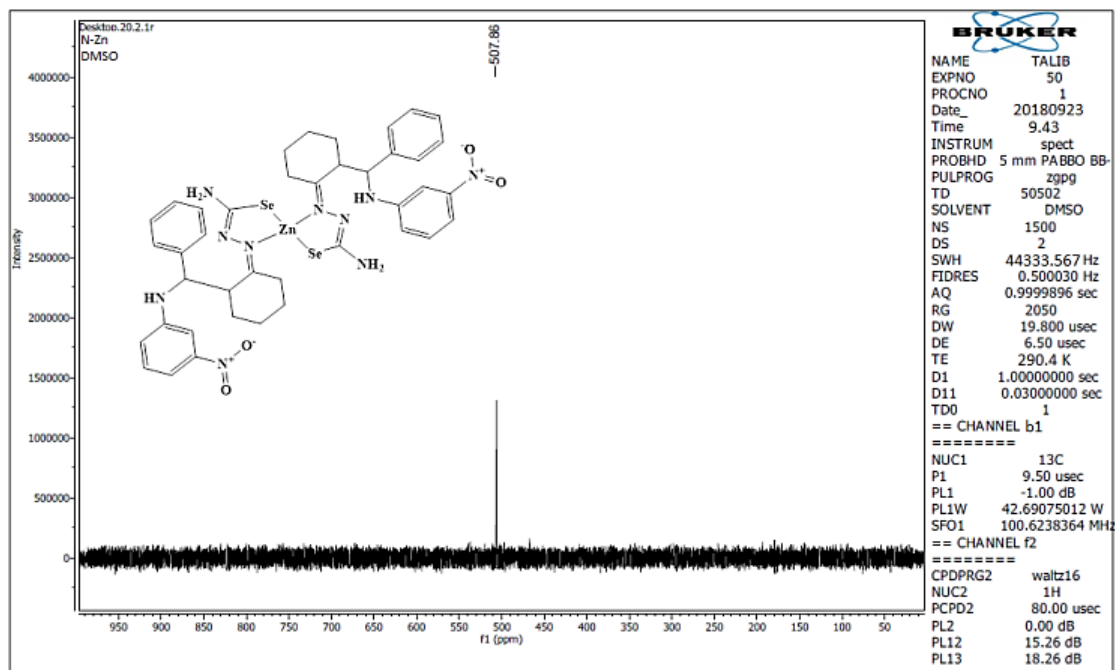
Figure (3-164): ^{77}Se-NMR chart of [Zn(L^4)$_2$] in DMSO-d^6.
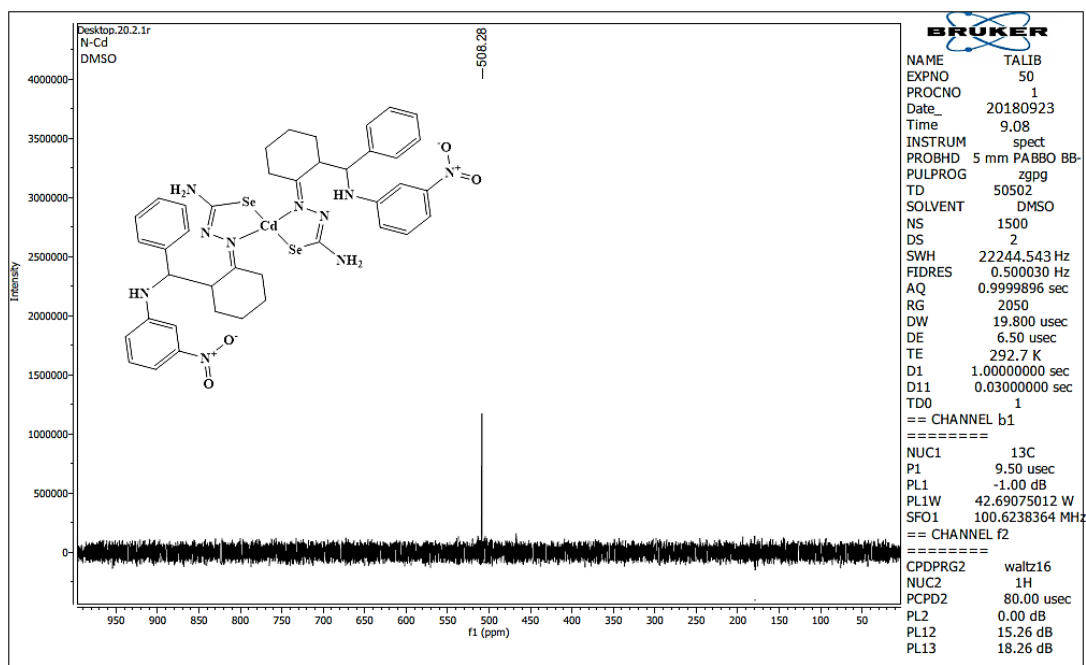
Figure (3-165): ^{77}Se-NMR chart of [Cd(L^4)$_2$] in DMSO-d^6.

245
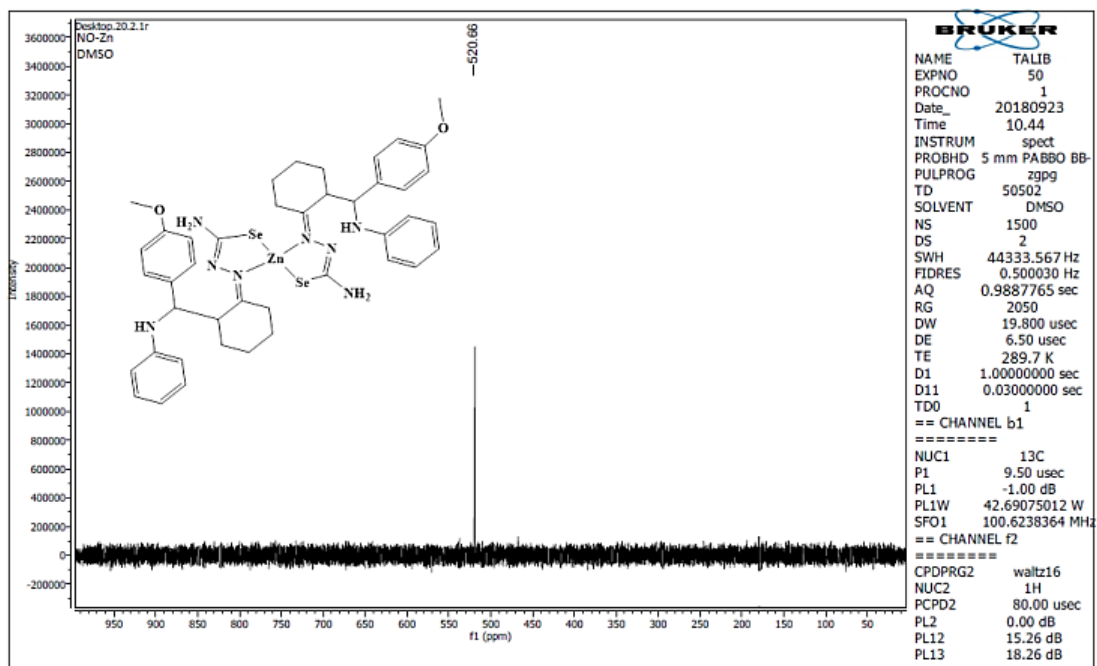
Figure (3-166): ^{77}Se-NMR chart of [Zn(L^5)$_2$] in DMSO-d^6.
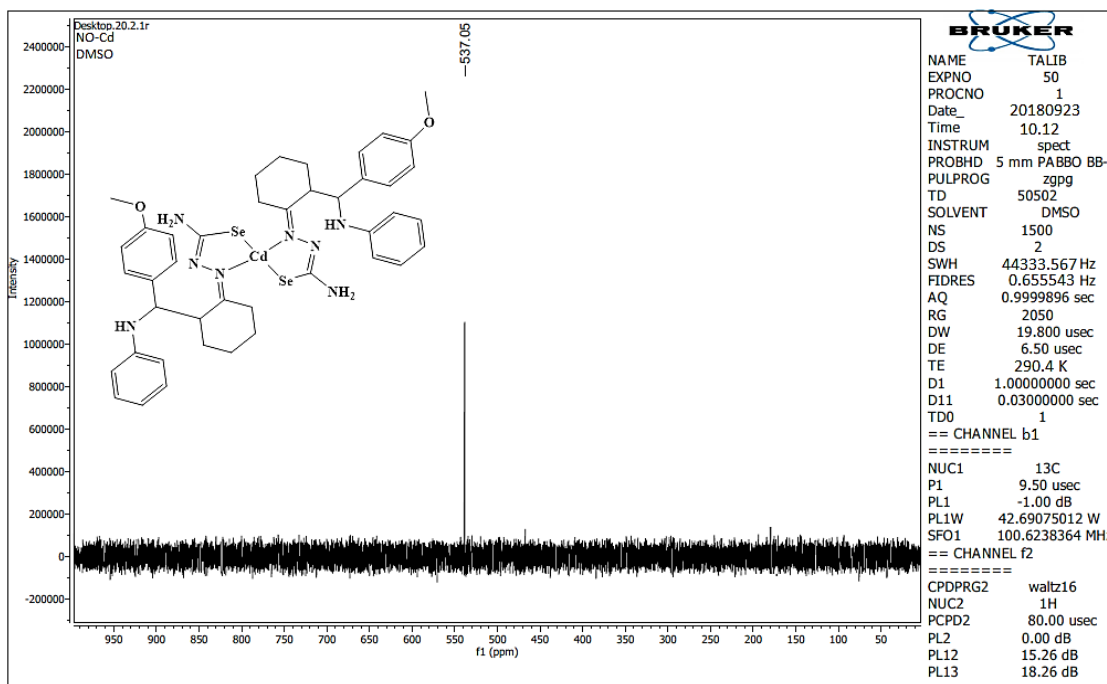
Figure (3-167): ^{77}Se-NMR chart of [Cd(L^5)$_2$] in DMSO-d^6.
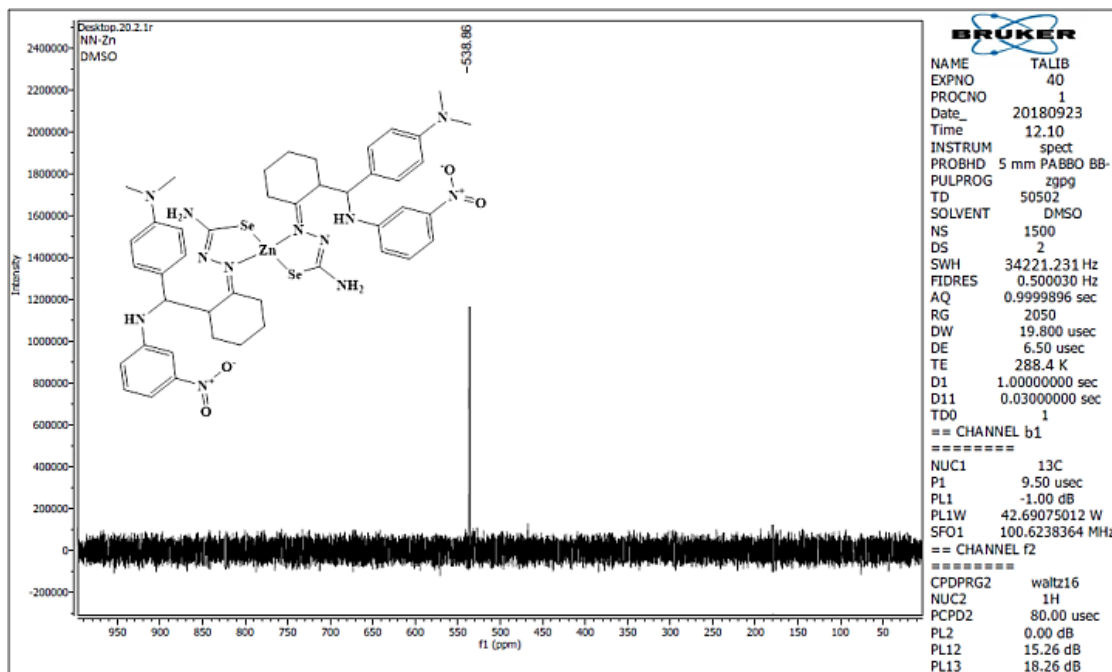
Figure (3-168): ^{77}Se-NMR chart of [Zn(L^6)$_2$] in DMSO-d^6.
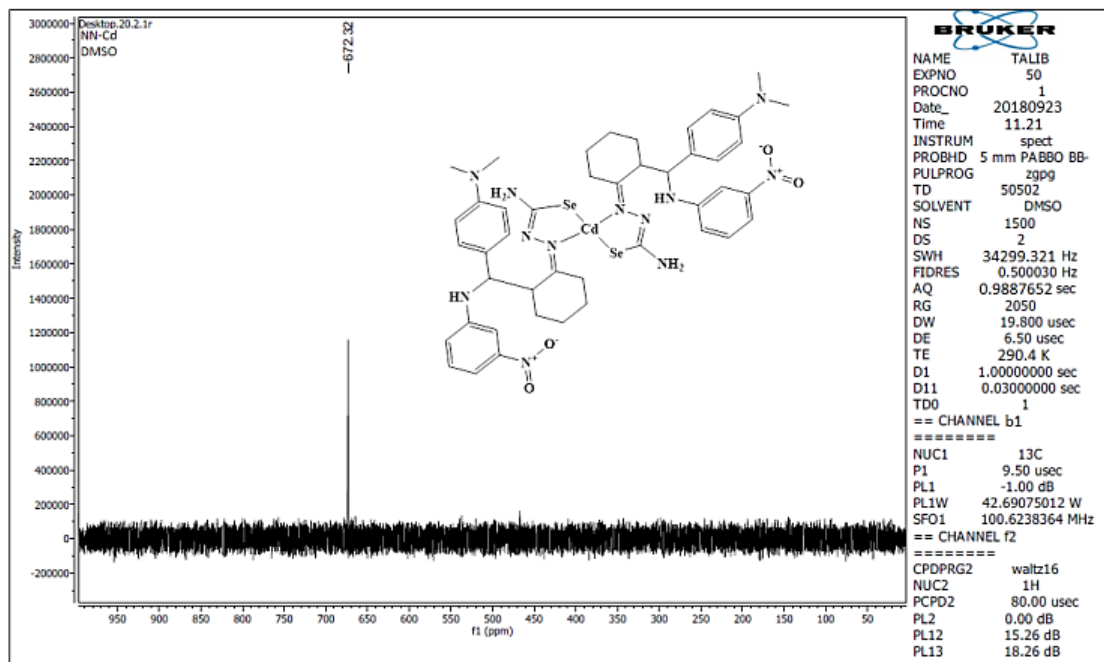
Figure (3-169): ^{77}Se-NMR chart of [Cd(L^6)$_2$] in DMSO-d^6.

247

Table (3-29): ^{77}**Se-NMR spectral records of HL^1-HL^6 complexes and their resonances in ppm (δ).**

Compound	Chemical shift for (C-Se) selenide group in ppm (δ)
$[Zn(L^1)_2]$	389.83
$[Cd(L^1)_2]$	392.55
$[Zn(L^2)_2]$	463.82
$[Cd(L^2)_2]$	437.75
$[Zn(L^3)_2]$	496.83
$[Cd(L^3)_2]$	492.70
$[Zn(L^4)_2]$	507.86
$[Cd(L^4)_2]$	508.28
$[Zn(L^5)_2]$	52066
$[Cd(L^5)_2]$	537.05
$[Zn(L^6)_2]$	538.86
$[Cd(L^6)_2]$	672.32

(3.12) Mass spectral data of complexes

(3.12.1) Mass spectral data of $K_2[Mn(L^1)_2Cl_2]$

The electrospray (+) mass spectrum of $K_2[Mn(L^1)_2Cl_2]$, Figure (3-170), shows the parent ion peak at m/z= 1025.1 (M)$^+$ (6%) calculated for $C_{42}H_{46}Cl_2K_2MnN_8Se_2$; requires= 1025.1. Peaks detected at m/z= 728.8 (25%), 626.8 (100%), 448.3 (44%), 346.3 (70%) and 116.8 (23%) related to $[M-(C_{12}H_{10}N+CH_3Cl+C_6H_7)]^+$, $[M-\{(C_{12}H_{10}N+CH_3Cl+C_6H_7)+(C_7H_4N)\}]^+$ and $[M-\{(C_{12}H_{10}N+CH_3Cl+C_6H_7)+(C_7H_4N)+(C_4H_9N_3Se)\}]^+$, $[M-\{(C_{12}H_{10}N+CH_3Cl+C_6H_7)+(C_7H_4N)+(C_4H_9N_3Se)+(C_7H_4N)\}]^+$ and $[M-\{(C_{12}H_{10}N+CH_3Cl+$

$C_6H_7) + (C_7H_4N) + (C_4H_9N_3Se) + (C_7H_4N) + (C_5H_8N_2SeMn)\}]^+$, respectively. The breaking steps are presented in Scheme (3-17).
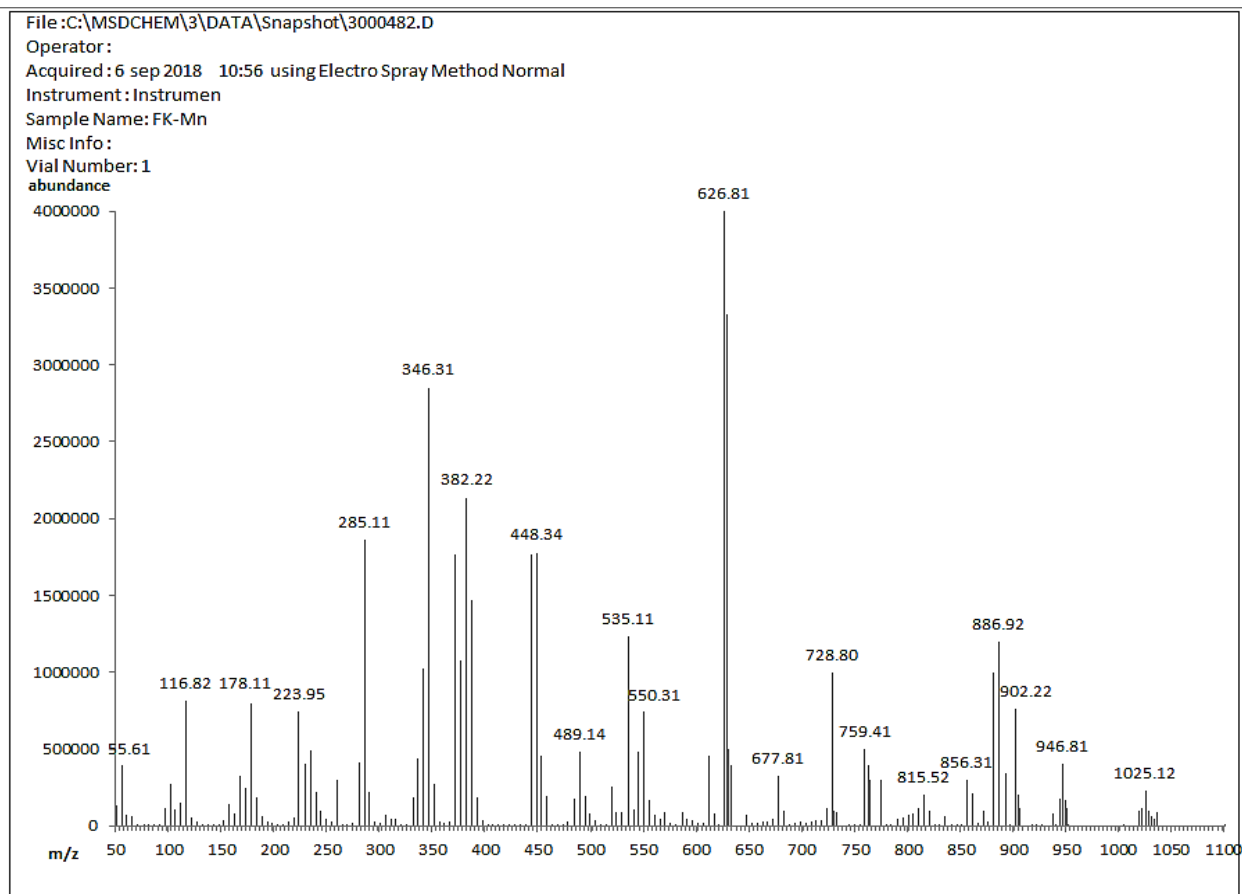
Figure (3-170): The electrospray (+) mass spectrum of $K_2[Mn(L^1)_2Cl_2]$.
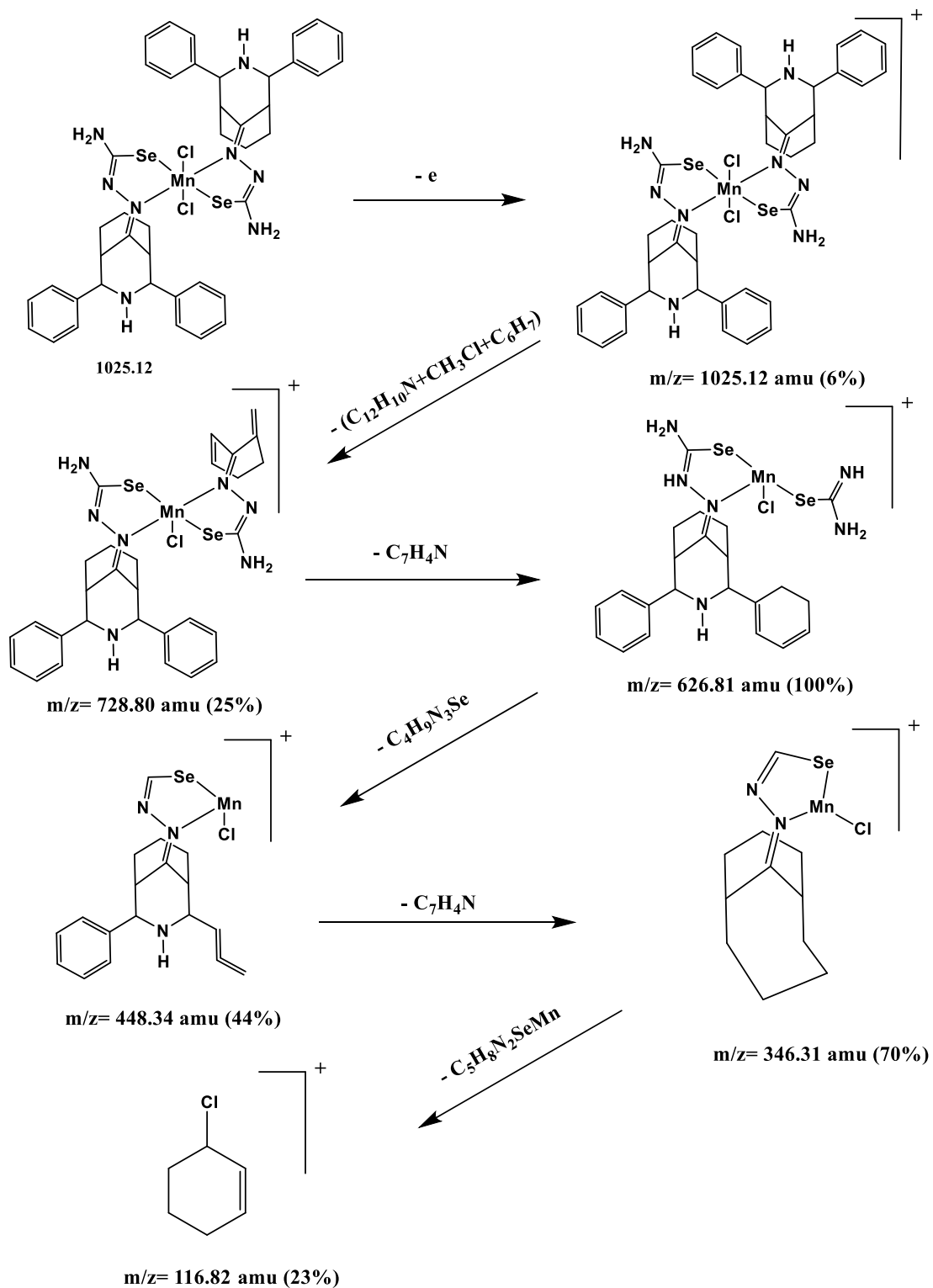
Scheme (3-17): Fragmentation steps and relative abundance of K$_2$[Mn(L^1)$_2$Cl$_2$].

(3.12.2) Mass spectral data of $[Zn(L^1)_2]$

The electrospray (+) mass spectrum of $[Zn(L^1)_2]$, Figure (3-171), reveals the parent ion peak at m/z= 886.21 $(M)^+$ (36%) calculated for $C_{42}H_{46}N_8Se_2Zn$; requires= 886.21. Fragments noticed at m/z= 631.92 (100%), 448.33 (53%), 346.32 (82%) and 116.83 (38%) related to $[M-(C_{19}H_{13}N)]^+$, $[M-\{(C_{19}H_{13}N)+(C_2H_{10}N_5Se)\}]^+$, $[M-\{(C_{19}H_{13}N)+(C_2H_{10}N_5Se)+(C_8H_6)\}]^+$ and $[M-\{(C_{19}H_{13}N)+(C_2H_{10}N_5Se)+(C_8H_6)+(C_6H_{10}NSeZn)\}]^+$, respectively. The fragmentation pattern is included in Scheme (3-18).

File :C:\MSDCHEM\3\DATA\Snapshot\3000482.D
Operator:
Acquired : 6 sep 2018   11:55 using Electro Spray Method Normal
Instrument : Instrumen
Sample Name: FK-Zn
Misc Info :
Vial Number: 1

Figure (3-171): The electrospray (+) mass spectrum of $[Zn(L^1)_2]$.

886.21

m/z= 886.21 amu (36%)

- e

- C$_{19}$H$_{13}$NH$_2$

- C$_2$H$_{10}$N$_5$Se

m/z= 631.92 amu (36%)

m/z= 448.33 amu (53%)

- C$_8$H$_6$

- C$_6$H$_{10}$NSeZn

m/z= 346.32 amu (82%)

m/z= 116.83 amu (38%)

Scheme (3-18): Fragmentation steps and relative abundance of [Zn(L^1)$_2$]

(3.12.3) Mass spectral data of [Cu(L^2)$_2$]

The electrospray (+) mass spectrum of [Cu(L^2)$_2$] is depicted in Figure (3-172). The parent ion peak recorded at m/z= 1005.21 (M)$^+$ (15%) calculated for $C_{46}H_{54}CuN_8O_4Se_2$; requires= 1005.21. Peaks detected at m/z= 842.31 (24%), 644.32 (100%), 407.81 (33%) and 110.80 (17%) assigned to [M-($C_{10}H_4O_2$)]$^+$, [M-{($C_{10}H_4O_2$)+($C_{12}H_{10}N_2O$)}]$^+$, [M-{($C_{10}H_4O_2$)+($C_{12}H_{10}N_2O$)+(CH_3CuSe_2)}]$^+$ and [M-{($C_{10}H_4O_2$)+($C_{12}H_{10}N_2O$)+(CH_3CuSe_2)+($C_{20}H_{13}N_2O$)}]$^+$ respectively. The fragmentation pattern is included in Scheme (3-19).

Figure (3-172): The electrospray (+) mass spectrum of [Cu(L^2)$_2$].

1005.21

m/z= 1005.21 amu (15%)

− e

− C$_{11}$H$_{15}$O

− C$_{13}$H$_{12}$NO

m/z= 842.31 amu (24%)

m/z= 644.32 amu (100%)

− C$_4$H$_4$N$_3$CuSe

− C$_{11}$H$_{14}$N$_4$OSe

m/z= 407.81 amu (33%)

m/z= 110.80 amu (17%)

Scheme (3-19): Fragmentation steps and relative abundance of [Cu(L^2)$_2$].

(3.12.4) Mass spectral data of [Zn(L^2)$_2$]

The electrospray (+) mass spectrum of [Zn(L^2)$_2$], Figure (3-173) exhibits the parent molecular ion fragment at m/z= 1007.21 (M+H)$^+$ (17%) calculated for C$_{46}$H$_{54}$N$_8$O$_4$Se$_2$Zn; requires= 1006.21. Peaks detected at m/z= 794.30 (64%), 568.83 (100%), 362.20 (38%), 190.72 (49%) and 55.71 (10%) related to [M+H-(C$_{14}$H$_{13}$O$_2$)]$^+$, [(M+H)-{(C$_{14}$H$_{13}$O$_2$)+(C$_{14}$H$_{12}$NO$_2$)}]$^+$, [(M+H)-{(C$_{14}$H$_{13}$O$_2$)+(C$_{14}$H$_{12}$NO$_2$)+(C$_8$H$_5$N$_2$Se)}]$^+$, [(M+H)-{(C$_{14}$H$_{13}$O$_2$)+(C$_{14}$H$_{12}$NO$_2$)+(C$_8$H$_5$N$_2$Se)+(C$_2$H$_5$ZnSe)}]$^+$ and [(M+H)-{(C$_{14}$H$_{13}$O$_2$)+(C$_{14}$H$_{12}$NO$_2$)+(C$_8$H$_5$N$_2$Se)+(C$_2$H$_5$ZnSe)+(C$_6$H$_9$N$_4$)}]$^+$ respectively. The fragmentation pattern is included in Scheme (3-20).
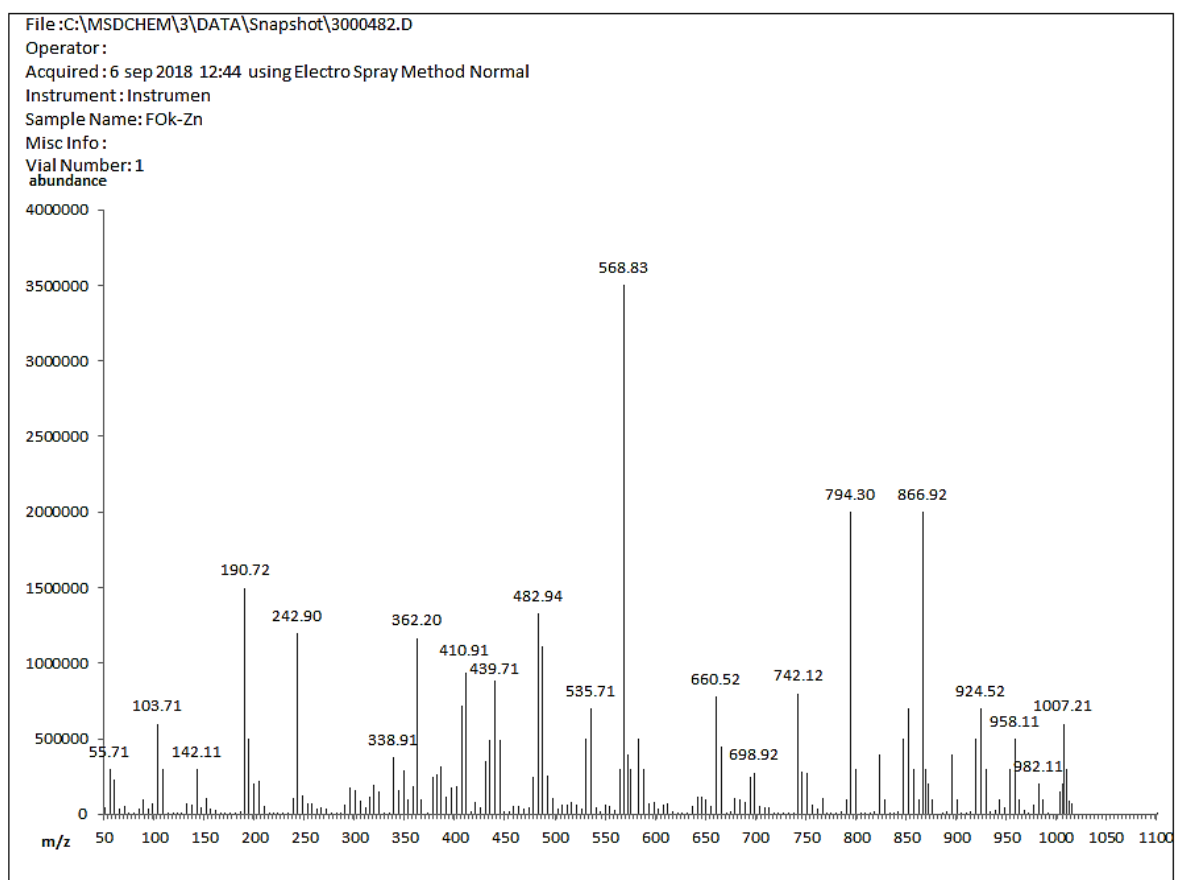
Figure (3-173): The electrospray (+) mass spectrum of [Zn(L^2)$_2$].

255

1006.21

m/z= 1007.21 amu (17%)

$- C_{14}H_{13}O_2$

$- C_{14}H_{12}NO_2$

m/z= 794.30 amu (64%)

$- C_8H_5N_2Se$

m/z= 568.83 amu (100%)

$- C_2H_5ZnSe$

m/z= 362.20 amu (38%)

m/z= 190.72 amu (49%)

$- C_6H_9N_4$

m/z= 55.71 amu (10%)
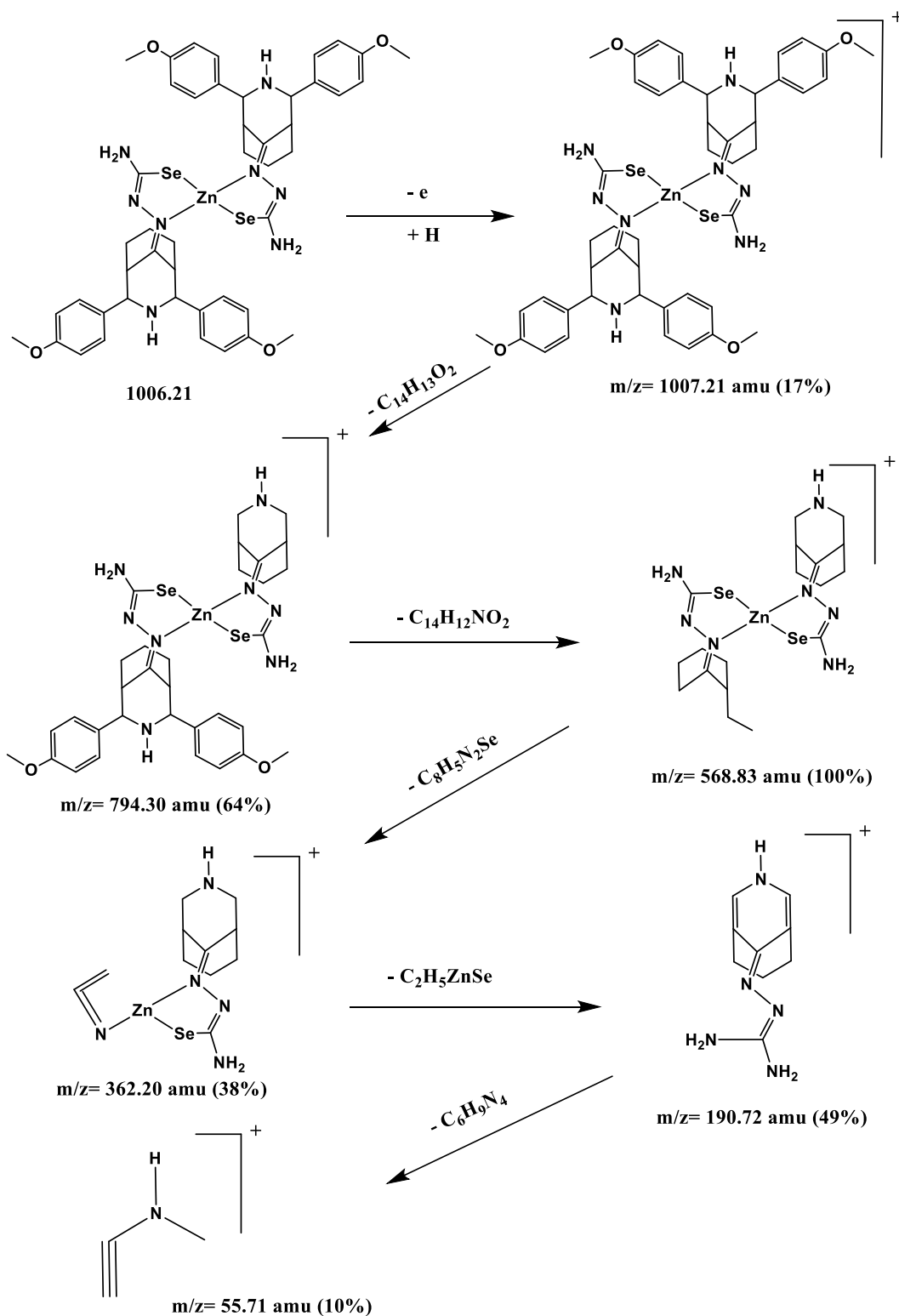
Scheme (3-20): Fragmentation steps and relative abundance of $[Zn(L^2)_2]$.

256

(3.12.5) Mass spectral data of K$_2$[Co(L^3)$_2$Cl$_2$]

The electrospray (+) mass spectrum of K$_2$[Co(L^3)$_2$Cl$_2$], Figure (3-174) exhibits the molecular ion peak at m/z= 1201.21 (M)$^+$ (13%) calculated for C$_{50}$H$_{66}$Cl$_2$CoK$_2$N$_{12}$Se$_2$; requires= 1201.21. Peaks detected at m/z= 1028.20 (19%), 804.61 (49%), 638.23 (100%), 378.21 (43%) and 118.21 (20%) related to [M-(C$_{11}$H$_{13}$N$_2$)]$^+$, [M-{(C$_{11}$H$_{13}$N$_2$)+(C$_3$H$_3$N$_2$Se+2K)}]$^+$, [M-{(C$_{11}$H$_{13}$N$_2$)+(C$_3$H$_3$N$_2$Se+2K)+(C$_8$H$_{14}$N$_4$)}]$^+$, [M-{(C$_{11}$H$_{13}$N$_2$)+(C$_3$H$_3$N$_2$Se+2K)+(C$_8$H$_{14}$N$_4$)+(C$_2$N$_2$CoCl$_2$Se)}]$^+$ and [M-{(C$_{11}$H$_{13}$N$_2$)+(C$_3$H$_3$N$_2$Se+2K)+(C$_8$H$_{14}$N$_4$)+(C$_2$N$_2$CoCl$_2$Se)+(C$_{16}$H$_{26}$N$_3$)}]$^+$ respectively. The fragmentation pattern is included in Scheme (3-21).
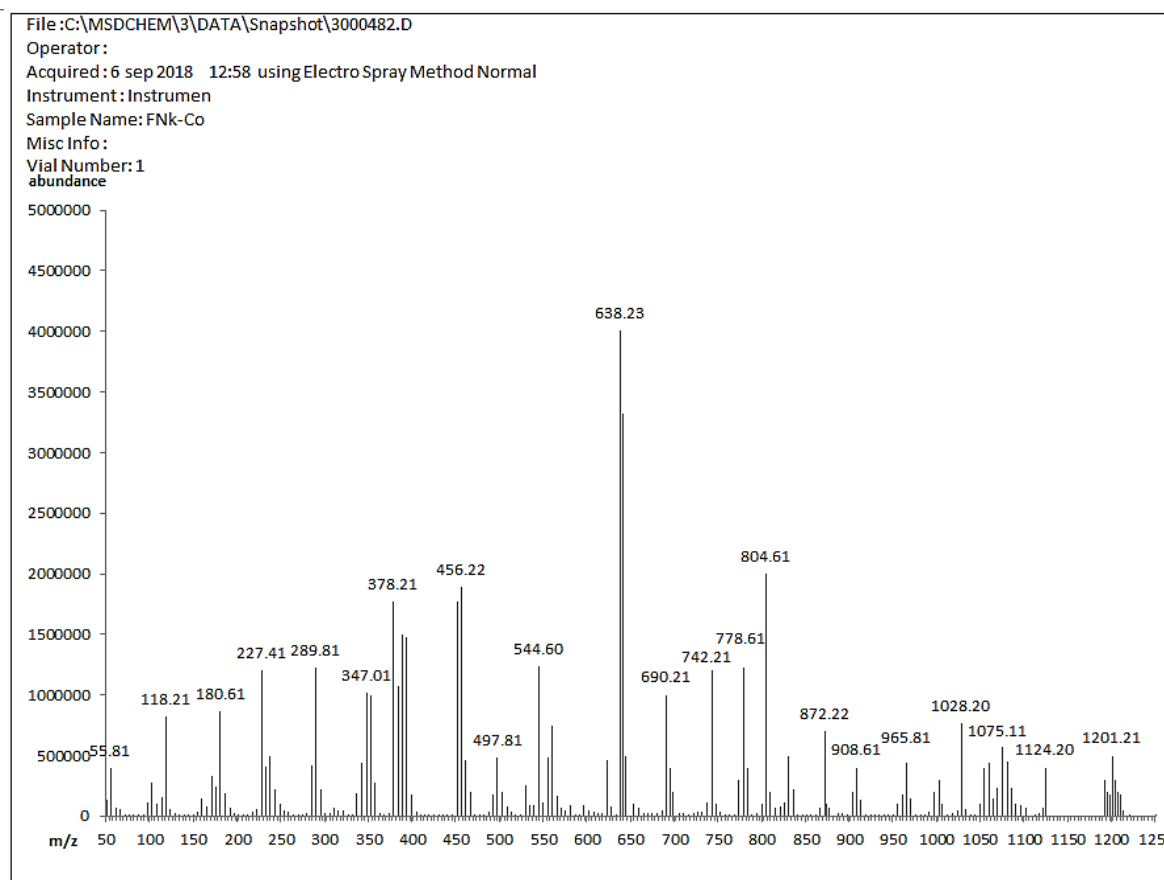
Figure (3-174): The electrospray (+) mass spectrum of K$_2$[Co(L^3)$_2$Cl$_2$].
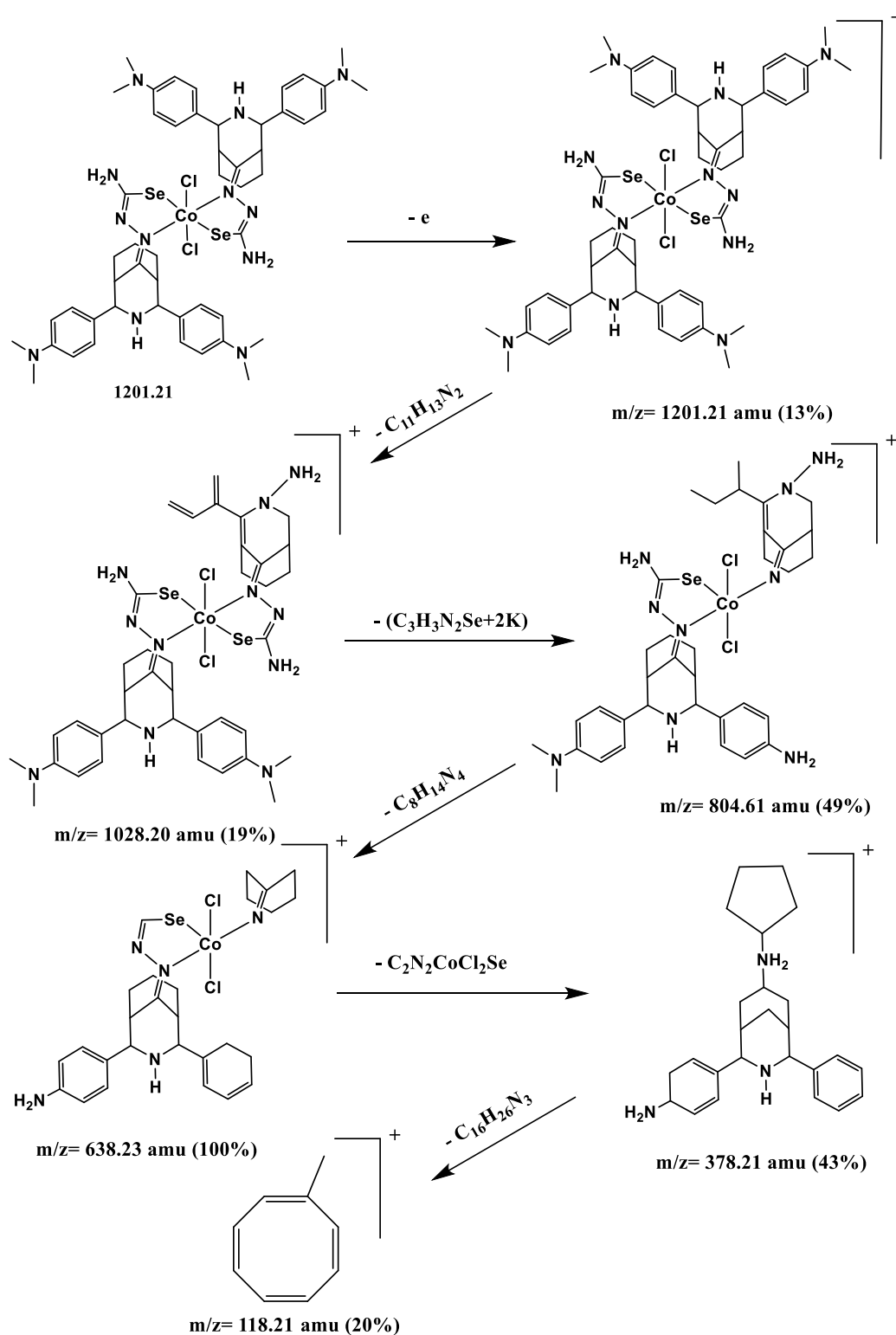
Scheme (3-21): Fragmentation steps and relative abundance of $K_2[Co(L^3)_2Cl_2]$.

(3.12.6) Mass spectral data of $[Cd(L^3)_2]$

The electrospray (+) mass spectrum of $[Cd(L^3)_2]$ is depicted in Figure (3-175). The spectrum exhibits the parent molecular ion at m/z= 1108.31 $(M)^+$ (18%) calculated for $C_{50}H_{66}CdN_{12}Se_2$; requires= 1108.31. Peaks detected at m/z= 903.81 (24%), 596.41 (64%), 331.43 (100%) and 77.11 (27%) related to $[M-(C_{12}H_{19}N_3)]^+$, $[M-\{(C_{12}H_{19}N_3)+(C_5H_{14}N_3CdSe)\}]^+$, $[M-\{(C_{12}H_{19}N_3)+(C_5H_{14}N_3CdSe)+(C_{10}H_{10}N_4Se)\}]^+$ and $[M-\{(C_{12}H_{19}N_3)+(C_5H_{14}N_3CdSe)+(C_{10}H_{10}N_4Se)+(C_{17}H_{22}N_2)\}]^+$ respectively. The fragmentation pattern is included in Scheme (3-22).
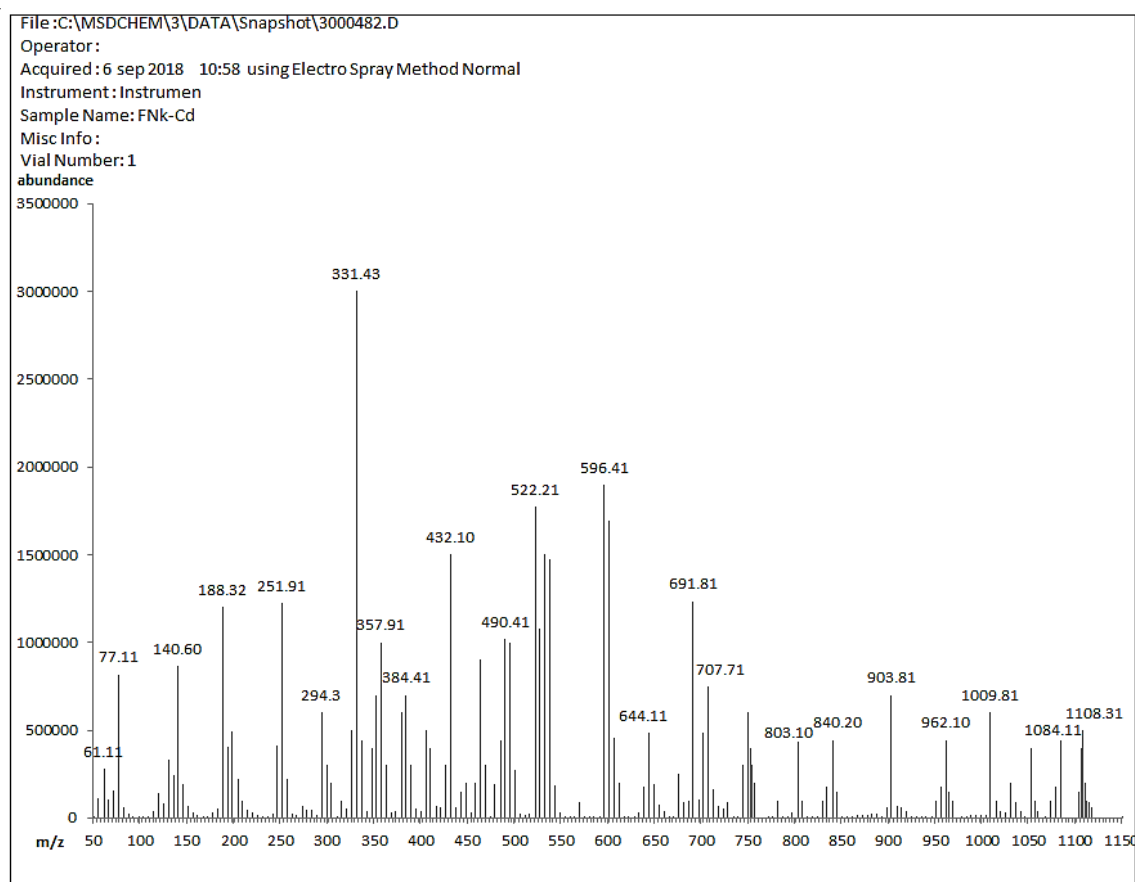
Figure (3-175): The electrospray (+) mass spectrum of $[Cd(L^3)_2]$.

1108.31

m/z= 1108.31 amu (18%)

- e

- C$_{12}$H$_{19}$N$_3$

m/z= 903.81 amu (24%)

- C$_5$H$_{14}$N$_3$CdSe

m/z= 596.41 amu (64%)

- C$_{10}$H$_{10}$N$_4$Se

m/z= 331.43 amu (100%)

- C$_{17}$H$_{22}$N$_2$

m/z= 77.11 amu (27%)
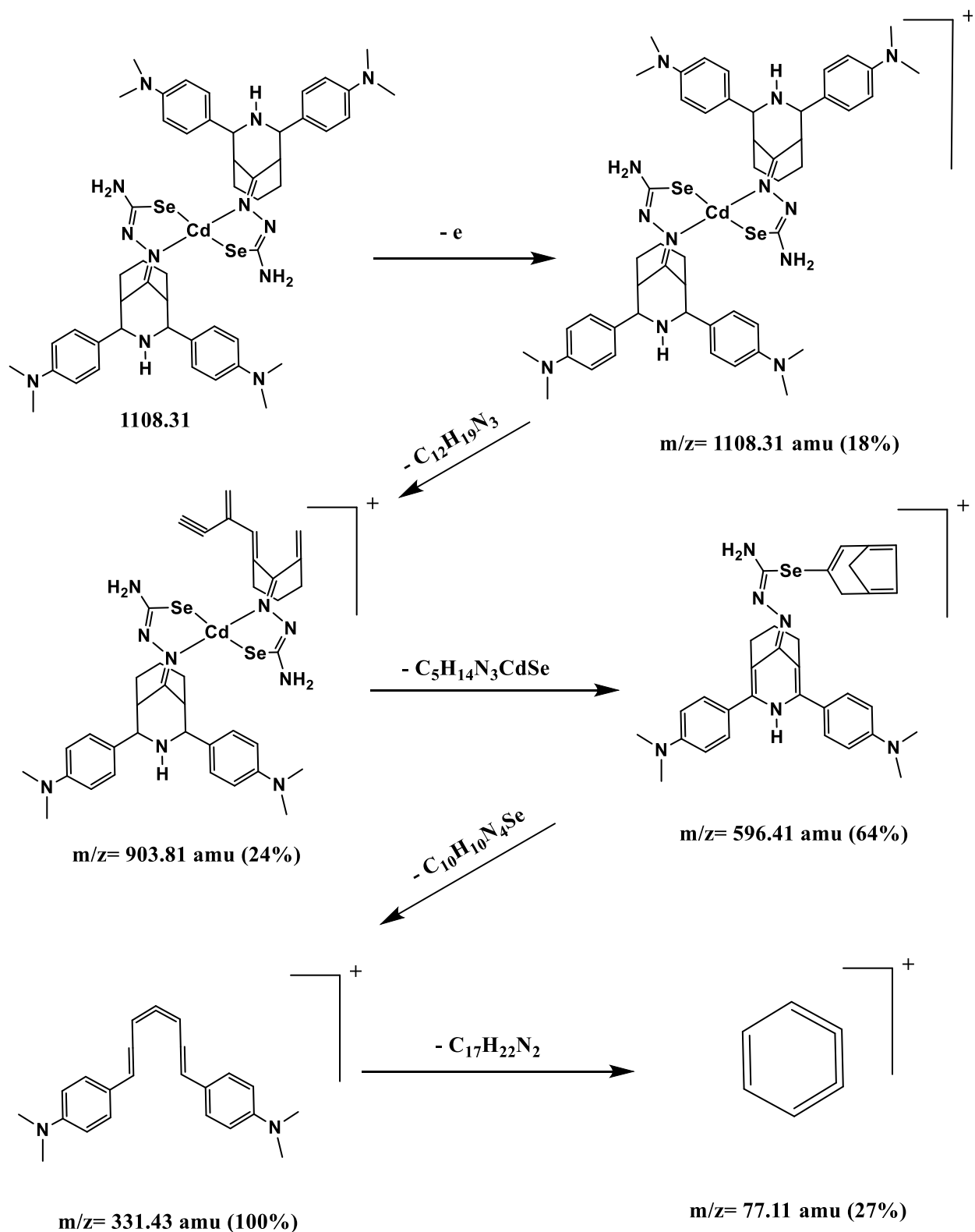
Scheme (3-22): Fragmentation steps and relative abundance of [Cd(L^3)$_2$].

(3.12.7) Mass spectral data of $K_2[Ni(L^4)_2Cl_2]$

The electrospray (+) mass spectrum of $K_2[Ni(L^4)_2Cl_2]$, Figure (3-176), recorded the parent ion peak at m/z= 1094.21 $(M)^+$ (15%) calculated for $C_{40}H_{44}Cl_2K_2N_{10}NiO_4Se_2$; requires= 1094.21. Peaks detected at m/z= 908.61 (21%), 726.63 (100%), 477.21 (53%), 352.22 (82%) and 92.22 (22%) related to $[M-(C_4H_{10}+NO_2+2K+4H_2)]^+$, $[M-\{(C_4H_{10}+NO_2+2K+4H_2)+(C_9H_4+2Cl)\}]^+$, $[M-\{(C_4H_{10}+NO_2+2K+4H_2)+(C_9H_4+2Cl)+(C_4H_7N_4NiSe)\}]^+$, $[M-\{(C_4H_{10}+NO_2+2K+4H_2)+(C_9H_4+2Cl)+(C_4H_7N_4NiSe)+(C_5H_5N+NO_2)\}]^+$ and $[M-\{(C_4H_{10}+NO_2+2K+4H_2)+(C_9H_4+2Cl)+(C_4H_7N_4NiSe)+(C_5H_5N+NO_2)+(C_{10}H_{19}N_3Se)\}]^+$, respectively. The fragmentation pattern is included in Scheme (3-23).
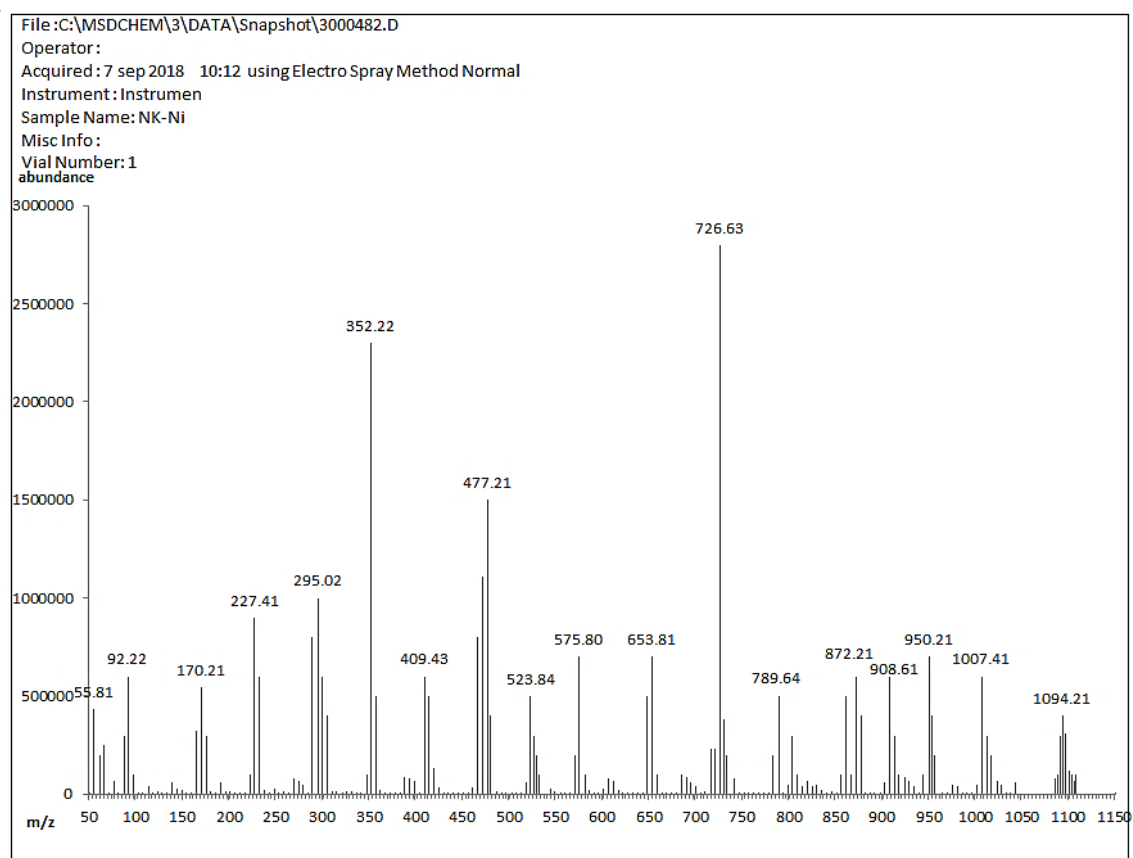
Figure (3-176): The electrospray (+) mass spectrum of $K_2[Ni(L^4)_2Cl_2]$.
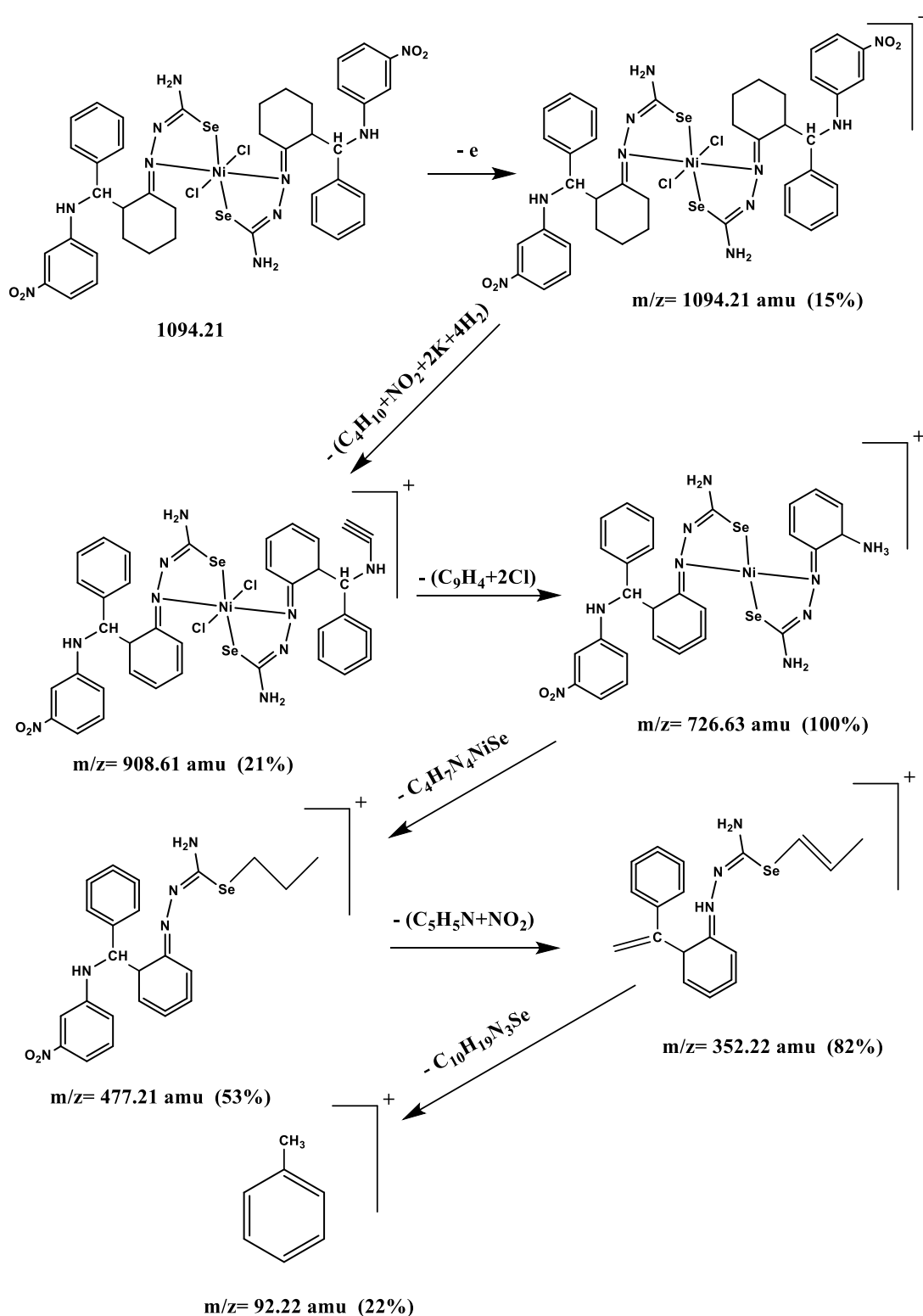
Scheme (3-23): Fragmentation steps and relative abundance of K$_2$[Ni(L^4)$_2$Cl$_2$].

(3.12.8) Mass spectral data of [Cd(L^4)$_2$]

The electrospray (+) mass spectrum of [Cd(L^4)$_2$], Figure (3-177) exhibits the parent ion peak at m/z= 1002.21 (M)$^+$ (15%) calculated for $C_{40}H_{44}CdN_{10}O_4Se_2$; requires= 1002.21. Peaks detected at m/z= 829.20 (22%), 519.62 (100%), 313.21 (54%) and 106.81 (33%) related to [M-(C$_9$H$_5$N+NO$_2$)]$^+$, [M-{(C$_9$H$_5$N+NO$_2$)+(C$_6$H$_5$N$_3$CdSe)}]$^+$, [M-{(C$_9$H$_5$N+NO$_2$)+(C$_6$H$_5$N$_3$CdSe)+(C$_6$H$_{13}$N$_3$Se)}]$^+$ and [M-{(C$_9$H$_5$N+NO$_2$)+(C$_6$H$_5$N$_3$CdSe)+ (C$_6$H$_{13}$N$_3$Se)+(C$_{11}$H$_{15}$N+NO$_2$)}]$^+$ respectively. The fragmentation pattern is included in Scheme (3-24).
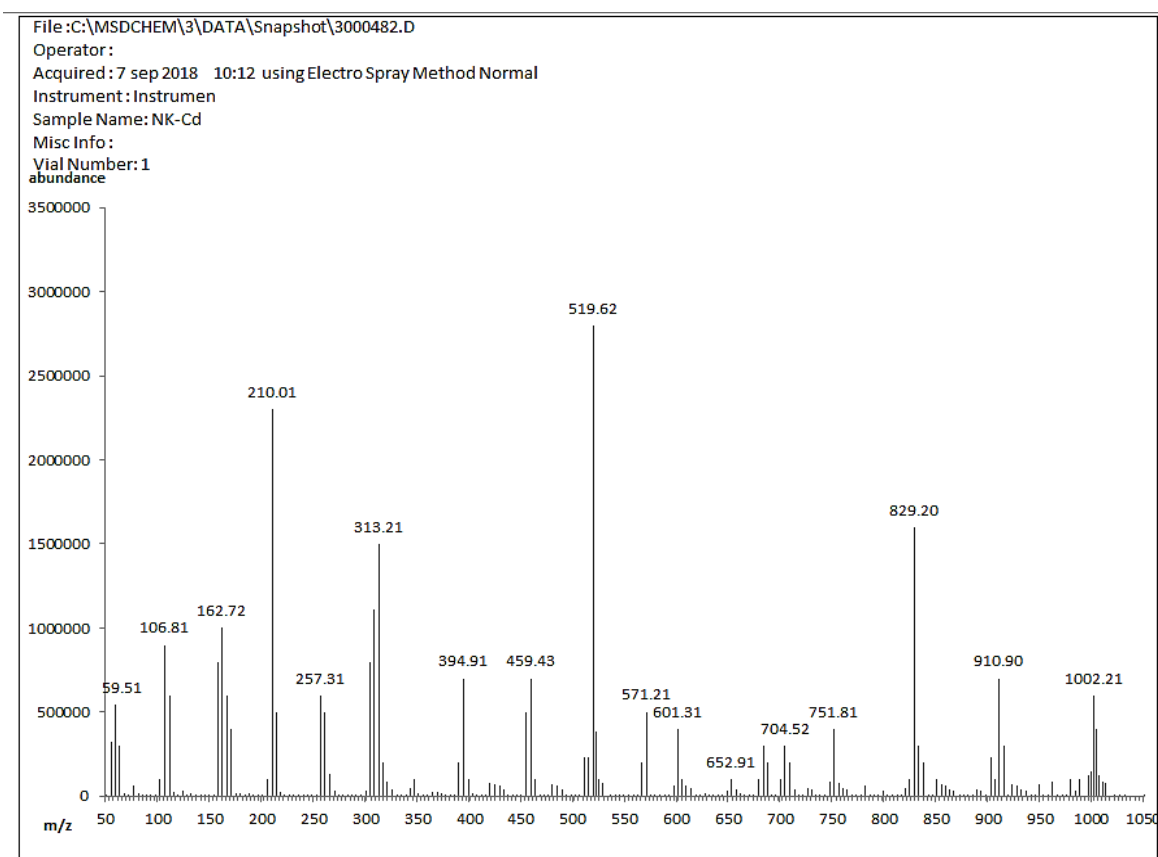
Figure (3-177): The electrospray (+) mass spectrum of [Cd(L^4)$_2$].
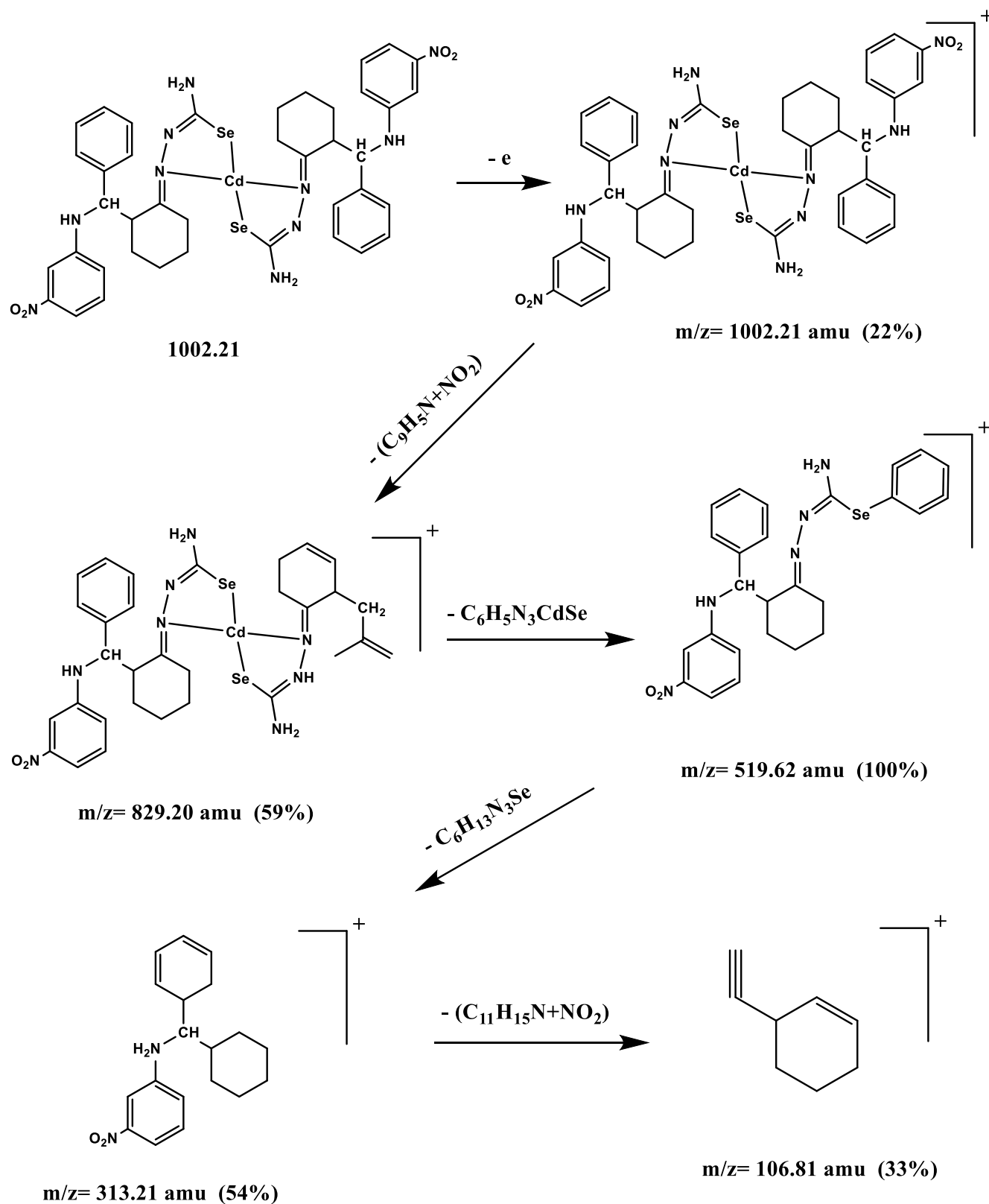
Scheme (3-24): Fragmentation steps and relative abundance of [Cd(L^4)$_2$].

(3.12.9) Mass spectral data of $K_2[Mn(L^5)_2Cl_2]$

The electrospray (+) mass spectrum of $K_2[Mn(L^5)_2Cl_2]$, Figure (3-178) showed the parent ion peak at m/z= 1061.11 $(M)^+$ (14%) calculated for $C_{42}H_{50}Cl_2K_2MnN_8O_2Se_2$; requires= 1061.21. Peaks detected at m/z= 846.12 (24%), 682.91 (100%), 484.32 (50%), 259.64 (31%) and 77.41 (17%) assigned to $[M-(C_4H_{10}N+OCH_2+Cl+2K)]^+$, $[M-\{(C_4H_{10}N+OCH_2+Cl+2K)+(CH_6N_2Se+2H_2+Cl)\}]^+$, $[M-\{(C_4H_{10}N+OCH_2+Cl+2K)+(CH_6N_2Se+2H_2+Cl)+(CH_6N_3MnSe+2H_2)\}]^+$, $[M-\{(C_4H_{10}N+OCH_2+Cl+2K)+(CH_6N_2Se+2H_2+Cl)+(CH_6N_3MnSe+2H_2)+(C_{15}H_{15}NO)\}]^+$ and $[M-\{(C_4H_{10}N+OCH_2+Cl+2K)+(CH_6N_2Se+2H_2+Cl)+(CH_6N_3MnSe+2H_2)+(C_{15}H_{15}NO)+(C_{15}H_2)\}]^+$ respectively. The fragmentation pattern is included in Scheme (3-25).
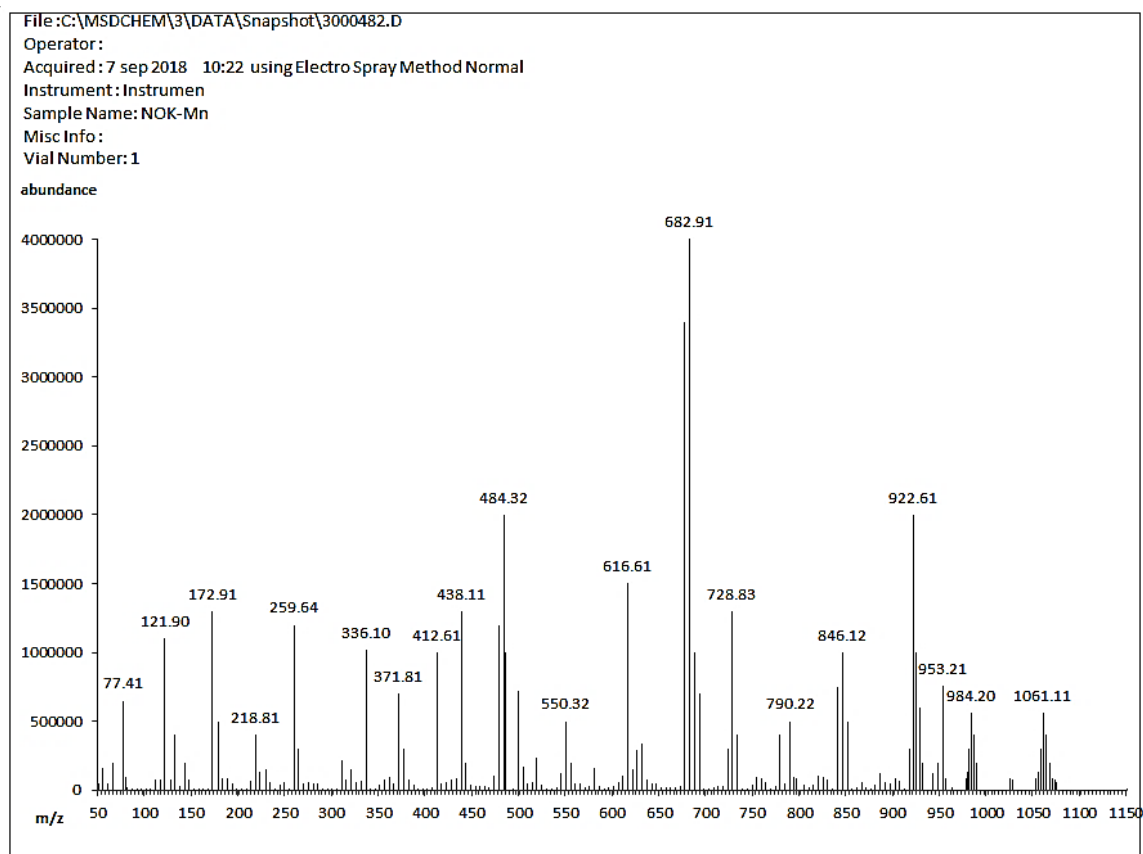
Figure (3-178): The electrospray (+) mass spectrum of $K_2[Mn(L^5)_2Cl_2]$.

1061.11

m/z= 1061.11 amu (14%)

$- (C_4H_{10}N + OCH_2 + Cl + 2K)$

$- (CH_6N_2Se + 2H_2 + Cl)$

m/z= 846.12 amu (24%)

m/z= 682.91 amu (100%)

$- (CH_6N_3MnSe + 2H_2)$

$- e$

$- C_{15}H_{15}NO$

m/z= 484.32 amu (50%)

m/z= 259.64 amu (31%)

$- C_{15}H_2$

m/z= 77.41 amu (17%)
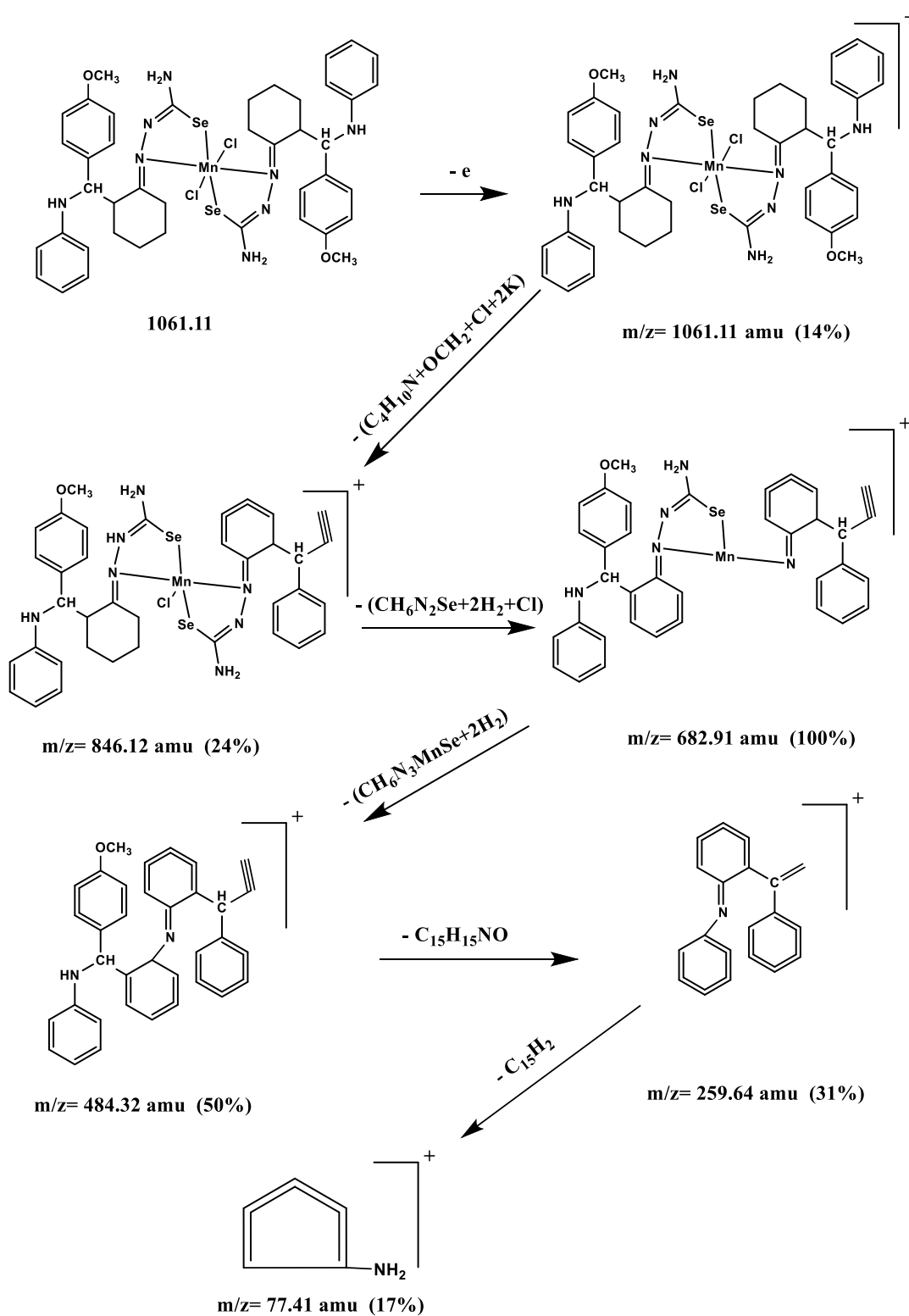
Scheme (3-25): Fragmentation steps and relative abundance of $K_2[Mn(L^5)_2Cl_2]$.

266

(3.12.10) Mass spectral data of [Zn(L^5)$_2$]

The electrospray (+) mass spectrum of the Zn(II) complex, [Zn(L^5)$_2$] (Figure (3-179)), showed the parent molecular ion at m/z= 922.31 (M)$^+$ (21%) calculated for $C_{42}H_{50}N_8O_2Se_2Zn$; requires= 922.31. Peaks detected at m/z= 819.11 (20%), 702.52 (100%), 501.11 (80%), 267.91 (48%) and 52.08 (8%) assigned to [M-($C_6H_{15}O$)]$^+$, [(M-{($C_6H_{15}O$)+(C_8H_7N)}]$^+$, [(M-{($C_6H_{15}O$)+(C_8H_7N)+(CH_3N_3ZnSe)}]$^+$, [(M-{($C_6H_{15}O$)+ (C_8H_7N)+(CH_3N_3ZnSe)+($C_8H_{17}N_3Se$)}]$^+$ and [(M-{($C_6H_{15}O$)+(C_8H_7N)+(CH_3N_3ZnSe)+ ($C_8H_{17}N_3Se$)+($C_{15}H_{10}NO$)}]$^+$ respectively. The fragmentation pattern is included in Scheme (3-26).

File : C:\MSDCHEM\3\DATA\Snapshot\3000482.D
Operator :
Acquired : 7 sep 2018 11:22 using Electro Spray Method Normal
Instrument : Instrumen
Sample Name : NOK-Zn
Misc Info :
Vial Number : 1
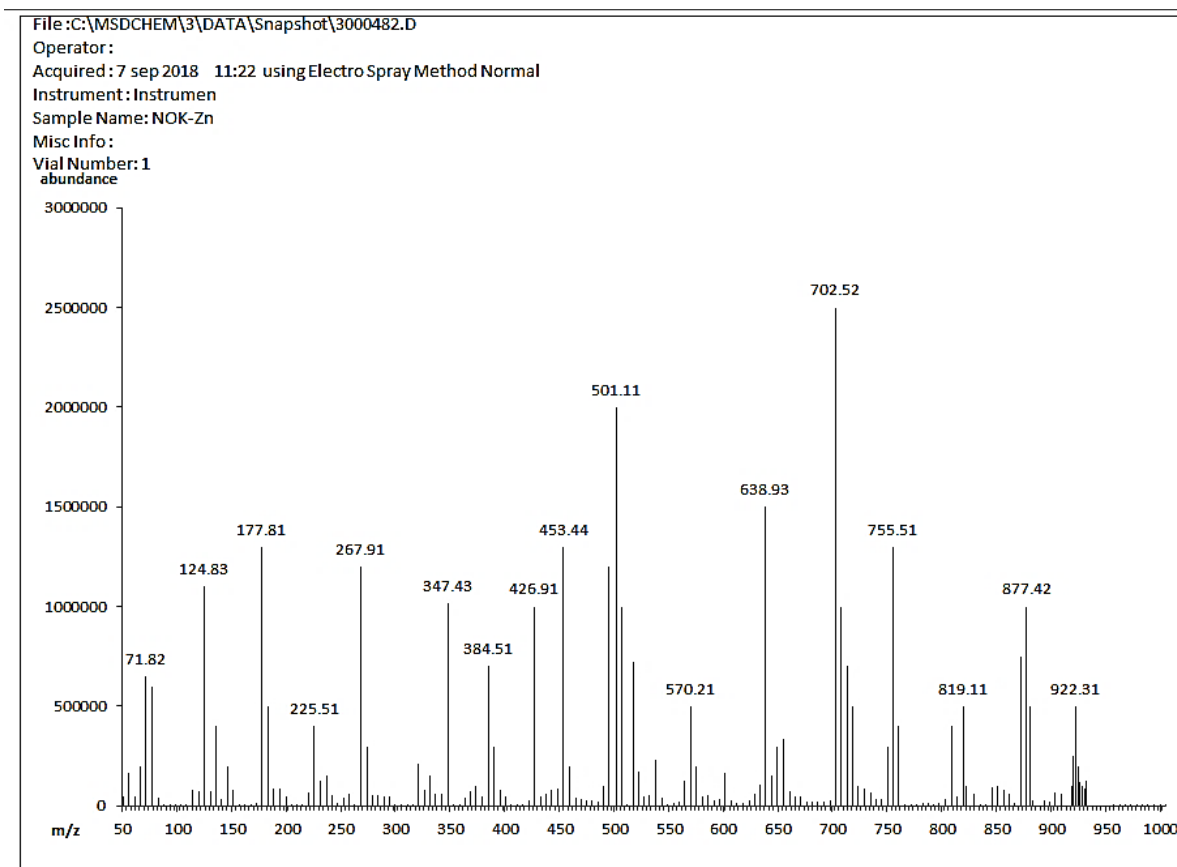
Figure (3-179): The electrospray (+) mass spectrum of [Zn(L^5)$_2$].
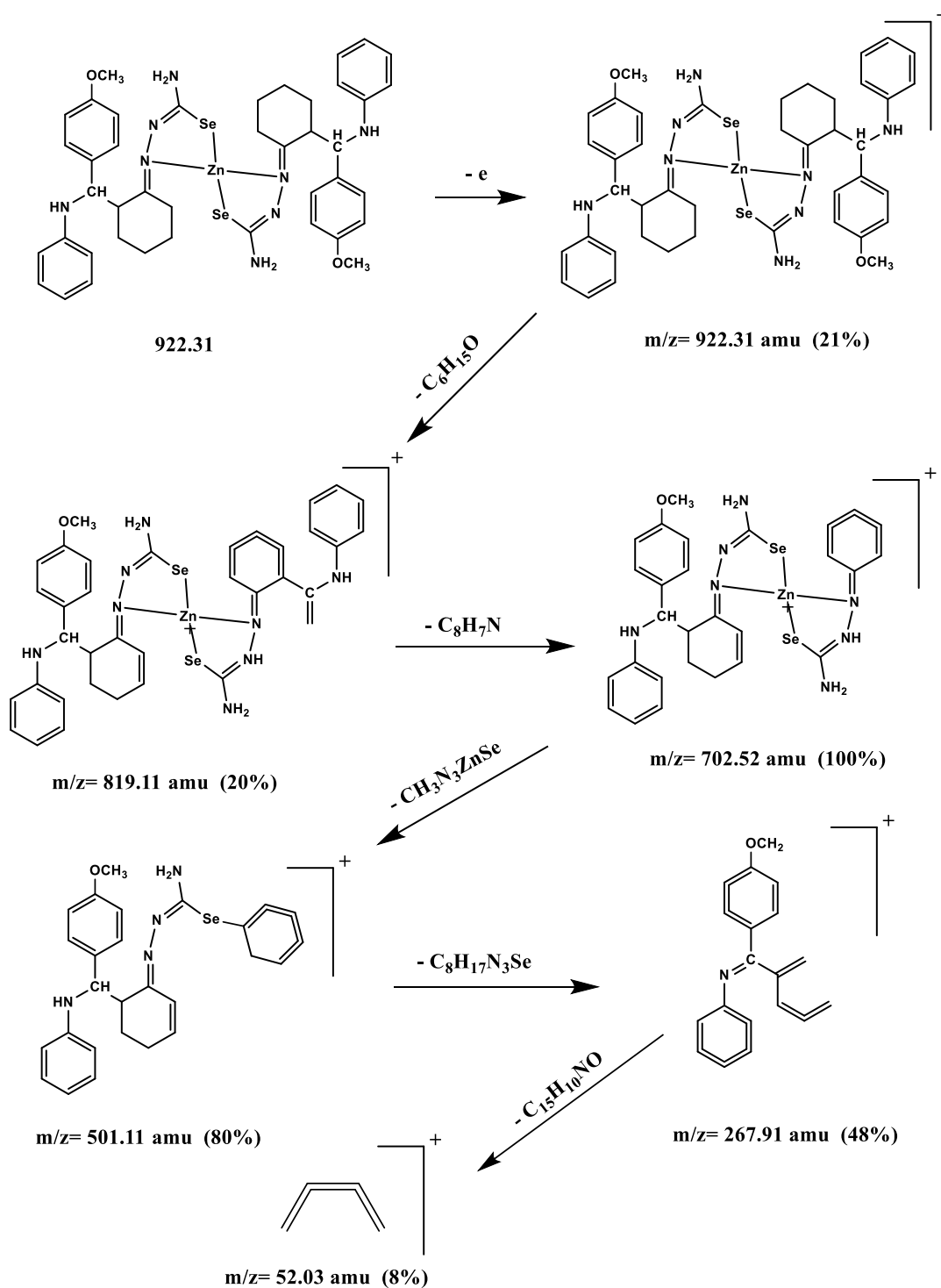
Scheme (3-26): Fragmentation steps and relative abundance of [Zn(L^5)$_2$].

(3.12.11) Mass spectral data of $[Cu(L^6)_2]$

The electrospray (+) mass spectrum of $[Cu(L^6)_2]$, Figure (3-180), showed peak at m/z= 1037.21 $(M)^+$ (24%) assigned to the parent molecular ion, calculated for $C_{44}H_{54}CuN_{12}O_4Se_2$; requires= 1037.21. Peaks detected at m/z= 819.72 (23%), 585.71 (90%), 440.11 (100%), 180.12 (71%) and 70.90 (30%) assigned to $[M-(C_{12}H_{14}N+NO_2)]^+$, $[(M-\{(C_{12}H_{14}N+NO_2)+(C_4HN_3CuSe)\}]^+$, $[(M-\{(C_{12}H_{14}N+NO_2)+(C_4HN_3CuSe)+(C_5H_{11}N_2+NO_2)\}]^+$, $[(M-\{(C_{12}H_{14}N+NO_2)+(C_4HN_3CuSe)+(C_5H_{11}N_2+NO_2)+(C_{11}H_7N_3Se)\}]^+$ and $[(M-\{(C_{12}H_{14}N+NO_2)+(C_4HN_3CuSe)+(C_5H_{11}N_2+NO_2)+(C_{11}H_7N_3Se)+(C_8H_{14})\}]^+$ respectively. The fragmentation pattern is included in Scheme (3-27).
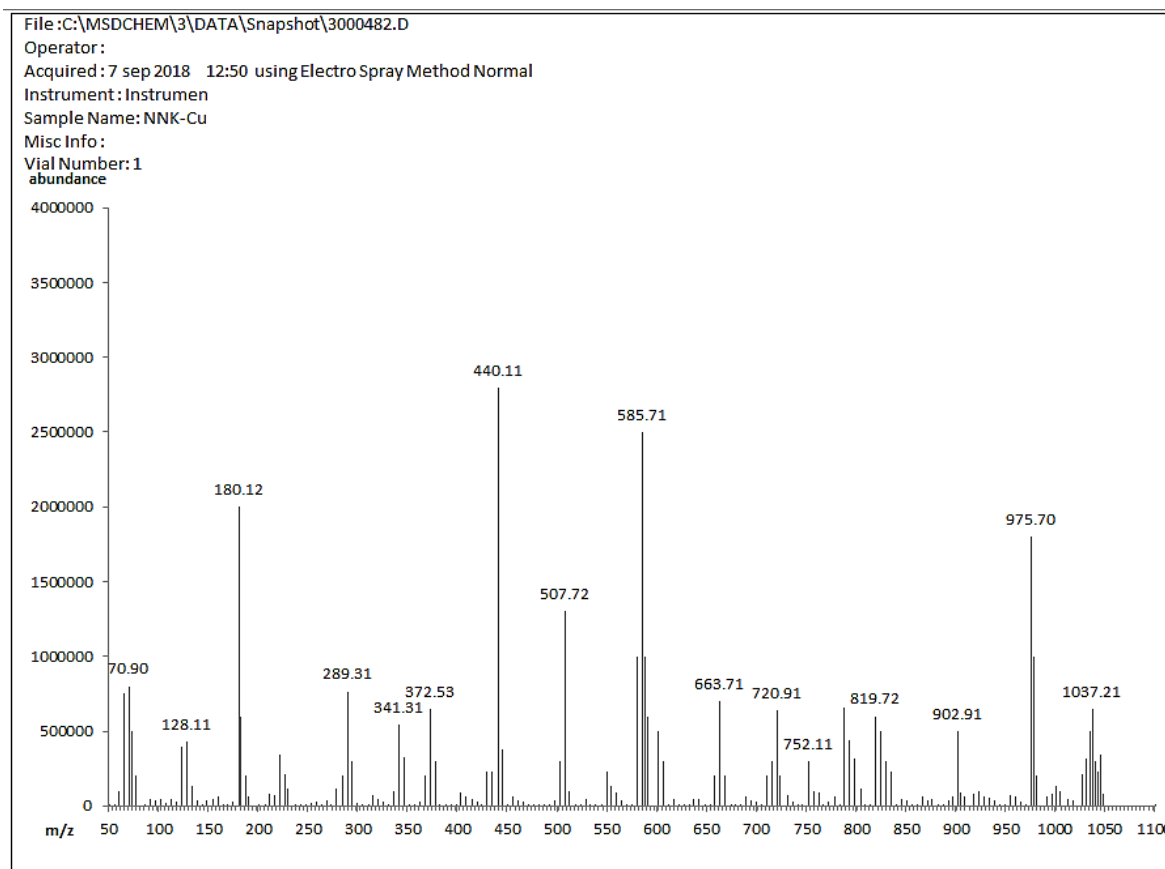
Figure (3-180): The electrospray (+) mass spectrum of $[Cu(L^6)_2]$.

1037.21

m/z= 1037.21 amu (24%)

− e

− (C$_{12}$H$_{14}$N+NO$_2$)

m/z= 819.72 amu (23%)

− C$_4$HN$_3$CuSe

m/z= 585.71 amu (90%)

− (C$_5$H$_{11}$N$_2$+NO$_2$)

m/z= 440.11 amu (100%)

− C$_{11}$H$_7$N$_3$Se

m/z= 180.12 amu (71%)

− C$_8$H$_{14}$

m/z= 70.90 amu (30%)
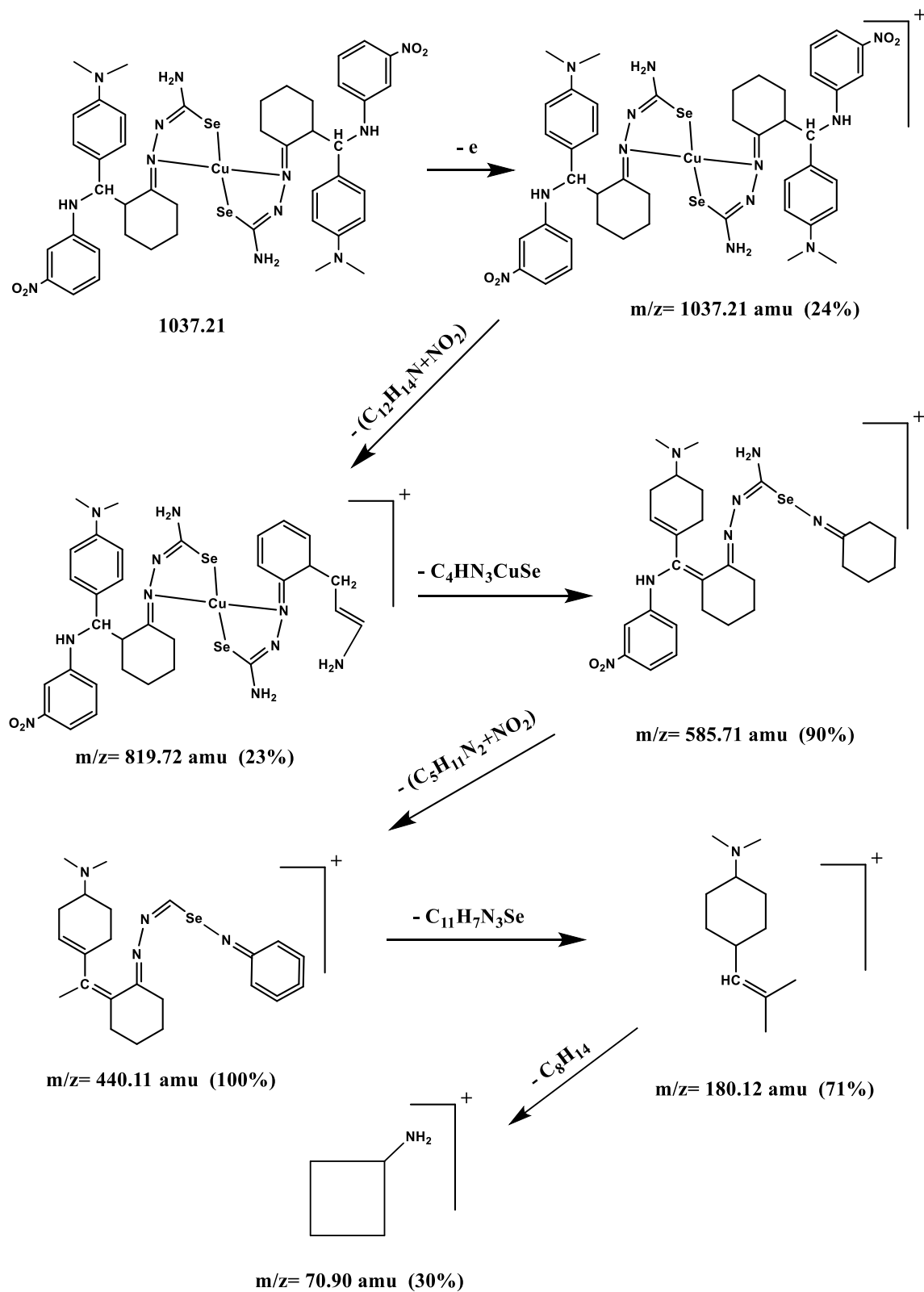
Scheme (3-27): Fragmentation steps and relative abundance of [Cu(L^6)$_2$].

270

(3.12.12) Mass spectral data of $[Zn(L^6)_2]$

The electrospray (+) mass spectrum of $[Zn(L^6)_2]$, Figure (3-181), indicated the parent molecular ion fragment at m/z= 1038.20 $(M)^+$ (23%) calculated for $C_{44}H_{54}N_{12}O_4Se_2Zn$; requires= 1038.20. Peaks detected at m/z= 876.11 (35%), 711.14 (57%), 466.71 (100%), 227.51 (28%) and 55.91 (20%) assigned to $[M-(C_7H_{13}N_2+NO_2)]^+$, $[(M-\{(C_7H_{13}N_2+NO_2)+(C_{11}H_{10}N)\}]^+$, $[(M-\{(C_7H_{13}N_2+NO_2)+(C_{11}H_{10}N)+(C_4H_{11}N_3ZnSe)\}]^+$, $[(M-\{(C_7H_{13}N_2+NO_2)+(C_{11}H_{10}N)+(C_4H_{11}N_3ZnSe)+(C_9H_{10}N_3Se)\}]^+$ and $[(M-\{(C_7H_{13}N_2+NO_2)+(C_{11}H_{10}N)+(C_4H_{11}N_3ZnSe)+(C_9H_{10}N_3Se)+(C_{10}H_{10}+NO_2)\}]^+$ respectively. The fragmentation pattern is included in Scheme (3-28).

File :C:\MSDCHEM\3\DATA\Snapshot\3000482.D
Operator:
Acquired : 7 sep 2018   10:56 using Electro Spray Method Normal
Instrument : Instrumen
Sample Name: NNK-Zn
Misc Info :
Vial Number: 1

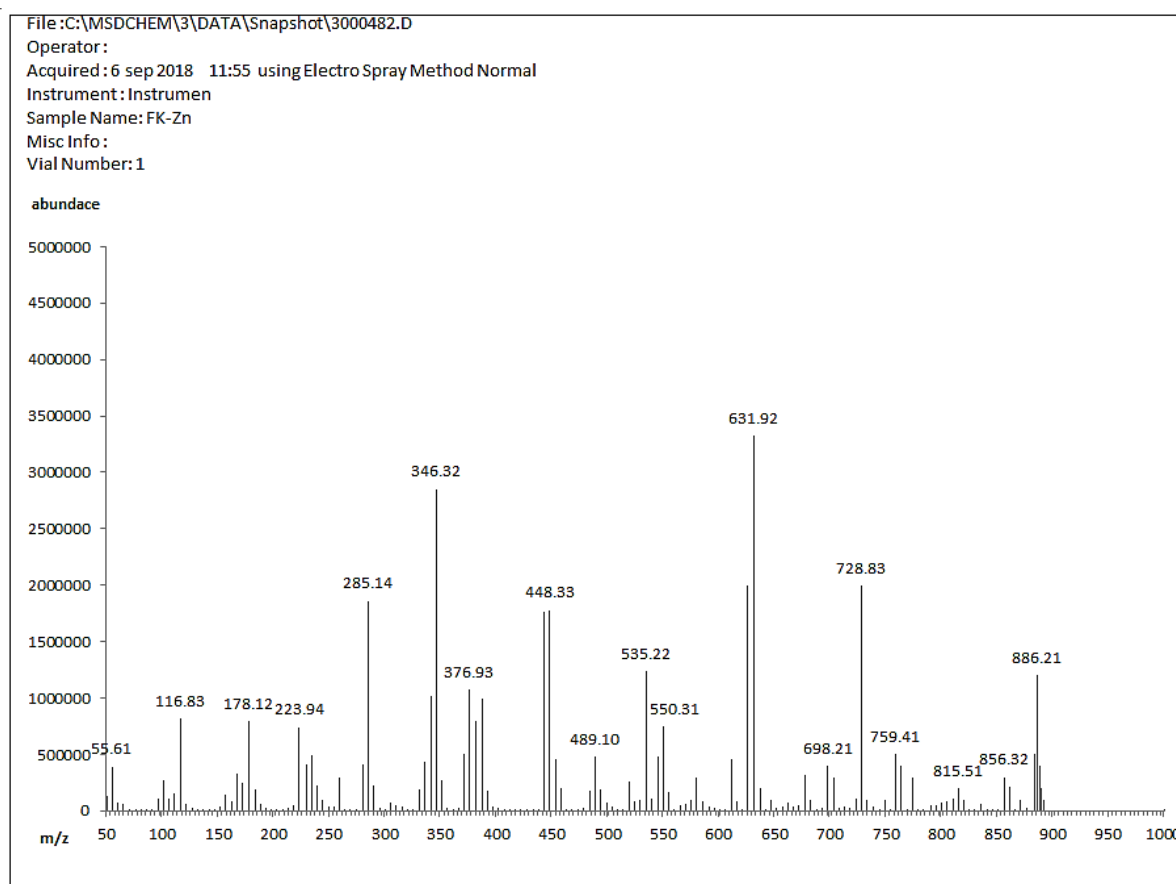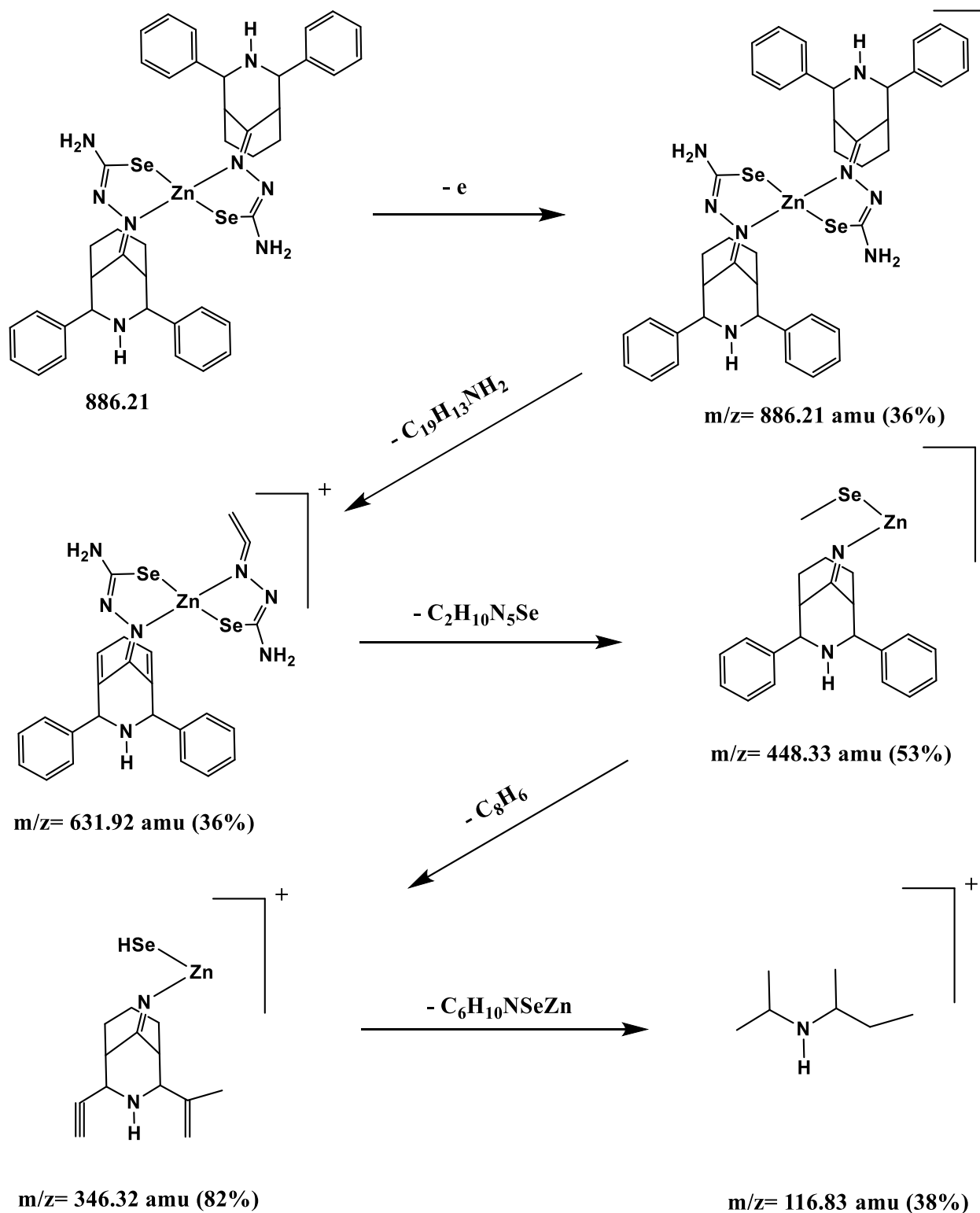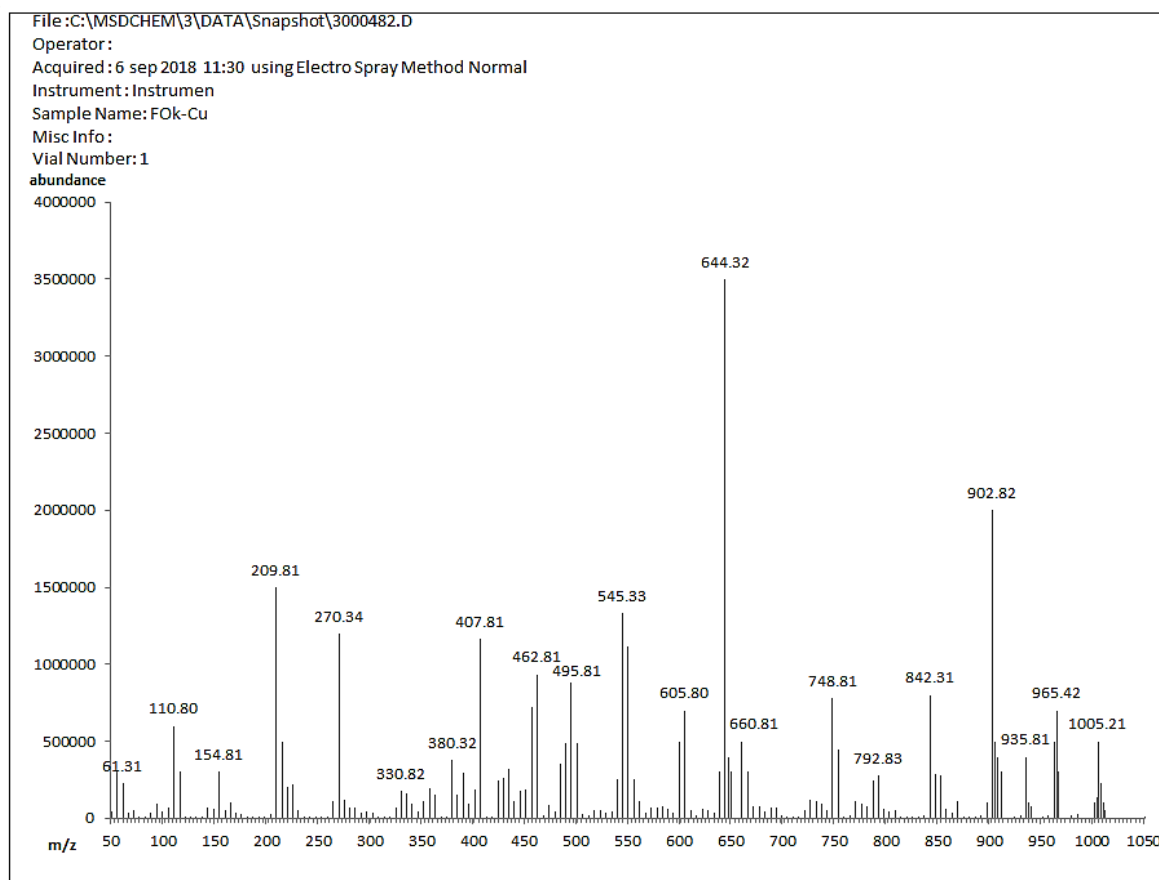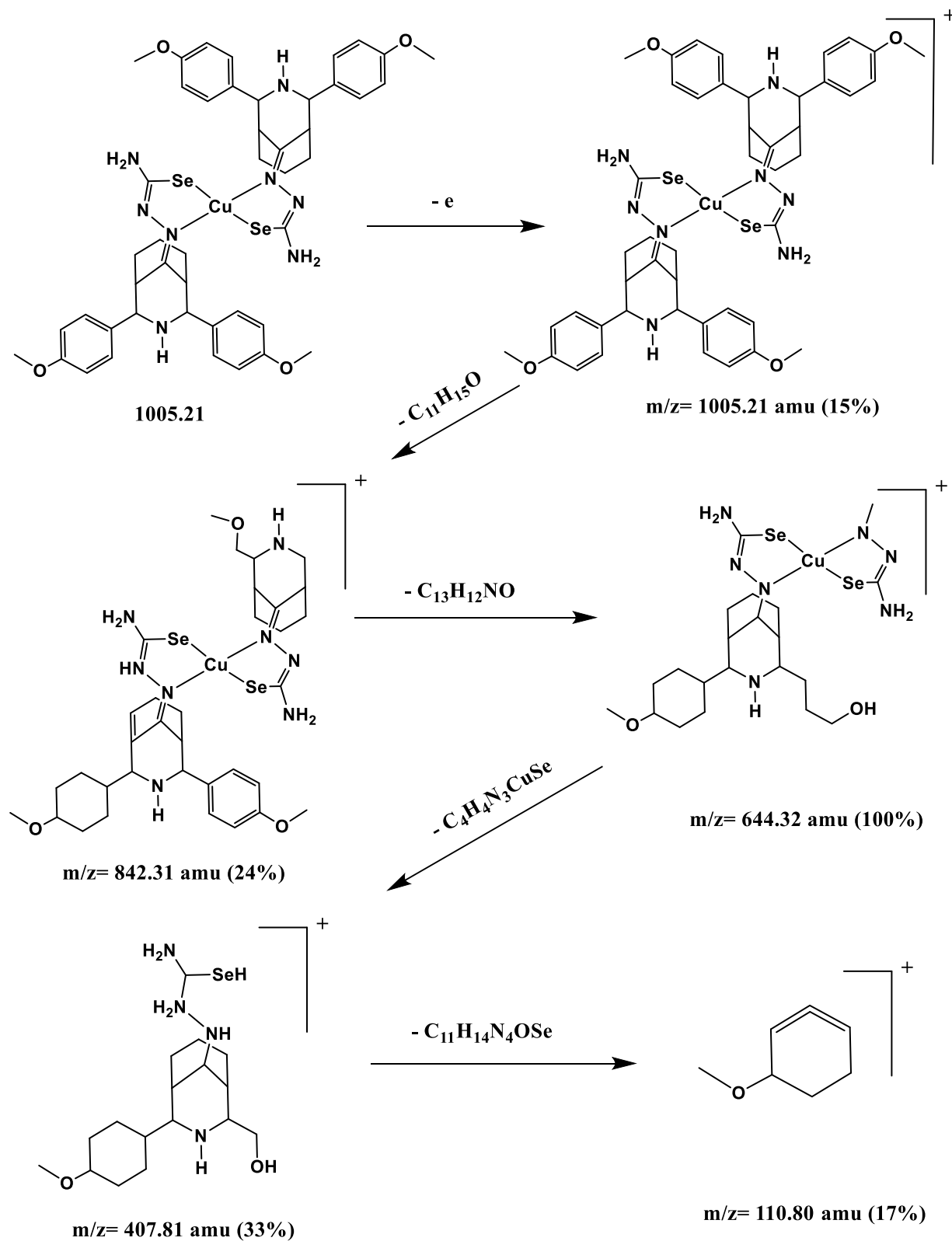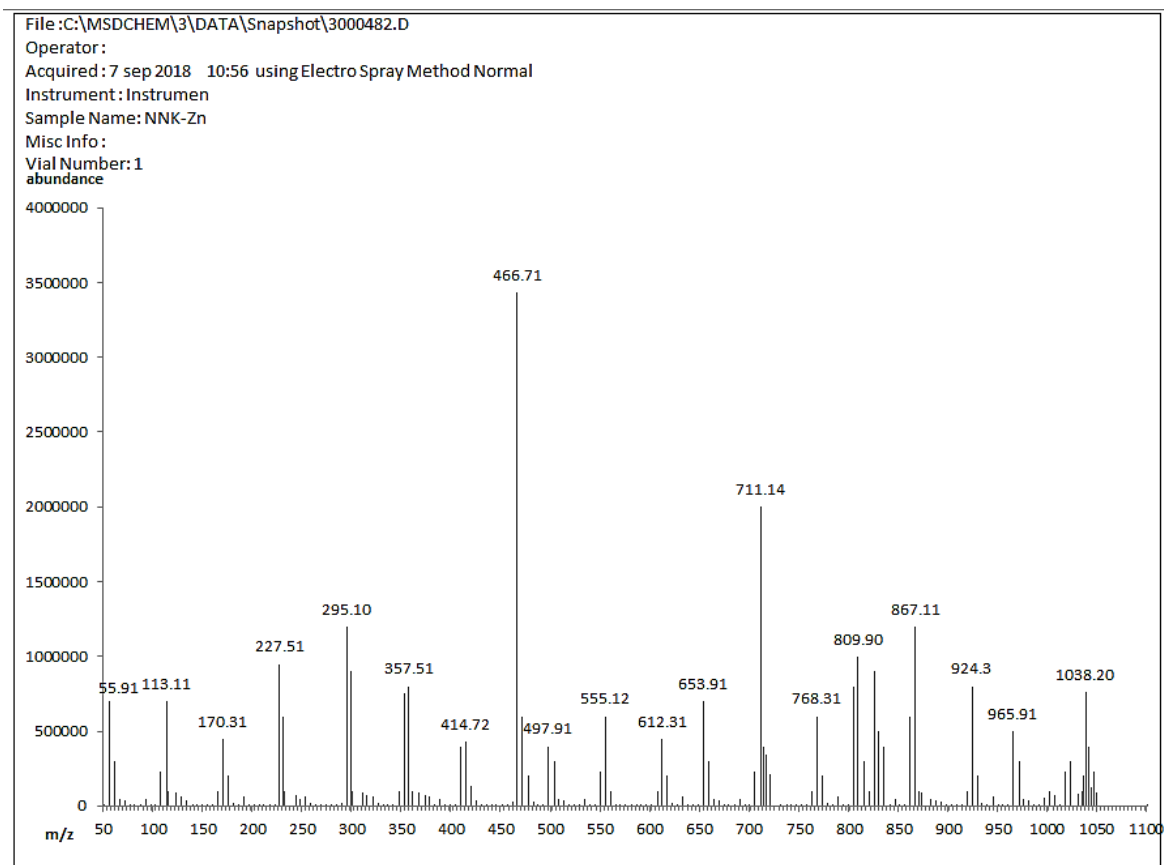**Figure (3-181): The electrospray (+) mass spectrum of $[Zn(L^6)_2]$.**

271
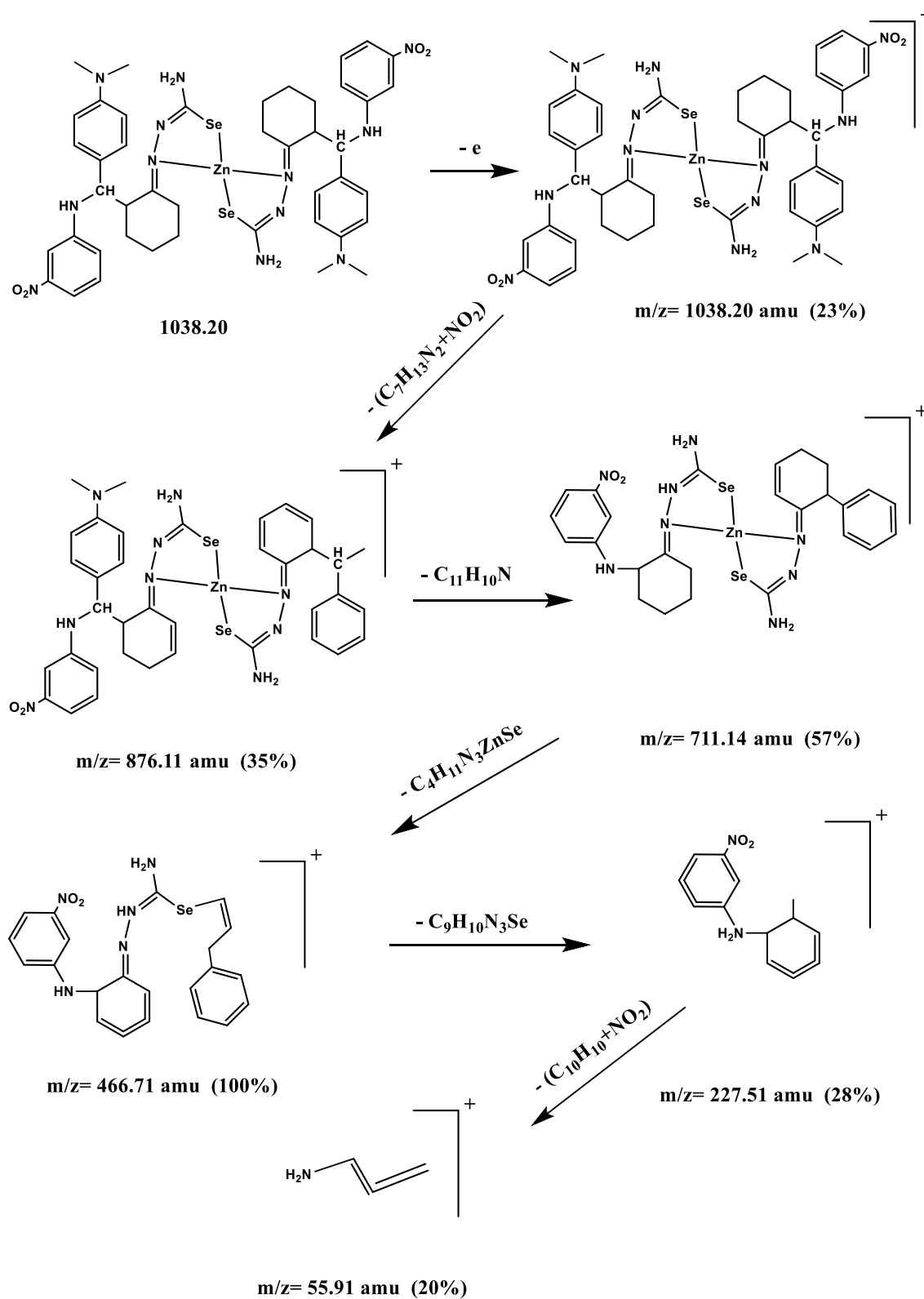
Scheme (3-28): Fragmentation steps and relative abundance of [Zn(L^6)$_2$].

(3.13) Thermal properties of ligands and complexes

Thermal analysis technique has used to determine thermal stability, melting points of ligands and their metal complexes and to conclude type of water molecule in complexes (hydrate or aquo) if there is/are water molecules. The TGA, DTG and DSC analysis data of ligands and selected metal complexes are listed in Table (3-30). The thermal analysis data of the prepared compounds in this work and their curves are discussed as follows:

(3.13.1) Thermal analysis of ligands

(3.13.1.1) Thermal analysis of HL^1

The TGA, DTG and DSC thermograms of selenosemicarbazone ligand (HL^1) are shown in Figure (3-182). The investigated sample exhibited stability up to 106.4 ºC. The associated exothermic or endothermic peaks have been detected over temperatures 108.4, 172.3, 250.7, 345.1 and 472.3 ºC, as revealed by DSC analysis. In general, the TGA curve indicated three decomposition steps. Peak observed between 108.4-259.7 °C attributed to the loss of $(CH_4+N_2H_2)$ fragments (obs.= 2.3785 mg; calc.= 2.3504 mg, 11.19%). The second step recorded at 361.5 ºC assigned to the loss of $(N_2+2CH_4+C_2H_4)$ fragment (obs.= 4.4723 mg; calc.= 4.4964 mg, 21.41%). The third peak that detected at 595.2 ºC is related to the loss of $(4CH_4+C_2H_6+H_2)$ fragments (obs.= 4.8768 mg; calc.= 4.9051 mg, 23.36%). The final weight that detected at 596.1 ºC (obs.= 9.2724 mg; calc.= 9.2479 mg, 44.04%) represents part of the ligand residue (C, Se and H) [81,82].
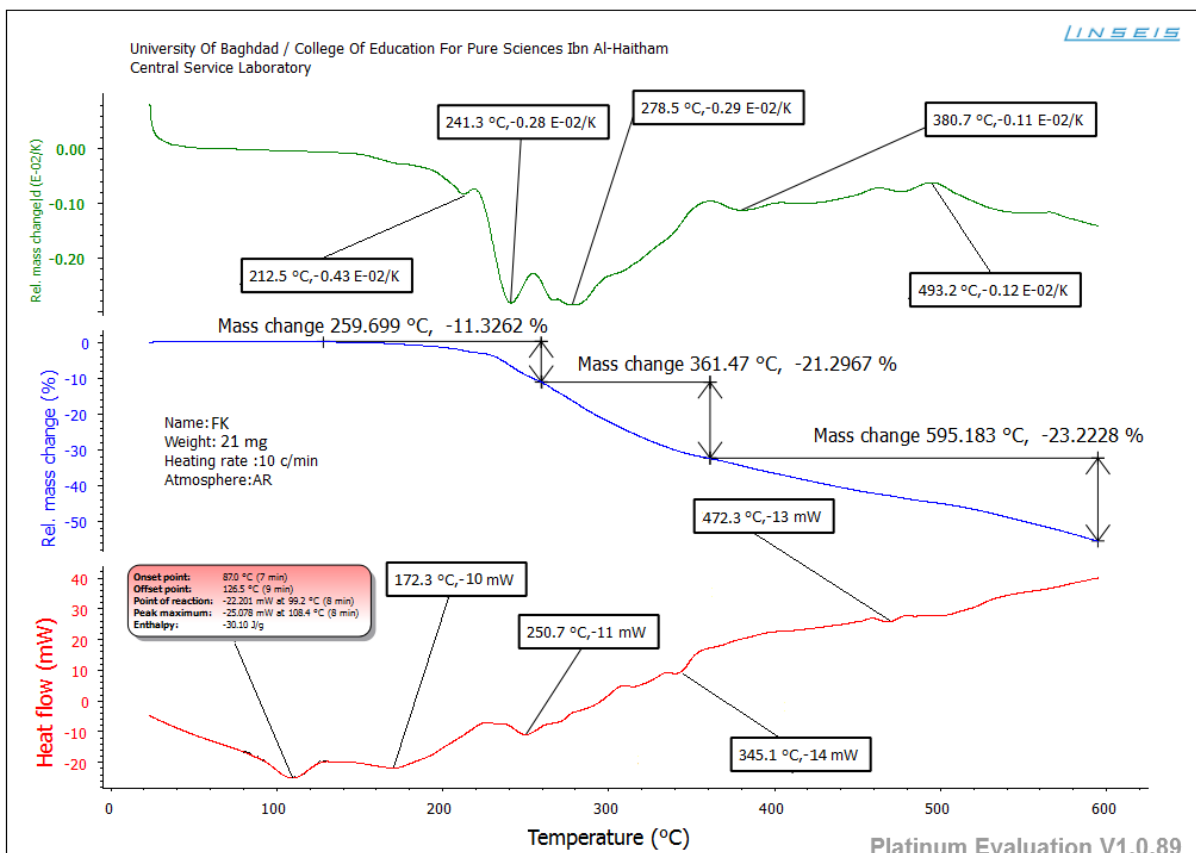
Figure (3-182): TGA, DTG and DSC thermograms of HL^1 in argon atmosphere.

(3.13.1.2) Thermal analysis of HL^2

The thermal analysis thermogram of selenosemicarbazone ligand (HL^2) is placed in Figure (3-183). The ligand appeared to be stable up to 235.3 ºC. The sample decomposes in a three exothermic and one endothermic decomposition processes over temperatures 253.7, 299.1, 336.0 and 511.3 ºC, as revealed by DSC analysis. Peaks between 241.3-376.4 ºC that combined the first and second decomposition steps is attributed to the loss of (C$_6$H$_{14}$) fragments (obs.= 3.7093 mg; calc.= 3.6441 mg, 18.22%). The third step occurs at 595.3 ºC corresponds to the loss of (N$_2$H$_4$+N$_2$+C$_2$H$_4$) fragments (obs.= 3.7188 mg; calc.= 3.7288

mg, 18.64%). The residue weight at 596.3 ℃ (obs.= 12.5719 mg; calc.= 12.6271 mg, 63.14%) represents part of the ligand residue [81,82].
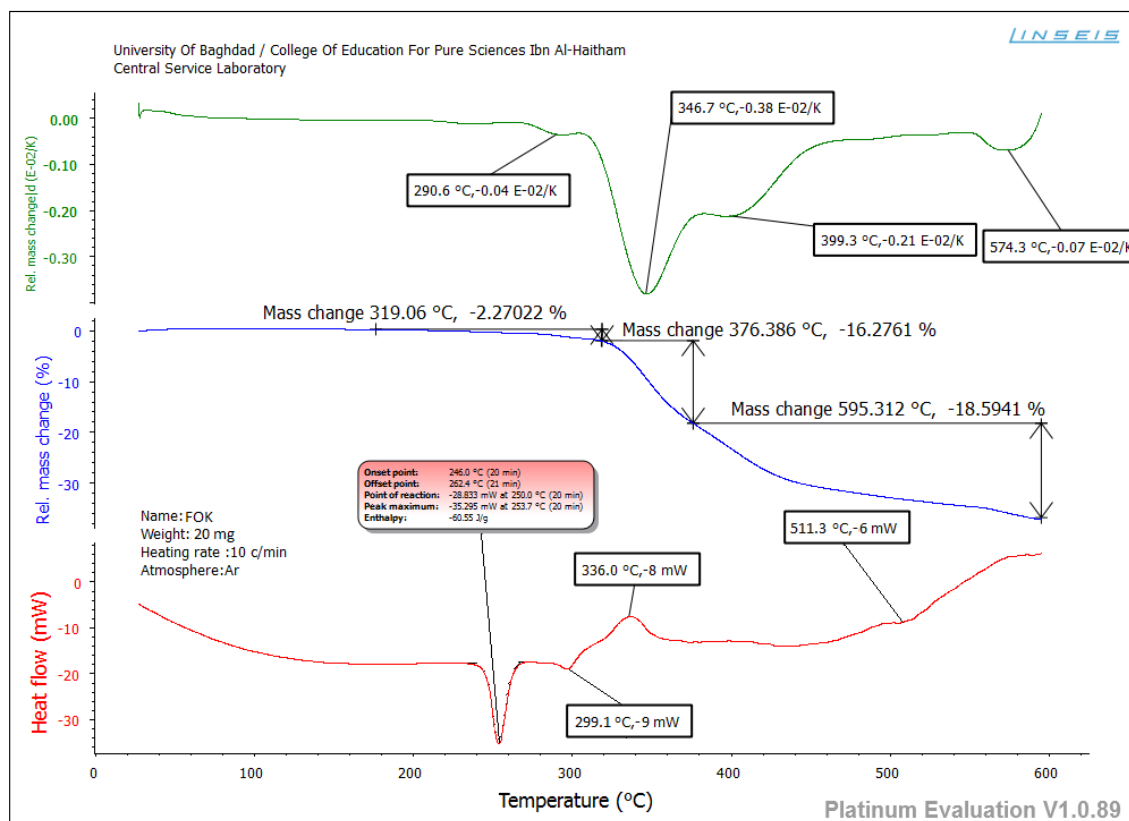
Figure (3-183): TGA, DTG and DSC thermograms of HL^2 in argon atmosphere.

(3.13.1.3)Thermal analysis of HL^3

The TGA, DTG and DSC thermograms of ligand (HL^3) are offered in Figure (3-184). The examination of sample appeared stable up to 168.6 ℃. The DSC analysis curve recorded peaks at 176.3, 288.5 and 414.3 ℃. The TGA thermogram curve indicated two decomposition steps. The first process was detected between 168.6-322.1 ℃ attributed to the loss of (2HCN+5CH$_4$+C$_4$H$_2$Se) fragments (obs.= 10.5857 mg; calc.= 10.5623 mg, 52.81%). While second process appeared at 448.0 ℃ due to elimination of (2C$_6$H$_6$+4CH$_4$)

fragments (obs.= 8.8315 mg; calc.= 8.8353 mg, 44.18%). The residue weight at 550.1 ºC is (obs.= 0.5828 mg; calc.= 0.6024 mg, 3.01%) represents part of the ligand residue [81,82].
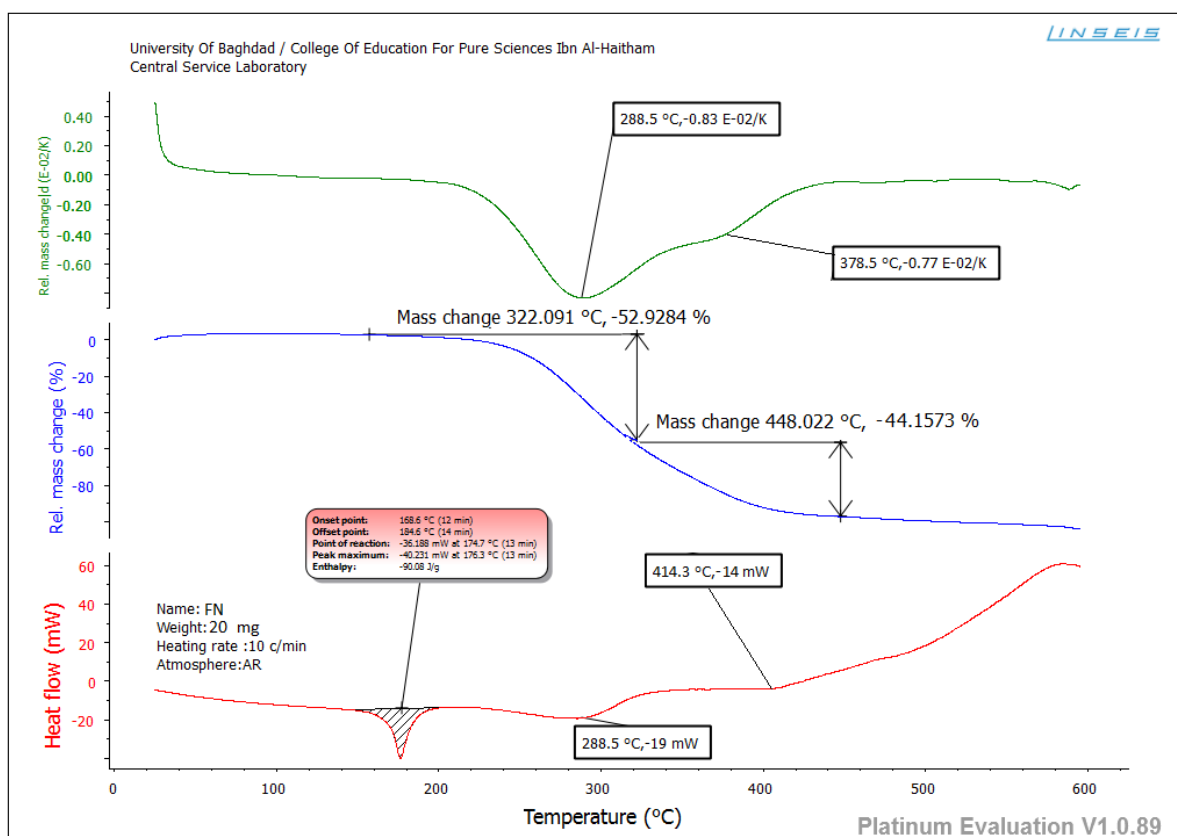
Figure (3-184): TGA, DTG and DSC thermograms of HL^3 in argon atmosphere.

(3.13.1.4)Thermal analysis of HL^4

The TGA, DTG and DSC thermograms of selenosemicarbazone ligand (HL^4) are shown in Figure (3-185). The ligand appeared to be stable up to 133.3 ºC. The sample decomposes in two exothermic and one endothermic peaks at 146.9, 294.4 and 348.9 ºC, respectively. The first step took place between 133.3-245.0 ºC attributed to the loss of ($N_2H_4+C_4H_8O+4CH_4$) segments (obs.= 7.4754 mg; calc.= 7.5676 mg, 37.84%). The second process at 344.7 ºC is related to the elimination of ($2HCN+C_4H_4Se+2H_2$) fragments, (obs.= 8.5211 mg; calc.= 8.5135 mg, 42.57%). While, the third process at 594.9 ºC is due to the removal of ($C_6H_6+CH_4+3H_2$) fragments, (obs.= 4.4816 mg; calc.= 4.5045 mg, 22.52%).

276

The residue weight at 596.1 ℃ is (obs.= 0.4781 mg; calc.= 0.5856 mg, 2.93%) represents part of the remaining ligand residue [81,82].
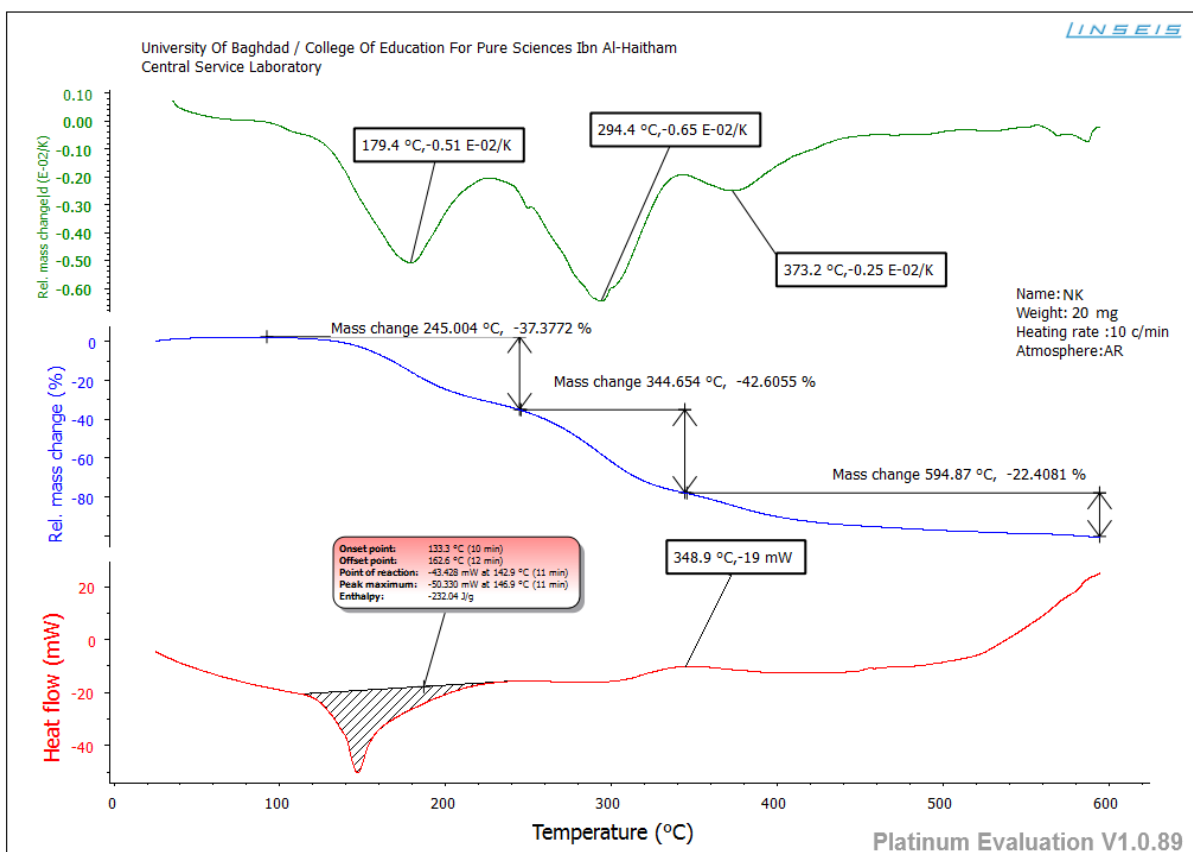
Figure (3-185): TGA, DTG and DSC thermograms of HL^4 in argon atmosphere.

(3.13.1.5) Thermal analysis of HL^5

The TGA, DTG and DSC analysis of selenosemicarbazone ligand (HL^5) are presented in Figure (3-186). The ligand appeared to be stable up to 52.3 ℃. The DSC analysis shows peaks at 83.9, 182.2, 250.2, 410.3, 526.2 and 564.3 ℃. The TGA curve indicated decomposition peak between 52.3-89.7 ℃ attributed to the loss of (NH_3) molecule (obs.= 0.8407 mg; calc.= 0.8322 mg, 3.96%). The second process at 253.1 ℃ is related to the loss of ($HCN+C_2H_4+C_4H_4O$) fragments, (obs.= 6.0811 mg; calc.= 6.0210 mg, 28.67%). Peak observed at 361.6 ℃ is due to the removal of ($HCN+C_2H_2$) segments,

(obs.= 2.5526 mg; calc.= 2.5944 mg, 12.35%). The four process that recorded at 594.4 ℃ is related to the loss of ($N_2H_2+CH_4$) molecules, (obs.= 2.2384 mg; calc.= 2.2518 mg, 10.72%). The residue weight at 597.1 ℃ (obs.= 9.2872 mg; calc.= 9.3006 mg, 44.29%) represents part of the ligand residue [81,82].
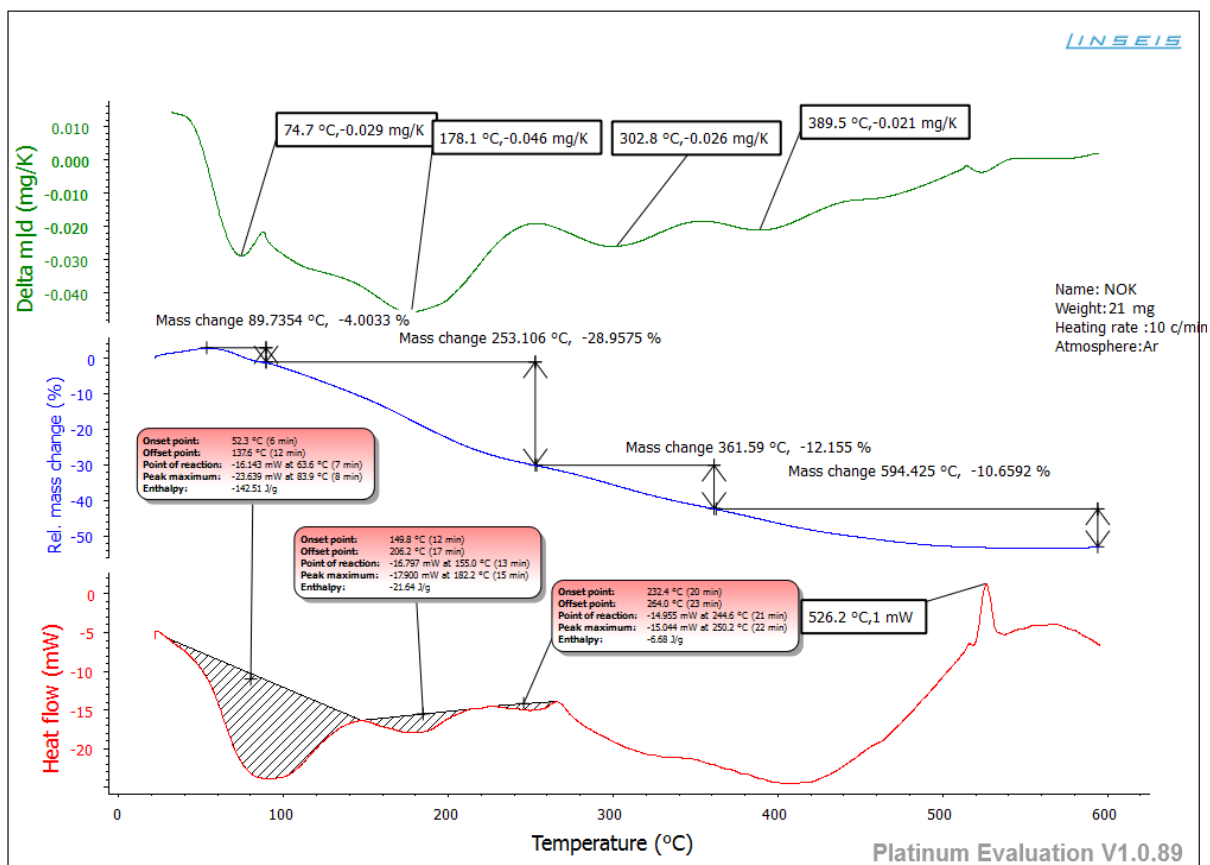
Figure (3-186): TGA, DTG and DSC thermograms of HL[5] in argon atmosphere.

(3.13.1.6) Thermal analysis of HL[6]

The TGA, DTG and DSC analysis of selenosemicarbazone ligand (HL[6]) are depicted in Figure (3-187). The ligand detected to be stable up to 70.2 ℃. The DSC technique indicated all peaks are exothermic at 80.9, 130.5, 155.7 and 455.3 ℃. The first

decomposition peak in the TGA is observed between 70.2-225.8 ℃. This decomposition process attributed to the loss of ($N_2H_2+C_4H_4O+CH_4$) segments (obs.= 4.6499 mg; calc.= 4.6721 mg, 23.36%). The second process at 304.9 ℃ is related to the loss of (C_4H_4N) molecule, (obs.= 2.7712 mg; calc.= 2.7049 mg, 13.53%). While, the third process at 363.0 ℃ is due to the removal of (NH_3+H_2) molecule, (obs.= 0.7717 mg; calc.= 0.7787 mg, 3.89%). The fourth process at 527.6 ℃ is related to the loss of ($C_3H_6+H_2Se$) fragment, (obs.= 5.0002 mg; calc.= 5.0410 mg, 25.21%). The final process, which detected at 594.3 ℃ is related to the loss of (CH_4) molecule (obs.= 0.5817 mg; calc.= 0.6557 mg, 3.27%). The residue weight that observed at 596.2 ℃ (obs.= 6.2253 mg; calc.= 6.1476 mg, 30.74%) represents part of the ligand residue [81,82]
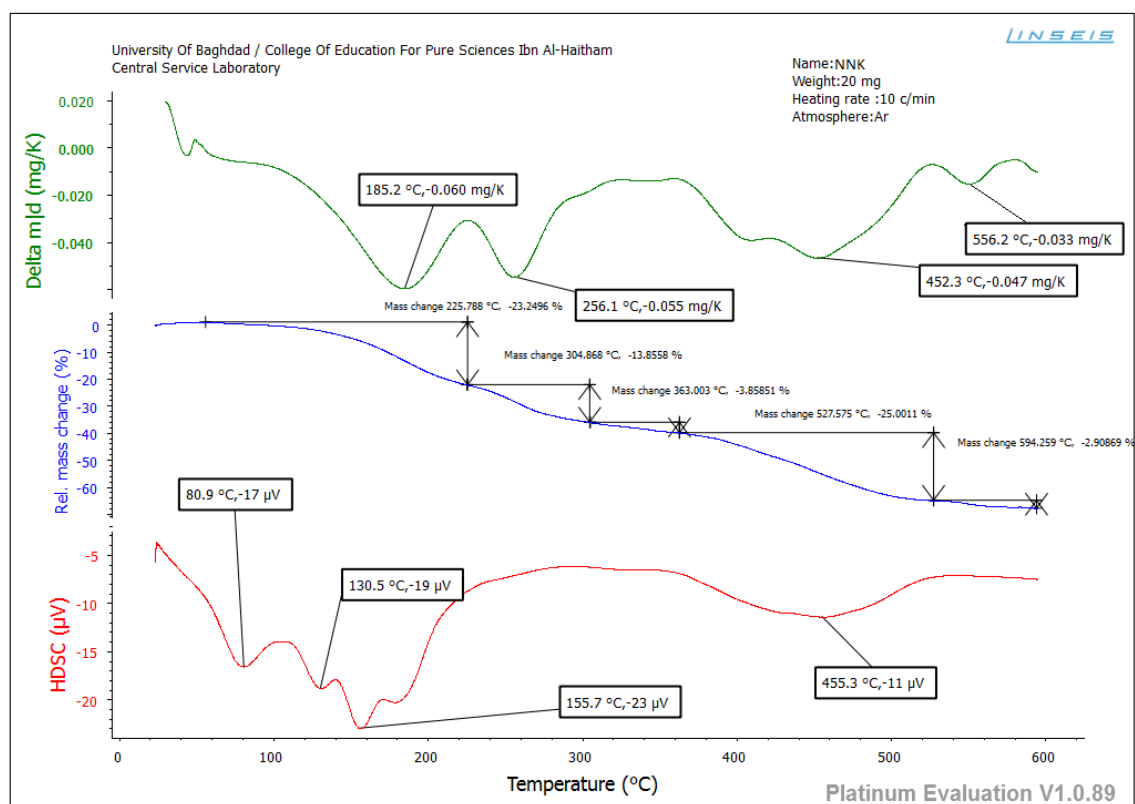
Figure (3-187): TGA, DTG and DSC thermograms of HL^6 in argon atmosphere.

(3.13.2) Thermal analysis of complexes

(3.13.2.1) Thermal analysis of $K_2[Ni(L^1)_2Cl_2]$

The thermal analysis thermogram of $K_2[Ni(L^1)_2Cl_2]$ complex is depicted in Figure (3-188). This complex appeared to be stable up to 171.1 ℃. The DSC curve analysis of the sample indicated peaks at 195.6, 307.4 and 417.5 ℃ that included exothermic processes. The TGA curve showed four decomposition steps. The first step that detected between 171.1-256.2 ℃, correlated to the removal of $(2CH_4)$ molecules (obs.= 0.6460 mg; calc.= 0.6531 mg, 3.11%). Peaks detected at 357.8, 447.0 and 595.4 ℃ attributed to the loss of $(2CH_4+C_4H_4+H_2Se)$ (obs.= 5.0288 mg; calc.= 5.0204 mg, 23.91%), $(N_2H_4+C_4H_4)$ (obs.= 1.7157 mg; calc.= 1.7143 mg, 8.16%) and $(N_2H_4+C_3H_8)$ (obs.= 1.5415 mg; calc.= 1.5510 mg, 7.39%), respectively. The final weight that displayed at 596.4 ℃ (obs.= 12.0680 mg; calc.= 12.0612 mg, 57.43%) represents the metallic and carbon residue [81,82].

Figure (3-188): TGA, DTG and DSC thermograms of $K_2[Ni(L^1)_2Cl_2]$ in argon atmosphere.

(3.13.2.2) Thermal analysis of [Cu(L^1)$_2$]

The thermal analysis thermogram of [Cu(L^1)$_2$] complex is exhibited in Figure (3-189). The complex appeared stable up to 161.2 °C. The DSC analysis indicated peaks at 183.2, 220.1, 329.3, 390.1 and 466.2 °C, which included exothermic and endothermic of the above temperatures. The TGA curve of the complex revealed four decomposition processes. The first step recorded between 161.2-262.6 °C indicated the loss of (N$_2$+C$_4$H$_2$Se) molecules (obs.= 3.5610 mg; calc.= 3.5520 mg, 17.76%). Peaks detected at 376.8, 473.0 and 595.4 °C attributed to the loss of (2C$_6$H$_6$) (obs.= 3.5359 mg; calc.= 3.5294 mg, 17.65%), (2NH$_3$+H$_2$) (obs.= 0.8019 mg; calc.= 0.8145 mg, 4.07%), and (C$_4$H$_4$) (obs.= 1.1695 mg; calc.= 1.1765 mg, 5.88%), respectively. The final weight at 596.5 °C (obs.= 10.9317 mg; calc.= 10.9276 mg, 54.64%) represents metallic and carbon residue [81,82].
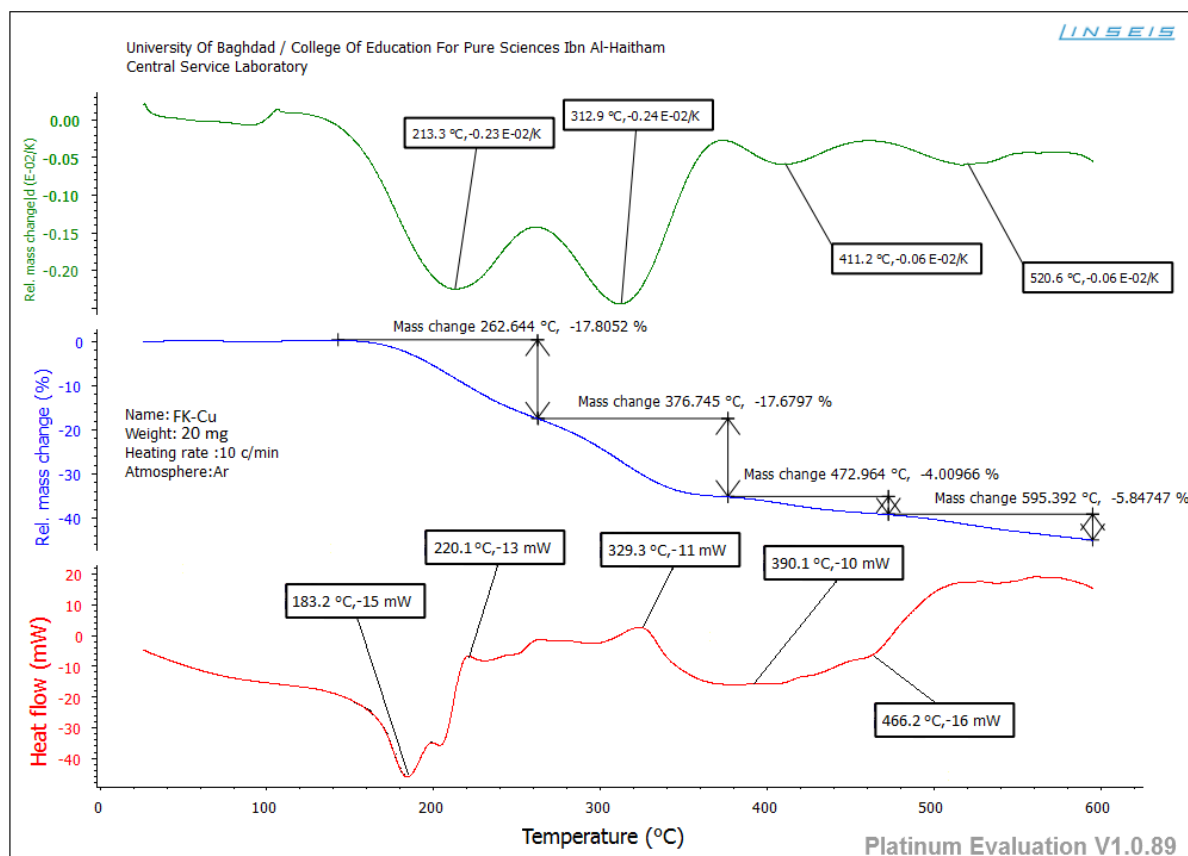
Figure (3-189): TGA, DTG and DSC thermograms of [Cu(L^1)$_2$] in argon atmosphere.

(3.13.2.3) Thermal analysis of $K_2[Mn(L^2)_2Cl_2]$

The thermal analysis curves of $K_2[Mn(L^2)_2Cl_2]$ are displayed in Figure (3-190). The complex appeared stable up to 164.1 ℃. The DSC curve shows four peaks that recorded over 170.7, 255.7, 323.2 and 570.5 ℃ represent exothermic and endothermic. The TGA curve exhibited three decomposition steps. The first step recorded between 164.1-257.0 ℃ that assigned to the loss of $(4N_2+3C_6H_6+2C_4H_4Se)$ molecules (obs.= 10.0564 mg; calc.= 10.0891 mg, 53.10%). Peaks detected at 344.1 and 595.5 ℃ attributed to the loss of $(2C_4H_4O+2C_5H_6)$ (obs.= 4.4208 mg; calc.= 4.4472 mg, 23.41%) and $(CH_4+C_6H_6+Cl_2)$ (obs.= 2.6899 mg; calc.= 2.7214 mg, 14.32%), respectively. The final weight that noticed at 596.6 ℃ (obs.= 1.8329 mg; calc.= 1.7423 mg, 9.17%) represents metallic and carbon residue [81,82].
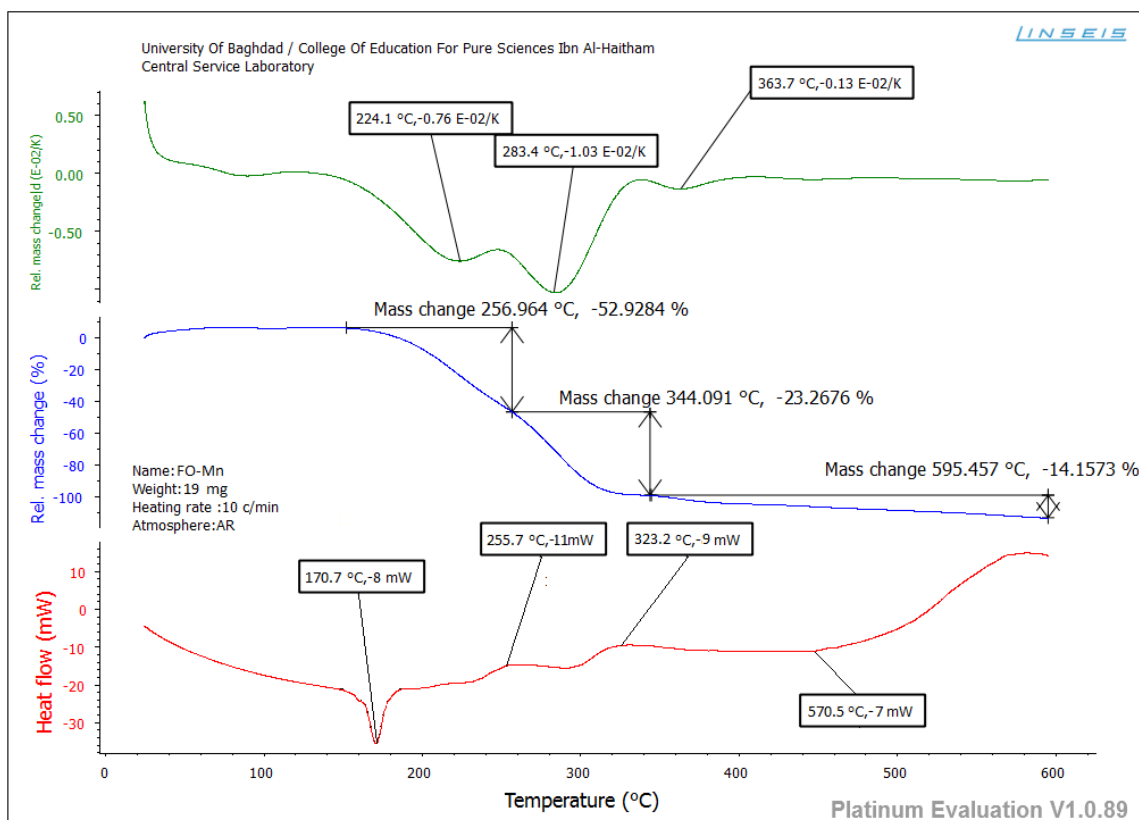
Figure (3-190): TGA, DTG and DSC thermograms of $K_2[Mn(L^2)_2Cl_2]$ in argon atmosphere.

(3.13.2.4) Thermal analysis of $[Cd(L^2)_2]$

The TGA thermal analysis curve of $[Cd(L^2)_2]$ complex is exhibited in Figure (3-191). This complex appeared to be stable up to 128.2 ºC. The DSC curve displayed peaks at 208.7, 291.7 and 415.2 ºC that refers for two exothermic and one endothermic decomposition process. The TGA curve showed peak detected between 128.2-257.0 ºC related to the removal of $(CH_4+C_4H_4Se+H_2)$ (obs.= 2.8315 mg; calc.= 2.8300 mg, 14.15%) represent first step. The second decomposition step at 382.4 ºC shows weight loss of $(4N_2+C_4H_4Se)$ (obs.= 4.6631 mg; calc.= 4.6154 mg, 23.08%). The third process at 595.3 ºC due to mass loss of $(C_4H_4O+C_3H_4)$ (obs.= 2.0398 mg; calc.= 2.0513 mg, 10.26%). The final weight at 596.3 ºC (obs.= 10.4656 mg; calc.= 10.5033 mg, 52.52%) represents metallic and carbon residue [81,82].
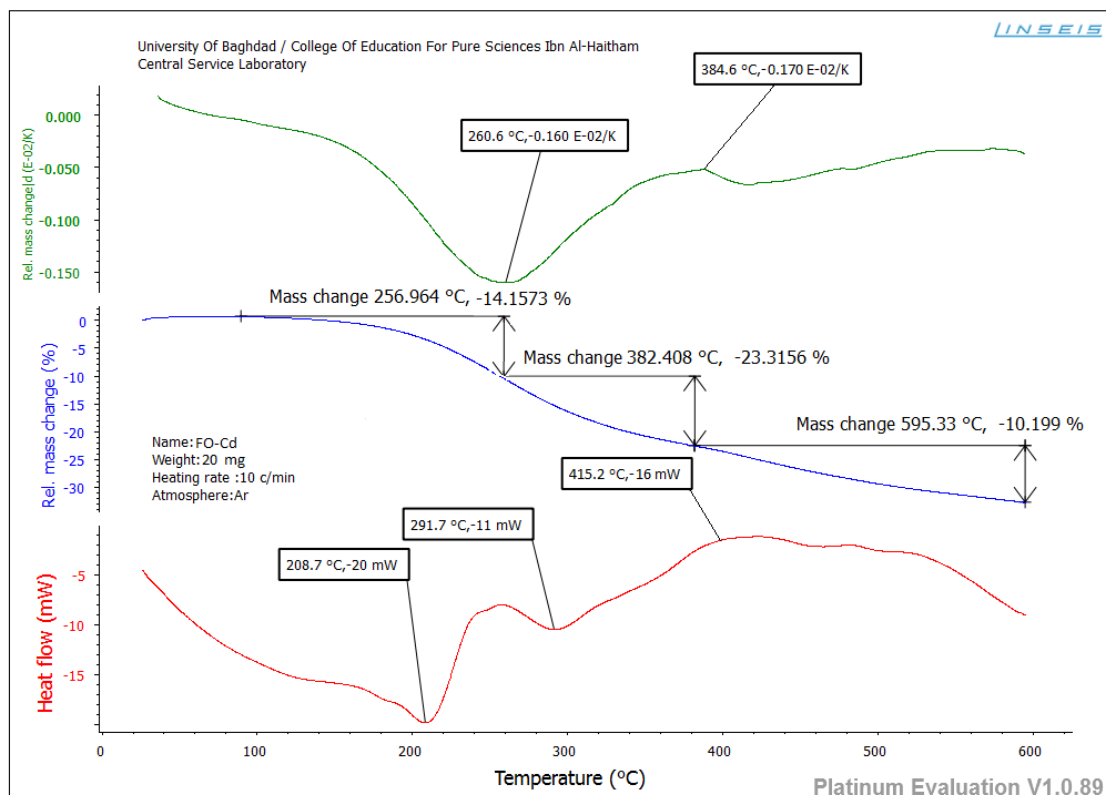
Figure (3-191): TGA, DTG and DSC thermograms of $[Cd(L^2)_2]$ in argon atmosphere.

(3.13.2.5) Thermal analysis of $K_2[Co(L^3)_2Cl_2]$

The thermal analysis thermogram of $K_2[Co(L^3)_2Cl_2]$ complex is displayed in Figure (3-192), which indicated the Co(II)-complex is stable up to 159.1 ℃. The DSC analysis curve confirmed three peaks at 260.1, 457.2 and 557.4 ℃ that due to exothermic decomposition processes. The TGA curve displayed three decomposition steps. Peak showed in the range 159.1-390.1 ℃ assigned to the removal of $(HCN+C_5H_6)$ molecules (obs.= 1.4648 mg; calc.= 1.4713 mg, 7.74%) represent first process. Whereas second process appeared at 522.1 ℃ due to loss $(N_2+HCN+C_4H_4N)$ molecules (obs.= 1.9378 mg; calc.= 1.9142 mg, 10.08%). Peak found at 595.6 ℃ attributed to the loss of $(C_6H_6+N_2H_4)$ (obs.= 1.7320 mg; calc.= 1.7402 mg, 9.16%). The final weight at 597.1 ℃ (obs.= 13.8654 mg; calc.= 13.8743 mg, 73.02%) represents metallic, carbon and selenium residue [81,82].
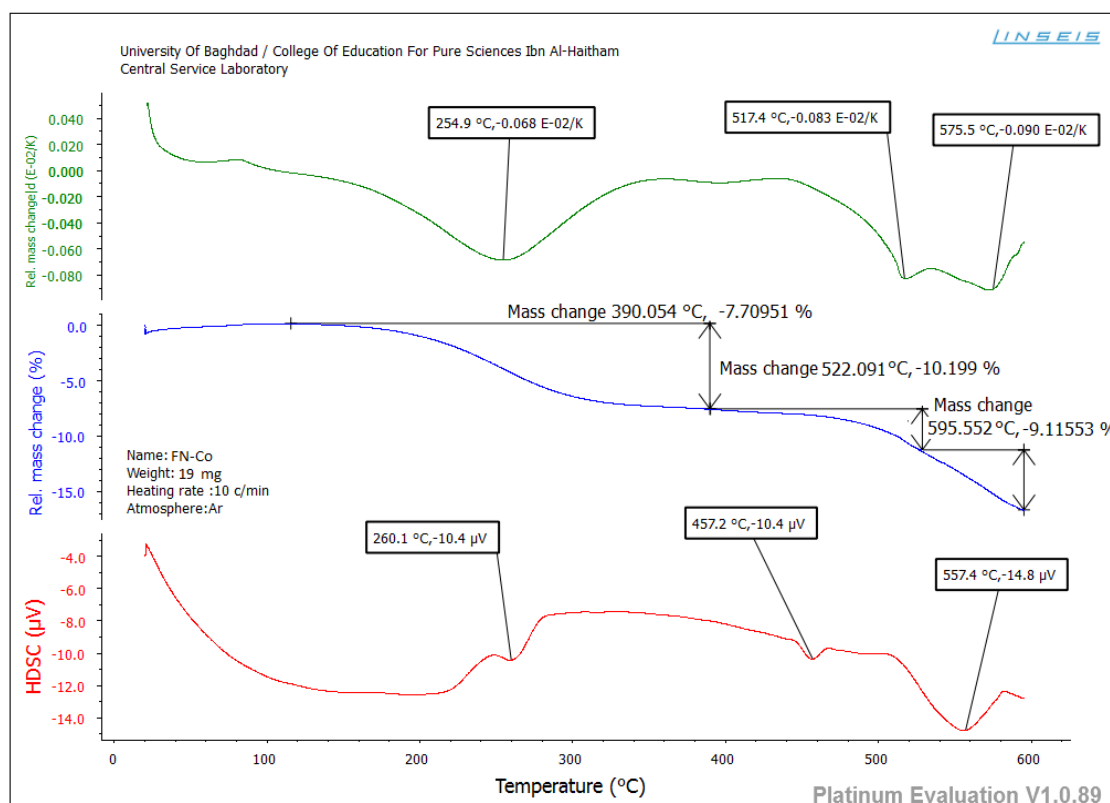
Figure (3-192): TGA, DTG and DSC thermograms of $K_2[Co(L^3)_2Cl_2]$ in argon atmosphere.

(3.13.2.6) Thermal analysis of [Zn(L^3)$_2$]

The TGA, DTG and DSC analyses curves of [Zn(L^3)$_2$] complex are depicted in Figure (3-193). The thermal analysis of complex appeared to be stable up to 120.2 ℃. The DSC analysis curve indicated three exothermic and one endothermic decomposition processes at 122.3, 246.1, 352.2 and 512.4 ℃. In the TGA curve found four peaks. The first peak displayed between 120.2-226.9 ℃ corresponds to the loss of (3CH$_4$+C$_4$H$_4$N) molecules (obs.= 2.3064 mg; calc.= 2.2606 mg, 10.77%). The second process showed at 288.9 ℃ attributed to loss of (N$_2$+2C$_4$H$_4$Se) molecules (obs.= 5.6830 mg; calc.= 5.7507 mg, 27.38%). Peak recorded at 370.1 ℃ attributed to the loss of (C$_6$H$_6$+C$_5$H$_{10}$) (obs.= 2.9364 mg; calc.= 2.9348 mg, 13.98%), while four process showed at 595.3 ℃ related to the elimination of (2N$_2$+3C$_6$H$_6$+C$_3$H$_8$) (obs.= 6.5941 mg; calc.= 6.6232 mg, 31.54%). The final weight at 597.2 ℃ (obs.= 3.4801 mg; calc.= 3.4307 mg, 16.34%) represents metallic and carbon residue [81,82].
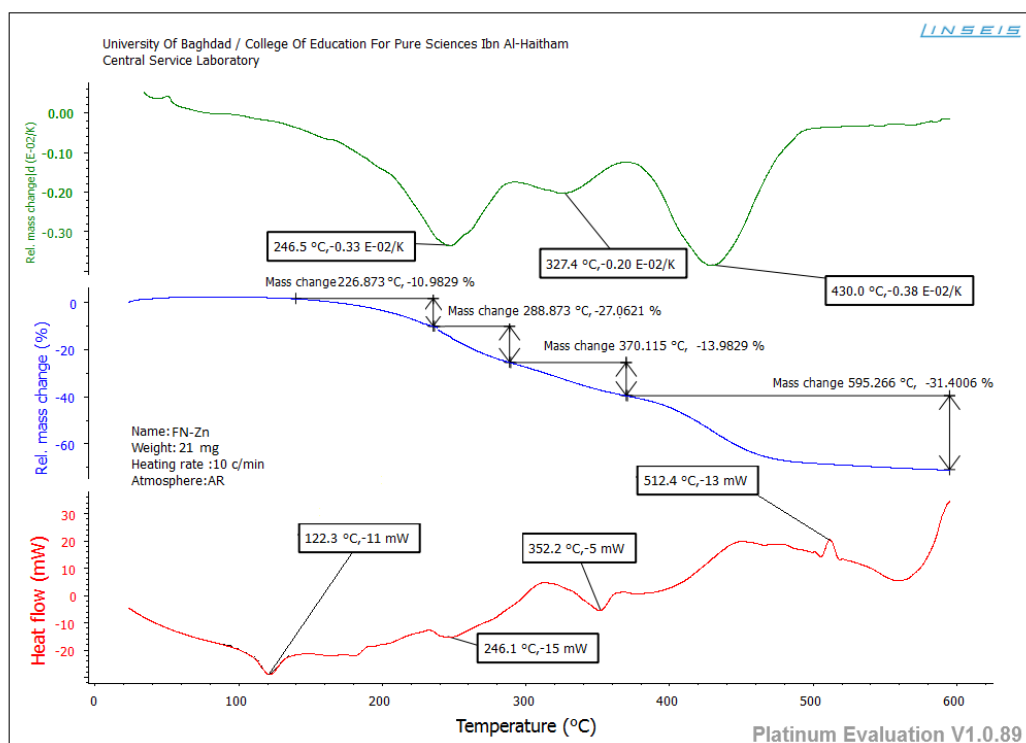
Figure (3-193): TGA, DTG and DSC thermograms of [Zn(L^3)$_2$] in argon atmosphere.

(3.13.2.7) Thermal analysis of $K_2[Mn(L^4)_2Cl_2]$

The thermal analysis thermogram of $K_2[Mn(L^4)_2Cl_2]$ complex is shown in Figure (3-194). The TGA indicated the Mn(II)-complex is stable up to 118.1 ℃. In the DSC analysis curve, peaks at 160.3, 215.3 and 398.4 ℃ related to two exothermic and one endothermic composition processes, respectively. The decomposition step displayed between 118.1-239.2 ℃, corresponds to the elimination of $(3CH_4+C_6H_6+C_3H_4+2HCl)$ molecules (obs.= 4.1322 mg; calc.= 4.1448 mg, 21.82%). Peak that attributed to the second step is recorded at 354.5 ℃. This step assigned to the loss of $(N_2H_4+HCN+C_4H_4Se+C_2H_6+H_2)$ (obs.= 3.8627 mg; calc.= 3.8662 mg, 20.35%). The third step seen at 595.2 ℃ related to the elimination of $(CH_4+C_6H_6)$ (obs.= 1.6279 mg; calc.= 1.6370 mg, 8.62%). The final weight at 597.1 ℃ (obs.= 9.3772 mg; calc.= 9.3555 mg, 49.24%) represents metallic and carbon residue.
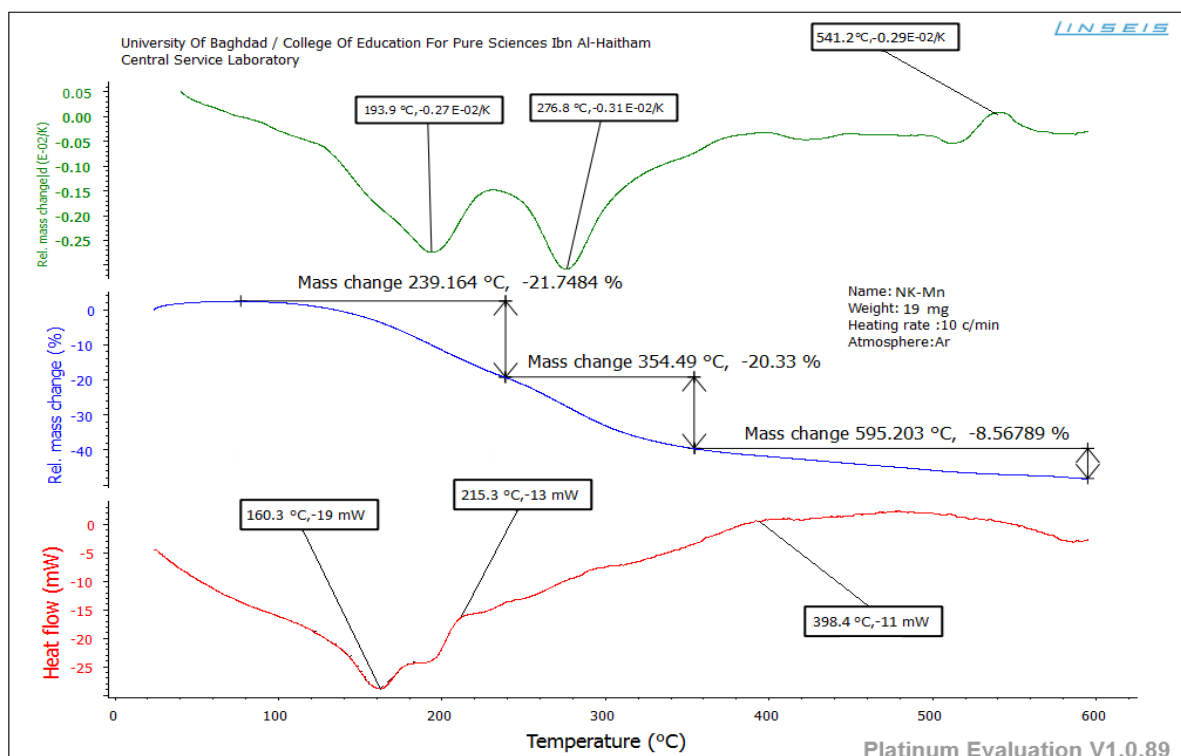
Figure (3-194): TGA, DTG and DSC thermograms of $K_2[Mn(L^4)_2Cl_2]$ in argon atmosphere.

(3.13.2.8) Thermal analysis of $[Cu(L^4)_2]$

The TGA thermal analysis curve of $[Cu(L^4)_2]$ complex is shown in Figure (3-195). The thermal analysis of sample appeared to be stable up to 76.4 °C. The DSC curve analysis displayed peaks at 194.7, 348.9, 480.3 and 565.8 °C, which due to two exothermic and two endothermic composition processes. The TGA decomposition process first displayed between 76.4-243.4 °C related to the mass of $(N_2+C_2H_4+3HCN)$ molecules (obs.= 3.0239 mg; calc.= 3.0284 mg, 14.42%). Peak corresponds to the second step at 352.3 °C attributed to the loss of (C_6H_4) (obs.= 1.6789 mg; calc.= 1.6800 mg, 8.00%). The third step observed at 595.4 °C related to the elimination of $(N_2H_4+CH_4+C_4H_4Se+H_2)$ (obs.= 3.9970 mg; calc.= 4.0011 mg, 19.05%). The final weight at 597.1 °C (obs.= 12.3002 mg; calc.= 12.2905 mg, 58.53%) represents metallic and carbon residue [81,82].
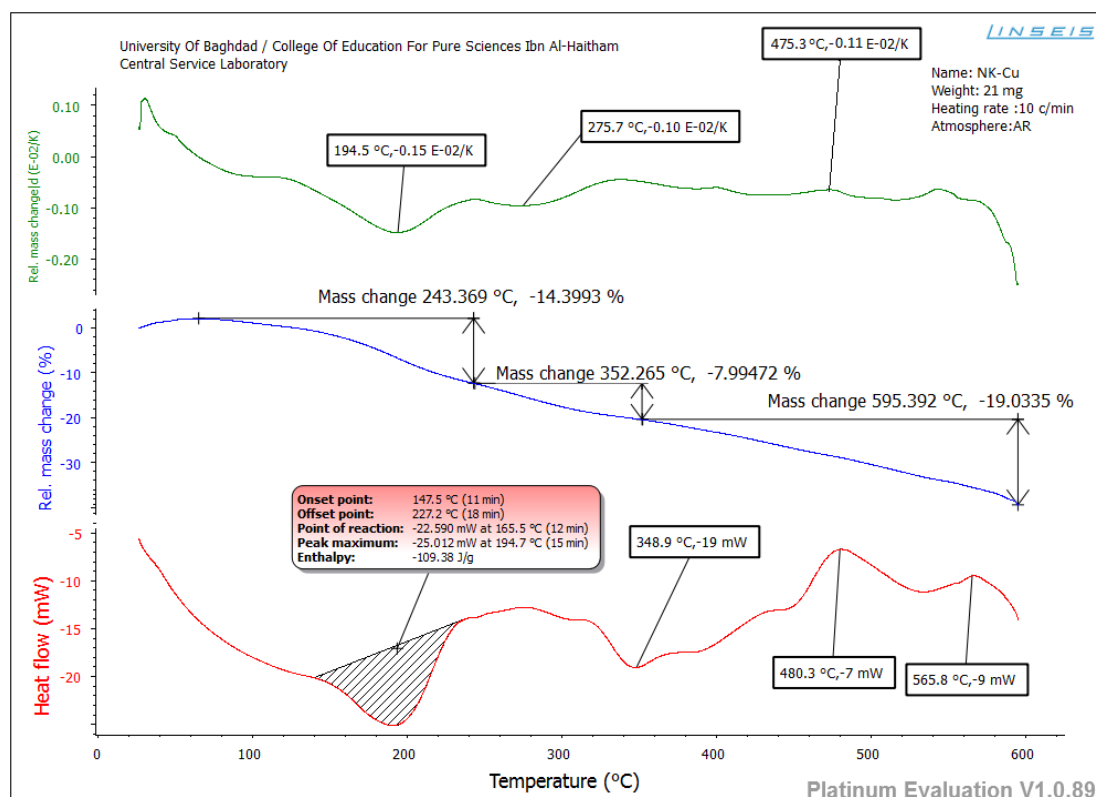
Figure (3-195): TGA, DTG and DSC thermograms of $[Cu(L^4)_2]$ in argon atmosphere.

(3.13.2.9) Thermal analysis of $K_2[Co(L^5)_2Cl_2]$

The TGA, DTG and DSC analyses thermograms of $K_2[Co(L^5)_2Cl_2]$ complex are exhibited in Figure (3-196). This complex appeared to be stable up to 141.2 ℃. The DSC analysis showed peaks at 191.7, 240.1 and 391.2 ℃, which indicated one exothermic and two endothermic composition processes. The TGA analysis indicated three decomposition steps. The first process displayed between 141.2-252.3 ℃ attributed to the mass loss of $(C_5H_8+3N_2+3C_6H_6+2HCl)$ molecules (obs.= 8.6112 mg; calc.= 8.6009 mg, 43.01%). The second step, which recorded at 346.8 ℃ attributed to the loss of $(N_2+2C_4H_4O+2C_6H_6+C_5H_{10})$ (obs.= 7.3416 mg; calc.= 7.3239 mg, 36.62%). The third step at 595.1 ℃ related to the elimination of $(2C_6H_6+3CH_4)$ (obs.= 3.8067 mg; calc.= 3.8310 mg, 19.15%). The final weight at 597.2 ℃ (obs.= 0.2405 mg; calc.= 0.02442 mg, 1.22%) represents metallic and carbon residue [81,82].
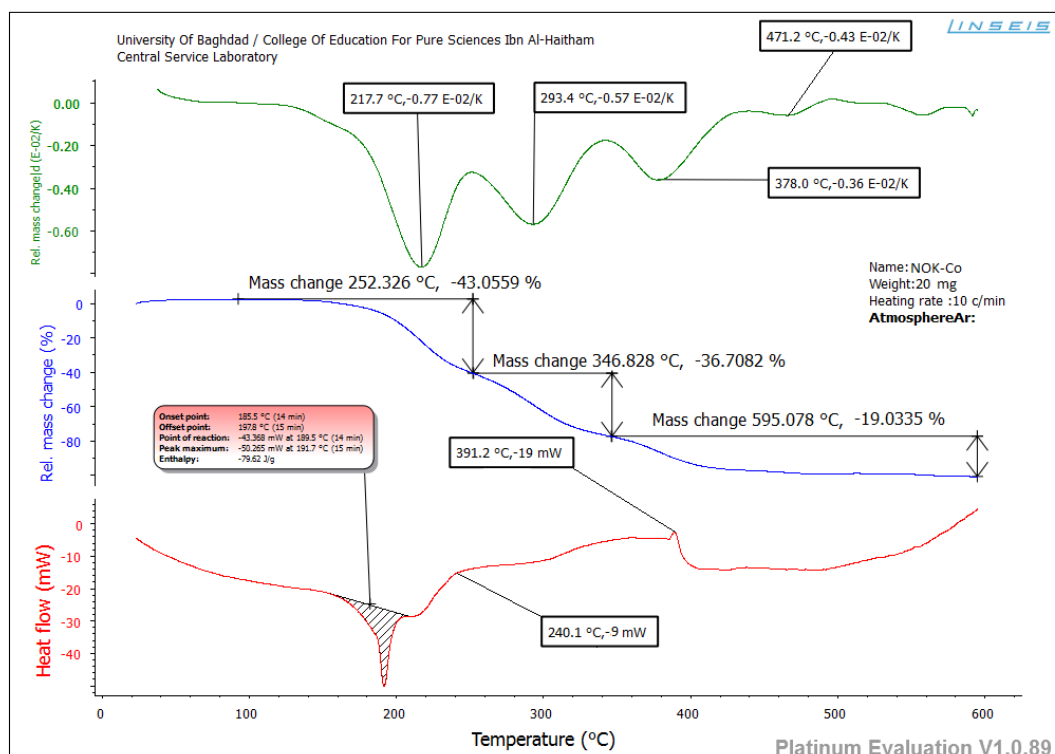
Figure (3-196): TGA, DTG and DSC thermograms of $K_2[Co(L^5)_2Cl_2]$ in argon atmosphere.

(3.13.2.10) Thermal analysis of [Cd(L^5)$_2$]

The thermal analysis thermogram of [Cd(L^5)$_2$] complex is displayed in Figure (3-197). The complex appeared to be stable up to 105.2 ℃. Peaks observed in the DSC curve analysis at 177.6, 209.6, 257.5, 334.1, 551.2 and 582.1 ℃ account for exothermic and endothermic composition processes. In the TGA, the first process recorded 105.2-252.3 ℃ correlated to the mass loss of ($3CH_4+C_4H_4Se+3H_2$) fragment, (obs.= 3.8067 mg; calc.= 3.8184 mg, 19.09%). While second process showed at 391.6 ℃ due to loss of ($3N_2H_2+2C_6H_6+7CH_4+2HCN+H_2$) (obs.= 8.5201 mg; calc.= 8.5449 mg, 42.73%). The third step that recorded at 595.1 ℃ has attributed to the elimination of (C_6H_3) (obs.= 1.5214 mg; calc.= 1.5480 mg, 7.74%). The final weight at 597.3 ℃ (obs.= 6.1518 mg; calc.= 6.0887 mg, 30.44%) represents metallic and carbon residue [81,82].
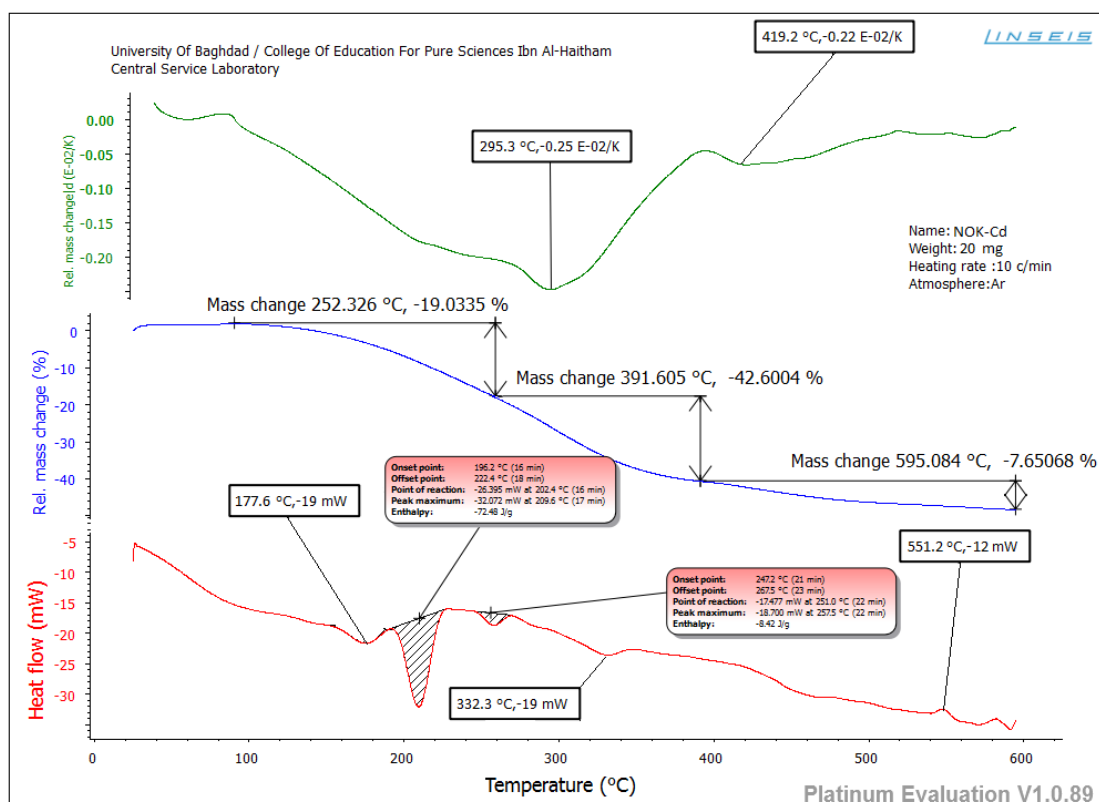
Figure (3-197): TGA, DTG and DSC thermograms of [Cd(L^5)$_2$] in argon atmosphere.

(3.13.2.11) Thermal analysis of $K_2[Ni(L^6)_2Cl_2]$

The TGA, DTG and DSC analyses curves of $K_2[Ni(L^6)_2Cl_2]$ complex are presented in Figure (3-198). The complex appeared to be stable up to 170.2 ℃. Peaks observed in the DSC curve analysis at 219.0, 295.4 and 496.4 ℃ confirmed two exothermic and one endothermic process. The TGA analysis indicated peak between 170.2-260.9 ℃ assigned to the mass loss of $(N_2H_2+2C_4H_4O)$ molecules (obs.= 2.6899 mg; calc.= 2.6706 mg, 14.10%) represented first process. Whereas, the second process showed at 350.9 ℃ due to loss of $(2N_2H_4+2C_6H_6+2C_4H_4N+Cl_2+C_4H_4Se)$ fragments (obs.= 8.9128 mg; calc.= 8.8967 mg, 46.83%). Peak which represents third step recorded at 594.4 ℃ attributed to the remove of $(N_2+2C_6H_6+C_4H_4Se)$ (obs.= 5.0446 mg; calc.= 5.0677 mg, 26.67%). The final weight loss (obs.= 2.3527 mg; calc.= 2.3650 mg, 12.45%) represents metallic and carbon residue [81,82].
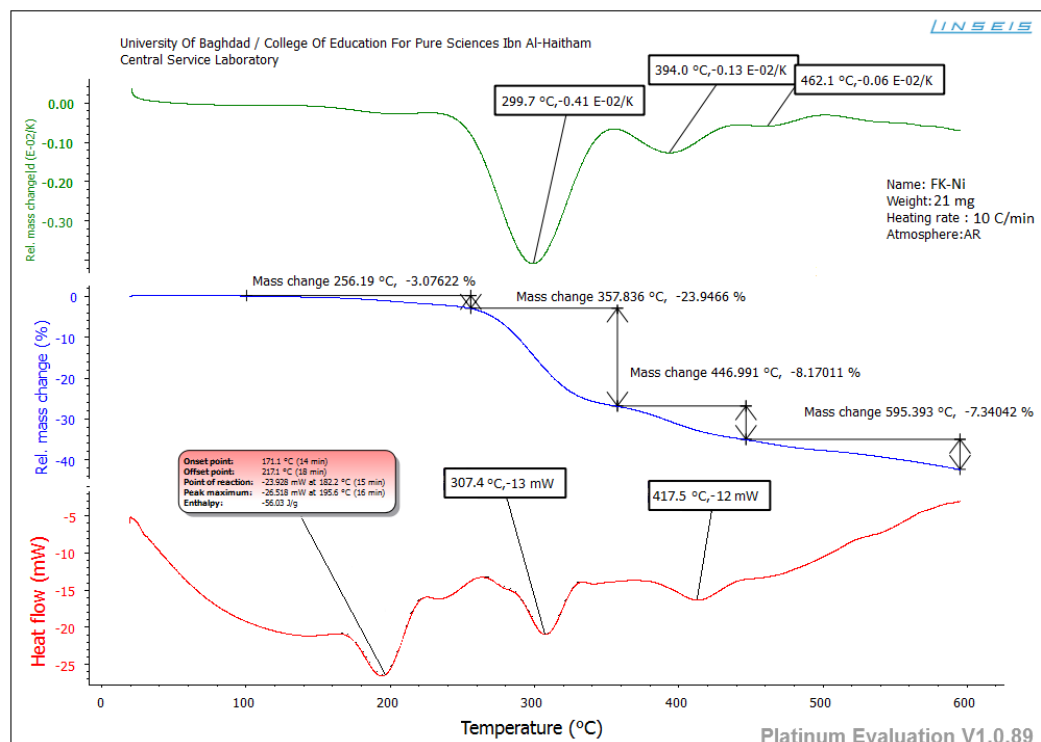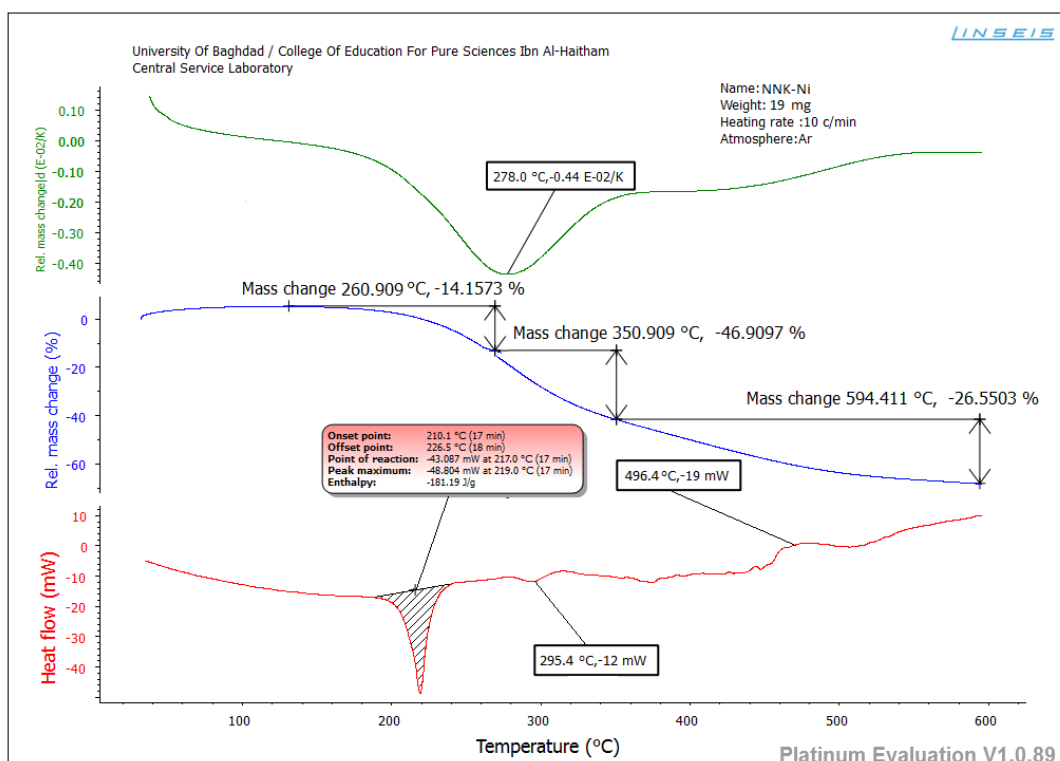

Figure (3-198): TGA, DTG and DSC thermograms of $K_2[Ni(L^6)_2Cl_2]$ in argon atmosphere.

(3.13.2.12) Thermal analysis of $[Zn(L^6)_2]$

The thermal analysis thermogram of $[Zn(L^6)_2]$ complex is displayed in Figure (3-199). The Zn(II)-complex appeared stable up to 110.1 ℃. The DSC technique indicated exothermic and endothermic peaks at 127.9, 274.7 and 480.1 ℃. The TGA curve showed peak between 110.1-282.4 ℃ related to the mass loss of $(N_2+C_6H_6)$ molecules (obs.= 2.0398 mg; calc.= 2.0424 mg, 10.21%). The second process that detected at 372.1 ℃ related to the mass loss of $(2N_2H_4)$ (obs.= 1.2068 mg; calc.= 1.2331 mg, 6.17%). The third peak, which represents the third step is recorded at 594.5 ℃ attributed to the remove of (C_2H_4) (obs.= 0.5542 mg; calc.= 0.5395 mg, 2.70%). The final weight at 596.2 ℃ (obs.= 16.1992 mg; calc.= 16.1850 mg, 80.93%) represents (metallic, carbon and selenium) residue [81,82].
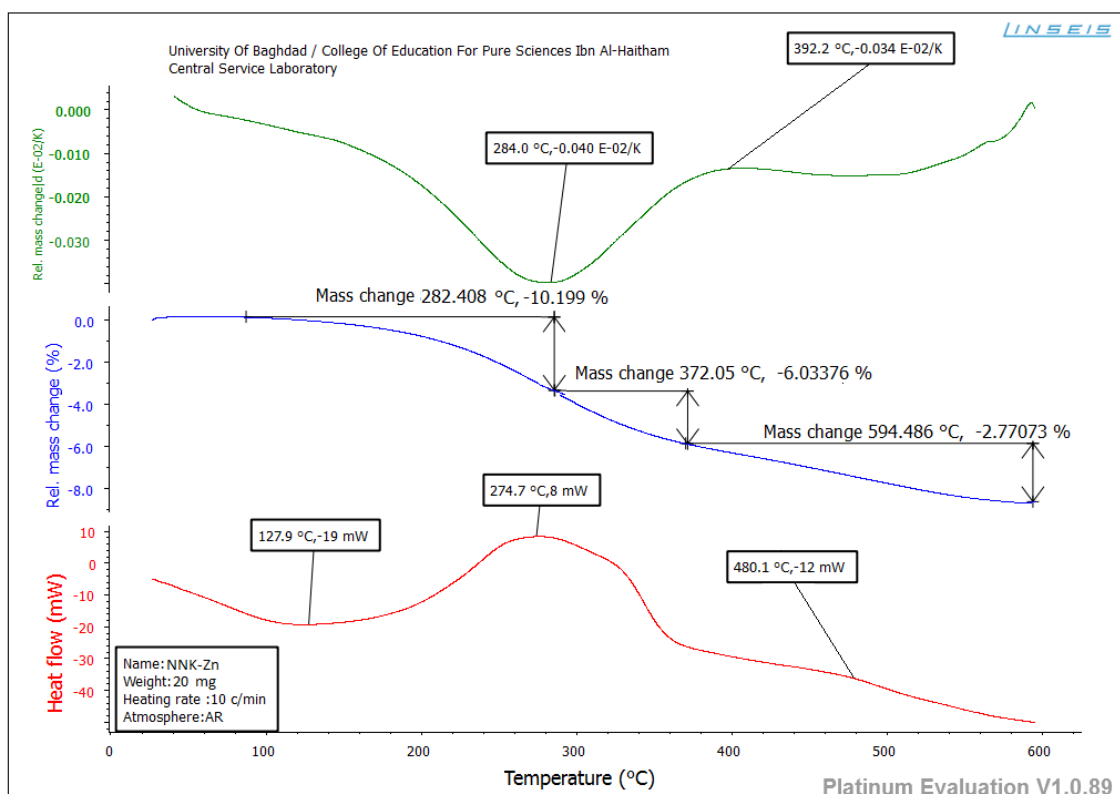
Figure (3-199): TGA, DTG and DSC thermograms of $[Zn(L^6)_2]$ in argon atmosphere.

Table (3-30): TGA/DTG/DSC information of ligands HL^1-HL^6 and selected complexes.

Compound	Stable up to °C	Stage	Decomposition temperature initial-final °C	Nature of transformation/intermediate formed% mass found (calc.)	Nature of DSC peak and temp. °C	DTG peak temp. °C
HL^1	106.4	1	107-260	2.3785 (2.3504)	108.4 Exo	212.5
					172.3 Exo	241.3
					250.7 Exo	
		2	262-362	4.4723 (4.4964)	345.1 Exo	278.5
		3	363-595	4.8768 (4.9051)	472.3 Exo	380.7
						493.2
K$_2$[Ni(L^1)$_2$Cl$_2$]	171.1	1	171-256	0.6460 (0.6531)	195.6 Exo	
		2	257-358	5.0288 (5.0204)	307.4 Exo	299.7
		3	359-447	1.7157 (1.7143)	417.5 Exo	394.0
		4	448-595	1.5415 (1.5510)		462.1
[Cu(L^1)$_2$]	161.2	1	161-263	3.5610 (3.5520)	183.2 Exo	213.3
					220.1 Endo	
		2	264-377	3.5359 (3.5294)	329.3 Endo	312.9
		3	378-473	0.8019 (0.8145)	390.1 Exo	411.2
		4	474-595	1.1695 (1.1765)	466.2 Exo	520.6
HL^2	235.3	1	235-376	3.7093 (3.6441)	253.7 Exo	290.6
					299.1 Exo	
		2	235-376	3.7093 (3.6441)	336.0 Endo	346.7
		3	377-595	3.7188 (3.7288)	511.3 Exo	399.3
						574.3
K$_2$[Mn(L^2)$_2$Cl$_2$]	164.1	1	164-257	10.0564 (10.0891)	170.7 Exo	224.1
					255.7 Endo	
		2	258-344	4.4208 (4.4472)	323.2 Endo	283.4
		3	345-596	2.6899 (2.7214)	570.5 Exo	363.7
[Cd(L^2)$_2$]	128.2	1	128-257	2.8315 (2.8300)	208.7 Exo	260.6
		2	258-382	4.6631 (4.6154)	291.7 Exo	
		3	383-595	2.0389 (2.0513)	415.2 Endo	384.6
HL^3	168.6	1	169-322	10.5857 (10.5623)	176.3 Exo	288.5
					288.5 Exo	378.5
		2	324-448	8.8315 (8.8353)	414.3 Exo	
K$_2$[Co(L^3)$_2$Cl$_2$]	159.1	1	159-390	1.4648 (1.4713)	260.1 Exo	254.9
		2	391-522	1.9378 (1.9142)	457.2 Exo	517.4
		3	523-596	1.7320 (1.7402)	557.4 Exo	575.5
[Zn(L^3)$_2$]	120.2	1	120-227	2.3064 (2.2606)	122.3 Exo	
		2	228-289	5.6830 (5.7507)	246.1 Exo	246.5
		3	290-370	2.9364 (2.9348)	352.2 Exo	327.4
		4	371-595	6.5941 (6.6232)	512.4 Endo	430.0

Compound	Stable up to °C	Stage	Decomposition temperature initial-final °C	Nature of transformation/intermediate formed% mass found (calc.)	Nature of DSC peak and temp. °C	DTG peak temp. °C
HL^4	133.3	1	133-245	7.4754 (7.5676)	146.9 Exo	179.4
		2	246-345	8.5211 (8.5135)	294.4 Exo	294.4
		3	346-595	4.4816 (4.5045)	348.9 Endo	373.2
$K_2[Mn(L^4)_2Cl_2]$	118.1	1	118-239	4.1322 (4.1448)	160.3 Exo	193.9
					215.3 Endo	
		2	240-355	3.8627 (3.8662)		276.8
		3	356-595	1.6279 (1.6370)	398.4 Endo	541.2
$[Cu(L^4)_2]$	76.4	1	76-243	3.0239 (3.0284)	194.7 Exo	194.5
		2	244-352	1.6789 (1.6800)	348.9 Exo	275.7
		3	353-595	3.9970 (4.0011)	480.3 Endo	475.3
					565.8 Endo	
HL^5	52.3	1	52-90	0.8407 (0.8322)	83.9 Exo	74.7
		2	91-253	6.0811 (6.0210)	182.2 Exo	178.1
					250.2 Exo	
		3	254-362	2.5526 (2.5944)		302.8
		4	363-594	2.2384 (2.2518)	410.3 Exo	389.5
					526.3 Endo	
					564.3 Exo	
$K_2[Co(L^5)_2Cl_2]$	141.2	1	141-252	8.6112 (8.6009)	191.7 Exo	217.7
					240.1 Endo	293.4
		2	253-347	7.3416 (7.3239)		378.0
		3	348-595	3.8067 (3.8310)	391.2 Endo	471.2
$[Cd(L^5)_2]$	105.2	1	105-252	3.8067 (3.8184)	177.6 Exo	295.3
					209.6 Exo	
		2	253-392	8.5201 (8.5449)	257.5 Exo	
		3	393-595	1.5214 (1.5480)	551.2 Endo	419.2
					582.1 Endo	
HL^6	70.2	1	70-226	4.6499 (4.6721)	80.9 Exo	185.2
					130.5 Exo	
					155.7 Exo	
		2	227-305	2.7712 (2.7049)		256.1
		3	306-363	0.7717 (0.7787)		
		4	364-528	5.0002 (5.0410)	455.3 Exo	452.3
		5	529-594	0.5817 (0.6557)		556.2
$K_2[Ni(L^6)_2Cl_2]$	170.2	1	170-261	2.6899 (2.6706)	219.0 Exo	
		2	262-351	8.9128 (8.8967)	295.4 Exo	278.0
		3	353-594	5.0446 (5.0677)	496.4 Endo	
$[Zn(L^6)_2]$	110.1	1	110-282	2.0398 (2.0424)	127.9 Exo	
		2	283-372	1.2068 (1.2139)	274.7 Endo	284.0
		3	373-595	0.5542 (0.5395)	480.1 Endo	392.2

293

(3.14) Magnetic moment measurements

Magnetic susceptibility technique is one of the most important measurements that used in coordination chemistry. It can provide an important information about the expected structure about metal centre that formed a complex. More, magnetic moment values of complexes can be used to indicate the status of system (high spin or low spin) of complexes.

The magnetic measurements were calculated using the Johnson Matthey balance [83,84]. The operative magnetic moment was achieved according to equation (3.1):

$$\mu = 2.83 \, (\chi PT)^{1/2} \tag{3.1}$$

Where: χP_{cor} = molar magnetic susceptibility that amended for diamagnetism of particles in the compound by Pascal's constant.

T= temperature in Kelvin (k).

(3.14.1) Magnetic susceptibility measurement

The molar magnetic susceptibility (χM) value was calculated of the multiplying of the mass susceptibility by molecular weight of compound;

$$\chi M = M\chi g \tag{3.2}$$

χM= Molar magnetic susceptibility
M= molecular weight of compound in *g/mol* unit
χg= Mass magnetic susceptibility

Diamagnetic corrections values were implemented upon the calculation of molar magnetic susceptibility. These values are due to the pair of electrons of ligand, associated ion electrons and metal ion core electrons [85].

$$\chi P = \chi M - \chi D \tag{3.3}$$

Where: $\chi D = \{\chi D(\text{core}) + \chi D(\text{ligand}) + \chi D(\text{counter ion})\}$

The diamagnetic improvement values are Pascal's constant [85].

The magnetic moment results were calculated according to Equation (3.1).

μ= 2.83 (χPT)$^{1/2}$ (3.1)

Where; T= temperature in Kelvin, during measurement time.

(3.14.2) Calculation of magnetic moment for $K_2[Mn(II)(L^1)_2Cl_2]$ complex

The Mn(II) complex of HL^1 was used as an example in the finding of the magnetic susceptibility:

χD= [24χD (C-ring) + 2χD (N-ring) + 18χD (C) + 6χD (N) + 46χD (H) +2χD (Se) + 2λ (C-Se) + 4λ (Ar-Ar) + 6λ (C-N) + 4λ (C=N) + 12λ (C=C) + 28λ (C-C)] $\times 10^{-6}$

χD= 24(-6.24) + 2(-4.61) + 18(-6) + 6(-5.57) + 46(-2.93) + 2(-23) + 2(-25) + 4(-0.5) + 6(-13) + 4(+8.15) + 12(+5.5) + 28(0)] $\times 10^{-6}$ emu mol^{-1}

χD= [-611.18 + 98.6] $\times 10^{-6}$ emu mol^{-1}
    = -512.58 $\times 10^{-6}$ emu mol^{-1}
    = -0.00051258 emu mol^{-1}

χD= [{χD(ligand)} + χD(core) + χD(counter ion)]

χD= [{χD(ligand)} + χD(-0.000014 for Mn) + (χD (Cl) + (χD (K)]]

χD for compound of $K_2[Mn(II)(L^1)_2Cl_2]$ = (-0.00051258) + (-0.000014 for Mn) + (-2 * 0.0000201) + (-2 * 0.0000149)

χD= -0.00059658 emu mol^{-1}

χM= $M\chi g$
    = 1025 $\times$ 0.15*10^{-4} emu mol^{-1}
    = 0.015375 emu mol^{-1}

χP= χM - χD
    = 0.015375 - (-0.00059658)
    = 0.01477842 emu mol^{-1}

χPT= 0.01477842 * 290 K
    = 4.2857418 emu K mol^{-1}

μ= 2.83 (χpT)$^{1/2}$
   = 2.83 (4.2857418)$^{1/2}$
   = 2.83 (2.0702033233)
   = 5.86 **μB**

Tables (3-31) to (3-33) represent Pascal's constants (values used to calculate χD):

Table (3-31): Values of χD of cations.

Cation	$\chi D/(1\times10^{-6}$ emu mol^{-1})
K^{+1}	-14.9
Mn^{+2}	-14
Co^{+2}	-12
Ni^{+2}	-12
Cu^{+2}	-11

Table (3-32): Values of χD of particles in covalent compounds.

Cation	$\chi D/(1\times10^{-6}$ emu mol^{-1})
C_{ring}	- 6.24
N_{ring}	- 4.61
C	- 6.??
O	- 4.6
N	- 5.57
H	- 2.93
Se	- 23.??

Table (3-33): Values of λi for explicit type of bond.

Bond	$\lambda i/(1\times10^{-6}$ emu mol^{-1})
Ar-Ar	- 0.5
Ar-NO$_2$	- 0.5
Ar-NR$_2$	+ 1
Ar-OR	- 1
NO$_2$	- 2
C=N	+ 8.15
C-N	- 13
C=C	+ 5.5
C-Se	- 25

(3.14.3) Calculation of magnetic moment (μ) of $K_2[M(L^n)_2Cl_2]$, (M= Mn(II), Co(II) and Ni(II)) and $[Cu(L^n)_2]$, (n= 1-6)

The magnetic susceptibility data are presented in Table (3-34). The calculated values of Mn(II)-complexes with the title ligands HL^n (n= 1-6) fall between 5.26 to 5.92 B.M. These numbers are characteristic to a high spin Mn(II) ion in which the geometry about metal centre is octahedral [86]. The Co(II)-complexes with HL^n (n= 1-6) revealed numbers around 3.61-3.90 B.M, indicating a high spin state and the geometry about Co(II) ion is octahedral [87]. The calculated magnetic values of Ni(II)-complexes with HL^n (n= 1-6), displayed μ_{eff} values between 2.53-2.80 B.M, Table (3-34). These values are close to the total spin-only values for a high spin octahedral geometry about Ni atom [88], see Table (3-34).

The measured magnetic data between 1.41-1.63 B.M of Cu(II)-complexes with HL^n (n= 1-6), indicated square planer geometry about Cu atom, (Table (3-34)).

Table (3-34): Results of magnetic moment values of HL^1-HL^6 complexes.

Complex	χg	M.Wt	χM	$\chi D*10^{-4}$	χP	μ_{eff}
K$_2$[Mn(L^1)$_2$Cl$_2$]	0.15*10^{-4}	1025	0.015375	-5.9658	0.01477842	5.86
K$_2$[Co(L^1)$_2$Cl$_2$]	0.065*10^{-4}	1029	0.006686	-5.9458	0.00609142	3.76
K$_2$[Ni(L^1)$_2$Cl$_2$]	0.035*10^{-4}	1029	0.0036015	-5.9458	0.00300692	2.64
[Cu(L^1)$_2$]	0.018*10^{-4}	884	0.0015912	-5.9358	0.00099762	1.52
K$_2$[Mn(L^2)$_2$Cl$_2$]	0.11*10^{-4}	1145	0.012595	-6.6642	0.01189308	5.26
K$_2$[Co(L^2)$_2$Cl$_2$]	0.055*10^{-4}	1149	0.0063195	-6.6442	0.00565508	3.62
K$_2$[Ni(L^2)$_2$Cl$_2$]	0.031*10^{-4}	1149	0.0035619	-6.6442	0.00289748	2.59
[Cu(L^2)$_2$]	0.0151*10^{-4}	1005	0.0015176	-6.6342	0.00085418	1.41
K$_2$[Mn(L^3)$_2$Cl$_2$]	0.12*10^{-4}	1197	0.014364	-8.2546	0.01353854	5.61
K$_2$[Co(L^3)$_2$Cl$_2$]	0.056*10^{-4}	1201	0.0067256	-8.2346	0.00590214	3.70
K$_2$[Ni(L^3)$_2$Cl$_2$]	0.035*10^{-4}	1201	0.0042035	-8.2346	0.00338004	2.80
[Cu(L^3)$_2$]	0.0175*10^{-4}	1057	0.0018498	-8.2246	0.00102729	1.55
K$_2$[Mn(L^4)$_2$Cl$_2$]	0.13*10^{-4}	1091	0.014183	-6.4206	0.01354094	5.61
K$_2$[Co(L^4)$_2$Cl$_2$]	0.057*10^{-4}	1095	0.0062415	-6.4006	0.00560144	3.61
K$_2$[Ni(L^4)$_2$Cl$_2$]	0.033*10^{-4}	1095	0.0036135	-6.4006	0.00297344	2.63
[Cu(L^4)$_2$]	0.0177*10^{-4}	946	0.0016744	-6.3906	0.00103536	1.55
K$_2$[Mn(L^5)$_2$Cl$_2$]	0.14*10^{-4}	1061	0.014854	-6.2230	0.0142317	5.75
K$_2$[Co(L)$_2$Cl$_2$]	0.061*10^{-4}	1065	0.0064965	-6.2030	0.0058762	3.69
K$_2$[Ni(L^5)$_2$Cl$_2$]	0.032*10^{-4}	1065	0.003408	-6.2030	0.0027877	2.55
[Cu(L^5)$_2$]	0.018*10^{-4}	920	0.001656	-6.193	0.0010367	1.55
K$_2$[Mn(L^6)$_2$Cl$_2$]	0.135*10^{-4}	1177	0.0158895	-7.8250	0.015107	5.92
K$_2$[Co(L^6)$_2$Cl$_2$]	0.062*10^{-4}	1181	0.0073222	-7.8050	0.0065417	3.90
K$_2$[Ni(L^6)$_2$Cl$_2$]	0.030*10^{-4}	1181	0.003543	-7.8050	0.0027625	2.53
[Cu(L^6)$_2$]	0.0185*10^{-4}	1037	0.00191845	-7.7950	0.00113895	1.63

(3.15) Molar conductance measurements

The conductivity measurements of Mn(II), Co(II), Ni(II), Cu(II), Zn(II) and Cd(II) complexes are used to determine the conductance behaviour of complexes (electrolyte or non-electrolyte) in solutions. The molar conductance of Mn(II), Co(II) and Ni(II)

complexes of ligands HL^1-HL^6 in DMSO solvents are summarised in Table (3-35). The title complexes recorded conductance values in the range 33.45-68.65 $S.cm^2.mol^{-1}$, confirming the 2:1 electrolyte-nature [89]. However, the Cu(II), Zn(II) and Cd(II) complexes of HL^1-HL^6 revealed non- electrolyte behaviour [90], see Table (3-35).

Table (3-35): Molar conductance values, in DMSO solutions, of complexes.

Complex	Λ_m $S.cm^2.mol^{-1}$	Behaviour
$K_2[Mn(L^1)_2Cl_2]$	37.34	2:1
$K_2[Co(L^1)_2Cl_2]$	41.23	2:1
$K_2[Ni(L^1)_2Cl_2]$	33.45	2:1
$[Cu(L^1)_2]$	3.11	non-electrolyte
$[Zn(L^1)_2]$	2.56	non-electrolyte
$[Cd(L^1)_2]$	2.67	non-electrolyte
$K_2[Mn(L^2)_2Cl_2]$	34.57	2:1
$K_2[Co(L^2)_2Cl_2]$	45.66	2:1
$K_2[Ni(L^2)_2Cl_2]$	50.23	2:1
$[Cu(L^2)_2]$	5.23	non-electrolyte
$[Zn(L^2)_2]$	6.98	non-electrolyte
$[Cd(L^2)_2]$	5.78	non-electrolyte
$K_2[Mn(L^3)_2Cl_2]$	63.12	2:1
$K_2[Co(L^3)_2Cl_2]$	39.66	2:1
$K_2[Ni(L^3)_2Cl_2]$	56.77	2:1
$[Cu(L^3)_2]$	8.90	non-electrolyte
$[Zn(L^3)_2]$	6.43	non-electrolyte
$[Cd(L^3)_2]$	5.89	non-electrolyte

Complex	Λ_m S.cm^2.mol^{-1}	Behaviour
$K_2[Mn(L^4)_2Cl_2]$	68.65	2:1
$K_2[Co(L^4)_2Cl_2]$	54.12	2:1
$K_2[Ni(L^4)_2Cl_2]$	45.67	2:1
$[Cu(L^4)_2]$	10.23	Non electrolyte
$[Zn(L^4)_2]$	6.87	Non electrolyte
$[Cd(L^4)_2]$	8.78	Non electrolyte
$K_2[Mn(L^5)_2Cl_2]$	43.22	2:1
$K_2[Co(L^5)_2Cl_2]$	45.12	2:1
$K_2[Ni(L^5)_2Cl_2]$	39.66	2:1
$[Cu(L^5)_2]$	4.33	Non electrolyte
$[Zn(L^5)_2]$	8.69	Non electrolyte
$[Cd(L^5)_2]$	3.80	Non electrolyte
$K_2[Mn(L^6)_2Cl_2]$	67.45	2:1
$K_2[Co(L^6)_2Cl_2]$	51.11	2:1
$K_2[Ni(L^6)_2Cl_2]$	42.33	2:1
$[Cu(L^6)_2]$	7.45	Non electrolyte
$[Zn(L^6)_2]$	6.23	Non electrolyte
$[Cd(L^6)_2]$	5.78	Non electrolyte

(3.16) Conclusions and proposed molecular structures of complexes

A range of physico-chemical measurements were used to confirm the entity of compounds and the expected arrangement of ligands about metal centre. These measurements indicated the formation of complexes with three types of geometries; octahedral, square planar and tetrahedral in both states (the solid and solution state).

(3.16.1) The proposed molecular structures for $K_2[M(L^n)_2Cl_2]$, (M= Mn (II), Co(II) and Ni(II)) and $[M(L^n)_2]$, (M = Cu(II), Zn(II) and Cd(II); (n= 1-6)

Based on the next analyses:

- ### FT-IR spectral data

The FT-IR spectral data of Mn(II), Co(II), Ni(II) Cu(II), Zn(II) and Cd(II) complexes with ligands (HL^1-HL^6) are presented in Tables (3-13) to (3-18) and depicted in Figures (3-62) to (3-97). The FT-IR of these compounds showed band in the range 1623-1646 cm^{-1}, assigned to ν(C=N)$_{imine}$ stretching. This band indicated lower shifting value, compared with that in the free ligand, confirming the involvement of the nitrogen atoms of these moieties in the coordination to the metal centre. A band that recorded in the range 702-762 cm^{-1} was assigned to ν(C-Se). This band has shifted to lower wave number, as compared with that in HL^1-HL^6, confirming complex formation and supported the participation of the selenium atoms in the organization to the metal centre. Moreover, band that related to N3-H group was no longer exists in the FT-IR of complexes, leading to the formation of N=C-Se segment. This was supported by the appearance of a peak in the range 1608-1619 cm^{-1} related to N=C-Se group. In addition, the spectra of complexes, as of that in the free ligands, revealed bands in the range 3358-3512 and 3304-3412 cm^{-1} due to ν(N4-H) and ν(N1-H), respectively. The appearance of these bands indicated the non-involvement of the nitrogen atoms in the coordination. New bands appeared in the range 405-474 and 333-375 related to ν(M-N) and ν(M-Se), respectively (M = Mn(II), Co(II), Ni(II), Cu(II), Zn(II) and Cd(II)). The spectra of Mn(II), Co(II) and Ni(II) complexes exhibited band in the range 252-285 related to ν(M-Cl).

▪ **Electronic and magnetic moments data**

The electronic spectra data of Mn(II), Co(II), Ni(II) Cu(II), Zn(II) and Cd(II) complexes with ligands HL^1-HL^6 are presented in Tables (3-19) to (3-24) and depicted in Figures (3-98) to (3-133). The electronic data of compounds detected bands in the range 275-396 nm attributed to intra-ligand field. Bands observed about 345-395 nm were related to C.T. The absorption spectra of Mn-complexes for ligands HL^1-HL^6 exhibited peaks at *ca*. 467 and 848 nm due to $^6A_1g^{(F)} \rightarrow ^4T_2g^{(G)}$ and $^6A_1g \rightarrow ^4T_1g^{(G)}$ transitions, indicating a distorted octahedral geometry around Mn atom. The calculated magnetic moments value μ_{eff} between 5.26 to 5.92 B.M are in a good agreement with proposed octahedral geometry. Peaks observed in the visible region in the range 541-831 nm, which assigned to d-d transitions, confirming octahedral geometries of Co-complexes for ligands HL^1-HL^6. The magnetic moments value μ_{eff} around 3.61-3.90 B.M indicated octahedral arrangement about Co atom. The spectral data of Ni-complexes for ligands HL^1-HL^6 showed peaks between 450-845 nm assigned to $^3A_2g^{(F)} \rightarrow ^3T_1g^{(P)}$, $^3A_2g^{(F)} \rightarrow ^3T_2g^{(F)}$ and $^3A_2g^{(F)} \rightarrow ^3T_1g^{(F)}$ transitions, confirming a distorted octahedral geometry about Ni atom. These data were supported by the experimental μ_{eff} values that found in the range 2.53-2.80 B.M, indicated distorted octahedral geometry. The Cu-complexes with ligands HL^1-HL^6 revealed bands around 676-871 nm due to $^2B_1g \rightarrow ^2B_2g$ and $^2B_1g \rightarrow ^2A_2g$, transitions, confirming a distorted square planar geometry around Cu atom. These data were supported by the magnetic moments value μ_{eff} among 1.41 to 1.63 B.M, Table (3-34). The electronic spectra for Zn- and Cd-complexes exhibit peaks related to $\pi \rightarrow \pi^*$, $n \rightarrow \pi^*$ and to charge transfer only, d^{10} system.

▪ **Mass spectrum**

The electrospray (+) mass spectra of precursors and ligands showed several peaks assigned to successive fragmentations of the title compound. The electrospray spectra

indicated the molecular parent ion of precursors and the title ligands (Figures (3-44) to (3-55)), Further, the electrospray (+) mass spectra of selected complexes revealed the parent ion peak with the successive fragmentations of the molecule (Figures (3-170) to (3-181)).

▪ ^{1}H-, ^{13}C- and ^{77}Se-NMR

The ^{1}H- and ^{13}C-NMR spectral data of precursors, ligands and diamagnetic complexes in DMSO-d^6 and CDCl$_3$ solvents exhibited peaks due to several protons and carbons nuclei supporting the expected structure and the purity of the title compounds. ^{77}Se-NMR spectra of ligands and their diamagnetic complexes in DMSO-d^6 displayed one signal in solution (with the appropriate chemical shift) indicated the presence of one isomer and confirming the purity of ligands and their complexes.

▪ Elemental microanalysis

The observed values of (C.H.N), chloride ratio and metal content for precursors, ligands and their complexes (see Tables (3-2) and (3-12)) agree well with the expected values. In addition, these obtained data supported the proposed structures of the title compounds.

▪ Molar Conductance

The conductivity values of Mn(II), Co(II) and Ni(II) complexes in DMSO solvents lie in the range 33.45-68.65 S.cm^2.mol^{-1}, Table (3-35). These numbers confirm the electrolyte nature of complexes with a 2:1 ratio. The experimental conductance values of Cu(II), Zn(II) and Cd(II) complexes indicated the non-electrolyte nature.

- **Thermal properties**

This tool was implemented to examine thermal stability and pyrolysis pathways of ligands and their complexes, which assisted in the characterisation of complexes. The thermal stability, melting points and chemical composition of ligands and some complexes have determined using TGA, DTG and DSC analysis. (see Table (3-30)).

- **Molecular modelling**

The proposed molecular structures of ligands and their metal complexes optimized by Chem. Office 2016 3DX program. The optimized computational calculations of Mn(II), Co(II), and Ni(II) complexes with HL^1-HL^6 indicated the most stable geometry about metal centre is octahedral geometry. While, the optimized computational calculations of Cu(II) complexes with the title ligands HL^1-HL^6 revealed the most stable arrangement about Cu atom is square planar. In addition, the computational calculations of Zn(II) and Cd(II) complexes with HL^1-HL^6 revealed the tetrahedral geometry is the most reasonable arrangement about the metal centre. The calculated structures were supported by the experimental spectroscopic and analytical data of the title complexes.

An example of the optimized calculated structure of the octahedral arrangement is depicted in Figure (3-200), which represents the proposed structure of $K_2[Mn(L^1)_2Cl_2]$. The calculated bond lengths and bond angles are found in Table (3-36). Further, Figure (3-201) symbolizes the optimized structure of $[Cu(L^1)_2]$, in which the optimized calculated data revealed square planar arrangement. The calculated bond lengths and bond angles are shown in Table (3-37). Finally, Figure (3-202) represents the optimized structure of the optimized tetrahedral arrangement of $[Zn(L^1)_2]$. The calculated bond lengths and bond angles are shown in Table (3-38).
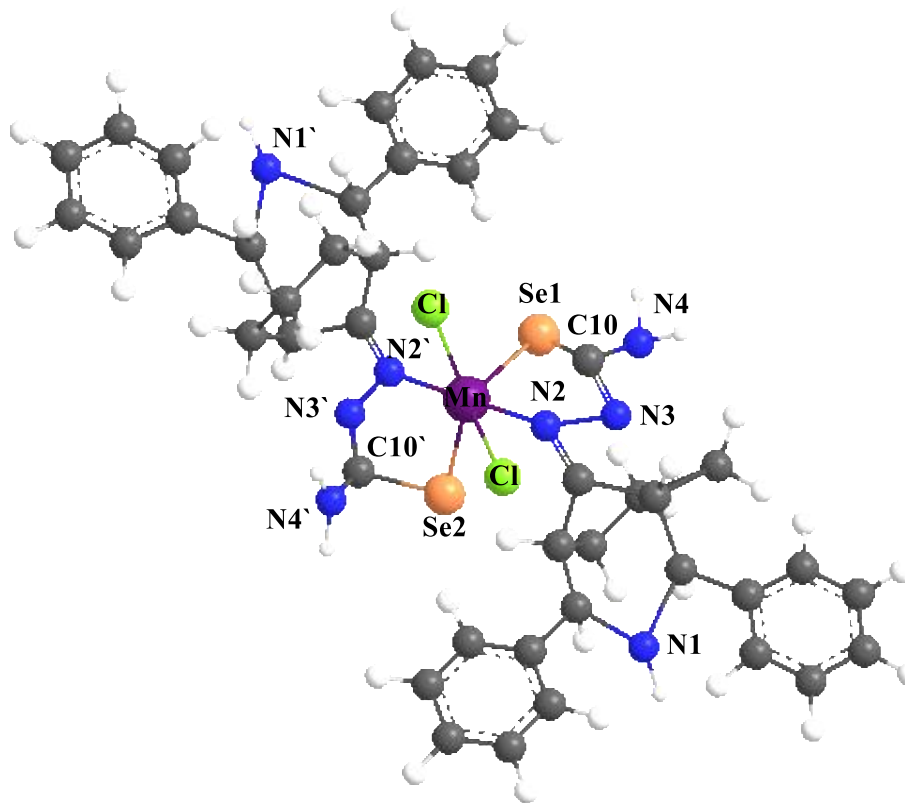
Figure (3-200): The optimized molecular structure of K$_2$[Mn(L^1)$_2$Cl$_2$].

⬤ Magnesium   ⬤ Nitrogen   ⬤ Selenium   ⬤ Chlorido

Table (3-36): Theoretical bond lengths and bond angles of K$_2$[Mn(L^1)$_2$Cl$_2$].

Atom	Bond lengths (A^o)	Atom	Bond angles (^{o})
Mn-Cl(10)	2.175	Mn-Cl(1)-N(2)	128.5
Mn-Cl(10`)	2.448	Mn-Cl(2)-N(2`)	156.1
Se(1)-Mn	2.780	Se(1)-Mn-N(2)	138.5
Se(2)-Mn	2.340	Se(2)-Mn-N(2`)	160.7
N(2)-Mn	1.917	N(2)-Mn- N(2`)	-78.1
N(2`)-Mn	1.929	N(2`)-Mn-N(2)	103.5
C(10)-N(2)	1.350	C(10)-N(2)-N(3)	-87.5
C(10`)-N(2`)	1.369	C(10`)-N(2`)-N(3`)	119.9
C(10)-Se(1)	1.636	N(2)-C(10)-Se(1)	103.3
C(10`)-Se(2)	1.921	C(10)-Se(1)-N(2)	77.6

305
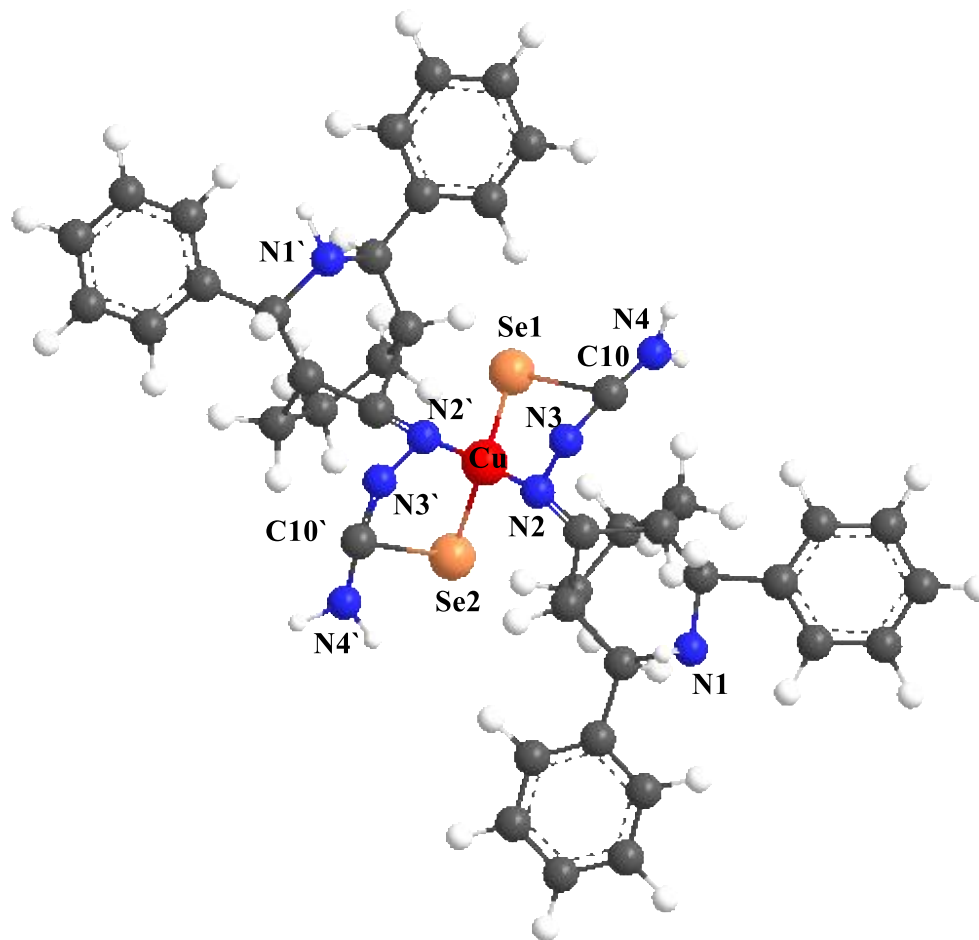
Figure (3-201): The optimized molecular structure of [Cu(L^1)$_2$].

🔴 Cupper   🔵 Nitrogen   🟠 Selenium

Table (3-37): Theoretical bond lengths and bond angles of [Cu(L^1)$_2$].

Atom	Bond lengths (A^o)	Atom	Bond angles (^{o})
Cu-Se(1)	2.339	C(10)-Se(1)-Cu	73.2
Se(2)-Cu	2.338	C(10`)-Se(2)-Cu	77.0
N(2)-Cu	1.303	Se(1)-Cu-N(2)	78.4
N(2`)-Cu	1.303	Se(2)-Cu-N(2`)	129.5
C(10)-N(2)	1.272	N(2)-Cu-N(2`)	139.9
C(10`)-N(2`)	1.976	N(2)-Cu-Se(1)	-128.2
C(10)-Se(1)	1.807	Se(1)-Cu-Se(2)	138.8
C(10`)-Se(2)	1.938	Cu-N(2)-C(10)	54.3
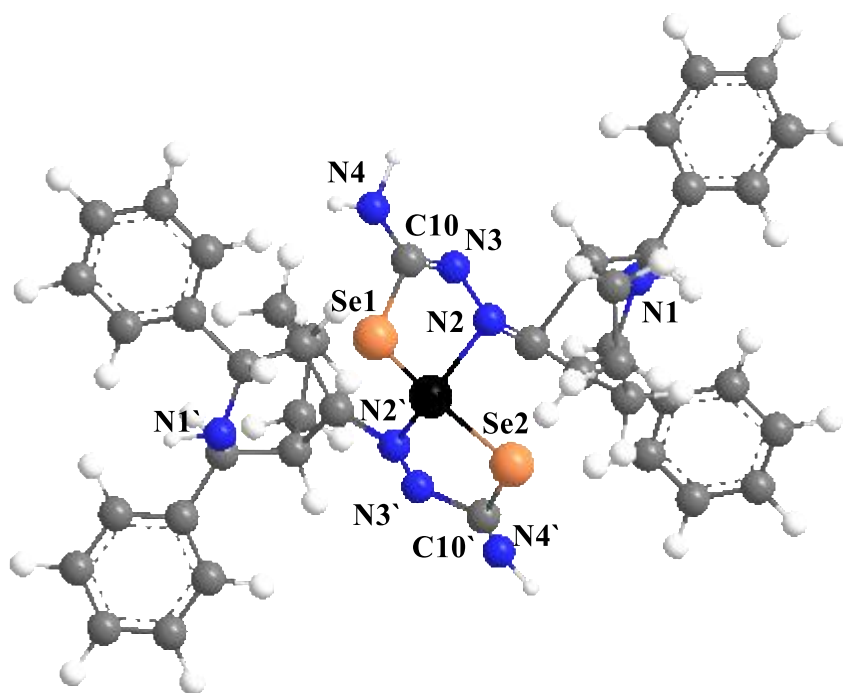
Figure (3-202): The optimized molecular structure of [Zn(L^1)$_2$].

Zinc	Nitrogen	Selenium

Table (3-38): Theoretical bond lengths and bond angles of [Zn(L^1)$_2$].

Atom	Bond lengths (A^o)	Atom	Bond angles (^{o})
Zn-Se(1)	2.418	N(2)-Zn-Se(1)	66.0
Zn-Se(2)	2.419	N(2`)-Zn-Se(2)	146.8
N(2)-Zn	1.935	N(2)-N(3)-Zn	35.8
N(2`)-Zn	1.937	N(2`)-N(3`)-Zn	130.8
C(10)-N(2)	1.415	C(10)-N(2)-N(3)	117.7
C(10`)-N(2`)	1.497	N(2)-Se(1)-N(3)	5.7
C(10)-Se(1)	2.045	Zn-N(2)-N(3)	130.8
C(10`)-Se(2)	1.943	N(2`)-Se(2)-N(3`)	23.2

CHAPTER FOUR

BIOLOGICAL ACTIVITY

(4) Biological activities

Selenosemicarbazone compounds (ligands and complexes) were investigated versus four types of bacterial species (Gram positive and Gram negative) and four of fungi species, as follows:

(4.1) Bacterial assay

Selenosemicarbazone compounds (ligands and complexes) were tested against their antimicrobial activity, adopting agar diffusion approach, using four bacterial strains (*Escherichia coli, Bacillus stubtilis, Staphylococcus aureus and Klebsiella Pneumoniae*). The bacterial strains were investigated using Mueller Hinton agar method [91]. In this method, the effect of the free solvent (DMSO) on the tested species was accomplished, which indicated there no effect on the studies bacteria. Table (4-1) and Figures (4-1 to 4-24). represent the obtained data regarding the inhibition zones of compounds against the expansion of tested bacteria. The concentration that used is 100 ppm in dimethyl sulfoxide, which loaded in the designated wells and incubated at 37 °C for one day.

The ligands and their complexes were showed different antimicrobial activity against the tested bacteria. In general, complexes showed more activity towards tested bacterial species compared with free ligands. The enhanced activity of metal complexes could be discussed according to chelation theory and Overtone's approach [92]. Regarding chelation approach, complexation may enhance the ability of metal complex to pass the cell layer of bacteria. Subsequently, the "chelation influence" will allow the distribution of the positive charge of the metal centre towards the coordinated ligand through the M-N and M-Se. Therefore, an increase in the lipophilic behaviour of the chelate ring will take place (due to redistribute of $d\pi$-electron across the whole chelate segment). Subsequently, this should favour the invasion of the chelate compound through the lipid of the cell membranes of tested species [93,94]. From the obtained data that included in Table (4-1), we can conclude the following important points:

- The ligands (HL^1-HL^6) and their complexes displayed activity against *Esherichia Coli* and *Bacillus subtilis* strains.

- Complexes of Mn(II), Ni(II) and Cu(II) with HL^1 and HL^3 showed no activity against *Staphylococcus aureus* and *Klebsiella Pneumoniae strains*.

- Ligand HL^1 exhibited no activity against *Staphylococcus aureus* and *Klebsiella Pneumoniae strains*. More, HL^3 shows no antimicrobial activity against *Staphylococcus aureus strain*.

- Zinc complex with HL^6 showed the highest antimicrobial activity against *E. coli strain,* compared with other complexes.

- Complexes of zinc and cadmium with the examined ligands (HL^1-HL^6) indicated the highest activity towards tested specie. This may be attributed to their d^{10} electronic system.

Figure (4-1): Inhibition diameter (mm) of HL^1 and its complexes against *Escherichia coli*.

Figure (4-2): Inhibition diameter (mm) of HL^{1} and its complexes against *Bacillus stubtilis*.

Figure (4-3): Inhibition diameter (mm) of HL^{1} and its complexes against *Staphylococcus aureus*.

Figure (4-4): Inhibition diameter (mm) of HL^1 and its complexes against *Klebsiella Pneumoniae.*
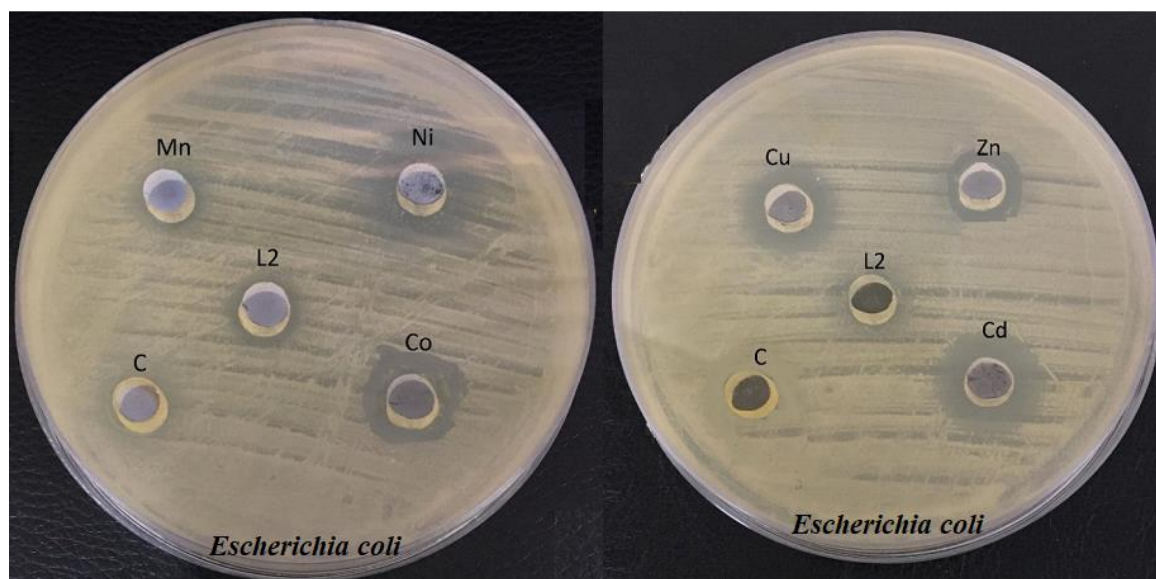
Figure (4-5): Inhibition diameter (mm) of HL^2 and its complexes against *Escherichia coli.*
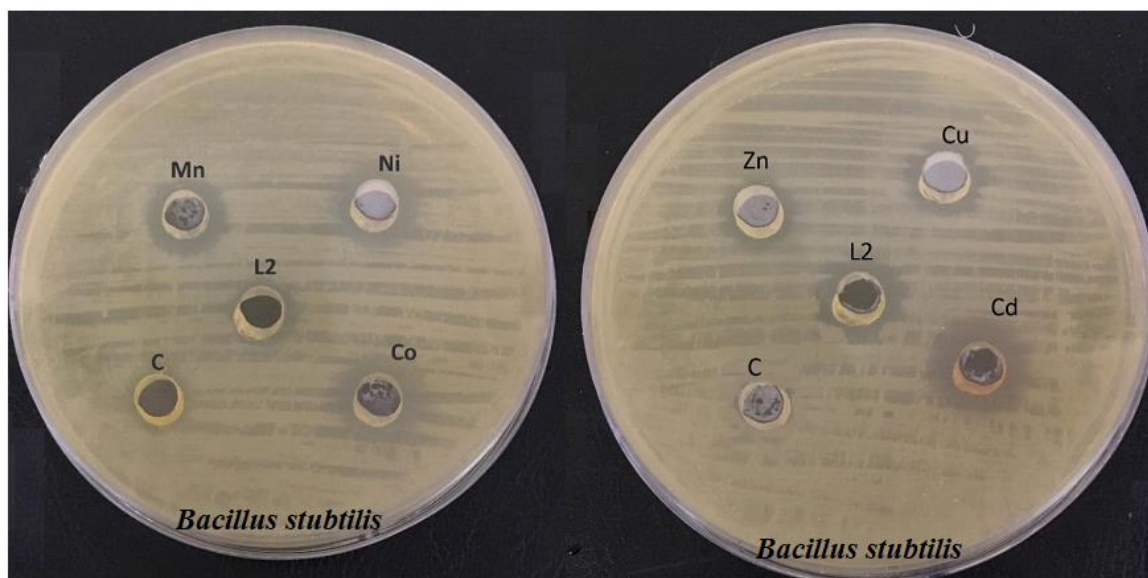
Figure (4-6): Inhibition diameter (mm) of HL^2 and its complexes against *Bacillus stubtilis*.
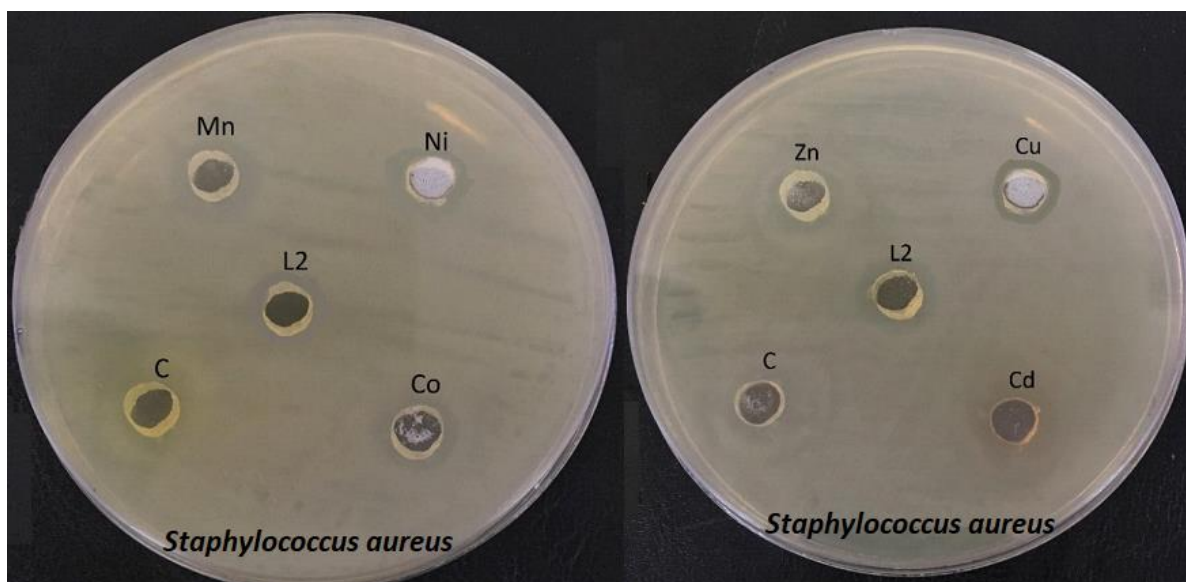
Figure (4-7): Inhibition diameter (mm) of HL^2 and its complexes against *Staphylococcus aureus*.
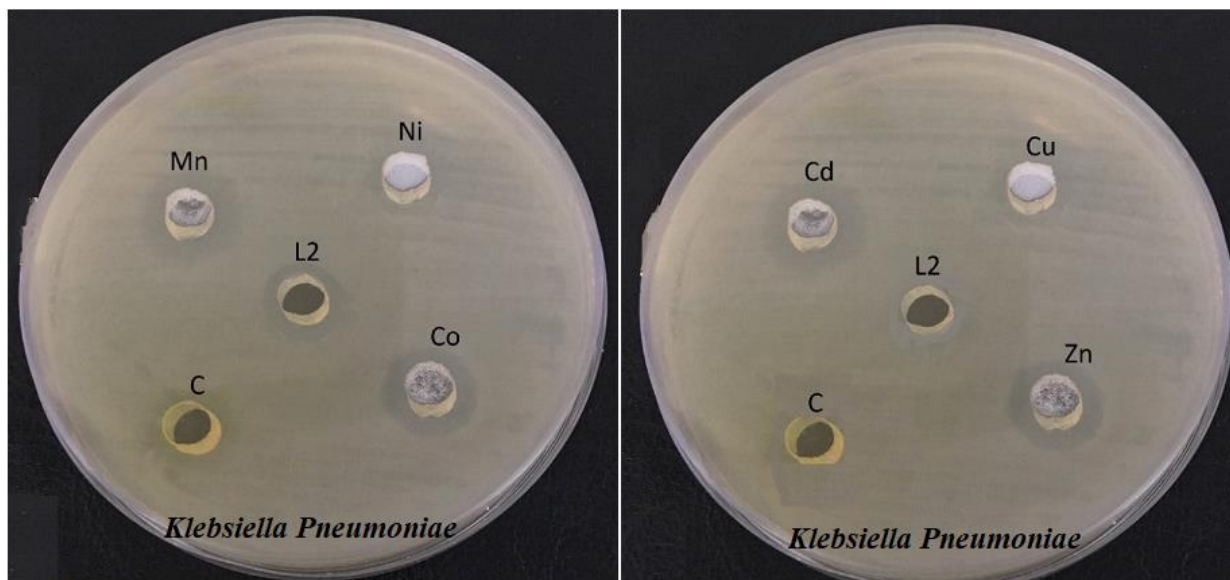
Figure (4-8): Inhibition diameter (mm) of HL^2 and its complexes against *Klebsiella Pneumoniae.*
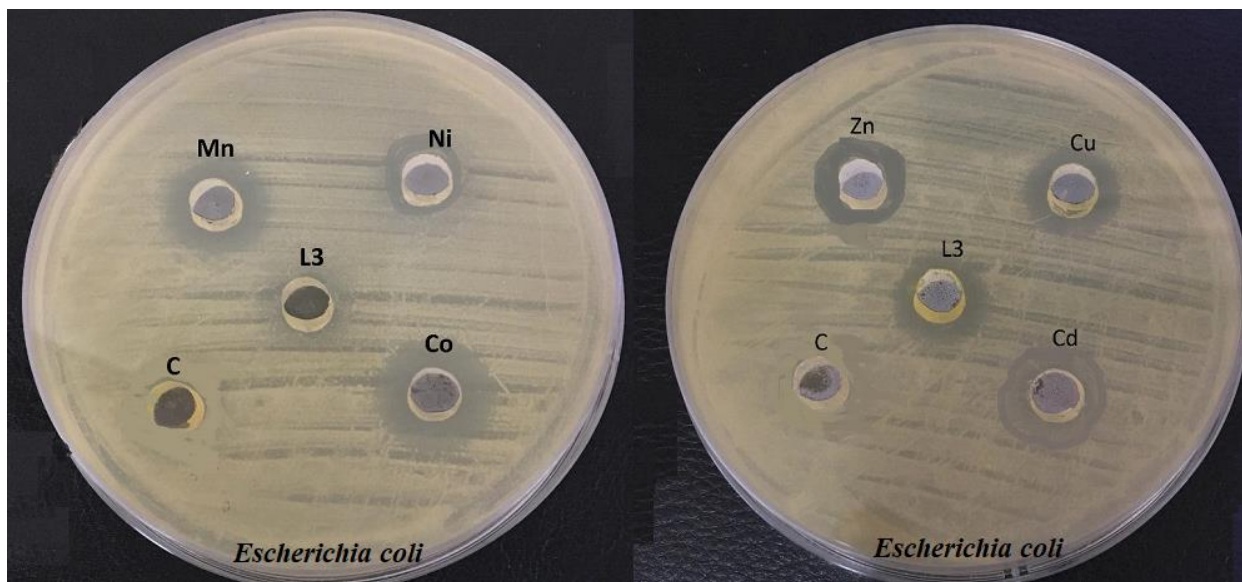
Figure (4-9): Inhibition diameter (mm) of HL^3 and its complexes against *Escherichia coli.*
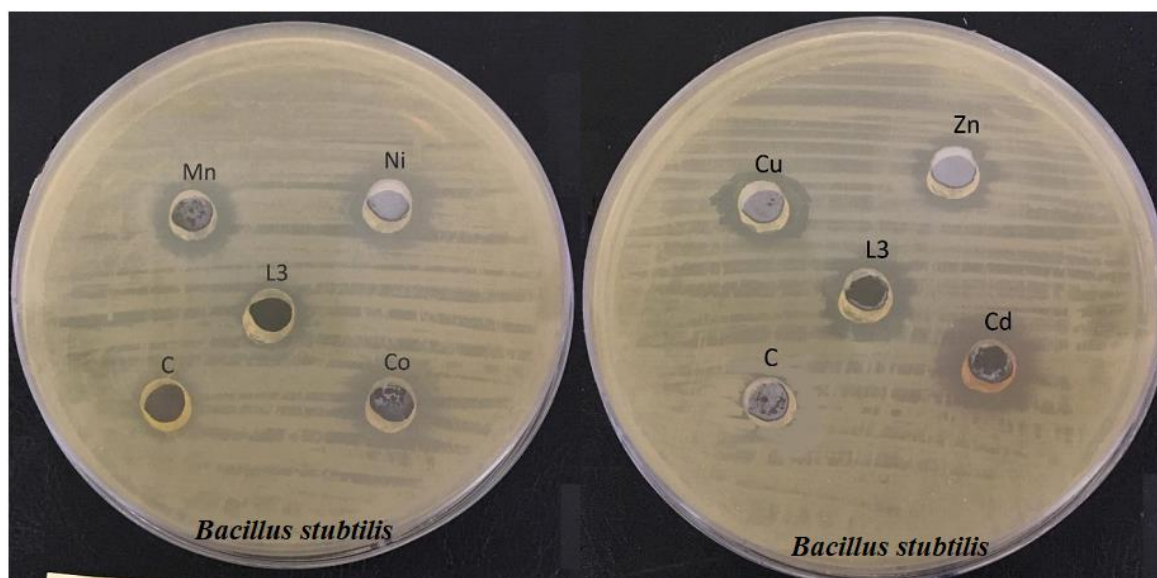
Figure (4-10): Inhibition diameter (mm) of HL^3 and its complexes against *Bacillus stubtilis*.
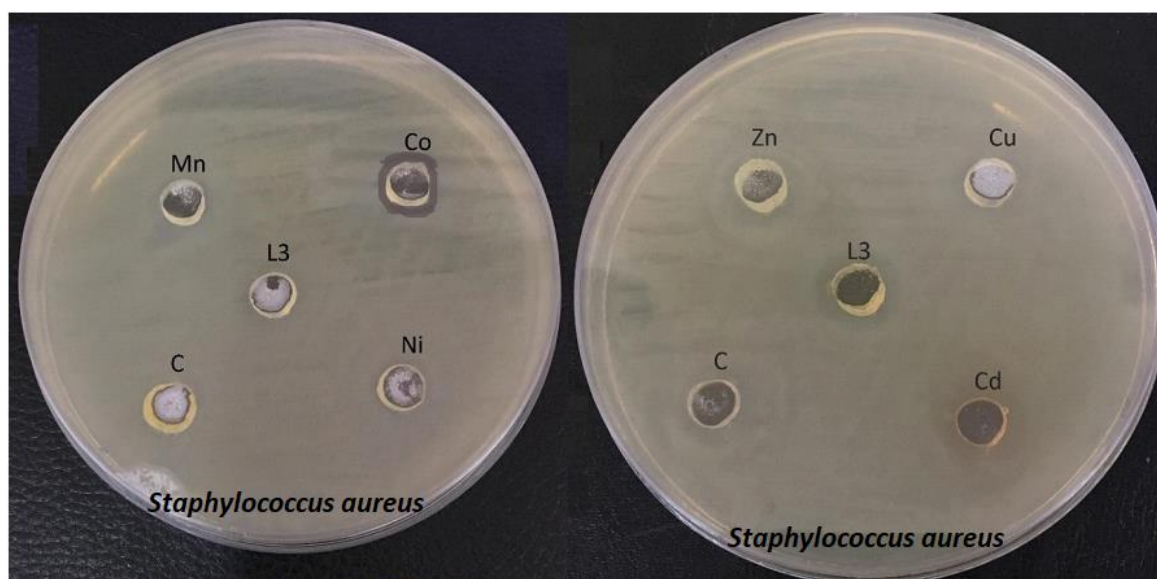
Figure (4-11): Inhibition diameter (mm) of HL^3 and its complexes against *Staphylococcus aureus*.
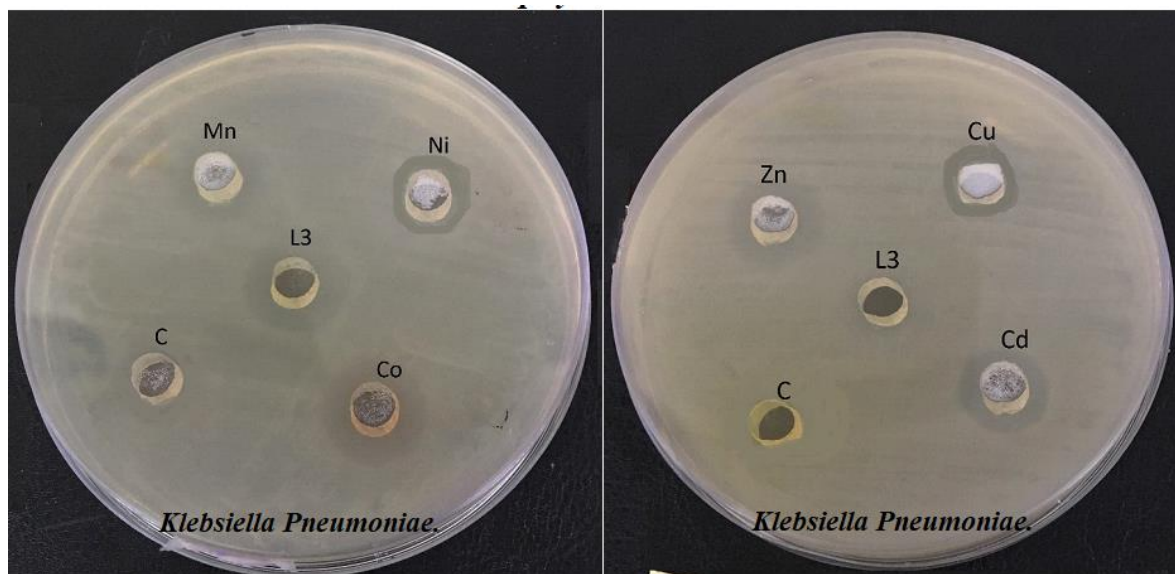
Figure (4-12): Inhibition diameter (mm) of HL^3 and its complexes against *Klebsiella Pneumoniae.*
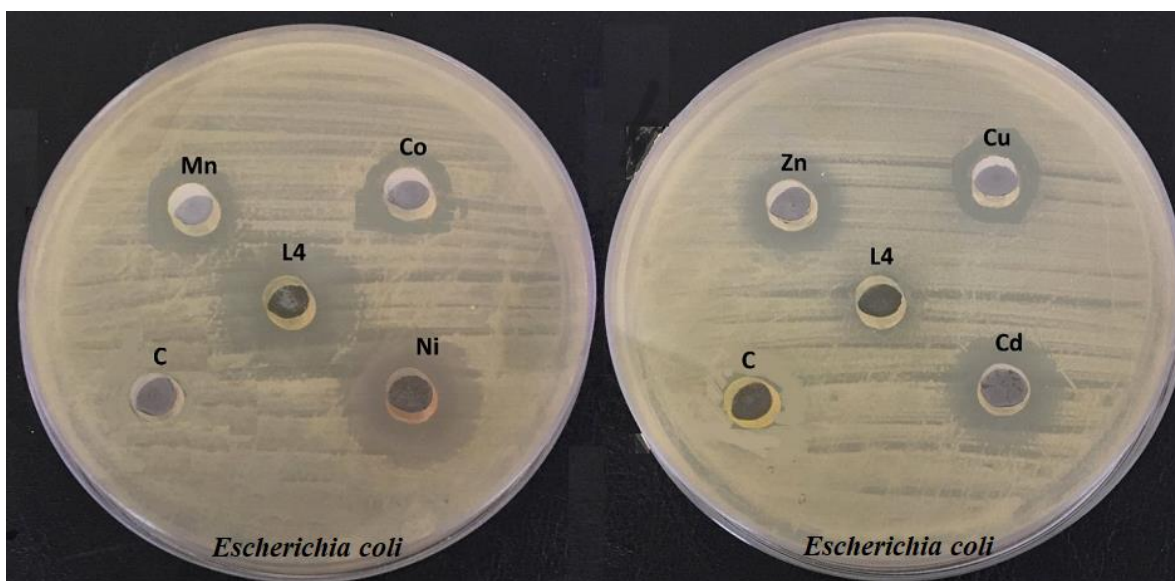
Figure (4-13): Inhibition diameter (mm) of HL^4 and its complexes against *Escherichia coli***.**
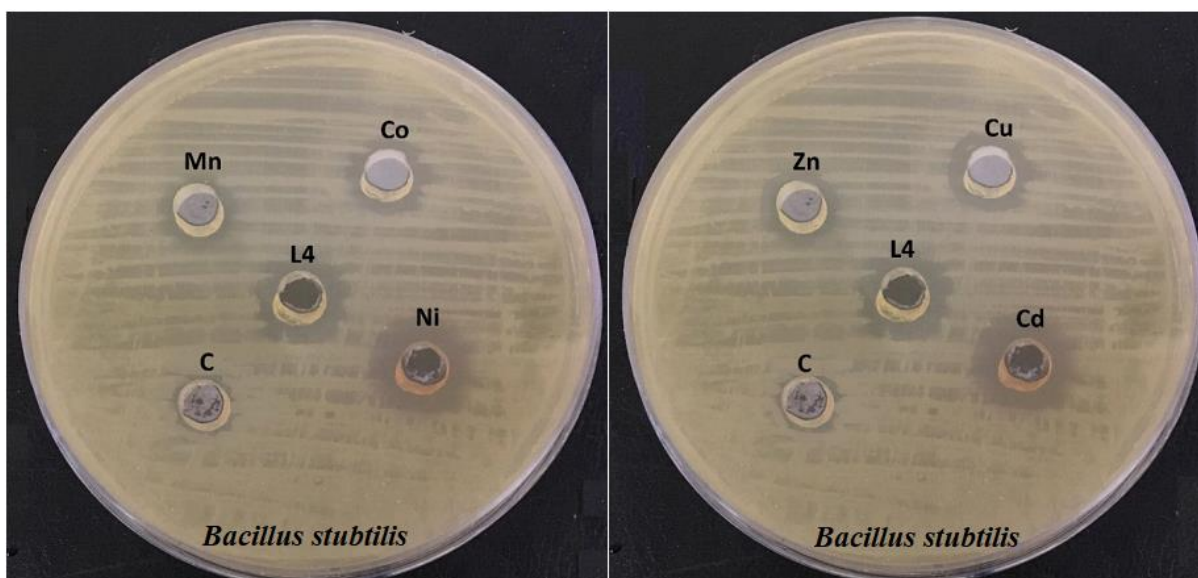
Figure (4-14): Inhibition diameter (mm) of HL^4 and its complexes against *Bacillus stubtilis*.
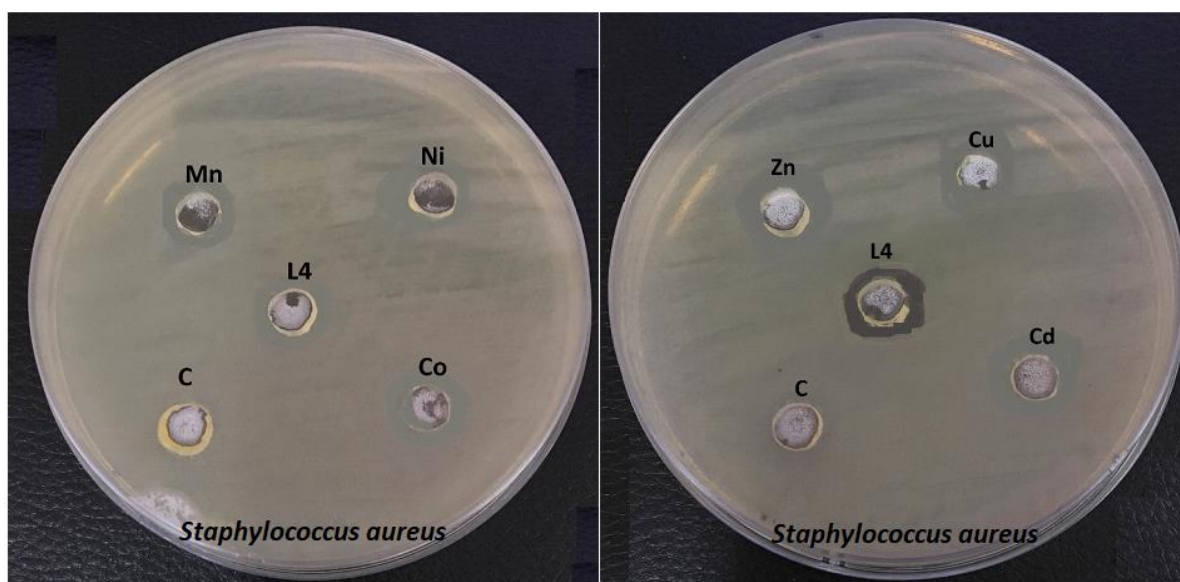
Figure (4-15): Inhibition diameter (mm) of HL^4 and its complexes against *Staphylococcus aureus*.
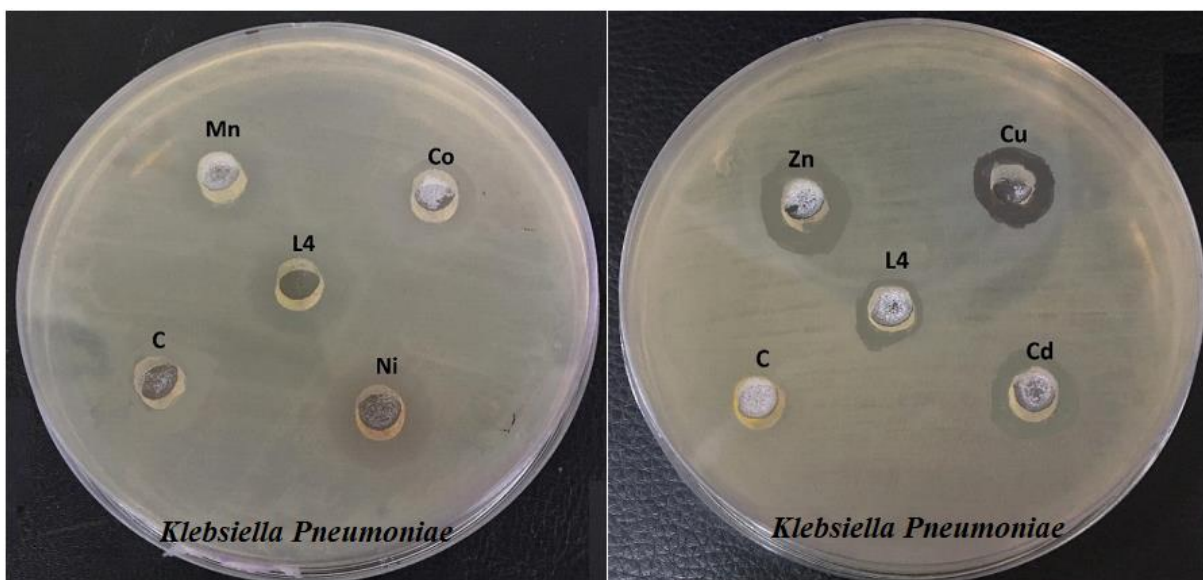
Figure (4-16): Inhibition diameter (mm) of HL^4 and its complexes against *Klebsiella Pneumoniae.*
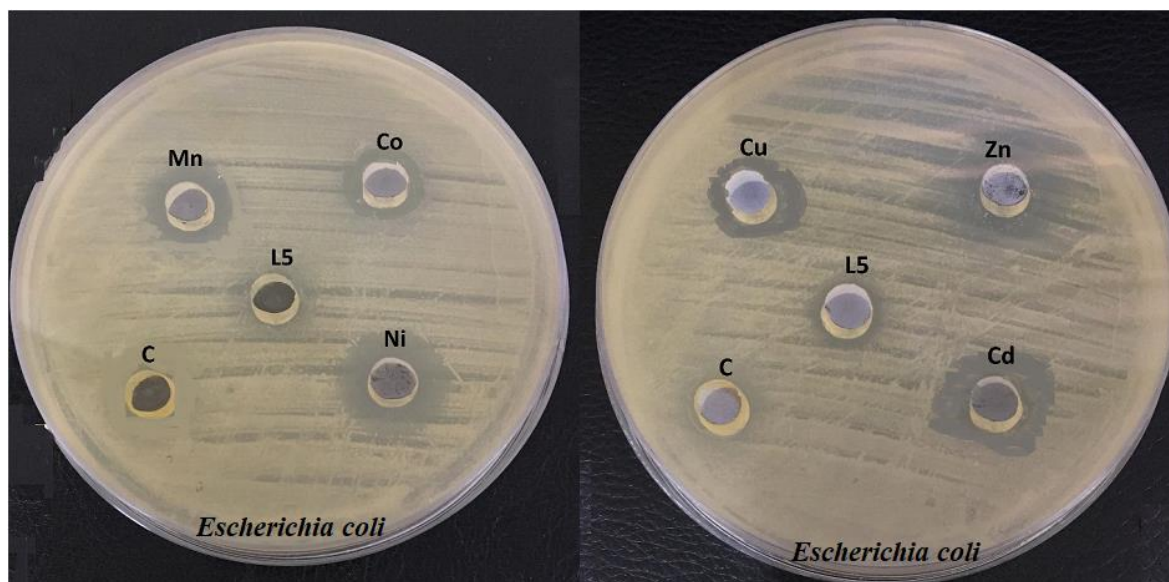
Figure (4-17): Inhibition diameter (mm) of HL^5 and its complexes against *Escherichia coli.*
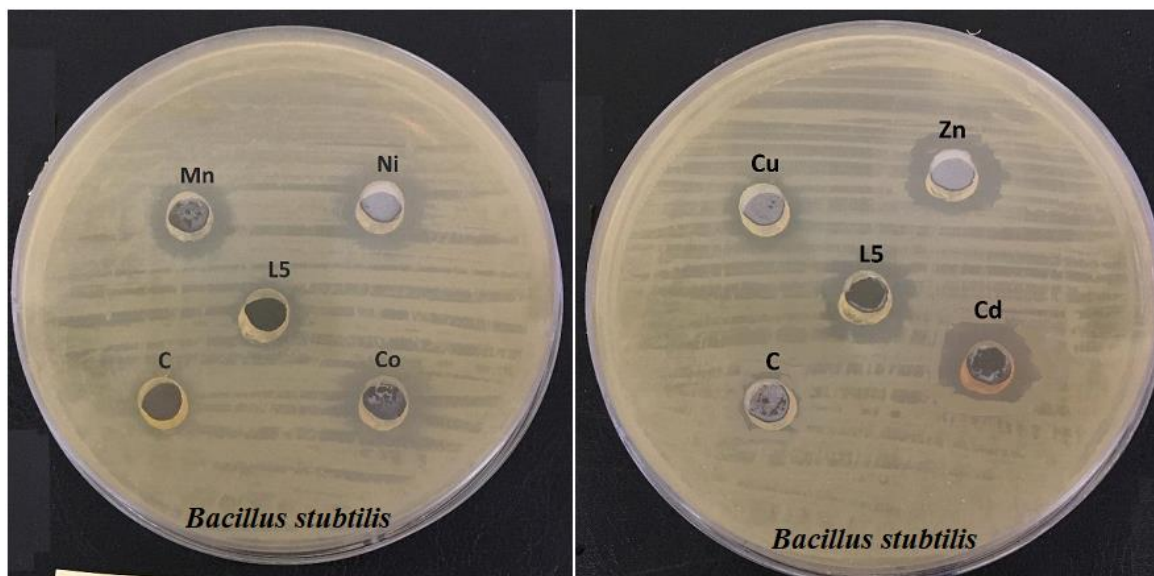
Figure (4-18): Inhibition diameter (mm) of HL^5 and its complexes against *Bacillus stubtilis*.
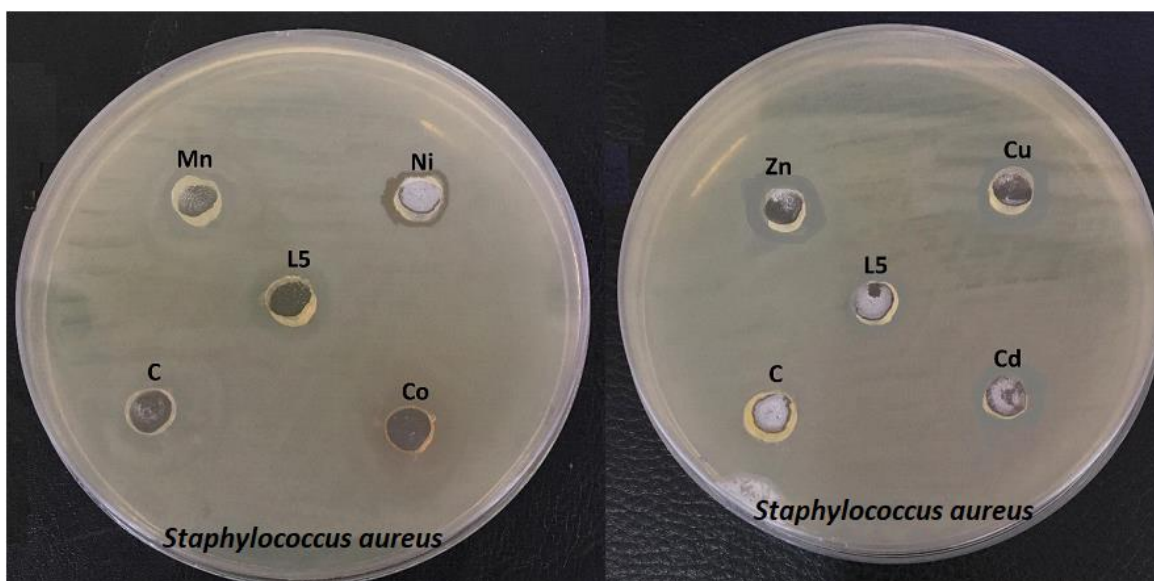
Figure (4-19): Inhibition diameter (mm) of HL^5 and its complexes against *Staphylococcus aureus*.
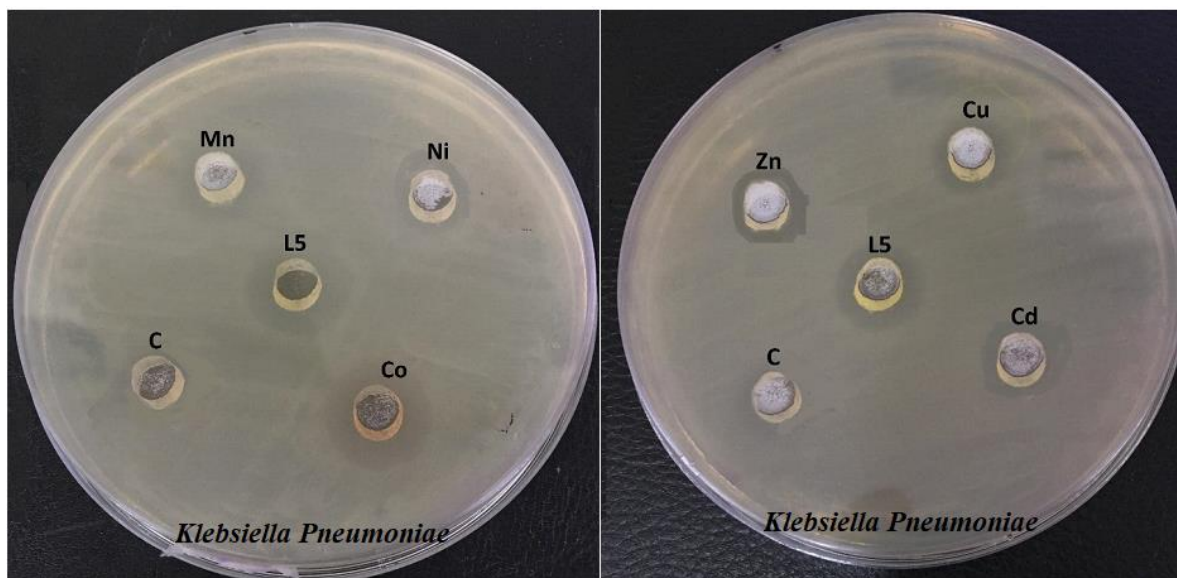
Figure (4-20): Inhibition diameter (mm) of HL^5 and its complexes against *Klebsiella Pneumoniae.*
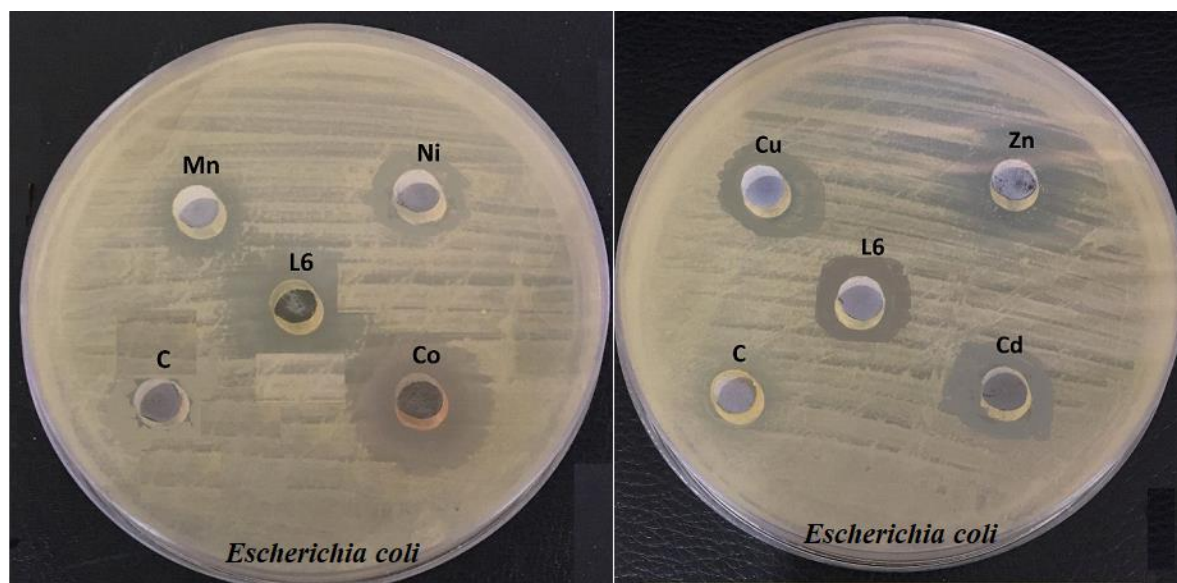
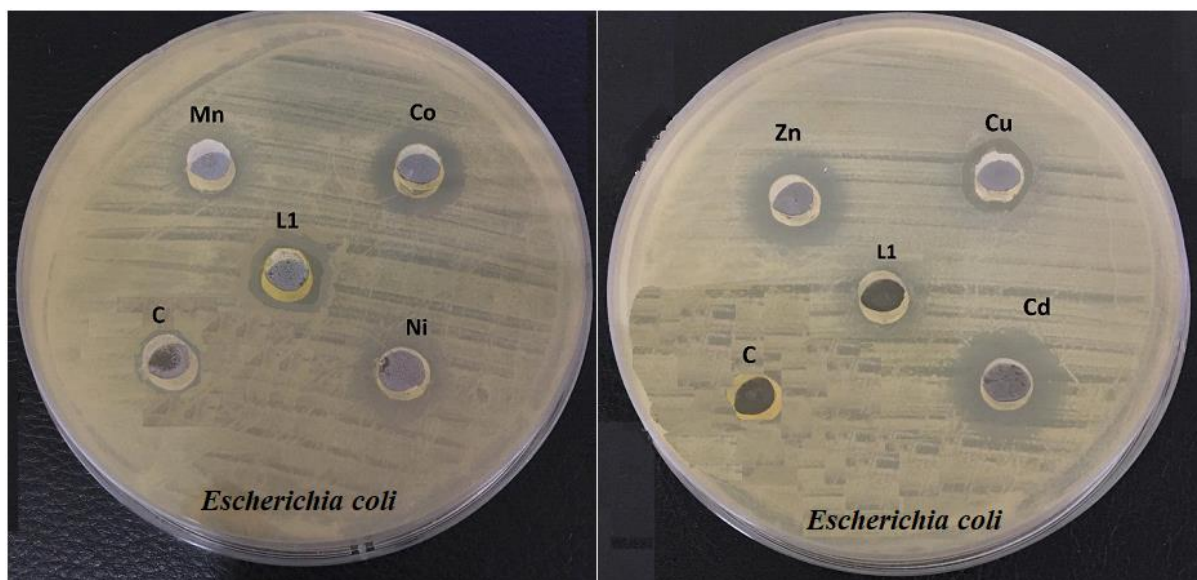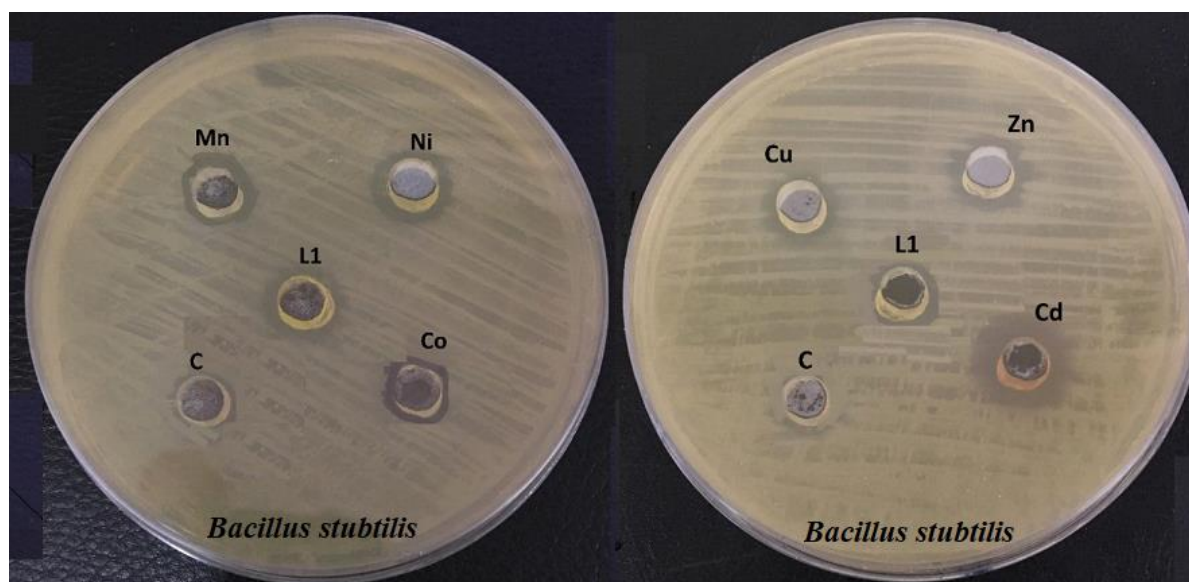**Figure (4-21): Inhibition diameter (mm) of HL^6 and its complexes against** *Escherichia coli.*
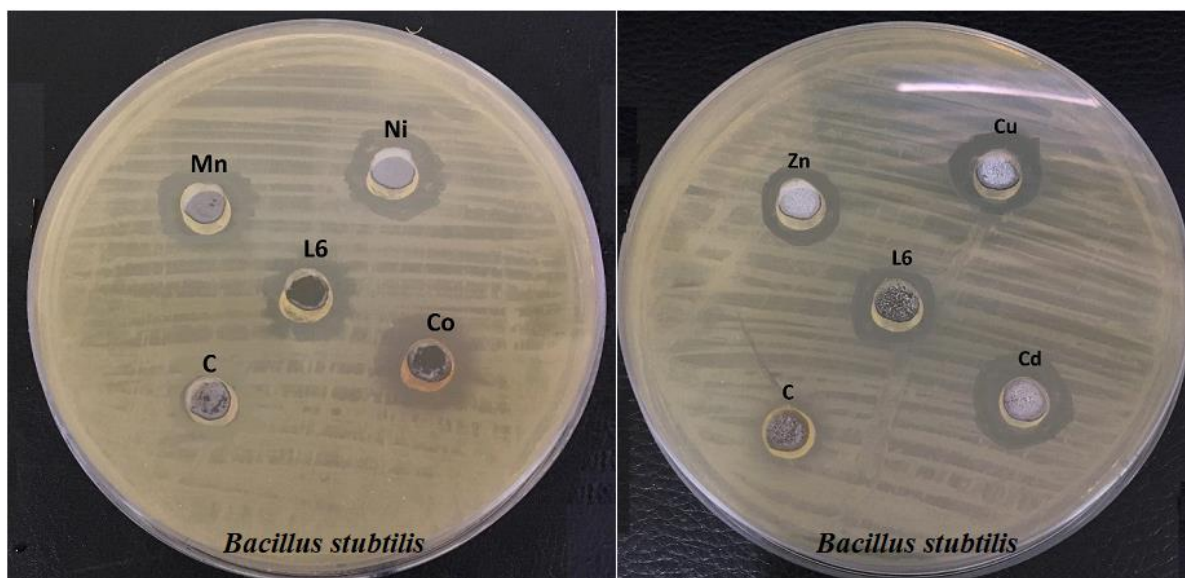
Figure (4-22): Inhibition diameter (mm) of HL^6 and its complexes against *Bacillus stubtilis.*
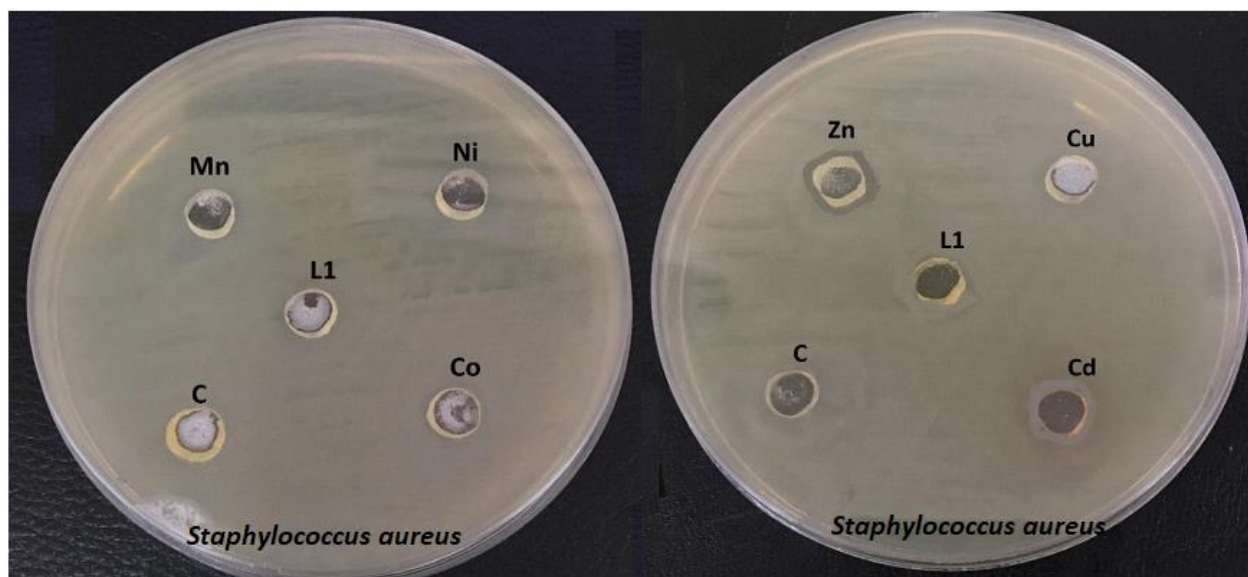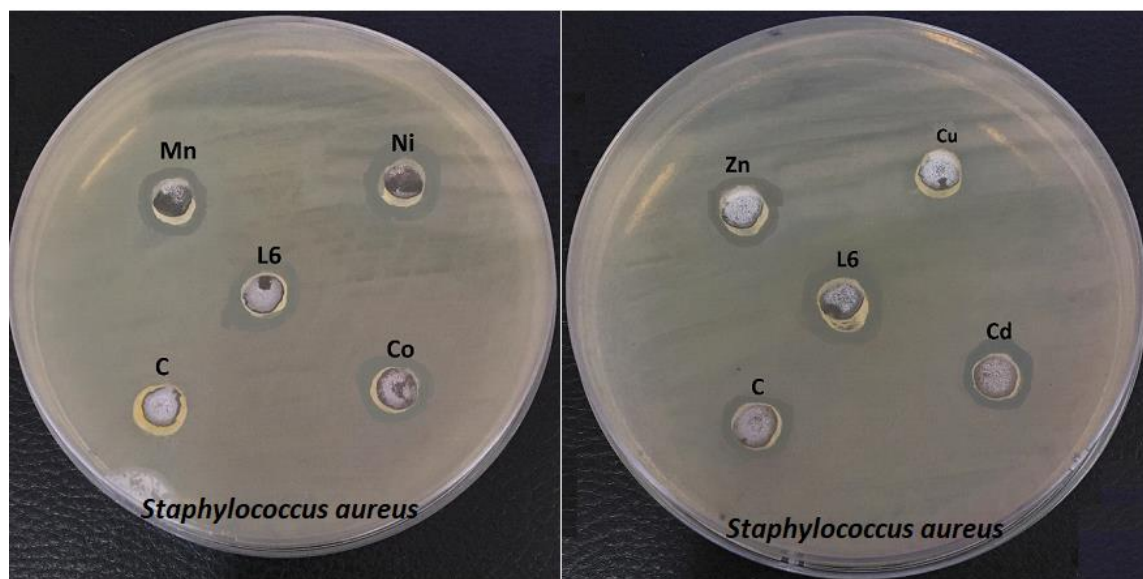

Figure (4-23): Inhibition diameter (mm) of HL^6 and its complexes against *Staphylococcus aureus.*
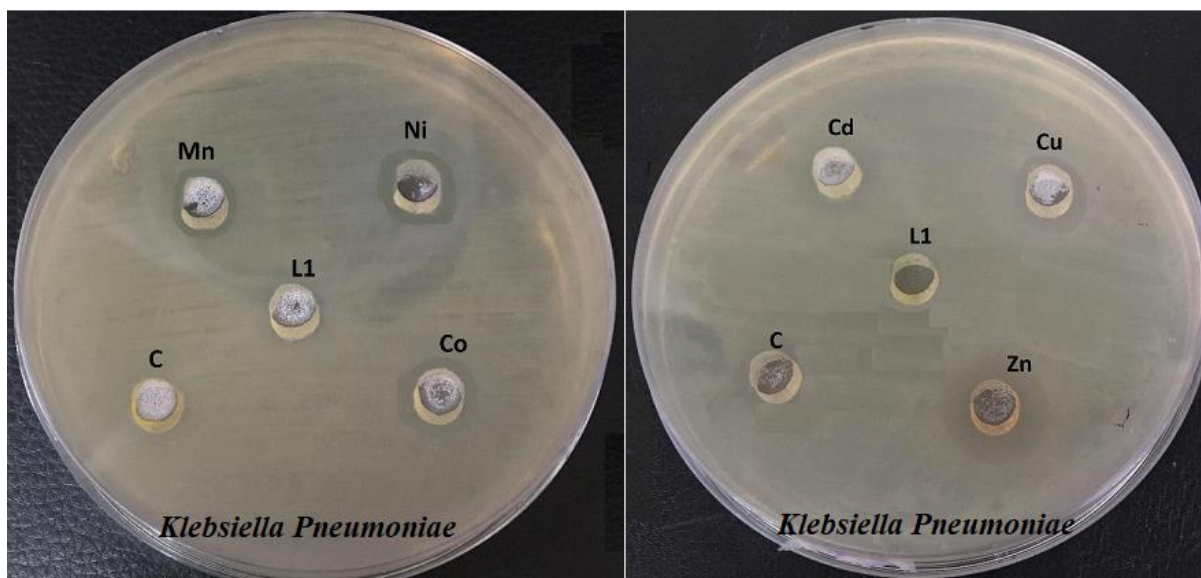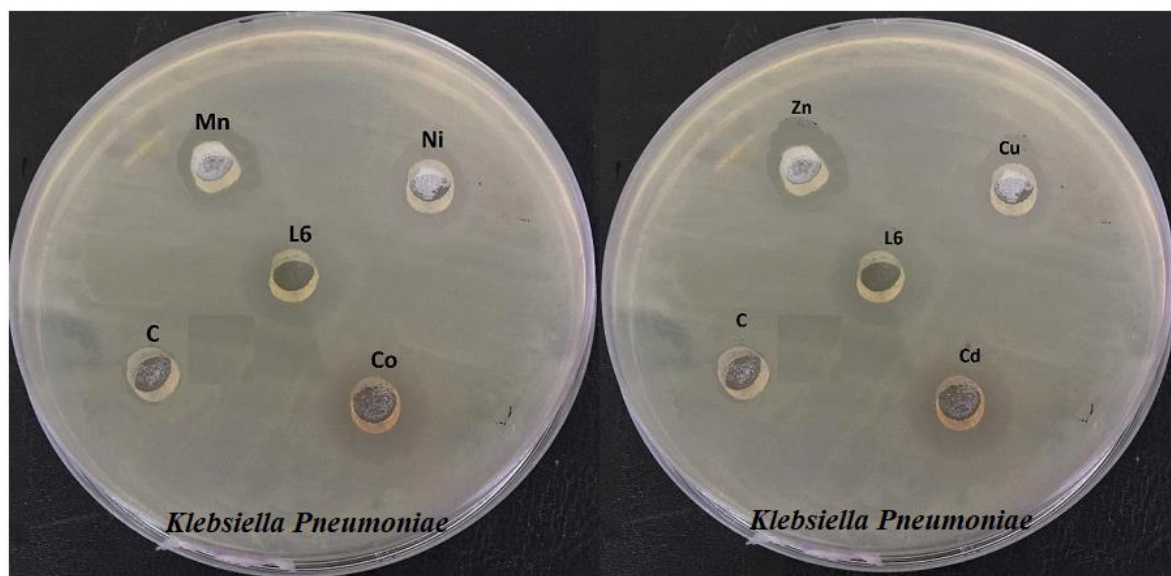
Figure (4-24): Inhibition diameter (mm) of HL^6 and its complexes against *Klebsiella Pneumoniae.*

Table (4-1): Bacterial activity of HL^1-HL^6 and their complexes.

Sample	Inhibition zone (mm)			
	E. coli	*B. subtilis*	*S. aureus*	*K. Pneumoniae*
HL^1	10	9	-	-
K$_2$[Mn(L^1)$_2$Cl$_2$]	17	15	-	13
K$_2$[Co(L^1)$_2$Cl$_2$]	18	12	12	15
K$_2$[Ni(L^1)$_2$Cl$_2$]	11	15	-	16
[Cu(L^1)$_2$]	12	15	-	19
[Zn(L^1)$_2$]	25	20	13	18
[Cd(L^1)$_2$]	22	21	14	20
HL^2	14	14	9	11
K$_2$[Mn(L^2)$_2$Cl$_2$]	17	17	15	12
K$_2$[Co(L^2)$_2$Cl$_2$]	19	19	14	14
K$_2$[Ni(L^2)$_2$Cl$_2$]	23	23	10	13
[Cu(L^2)$_2$]	21	21	16	15
[Zn(L^2)$_2$]	16	16	17	19
[Cd(L^2)$_2$]	20	20	19	16
HL^3	12	13	-	11
K$_2$[Mn(L^3)$_2$Cl$_2$]	13	14	-	12
K$_2$[Co(L^3)$_2$Cl$_2$]	15	14	15	19
K$_2$[Ni(L^3)$_2$Cl$_2$]	16	16	-	12
[Cu(L^3)$_2$]	17	16	-	13
[Zn(L^3)$_2$]	18	14	13	20
[Cd(L^3)$_2$]	19	19	18	22

Sample	Inhibition zone (mm)			
	E. coli	*B. subtilis*	*S. aureus*	*K. Pneumoniae*
HL^4	14	12	11	12
$K_2[Mn(L^4)_2Cl_2]$	15	13	12	13
$K_2[Co(L^4)_2Cl_2]$	16	17	13	17
$K_2[Ni(L^4)_2Cl_2]$	18	19	12	13
$[Cu(L^4)_2]$	20	21	18	14
$[Zn(L^4)_2]$	22	21	19	21
$[Cd(L^4)_2]$	21	20	18	19
HL^5	11	10	10	12
$K_2[Mn(L^5)_2Cl_2]$	13	13	12	14
$K_2[Co(L^5)_2Cl_2]$	15	16	13	15
$K_2[Ni(L^5)_2Cl_2]$	16	15	11	13
$[Cu(L^5)_2]$	17	18	19	17
$[Zn(L^5)_2]$	20	21	18	16
$[Cd(L^5)_2]$	22	19	14	13
HL^6	15	14	12	13
$K_2[Mn(L^6)_2Cl_2]$	16	17	13	15
$K_2[Co(L^6)_2Cl_2]$	20	21	14	16
$K_2[Ni(L^6)_2Cl_2]$	19	18	16	14
$[Cu(L^6)_2]$	20	22	13	14
$[Zn(L^6)_2]$	29	21	13	15
$[Cd(L^6)_2]$	23	21	19	20

(4.2) Fungi activity

Ligands (HL^1-HL^6) and their metal complexes were investigated against four types of fungi (*Candida albicans*, *Candida glabrat*a, *Candida tropicali*s and *Candida parapsilsis*). All tested compounds (ligands and metal complexes) were dissolved in DMSO with a final concentration of 100 ppm. The observed activity measurements of tested compounds against Fungi are listed in Table (4-2). The inhibition capacity of ligands

and their metal complexes on the tested fungi types are shown Figures (4-25 to 4-48). From the obtained data the following observation are noticed as follow:

- Ligands (HL^1-HL^6) and their metal complexes showed activity against *Candida glabrata*.

- Ligands (HL^1-HL^5) displayed no activity against *Candida parapsilsis*.

- All complexes of HL^1 exhibited no activity against *Candida parapsilsis*.

- Ligands (HL^1-HL^3) did not show any activity against *Candida albican*s.

- Complexes of Ni(II) and Cd(II) with HL^1 and complex Cd(II) with HL^4 showed no activity against *Candida albican*s.

- Regarding the activity of tested compounds against *Candida tropicalis*, the following results are observed:

  a- Complexes of Ni(II) and Cd(II) with HL^1 displayed no activity.

  b- Ligands HL^2 and HL^3 showed no activity.

  c- Complex of Ni(II) with HL^4 did not exhibit any activity.

  d- Ligands (HL^5 and HL^6) and their metal complexes exhibited higher activity in comparison with other compounds.

Generally, complexes showed more resistance toward fungi as compared with free ligands confirming that complexation enhanced the resistance ability of ligands. This can be defined according to chelation theory [95] which described by the redistribution of π- electrons of the title ligand through the chelate ring. As a result, the polarity of the chelation system decreases that improves the activity of the ligand. Subsequently, the lipophilic behaviour of the chelate system will allow the penetration of the complex across lipid layer of the cell membranes of fungi.
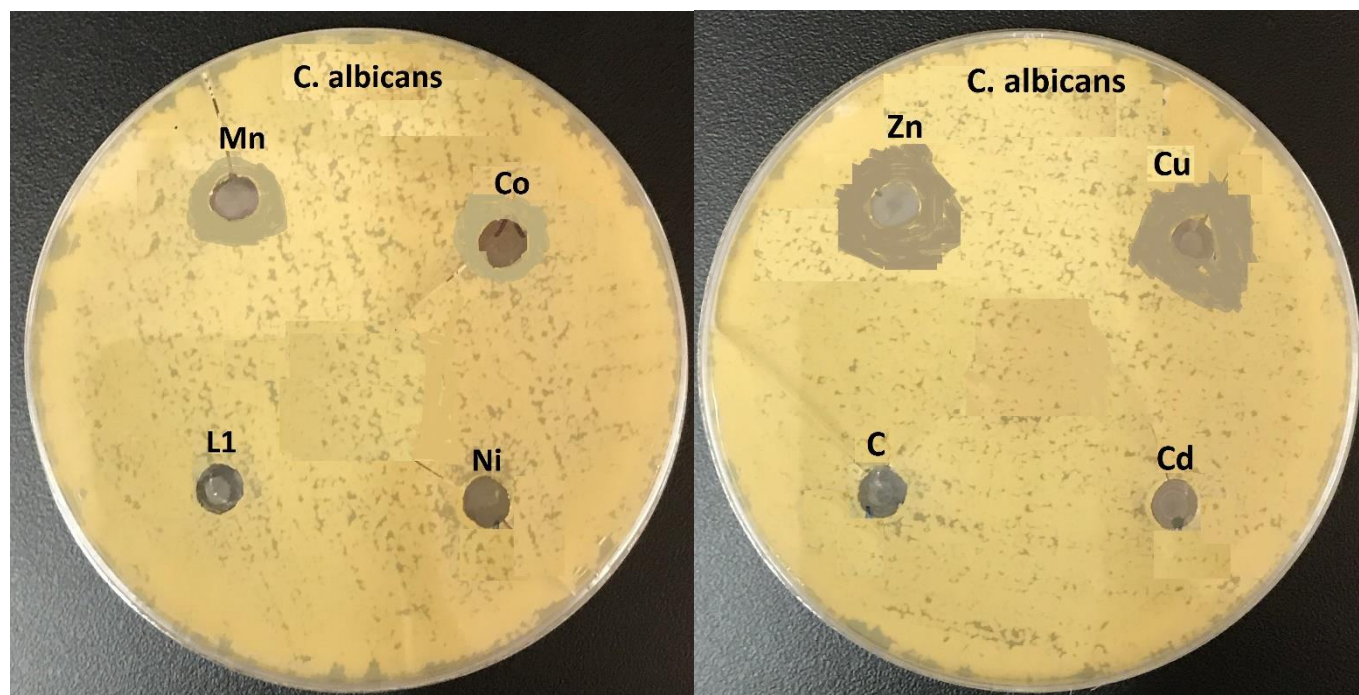
Figure (4.25): The influence of HL^1 and its complexes on *Candida albicans*.
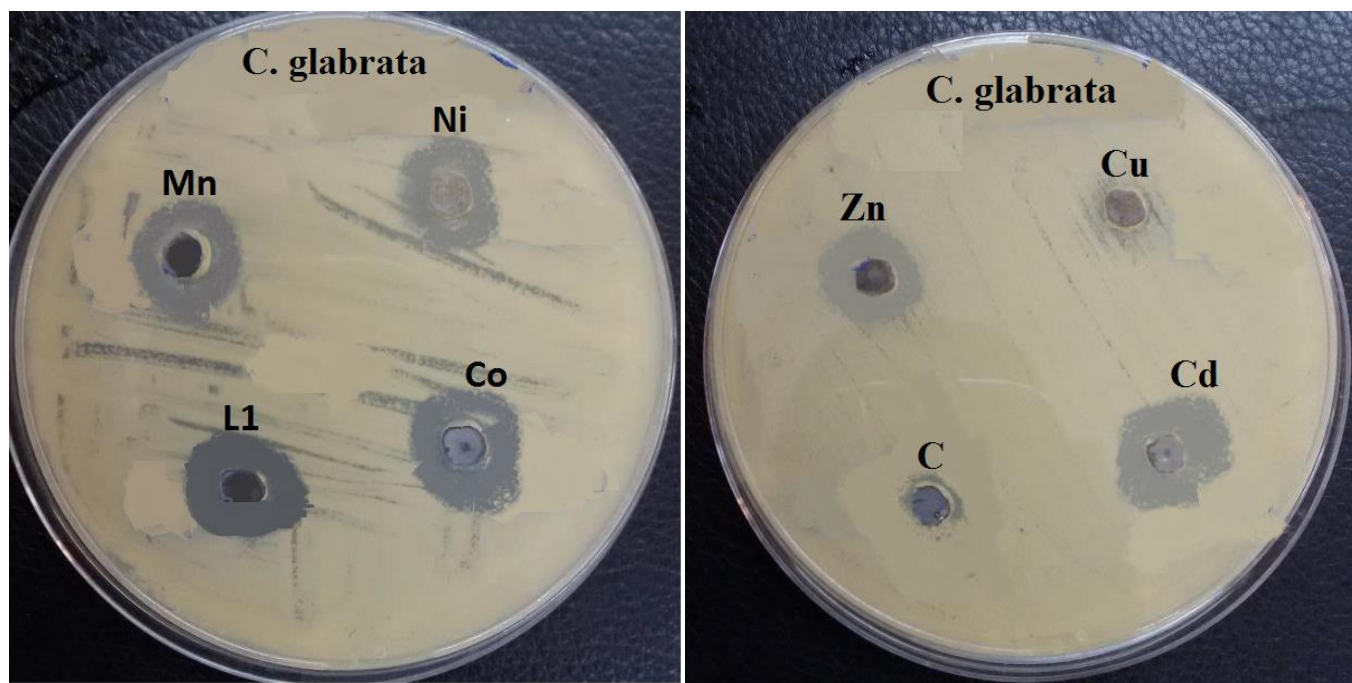
Figure (4.26): The influence of HL^1 and its complexes on *Candida glabrata*.
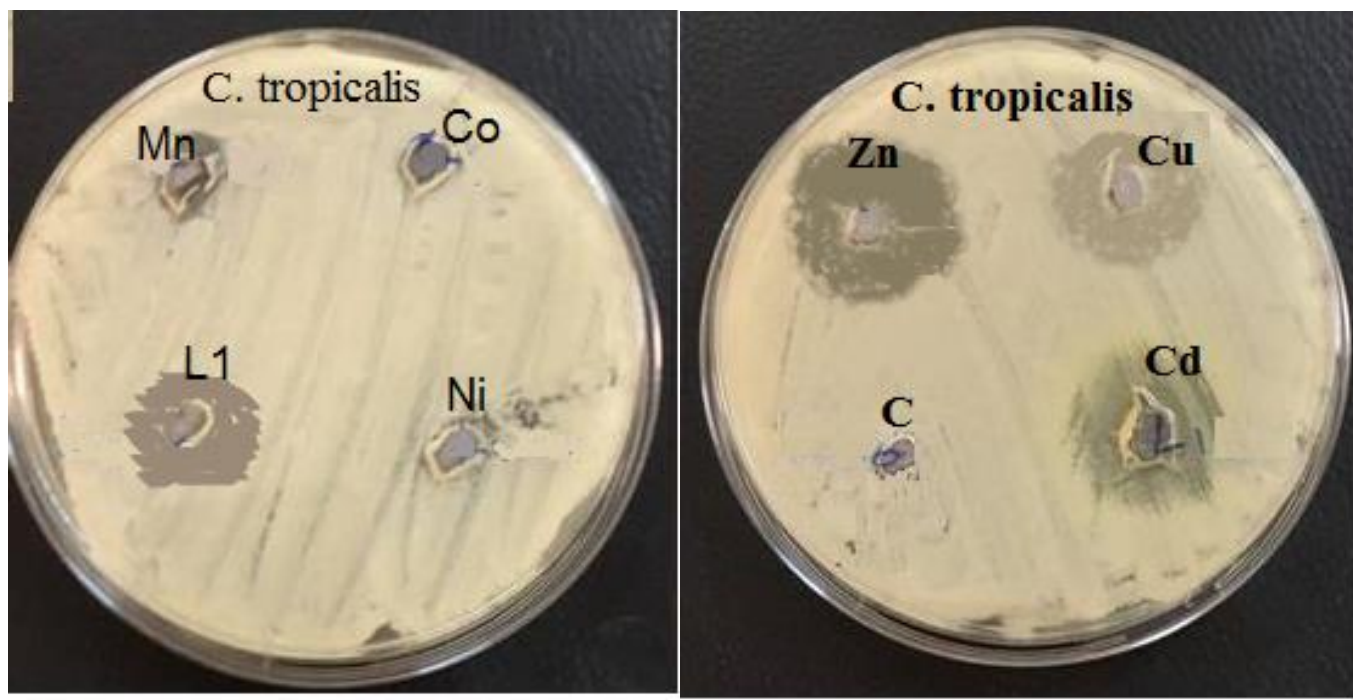
Figure (4.27): The influence of HL^1 and its complexes on *Candida tropicalis*.
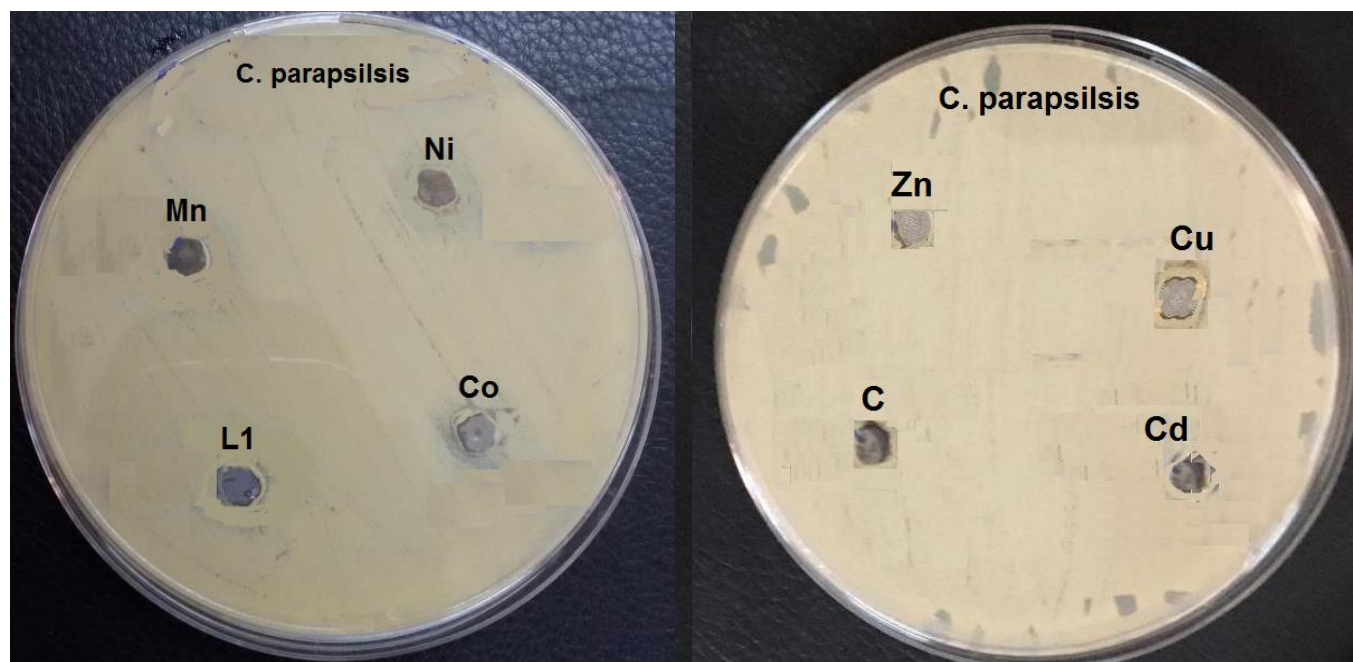
Figure (4.28): The influence of HL^1 and its complexes on *Candida parapsilsis*.
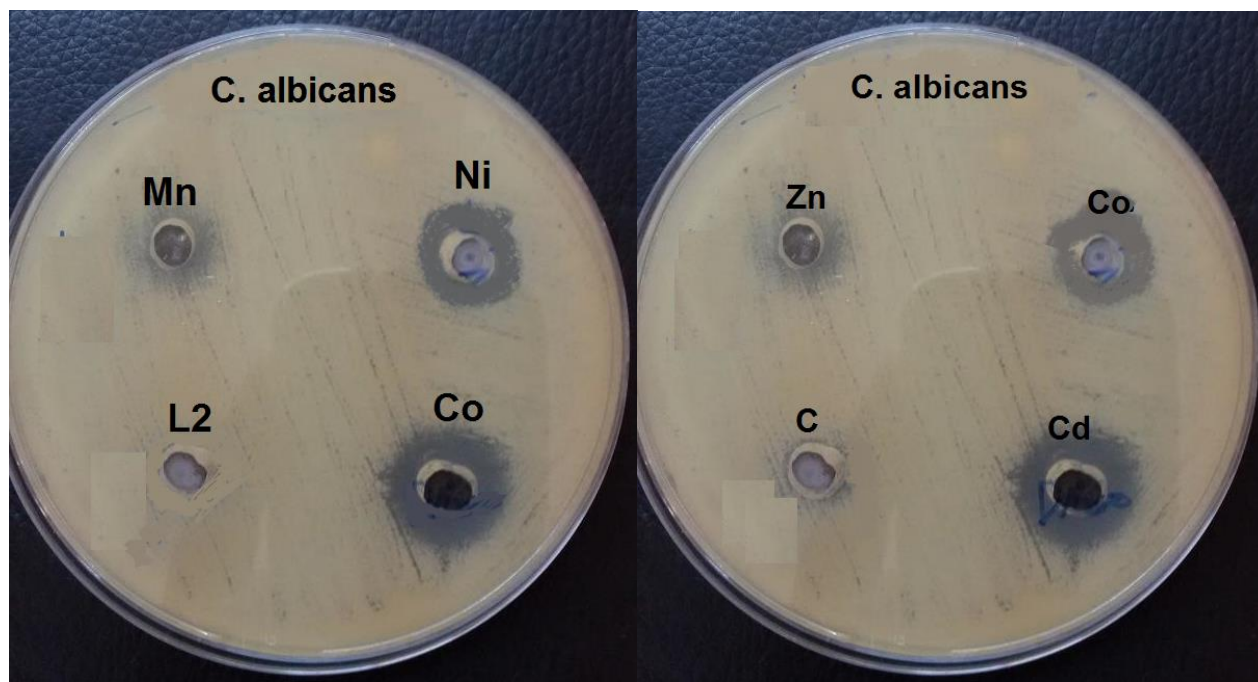
Figure (4.29): The influence of HL^2 and its complexes on *Candida albicans*.
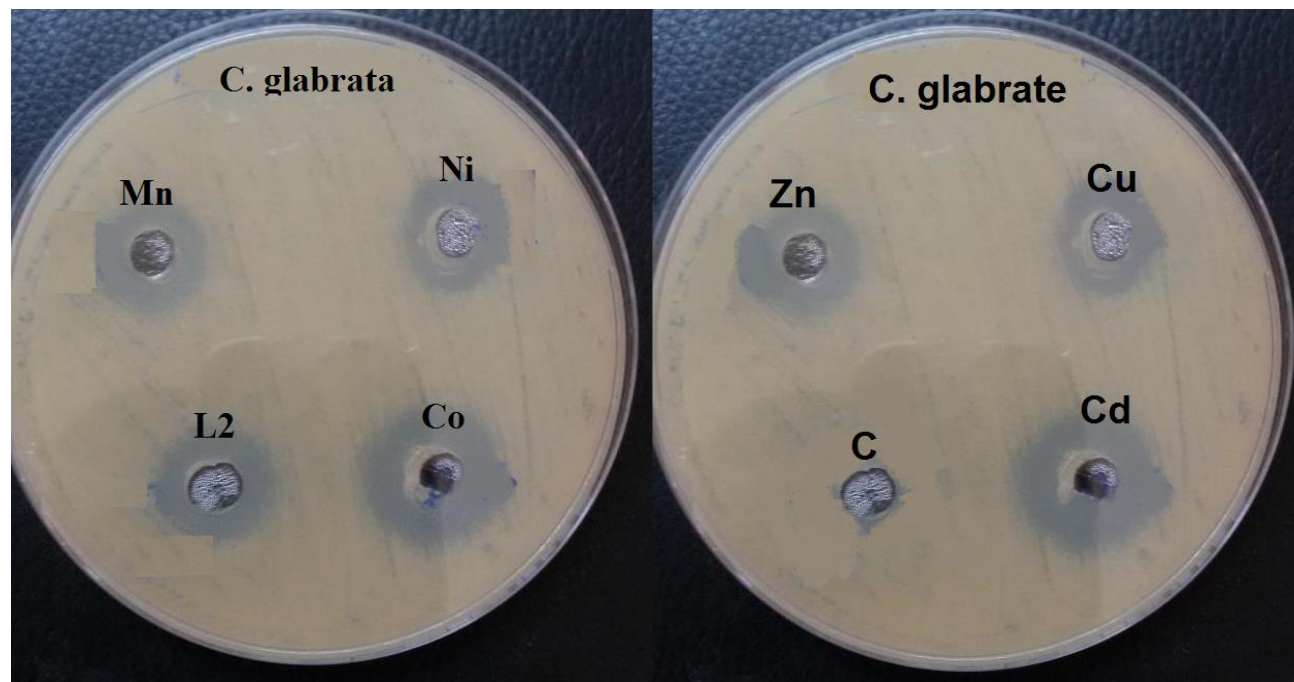
Figure (4.30): The influence of HL^2 and its complexes on *Candida glabrata*.

327
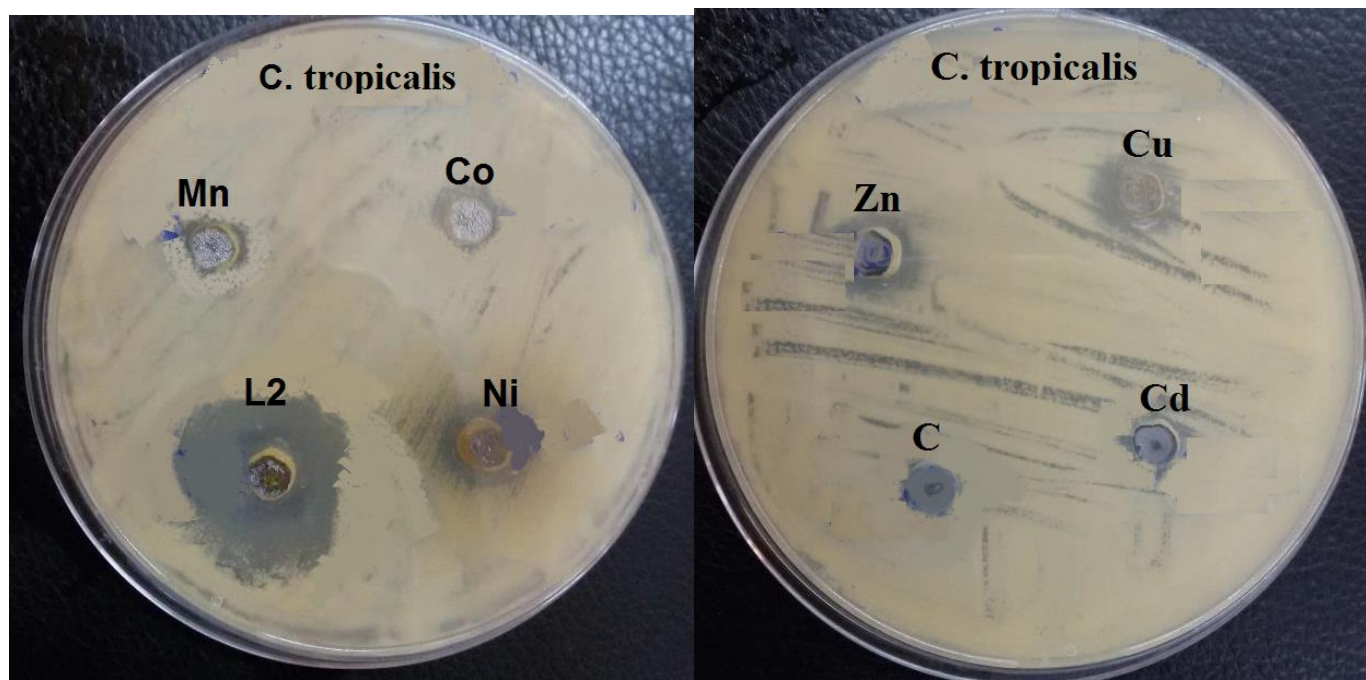
Figure (4.31): The influence of HL^2 and its complexes on *Candida tropicalis*.
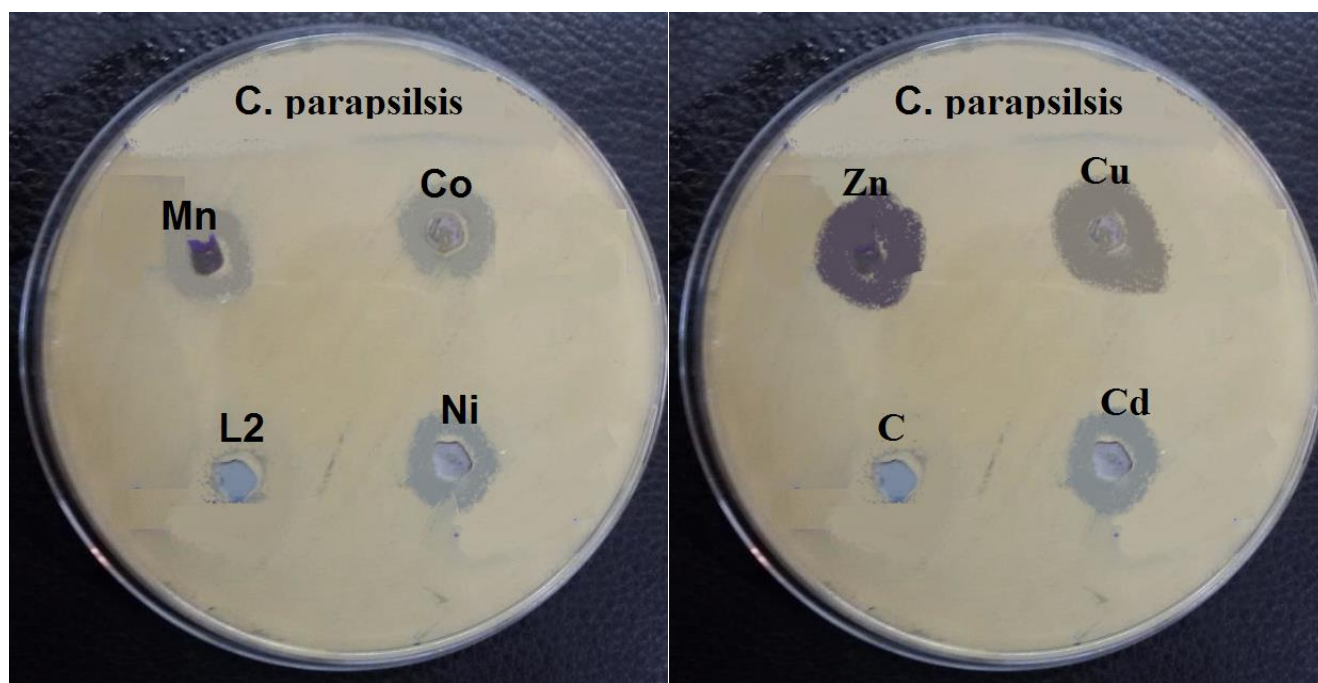
Figure (4.32): The influence of HL^2 and its complexes on *Candida parapsilsis*.
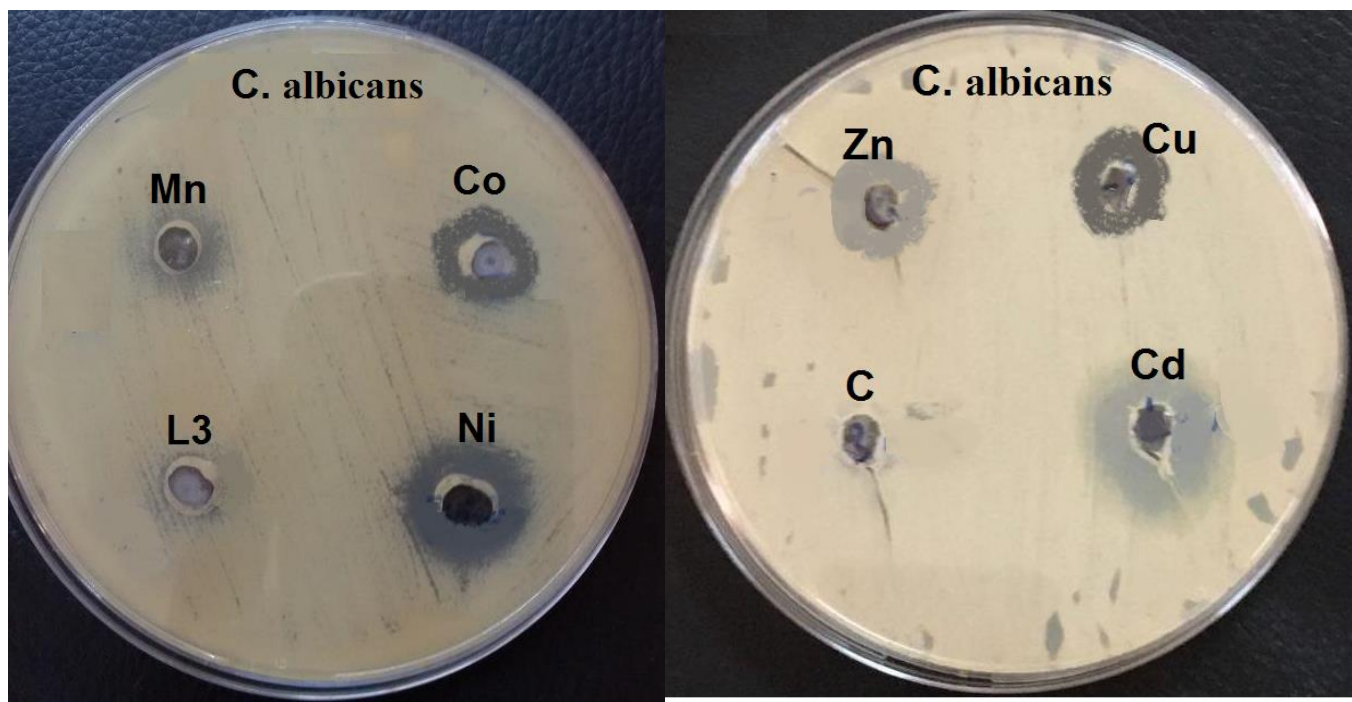
Figure (4.33): The influence of HL^3 and its complexes on *Candida albicans*.
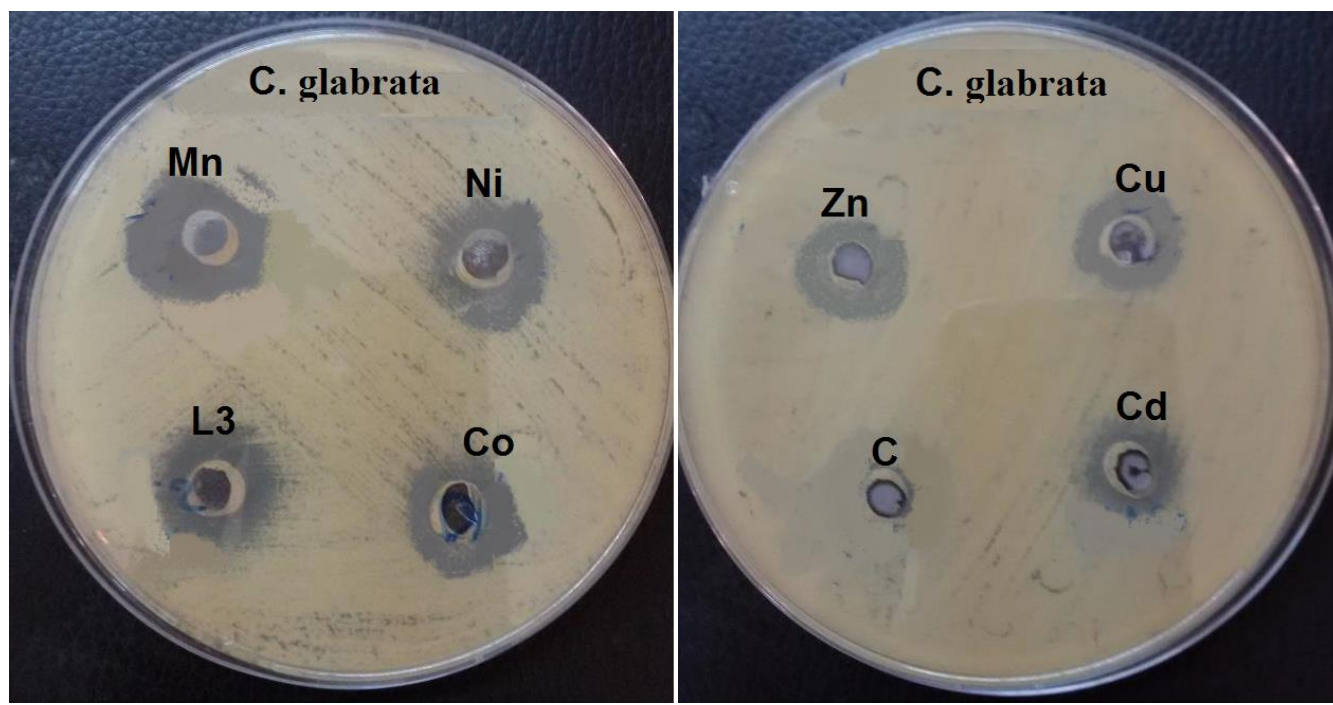
Figure (4.34): The influence of HL^3 and its complexes on *Candida glabrata*.
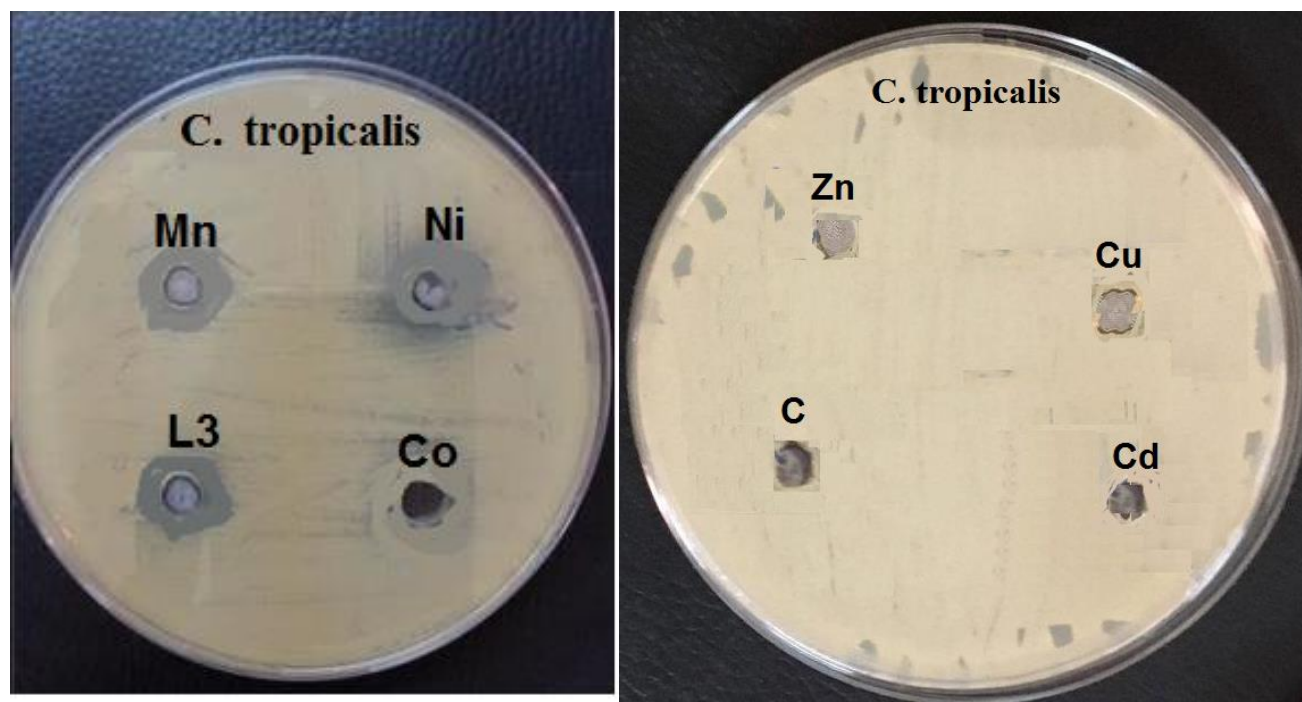
Figure (4.35): The influence of HL^3 and its complexes on *Candida tropicalis*.
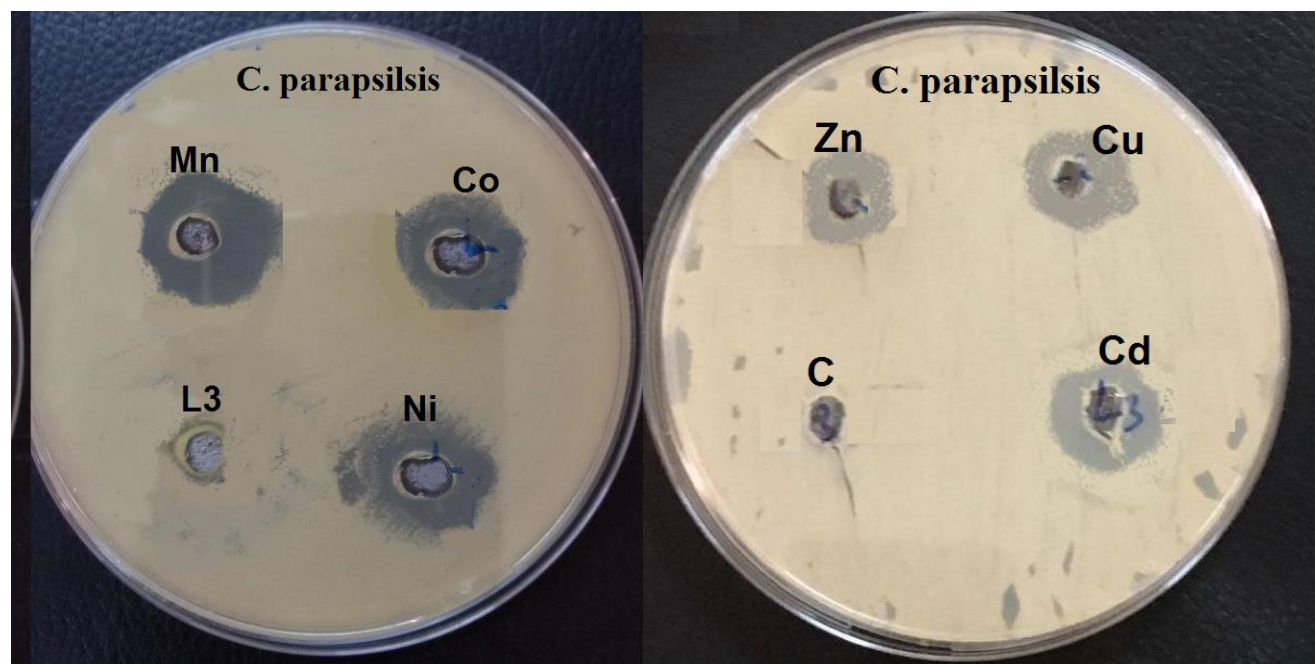
Figure (4.36): The influence of HL^3 and its complexes on *Candida parapsilsis*.
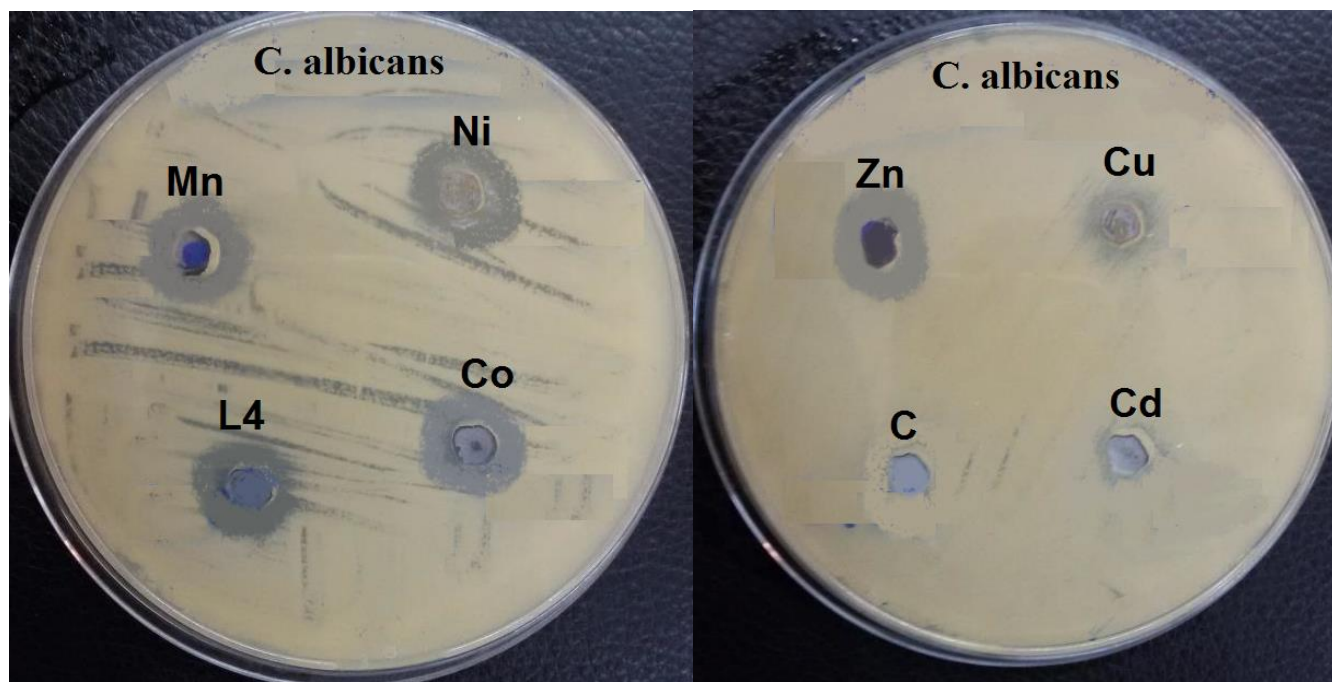
Figure (4.37): The influence of HL^4 and its complexes on *Candida albicans*.
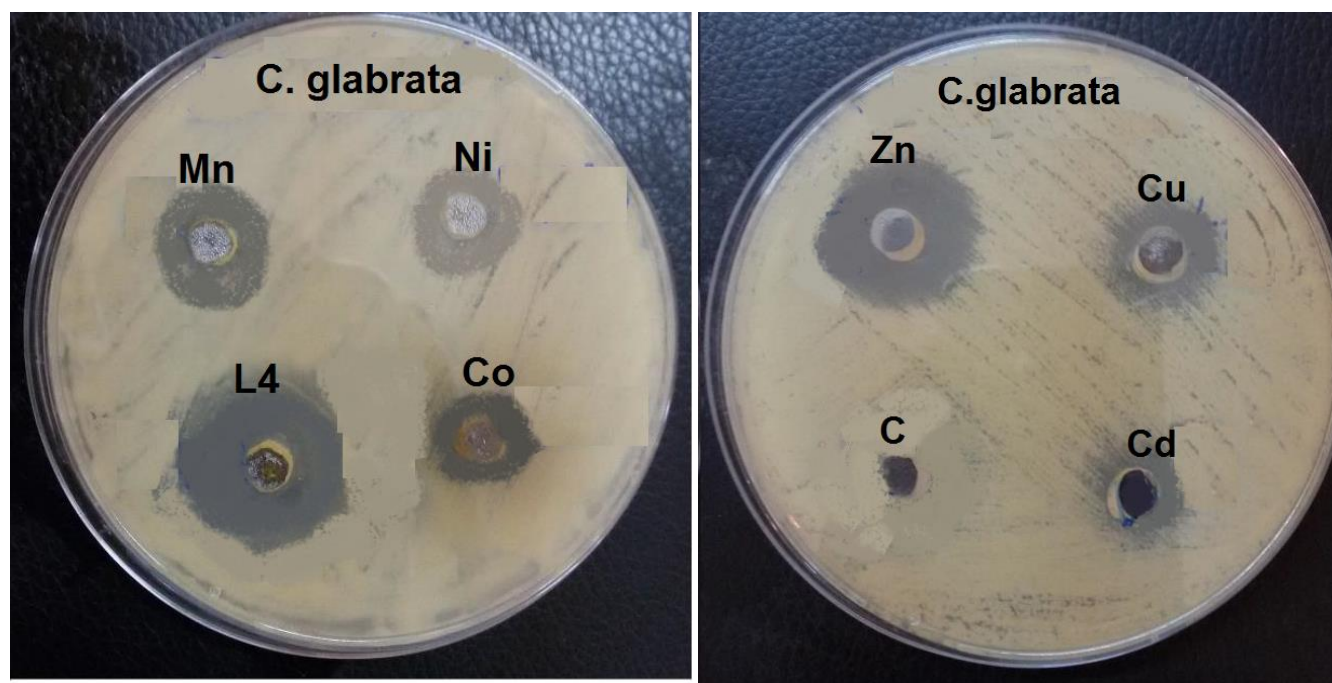
Figure (4.38): The influence of HL^4 and its complexes on *Candida glabrata*.
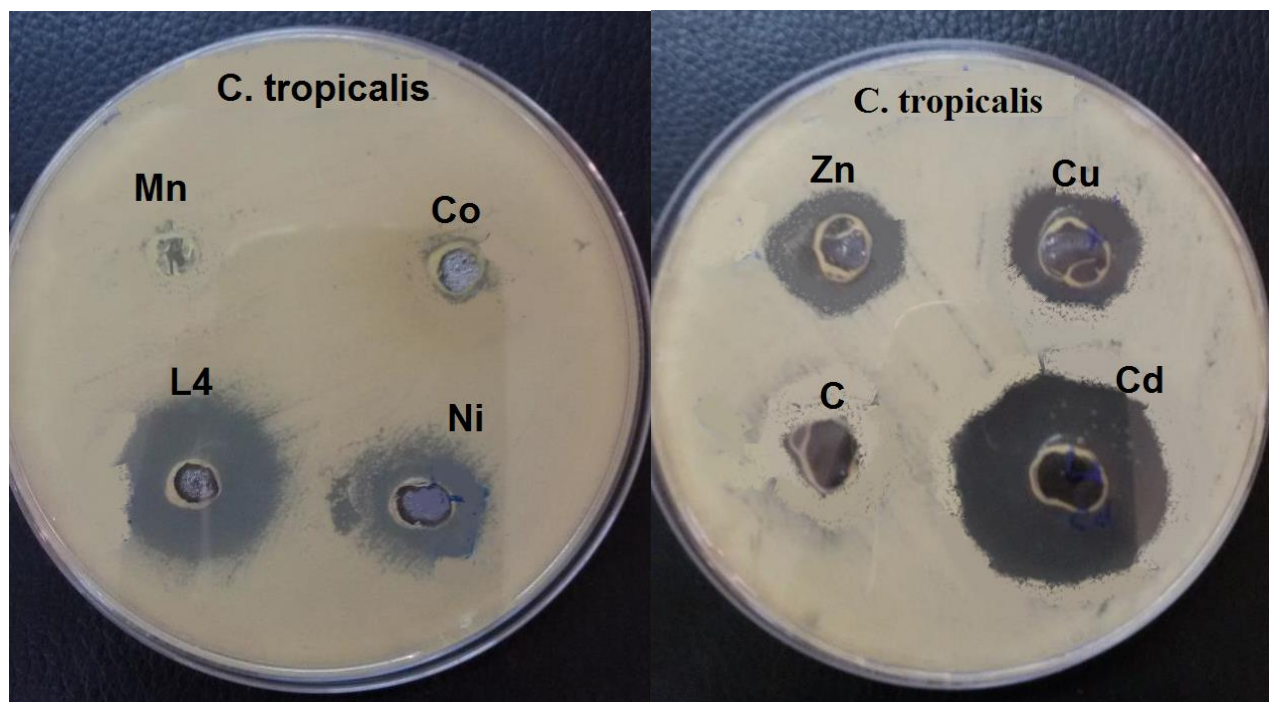
Figure (4.39): The influence of HL^4 and its complexes on *Candida tropicalis*.
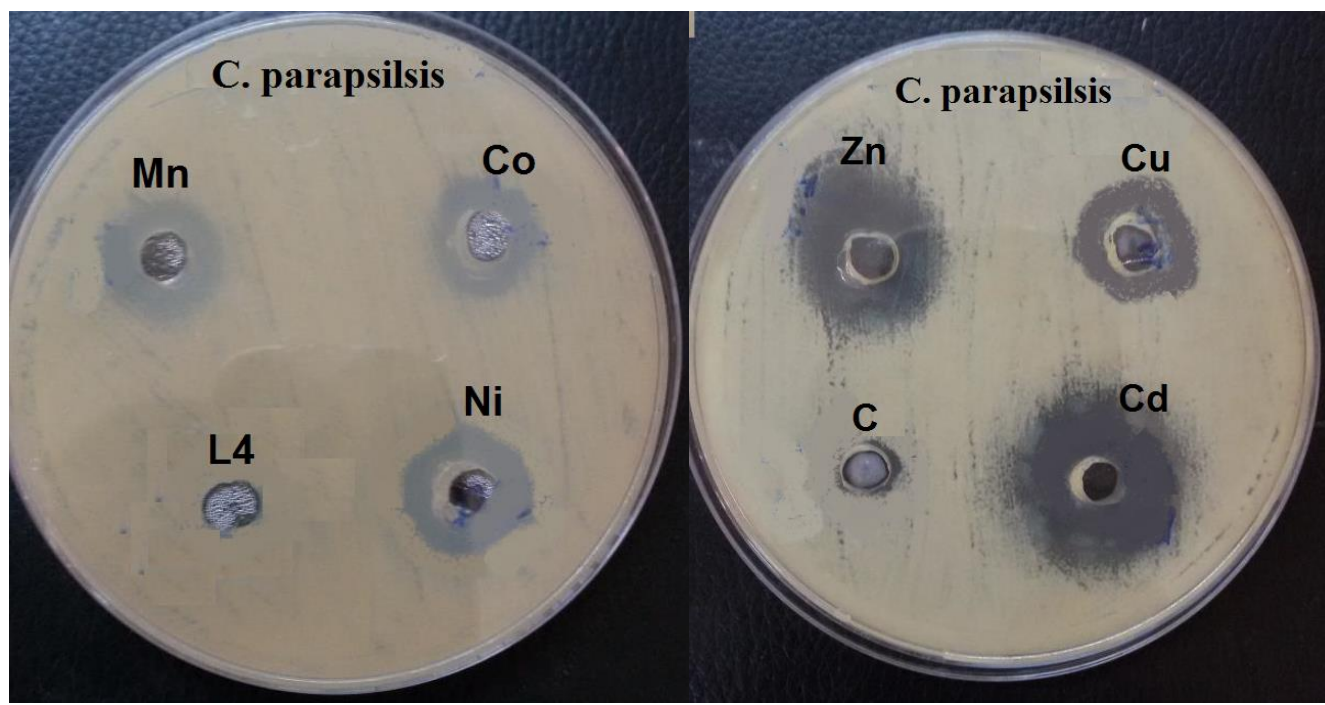
Figure (4.40): The influence of HL^4 and its complexes on *Candida parapsilsis*.
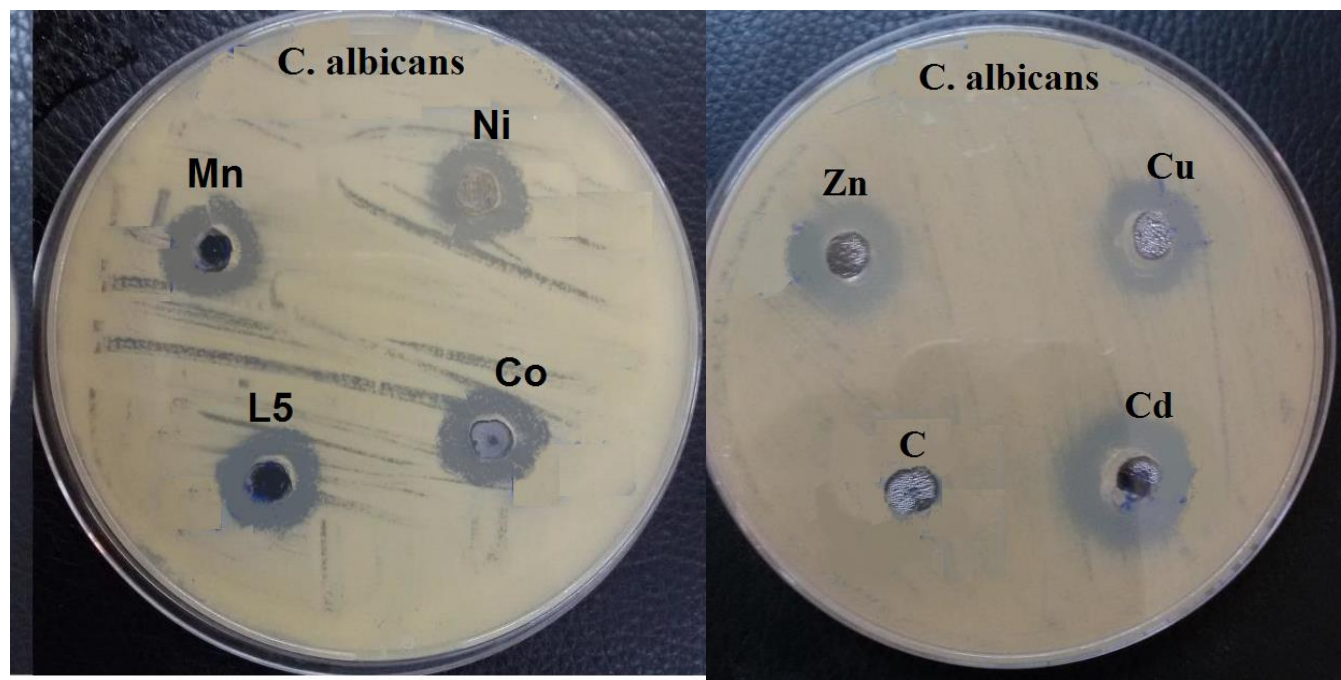
Figure (4.41): The influence of HL^5 and its complexes on *Candida albicans*.
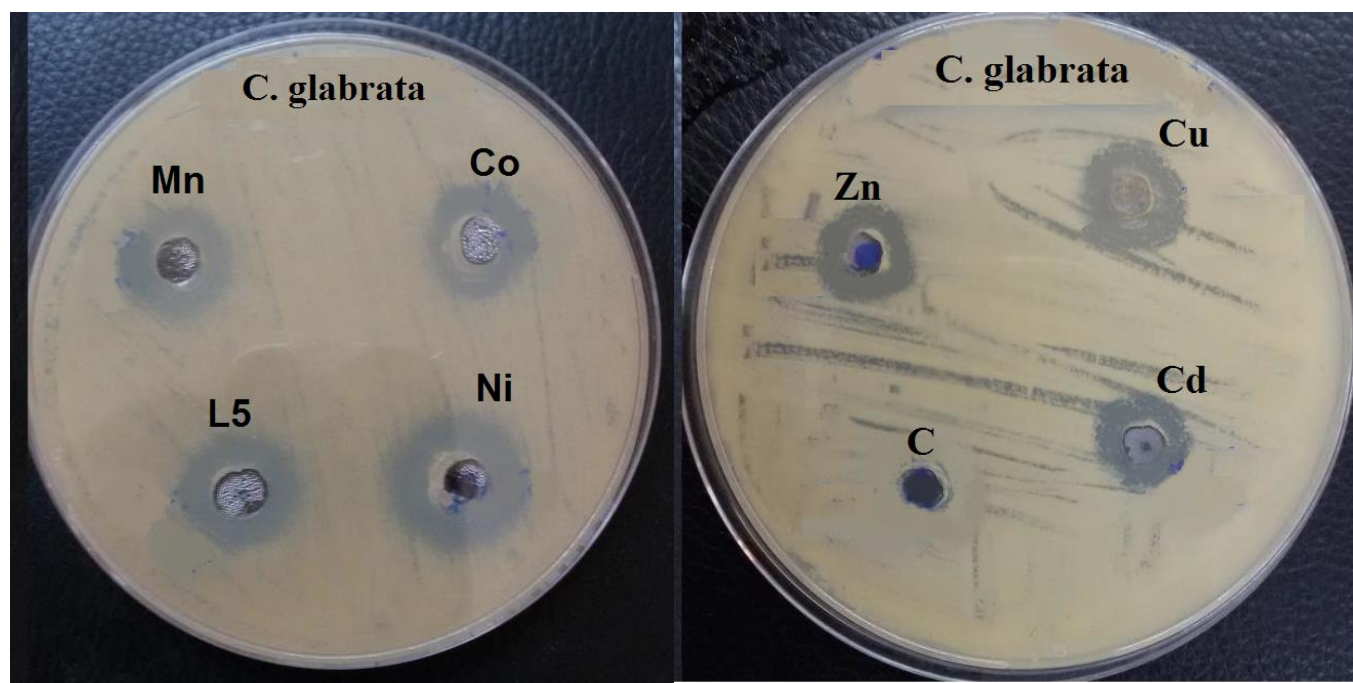
Figure (4.42): The influence of HL^5 and its complexes on *Candida glabrata*.
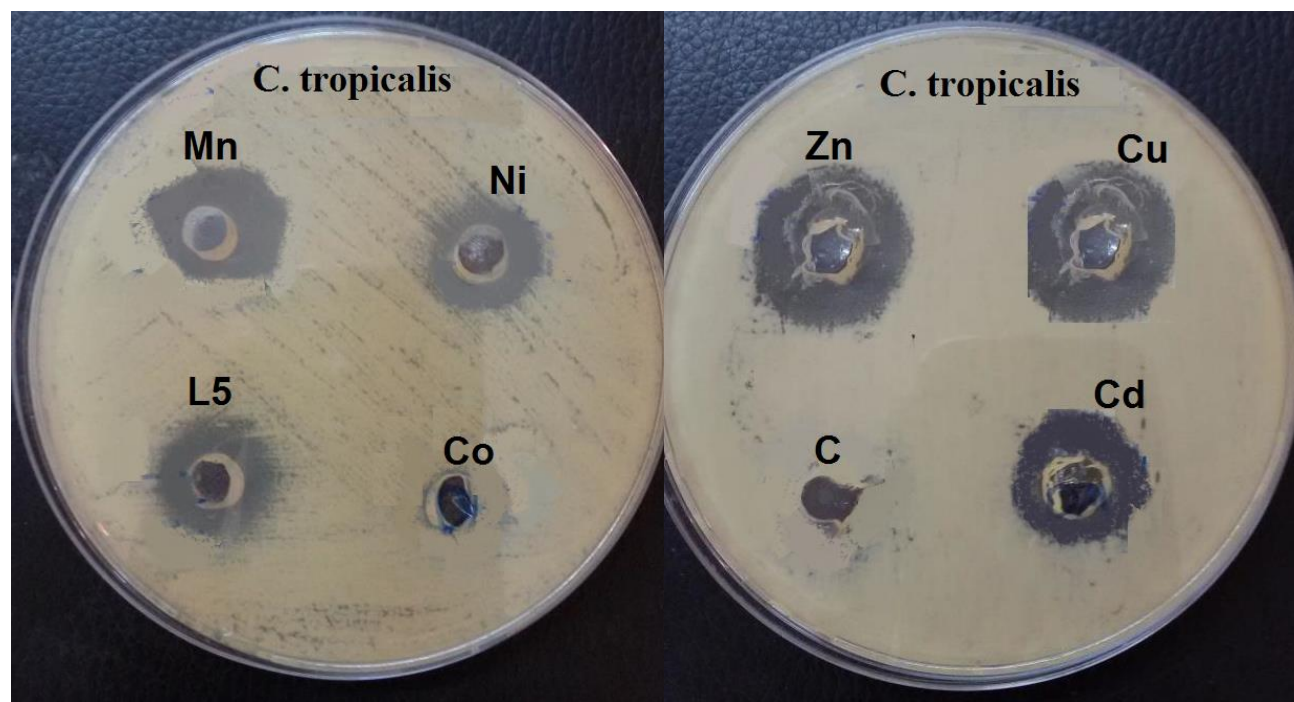
Figure (4.43): The influence of HL^5 and its complexes on *Candida tropicalis*.
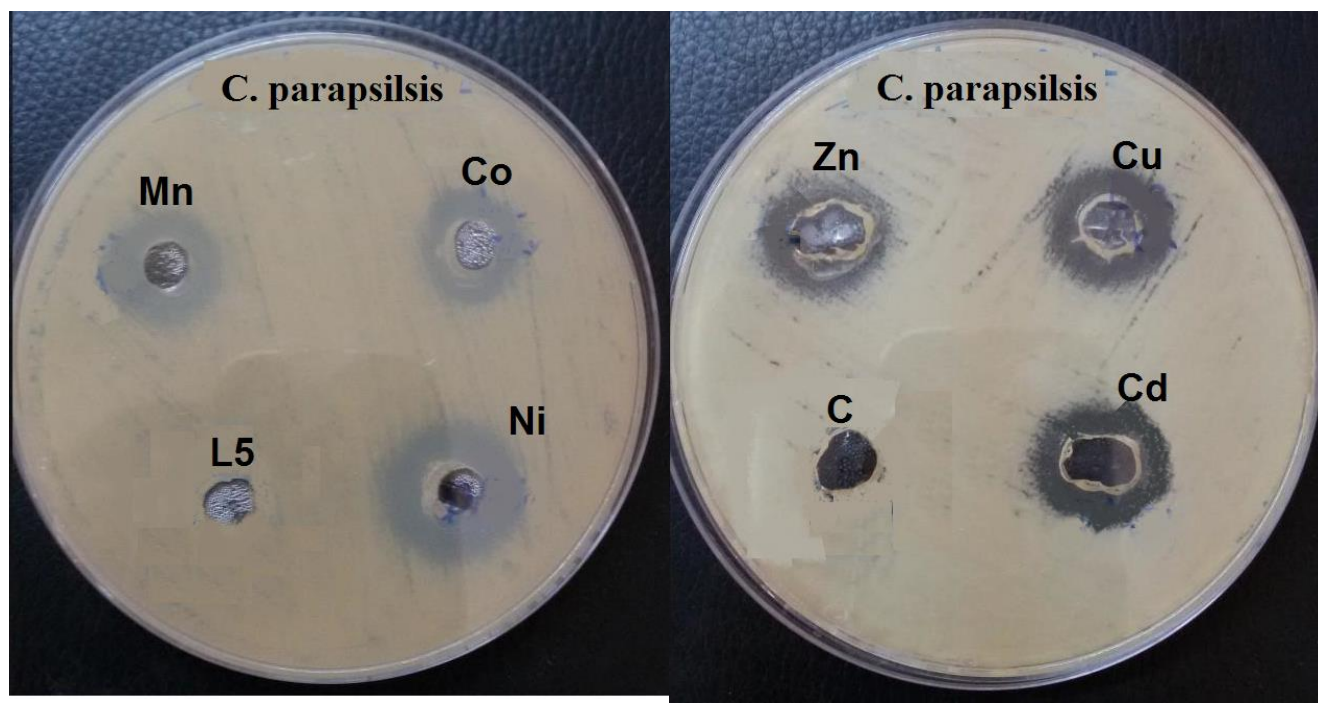
Figure (4.44): The influence of HL^5 and its complexes on *Candida parapsilsis*.
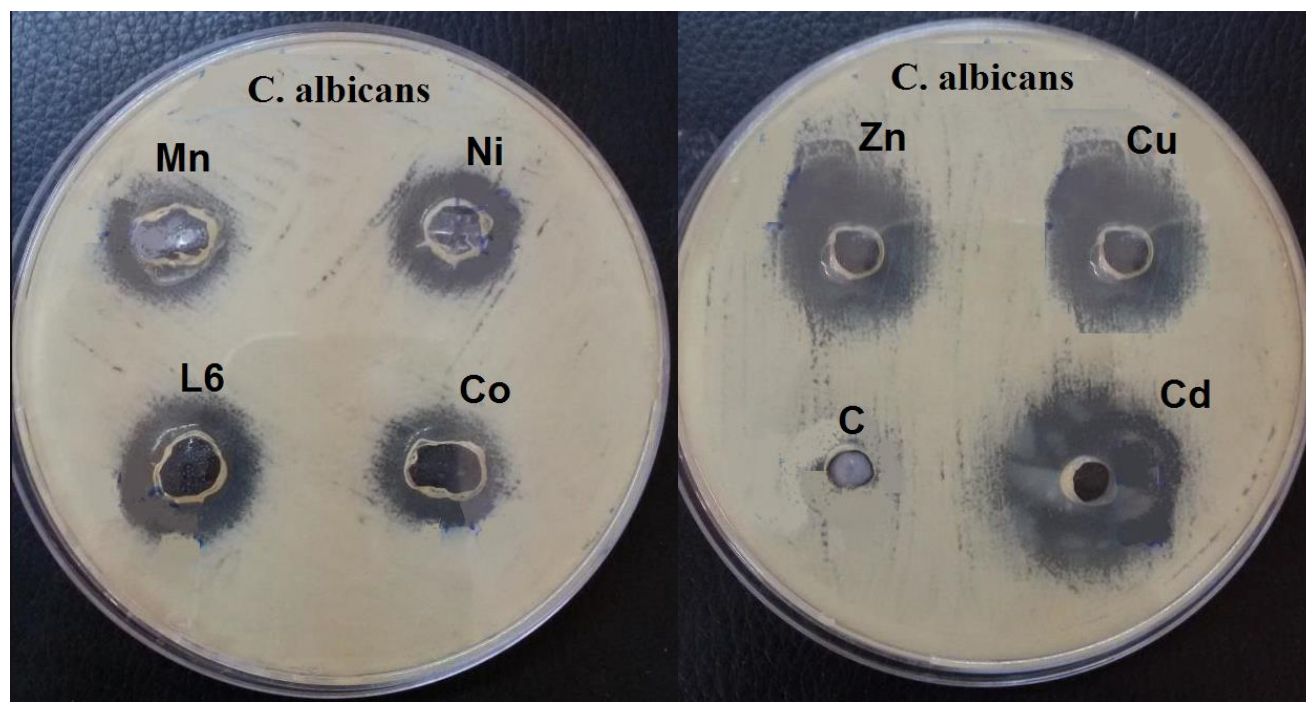
Figure (4.45): The influence of HL^6 and its complexes on *Candida albicans*.
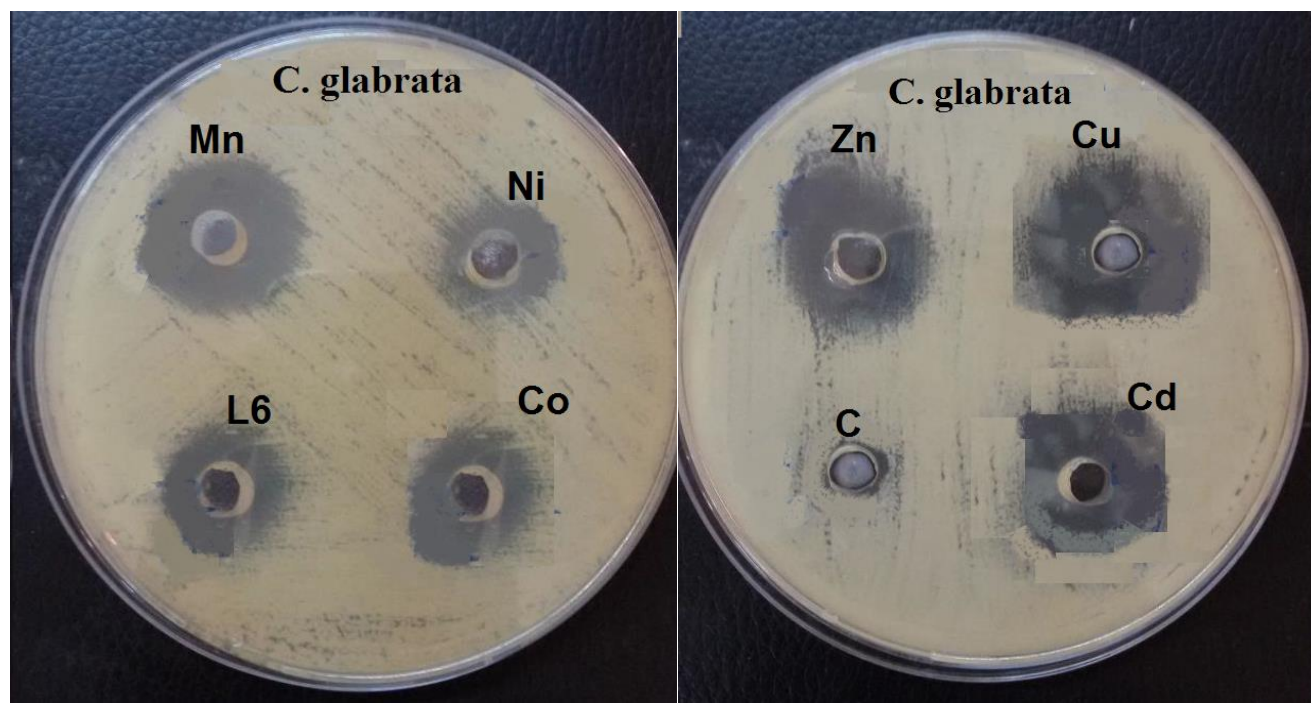
Figure (4.46): The influence of HL^6 and its complexes on *Candida glabrata*.
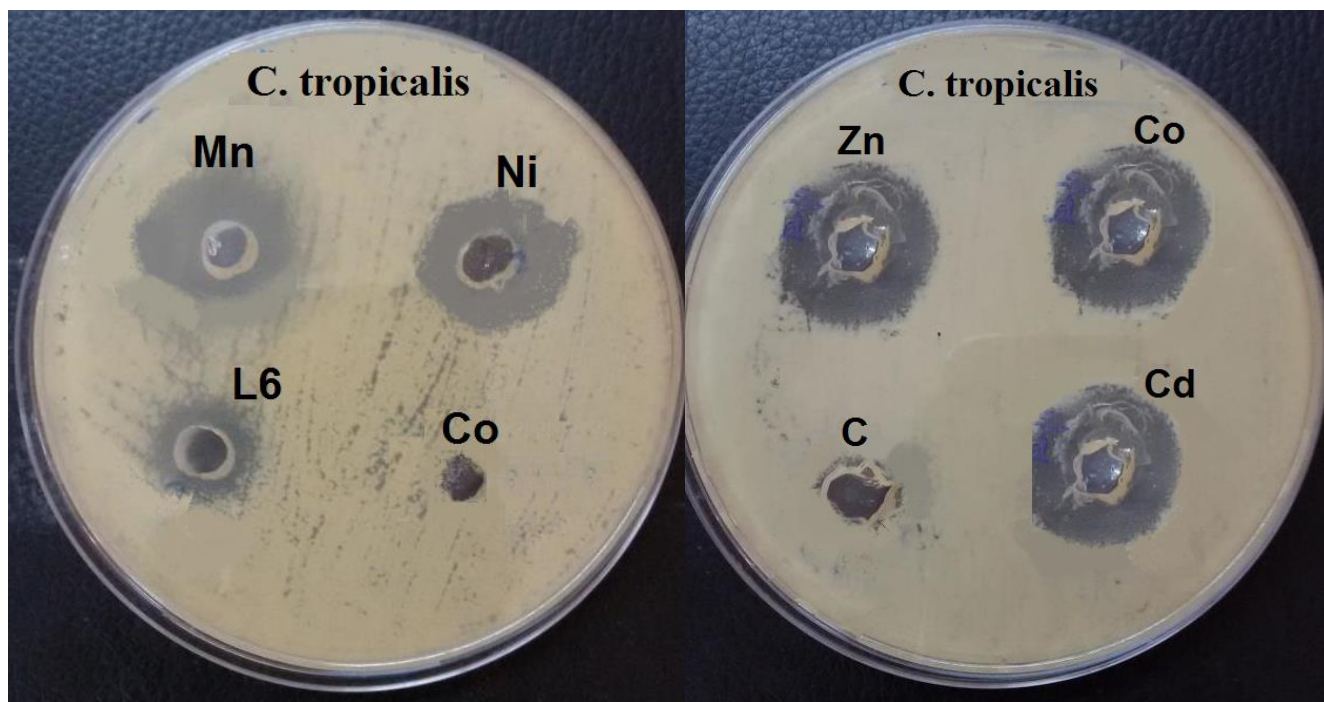
Figure (4.47): The influence of HL^6 and its complexes on *Candida tropicalis*.
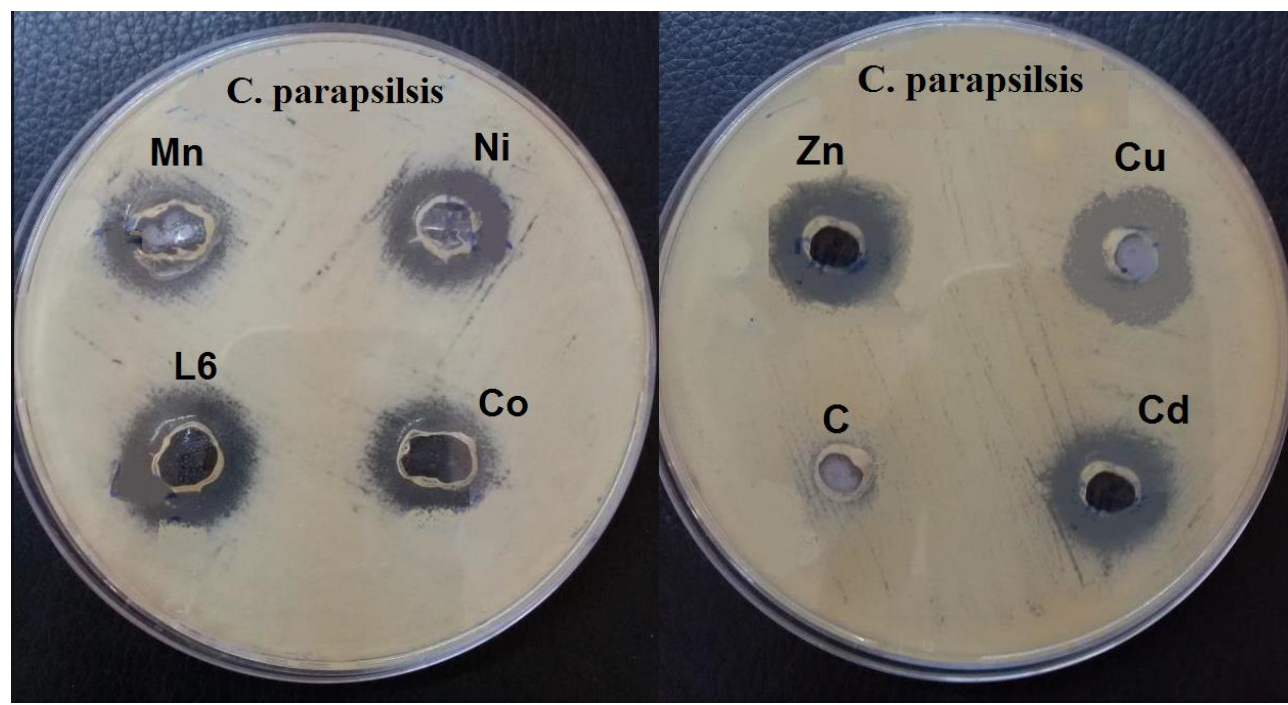
Figure (4.48): The influence of HL^6 and its complexes on *Candida parapsilsis*.

Table (4-2): Fungi activity of HL^1-HL^6 and their complexes.

Sample	*Candida albicans*	*Candida glabrata*	*Candida tropicalis*	*Candida parapsilsis*
HL^1	_	13	9	_
K$_2$[Mn(L^1)$_2$Cl$_2$]	15	13	_	_
K$_2$[Co(L^1)$_2$Cl$_2$]	14	18	_	_
K$_2$[Ni(L^1)$_2$Cl$_2$]	_	15	_	_
[Cu(L^1)$_2$]	19	8	15	_
[Zn(L^1)$_2$]	20	10	18	_
[Cd(L^1)$_2$]	_	13	17	_
HL^2	_	11	12	_
K$_2$[Mn(L^2)$_2$Cl$_2$]	13	19	_	11
K$_2$[Co(L^2)$_2$Cl$_2$]	17	20	_	16
K$_2$[Ni(L^2)$_2$Cl$_2$]	18	22	11	11
[Cu(L^2)$_2$]	16	23	12	9
[Zn(L^2)$_2$]	11	20	15	8
[Cd(L^2)$_2$]	10	21	_	10
HL^3	_	12	13	_
K$_2$[Mn(L^3)$_2$Cl$_2$]	11	15	11	13
K$_2$[Co(L^3)$_2$Cl$_2$]	10	16	_	12
K$_2$[Ni(L^3)$_2$Cl$_2$]	15	17	11	18
[Cu(L^3)$_2$]	13	9	_	12
[Zn(L^3)$_2$]	14	10	_	17
[Cd(L^3)$_2$]	11	13	_	11

Sample	*Candida albicans*	*Candida glabrata*	*Candida tropicalis*	*Candida parapsilsis*
HL^4	10	15	16	_
$K_2[Mn(L^4)_2Cl_2]$	17	10	_	10
$K_2[Co(L^4)_2Cl_2]$	16	9	_	11
$K_2[Ni(L^4)_2Cl_2]$	13	11	11	16
$[Cu(L^4)_2]$	15	12	12	17
$[Zn(L^4)_2]$	11	13	15	19
$[Cd(L^4)_2]$	_	11	17	20
HL^5	11	15	10	_
$K_2[Mn(L^5)_2Cl_2]$	12	16	11	9
$K_2[Co(L^5)_2Cl_2]$	13	17	_	11
$K_2[Ni(L^5)_2Cl_2]$	14	11	13	10
$[Cu(L^5)_2]$	16	10	18	12
$[Zn(L^5)_2]$	17	12	17	13
$[Cd(L^5)_2]$	11	11	16	15
HL^6	17	16	12	11
$K_2[Mn(L^6)_2Cl_2]$	13	17	11	9
$K_2[Co(L^6)_2Cl_2]$	19	18	-	8
$K_2[Ni(L^6)_2Cl_2]$	20	19	19	15
$[Cu(L^6)_2]$	22	20	20	14
$[Zn(L^6)_2]$	21	21	18	13
$[Cd(L^6)_2]$	20	11	17	11

(4.3) Prospective Studies

- Synthesis of a range of selenosemicarbazone ligands with different substituents and studying the impact of the substituent on the complexation nature of the metal ion.

- Studying complex formation of selenosemicarbazone ligands with other metal ions such as lanthanide and actinide ions.

- Investigating the role of selenosemicarbazone ligands against other types of microorganisms.

- Study the uses of selenosemicarbazone ligands and their complexes in the DNA binding approach.

- Studying the electrochemistry of the selenosemicarbazone ligands and their metal complexes.
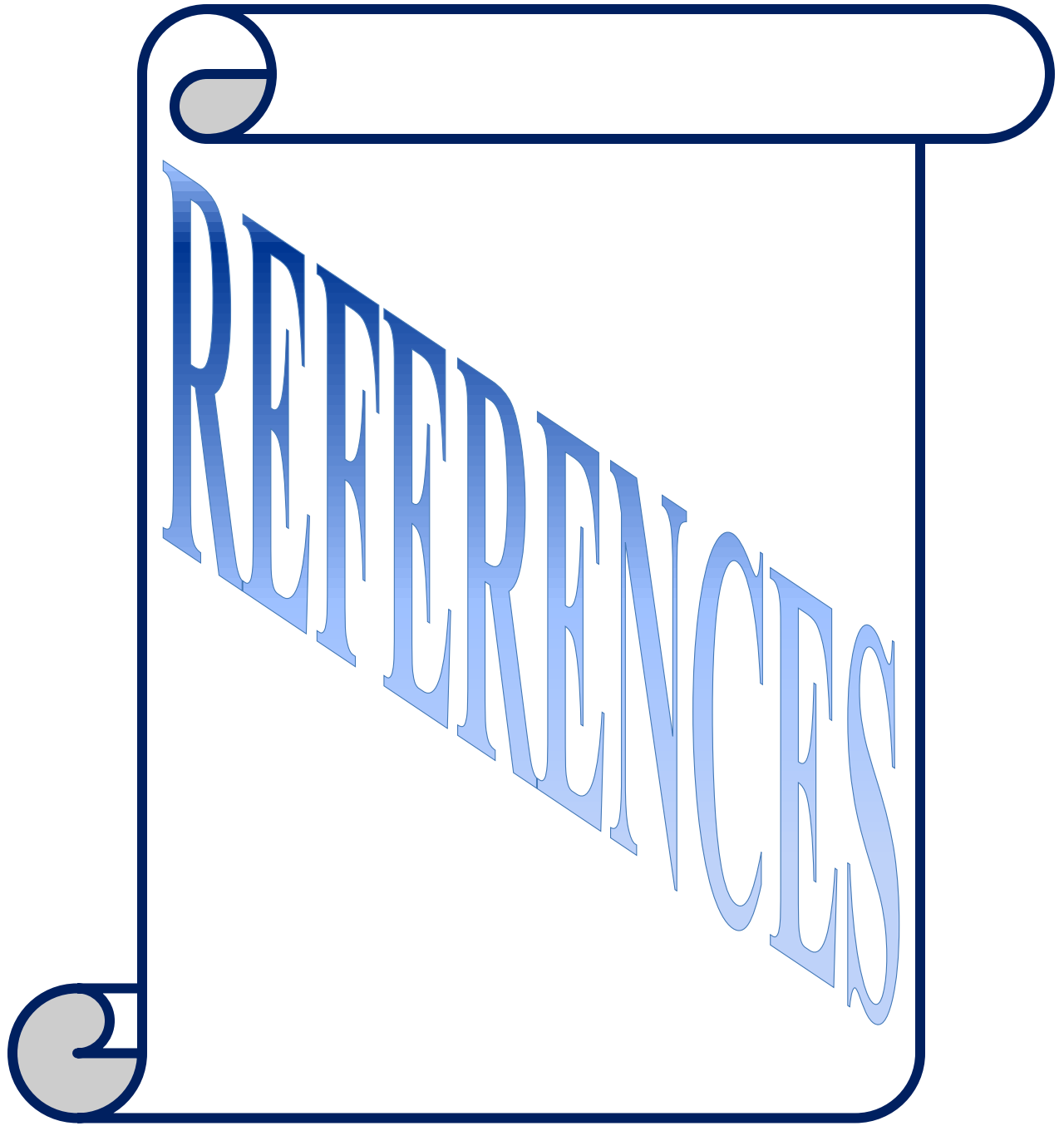
REFERENCES

REFERENCES

1. G. L. Sommen1, A. Linden, H. Heimgartner, "Selenium-Containing Heterocycles from Isoselenocyanates: Use of Hydrazine for the Synthesis of 1,3,4-Selenadiazine Derivatives", *Helvetica Chimica Acta*, **89**, 1322-1329, (2006).

2. V. Zaharia, A. Ignat, B. l. Ngameni, V. K. Marlyse, L. Moungang, C. N. Fokunang, M. Vasilescu, N. Palibroda, C. Cristea, L. S. Dumitrescu, B. T. Ngadjui, "Heterocycles 23: Synthesis, Characterization And Anticancer Activity Of New Hydrazinoselenazole Derivatives", *Med Chem Res*, **22**, 5670-5679, (2013).

3. T. R. Todorovic, A. Bacchi, N. O. Juranic, D. M. Sladic, G. Pelizzi, T. T. Bozˇic, N. R. Filipovic, K. K. elkovic, "Synthesis And Characterization Of Novel Cd(II), Zn(II) And Ni(II) Complexes With 2-Quinolinecarboxaldehyde Selenosemicarbazone. Crystal Structure Of Bis(2-Quinolinecarboxaldehyde Selenosemicarbazonato)Nickel(II)", *Polyhedron* **26,** 3428-3436, (2007).

4. H. Beraldo, "Semicarbazonas E Tiossemicarbazonas: O Amplo Perfil Farmacológico E Usos Clínicos", *Quim. Nova*, **27**, 3, 461-471, (2004).

5. I. R. Parrey, A. a. Hashmi, "Synthesis of Schiff Base Complexes of Mn(II) and Co(II) and their Catalytic Oxidation towards Olefins and Alcohols", *Canadian Chemical Transactions*, **3**, 1, 65-71, (2015).

6. D. Plano, E. Lizarraga, M. Font, J. A. Palop, C. Sanmartı´n, "Thermal Stability And Decomposition Of Sulphur And Selenium Compounds", *J Therm Anal Calorim* **98**, 559-566, (2009).

7. Javier Fernández-Lodeiro, Marcos Felipe Pinatto-Botelho, Antônio A. Soares-Paulino, Augusto Cesar Gonçalves, Bruno A. Sousa, Cleverson Princival, Alcindo A. Dos Santos, "Synthesis and Biological Properties of Selenium- and Tellurium containing Dyes", *Dyes and Pigments*, **14**, 143-7208, (2014).

8. H. Lu, R. Wu, H. Cheng, S. Nie, Y. Tang, Y. Gao, Z. Luo, "An Efficient And Mild One-Pot Three-Component Mannich Reaction Catalyzed By $(C_4H_{12}N_2)_2[Bicl_6]Cl.H_2O$ In Neat", *Synthesis*, **10**, 1-29, (2015).

9. V. C. Mannich, W. Krösche, "Ueber ein Kondensationsprodukt aus Formaldehyd, Ammoniak und Antipyrin", *Losckann Chem-Ztg*, **14**, 1408, (1890).

REFERENCES

10. C. Mannich, W. Krösche, "Ueber ein Kondensationsprodukt aus Formaldehyd, Ammoniak und Antipyrin", *Archiv der Pharmazie (in German)*. **250**, (1), 647-667, (1912).

11. Blicke, F. F. "The Mannich Reaction", Organic Reactions. **1**, (10), 303-341, (2011).

12. P. Bippus, A. Molter, D. Müller, F. Mohr, "Cyclohexanone Selenosemicarbazone: Aconvenient Starting Material For The Preparation Of Functionalized Selenosemicarbazones And Their Pt And Pd Complexes", *J. of Organometallic Chemistry*, **695**, 1657-1662, (2010).

13. C. Pizzo, P. F. Tello, G. Yaluff, E. Serna, S. Torres, N. Vera, C. Saiz, C. Robello, G. Mahler, "New Approach Towards The Synthesis Of Selenosemicarbazones, Useful Compounds For Chagas' Disease", *European Journal of Medicinal Chemistry*, **109**, 107-113, (2016).

14. A. Molter, J. Rust, C. W. Lehmann, F. Mohra, "Synthesis And Structural Studies Of Some Selenoureas And Their Metal Complexes", *ARKIVOC*, (**vi**), 10-17, (2011).

15. K. Z. Łaᵎczkowski, K. Motylewska, A. B. Łaᵎczkowska, A. Biernasiuk, K. Misiura, A. Malm, B. Fernandez, "Synthesis, Antimicrobial Evaluation And Theoretical Prediction Of NMR Chemical Shifts Of Thiazole And Selenazole Derivatives With High Antifungal Activity Against Candida Spp", *J. of Molecular Structure*, **1108**, 427-437, (2016).

16. I. Yavari1, S. Mosaferi, "A One-Pot Synthesis Of 2H-Pyrido[1,2-A][1,3,5]Triazine-2-Selenones From Acyl Isoselenocyanates And Pyridin-2-Amine", *Monatsh Chem.*, **148**, 963-966, (2017).

17. A. Ilie, O. Crespo, M. C. Gimeno, M. C. Holthausen, A. Laguna, M. Diefenbach, C. Silvestru, "(N,Se) And (Se,N,Se) Ligands Based On Carborane And Pyridine Fragments-Reactivity Of $2,6-[(1'-Me-1',2'-Closo-C_2B_{10}H_{10})Sech_2]_2C_5H_3N$ Towards Copper And Silver", *Eur. J. Inorg. Chem.*, 2643-2652, (2017).

18. A. A. Jadhav, V. P. Dhanwe, P. G. Joshi, P. K. Khanna, "An Efficient Solventless Synthesis Of Cycloalkeno-1,2,3-Selenadiazoles, Their Antimicrobial Studies, And Comparison With Parent Semicarbazones", *Chemistry of Heterocyclic Compounds*, **51**, (1), 102-106, (2015).

19. D. R. Garud, M. Koketsu, H. Ishihara, "Isoselenocyanates: A Powerful Tool For The Synthesis Of Selenium-Containing Heterocycles", *Molecules*, **12**, 504-535, (2007).

20. R. A. Popa, A. Silvestru, A. Pop, "Silver(I) Complexes Of A New Multidentate Macrocyclic Ligand With N/S/Se Donor Atoms", *Polyhedron*, **110**, 197-202, (2016).

21. S. K. Tripathi, B. L. Khandelwal, S. K. Gupta, "A New Family Of Chalcogen Bearing Macrocycles: Synthesis And Characterization Of $N_4O_2E_2$ (E= Se,Te) Type Compounds", *Phosphorus, Sulfur and Silicon*, **177**, 2285-2293, (2002).

22. D. Dekanski, T. Todorović, D. Mitić, N. Filipović, N. Polović, K. Anđelković, "High Antioxidative Potential And Low Toxic Effects Of Selenosemicarbazone Metal Complexes", *J. Serb. Chem. Soc,* **78**, (10), 1503-1512, (2013).

23. A. Pop, R. Mitea, A. Silvestru, "Diorganochalcogen(II) Ligands Of Type $[R_2C(OH)CH_2](2-Me_2NCH_2C_6H_4)$ E (E ¼ S, Se, Te; R ¼ Me, Ph), And Their Silver(I) Complexes", *J. of Organometallic Chemistry*, **768**, 121-127, (2014).

24. A. K. Asatkar, M. Tripathi, S. Panda, R. Pande, S. S. Zade, "Cu(I) Complexes Of Bis(Methyl)(Thia/Selena) Salen Ligands: Synthesis, Characterization, Redox Behavior And DNA Binding Studies", *Spectrochimica Acta Part A: Molecular and Biomolecular Spectroscopy,* **171**, 18-24, (2017).

25. M. Koketsu, Y. Yamamura, H. Aoki, H. Ishihara, "The Preparation Of Acylselenourea And Selenocarbamate Using Isoselenocyanate"' *Phosphorus, Sulfur, and Silicon,* **181**, 2699-2708, (2006).

26. A. Pöllnitz, A. Rotar, A. Silvestru, C. Silvestru, M. Kulcsar, "Group 12 Metal Aryl Selenolates. Crystal And Molecular Structure Of [2-(Et2NCH2)C6H4]2Se2 And $[2-(Me_2NCH_2)C_6H_4Se]2M$ (M¼ Zn, Cd)", *J. of Organometallic Chemistry*, **695**, 2486-2492, (2010).

27. S. Bjelogrlić, T. Todorović, A. Bacchi, M. Zec, D. Sladić, T. Srdić-Rajić, D. Radanović, S. Radulović, G. Pelizzi, K. Anđelković, "Synthesis, Structure And Characterization Of Novel Cd(II) And Zn(II) Complexes With The Condensation Product Of 2-Formylpyridine And Selenosemicarbazide Antiproliferative Activity Of The Synthesized Complexes And Related Selenosemicarbazone Complexes", *J. of Inorganic Biochemistry*, **104**, 673-682, (2010).

28. N. Filipovic, N. Polovic, B. Rasˇkovic, S. Misirlic´-Dencˇic, M. Dulovic, M. Savic, M. Niksˇic, D. Mitic, K. Andelkovic, T. Todorovic, "Biological Activity Of Two Isomeric N-Heteroaromatic Selenosemicarbazones And Their Metal Complexes", *Monatsh Chem.* **145**, 1089-1099, (2014).

29. P. K. Atanassov, Y. Zhou, A. Linden, H. Heimgartner, "Synthesis Of Bis(2,4-Diarylimidazol-5-Yl) Diselenides From N-Benzylbenzimidoyl Isoselenocyanates", *HELVECA CHIMICA*, **85**, 1102-1117, (2002).

30. T. R. Todorovic, A. Bacchi, G. Pelizzi , N. O. Juranic, D. M. Sladic, I. D. Brcˇeski, K. K. Andelkovic, "Synthesis And Characterization Of Zn(II) And Cd(II) Complexes With 2,6-Diacetylpyridine-Bis(Selenosemicarbazone). Crystal Structure Of A Ni(II) Complex With A Modified 2,6-Diacetylpyridine-Bis(Selenosemicarbazone)", *Inorganic Chemistry Communications,* **9**, 862-865, (2006).

31. D. L. Klayman, J. P. Scovill, J. F. Bartosevich, J. Bruce, "2-Acetylpyridine Thiosemicarbazones. 5.1-[L-(2-Pyridyl)Ethyl]-3-Thiosemicarbazideass Potential Antimalarial Agents1,2", *J. Med. Chem.*, **26**, 35-39, (1983).

32. M. Zhou, S. Ji, Z. Wu, Y. Li, W. Zheng, H. Zhou,T. Chen, "Synthesis Of Selenazolopyridine Derivatives With Capability To Induce Apoptosis In Human Breast Carcinoma MCF-7 Cells Through Scavenge Of Intracellular ROS", *European Journal of Medicinal Chemistry*, **96**, 92-97, (2015).

33. M. Alsharif, MD, S. E. H. Cameron, MD, J. H. Young, MD, K. Savik, MS, J. C. Henriksen, H. E. Gulbahce, MD, S. E. Pambuccian, MD, "Time Trends In Fungal Infections As A Cause Of Death In Hematopoietic Stem Cell Transplant Recipients", *Am. J. Clin. Pathol.*, **132**, 746-755, (2009).

34. M.A. Pfaller, R.N. Jones, G.V. Doern, A.C. Fluit, J. Verhoef, H.S. Sader, S.A. Messer, A. Houston, S. Coffman, R.J. Hollis, "International Surveillance Of Blood Stream Infections Due To Candida Species In The European SENTRY Program: Species Distribution And Antifungal Susceptibility Including The Investigational Triazole And Echinocandin Agents", *DIAGN MICROBIOL INFECT DIS,* **35**, 19-25, (1999).

35. T. J. Walsh, A. Groll, J. Hiemenz, R. Fleming, E. Roilides, E. Anaissie, "Infections Due To Emerging And Uncommon Medically Important Fungal Pathogens", *European Society of Clinical Microbiology and Infectious Diseases, CMI*, **10**, 48-66, (2004).

36. P. C. Srivastava, R. K. Robins, "Synthesis And Antitumor Activity Of 2-*B*-D-Ribofuranosylselenazole-4-Carboxamide And Related Derivatives", *Journal of Medicinal Chemistry*, **26**, 3, 445-448, (1983).

37. R. A. Hussaina, A. Badshash, M. Sohailb, B. Lala, A. A. Altaf. "Synthesis, Chemical Characterization, DNA Interaction And Antioxidant Studies Of Ortho, Meta And Para Fluoro Substituted Ferrocene Incorporated Selenoureas", *Inorganica Chimica Acta.*, **13**, 1-28, (2013).

38. G. Mugesh, W. du Mont, H. Sies, "Chemistry of Biologically Important Synthetic Organoselenium Compounds", *Chem. Rev.*, **101**, 2125-2179, (2001).

39. M. Al-Smadi, S. Ratrout, "New 1,2,3-Selenadiazole and 1,2,3-Thiadiazole Derivatives", *Molecules*, **9**, 957-967, (2004).

40. S. R. TURK, C. SHIPMAN, JR, J. C. DRACH, "Structure-Activity Relationships among at-(N)-Heterocyelic Acyi Thiosemicarbazones and Related Compounds as lnhibitors of Herpes Simplex Virus Type 1-specified Ribonueleoside Diphosphate Reductase", *J. gen. Virol.* **67**, 1625-1632, (1986).

41. D. X. West, S. B. Padhye, P. B. Sonawane, "Structural and Physical Correlations in the Biological Properties of Transition Metal Heterocyclic Thiosemicarbazone and S-alkyldithiocarbazate Complexes", *Structure and Bonding*, **76**, 1-50, (1991).

42. T. SR, S. C. Jr, D. JC., "Structure-activity relationships among alpha-(N)-heterocyclic acyl thiosemicarbazones and related compounds as inhibitors of herpes simplex virus type 1-specified ribonucleoside diphosphate reductase", *J Gen Virol.* **67** (Pt 8):1625-32, (1986).

43. G. Mugesh, H. B. Singh, "Synthetic Organoselenium Compounds As Antioxidants: Glutathione Peroxidase Activity", *Chem. Soc. Rev.*, **29**, 347-357, (2000).

44. A. J. Mukherjee, S. S. Zade, H. B. Singh, R. B. Sunoj, "Organoselenium Chemistry: Role of Intramolecular Interactions", *Chem. Rev.*, **110**, 4357-4416, (2010).

45. A. Kumar, G. K. Rao, F. Saleem, A. K. Singh, "Organoselenium Ligands In Catalysis", *Dalton Trans.*, **41**, 11949-11977, (2012).

46. M. Schuster, K.H. Konig, "Zur Chromatographic von Metallchelaten XVII. Diinnschicht-Chromatographie yon N,N-Dialkyl-N'benzoylselenoharnstoff-Chelaten", *Fresenius Z Anal Chem.*, **327**, 102-104, (1987).

47. M. Schuster, K.H. Konig, "Zur Chromatographic von Metallchelaten XVIII*.liir Einflufl der Koordinationsstellen auf die chromatographischen Eigenschaften von N,N-Dialkyl-N'-benzoylharnstoff-Chelaten", *Fresenius Z. Anal. Chem*. **331**, 383-386, (1988).

48. H. R. El-Ramady, É. D. Szabolcsy, T. A. Shalaby, J. Prokisch, M. Fári, "Selenium in Agriculture: Water, Air, Soil, Plants, Food, Animals and Nanoselenium", *Environmental Chemistry for a Sustainable World*, **5,** 155-232, (2015).

49. D. L. Klayman, W. H. H. Gunther, "Organic Selenium Compounds: Their Chemistry and Biology", *Wiley-Interscience, New York*, **2**, 1188, (1973).

50. G. R. Waitkins and R. Schutt, "Inorganic Syntheses", *New York: Wiley*, **2**, 186 (1946).

51. N. Sampath, S. M. Malathy Sony, M. N. Ponnuswamy and M. Nethaji, "Crystal structure of 2,6- diphenyl azabicyclo [3.3.1] nonan9-one thiosemicarbazone", *Cryst. Res. Technol.,* **39**, 9, 821-826, (2004).

52. P. Kulkarni, B. Totawar, P. K. Zubaidha, "An efficient synthesis of b-aminoketone compounds through three-component Mannich reaction catalyzed by calcium chloride", *Monatsh Chem* 143:625-629, (2012).

53. M. J. Al-Jeboori, M. S. Al-Fahdawi and A. A. Sameh, "New homoleptic metal complexes of Schiff bases derived from 2,4-di-ptolyl-3-azabicyclo[3.3.1]nonan-9-one", *J. Coord. Chem.,* **62**, 3853-3863, (2009).

54. R. M. Silverstein, G. C. Basslev, T. C. Morrill, "Spectromeric Identification of Organic Compound", *4th Edn., John Wiley and Sons. New York,* P. **172**, (1981).

55. A. G. Sykes, G. Wilkinson, R. D. Gillard, McCleverty J. A., Eds, "Comprehensive Coordination Chemistry", *Pergamon Press: Oxford, UK.,* 229, (1987).

56. I. D. Br_ceski, V. M. Leovac, G. A. Bogdanovi, S. Sovilj, M Revenco, "Synthesis, physicochemical properties and crystal structure of isothiocianato [2-(diphenylphosphino)benzaldehyde selenosemicarbazonato(1)] nickel(II)", *Inorganic Chemistry Communications*, **7,** 253-256, (2004).

57. T. Kano, S. Song, Y. Kubota and K. Maruka, "Highly diastereo- and enantioselective mannich reactions of synthetically flexible ketimines with secondary amine organocatalysts", *Ang. Chem. Int. Ed.,* **51**, 5, 1191-1194, (2012).

58. T. Kano, S. Song and K. Maruoka, "Molecular recognation ketomalonates by asymmetric aldol reaction of aldehydes with secondery amine organocatalysts", *Chem. Commun,* **48**, 56, 7037-7039, (2012).

59. J. Li-li, L. Yun-tao, "One-pot Three-component Mannich Reaction Catalyzed by 2-Hydroxylpyridine", *Chem. Res. Chin. Univ.*, **29,** (4), 710-713, (2013).

60. V. Orescanin, L. Mikelic, V. Roje and S. Lulic, "Determination of lanthanides by source excited energy dispersive X-ray fluorescence (EDXRF) method after preconcentration with ammonium pyrrolidine dithiocarbamate (APDC)", *Anal. Chim. Acta.,* **570**, 2, 277-282, (2006).

61. T. R. N. Jowit, and P. C. H. Mitchell, "Complexes of molybdenum(VI) and molybdenum(V) with dithiocarbamate, dithiocarbonate, and phosphorothiolothionate", *J. Chem. Soc.* part A, 1702-1708, (1970).

62. L. Ronconi, L. Giovagnini, C. Marzono, F. Bettio, R. Graziani, G. Pilloni and D. Fregona, "Gold dithiocarbamate derivatives as potential antineoplastic agents:Design, spectroscopic properties, and in vitro antitumor activity", *Inorg. Chem.,* **44**, 6, 1867-1881, (2005).

63. K. Nakamoto, "Infrared Spectra of Inorganic and Coordination Compounds", *John Wiley and Sons, New York*, **4th** Edn., (1996).

64. W. A. Volkert, T. J. Hofman, "Therapeutic radiopharmaceuticals", *Chem. Rev.,* **99,** 2269, (1999).

65. Bal, S. S. Bal, "Cobalt(II) and Manganese(II) Complexes of Novel Schiff Bases, Synthesis, Charcterization, and Thermal, Antimicrobial, Electronic, and Catalytic Features", *Advances in Chem.*, **2014,** 12, (2014).

66. P. H. Smith, J. R. Morris, G. D. Ryan, "Prediction of q-values and conformations of gadolinium chelates for magnetic resonance imaging", *J. Am. Chem. Soc*.**, 111,** 7437, (1989).

67. K. J. Oberhausen, J. F. Richandon, R. M. Buchanan, "Century-Known Copper Salt Cu(OAc)(OMe) Proven To Be a Unique", *Inorg. Chem.*, **30,** 1357, (1991).

68. M. J. Al-Jeboori, A. J. Abdul-Ghani and A. J. Al-Karawi, "Synthesis and structural studies of new Mannich base ligands and their metal complexes", *Transition Met. Chem.,* **33**, 925–930, (2008).

69. T. R. Todorovic, A. Bacchi , D. M. Sladic, N M. Todorovic, T. T. Bozˇic,D. D. Radanovic, N. R. Filipovic, G. Pelizzi, K. K. Andelkovic, "Synthesis, characterization and biological activity evaluation of Pt(II), Pd(II),Co(III) and Ni(II) complexes with N-heteroaromatic selenosemicarbazones", Inorganica Chimica Acta 362, 3813-3820, (2009).

70. .J. Al-Jeboori, A. A. Ameer and N. A. Aboud, "Novel Pentadentate Ligand of N_3S_2 Donor Atoms and It's Complexes With (NiII, CoII, CuII, FeII, HgII, AgI and ReV)", J. Ibn Al-Haitham Pure Appl. Sci., **17**, 3, 80, (2004).

71. A. Z. El-Sonbati, A. S. Al-Shihri and A. A. El-Bindary, "Stereochemistry of new nitrogen containing heterocyclic aldehyde: Part XI. Novel ligational behaviour of quinoline as chelate ligand toward transition metal ions", Spectro chimica Acta Part A: Molecular and Biomolecular Spectroscopy, **60**, 1763–1768, (2004).

72. F. H. Al-Jeboori, PhD., "Novel Acyclic and Cyclic Polydentate Ligands Derived From 2,6- diformyl-4-methylphenol and Their Metal Complexes Synthesis and Physico-Chemical Studies"University of Baghdad, College of Education - Ibn-Al-Haitham,(2006).

73. B. K. Salman, Mc. "Synthesis and Characterisation of Novel Ligand Derived from (4-Benzaldehyde azo salicyladehyde) and its Metal Complexes", University of Baghdad, College of Education-Ibn-Al-Haitham, (2008).

74. N. S. Yousif, K. H. Hegab and A. E. Eid, "Synthesis and Coordinating Properties of New Chromone Thiosemicarbazones Towards Some Transition Metal Ions", Inorganic and nano- metal chemistry, **33**, 1647-1666, (2003).

75. R. M. Ahmad, PhD., "Synthesis, Characterisation and Theoretical Studies of Polymeric Chain-Assemblies of Transition Metal Complexes with Mixed Azido-Carboxylato Bridges", University of Baghdad, College of Education - Ibn-Al-Haitham, (2012).

76. A. B. P. Lever, "Inorganic Electronic Spectroscopy" 2nd Ed., New York, (1984).

77. A. J. Abdul-Gganiy, M. J.AL-jeboori and A. J. Al-karawi, "Synthesis and spectral studies of new N2S2 and N2O2 Mannich base ligands and their metal complexes", Journal of Coordination Chemistry, **62**, 16, 20 August, 2736–2744, (2009).

78. R. N. Jowitt, and P. C. H. Mitchell, "Complexes of molybdenum(VI) and molybdenum(V) with dithiocarbamate, dithio carbonate, and phosphorothiolothionate", J. Chem. Soc. part A, 1702-1708, (1970).

79. P. K. Pandey, A. N. Mishra, K. K.Ojha, and K. S. Rubish, "Phesco chemical studies of menganese(II), cobalt(II), Zinc(II), and copper(II) complexes derived from 2-substituted benzaldehyde thiosemi carbazones", *Indian J. Sci. Res.,* **3**, 1, 119-122, (2012).

80. T. H. Mawat, Mc, "Transition Metals Complexes with N, O and S Coordination Sphere; Spectroscopic and Structural Studies", *University of Baghdad, College of Education - Ibn-Al-Haitham*, (2016).

81. E. I. Yousif, H. A. Hasan, R. M. Ahmad, M. J. Al-Jeboori, "Formation of macrocyclic complexes with bis(dithiocarbamate) ligand; synthesis, spectral characterisation and bacterial activity" *Der Chemica Sinica*, 7, 2, 53-65, (2016).

82. T. H. Mawat, M.J. Al-Jeboori, "Phenoxo- and azido-bridged complexes with N_2OS_2 Schiff-base ligand; synthesis, spectral investigation and bacterial activity", *Chem Xpress*, **9**, 2, 156-171, (2016).

83. D. Evans, "A new type of megnetic balance", *J. phys. E; Sci. instrum.,***7**,4, 274, (1974).

84. O. Senqupta, B. Gole, S. Mukheriee and P. S. Mukheriee, "A series of transition metal–azido extended complexes with various anionic and neutral co-ligands: synthesis, structure and their distinct magnetic behavio", *Dalton Trans.,* **39**, 32, 7451-7465, (2010).

85. G. A. Bain and J. F. Berry, "Diamagnetic corrections and Pascal's constants", *J. Chemi. Educ.,* **85**, 4, 532, (2008).

86. Y. Ma, Y. Q. Wen, J. Y. Zhang, E. Q. Gao, C. M. Liu, "Structures and magnetism of azide- and carboxylate-bridged metal(II) systems derived from 1,2-bis(N-carboxymethyl-4-pyridinio)ethane", *Dalton Trans*., **39**, 1846-1854, (2010).

87. Z. Guo, G. Li, L. Zhou, S. Su, Y. Li, S. Dang, H. Zhang., "Magnetic Exchange Coupling in Actinide-Containing Molecules", *Inorg. Chem.*, **48**, 8069, (2009).

88. P. Albores, E. Rentschler, "A New Hexanuclear Iron-Selenium Nitrosyl Cluster: Primary Exploration of the Preparation Methods, Structure, and Spectroscopic and Electrochemical Properties", *Inorg. Chem*., **49**, 8953-8961, (2010).

89. E. Canpolat and M. Kaya, "Spectroscopic characterization of N,Nbis(2-{[(2,2-Dimethyl1,3Dioxolan4yl)Methyl]Amino}Ethyl)N',N'Dihydroxyethanediimidame and its complexes", *J. Coord. Chem.,* **31**, 7, 511-515, (2005).

90. W. J. Geary, "The use of conductivity measurements in organic solvents for thecharacterisation of coordination compound", *Russian J. Coord. Chem. Rev.,***7**, 81-122, (1971).

91. A. Rahman, M. Choudhary and W. Thomsen, "Bioassay Techniques For Drug Development", *Harwood Academic. Amsterdam. The Netherlands,* (2001).

92. R. V. Singh, R. Dwivedi, S. C. Joshi, "Synthetic, magnetic, spectral, antimicrobial and antifertility studies of dioxomolybdenum(VI) unsymmetrical imine complexes having a *N ∩ N* donor system", *Transition Met. Chem.*, **29**, (1), 70-74, (2004).

93. R. V. Singh, R. Dwivedi and S. C. Joshi, "Synthetic, magnetic, spectral, antimicrobial and antifertility studies of dioxomolybdenum(VI) unsymmetrical imine complexes having a N ∩↓ Ndonor system", *Trans .Met .Chemi,* **29**, 1,70–74, (2004).

94. B. G. Tweedy, "Plant extracts with metal ions as potential antimicrobial agents", *Phytopathology,* **55**, 910-914, (1964).

95. M. Balouiri. , M. Sadiki and S. *K.* Ibnsouda "Methods for in vitro evaluating antimicrobial activity: A review", *Journal of Pharmaceutical Analysis,* **6**, 71-79, (2016).
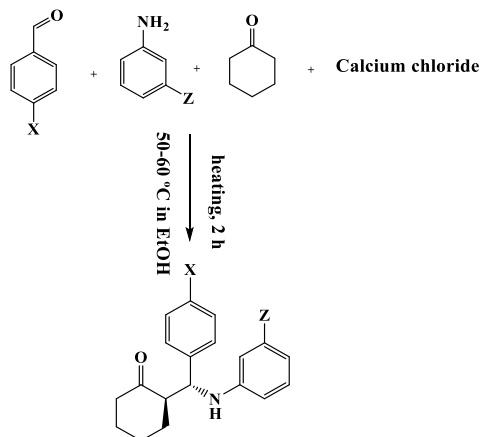
الخلاصة

تضمنت الاطروحة تحضير وتشخيص طيفي وفحص حراري والفعالية البايلوجية لستة ليكاندات لسيلينوسيميكاربزون الجديدة ومعقداتها الفلزية. اعتمد تحضير الليكاندات على المادة الأولية و المحضرة حسب تفاعل مانخ. الهدف من استخدام مركبات سيلينوسيميكاربزون يعود الى دورها المهم وتطبيقاتها في الكيمياء اللاعضوية و الطب وصناعة الادوية والكيمياء التحليلية والفعالية البايلوجية. كذلك بينت الادبيات هناك عدد محدود من النشريات تشمل هذا النوع من الليكاندات ومعقداتها، وهذا السبب شجعنا الى دراسة وتحضير هذه المركبات. علما بان هذه الاطروحة هي الاولى في العراق والتي تشمل تحضير ليكاندات سيلينوسيميكاربزون ومعقداتها الفلزية. تتالف الاطروحة من اربعة فصول وكما يلي:
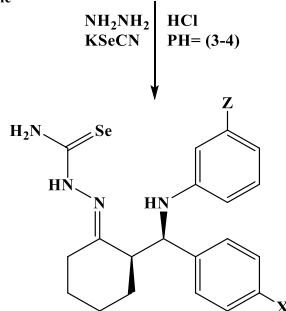
الفصل الاول تناول مقدمة عن تفاعلات مانخ وعرض المراجع والدراسات السابقة والتي غطت المرحلة الزمنية الخاصة بتحضير المعقدات الفلزية نوع N و Se كمراكز تناسق. حيث غطت الدراسات السابقة البحوث الخاصة بالليكاندات الحلقية وغير الحلقية الكبيرة ومعقداتها الفلزية. علاوة على ذلك اشتمل الفصل التطبيقات والاستخدامات لمركبات السلينيوم مع مصادرها مع تضمين الهدف من العمل.

الفصل الثاني تضمن الجزء العملي الذي شمل قائمة المواد المستعملة في هذا العمل، وكذلك التقنيات الكيمو- فيزياوية وطرق التحضير الخاصة بالمشتقات العضوية وليكاندات السيلينوسيميكاربزون ومعقداتها الفلزية. حضرت الليكاندات بخطوات متعددة حيث تم تقسيم الليكاندات الى مجموعتين اعتمادا على نوع المشتق الذي استخدم في تحضير الليكاند المطلوب. مشتقات المجموعة الأولى تضم ال F1, F2, F3 و التي تم الحصول عليها من تفاعل مانخ بخطوة واحدة من خلال التفاعل التكثيفي للبنزالديهايد، 4 ميثوكسي بنزيالديهايد و4،4 داي مثيل امينو بنزالديهايد مع سايكلوهكسانون وخلات الامونيوم بنسبة 2:1:1 مع استخدام الايثانول كوسط للتفاعل للحصول على مشتقات ال F1 F2, F3 على التوالي.

المجموعة الثانية شملت تحضير المشتقات N1, N2, N3 من خلال تفاعل مانخ بواسطة مزج كلوريد الكالسيوم والالديهايد مع امين اروماتي مع سايكلوهكسانون بنسبة 1:1:1:1 باستخدام الايثانول كوسط للتفاعل من خلال تفاعل البنزالديهايد وميتا-نايترو انيلين للمشتق N1 و 4 ميثوكسي بنزالديهايد وانيلين للمشتق N2 والمشتق N3 حضر بنفس طريقة تحضير المشتق N1 ولكن باستعمال 4؛4 داي مثيل امينو بنزالديهايد وميتا-نايترو انيلين. تم تحضير ليكاندات سيلينوسيميكاربزون الستة الجديدة من تفاعل المشتقات اعلاه مع KSeCN و NH_2NH_2 بنسبة 3:1:1: في مزيج CHCl$_3$:EtOH (1:3) كمذيب. تم تحضير ستة وثلاثون معقد جديد من تفاعل الليكاندات مع املاح الفلزات بنسبة 2:1 بوجود KOH كقاعدة في مزيج من الايثانول والكلوفورم بنسبة 1:3 (انظر المخطط).

Calcium chloride

heating, 2 h
50-60 °C in EtOH

X = 0, Z = NO₂, N1 = 2-(((3-nitrophenyl)amino)(phenyl)methyl)cyclohexan-1-one
X = OMe, Z = 0, N2 = 2-((4-methoxyphenyl)(phenylamino)methyl)cyclohexan-1-one
X = N(Me)₂, Z = NO₂, N3 = 2-((4-(dimethylamino)phenyl)((3-nitrophenyl)amino)methyl)cyclohexan-1-one

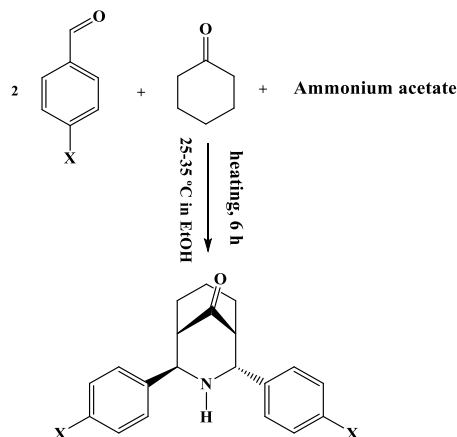NH₂NH₂ | HCl
KSeCN | PH= (3-4)

X = 0, Z = NO₂ (HL⁴)
X = OMe, Z = 0, (HL⁵)
X = N(Me)₂, Z = NO₂, (HL⁶)

+ MCl₂.b(H₂O)   KOH   EtOH/CHCl₃

R= 0, Y= NO₂ = HL⁴; R= OCH₃, Y= 0 = HL⁵; R= N(CH₃)₂, Y= NO₂ = HL⁶
M= Mn(II), Co(II), Ni(II); n= 2; X= Cl; Z= -2
M= Cu(II), Zn(II), Cd(II); n= 0; X= 0; Z= 0
b= Number of water molecules

2 + + Ammonium acetate

heating, 6 h
25-35 °C in EtOH

X = 0, F1 = 2,4-diphenyl-3-azabicyclo[3.3.1]nonan-9-one
X = OMe, F2 = 2,4-bis(4-methoxyphenyl)-3-azabicyclo[3.3.1]nonan-9-one
X = N(Me)₂, F3 = 2,4-bis(4-(dimethylamino)phenyl)-3-azabicyclo[3.3.1]nonan-9-one

NH₂NH₂ | HCl
KSeCN | PH= (3-4)

X = 0, (HL¹)
X = OMe, (HL²)
X = N(Me)₂, (HL³)

+ MCl₂.b(H₂O)   KOH   EtOH/CHCl₃

R= 0 = HL¹; R= OCH₃ = HL²; R= N(CH₃)₂ = HL³
M= Mn(II), Co(II), Ni(II); n= 2; X= Cl; Z= -2
M= Cu(II), Zn(II), Cd(II); n= 0; X= 0; Z= 0
b= Number of water molecules

مخطط يوضح تحضير الليكاندات الستة مع معقداتها الفلزية.

ب

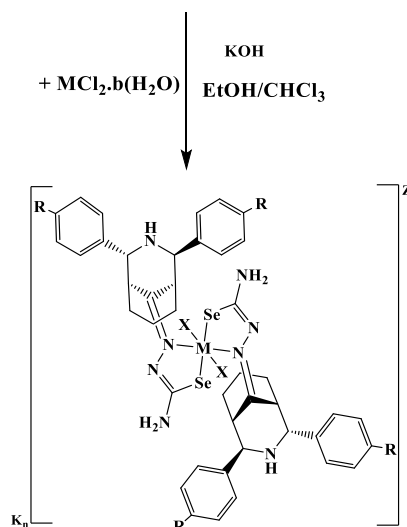تناول الفصل الثالث (النتائج والمناقشة) عرض وتحليل بيانات التحاليل الطيفية (الاشعة تحت الحمراء، الاشعة فوق البنفسجية، الرنين النووي المغناطيسي للبروتون والكاربون والسيلينيوم وطيف الكتلة) لتحديد البنية الكيميائية للمشتقات والليكاندات ومعقداتها الفلزية. كذلك اشتملت القياسات تقنيات التحليل الدقيق للعناصر (C.H.N)، الامتصاص الذري للعناصر الفلزية، التحليل الحراري، محتوى الكلور، التوصيلية المولارية، نقطة الانصهار والحساسية المغناطيسية.

اثبتت الازاحة الكيميائية لطيف الرنين النووي المغناطيسي للسيلينوم وجود ذرة السيلينوم في المركب العضوي بالنسبة لليكاندات ومعقداتها الفلزية. بالاضافة لظهور اشارة واحدة في طيف الليكاندات ومعقداتها الدايامغناطيسية مؤكدة نقاوتها من جهة ووجودها كايزومر واحد لليكاندات المرتبطة بالذرة المركزية. اثبتت نتائج طيف الكتلة للمشتقات و الليكاندات وبعض معقداتها الحصول على الوزن الجزيئي لهذه المركبات المحضرة. اكد طيف الاشعة تحت الحمراء ان الليكاندات هي ثنائية السن وترتبط بشكل انيون (1-) مع ذرة العنصر المركزية. تم استخدام التحليل الحراري لليكاندات وبعض معقداتها لدراسة الاستقرارية الحرارية لهذه المركبات في درجات حرارة مختلفة واسلوب التشظي.

تم استخدام طيف الاشعة فوق البنفسجية لبيان ترتيب الليكاندات حول العناصر الفلزية والشكل الفراغي المتوقع. بينت التوصيلية المولارية للمعقدات بانها تسلك سلوك الالكتروليتي بنسبة 2:1 وغير الالكتروليتي (متعادل).

تم استخدام برنامج 3D Chem 16 النظري لاثبات نوع التناسق والشكل الهندسي المفضل حول الذرة المركزية في المعقدات الفلزية وتم مقارنة هذه النتائج مع النتائج العملية التي تم حصول عليها من التشخيص والطرق التحليلية للمعقدات.

استنادا الى النتائج اعلاه فان نوع الارتباط والشكل الفراغي المقترح للمعقدات يكون كالاتي:

معقدات (Mn(II), Co(II), Ni(II مع الليكاندات (HL^1-HL^6) التي اظهرت تناسق سداسي والشكل هو ثماني السطوح، اما معقدات ((Zn(II) Cd(II) و(Cu(II مع ليكاندات (HL^1-HL^6) فالتناسق المحتمل كان رباعي التناسق والمربع المستوي على التوالي.

تم اختبار الفعالية البايلوجية لليكاندات ومعقداتها الفلزية ضد اربعة انواع من البكتريا واربع انواع من الفطريات. شملت دراسة البكتريا:

(*E. coli*, *St. aureus*, *B. stubtilis* and *Klebsiella Pneumoniae*)

اما الفطريات المرضية فكانت:

<div dir="rtl">

الخلاصة

(*Candida albicans*, *Candida glabrata*, *Candida tropicalis* and *Candida parapsilsis*).

وقد بينت النتائج ما يلي:

- اظهرت الليكاندات (HL^1-HL^6) ومعقداتها فعالية بايلوجية ضد *E. coli strains* و strains *Bacillus subtilis*.

- لم تبين معقدات ال Mn(II), Ni(II) and Cu(II) لليكاندات HL^1 و HL^3 اي فعالية اتجاه *Staphylococcus aureus strains* و . *Klebsiella Pneumoniae strains*.

- لم يظهر ليكاند HL^1 اي فعالية ضد *Staphylococcus aureus* and *Klebsiella Pneumoniae strains*. كذلك لم يبين ليكاند HL^3 اي نشاط ضد *Staphylococcus aureus strain*.

- اظهر معقد الزنك مع ليكاند HL^6 ضد *E. coli strains*. مقارنة مع بقية المعقدات.

- لوحظ نشاط بايلوجي عالي لمعقدات الزنك والكادميوم مع ليكاندات (HL^1-HL^6) مقارنة مع بقية المعقدات والسبب يعود للترتيب الالكتروني لها (d^{10}) .

- اظهرت جميع الليكاندات (HL^1-HL^6) ومعقداتها فعالية ضد *Candida glabrata*.

- لم تظهر ليكاندات (HL^1-HL^5) اي فعالية ضد *Candida parapsilsis* .

- لم تظهر معقدات الليكاند HL^1 فعالية ضد *Candida parapsilsis*.

- لم تبين ليكاندات (HL^1-HL^3) ومعقدات Ni(II), Cd(II) لليكاند HL^1 ومعقد الكادميوم لليكاند HL^4 اي فعالية ضد *Candida albicans*.

- بالنسبة للمركبات التي فحصت ضد *Candida tropicalis* كانت النتائج كما يلي:

  أ- لم تظهر معقدات النيكل والكادميوم مع ليكاند HL^1 اي فعالية بايلوجية.

  ب- لم تسجل الليكاندين HL^2 و HL^3 اي فعالية بايلوجية.

  ت- لم يلاحظ اي نشاط لمعقد النيكل مع ليكاند HL^4.

  ث- اظهرت ليكاندات HL^5 و HL^6 ومعقداتهما نشاط بايلوجي عالي مقارنة مع باقي المركبات.

</div>

<div dir="rtl" align="center">

ث

</div>

المعقدات الفلزية المشتقة من ليكاندات ثنائية السن (N,Se)؛ تحضير، التشخيص الطيفي والفعالية البايلوجية

اطروحة مقدمة إلى

مجلس كلية التربية للعلوم الصرفة – ابن الهيثم – جامعة بغداد

وهي جزء من متطلبات نيل درجة الدكتوراة فلسفة في علوم الكيمياء

من قبل

طالب حامد موات

بكالوريوس علوم كيمياء (2013)

ماجستير علوم كيمياء (2016)

كلية التربية للعلوم الصرفة – ابن الهيثم – جامعة بغداد

بإشراف

أ. د. محمد جابر الجبوري